

CHARACTERIZATION OF CARBON FIBER-EPOXY COMPOSITE MATERIALS

by
Neha Shakelly

A Thesis

*Submitted to the Faculty of Purdue University
In Partial Fulfillment of the Requirements for the degree of*

Master of Science in Aeronautics and Astronautics



School of Aeronautics and Astronautics

West Lafayette, Indiana

May 2020

THE PURDUE UNIVERSITY GRADUATE SCHOOL
STATEMENT OF COMMITTEE APPROVAL

Dr. R. Byron Pipes, Chair

School of Aeronautics and Astronautics

Dr. Tyler N. Tallman

School of Aeronautics and Astronautics

Dr. Wenbin Yu

School of Aeronautics and Astronautics

Approved by:

Dr. Gregory A. Blaisdell

Associate Head for the Gambaro Graduate Program of Aeronautics and Astronautics

ACKNOWLEDGMENTS

Firstly, I would like to thank my advisor, mentor, Dr. R. Byron Pipes, for giving me the opportunity to work with him and giving me access to all the resources at his facility. His vision guided, motivated and taught me the right path to start and conduct research.

My sincere thanks go to Dr. Sergii G. Kravchenko for guiding me every time I had any problems and for helping me learn how to be a better researcher.

I thank all my fellow group mates and friends, especially, Akshay Jacob Thomas, Sushrut Karmarkar and Xin Liu for helping me build up and widen my knowledge by having a lot of stimulating discussions with me. I would also like to thank Garam Kim for training and helping me to make the test specimen for all the experiments.

I dedicate all my achievements to my parents and my brother for being a constant source of support for me as I could have never advanced anywhere if not for their unconditional love.

TABLE OF CONTENTS

TABLE OF CONTENTS.....	4
LIST OF TABLES.....	11
LIST OF FIGURES	13
ABSTRACT.....	22
1. INTRODUCTION	23
1.1 Test Specimen Fabrication for physical testing.....	23
1.1.1 Description of composites and its basic constituents.....	24
1.1.2 Fabrication process and possible sources of error	24
1.2 Micromechanical Analysis of Fiber and Matrix properties	25
1.2.1 Representative Volume Element (RVE) Analysis.....	27
1.2.2 Voigt and Reuss Rules of Mixtures	29
1.2.3 SwiftComp Results	30
1.3 References.....	31
1.4 Appendix.....	33
1.4.1 AS4C Fiber Data Sheet:.....	34
1.4.2 F155 matrix Data Sheet:	35
1.4.3 Images.....	39
2. MODELING OF SPECIMEN FOR TENSILE TEST.....	41
2.1 Introduction.....	41
2.1.1 Tensile test of a material	41
2.1.2 Modeling in Abaqus.....	41
2.1.3 Constitutive relations	42
2.1.3.1 Young's Modulus.....	42
2.1.3.2 Ultimate Tensile Stress.....	43
2.1.3.3 Poisson's Ratio.....	43
2.2 Overview of the experimental procedure.....	43
2.2.1 Testing of the specimen in MTS	43
2.2.2 Digital Image Correlation	45
2.3 Micromechanical Analysis.....	45

2.4	Comparison of experimental and simulation results.....	49
2.5	Specimen geometry and material properties.....	54
2.5.1	Material Properties.....	55
2.5.2	Orientation of plies in the laminate.....	56
2.6	Mesh Parameters and convergence studies.....	56
2.7	Boundary and Load conditions.....	60
2.8	Step Outputs.....	60
2.9	References.....	61
2.10	Appendix.....	62
2.10.1	Arc-Resistant GP03 Fibre Glass sheet Data Sheet:	62
2.10.2	Poisson's Ratio data:.....	63
2.10.3	Images.....	65
3.	MODELING OF SPECIMEN FOR CTE TEST.....	66
3.1	Introduction.....	66
3.1.1	Coefficient of Thermal Expansion (CTE).....	66
3.1.2	Constitutive relations for thermal expansion.....	67
3.1.3	Residual stresses in composite laminates.....	68
3.1.4	Coefficient of Thermal Expansion for composite laminates.....	69
3.2	Overview of the experimental procedure.....	70
3.2.1	Set-up of the experiment.....	70
3.2.2	Prediction of CTE from cdmHUB data.....	74
3.3	Comparison of cdmHUB results with experimental data.....	75
3.4	Specimen geometry and material properties.....	75
3.5	Mesh Parameters and convergence studies.....	76
3.6	Boundary and Load conditions.....	78
3.7	Step Outputs.....	80
3.8	References.....	81
3.9	Appendix.....	81
4.	OFF AXIS TENSION.....	82
4.1	Introduction.....	82
4.1.1	Analysis of shear strength.....	82

4.1.2	Effect of end-constraints (tabs) on the test specimen	83
4.1.3	Determination of failure in off-axis specimen	84
4.1.3.1	Maximum Stress Failure	84
4.1.3.2	Maximum Strain Failure	85
4.1.3.3	Tsai-Wu Failure.....	85
4.2	Experimental Procedure.....	86
4.3	Processing of experimental results.....	87
4.4	Modeling and analysis of simulation for off-axis test	96
4.4.1	Analysis of simulation results for [15]8, [30]8, [45]8, [60]8, [75]8 laminates ..	96
4.4.1.1	Displacement.....	96
4.4.1.1.1	In-plane deformation	96
4.4.1.1.2	Out-of-plane deformation.....	98
4.4.1.1.3	Axial deformation	103
4.4.1.2	Stress	108
4.4.1.2.1	Axial Stress	108
4.4.1.2.2	Transverse Stress.....	115
4.4.1.2.3	Normal Stress	120
4.4.1.2.4	In-plane Shear Stress.....	125
4.4.1.3	Strain	131
4.4.1.3.1	Axial Strain	131
4.4.1.3.2	Transverse Strain.....	135
4.4.1.3.3	In-plane Shear Strain.....	140
4.5	Conclusions.....	145
4.6	References.....	146
4.7	Appendix.....	147
4.7.1	Images	147
5.	LAMINATE TENSION	148
5.1	Introduction.....	148
5.1.1	Global and Local coordinate systems	148
5.1.2	Obtaining elastic constants from the stiffness matrix using Classical Laminate Plate Theory (CLPT)	150

5.2	Experimental Procedure.....	154
5.3	Processing of experimental results.....	156
5.3.1	Stress-Strain plots of the laminates.....	158
5.3.2	Transverse Strain-Longitudinal Strain plots for the laminates	160
5.3.3	Homogenization of elastic constants for the laminates.....	162
5.3.4	Comparison of theoretical and experimental data	166
5.4	Modeling and analysis of simulation	167
5.4.1	Analysis of simulation results.....	168
5.4.1.1	[02 / ±45]s Laminate.....	168
5.4.1.2	[0 / ±45 /90]s Laminate.....	172
5.4.1.3	[±30] 2s Laminate	176
5.4.1.4	[902 / ±45]s Laminate	180
5.5	Comparison between theoretical and simulation results.....	184
5.5.1	Theoretical variation of stress through the thickness of the laminate.....	184
5.5.2	Variation of stress through the thickness of the laminate from the simulation	187
5.6	Conclusions.....	189
5.7	References.....	190
6.	OPEN HOLE TENSION AND CTE ANALYSIS	191
6.1	Introduction.....	191
6.1.1	Finite and Infinite width specimen	191
6.1.2	Point Stress Criteria (PSC).....	193
6.1.3	Average Stress Criteria (ASC).....	194
6.1.4	Modified Point Stress Criteria (MPSC)	196
6.1.5	CTE for [±30] 2s laminate from CLPT	197
6.2	Experimental Procedure for tensile test	198
6.3	Experimental procedure for CTE test	199
6.4	Processing of experimental results for tensile test.....	199
6.4.1	[02 / ±45]s	199
6.4.2	[±30]2s	205
6.4.3	[0/±45/90]s	211
6.5	Modeling the geometry for simulations.....	221

6.5.1	Geometry, Load, and Boundary conditions	221
6.5.2	Mesh.....	221
6.6	Analysis of simulation results for tensile test	225
6.6.1	Distribution of stress on laminates.....	225
6.6.1.1	[02 / ±45]s	225
6.6.1.2	[±30]2s	231
6.6.2	[0/±45/90]s.....	237
6.6.3	Variation of stress across the width of the specimen from the hole	242
6.6.4	Strain distribution around the hole.....	244
6.6.4.1	[02 / ±45]s.....	244
6.6.4.2	[±30]2s	247
6.6.5	[0/±45/90]s.....	250
6.7	Analysis of simulation results for [±30]2s CTE test	253
6.7.1	Deformation along X-axis.....	254
6.7.2	Deformation along Y-axis.....	257
6.7.3	Stress in X-direction	261
6.7.4	Effect of negative CTE on the deformation of the hole during heating.....	267
6.8	Conclusions.....	269
6.9	References.....	270
7.	FREE EDGE EFFECTS	271
7.1	Introduction.....	271
7.1.1	Stress distributions at the free edge	271
7.1.2	Axial displacement and interlaminar shear strain across the thickness	272
7.1.3	Variation of stresses across the width.....	274
7.2	Experimental Procedure.....	278
7.3	Processing of experimental results.....	279
7.3.1	[±30] 2s laminate	280
7.3.2	[±302] 2s laminate.....	281
7.3.3	[±30/902] s laminate	283
7.3.4	[±302/904] s laminate	284
7.4	Modeling of geometry for simulations	286

7.4.1	Mesh.....	286
7.5	Analysis of simulation results and comparison with theoretical results	287
7.5.1	[± 30] 2s laminate	288
7.5.1.1	Axial displacement across thickness at the free edge	288
7.5.1.2	Stresses across thickness at the free edge.....	291
7.5.1.2.1	Variation of normal and transverse stresses through thickness.....	296
7.5.1.3	Stresses across width.....	300
7.5.1.4	Stresses across thickness at the laminate center.....	304
7.5.1.5	Axial displacement across the width.....	307
7.5.2	[$\pm 30/902$] s laminate	309
7.5.2.1	Axial displacement across thickness at the free edge	309
7.5.2.2	Stresses across thickness at the free edge.....	312
7.5.2.2.1	Variation of normal and transverse stresses through thickness.....	317
7.5.2.3	Stresses across width.....	321
7.5.2.4	Stresses across thickness at the laminate center.....	325
7.5.2.5	Axial displacement across the width.....	328
7.6	Conclusions.....	330
7.7	References.....	332
8.	MODE I- INTERLAMINAR FRACTURE.....	333
8.1	Introduction.....	333
8.1.1	Common failure modes in a composite laminate.....	333
8.1.2	Compliance and strain energy release rate for interlaminar fracture	334
8.1.3	Load and displacement control for DCB specimen	337
8.1.4	Calculation of strain energy release rate	338
8.1.4.1	Simple Beam Theory.....	338
8.1.4.2	Modified Beam Theory	338
8.1.4.3	Compliance Calibration Method	339
8.1.4.4	Modified Compliance Calibration Method	340
8.2	Experimental Procedure.....	340
8.3	Processing of experimental results.....	342
8.3.1	Data reduction from Modified Beam Theory	342

8.3.2	Data reduction from Compliance Calibration	343
8.3.3	Data reduction from Modified Compliance Calibration	344
8.3.4	Force-displacement plots for the tested samples	344
8.3.5	GIC calculated from different methods and propagation of the crack.....	346
8.4	Modeling of geometry for simulation	349
8.5	Boundary conditions and Interactions	351
8.5.1	Boundary conditions	351
8.5.2	Interaction properties to model cohesion	352
8.6	Mesh parameters and convergence studies	354
8.6.1	Convergence studies	355
8.7	Step Outputs.....	356
8.8	Analysis of simulation results	356
8.8.1	Force-displacement curve	356
8.8.2	Compliance and Strain energy release rate calculations	359
8.9	Conclusions.....	363
8.10	References	364
9.	FUTURE WORK.....	365
9.1	Failure Analysis	365

LIST OF TABLES

Table 2.1: Sample-wise data for [0]8	50
Table 2.2: Statistical averages of properties of [0]8.....	50
Table 2.3: Sample-wise data for [90]8.....	51
Table 2.4: Statistical averages of properties of [90]8	51
Table 2.5: Sample-wise data for [90]16.....	52
Table 2.6: Statistical averages of properties of [90]16	52
Table 2.7: Summary of material properties	53
Table 2.8: Comparison of experimental, simulation data with material datasheet.....	53
Table 2.9: Elastic constants from simulation and experiments.....	54
Table 2.10: Mesh convergence study data for tensile test specimen	59
Table 3.1: Comparison of CTE data for $[\pm 30]_2s$	75
Table 3.2: Mesh convergence study data for CTE specimen.....	78
Table 4.1: Off-axis sample dimensions	88
Table 4.2: Failure angles of the off-axis specimens	89
Table 4.3: Off-Axis tensile properties	90
Table 5.1: Dimensions of the test samples.....	155
Table 5.2: Comparison of modulus data	167
Table 5.3: Comparison of Poisson's ratio data	167
Table 6.1: Comparison of strength data of notched and un-notched laminates.....	220
Table 6.2: Parameters a_0 and d_0 for the laminates with all the hole sizes	220
Table 6.3: Deformation of holes in the cooling cycle.....	269
Table 6.4: Deformation of holes in the heating cycle	269
Table 7.1: Average and standard deviation values of sample dimensions	280
Table 7.2: Summary of the results	331
Table 8.1: DCB Specimen Dimensions	341
Table 8.2: Results from MBT method	348
Table 8.3: Results from CC Method.....	348
Table 8.4: Results from MCC method.....	349

Table 8.5: Mesh convergence study data for DCB specimen	355
Table 8.6: Experimental Compliance data.....	359
Table 8.7: Simulation Compliance data.....	360
Table 8.8: Experimental Strain energy release rate (KJ/m ²) data.....	362
Table 8.9: Simulation Strain energy release rate (KJ/m ²) data.....	362
Table 8.10: Percentage error of strain energy release rate using different methods.....	363
Table 9.1: Hashin Damage parameters	366
Table 9.2: Damage Evolution parameters.....	366
Table 9.3: Damage Stabilization parameters	366

LIST OF FIGURES

Figure 1.1: Analysis of plate-like structures approximated over an SG	26
Figure 1.2: Composite models	26
Figure 1.3: Flowchart of the Mechanics of Structure Genome.....	27
Figure 1.4: Representative Volume Element	28
Figure 1.5: Bound on modulus with ROM	29
Figure 1.6: Mesh of hexagonal micromechanics model (left), Homogenization parameters (Right)	30
Figure 1.7: Different reinforcement systems	39
Figure 1.8: Manufacturing of a composite laminate.....	39
Figure 1.9: Trend of variation in material properties.....	40
Figure 2.1: ASTM D3039/D3039M test fixture	44
Figure 2.2: Tensile test specimen geometries	44
Figure 2.3: Simulation images from SwiftComp.....	46
Figure 2.4: SwiftComp simulation results	47
Figure 2.5: Geometry of the tensile coupons, One-inch width (Left), Half-inch width (Right)...	55
Figure 2.6: Mesh on the tensile test part geometries	57
Figure 2.7: Mesh convergence study plots for tensile test specimen.....	59
Figure 2.8: Load and Boundary Conditions on the tensile coupon.....	60
Figure 2.9: Mechanical behavior of composites	65
Figure 2.10: Stress-strain curve for matrix and fibers	65
Figure 3.1: Potential Energy Vs interatomic distance	66
Figure 3.2: Different types of cross-linking in polymers.....	66
Figure 3.3: Variation of the physical property with temperature.....	67
Figure 3.4: Unconstrained and constrained expansion in unidirectional and cross-ply laminates	69

Figure 3.5: Speckled specimen before analysis	71
Figure 3.6: Set-up of the specimen in the apparatus	72
Figure 3.7: Apparatus.....	73
Figure 3.8: DIC analysis of the sample with two different regions of interest	73
Figure 3.9: X and Y deformation on the sample with a hole diameter 3.683 mm for cooling (left) and heating (right) cycles respectively with a maximum temperature of 100oC	74
Figure 3.10: Laminate properties from cdmHUB for $[\pm 30]_2s$	75
Figure 3.11: Geometry of the CTE specimen, 1/8-inch hole diameter (Left), 1/4-inch hole diameter (Right)	76
Figure 3.12: Mesh on the CTE part geometries	77
Figure 3.13: Mesh convergence study plots for CTE specimen	78
Figure 3.14: Boundary conditions on CTE specimen	79
Figure 3.15: Load and Boundary Conditions on the tensile coupon.....	80
Figure 3.16: Pushrod dilatometer.....	81
Figure 4.1: DIC Set-up.....	87
Figure 4.2: Failure angles of specimens	89
Figure 4.3: Stress Vs Strain curves for off-axis specimens	90
Figure 4.4: Shear modulus Vs Angle	91
Figure 4.5: Axial Modulus Vs Angle.....	92
Figure 4.6: Tensile failure strength Vs Angle.....	92
Figure 4.7: Poisson's ratio Vs Angle.....	93
Figure 4.8: Axial modulus vs off-axis angle.....	94
Figure 4.9: Failure stress Vs Angle.....	95
Figure 4.10: DIC image with the transverse displacement of the specimen.....	95
Figure 4.11: In-plane deformation (U3) of the off-axis specimen.....	97
Figure 4.12: Out-of-plane deformation (U2) of the off-axis specimen	99

Figure 4.13: Axial deformation (U_1) of the off-axis specimen	104
Figure 4.14: Axial stress (σ_{11}) on the off-axis specimen	110
Figure 4.15: Transverse stress (σ_{22}) on the off-axis specimen.....	116
Figure 4.16: Normal stress (σ_{33}) on the off-axis specimen	121
Figure 4.17: In-plane shear stress (σ_{12}) on the off-axis specimen	126
Figure 4.18: Axial strain (ϵ_{11}) on the off-axis specimen.....	131
Figure 4.19: Transverse strain (ϵ_{22}) on the off-axis specimen	136
Figure 4.20: In-plane shear strain (ϵ_{12}) on the off-axis specimen.....	141
Figure 4.21: Off-axis coupon without and with constraints	147
Figure 4.22: Failure envelope for a typical anisotropic material	147
Figure 5.1: Local and global coordinate systems.....	148
Figure 5.2: In-plane forces and moments	149
Figure 5.3: In-plane forces and moments per unit length	150
Figure 5.4: Laminate stacking across the thickness.....	152
Figure 5.5: Laminate tension samples	154
Figure 5.6: Speckled samples for DIC analysis	155
Figure 5.7: Load cell and DIC set-up for the experiment	156
Figure 5.8: Fractured specimens	157
Figure 5.9: Stress-Strain plots for the laminates.....	159
Figure 5.10: Transverse strain Vs Longitudinal strain for the laminates.....	161
Figure 5.11: Analytical results for $[0_2 / \pm 45]_s$	163
Figure 5.12: Analytical results for $[0 / \pm 45 / 90]_s$	164
Figure 5.13: Analytical results for $[\pm 30]_2$	165
Figure 5.14: Analytical results for $[90_2 / \pm 45]_s$	166
Figure 5.15: Variation of stresses for $[0_2 / \pm 45]_s$ laminate.....	169

Figure 5.16: Variation of stresses for $[0 / \pm 45 / 90]_s$ laminate.....	173
Figure 5.17: Variation of stresses for $[\pm 30]_2s$ laminate.....	177
Figure 5.18: Variation of stresses for $[90_2 / \pm 45]_s$ laminate	181
Figure 5.19: Stress Vs thickness plots from CLPT.....	185
Figure 5.20: Stress Vs thickness plots from Simulations	188
Figure 6.1: Finite plate.....	192
Figure 6.2: Normal stress distribution for quasi-isotropic laminates with 2 hole sizes.....	193
Figure 6.3: Experimental data on predicted values from PSC.....	194
Figure 6.4: Graphical representation of PSC	194
Figure 6.5: Experimental data on predicted values from ASC	195
Figure 6.6: Graphical representation of ASC	195
Figure 6.7: Experimental data on predicted values from MPSC	196
Figure 6.8: Curve fit to calculate parameters in MPSC	197
Figure 6.9: Elastic constants and CTE values of $[\pm 30]_2s$ laminate	197
Figure 6.10: Specimen tested with DIC.....	198
Figure 6.11: Experimental Set-up.....	198
Figure 6.12: Strength distribution for $[0_2 / \pm 45]_s$ laminate	199
Figure 6.13: Stress distribution as a function of hole size for $[0_2 / \pm 45]_s$ laminate	201
Figure 6.14: Failed specimen for $[0_2 / \pm 45]_s$ laminate	203
Figure 6.15: Delamination observed in $[0_2 / \pm 45]_s$ laminate.....	204
Figure 6.16: Strain distribution around the big hole of $[0_2 / \pm 45]_s$ laminate.....	204
Figure 6.17: Force-displacement curve for $[0_2 / \pm 45]_s$ laminate with smallest hole.....	205
Figure 6.18: Strength distribution for $[\pm 30]_2s$ laminate	206
Figure 6.19: Stress distribution as a function of hole size for $[\pm 30]_2s$ laminate	208
Figure 6.20: Failed specimen for $[\pm 30]_2s$ laminate	210

Figure 6.21: Strain distribution around the big hole of $[\pm 30]_2s$ laminate	211
Figure 6.22: Stress-Strain curve for $[\pm 30]_2s$ laminate with the largest hole.....	211
Figure 6.23: Strength distribution for $[0 / \pm 45 / 90]_s$ laminate	212
Figure 6.24: Stress distribution as a function of hole size for $[0 / \pm 45 / 90]_s$ laminate	214
Figure 6.25: Failed specimen for $[0 / \pm 45 / 90]_s$ laminate	216
Figure 6.26: Strain distribution around the big hole of $[0 / \pm 45 / 90]_s$ laminate.....	217
Figure 6.27: Comparison of strain data around the hole in $[0 / \pm 45 / 90]_s$ laminate with hole size increasing from left to right	218
Figure 6.28: Force displacement curve for $[0 / \pm 45 / 90]_s$ laminate	218
Figure 6.29: Mesh on open-hole tensile test specimen	222
Figure 6.30: Variation of axial stress σ_{11} on the $[02 / \pm 45]_s$ laminate with a hole of diameter 3.683 mm	225
Figure 6.31: Variation of axial stress σ_{11} on the $[02 / \pm 45]_s$ laminate with a hole of diameter 5.715 mm	227
Figure 6.32: Variation of axial stress σ_{11} on the $[02 / \pm 45]_s$ laminate with a hole of diameter 6.604 mm	229
Figure 6.33: Variation of axial stress σ_{11} on the $[\pm 30]_2s$ laminate with a hole of diameter 3.683 mm	231
Figure 6.34: Variation of axial stress σ_{11} on the $[\pm 30]_2s$ laminate with a hole of diameter 5.715 mm	233
Figure 6.35: Variation of axial stress σ_{11} on the $[\pm 30]_2s$ laminate with a hole of diameter 6.604 mm	235
Figure 6.36: Variation of axial stress σ_{11} on the $[0 / \pm 45 / 90]_s$ laminate with a hole of diameter 3.683 mm	237
Figure 6.37: Variation of axial stress σ_{11} on the $[0 / \pm 45 / 90]_s$ laminate with a hole of diameter 5.715 mm	239
Figure 6.38: Variation of axial stress σ_{11} on the $[0 / \pm 45 / 90]_s$ laminate with a hole of diameter 6.604 mm	241
Figure 6.39: Normalized variation of axial stress σ_{11} across the width of the specimen with three different hole sizes	243

Figure 6.40: Variation of axial strain ϵ_{11} on the $[02 / \pm 45]_s$ laminate for three different hole sizes	245
Figure 6.41: Variation of axial strain ϵ_{11} on the $[\pm 30]_2s$ laminate for three different hole sizes	248
Figure 6.42: Variation of axial strain ϵ_{11} on the $[0 / \pm 45 / 90]_s$ laminate for three different hole sizes	251
Figure 6.43: Deformation along X-axis U_1 due to temperature change on the $[\pm 30]_2s$ laminate for two different hole sizes	254
Figure 6.44: Deformation along Y-axis U_2 due to temperature change on the $[\pm 30]_2s$ laminate for two different hole sizes	258
Figure 6.45: Variation of stress in X-direction, σ_{11} due to temperature change on the $[\pm 30]_2s$ laminate for two different hole sizes.....	261
Figure 6.46: Effect of temperature change on the $[\pm 30]_2s$ laminate for two different hole sizes	267
Figure 7.1: Stress state at the free edge of the specimen	272
Figure 7.2: Axial displacement across the thickness	273
Figure 7.3: Interlaminar shear strain across the thickness	274
Figure 7.4: Axial displacement across width and thickness of the laminate	276
Figure 7.5: Interlaminar shear stresses through the thickness	277
Figure 7.6: Simplified and Actual shear stress distributions across the width of the sample.....	278
Figure 7.7: Variation of stresses at the interface of $[\pm 45]_s$ laminate	278
Figure 7.8: Experimental Setup	279
Figure 7.9: Load Displacement and stress-strain plot for $[\pm 30]_2s$ laminate	281
Figure 7.10: Load Displacement and stress-strain plots for $[\pm 30]_2s$ laminate	282
Figure 7.11: Delamination failure at the edge of the specimen for $[\pm 30]_2s$ laminate	283
Figure 7.12: Load Displacement and stress-strain plot for $[\pm 30/90]_s$ laminate.....	284
Figure 7.13: Load Displacement and stress-strain plot for $[\pm 30/90]_s$ laminate.....	285
Figure 7.14: Evident delamination at the edges for $[\pm 30/90]_s$ laminate.....	286

Figure 7.15: Mesh on the edges of free-edge coupon with a width of $5t$	287
Figure 7.16: Variation of axial displacement $U1$ across thickness at the free edge of $[\pm 30] 2s$ laminate.....	289
Figure 7.17: Contoured variation of axial displacement $U1$ on the $[\pm 30] 2s$ laminate.....	290
Figure 7.18: Variation of stresses across thickness at the free edge of $[\pm 30] 2s$ laminate	293
Figure 7.19: Contoured variation of stresses on $[\pm 30] 2s$ laminate	294
Figure 7.20: Variation of normal and transverse components of stresses across thickness at the free edge of $[\pm 30] 2s$ laminate.....	297
Figure 7.21: Contour variation of normal and transverse components of stresses across thickness at the free edge of $[\pm 30] 2s$ laminate.....	298
Figure 7.22: Variation of stresses across the width on $[\pm 30] 2s$ laminate	302
Figure 7.23: Contoured variation of stresses across the width and at the edge of $[\pm 30] 2s$ laminate	304
Figure 7.24: Variation of stresses across thickness at the center of $[\pm 30] 2s$ laminate.....	305
Figure 7.25: Contoured variation of stresses at the center of $[\pm 30] 2s$ laminate	306
Figure 7.26: Variation of axial displacement $U1$ across width of $[\pm 30] 2s$ laminate	308
Figure 7.27: Variation of axial displacement $U1$ across thickness at free edge of $[\pm 30/90]_2 s$ laminate.....	310
Figure 7.28: Contoured variation of axial displacement $U1$ on the $[\pm 30/90]_2 s$ laminate	311
Figure 7.29: Variation of stresses across thickness at the free edge of $[\pm 30/90]_2 s$ laminate .	313
Figure 7.30: Contoured variation of stresses on $[\pm 30/90]_2 s$ laminate	314
Figure 7.31: Variation of normal and transverse components of stresses across thickness at the free edge of $[\pm 30/90]_2 s$ laminate	317
Figure 7.32: Contour variation of normal and transverse components of stresses across thickness at the free edge of $[\pm 30/90]_2 s$ laminate	318
Figure 7.33: Variation of stresses across width on $[\pm 30/90]_2 s$ laminate.....	322
Figure 7.34: Contoured variation of stresses across the width and at the edge of $[\pm 30/90]_2 s$ laminate.....	324
Figure 7.35: Variation of stresses across thickness at the center of $[\pm 30/90]_2 s$ laminate	325

Figure 7.36: Contoured variation of stresses at the center of $[\pm 30/90]_s$ laminate	327
Figure 7.37: Variation of axial displacement U_1 across width of $[\pm 30/90]_s$ laminate	329
Figure 8.1: Modes of failure in a composite material	333
Figure 8.2: Fiber bridging	334
Figure 8.3: DCB specimen with hinge loading	335
Figure 8.4: DCB specimen under loading	335
Figure 8.5: Variation of stress from near the notch to the end of the laminate	336
Figure 8.6: MBT with correction factor	339
Figure 8.7: Compliance Calibration	339
Figure 8.8: Modified Compliance Calibration	340
Figure 8.9: DCB specimen with hinges	341
Figure 8.10: Loading of the DCB specimen in the 5-kip load frame	342
Figure 8.11: Data reduction from Modified Beam Theory	343
Figure 8.12: Data reduction from Compliance Calibration	343
Figure 8.13: Data reduction from Modified Compliance Calibration	344
Figure 8.14: Load Vs Displacement curves for the DCB samples	345
Figure 8.15: Comparison of GIC values obtained from different methods	346
Figure 8.16: Propagation of crack across the length of the sample	347
Figure 8.17: Fiber Bridging while testing the DCB samples	347
Figure 8.18: Shearing of hinges during the test	348
Figure 8.19: Parts modeled for DCB analysis	350
Figure 8.20: DCB part assembly	351
Figure 8.21: Boundary conditions on the DCB specimen	352
Figure 8.22: Interactions on the DCB specimen	353
Figure 8.23: Mesh on the DCB part assembly	354

Figure 8.24: Mesh convergence study plots for DCB specimen	356
Figure 8.25: Force-displacement plot for crack propagation on DCB specimen for different simulation parameters	358
Figure 8.26: Force-crack length validation plot for DCB specimen.....	361
Figure 8.27: Compliance-crack length validation plot for DCB specimen	361
Figure 9.1: Hashin failure criterion on $[\pm 30]$ 2s laminate.....	367
Figure 9.2: Axial stress on $[\pm 30]$ 2s laminate	369

ABSTRACT

Characterization of a material is very important to determine its behavior and properties in different load conditions. There are different experimental tests that are used to determine these properties, but, making the samples and conducting the test can be very time and labor-consuming. The main aim of this work is to develop a digital finite element method that can be used to predict the behavior and the distribution of various parameters along with the specimen before or without actually conducting the experiments. This is a part of the process of development of a virtual lab that provides a common platform for learning and integrating different concepts required to characterize composites. The material properties that were given as an input for the simulations were predicted by using a micromechanical analysis of the fiber and matrix properties that were obtained from their respective datasheets and were validated with the experimental results. Hence, this method can be used for the analysis of any kind of material that has basic data available on its datasheets. Five main test methods are discussed in this work, namely, off-axis tension, laminate tension, open hole tension and CTE analysis, free-edge effects and mode I fracture (Double Cantilever Beam) test. The results obtained from the simulation were compared to the analytical and experimental results for validation. Only linear elastic analysis was carried out for all the tensile specimen and the prediction of failure properties is a potential extension of this work.

1. INTRODUCTION

Characterization of material is very crucial to determine its mechanical, microstructural properties. The behavior of the material can be analyzed and it helps the manufacturer to make crucial decisions about the applications of the material. Various failure and process-related problems can be solved by the data obtained by the characterization of the material. The material used was HEXCEL® AS4C-GP 12K / F155 40% RW; 145 AW; 24” unidirectional tape. It has carbon fiber as reinforcement and epoxy resin as the matrix system. Where HEXCEL is the name of the prepreg manufacturing company, F155 is the name of the resin system, AS4C-GP is the name of the fiber reinforcement which has 12K, that is, 12,000 filaments per tow with 145 grams of reinforcement per square meter. 40% RW denotes the weight percentage of the resin in the prepreg and the material has a unidirectional reinforcement type.

The typical process of specimen fabrication and testing is very time, labor and cost consuming. Hence, digital twins were created for each of the characterization experiments in order to directly predict the properties of the material. The results from experiments and simulations were also validated. The modulus for the material was predicted by using a micromechanical analysis of the fiber and matrix properties as obtained from the material datasheets. Hence, these properties can be predicted in a similar manner and the test methods can be generalized for any given material. This would greatly increase the efficiency in the characterization of composite materials.

1.1 Test Specimen Fabrication for physical testing

Test specimen fabrication is one of the most crucial steps in the characterization of the material. A lot of care has to be taken in this process as the results can vary largely when there is any mistake in the fabrication of the test coupons. Even to make a prepreg material, a lot of processing is done in which the fibers are impregnated with the resin material. A combination of these two components forms a composite material. The final property of the composite is hence a combination of the properties of the fiber and matrix. The material used to make the samples is comprised of carbon fibers impregnated with epoxy resin. Enough care should also be taken during the bagging process in order to avoid any vacuum leaks or formation of wrinkles. The plates are

then cured with a prescribed cure cycle and it was observed that the plates with symmetrical orientations did not have any curvature, but the ones with unsymmetrical orientations have a curvature due to the residual stresses caused by the CTE mismatch.

1.1.1 Description of composites and its basic constituents

Composites are materials made from two or more materials which have different chemical and physical properties, but, have different properties from the individual components when combined together. There are many advantages of composite materials. They are lighter and stronger than traditional materials and have a wide range of applications in many different industries. The two main constituents in a composite are matrix and reinforcement. The reinforcement material provides different physical properties that increase the performance of the matrix. Whereas, the matrix helps in binding the reinforcement materials to their relative positions and providing them enough support. There are a wide range and variety of materials from which one can choose any combination to make a composite material. A few of the typical reinforcement systems are shown in Figure 7 (in Appendix).

1.1.2 Fabrication process and possible sources of error

Over the last few decades, the cost of composites has dropped and the applications are increasing at a very fast rate. The usage of composites is still expensive in many industries because of the high-quality material needed.

The typical process of making a laminate from the fiber and the reinforcements is shown in Figure 8 (In Appendix). The fibers are impregnated with the resin to make a prepreg roll. The material is then cut from the prepreg roll into the required size with the required ply orientation and it is then laid up and cured as prescribed by the manufacturer. The laminate is then un-bagged and prepared for the required application.

Hand lay-up is one of the most traditional methods used in the manufacturing of a composite part. It is highly labor-intensive and requires a lot of preparation in advance. The material has to be taken out of the freezer and has to be let to thaw to room temperature. But, care should be taken that the condensed water droplets do not enter into the material. The presence of water droplets on

the material can lead to a lot of problems while curing the part. While laying the plies on top of one another, a lot of care has to be taken while removing the bagging on the material. It has to be removed along the fiber direction so that the fibers do not get ripped apart.

The bagging process is also very important and enough care has to be taken that there is no leak in the bag. This process can get really complicated while manufacturing complex parts. There should not be any wrinkles on the lay-up as there is a high chance that it gets transferred onto the part. Enough pressure should also be given as it is needed for the ply layers to adhere to each other. This data is usually given by the manufacturer itself and it depends on the fiber and matrix that is used to make the material.

The ply orientation also plays a crucial role in the final part. Some of the plates that were manufactured had a curvature as they had an unsymmetrical lay-up. This is because of the residual stresses caused as a result of the CTE mismatch between the different layers in the laminate plate. This degree of curvature can usually be quantified by using the extension-bending coupling stiffness matrix for the given ply orientations. Hence, while formulating a ply sequence, care should be taken that the plies are symmetric and balanced. In this way, there is a consistency in the final part that we get and there will not be any presence of unanticipated curvatures in it.

1.2 Micromechanical Analysis of Fiber and Matrix properties

Composites are usually highly anisotropic and it is usually very difficult to conduct detailed simulations at the macroscopic level as it is very computationally expensive to consider all the factors that affect the performance of a composite. Micromechanics is the study of the composite material by understanding the interaction between constituent materials on a microscopic scale. This helps in computing the material properties and failure mechanisms of composite materials. The main goal of micromechanics is to predict the anisotropic response of the heterogeneous material on the basis of the geometries and properties of the individual phases. A good micromechanical model does not require high computing power. The composites can be modeled based on various different dimensions of the structural genome where a simpler model is made to

approximate the structure. Figure 1 shows the different approximations that can be used in order to analyze plate-like structures.

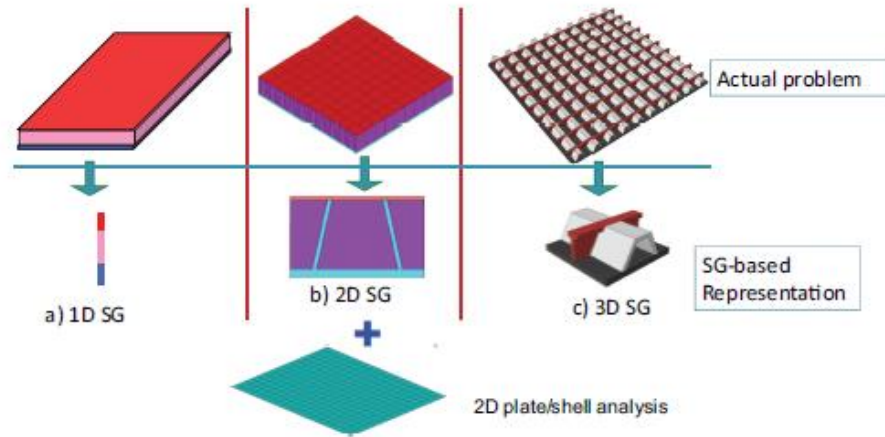


Figure 1.1: Analysis of plate-like structures approximated over an SG
(Image from Multiscale Structural Mechanics (2017))

Figure 2 shows the transition between micromechanical studies to the laminate theory. There is an entire process involved in analyzing the properties of a composite by using the Mechanics of Structure Genome. The flowchart that describes this process is shown in Figure 3. The constitutive modeling over the structural genome was done using SwiftComp in order to get an approximation of the elastic constants.

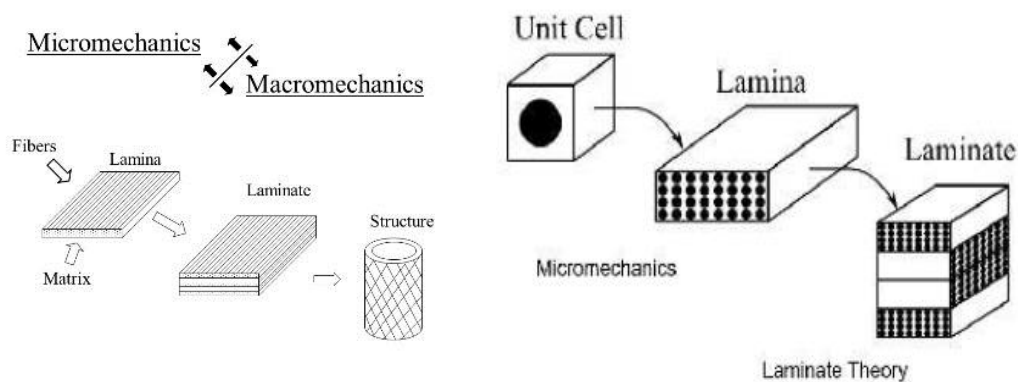


Figure 1.2: Composite models
(Image from Multiscale Structural Mechanics (2017))

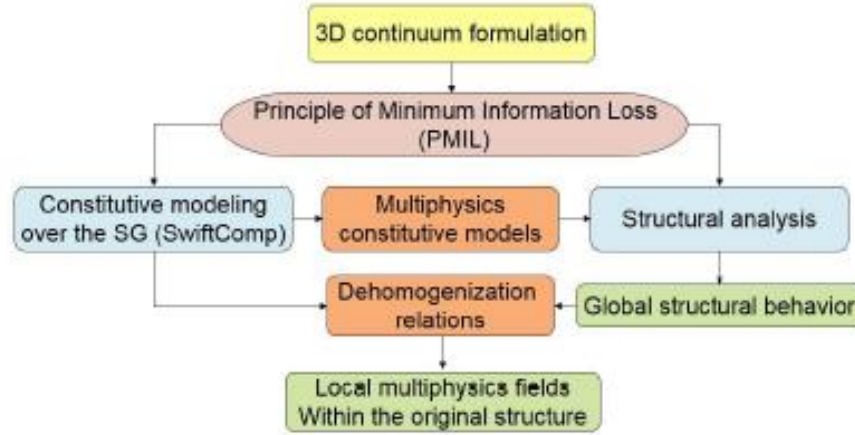


Figure 1.3: Flowchart of the Mechanics of Structure Genome
(Image from Multiscale Structural Mechanics (2017))

1.2.1 Representative Volume Element (RVE) Analysis

The ply properties can be evaluated from the known properties of composite constituents (fiber and matrix phases). The microstructure of physical material is complex and uniform. There are different methods that can be used to determine the properties of the composite plate. The upper and lower bounds for the elastic properties are determined by the Voigt and Reuss rules of mixtures. A Representative Volume Element (RVE) method can also be used in order to get more close approximations of these values. An RVE is an elementary repetitive element that is present in the structure. Usually, this element can be used to determine the properties of the entire structure. There are different types of RVEs as shown in Figure 4. The common ones that are used are square array and hexagonal array.

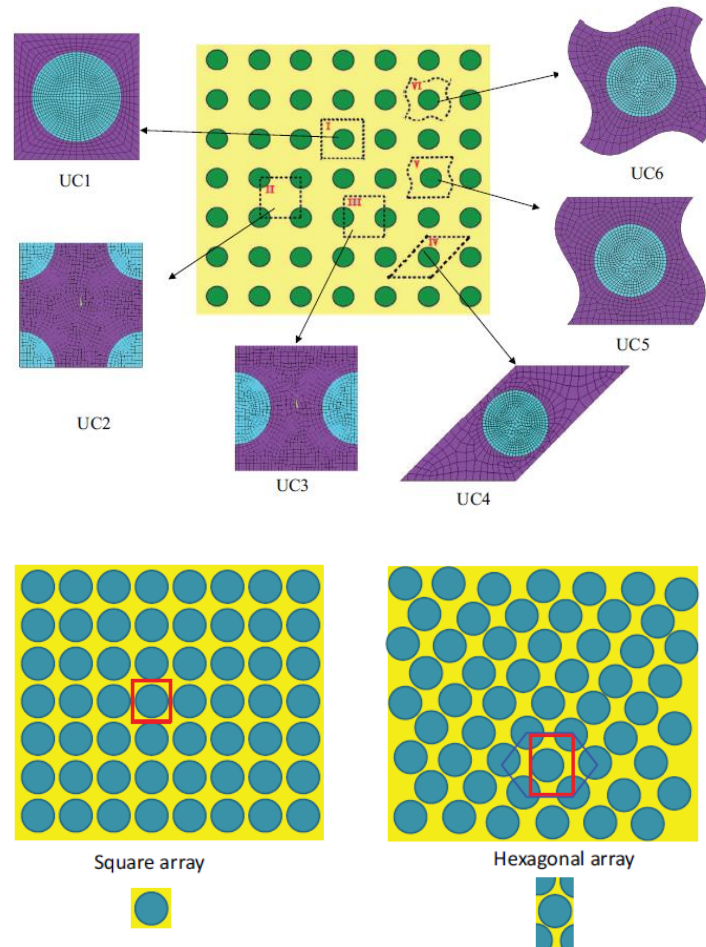


Figure 1.4: Representative Volume Element
(Image from Multiscale Structural Mechanics (2017))

A hexagonal unit cell is still a better representation as all its six neighbors are identical and the distance between the centroids is the same for all of the neighbors. For a square array, there are two kinds of neighbors. One where the neighbors have a common edge and another set of neighbors where they have a common edge. They form a better fit for curved surfaces and have reduced edge effects. They also have the lowest perimeter to area ratio of any regular tessellation of the plane. The arrangement also minimizes the amount of material used to create a lattice of cells with a given volume.

1.2.2 Voigt and Reuss Rules of Mixtures

To get an upper and lower bound of the properties, general rules of mixtures are used. The Voigt model is used for axial loading and the Reuss model is used for transverse loading. The stiffness calculated by the Voigt ROM is the upper limit and Reuss ROM is the lower limit for composite stiffness. This plot is shown in Figure 5.

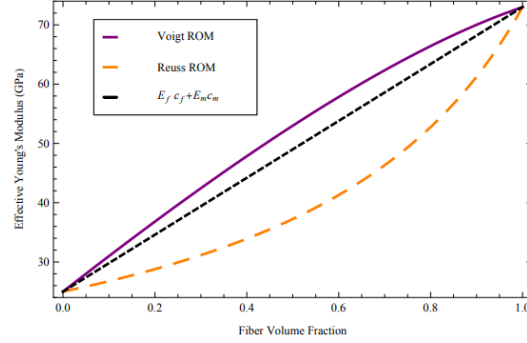


Figure 1.5: Bound on modulus with ROM
(Image from Multiscale Structural Mechanics (2017))

The Voigt ROM assumes that the strain field within the RVE is constant, that is, $\varepsilon_{ij} = \bar{\varepsilon}_{ij}$. It assumes that the fiber and matrix act as springs in parallel and is appropriate for properties dominated by fibers. The effective stiffness is the volume average of the stiffness of the constituents.

$$\bar{\sigma}_{ij} = \langle \sigma_{ij} \rangle$$

$$C_{ijkl}^{V*} = \langle C_{ijkl} \rangle$$

The Reuss ROM assumes that the stress field within the RVE is constant, that is, $\sigma_{ij} = \bar{\sigma}_{ij}$. It assumes that the fiber and matrix act as springs in series and is appropriate for properties dominated by matrix. Effective compliance is the volume average of the compliance of the constituents.

$$\bar{\varepsilon}_{ij} = \langle \varepsilon_{ij} \rangle$$

$$S_{ijkl}^{R*} = \langle S_{ijkl} \rangle = \langle C_{ijkl}^{-1} \rangle$$

It can be observed that the elastic properties can be extracted from the compliance matrix. The modulus of elasticity usually reduces with the decrease in the fiber volume fraction of the sample. The trend of the variation in the material properties is shown in Figure 9 (In Appendix).

1.2.3 SwiftComp Results

The micromechanical analysis was done on the material by using a 2D Structural Genome with a hexagonal unit cell in order to get the approximate values of the material properties of the composite. The material properties of the fiber and the matrix were found from their respective data sheets (Given in Appendix). The carbon tape that was used in this resin system weighs 145 grams/ m² and hence the corresponding material properties are used. A few properties were taken from similar materials with the same fiber volume fractions. Figure 6 shows the mesh of this structure with an unstructured mesh of an element size factor of 0.01.

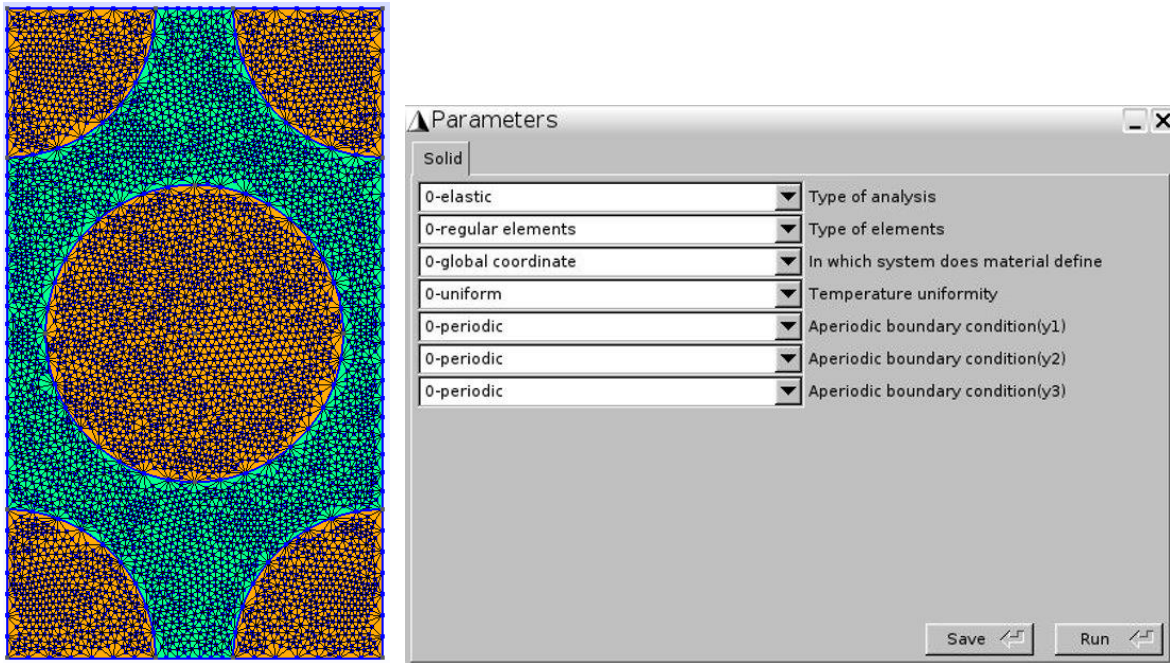


Figure 1.6: Mesh of hexagonal micromechanics model (left), Homogenization parameters (Right)

This model was homogenized to be a solid element for the analysis and the stiffness and the compliance matrices were obtained and the elastic constants of the composite material were hence deduced from these matrices as follows:

The Effective Stiffness Matrix

1.3739533E+11	7.5946262E+09	7.5946303E+09	2.8212529E+03	0.0000000E+00	0.0000000E+00
7.5946262E+09	1.4137955E+10	9.0471836E+09	1.9126601E+04	0.0000000E+00	0.0000000E+00
7.5946303E+09	9.0471836E+09	1.4137972E+10	-8.0798684E+03	0.0000000E+00	0.0000000E+00
2.8212529E+03	1.9126601E+04	-8.0798684E+03	2.5454251E+09	0.0000000E+00	0.0000000E+00
0.0000000E+00	0.0000000E+00	0.0000000E+00	0.0000000E+00	3.9901516E+09	3.7556265E+04
0.0000000E+00	0.0000000E+00	0.0000000E+00	0.0000000E+00	3.7556265E+04	3.9900636E+09

The Effective Compliance Matrix

7.5517365E-12	-2.4736807E-12	-2.4736790E-12	2.3653203E-18	0.0000000E+00	0.0000000E+00
-2.4736807E-12	1.2059267E-10	-7.5840957E-11	-1.1441444E-15	0.0000000E+00	0.0000000E+00
-2.4736790E-12	-7.5840957E-11	1.2059253E-10	9.5541228E-16	0.0000000E+00	0.0000000E+00
2.3653203E-18	-1.1441444E-15	9.5541228E-16	3.9286169E-10	0.0000000E+00	0.0000000E+00
0.0000000E+00	0.0000000E+00	0.0000000E+00	0.0000000E+00	2.5061704E-10	-2.3589198E-15
0.0000000E+00	0.0000000E+00	0.0000000E+00	0.0000000E+00	-2.3589198E-15	2.5062257E-10

The Engineering Constants (Approximated as Orthotropic)

E1	=	1.3241987E+11
E2	=	8.2923783E+09
E3	=	8.2923878E+09
G12	=	3.9900636E+09
G13	=	3.9901516E+09
G23	=	2.5454251E+09
nu12	=	3.2756449E-01
nu13	=	3.2756426E-01
nu23	=	6.2890190E-01

1.3 References

- [1] “The Design of Composite Materials and Structures.” [Online]. Available: <http://www.mse.mtu.edu/~drjohn/my4150/compositesdesign/cd1/cd2.html>. [Accessed: 03-Sep-2019].
- [2] Carlsson, L. A., Adams, D. F., & Pipes, R. B. (2014). Experimental characterization of advanced composite materials. Boca Raton, FL: CRC Press.
- [3] Dr. Wenbin Yu. (2017) Multiscale Structural Mechanics. Wiley-Interscience. John Wiley & Sons, INC., Publication
- [4] Bay, R. S., & Tucker, C. L. (1992). Stereological measurement and error estimates for three-dimensional fiber orientation. Polymer Engineering and Science, 32(4), 240–253. DOI: 10.1002/pen.760320404
- [5] Sharma, B. N., Naragani, D., Nguyen, B. N., Tucker, C. L., & Sangid, M. D. (2017). Uncertainty quantification of fiber orientation distribution measurements for long-fiber-reinforced thermoplastic composites. Journal of Composite Materials, 52(13), 1781–1797. DOI: 10.1177/0021998317733533

- [6] Dr. Ben Denos, 26th August 2019, Monday, Microscopy and Inspection Lecture, Presentation. PPT. (2019)
- [7] Akshay, Swapneel, Hayden 30th August 2019, Friday, Lab 2- Microscopy, Presentation. PPT. (2019)
- [8] Neha Shakelly, 26th August 2019, Wednesday, Micromechanical Analysis for Elastic Constants. PPT. (2019)
- [9] Dr. Byron Pipes, 19th August 2019, Monday, Introduction, Presentation. PPT. (2019).
- [10] Garam Kim, 23rd August 2019, Friday, Lab 1- Autoclave Curing, Presentation. PPT. (2019).
- [11] Claire Specty. 30th August 2017, Laboratory Report 1, Test Specimen Fabrication
- [12] https://www.heatcon.com/wp-content/uploads/2017/09/HCS2403-015_Hexcel-F155-71-TDS_Prepeg.pdf

1.4 Appendix

Physical Properties

	Property	Kevlar Fabrics		Glass Fabrics		Carbon Tapes		Carbon Fabrics	
Prepreg	Material	K120	K285	120	1581	95 g/m ²	145 g/m ²	W3T282 or W3C282	F3T584 or F3C584
	% Flow @ 250°F 50 psi (121°C 345 kPa)	14-26	14-26	8-20	8-20	4-16	4-16	4-16	4-16
	% Resin content (dry)	54-60	49-55	42-48	36-40	38-40	38-40	40-44	40-44
Laminate	Cured thickness per ply, in (cm)	0.0045 (0.011)	0.0010 (0.0025)	0.0047 (0.012)	0.0104 (0.026)	0.0037 (0.0094)	0.0056 (0.014)	0.0086 (0.022)	0.0150 (0.038)
	% Fiber volume	42	46	38	45	57	57	50	51

1.4.1 AS4C Fiber Data Sheet:

Carbon Fiber Certification

The carbon fiber is manufactured to Hexcel aerospace grade specification HS-QP-4000. A copy of this specification is available upon request. A Certification of Analysis will be provided with each shipment of HS-QP-4000 fiber.

Available Sizing

Sizing compatible with various resin systems, based on application are available to improve handling characteristics and structural properties. Please see additional information on available Sizes on our website or contact our technical team for additional information.

Packaging

Standard packaging of HexTow® AS4C is as follows:

Filament Count	Nominal Weight		Nominal Length	
	(lb)	(kg)	(ft)	(m)
8K	4.0	1.8	20,760	9,070
8K	4.0	1.8	14,490	4,540
12K	8.0	3.6	14,490	4,540

Other package sizes may be available upon request. The fiber is wound on a 8-inch ID by 11-inch long cardboard tube and overwrapped with plastic film.

Safety Information

Obtain, read, and understand the Material Safety Data Sheet (MSDS) before use of this product.

For more information

Hexcel is a leading worldwide supplier of composite materials to aerospace and industrial markets.

Our comprehensive range includes:

- HexTow® carbon fibers
- HexFlow® RTM resins
- HexForce® reinforcements
- HexTool® tooling materials
- HexPly® prepregs
- HexMC® molding compounds
- Acousti-Cap® sound attenuating honeycomb
- Redux® adhesives
- Engineered core
- Engineered products

For US quotes, orders and product information call toll-free 1-800-550-2882. For other worldwide sales office telephone numbers and a full address list, please go to:

<http://www.hexcel.com/contact/salesoffice>

©2009 Hexcel Corporation - All rights reserved. Hexcel Corporation and its subsidiaries ("Hexcel") believe that the technical data and other information provided herein was reasonably accurate as of the date this document was issued. Hexcel reserves the right to update, revise or modify such technical data and information at any time. Any performance values provided are considered representative but do not and should not constitute a warranty for your own testing or application. Hexcel does not warrant the accuracy of the information provided herein for any purpose other than the intended use of the product. Hexcel is not responsible for any damage or injury resulting from the use of the product. Hexcel is not responsible for any damage or injury resulting from the use of the product. Hexcel is not responsible for any damage or injury resulting from the use of the product.

HexTow® AS4C carbon fiber is a continuous, high strength, high strain, PAN based fiber available in 3,000 (3K), 6,000 (6K) and 12,000 (12K) filament count tows. The fiber has been surface treated and can be sized to improve its interlaminar shear properties, handling characteristics, and structural properties, and is suggested for use in weaving, prepregging, filament winding, braiding, and pultrusion.

Typical Fiber Properties	U.S. Units	SI Units
Tensile Strength	8K	675 ksi
	6K	4,654 MPa
	6K	4,447 MPa
Tensile Modulus (Chord 6000-1000)	12K	660 ksi
	6K	4,482 MPa
Ultimate Elongation at Failure		
8K	1.8%	1.8%
6K	1.7%	1.7%
12K	1.8%	1.8%
Density	0.0843 lb/in ³	1.78 g/cm ³
Weight Length	8K	11.2 x 10 ⁻⁴ lb/in
	6K	22.4 x 10 ⁻⁴ lb/in
	12K	44.8 x 10 ⁻⁴ lb/in
Approximate Yield	8K	7.441 lb/in
	6K	8.221 lb/in
	12K	1.681 lb/in
Tow Cross-Sectional Area	8K	1.74 x 10 ⁻⁴ in ²
	6K	8.48 x 10 ⁻⁴ in ²
	12K	6.97 x 10 ⁻⁴ in ²
Filament Diameter	0.272 mil	6.9 microns
Carbon Content	94.0%	94.0%
Twist	None/Twisted	None/Twisted

Typical HexPly 8550 Composite Properties (at Room Temperature)	U.S. Units	SI Units	Test Method
0° Tensile Strength	320 ksi	2,203 MPa	ASTM D3039
0° Tensile Modulus	20.5 ksi	1,417 GPa	
0° Tensile Strain	1.6%	1.6%	
0° Short Beam Shear Strength	18.5 ksi	128 MPa	ASTM D2344
0° Compressive Strength	270 ksi	1,862 MPa	ASTM Mod D695
Fiber Volume	60%	60%	

1.4.2 F155 matrix Data Sheet:

Availability

Form	Hexcel Designation	Fiber	Fiber Area Wt. g/m ²	Weave	Count Warp x Fill	Widths Available Standard Width in (cm)
Carbon Fabrics	W3728-42*-F155	T300	194	Plain	12.6 x 12.6	42", 60" (106.7, 162.4)
	W37282-42*-F155	T300*				
	F37684-42*-F155	T300	370	8 Harness Satin	24 x 24	42", 60" (106.7, 162.4)
	F37684-42*-F155	T300*				
Glass Fabrics	120-38*-F155	450-1/2	116	Crowfoot MIL-C-9084 TYVII	60 x 68	38", 60", 60" (96.6, 127, 162.4)
	1681-38*-F155	160-1/2	303	8 Harness Satin MIL-C-9084 TYVIIIA	67 x 64	38", 60", 60", 72" (96.6, 127, 162.4, 182.9)
	7781-38*-F155	76-1/0	303	8 Harness Satin MIL-C-9084 TYVIIIB	67 x 64	38", 60", 60", 72" (96.6, 127, 162.4, 182.9)
	K120-38*-F155	Kev. 49 106	61	Plain	34 x 34	38", 60", 60" (96.6, 127, 162.4)
Kevlar® Fabrics	K285-38*-F155	Kev. 49 1140	170	Crowfoot	17 x 17	38", 60", 60" (96.6, 127, 162.4)
	K281-38*-F155	Kev. 49 1140	170	Plain	17 x 17	38", 60", 60" (96.6, 127, 162.4)
Carbon Tapes	T00065-12*-F155	Various	96			
	T00145-12*-F155	Various	145			
	T00160-12*-F155	Various	160			
Glass Tape	T2E285-12*-F155	E-Glass 1082	285	n/a	n/a	12", 3"-24" (30.6, 7.6-61)
	T7D160-12*-F155	Kev. 49 7100	160			

Note: All Hexcel carbon, glass, and Kevlar resins may be used with the HexPly® F155 Resin System. Also, HexPly® F155 carbon tapes may be produced with various carbon fiber types and tow sizes. In designating carbon tape, the second digit represents tow size and the third digit represents fiber source. Contact the nearest Hexcel Sales Office for additional information.

Description

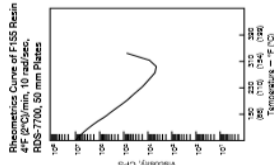
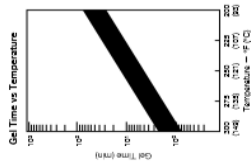
HexPly® F155 is an advanced modified epoxy formulation designed for autoclave curing to offer very high laminate strengths, coupled with increased fracture toughness and adhesive properties. HexPly® F155 is a controlled flow epoxy resin for lamination and co-curing at 250°F (121°C) cure. HexPly® F155 will pass MIL-R-9300, co-cure as a honeycomb facing, and bond metal to metal.

Features

- Uncured**
 - Controlled flow in the basic formulation to offer balanced tool and bagside sandwich peels
 - Good tack and drap properties for layup and assembly purposes
 - Can be adapted for use on various weaves and fiber reinforcements
 - Long out time
- Cured**
 - High laminate strengths
 - Good sandwich panel and metal-to-metal bonding
 - Self-extinguishing properties
 - Certified to MIL-R-9300, Type 1, Grade O, Form B

Next Resin Properties

- Specific gravity**
1.335
250°F (121°C)
9.4%
- Equilibrium moisture absorption**
2.93 x 10⁻³ in/in/°F (6.27 x 10⁻² cm/cm/°C)
- Linear coefficient of thermal expansion**
11.6 in/in (80 MPa)
- Tensile strength**
0.47 ksi (3.24 GPa)
- Tensile modulus**
6.2%
- Tensile strain**
1.50 ksi $\sqrt{\text{in}}$ (1.05 MPa $\sqrt{\text{m}})$
- Fracture toughness, K1C**
4.18 in-lb/in^{3/2} (0.73 kJ/m²)
- Strain energy release rate, G1C**
4-10 min
- Gel time @ 250°F (121°C)**



Copyright © 2016 - Hexcel Corporation. All Rights Reserved.

Copyright © 2016 - Hexcel Corporation. All Rights Reserved.



HexPly® F155

Resin Systems for Advanced Composites



Product Data Sheet

Physical Properties

Property	Kevlar® Fibers	Glass Fabrics	Carbon Tapes	Carbon Fabrics
Material	K120	K285	W3T282 or W3C282	F3T584 or F3C584
% Flow @ 260°F 60 psi (121°C)	14-26	8-20	4-16	4-16
% Resin content (by wt)	54-60	49-55	38-40	40-44
Cured thickness per ply, in (cm)	0.0046 (0.011)	0.0047 (0.012)	0.0066 (0.014)	0.0086 (0.022)
% Fiber volume	42	46	57	61

Mechanical Properties

Property	Temp. °F (°C)	Kevlar 49 Fabrics		Glass Fabrics		Carbon Tapes			Carbon Fabric
		120	285	120	220	161	T3T095	T2C145	
Tensile strength, ksi (MPa)	75 (24)	62 (427)	82.8 (571)	67.0 (333)	60.3 (416)	70 (483)	225 (1552)	266 (1834)	225 (1518)
	75 (24)	3.9 (26.7)	4.4 (30.3)	3.0 (20.7)	3.0 (20.7)	3.4 (23.4)	18.3 (128.2)	18.3 (128.2)	18.1 (124.8)
Tensile strain	75 (24)	15,000	—	—	—	—	10,180	10,370	10,470
Tensile strength, ksi (MPa)	160 (71)	68 (400)	79.3 (547)	—	62.7 (383)	62 (427)	—	248 (1710)	226 (1588)
	160 (71)	3.7 (26)	3.9 (26.9)	—	2.7 (18.6)	3.1 (21.4)	—	17.2 (119)	17.0 (117)
Tensile strain	160 (71)	—	—	—	—	—	—	—	—
Tensile strength, ksi (MPa)	200 (93)	—	—	46.3 (319)	47.9 (330)	67 (393)	—	—	—
	200 (93)	—	—	2.6 (17.9)	2.6 (17.9)	2.9 (20)	—	—	—
Tensile modulus, ksi (GPa)	200 (93)	—	—	—	—	—	—	—	—
Tensile strain	200 (93)	—	—	—	—	—	—	—	—

Copyright © 2016 - Hexcel Corporation - All Rights Reserved

3



HexPly® F155

Resin Systems for Advanced Composites



Product Data Sheet

Property	Temp. °F (°C)	Kevlar® 49 Fabrics		Glass Fabrics			Carbon Tapes		Carbon Fabric W3T282	
		120	285	120	220	161	T3T095	T2C145		T2C190
Compression strength, ksi (MPa)	76 (24)	32.0 (221)	37.9 (261)	64.4 (444)	71.9 (496)	76 (517)	168 (1158)	193 (1331)	170 (1172)	131 (904)
Compression modulus, ksi (GPa)	76 (24)	3.0 (20.9)	3.4 (23.4)	3.0 (20.7)	3.2 (22.1)	3.7 (26.5)	16.9 (109.6)	-	-	8.3 (57.2)
Compression strength, ksi (MPa)	160 (71)	24 (166)	28.3 (195)	-	67.4 (460)	68 (466)	134 (924)	170 (1172)	140 (966)	72.0 (496)
Compression modulus, ksi (GPa)	160 (71)	3.0 (21)	3.4 (23.4)	-	3.0 (20.7)	3.4 (23.4)	16.6 (117)	-	-	-
Compression strength, ksi (MPa)	200 (93)	-	-	43.8 (302)	49.6 (341)	48 (331)	-	-	-	-
Compression modulus, ksi (GPa)	200 (93)	-	-	2.8 (19.3)	2.7 (18.6)	3.2 (22.1)	-	-	-	-
Compression interlaminar shear strength, ksi (MPa)	RT	-	-	9.6 (61)	9.8 (63)	10 (68.9)	-	13.0 (89.6)	-	-
Compression interlaminar shear strength, ksi (MPa)	160 (71)	-	-	-	7.7 (53)	7 (48)	-	10.4 (71.7)	-	131 (904)
Compression interlaminar shear strength, ksi (MPa)	200 (93)	-	-	6.8 (47)	6.2 (43)	6.4 (37)	-	-	-	-
Flatwise tensile strength, psi (kPa)	76 (24)	800 (5516)	740 (5164)	846 (5833)	874 (6026)	780 (5378)	-	670 (4620)	-	940 (6481)
Flatwise tensile strength, psi (kPa)	160 (71)	600 (4137)	640 (4413)	-	799 (5509)	700 (4826)	-	-	-	-
Flatwise tensile strength, psi (kPa)	200 (93)	-	-	667 (4544)	660 (4544)	610 (4206)	-	-	-	-
Long beam flexure, lb (kg)	76 (24)	66 (23.6)	129 (58.5)	122 (55.5)	112 (50.9)	216 (98.2)	-	-	-	-
Long beam flexure, lb (kg)	160 (71)	6.6 (2.9)	107 (48.6)	-	104 (47.3)	177 (80.4)	-	-	-	-
Long beam flexure, lb (kg)	200 (93)	-	-	93 (42.3)	85 (38.7)	166 (75.1)	-	-	-	-
Drum peel, in-lb/3" width (cm-kg/7.6 cm)	76 (24)	8 (0.2)	29 (33)	11 (13)	14 (16)	14 (16)	-	-	-	-

All mechanical property values are based on the calculated fiber volume found on the previous table.

Reported property values are averages to which no statistical assurance should be associated. While Hexcel believes that the data contained herein are factual, the data are not to be taken as a warranty or representation for which Hexcel assumes legal responsibility. They are offered solely for your consideration, investigation, and reference.

Copyright © 2016 - Hexcel Corporation - All Rights Reserved

4



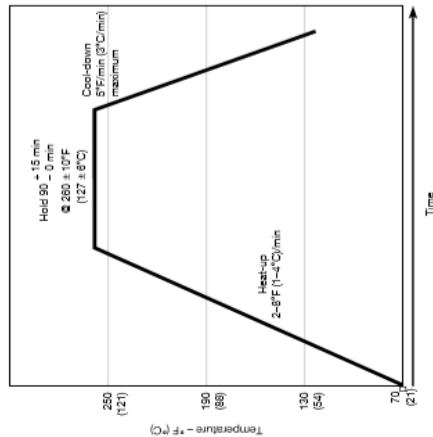
HexPly® F155

Resin Systems for Advanced Composites



Product Data Sheet

Cure Cycle



Cure Procedure

- Apply vacuum of 22 inches (7.4 kPa) Hg minimum.
- Apply 85 ± 15 – 0 psig (588 ± 103 – 0 kPa) pressure for laminates.
- Apply 45 ± 15 – 0 psig (310 ± 103 – 0 kPa) pressure for sandwich.*
- Vent vacuum bag to atmosphere when pressure reaches 20 psi (138 kPa).
- During cool-down when the part temperature falls below 140°F (60°C), pressure can be released and the test panel removed from the autoclave and degassed.

* * * Total for Hexcel HexPly® F155 – 16 – 16 – 3.0 honeycomb.

Storage

HexPly® F155 has a storage life of 180 days from date of receipt when stored at 10°F (-12°C), plus a handling life of 200 hours at 75°F (24°C) and mechanical life of 200 hours at 75°F (24°C).

Copyright © 2016 - Hexcel Corporation - All Rights Reserved



HexPly® F155

Resin Systems for Advanced Composites



Product Data Sheet

Shipping

Prepreg fabric and tape are generally shipped in sealed polyethylene bags in insulated containers packed with dry ice.

Disposal of Scrap

Disposal of this material should be in a secure landfill in accordance with state and federal regulations.

Corrosion of Potential

A need for the management of corrosion potential is necessary when graphite composites are placed in contact with metallo honeycomb, skins, or fasteners.

Handling and Safety Precautions

Hexcel recommends that customers observe established precautions for handling epoxy resins and fire flammable materials. Operators working with this product should wear clean, impervious gloves to reduce the possibility of skin contact and to prevent contamination of the material.

Airborne graphite as a result of sawing, grinding, etc., can present electrical shorting hazards; refer to NASA Technical Memorandum 78052. Material Safety Data Sheets (MSDS) have been prepared for all Hexcel products and are available to company safety officers on request from your nearest Hexcel Sales Office.

For more information

Hexcel is a leading worldwide supplier of composite materials to aerospace and industrial markets.

Our comprehensive range includes:

- HexTow® carbon fibers
- HexFlow® RTM resins
- HexForce® reinforcements
- Redux® adhesives
- HexPly® prepregs
- HexTool® tooling materials
- HexMOC® molding compounds
- HexWeb® honeycombs
- Acoust-Cap® sound attenuating honeycomb
- Engineered core
- Engineered products

For US quotes, orders and product information call toll-free 1-800-888-7734. For other worldwide sales office telephone numbers and a full address list, please go to:

<http://www.hexcel.com/contact/salesoffice>

©2016 Hexcel Corporation - All rights reserved. Hexcel Corporation and its subsidiaries ("Hexcel") believe that the technical data and other information provided herein was reasonably accurate as of the date this document was issued. Hexcel reserves the right to update, revise or modify such technical data and information without notice and without obligation. Hexcel does not warrant the accuracy, completeness or reliability of the information provided herein, and the implied warranties of merchantability and fitness for a particular purpose, and disclaims any liability arising out of or related to, the use of or reliance upon any of the technical data or information contained in this document.

Physical Properties

	Property	Kevlar Fabrics		Glass Fabrics		Carbon Tapes			Carbon Fabrics	
Prepreg	Material	K120	K285	120	1581	95 g/m ²	145 g/m ²	190 g/m ²	W3T282 or W3C282	F3T584 or F3C584
	% Flow @ 250°F 50 psi (121°C 345 kPa)	14–26	14–26	8–20	8–20	4–16	4–16	4–16	4–16	4–16
	% Resin content (dry)	54–60	49–55	42–48	36–40	38–40	38–40	38–40	40–44	40–44
Laminate	Cured thickness per ply, in (cm)	0.0045 (0.011)	0.0010 (0.0025)	0.0047 (0.012)	0.0104 (0.026)	0.0037 (0.0094)	0.0056 (0.014)	0.0074 (0.019)	0.0086 (0.022)	0.0150 (0.038)
	% Fiber volume	42	46	38	45	57	57	57	50	51

Mechanical Properties

Property	Temp. °F (°C)	Kevlar® 49 Fabrics		Glass Fabrics			Carbon Tapes			Carbon Fabric
		120	285	120	220	181	T3T095	T2C145	T2C190	W3T282
Tensile strength, ksi (MPa)	75 (24)	62 (427)	82.8 (571)	57.0 (393)	60.3 (416)	70 (483)	225 (1552)	266 (1834)	225 (1518)	123 (848)
Tensile modulus, msi (GPa)	75 (24)	3.9 (26.7)	4.4 (30.3)	3.0 (20.7)	3.0 (20.7)	3.4 (23.4)	18.3 (126.2)	18.3 (126.2)	18.1 (124.8)	8.4 (58)
Tensile strain	75 (24)	15,900	–	–	–	–	10,180	10,370	10,470	10,490
Tensile strength, ksi (MPa)	160 (71)	58 (400)	79.3 (547)	–	52.7 (363)	62 (427)	–	248 (1710)	226 (1558)	–
Tensile modulus, msi (GPa)	160 (71)	3.7 (25)	3.9 (26.9)	–	2.7 (18.6)	3.1 (21.4)	–	17.2 (119)	17.0 (117)	–
Tensile strain	160 (71)	–	–	–	–	–	–	–	–	–
Tensile strength, ksi (MPa)	200 (93)	–	–	46.3 (319)	47.9 (330)	57 (393)	–	–	–	–
Tensile modulus, msi (GPa)	200 (93)	–	–	2.6 (17.9)	2.6 (17.9)	2.9 (20)	–	–	–	–
Tensile strain	200 (93)	–	–	–	–	–	–	–	–	–

1.4.3 Images

Type of Fiber	Tensile Strength (Ksi)	Tensile Modulus (Msi)	Elongation at Failure (%)	Density (gm/cm ³)	Coefficient of Thermal Expansion (10 ⁻⁶ °C)	Fiber Diameter (μm)
Glass						
E-Glass	500	11.0	4.7	2.58	4.9-6.0	5-20
S-2 Glass	650	12.6	5.6	2.48	2.9	5-10
Quartz	490	10.0	5.0	2.15	0.5	9
Organic						
Kevlar 29	525	12.0	4.0	1.44	-2.0	12
Kevlar 49	550	19.0	2.8	1.44	-2.0	12
Kevlar 149	500	27.0	2.0	1.47	-2.0	12
Spectra 1000	450	25.0	0.7	0.97	-----	27
PAN Based Carbon						
Standard Modulus	500-700	32-35	1.5-2.2	1.80	-0.4	6-8
Intermediate Modulus	600-900	40-43	1.3-2.0	1.80	-0.6	5-6
High Modulus	600-800	50-65	0.7-1.0	1.90	-0.75	5-8
Pitch Based Carbon						
Low Modulus	200-450	25-35	0.9	1.9	-----	11
High Modulus	275-400	55-90	0.5	2.0	-0.9	11
Ultra High Modulus	350	100-140	0.3	2.2	-1.6	10

Note: Representative only. For specific properties, contact the fiber manufacturer.

Figure 1.7: Different reinforcement systems

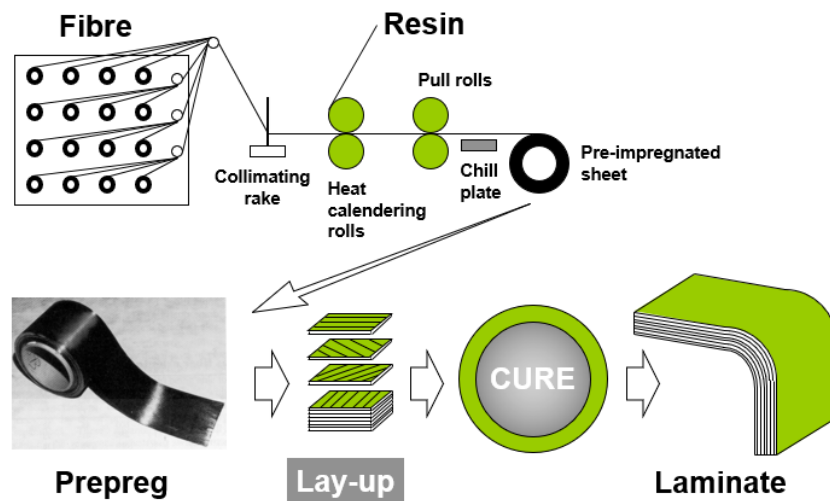


Figure 1.8: Manufacturing of a composite laminate

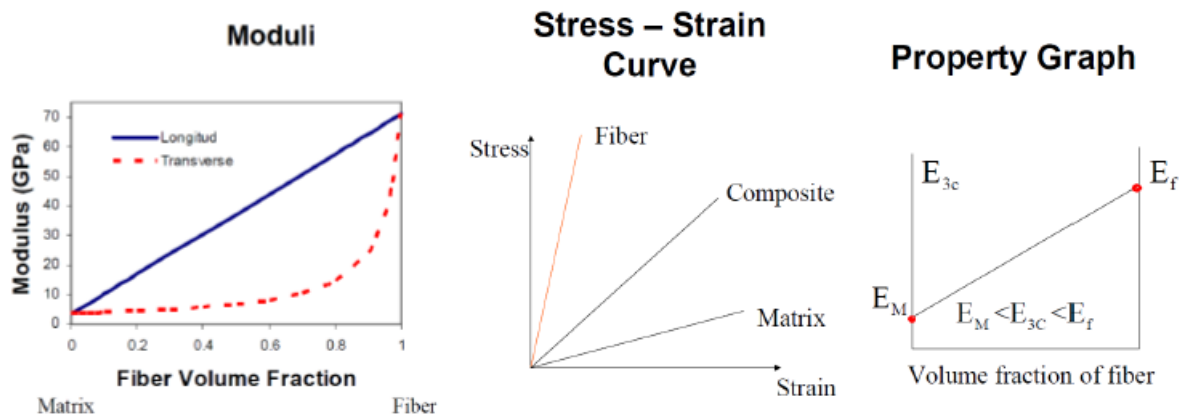


Figure 1.9: Trend of variation in material properties

2. MODELING OF SPECIMEN FOR TENSILE TEST

2.1 Introduction

2.1.1 Tensile test of a material

The tensile test is the most basic mechanical test that can be performed while characterizing a material. In this test, the specimens are subjected to a tensile load until they reach their fracture point. The behavior of the material under a tensile load is determined. The data that is obtained from these tests is further used to determine properties like the ultimate tensile strength, yield strength and also the elongation of the specimen at fracture. Some of the elastic constants are also obtained from this data.

When a composite material is under tension, the load is typically carried by both the fiber and the matrix. For a brittle fiber and a ductile matrix, there are three stages as shown in Figure 9 (In Appendix). Stage 1 comprises elastic deformation, in stage 2 the fiber has elastic behavior whereas the matrix has plastic behavior. In stage 3 both the matrix and the fiber have a plastic deformation.

2.1.2 Modeling in Abaqus

Abaqus is one of the most efficient software that is used to solve finite element problems of a wide range. In this work, five different tests that are used to characterize a composite material were modeled using Abaqus. The test specimens were modeled to full scale along with the glass fiber tabbing on them to study the end effects of these tabs. The Double Cantilever Beam (DCB) specimens were modeled with their respective stainless-steel hinges. These models hence act as the digital twins for the actual specimen that are tested in the experiment.

The system of units is unique in Abaqus and care has to be taken that there is consistency in entering the values as input. For all the modeling that was carried out in this work, the following units were used:

Length (mm), Force (N), Mass (tonne; $10^3 kg$), Time (s), Stress (MPa), Energy (mJ; $10^{-3} J$),

$$Density \left(\frac{tonne}{mm^3} \right)$$

2.1.3 Constitutive relations

Stress and strain are the most basic terms in the mechanics of materials. Tensile tests are used to plot the stress versus strain plots. The following equations are the basic descriptions of stress and strain:

$$\sigma = \frac{\text{Force}}{\text{Area}}$$
$$\varepsilon = \frac{\Delta L}{L}$$

Where stress is defined as the force acting per unit cross-section area and strain is defined as the ratio of change in length to the original length of the sample. Young's modulus or elastic modulus is the measure of the stiffness of a material. It relates the proportion of stress to strain under elastic deformation. The relation is known as Hooke's law and is formulated as,

$$\sigma = E * \varepsilon$$

Figure 10 (In Appendix) shows a plot of stress versus strain for composite material. The constitutive relations which determine the mechanical properties of the material are listed as follows:

$$\varepsilon_{ij} = \frac{1}{2} \left(\frac{\partial u_i}{\partial x_j} + \frac{\partial u_j}{\partial x_i} \right)$$
$$\varepsilon_{ij,kl} + \varepsilon_{kl,ij} - \varepsilon_{jl,ik} - \varepsilon_{ik,jl} = 0$$
$$\sigma_{ji,j} + f_i = 0$$
$$\sigma_{ij} = f_{ij}(\varepsilon_{11}, \varepsilon_{22}, \varepsilon_{33}, \varepsilon_{23}, \varepsilon_{13}, \varepsilon_{12})$$

2.1.3.1 Young's Modulus

The Young's modulus of composite material is determined by the rules of mixtures. The strength of the composite, when measured along the direction of the fibers, is known as the longitudinal strength. If the load is applied parallel to the fiber direction, the fiber and the matrix have the same strain and hence deform the same amount as in the following equation:

$$\varepsilon_c = \varepsilon_f = \varepsilon_m$$

Assuming a length of 1, hence, considering the areas as volumes, and applying the equal strain condition, the rules of mixtures can be applied to calculate the young's modulus as follows:

$$E_c = E_f V_f + E_m V_m$$

The strength of a composite when measured perpendicular to the fiber direction is known as transverse loading. In this case, the loads on the matrix and the fiber are equal, hence

$$P_c = P_f = P_m$$

The area normal to the loading direction is equal. Hence, the constituent stresses are equal as follows:

$$\sigma_c = \sigma_f = \sigma_m$$

For an iso-stress case, substituting these relations, we get,

$$\frac{E_T}{E_m} = \frac{E_f}{E_m V_f + E_f V_m}$$

2.1.3.2 Ultimate Tensile Stress

Ultimate Tensile Stress is the maximum load the specimen can carry during the test. This value is the strength of the specimen at its first fracture and may always not be equal to the strength at the break. Tensile strength is defined as the ultimate stress at failure.

2.1.3.3 Poisson's Ratio

Poisson's ratio is defined as the ratio of transverse contraction strain to longitudinal extension strain in the direction in which the stretching force acts. In this experiment, only ν_{12} and ν_{21} were considered and they can be formulated as follows:

$$\nu_{12} = \frac{-\varepsilon_2}{\varepsilon_1}; \quad \nu_{21} = \frac{-\varepsilon_1}{\varepsilon_2}$$

2.2 Overview of the experimental procedure

2.2.1 Testing of the specimen in MTS

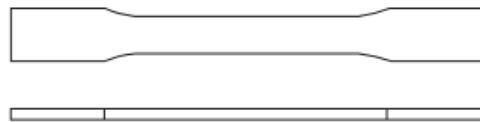
The composites in which the fibers are continuously aligned along the axis have high strengths as they have high orthotropy. These laminates are strong longitudinally, whereas, they are weak transversely. This is because the orthotropic fibers are capable of carrying higher tensile loads along their length than an isotropic matrix. The test method that was used was an ASTM D3039/D3039M standard (test fixture as shown in figure 1).



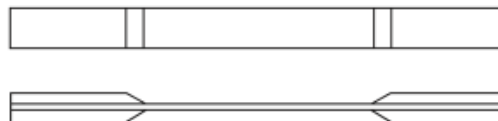
Figure 2.1: ASTM D3039/D3039M test fixture

(Image from Experimental characterization of advanced composite materials (2014))

Wedge hydraulic grips are used in these tests. These grips perform well. But, they are heavier and bulkier than the mechanical wedge grips. These grips can also be changed if more friction has to be given to the specimens. The transfer of this load onto the specimen is very crucial. For high stress-bearing structures, holes cannot be drilled through them for the fixture as it might lead to local failure around the holes due to high-stress concentrations. Hence, clamping grips or tabs are used on the specimen. In this method, the load is transferred onto the specimen by shear on the clamp-specimen interface. Figure 2 shows the different types of test specimen geometries. These tabs are used to protect the end of the specimen from the grip damage. But they induce stress concentrations due to sudden change in the thickness.



(a) Dog bone samples



(b) End-tabbed samples

Figure 2.2: Tensile test specimen geometries

(Image from Experimental characterization of advanced composite materials (2014))

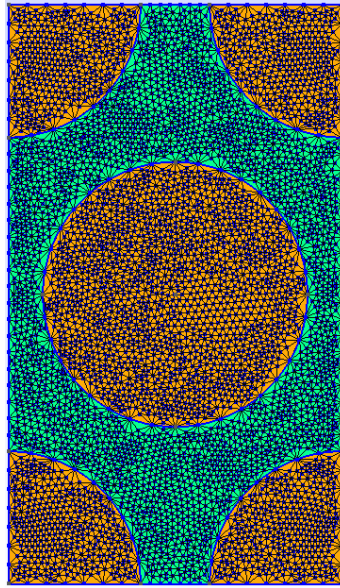
The geometry of the test specimens was also set according to the standards. This was done to avoid the loading eccentricities on the sample. The typical width of a 0° laminate with 6-8 plies is 12.7 mm width and for a 90° laminate with 16-24 plies, the width is 25 mm. The tab length is required to be greater than 38 mm and its thickness should be between 1.6-3.2 mm. The gauge length should be between 125-155 mm.

2.2.2 Digital Image Correlation

Digital Image Correlation (DIC) is an optical method that is used to measure the deformation on the surface of an object. This method tracks the changes in the speckle pattern on the sample. It is then used to determine the displacement and further translated into the strain field. Two cameras were used in order to generate a 3Dimensional image of the sample.

2.3 Micromechanical Analysis

A micromechanical analysis was done for the three laminates to predict the material properties. The material properties of the fiber and the matrix were considered and the properties of the laminate were calculated by Representative Volume Element (RVE) method, where a hexagonal unit cell was considered. Figure 3 shows an RVE with a mesh size of 0.01 and a one-dimensional SG element.



(a) Hexagonal Unit Cell in an RVE



(b) 1-D SG element (8 plies)



(c) 1-D SG element (16 plies)

Figure 2.3: Simulation images from SwiftComp

The data for the stiffness, compliance matrices along with the elastic constants for the three laminates is given in Figure 4. It can be observed that the values of the elastic constants are the same for the $[90]_8$ and $[90]_{16}$ samples and the data for the $[0]_8$ sample is the same as the data obtained for the composite laminate in general.

The Effective Stiffness Matrix					
1.3739533E+11	7.5946262E+09	7.5946303E+09	2.8212529E+03	0.0000000E+00	0.0000000E+00
7.5946262E+09	1.4137955E+10	9.0471836E+09	1.9126601E+04	0.0000000E+00	0.0000000E+00
7.5946303E+09	9.0471836E+09	1.4137972E+10	-8.0798684E+03	0.0000000E+00	0.0000000E+00
2.8212529E+03	1.9126601E+04	-8.0798684E+03	2.5454251E+09	0.0000000E+00	0.0000000E+00
0.0000000E+00	0.0000000E+00	0.0000000E+00	0.0000000E+00	3.9901516E+09	3.7556265E+04
0.0000000E+00	0.0000000E+00	0.0000000E+00	0.0000000E+00	3.7556265E+04	3.9900636E+09
The Effective Compliance Matrix					
7.5517365E-12	-2.4736807E-12	-2.4736790E-12	2.3653203E-18	0.0000000E+00	0.0000000E+00
-2.4736807E-12	1.2059267E-10	-7.5840957E-11	-1.1441444E-15	0.0000000E+00	0.0000000E+00
-2.4736790E-12	-7.5840957E-11	1.2059253E-10	9.5541228E-16	0.0000000E+00	0.0000000E+00
2.3653203E-18	-1.1441444E-15	9.5541228E-16	3.9286169E-10	0.0000000E+00	0.0000000E+00
0.0000000E+00	0.0000000E+00	0.0000000E+00	0.0000000E+00	2.5061704E-10	-2.3589198E-15
0.0000000E+00	0.0000000E+00	0.0000000E+00	0.0000000E+00	-2.3589198E-15	2.5062257E-10
The Engineering Constants (Approximated as Orthotropic)					
E1 =	1.3241987E+11				
E2 =	8.2923783E+09				
E3 =	8.2923878E+09				
G12 =	3.9900636E+09				
G13 =	3.9901516E+09				
G23 =	2.5454251E+09				
nu12=	3.2756449E-01				
nu13=	3.2756426E-01				
nu23=	6.2890190E-01				

(a) $[0]_8$

Figure 2.4: SwiftComp simulation results

Figure 2.4 continued

The Effective Stiffness Matrix					
1.4137956E+10	7.5946262E+09	9.0471836E+09	0.0000000E+00	0.0000000E+00	8.7978495E-08
7.5946262E+09	1.3739533E+11	7.5946303E+09	0.0000000E+00	0.0000000E+00	7.4593589E-06
9.0471836E+09	7.5946303E+09	1.4137972E+10	0.0000000E+00	0.0000000E+00	-8.8943237E-08
0.0000000E+00	0.0000000E+00	0.0000000E+00	3.9901516E+09	8.8463984E-08	0.0000000E+00
0.0000000E+00	0.0000000E+00	0.0000000E+00	8.8463984E-08	2.5454251E+09	0.0000000E+00
8.7978495E-08	7.4593589E-06	-8.8943237E-08	0.0000000E+00	0.0000000E+00	3.9900636E+09
The Effective Compliance Matrix					
1.2059267E-10	-2.4736808E-12	-7.5840956E-11	0.0000000E+00	0.0000000E+00	2.7492583E-28
-2.4736808E-12	7.5517368E-12	-2.4736791E-12	0.0000000E+00	0.0000000E+00	-1.4118447E-26
-7.5840956E-11	-2.4736791E-12	1.2059253E-10	0.0000000E+00	0.0000000E+00	8.9849001E-27
0.0000000E+00	0.0000000E+00	0.0000000E+00	2.5061704E-10	-8.7099723E-27	0.0000000E+00
0.0000000E+00	0.0000000E+00	0.0000000E+00	-8.7099723E-27	3.9286169E-10	0.0000000E+00
2.7492583E-28	-1.4118447E-26	8.9849001E-27	0.0000000E+00	0.0000000E+00	2.5062257E-10
The Engineering Constants (Approximated as Orthotropic)					
E1 =	8.2923783E+09				
E2 =	1.3241987E+11				
E3 =	8.2923878E+09				
G12 =	3.9900636E+09				
G13 =	2.5454251E+09				
G23 =	3.9901516E+09				
nu12=	2.0512697E-02				
nu13=	6.2890190E-01				
nu23=	3.2756426E-01				

(b) $[90]_8$

The Effective Stiffness Matrix					
1.4137956E+10	7.5946262E+09	9.0471836E+09	0.0000000E+00	0.0000000E+00	8.7978495E-08
7.5946262E+09	1.3739533E+11	7.5946303E+09	0.0000000E+00	0.0000000E+00	7.4593589E-06
9.0471836E+09	7.5946303E+09	1.4137972E+10	0.0000000E+00	0.0000000E+00	-8.8943237E-08
0.0000000E+00	0.0000000E+00	0.0000000E+00	3.9901516E+09	8.8463984E-08	0.0000000E+00
0.0000000E+00	0.0000000E+00	0.0000000E+00	8.8463984E-08	2.5454251E+09	0.0000000E+00
8.7978495E-08	7.4593589E-06	-8.8943237E-08	0.0000000E+00	0.0000000E+00	3.9900636E+09
The Effective Compliance Matrix					
1.2059267E-10	-2.4736808E-12	-7.5840956E-11	0.0000000E+00	0.0000000E+00	2.7492583E-28
-2.4736808E-12	7.5517368E-12	-2.4736791E-12	0.0000000E+00	0.0000000E+00	-1.4118447E-26
-7.5840956E-11	-2.4736791E-12	1.2059253E-10	0.0000000E+00	0.0000000E+00	8.9849001E-27
0.0000000E+00	0.0000000E+00	0.0000000E+00	2.5061704E-10	-8.7099723E-27	0.0000000E+00
0.0000000E+00	0.0000000E+00	0.0000000E+00	-8.7099723E-27	3.9286169E-10	0.0000000E+00
2.7492583E-28	-1.4118447E-26	8.9849001E-27	0.0000000E+00	0.0000000E+00	2.5062257E-10
The Engineering Constants (Approximated as Orthotropic)					
E1 =	8.2923783E+09				
E2 =	1.3241987E+11				
E3 =	8.2923878E+09				
G12 =	3.9900636E+09				
G13 =	2.5454251E+09				
G23 =	3.9901516E+09				
nu12=	2.0512697E-02				
nu13=	6.2890190E-01				
nu23=	3.2756426E-01				

(c) $[90]_{16}$

2.4 Comparison of experimental and simulation results

Tensile tests on the 0° and 90° samples are very crucial to determine the values of the longitudinal and transverse Young's modulus and Poisson's ratio on a composite laminate. It was observed that the 0° sample was much stiffer than the 90° sample as all the fibers were aligned along the loading direction. These properties along with the tensile strength are intrinsic to the material and they do not depend on the thickness of the specimen. Hence, the properties obtained for the $[90]_8$ and the $[90]_{16}$ samples were very close to each other. The 0° samples were used to obtain the values of E_1 and ν_{12} and the 90° samples were used to calculate the E_2 of the material. The value of ν_{21} was obtained from these 3 values by utilizing the symmetric property of the compliance matrix. The 0° samples also appeared to stiffen with the application of the load and this might be because the fibers get aligned along the direction of the load and hence make it stiffer along the loading direction.

Table 1 shows the values of Young's modulus and the Poisson's ratio that were obtained for each of the $[0]_8$ samples and Table 2 shows the statistical values of a combination of these values.

Table 2.1: Sample-wise data for $[0]_8$

Sample	Tensile Modulus, E_1 (GPa)		Poissons ratio, ν_{12}	Tensile Strength X_1 (MPa)
	0.001 to 0.003 $\mu\epsilon$	0.008 to 0.0014 $\mu\epsilon$		
1	108.605	123.521	0.336	1890.650
2	101.849	115.741	0.465	1730.500
3	104.588	119.594	0.366	1868.974
4	102.653	120.652	0.304	1755.318
5	106.227	121.331	0.305	1841.700
6	108.911	124.365	0.413	1884.959
7	104.182	120.478	0.337	1862.802
8	113.141	123.057	0.419	1922.212
9	110.208	122.632	0.413	1818.364
10	105.550	120.514	0.335	1872.303
11	112.314	125.278	0.349	1873.674

Table 2.2: Statistical averages of properties of $[0]_8$

	Mean	Standard deviation	Co-variance
E_1 (GPa)	107.112	3.798	3.545
E_1 Tangent Modulus	121.564	2.642	2.173
ν_{12}	0.367	0.053	14.320
X_1 (MPa)	1847.405	58.233	3.152

Table 3 consists of specimen-wise data for the elastic constants and Table 4 consists of the statistical averages of the data for the $[90]_8$ samples. Table 5 consists of specimen-wise data for the elastic constants and Table 6 consists of the statistical averages of the data for the $[90]_{16}$ samples.

Table 2.3: Sample-wise data for $[90]_8$

Sample	Tensile Modulus, E_2 (GPa)	Poisons ratio, ν_{21}	Tensile Strength X_2 (MPa)
1	6.910	0.005	52.765
2	6.574	0.021	54.832
3	6.932	0.001	54.785
4	7.095	0.053	57.474
5	6.928	-0.007	51.342
6	7.225	0.041	53.370
7	7.038	-0.061	58.419
8	7.451	0.074	48.303
9	7.250	0.020	50.545

Table 2.4: Statistical averages of properties of $[90]_8$

	Mean	Standard deviation	Co-variance
$E_2(\text{GPa})$	7.045	0.252	3.578
ν_{21}	0.016	0.039	240.217
$X_2(\text{MPa})$	53.537	3.247	6.065

Table 2.5: Sample-wise data for $[90]_{16}$

Sample	Tensile Modulus, E_2 (GPa)	Poissons ratio, ν_{21}	Tensile Strength (MPa), X_2
1	7.518	-0.013	59.166
2	7.531	0.047	54.484
3	7.065	0.031	52.684
4	7.550	-0.017	58.856
5	6.993	0.045	52.721
6	7.143	0.014	57.965
7	7.426	0.025	59.108
8	7.671	0.012	59.352
9	7.747	0.048	59.309
10	7.617	-0.036	57.734

Table 2.6: Statistical averages of properties of $[90]_{16}$

	Mean	Standard deviation	Co-variance
E_2 (GPa)	7.426	0.265	3.570
ν_{21}	0.016	0.029	187.850
X_2 (MPa)	57.138	2.748	4.810

Table 7 shows the values of tensile modulus, Poisson's ratio and the ultimate tensile strength of the $[0]_8$, $[90]_8$ and $[90]_{16}$ samples and Table 8 shows the data for $[0]_8$ samples compared with the simulation results and the material datasheet. The values of ν_{21} were calculated by using the formula $\nu_{21} = \nu_{12} \left(\frac{E_2}{E_1} \right)$ by utilizing the symmetry of the compliance matrix as the DIC is very sensitive in obtaining this data.

Table 2.7: Summary of material properties

	[0]₈	[90]₈	[90]₁₆
Tensile modulus (GPa)	107.112	7.045	7.426
Poisson's ratio	0.367	0.016 (0.024)	0.016 (0.025)
Ultimate strength (MPa)	1847.405	53.537	57.138

Table 2.8: Comparison of experimental, simulation data with material datasheet

	Experimental results		Simulation results	Material Data Sheet
Tensile Modulus, E_1 (GPa)	107.112 (15.12% error) 0.001-0.003 $\mu\epsilon$	121.563 (3.67% error) 0.008-0.0014 $\mu\epsilon$	132.420	128.2
Transverse Modulus, E_2 (GPa)	7.235		8.347	-
ν_{12}	0.367		0.327	-
ν_{21}	0.025		0.020	-
Tensile strength, X_1 (MPa)	1847.4 (0.72% error)		-	1834
X_1 (Method2*)	1711.650 0.01598*107.1	1942.529 0.01598*121.563		
Tensile strength, X_2 (MPa)	55.34		-	-

After conducting all the experiments on the tensile coupons, the elastic constants were measured and was compared to the values obtained from the simulation. Table 9 shows the comparison of simulation and experimental data. The values are obtained to be very close to each other.

Table 2.9: Elastic constants from simulation and experiments

Elastic Constants	Simulation	Experiments
E_1	132.4 <i>GPa</i>	128.2 <i>GPa</i>
$E_2 = E_3$	8.3 <i>GPa</i>	7.4 <i>GPa</i>
$G_{12} = G_{13}$	4.0 <i>GPa</i>	3.9 <i>GPa</i>
G_{23}	2.5 <i>GPa</i>	-
$\nu_{12} = \nu_{13}$	0.33	0.37
ν_{23}	0.63	-
α_{11}	$0.9 \frac{\mu\epsilon}{^\circ\text{C}}$	$1.1 \frac{\mu\epsilon}{^\circ\text{C}}$
$\alpha_{22} = \alpha_{33}$	$38.0 \frac{\mu\epsilon}{^\circ\text{C}}$	$35.5 \frac{\mu\epsilon}{^\circ\text{C}}$

2.5 Specimen geometry and material properties

For all the tensile tests that are discussed in this document, 8-plyed composite plates were used with different stacking sequences. The off-axis tensile specimens were made to be half-inch (12.7 mm) wide and the other specimen was one inch (25.4 mm) wide. Figure 5 shows the geometry of the tensile coupon modeled to full-scale with the glass fiber tabbing on both sides. The tabs were modeled with a thickness of 3.175 mm (1/8th inch) and a length of 50.8 mm (2 inches). Hence, the gage length of the coupons was 152.4 mm (6 inches). The ply thickness was set to be 0.14224 mm as obtained from the physical measurements of the test specimen. For the respective tests, there can be small changes in the geometry of the coupons. The laminate is assumed to be perfectly bonded to the tabs. But, this is a very basic outline of all the tensile coupons in general. The specimens are modeled to have straight tabs. But, it is observed that the deformed tabs obtain an oblique shape after the specimens undergo tensile loading. Hence, in most of the cases, the experimental specimens are manufactured with oblique tabs. It can be observed that the transverse

and the normal directions are along the Z and Y directions respectively in the Abaqus model. Hence, the stresses, strains, and displacements have the respective nomenclatures. X, Y and Z directions are denoted by 1, 2 and 3 respectively in the output parameters.

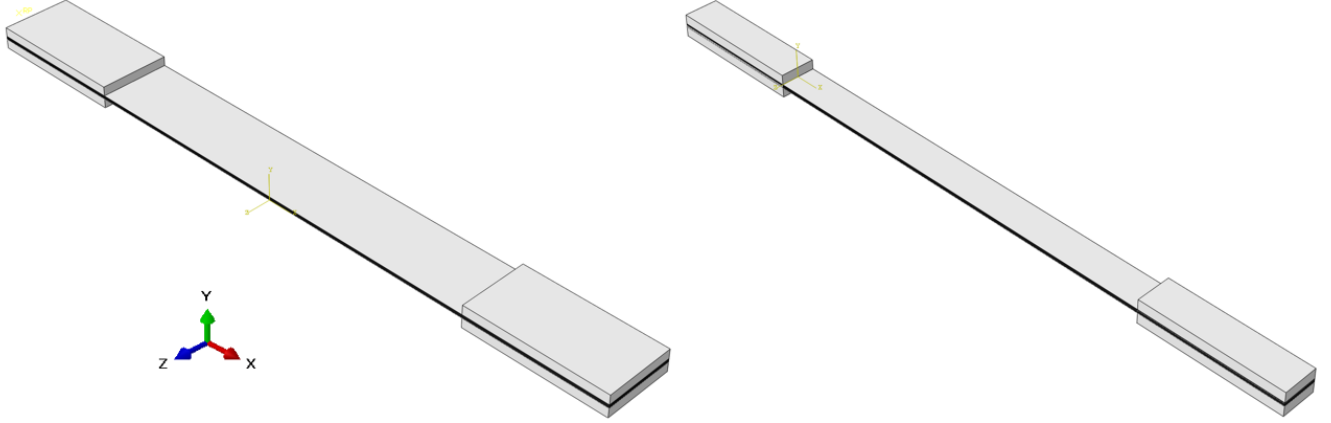


Figure 2.5: Geometry of the tensile coupons, One-inch width (Left), Half-inch width (Right)

2.5.1 Material Properties

The laminate was modeled to be an elastic orthotropic material with the material properties as obtained from the micromechanical analysis of the fiber-matrix properties as shown in the SwiftComp results for $[0]_8$ laminate in Figure 6. The elastic constants that were given as the input for the lamina properties are as follows:

$$E_1 = 132419.87 \text{ MPa}, E_2 = 8292.3783 \text{ MPa}, E_3 = 8292.3878 \text{ MPa}$$

$$\nu_{12} = 0.32756449, \nu_{13} = 0.32756426, \nu_{23} = 0.6289019$$

$$G_{12} = 3990.0636 \text{ MPa}, G_{13} = 3990.1516 \text{ MPa}, G_{23} = 2545.4251 \text{ MPa}$$

The main purpose of using the micromechanical analysis to get the material properties is that they can be predicted from the details from the datasheet and hence, this method can be generalized to any composite material system with any laminate orientation. Another method would be to use a black Aluminum approach where the global elastic constants are predicted and they can be used as input without having any separate orientations for each lamina. But this approach would not give the variation of stresses across the thickness of the laminate and the properties would constantly be varying every time the stacking sequence of the laminate is changed.

All the tensile test specimens were modeled with elastic isotropic fiberglass tabs on them and the input material properties for the tabs as obtained from their datasheet are as follows:

$$E = 11721.0874 \text{ MPa}, \nu = 0.3$$

The Double Cantilever Beam (DCB) specimen were modeled with stainless steel hinges on them and the properties of those hinges are as follows:

$$E = 210000 \text{ MPa}, \nu = 0.3$$

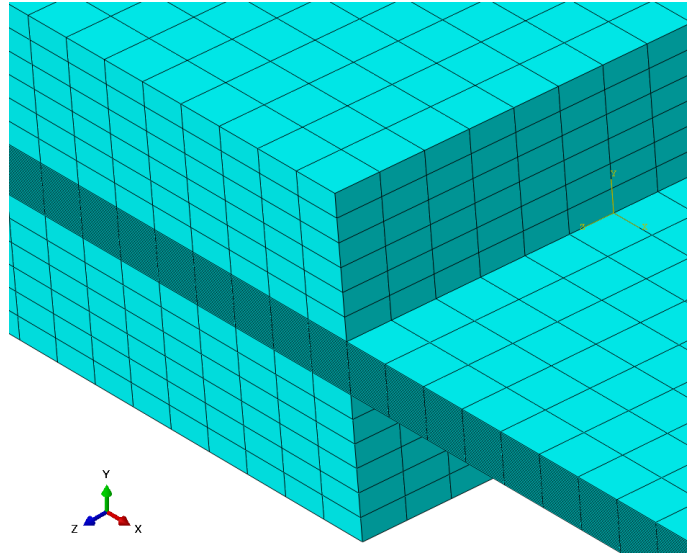
2.5.2 Orientation of plies in the laminate

As mentioned in the previous section, since each of the laminae is modeled as an orthotropic material, it is crucial to assign the material orientations accordingly. Hence, sections were created across the thickness of the laminate and local material orientations were assigned. For the off-axis tension test, 5 different laminates were modeled such as, $[15]_8$, $[30]_8$, $[45]_8$, $[60]_8$, $[75]_8$. For the laminate tension test, laminates with 4 different stacking sequences such as $[0 / \pm 45 / 90]_s$, $[0_2 / \pm 45]_s$, $[90_2 / \pm 45]_s$, $[\pm 30]_{2s}$. For the open-hole tension test, 3 laminates with three different hole sizes were modeled with stacking sequences as $[0_2 / \pm 45]_s$, $[0 / \pm 45 / 90]_s$, $[\pm 30]_{2s}$ and the CTE analysis conducted for the $[\pm 30]_{2s}$ laminate. For the test on free-edge effects, two different laminates, $[\pm 30]_{2s}$ and $[\pm 30 / 90_2]_s$ were compared. The Double Cantilever Beam (DCB) test was modeled for $[0]_{24}$ specimen.

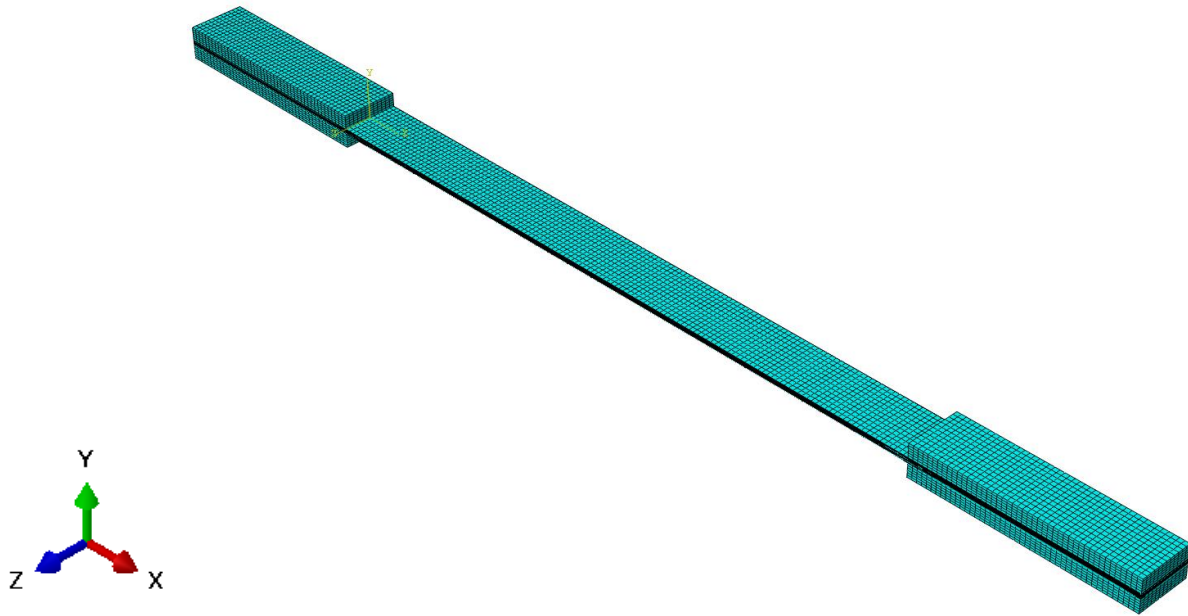
Since local material orientations were assigned for each ply individually, while post-processing the data it is very crucial to transforming all the results back to the global coordinate system in order to obtain the global displacements, stresses, and strains.

2.6 Mesh Parameters and convergence studies

A structured mesh with a mesh type of an 8-node linear brick, reduced integration, hourglass control with a global size of 1 was used to mesh the part. Few edges were seeded by assigning them a certain number of nodes for more accuracy of solutions at those locations. Each ply was seeded with 4 elements across the thickness. Each of the tabs was also seeded with 6 elements across the thickness. Figure 6 shows the mesh on half-inch (12.7 mm) and one-inch (25.4 mm) wide tensile coupons along with the seeded edges. The former and the latter parts have a total of 121576 and 233800 elements on them respectively.



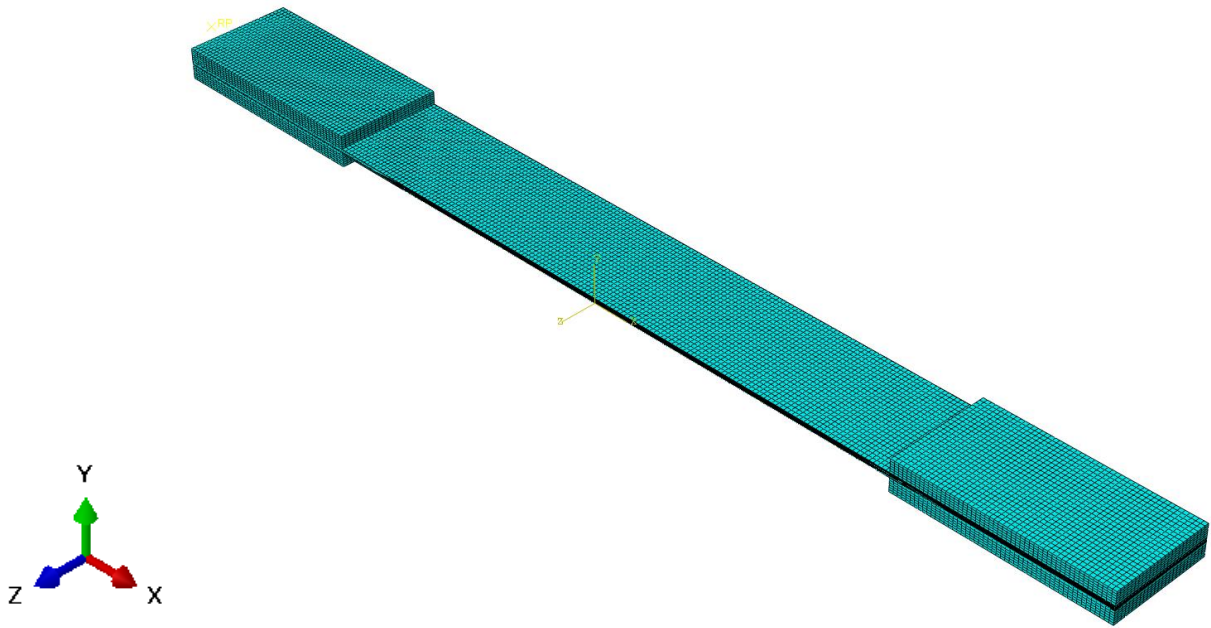
(a) Seeded edges at the laminate and the tabs



(b) Mesh on the entire coupon (width: 12.7 mm)

Figure 2.6: Mesh on the tensile test part geometries

Figure 2.6 continued



(c) Mesh on the entire coupon (width: 25.4 mm)

A mesh convergence study was carried out for the parameters described in Table 10. Figure 9 also shows the variation of these parameters with the number of elements in the model. The number of elements is varied depending on the global mesh size that was assigned to the geometry. This study was done to check the variation of parameters with the increase in the number of elements in the geometry. Hence, the computational time can be significantly reduced when the number of elements is reduced without significantly reducing the parameters that are studied. Two plots are made for mesh convergence because of the difference in the scale and to make the plots more defined.

Table 2.10: Mesh convergence study data for tensile test specimen

Mesh Size	Number of elements	Number of nodes	Max S. Mises (MPa)	Max S11 (MPa)	Max RF mag (N)
0.5	468400	501852	1120.8	1156.8	57.93
0.6	327768	353958	1120.5	1156.4	57.62
0.7	241200	262599	1119.6	1155.9	57.32
0.8	187200	205275	1119.4	1155.2	57.11
0.9	144704	160110	1119	1154.8	56.85
1	121576	135282	1118	1154	56.16
1.1	101952	114192	1110.6	1148.7	58.31
1.2	85360	96336	1092	1129.4	86.65
1.3	71760	81708	1075.6	1102.6	94.81
1.4	59904	68940	1010.9	1047.6	100.8
1.5	50048	58347	1006	1035	121.2

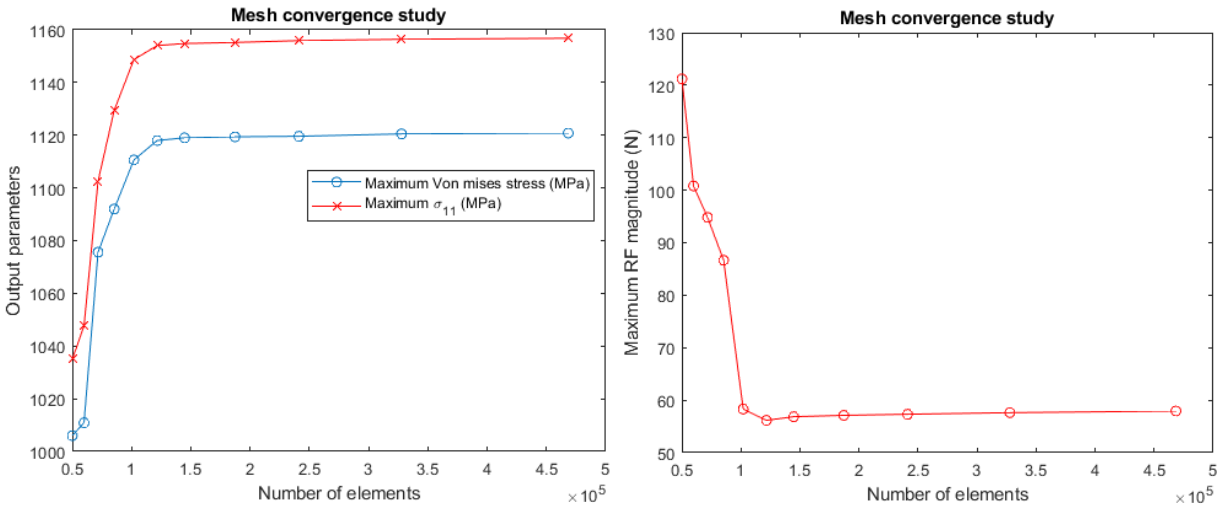


Figure 2.7: Mesh convergence study plots for tensile test specimen

2.7 Boundary and Load conditions

The sample is gripped by the wedges in the MTS. The grips apply a pressure of 1500 psi (10.3421 N/mm^2) on the surface of the tabs. The movement of the sample is restricted in the transverse and the normal directions and the load is applied on one side of the sample by using a method of displacement control where the rate of displacement is 2 mm/min . This load is applied in a quasi-static manner where a displacement of 2 mm is applied for a time period of 60 s . Figure 8 shows the load and boundary conditions applied to the sample. The grip pressure is applied on the sample as a ‘Total Force’ where the pressure is uniformly distributed and its magnitude is the total magnitude of the applied force.

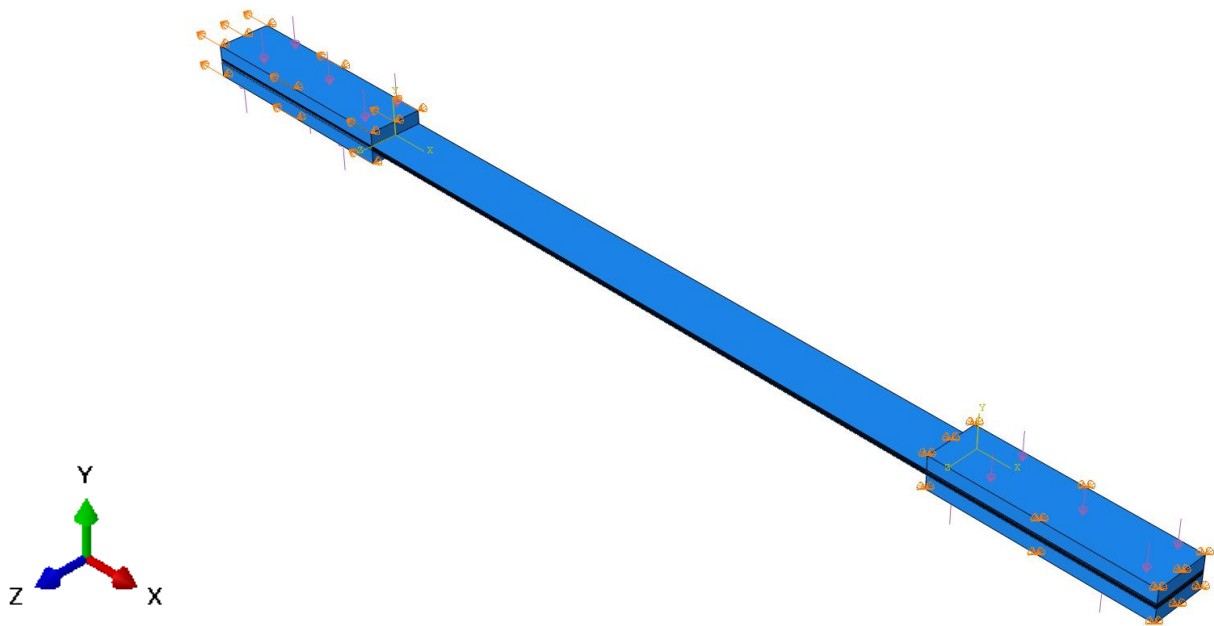


Figure 2.8: Load and Boundary Conditions on the tensile coupon

2.8 Step Outputs


A step was created with a type of static, general and the simulation was run for a time period of 60 s with the initial and maximum increment size of 1 and a minimum increment of 0.0006 . The maximum number of increments was set to be 100 . All the loads and boundary conditions were applied in this step in linear increments. Each unit time interval displays how the tensile coupon deforms at every second and how the stresses and strains are varied gradually.

Hence, a linear elastic analysis was carried out for the tensile tests and the results were analyzed for the different outputs that are required from the respective tests.

2.9 References


- [1] Carlsson, L. A., Adams, D. F., & Pipes, R. B. (2014). *Experimental characterization of advanced composite materials*. Boca Raton, FL: CRC Press.
- [2] Dr. Wenbin Yu. (2017) Multiscale Structural Mechanics. Wiley-Interscience. John Wiley & Sons, INC., Publication
- [3] W.D. Callister, Fundamentals of Materials Science Engineering, 5th ed. Wiley. (2001)
- [4] Lecompte, D., et al. 2006. Quality assessment of speckle patterns for digital image correlation. *Optics and Lasers in Engineering*. Vol 44, Issue 11. 1132-1145.
- [5] Rajan Jain, Peter Hong, Vasudha Kapre 6th September 2019, Friday, Lab 3- Tensile Test, Presentation. PPT. (2019)
- [6] Neha Shakelly, 26th August 2019, Wednesday, Micromechanical Analysis for Elastic Constants. PPT. (2019)

2.10.1 Arc-Resistant GP03 Fibre Glass sheet Data Sheet:



RÖCHLING

Glastic Composites



RÖCHLING

Glastic Composites

Grade UTR

Arc/Track & Flame Resistant Laminate

- 1,000 Minutes Track Resistance
- Electrically Insulating
- Highly Flame-Resistant
- Low Smoke & Smoke Toxicity
- UL® Recognized
- NEMA Grade GPO-3

Grade UTR is a fiberglass reinforced thermoset polyester material. It is available in sheet form as well as a wide selection of channel, angle, and tube sizes. These materials are the industry standard for flame and arc/track resistant electrical insulation. In addition, the excellent combination of high strength, flame resistance, and low smoke generation has given it application in many other areas such as transit and marine where safe, yet economical materials are required. Additional information and samples can be obtained through Röchling Glastic Composites Customer Service or your local authorized distributor.

Grade UTR


Hemo & Smoke Characteristics

UL Subject 94	0.94" & Thicker Less than 0.93"	UL 94	V0
Oxygen Index	%OI	D2663	39
Hemo Resistance			
Ignition Time	Min.	-	85
Burn Time	Min.	-	49
Flamed Test			
Hemo Spread		ASTM E 84/UL 723	25
Smoke Density			115
Fuel Contributed			0
Cone Calorimeter			
Time to Ignition	Sec.		100
Heat Rate of Heat Release	MW/m ²		180 S
Heat Release Rate @ 300 sec.	MW/m ²	ASTM E 1554	77.2
Caloric Content	MJ/kg		713
Average Smoke Eviction Area	m ² /kg		336.1
Hazard Panel Hemo Spread			
Specific Optical Density of Smoke		ASTM E 162	11
(Is @ 4.0 mm) (Average)		ASTM E667	
(Unit/cm) (Average)			
Composition of Smoke			
Material:			
Hydrogen Chloride			0
Aldehydes as HCHO			4
Ammonia			0
Carbon Monoxide		ppm	270
Carbon Dioxide			3,775
Oxides of Nitrogen as NO _x			10
Cyanides of KCN			0
Thermal Properties			
Coefficient of Thermal Expansion	In/in/°C x 10 ⁻⁵	ASTM D596	2
Thermal Conductivity	BTU/hr-ft ² /in ² /°F	ASTM C177	1.9

*Typical average values for 0.03" thick laminate.
Properties vary with material thickness and form.


All of the information, suggestions, and recommendations appearing in this prospectus and cover of the brochure have been prepared by Röchling Glastic Composites based on tested specimens and data submitted to the Bureau of Standards. The user must understand that the availability of any material described herein for the use contemplated, the manner of such use, and the results thereof will be determined by the user and are the responsibility of the user. THE INFORMATION CONTAINED HEREIN IS FOR INFORMATIONAL PURPOSES ONLY. IT DOES NOT CONSTITUTE AN OFFER OF ANY PRODUCT OR SERVICE. Röchling Glastic Composites does not warrant the accuracy of the information contained herein nor its suitability for any particular use or circumstances. We do not accept liability for accidents resulting from the use of our products.

Customer Support Department
Röchling Glastic Composites, Inc., P.O. Box 100
4000 Röchling Drive, Suite 100
Gastic Composites Laboratory, Inc.
Houston, Texas 77058-1000
©2000 Röchling Glastic Composites. All Rights Reserved. Printed in USA.



RÖCHLING

Glastic Composites



RÖCHLING

Glastic Composites

Grade UTR

Arc/Track & Flame Resistant Laminate

- 1,000 Minutes Track Resistance
- Electrically Insulating
- Highly Flame-Resistant
- Low Smoke & Smoke Toxicity
- UL® Recognized
- NEMA Grade GPO-3

Grade UTR is a fiberglass reinforced thermoset polyester material. It is available in sheet form as well as a wide selection of channel, angle, and tube sizes. These materials are the industry standard for flame and arc/track resistant electrical insulation. In addition, the excellent combination of high strength, flame resistance, and low smoke generation has given it application in many other areas such as transit and marine where safe, yet economical materials are required. Additional information and samples can be obtained through Röchling Glastic Composites Customer Service or your local authorized distributor.

Grade UTR

Low Profile Switchgear Cabinet - Interphase and end barriers are fabricated from Grade UTR laminate.

General Information	UNIT	Procedure	Typical Value*
Part Number			1491, 1494, 1497
Standard Color			White, Red, Black
NEMA Grade		NEMA L11	GPO-3
Mechanical Properties			
Tensile Strength	Psi	ASTM D638	7,800
Elongation Modulus	Psi X 10 ⁶	ASTM D638	1.7
Flexural Strength	Psi	ASTM D790	22,100
Flexural Modulus	Psi	ASTM D790	13,100
Compressive Strength	Psi	ASTM D695	33,100
Shear Strength	Psi	ASTM D732	11,600
200 Impact Strength (notched)	ft. lb./in.	ASTM D256	8.9
Water Absorption	% by wt.	ASTM D570	0.4
Specific Gravity	-	ASTM D792	1.81
Electrical Properties			
Electrical Strength - Perpendicular S/I in air	Vpm	ASTM D149	450
Electrical Strength - Perpendicular S/I in oil	Vpm	ASTM D149	584
Electrical Strength - Parallel S/S in oil	KV	ASTM D149	47
Arc Resistance	Sec.	ASTM D495	180
Inclined Plane Track Resistance - 1/8" thick	V	UL 766A	>1,000
EC Track Resistance (C11)	V	UL 766A	>500
UL High Voltage Track Rate	In./Min.	UL 766A	0
Permittivity, 60 Hz	-	ASTM D150	4.1
Dielectric Factor, 60 Hz	-	ASTM D150	4.1
Permittivity, MHz	-	ASTM D150	0.013
Dielectric Factor, MHz	-	ASTM D150	0.010
Insulation Resistance	Ohm x 10 ⁹	ASTM D257	3.1

2.10.2 Poisson's Ratio data:



Alro

Plastics



EXTREN®

FIBERGLASS STRUCTURAL SHAPES AND PLATE



Introduction

What you see below is not the erection of a steel structure. Rather, it is a structure being assembled using EXTREN® fiberglass structural members. Today, EXTREN® is replacing steel, aluminum, and wood in a wide variety of structural applications. Why? Because EXTREN® is a problem solving material. This brochure provides basic information about the EXTREN® product line and shows many examples of how EXTREN® provides long-term, cost effective structural solutions for end users in a variety of markets and applications.

The features of EXTREN® fiberglass structural shapes are readily translated into user benefits:

- Corrosion Resistant
- Low in Conductivity — Thermally and Electrically
- Nonmagnetic — Electromagnetic Transparency
- Lightweight — Weights 80% less than Steel
- High Strength
- Dimensional Stability
- Low Maintenance
- Custom Colors



Stronach's 388,000 sq. ft. Bristol, Virginia facility is the world's largest pollution operation.






2

Quality and Availability

Strongwell manufacturing facilities are ISO-9001:2008 certified. This ensures the utmost quality standards for producing EXTREME® structural shapes in a world class facility. A "first article" series of tests on each EXTREME® production run is designed to assure the end user that the structural members meet or exceed published minimum criteria. While distributors stock the most popular shapes of EXTREME® for immediate delivery to their customers, Strongwell also maintains a large inventory to service distributors and prevent long lead times to end users.



Left: Strongwell can perform incoming resin tests to verify the suppliers' conformance to specified requirements.

Right: Strongwell's Techno-Matrix™ Test Chamber is a state-of-the-art piece of equipment.

Bottom: Strongwell's laboratory and research facility is large, well-equipped and professionally staffed.



Properties

MECHANICAL												
D638	Tensile Stress, LW	psi	30,000	30,000	30,000	20,000	20,000	20,000	20,000	20,000	20,000	20,000
	Tensile ¹	267	267	158	158	158	158	158	158	158	158	
D638	Tensile Stress, CW	psi	7,000	7,000	7,500	10,000	7,500	10,000	7,500	10,000	10,000	
	Tensile ¹	413	413	517	517	517	517	517	517	517	517	
D638	Tensile Modulus, LW	10 ⁶ psi	2.5	2.5	2.5	1.8	1.8	1.8	1.8	1.8	1.8	
	Tensile ¹	172	172	172	172	172	172	172	172	172	172	
D638	Tensile Modulus, CW	10 ⁶ psi	0.8	0.8	0.7	0.9	1.0	1.0	1.0	1.0	1.0	
	Tensile ¹	552	552	483	521	525	589	538	585	585	585	
D695	Compressive Stress, LW	psi	30,000	30,000	24,000	24,000	24,000	24,000	24,000	24,000	24,000	
	Compressive ¹	267	267	165	165	165	165	165	165	165	165	
D695	Compressive Stress, CW	psi	15,000	15,000	15,500	15,500	20,000	15,500	17,500	17,500	17,500	
	Compressive ¹	163	119	107	114	138	114	121	121	121	121	
D695	Compressive Modulus, LW	10 ⁶ psi	2.5	2.5	1.8	1.8	1.8	1.8	1.8	1.8	1.8	
	Compressive ¹	552	552	483	521	525	589	538	585	585	585	
D695	Compressive Modulus, CW	10 ⁶ psi	0.8	0.8	0.7	0.9	1.0	1.0	1.0	1.0	1.0	
	Compressive ¹	267	267	165	165	165	165	165	165	165	165	
D790	Flexural Stress, LW	psi	30,000	30,000	24,000	24,000	24,000	24,000	24,000	24,000	24,000	
	Flexural ¹	267	267	165	165	165	165	165	165	165	165	
D790	Flexural Stress, CW	psi	10,000	10,000	10,000	13,000	17,000	10,000	13,000	17,000	17,000	
	Flexural ¹	58.9	58.9	58.9	86.5	117	68.9	86.5	117	117	117	
D790	Flexural Modulus, LW	10 ⁶ psi	1.6	1.6	1.1	1.1	1.1	1.1	1.1	1.1	1.1	
	Flexural ¹	111.9	111.9	79.8	79.8	65.6	79.8	65.6	79.8	65.6	65.6	
D790	Flexural Modulus, CW	10 ⁶ psi	0.8	0.8	0.8	0.8	1.3	0.8	0.8	1.3	1.3	
	Flexural ¹	552	552	552	552	552	836	551	551	836	836	
W 4 x 13	Modulus of Elasticity Ⓢ	10 ⁶ psi	2.6	2.6	2.6	2.6	2.6	2.6	2.6	2.6	2.6	
	Modulus of Elasticity: W 4 x 13 shapes > 4"	10 ⁶ psi	17.9	19.3	19.3	19.3	19.3	19.3	19.3	19.3	19.3	
W 6 x 15	Modulus of Elasticity: W 6 x 15 shapes > 100mm	10 ⁶ psi	2.5	2.5	2.5	2.5	2.5	2.5	2.5	2.5	2.5	
	Modulus of Elasticity: W 6 x 15 shapes > 100mm	10 ⁶ psi	17.2	17.2	17.2	17.2	17.2	17.2	17.2	17.2	17.2	
S 12 x 19	Shear Modulus, LW Ⓢ	10 ⁶ psi	0.825	0.825	0.825	0.825	0.825	0.825	0.825	0.825	0.825	
	Shear Modulus, CW Ⓢ	10 ⁶ psi	2.58	2.58	2.58	2.58	2.58	2.58	2.58	2.58	2.58	
C2044	Short Beam Shear, LW Ⓢ	psi	4,500	4,500	4,500	4,500	4,500	4,500	4,500	4,500	4,500	
	Short Beam Shear, CW Ⓢ	psi	1,500	1,500	1,500	1,500	1,500	1,500	1,500	1,500	1,500	
D963	Bearing Stress, LW	psi	30,000	30,000	32,000	32,000	32,000	32,000	32,000	32,000	32,000	
	Bearing ¹	267	267	267	220.6	221	221	221	221	221	221	
C1019	Poisson's Ratio, LW Ⓢ	in/in	0.33	0.33	0.31	0.31	0.31	0.32	0.32	0.32	0.32	
	Poisson's Ratio, CW Ⓢ	in/in	0.30	0.30	0.30	0.30	0.30	0.30	0.30	0.30	0.30	
I 10 x 15.3	Notched Irod Impact, LW	ft-lb/in	25	25	15	10	10	15	10	10	10	
	Notched Irod Impact, LW	ft-lb/in	133	133	81	53	53	81	53	53	53	
I 10 x 15.3	Notched Irod Impact, CW	ft-lb/in	4	4	5	5	5	5	5	5	5	
	Notched Irod Impact, CW	ft-lb/in	214	214	267	267	267	267	267	267	267	

PHYSICAL

Bend Hardness	psi	45	45	45	45	45	45	45	45	45	45	45
24 hr Water Absorption Ⓢ	% Max	0.6	0.6	0.6	0.6	0.6	0.6	0.6	0.6	0.6	0.6	0.6
Density	lb/in ³	0.023	0.023	0.023	0.023	0.023	0.023	0.023	0.023	0.023	0.023	0.023
Coefficient of Thermal Expansion, LW Ⓢ	10 ⁻⁶ in/in-°F	1.72-1.84	1.72-1.84	1.72-1.84	1.72-1.84	1.72-1.84	1.72-1.84	1.72-1.84	1.72-1.84	1.72-1.84	1.72-1.84	1.72-1.84
Coefficient of Thermal Expansion, LW Ⓢ	10 ⁻⁶ in/in-°C	3.1	3.1	3.1	3.1	3.1	3.1	3.1	3.1	3.1	3.1	3.1
Thermal Conductivity Ⓢ	BTU-in/hr-ft ² -°F	4	4	4	4	4	4	4	4	4	4	4

All values are minimum ultimate properties from coupon tests except as noted.

Ⓢ This value is determined from full section sample beam bending of EXTREME® structural shapes.

Ⓢ The Shear Modulus value has been determined from tests with full sections of EXTREME® structural shapes. (See Strongwell's Design Manual for further information.)

Ⓢ Values would be 50 if the surface were not sand blasted.

Ⓢ Values are determined from standard Charpy impact tests on standard Charpy impact test specimens.

Ⓢ Values apply to Series 525 and 525.

Ⓢ Measured as a percentage maximum by weight.

Ⓢ Span to depth ratio of 3:1. EXTREME® angles will have a minimum value of 4000 psi and the LW shapes are tested in the web.

Ⓢ Typical values because these are shape and composite dependent tests.

LW — Lengthwise
CW — Crosswise
PL — Perpendicular to laminate face
NLT — Not Tested

2.10.3 Images

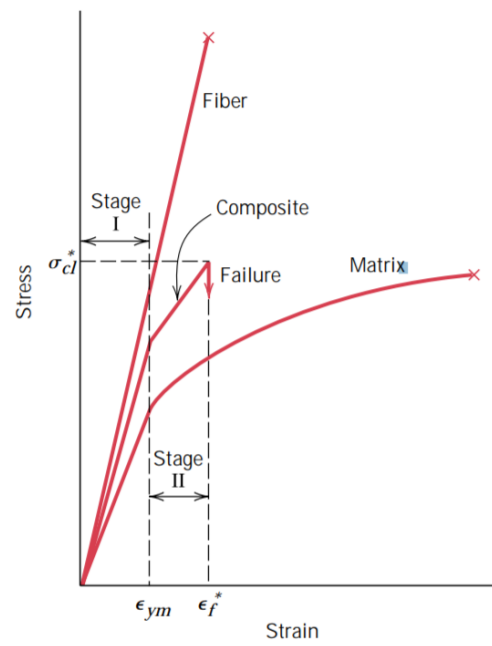


Figure 2.9: Mechanical behavior of composites

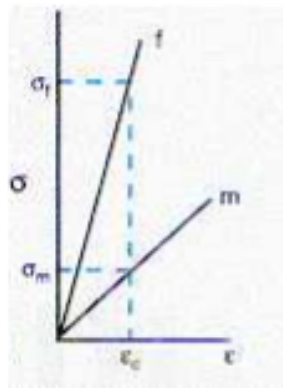


Figure 2.10: Stress-strain curve for matrix and fibers

3. MODELING OF SPECIMEN FOR CTE TEST

3.1 Introduction

3.1.1 Coefficient of Thermal Expansion (CTE)

The coefficient of thermal expansion (CTE) is a material property that is indicative of the extent to which a material expands upon heating. It is related to the binding energy of the material. Larger the bonding energy, lower the CTE of the material. The thermal expansion is due to the asymmetric curvature of the potential energy trough as shown in Figure 1a. It is also reflected by an increase in the average interatomic distance as shown in Figure 1b.

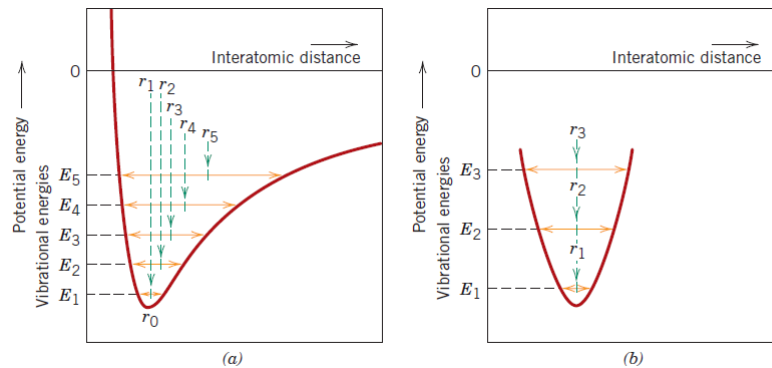


Figure 3.1: Potential Energy Vs interatomic distance

(Image from Callister. Materials Science and Engineering: An Introduction. 7th Ed)

For polymers, the magnitude of CTE reduces with the increase in crosslinking. The lowest CTE is found in the thermosetting network of polymers where the covalent bonds are strong. Figure 2 shows the different kinds of cross-linking in polymers.

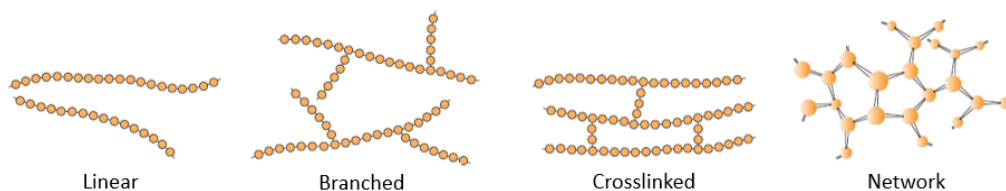


Figure 3.2: Different types of cross-linking in polymers

(Image from Callister. Materials Science and Engineering: An Introduction. 7th Ed)

Composites are used in the temperature ranges between -50 °C to 170 °C in the aerospace industry. Hence, it is very important to analyze their properties between wide ranges of temperatures. CTE is often defined by the glass transition temperatures of the material. Glass transition temperature of a material can be defined as the temperature, below which the physical properties of plastics change to those of a glassy or crystalline state. The material is hard and brittle below the glass transition temperature and it is soft, flexible and in a rubbery state above the glass transition temperature. Figure 3 shows the variation of the physical property of the material with respect to temperature.

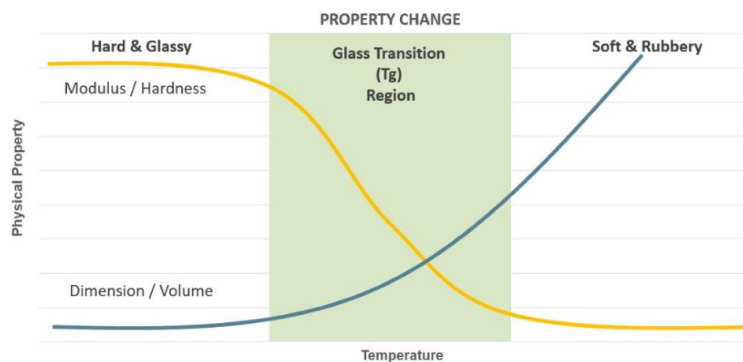


Figure 3.3: Variation of the physical property with temperature

(Image from Callister. Materials Science and Engineering: An Introduction. 7th Ed)

3.1.2 Constitutive relations for thermal expansion

The thermal expansion of a body is defined as the change in dimensions of it as a result of the change in temperature. There are many structures that undergo a change in temperature as they are subjected to different conditions as a part of their application. The coefficient of thermal expansion of a material is defined as follows:

$$\alpha = \frac{\Delta \epsilon}{\Delta T}$$

Where $\Delta \epsilon$ is the increment of strain for an unconstrained material that is subjected to a temperature change of ΔT . Hence, for small temperature ranges, thermal expansion of uniform linear objects is proportional to the temperature change. If the value of CTE of material is negative, it implies that it contracts upon heating. Composite laminae are orthotropic and hence, the in-plane thermal deformation in the orthotropic composite lamina can be given by:

$$\alpha_1 = \frac{\Delta \varepsilon_1}{\Delta T}; \quad \alpha_2 = \frac{\Delta \varepsilon_2}{\Delta T}$$

Where $\Delta \varepsilon_1$ and $\Delta \varepsilon_2$ are the thermally induced strains in the principal material directions. Hyer and Wass determined a self-consistent field relationship for CTE which is given by the following equations. Here, the fiber(f) and matrix(m) properties are used to determine the values of CTE in the principal material coordinate system.

$$\alpha_1 = \frac{\alpha_{1f}E_{1f}V_f + \alpha_m E_m V_m}{E_{1f}V_f + E_m V_m}$$

$$\alpha_2 = \alpha_3 = (\alpha_{2f} + \nu_{12f}\alpha_{1f})V_f + \alpha_m(1 + \nu_m)(1 - V_f) - (\nu_{12f}V_f + \nu_m V_m) \left[\frac{\alpha_{1f}E_{1f}V_f + \alpha_m E_m V_m}{E_{1f}V_f + E_m V_m} \right]$$

The composite laminates exhibit transversely isotropic CTEs and its value in the fiber direction is close to zero. The CTE of the matrix phase is restricted by the fibers in the fiber direction. The laminates expand more in the transverse direction as the CTE is unconstrained by the fibers in the transverse direction.

3.1.3 Residual stresses in composite laminates

Residual stresses can be defined as the internal stress distributions that are locked into the material. They are present even after the external loading forces have been removed. These stresses can be caused by thermal stresses and chemical shrinkage in composites and are a result of the material obtaining equilibrium after it has undergone plastic deformation. A unidirectional laminate has no residual stresses in the ply-scale as there is no inhibition to its desire to expand in the transverse direction, whereas, in a cross-ply laminate, the expansion of one layer is restrained by its neighboring layer that desires to expand in the opposite direction. This leads to the formation of stresses between the layers. Figure 4 shows the constrained and unconstrained expansions in unidirectional ply and cross-ply laminates respectively.

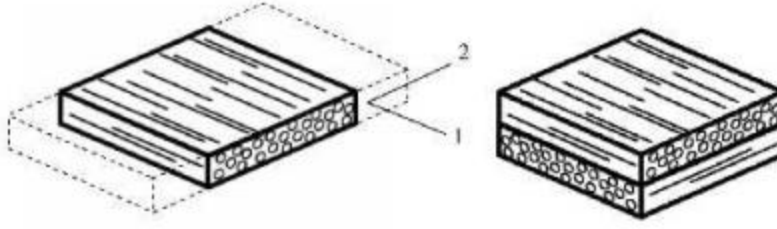


Figure 3.4: Unconstrained and constrained expansion in unidirectional and cross-ply laminates
(Image from Multiscale Structural Mechanics (2017))

3.1.4 Coefficient of Thermal Expansion for composite laminates

The coefficient of thermal expansion in a composite laminate can be determined theoretically by using composite laminate plate theory. It assumes the thickness of the laminate is much smaller than its length or width, which allows the elimination of out of plane shear and strain. The stiffness form of the laminate constitutive relations is written as follows:

$$\begin{bmatrix} N \\ M \end{bmatrix} = \begin{bmatrix} A & B \\ B & D \end{bmatrix} \begin{bmatrix} \varepsilon^0 \\ \kappa \end{bmatrix}$$

Where N is the force per unit width, M is the laminate resultant moment per unit width, ε^0 are the mid-plane strains κ are the laminate mid-plane curvatures. The following equation represents the compliance form of the laminate constitutive equations as follows:

$$\begin{bmatrix} \varepsilon^0 \\ \kappa \end{bmatrix} = \begin{bmatrix} a & b \\ b & d \end{bmatrix} \begin{bmatrix} N \\ M \end{bmatrix}$$

For a symmetric and balanced laminate, $b = c = 0$ and hence, the equation reduces to the following:

$$\begin{bmatrix} \varepsilon^0 \\ \kappa \end{bmatrix} = \begin{bmatrix} a & 0 \\ 0 & d \end{bmatrix} \begin{bmatrix} N^T \\ M^T \end{bmatrix}$$

For a thermal analysis, N^T and M^T are thermally induced forces and moments. In this experiment, $M^T = 0$. Hence, the equation is reduced to the following:

$$[\varepsilon^0] = [a][N^T]$$

$$[\kappa] = [0]$$

$$\begin{bmatrix} \varepsilon_x \\ \varepsilon_y \\ \gamma_{xy} \end{bmatrix} = \begin{bmatrix} a_{11} & a_{12} & 0 \\ a_{12} & a_{22} & 0 \\ 0 & 0 & a_{66} \end{bmatrix} \begin{bmatrix} N_x^T \\ N_y^T \\ 0 \end{bmatrix}$$

$\gamma_{xy} = 0$ shows that the balanced laminate will not deform in shear due to the temperature change.

Hence, reducing to the in-plane terms, we get the following relation:

$$\begin{bmatrix} \varepsilon_x^0 \\ \varepsilon_y^0 \end{bmatrix} = \begin{bmatrix} A_{11} & A_{12} \\ A_{12} & A_{22} \end{bmatrix}^{-1} \begin{bmatrix} N_x^T \\ N_y^T \end{bmatrix}$$

Combining the equation with the relation of the CTE, $L = L_0(1 + \alpha\Delta T)$, we get the following relation:

$$\begin{bmatrix} \alpha_x \Delta T \\ \alpha_y \Delta T \end{bmatrix} = \begin{bmatrix} A_{11} & A_{12} \\ A_{12} & A_{22} \end{bmatrix}^{-1} \begin{bmatrix} N_x^T \\ N_y^T \end{bmatrix}$$

$$\alpha_x = \frac{a_{11}N_x^T + a_{12}N_y^T}{\Delta T}$$

$$\alpha_y = \frac{a_{12}N_x^T + a_{22}N_y^T}{\Delta T}$$

3.2 Overview of the experimental procedure

The procedure carried out in this experiment is not the ASTM standard and the most commonly used ASTM standards used to estimate the coefficient of thermal expansion are D696 and E228 which use a push rod dilatometer for a temperature range of -30 to 30 °C and -180 to 900 °C respectively. E289 is another method using an interferometer which is a non-contact and absolute measurement that is suitable for low CTEs as in the case of a fiber. The precision is greater than 40 nm/m/K. Figure 16 (In Appendix) shows the pushrod dilatometer that is used for the determination of CTE with ASTM standards.

3.2.1 Set-up of the experiment

The samples ($[\pm 30]_{2s}$ laminates) were prepared and speckled using the high-temperature paint. Holes of two sizes of diameter, $\frac{1}{8}$ " (3.175 mm) and $\frac{1}{4}$ " (6.35 mm) were drilled on the laminates. Only one layer of the paint was applied as the CTE of the material is quite low and if more layers of paint are applied, we would measure the CTE along with the CTE of the paint. Figure 5 shows the speckled samples that were used for the CTE analysis. INSTEC temperature controller was used to create the recipe and the sample was placed in the set-up to conduct the analysis. DIC set-

up was used for obtaining the 2D strain on the specimen. Only one camera was used in this case and the aperture was set in such a way that the displacement of the sample is perpendicular to it. It is ensured that the specimen has proper lighting and focus and the program is run with the set recipe. Figure 6b shows the extent of the focus of the specimen. It can be seen that the specimen is properly focused for the analysis.

Figure 7 shows the INSTEC mk2000 temperature controller that was used to conduct the analysis. The temperature stability is ± 0.01 °C and it has a temperature resolution of ± 0.1 °C. Figure 7b shows the experimental set-up and the apparatus used for CTE analysis.

The DIC images were taken every 15 seconds and the temperature data is taken about once every second and is automatically written into a file. Figure 6b shows the DIC set focusing on the sample. An area of interest is chosen on the DIC images as shown in Figure 8. The area is partitioned into 50 subsets and the strain data was averaged within each subset. All the DIC images are analyzed according to the area of interest and the strain is collected into a single data file. Figure 9 shows the variation of X for the cooling cycle and the variation of Y for the heating cycle on the specimen with a hole diameter of 3.683 mm. To avoid the free-edge effects around the hole, the region surrounding it is removed during the analysis.

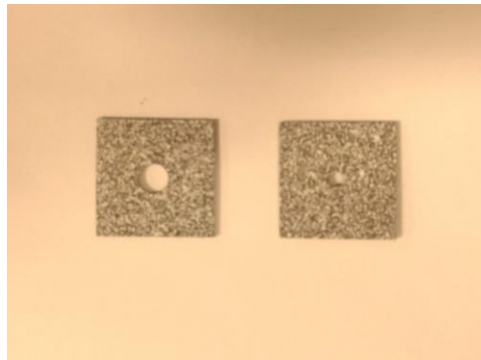
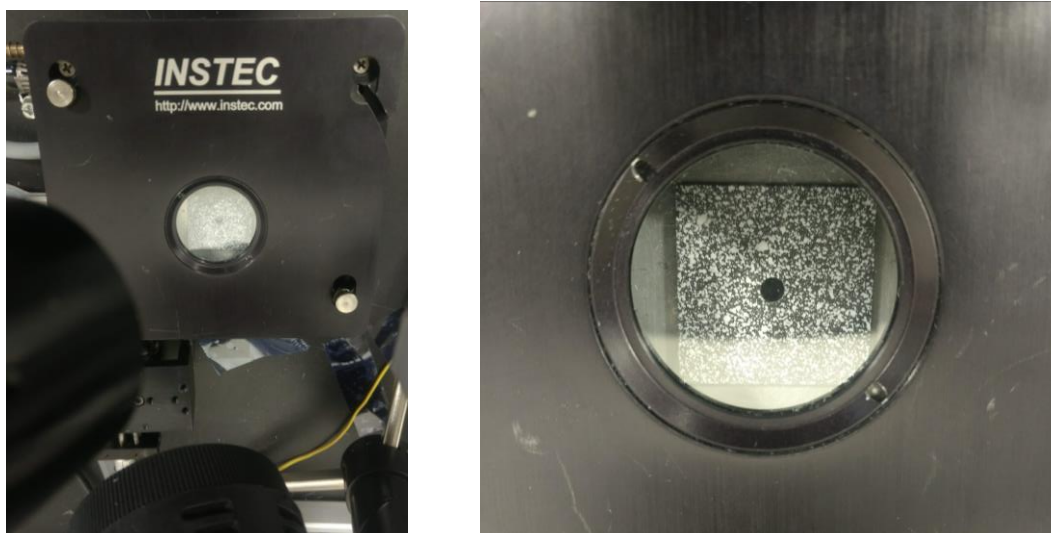
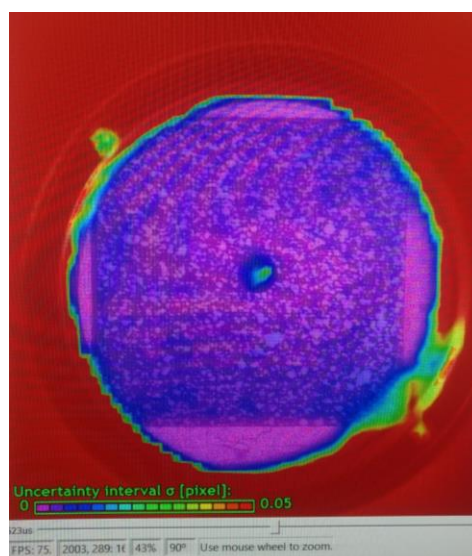


Figure 3.5: Speckled specimen before analysis



(a) Placement of the sample

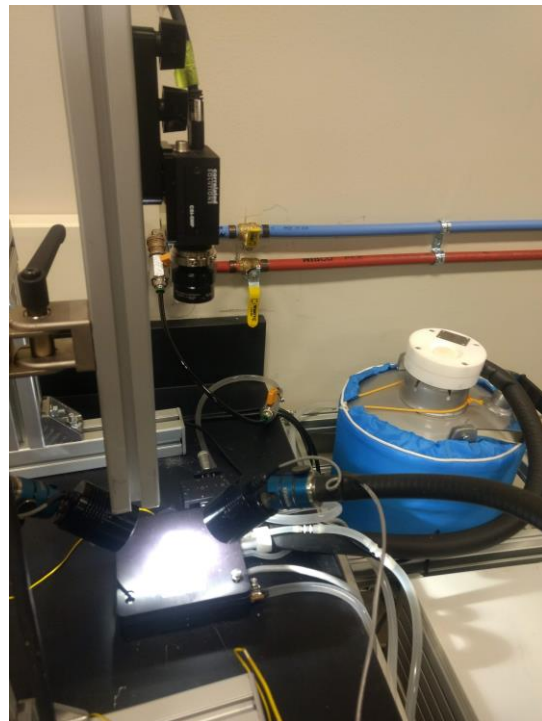


(b) Focus of sample in DIC

Figure 3.6: Set-up of the specimen in the apparatus



(a) INSTEC mk2000 temperature controller



(b) Experimental apparatus

Figure 3.7: Apparatus

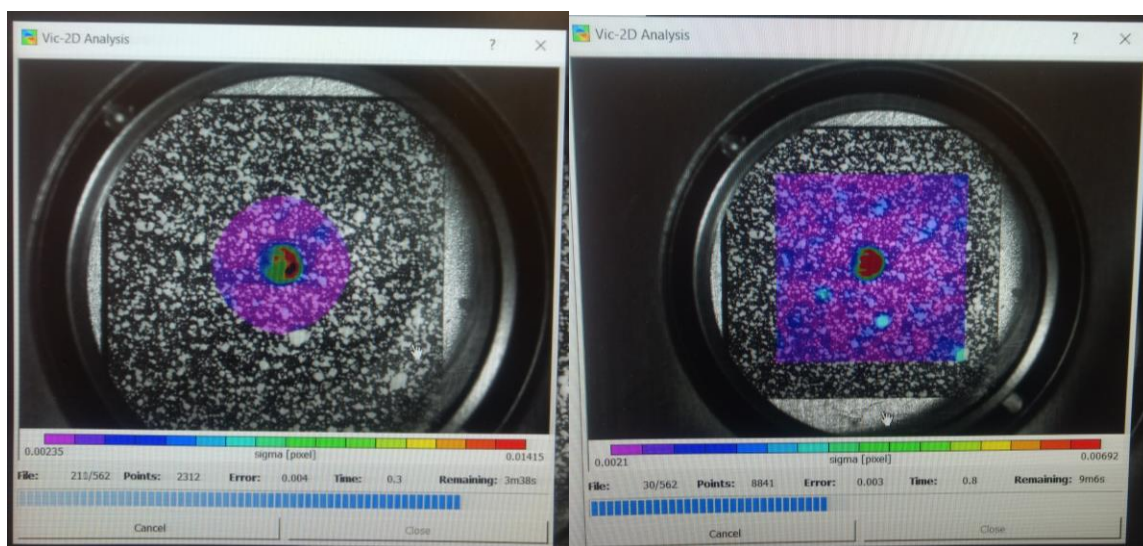


Figure 3.8: DIC analysis of the sample with two different regions of interest

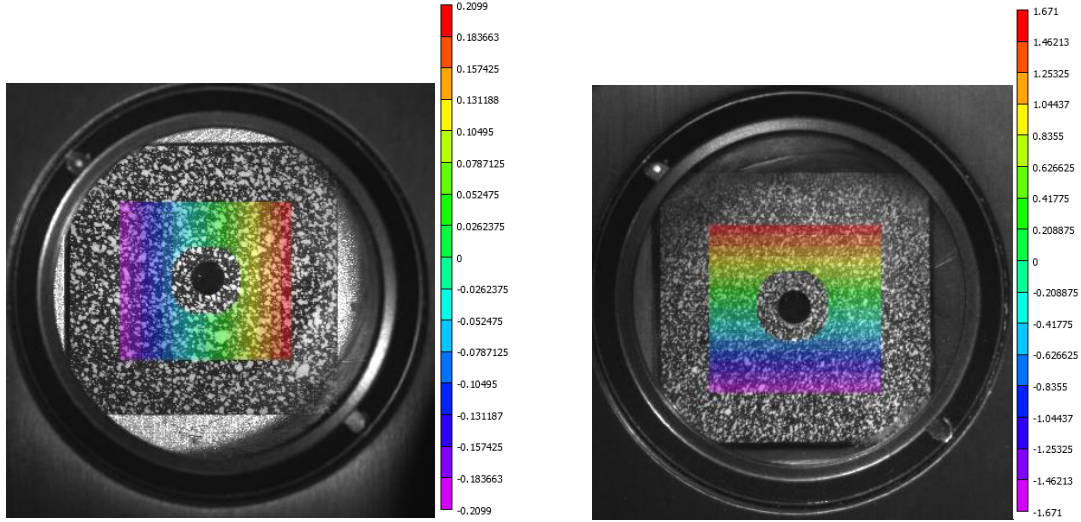


Figure 3.9: X and Y deformation on the sample with a hole diameter 3.683 mm for cooling (left) and heating (right) cycles respectively with a maximum temperature of 100°C

The samples were heated or cooled with a series of steps with two stages. Stage 1 was where they were heated or cooled 10 degrees at a rate of 4 °C/min and stage 2 was where they were held at the same temperature for 5 minutes. In the heating cycle, the samples were heated from 30 °C to 180 °C and brought back to 30 °C. In the cooling cycle, the samples were cooled from 20 °C to -50 °C and brought back to 20 °C.

3.2.2 Prediction of CTE from cdmHUB data

Figure 11 shows the properties obtained from cdmHUB for the $[\pm 30]_{2s}$ laminate. It can be observed that the CTE is predicted to be negative in the longitudinal direction and positive in the transverse directions. This implies that the sample shrinks in the longitudinal direction when it is heated.

```

Laminate Properties:
Ex (Pa)
4.2043e+10
Ey (Pa)
9.01145e+09
Gxy (Pa)
2.6534e+10
nuxy
1.48
alphax
-4.5e-06
alphay
2.41e-05
alphaxxy
0

```

Figure 3.10: Laminate properties from cdmHUB for $[\pm 30]_{2s}$

3.3 Comparison of cdmHUB results with experimental data

Tables 1 shows the comparison of the CTE data from the experiment with the results obtained from cdmHUB. The average values of α_1 was obtained to be $-8.83 \mu\epsilon/^\circ\text{C}$ and $-2.75 \mu\epsilon/^\circ\text{C}$ for heating and cooling respectively. Similarly, the average values of α_2 was obtained to be $31.95 \mu\epsilon/^\circ\text{C}$ and $18.5 \mu\epsilon/^\circ\text{C}$ for heating and cooling respectively. The average value of the heating and cooling cycles was obtained to be close to the experiment.

Table 3.1: Comparison of CTE data for $[\pm 30]_{2s}$

Laminate CTE	Analytical ($\mu\epsilon/^\circ\text{C}$)	Experiment heating cycle ($\mu\epsilon/^\circ\text{C}$)	Experiment cooling cycle ($\mu\epsilon/^\circ\text{C}$)	Average from experiment ($\mu\epsilon/^\circ\text{C}$)
α_x	-4.5	-8.83	-2.75	-5.79
α_y	24.1	31.95	18.5	25.23

3.4 Specimen geometry and material properties

For the CTE tests that are discussed in this document, 8-plyed composite plates with a stacking sequence of $[\pm 30]_{2s}$ were used. The specimens were manufactured in such a way that they have dimensions of a square with a side of one-inch (25.4 mm). Figure 12 shows the geometry of the CTE specimen modeled to full-scale with holes of two sizes of diameter $[1/$

8" (3.175 mm) and ¼" (6.35 mm)] cut through them. The ply thickness was set to be 0.14224 mm as obtained from the physical measurements of the test specimen. They were modeled as a squared specimen with a side of one-inch (25.4 mm).

The input of lamina material properties for the CTE specimen is the same as the tensile test specimen. However, in the definition of material behavior, a tab for expansion was also created defining the values of Co-efficient of Thermal Expansion (CTE) for the orthotropic lamina at a reference temperature of 20° C. The values of lamina CTE that were given as input are as follows:

$$\alpha_{11} = 0.898 \mu\epsilon/^{\circ}\text{C}, \alpha_{22} = \alpha_{33} = 38 \mu\epsilon/^{\circ}\text{C}$$

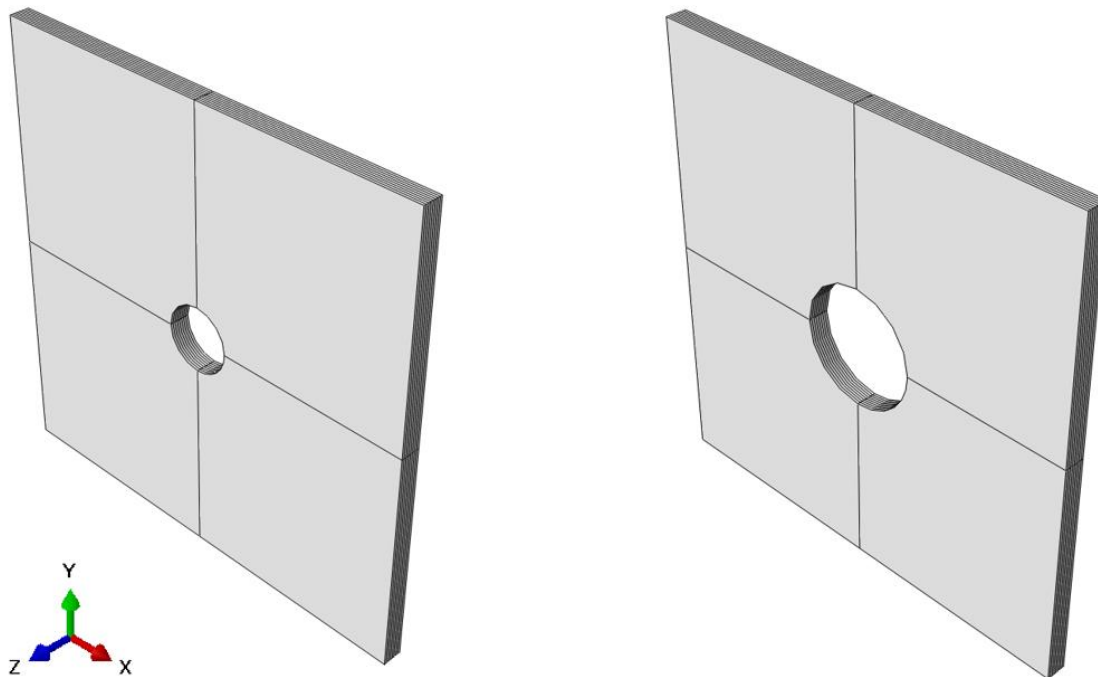


Figure 3.11: Geometry of the CTE specimen, 1/8-inch hole diameter (Left), 1/4-inch hole diameter (Right)

3.5 Mesh Parameters and convergence studies

A structured mesh with a mesh type of an 8-node linear brick, reduced integration, hourglass control with a global size of 0.3 was used to mesh the part. Few edges were seeded by assigning them a certain number of nodes for more accuracy of solutions at those locations. Each ply was seeded with 4 elements across the thickness. The region around the hole was seeded with 40 elements along the circumference. Figure 13 shows the mesh on the CTE specimen with two

different sizes of hole diameter [$1/8''$ (3.175 mm) and $1/4''$ (6.35 mm)] through them. The former and the latter parts have a total of 216800 and 195968 elements on them respectively. Different sections were created on the part (as shown in Figure 12) in order to get a structured mesh around the hole.

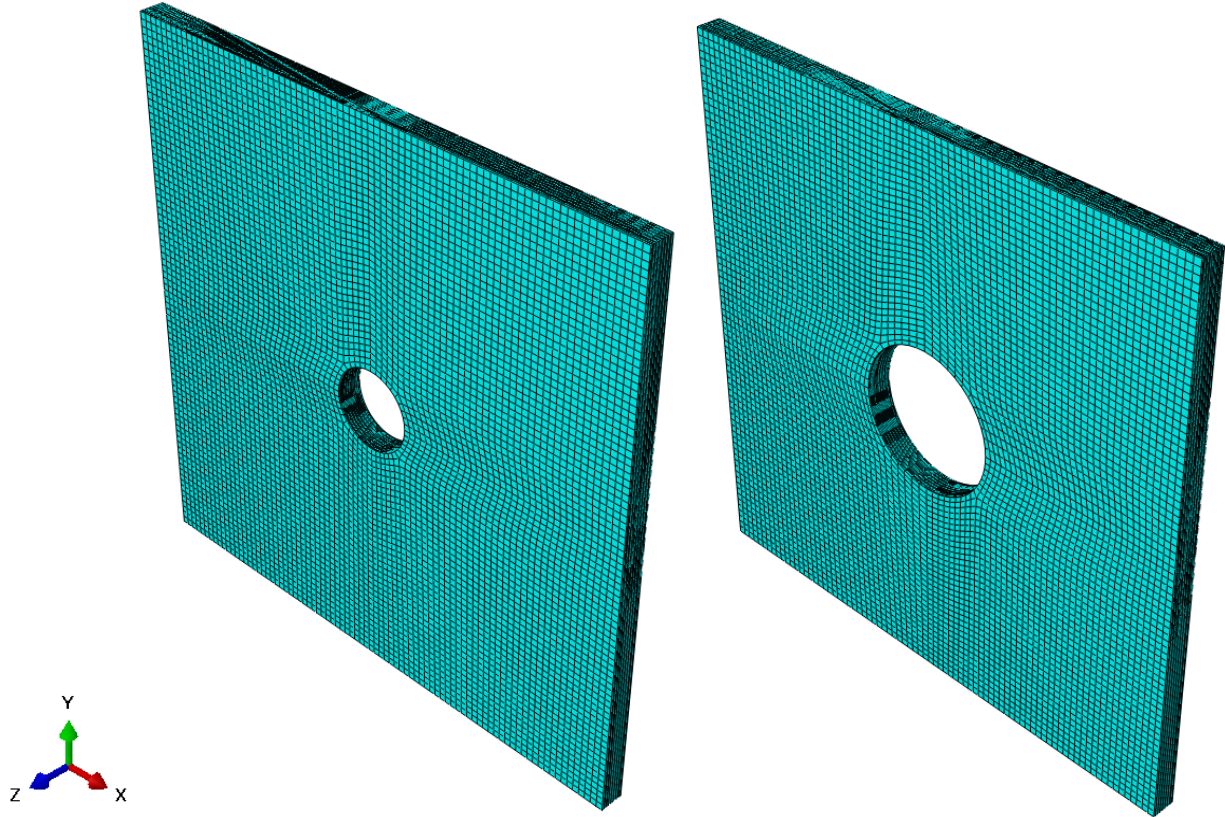


Figure 3.12: Mesh on the CTE part geometries

A mesh convergence study was carried out for the parameters described in Table 2. Figure 14 also shows the variation of these parameters with the number of elements in the model. The number of elements is varied depending on the global mesh size that was assigned to the geometry. This study was done to check the variation of parameters with the increase in the number of elements in the geometry. Hence, the computational time can be significantly reduced when the number of elements is reduced without significantly reducing the parameters that are studied. Two plots are made for mesh convergence because of the difference in the scale and to make the plots more defined.

Table 3.2: Mesh convergence study data for CTE specimen

Mesh Size	Number of elements	Number of nodes	Max S. Mises (MPa)	Max S11 (MPa)	Max E22
0.1	1899008	1975512	3787.9	1150.7	0.216
0.2	476800	500610	3786.2	1149.2	0.214
0.3	216800	229746	3785	1148	0.213
0.4	129152	138072	3672.4	1042.5	0.204
0.5	79360	85800	3467	984.6	0.192
0.6	55808	60984	3258	911.3	0.175
0.7	42112	46464	3174	900.6	0.1742
0.8	33408	37224	3125	889.1	0.1659
0.9	25728	29040	2987	876.4	0.1634
1	22272	25344	2935	863.7	0.1621

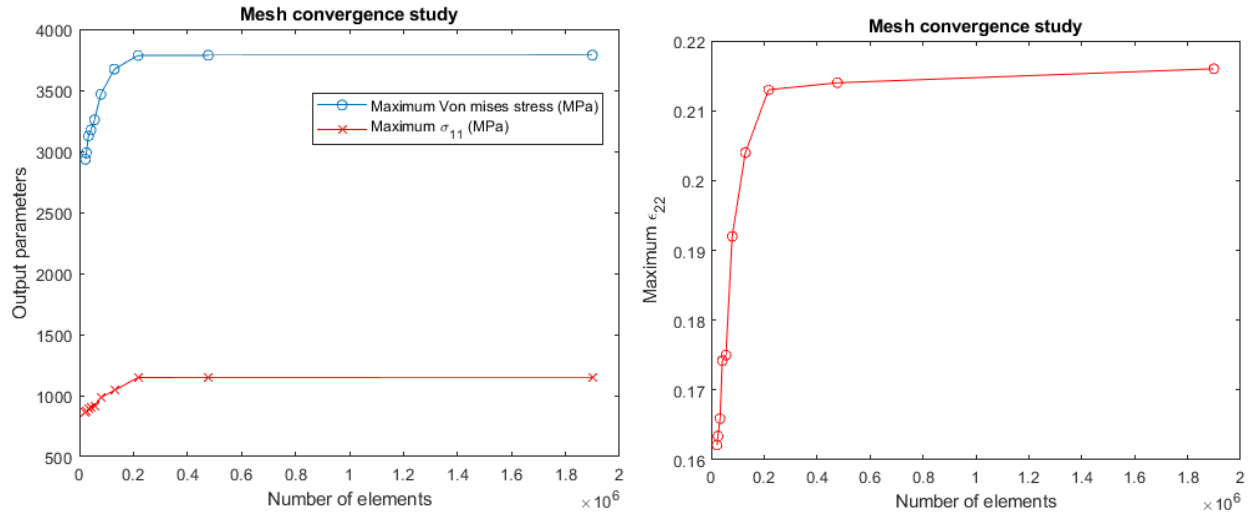


Figure 3.13: Mesh convergence study plots for CTE specimen

3.6 Boundary and Load conditions

As described in the experimental procedure section, the samples were placed in INSTEC mk2000 temperature controller to conduct the tests. They were modeled ensuring that the boundary conditions are the same as the test apparatus. In order to avoid free body translation, the two mutually perpendicular midplanes of the specimen were constrained from the motion along X and

Y directions respectively. The bottom face was constrained from movement along the Z direction. Figure 15 shows the boundary conditions applied to the specimen.

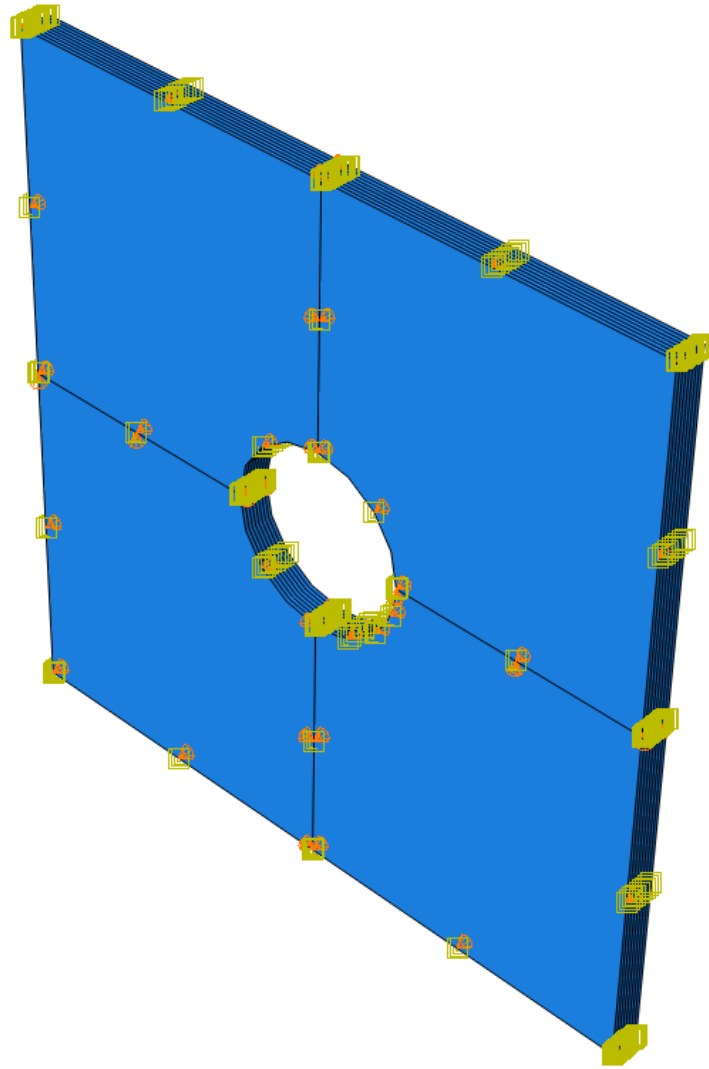


Figure 3.14: Boundary conditions on CTE specimen

For applying the temperature boundary conditions on the specimen, predefined fields were created for both the initial conditions and for the temperature ramp to be applied in the step. The predefined field was temperature and it was set to be constant throughout the region that contained the specimen. The initial value of the temperature was set to be 30°C for the heating cycles and 20°C for the cooling cycles. The magnitudes of temperature in heating and cooling ramps were given as an amplitude as shown in Figure 16. The ramp was an increase or decrease of 10°C at a rate of

$4^{\circ}\text{C}/\text{min}$ and the specimen was held at that temperature for 5 minutes. The maximum temperature in the heating cycle was 180°C and the minimum temperature in the cooling cycle was -100°C according to the limitations of the experimental apparatus. The heating cycle has a total time period of 13200 s and the cooling cycle has a total time period of 10500 s. For the first half of these cycles, the temperature is ramped to reach the maximum or the minimum value and in the second half, it is brought back to room temperature. Simulations were also carried out for the cooling cycle with a minimum temperature of -180°C . This was done to compare the variation of deformation between 180°C and -180°C since there is no limitation on the minimum temperature in Abaqus.

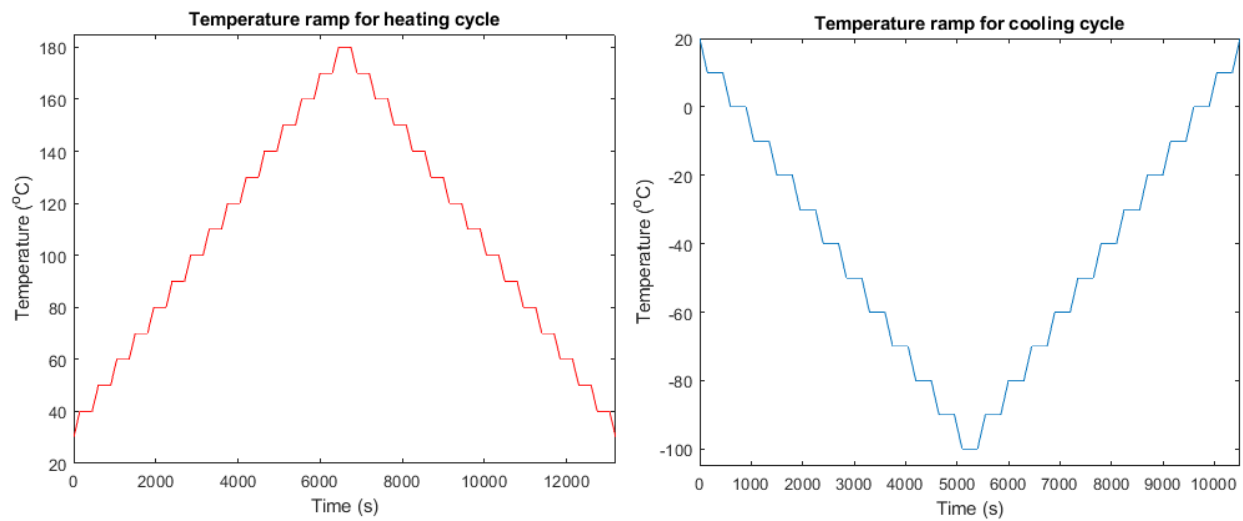


Figure 3.15: Load and Boundary Conditions on the tensile coupon

3.7 Step Outputs

A step was created with a type of static, general and the simulation was run for a time period of 1s with the initial and maximum increment size of 1 and a minimum increment of $1\text{e-}5$. The maximum number of increments was set to be 100. All the loads and boundary conditions were applied in this step in linear increments. The whole analysis was carried out in this single step as the main output required was the final deformation of the laminate and not on how it deforms for every unit time interval.

3.8 References

- [1] Carlsson, L. A., Adams, D. F., & Pipes, R. B. (2014). *Experimental characterization of advanced composite materials*. Boca Raton, FL: CRC Press.
- [2] Dr. Wenbin Yu. (2017) *Multiscale Structural Mechanics*. Wiley-Interscience. John Wiley & Sons, INC., Publication
- [3] Brian Seekatz, Zane Smith, 11th October 2019, Friday, Lab 8- Lamina Thermal Expansion, Presentation, PPT. (2019).
- [4] Dr. Byron Pipes, 30th September 2019, Monday, CTE of Lamina and Laminates, Presentation, PPT. (2019).
- [5] Daw, Joshua & Rempe, Joy & Knudson, D. & Condie, K. & Crepeau, John. (2008). Viability of Pushrod Dilatometry Techniques for High Temperature In-Pile Measurements. 10.2172/926333.
- [6] Callister, W. D. (2006). *Materials science and engineering: An introduction*. 7th Ed. New York: John Wiley & Sons.
- [7] Andrew Sarnowski, Philip Steckler, 18th October 2019, Friday, Lab 9- Laminate Coefficient of Thermal Expansion, Presentation, PPT. (2019).
- [8] Dr. Byron Pipes, 30th September 2019, Monday, CTE of Lamina and Laminates, Presentation, PPT. (2019).

3.9 Appendix

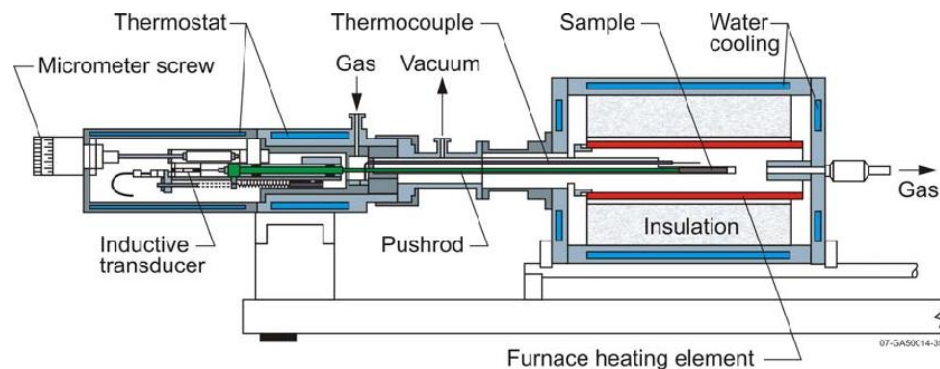


Figure 3.16: Pushrod dilatometer

4. OFF AXIS TENSION

4.1 Introduction

4.1.1 Analysis of shear strength

In the characterization of a composite laminate, it is very important to analyze its shear strength. This is because most of the applications of the composite materials are not in the axial loading direction and the overall strength of the composite material depends on the shear strength of the material. Typically, $[\pm 45]_s$ laminates were used to calculate the shear properties of the material. But, the fracture mechanism in these laminates is quite difficult to analyze due to the complex interactions between the $+45^\circ$ and -45° plies which causes difficulty in defining locations where the ply failure may happen. For this reason, the off-axis tensile test is used where the laminates are designed to have failures that are shear-dominated.

The plane stress reduced stiffness and compliance matrices in the laminate coordinate system are as follows:

$$\begin{bmatrix} \sigma_1 \\ \sigma_2 \\ \tau_{12} \end{bmatrix} = \begin{bmatrix} m^2 & n^2 & 2mn \\ n^2 & m^2 & -2mn \\ -mn & mn & (m^2 - n^2) \end{bmatrix} \begin{bmatrix} \sigma_x \\ \sigma_y \\ \tau_{xy} \end{bmatrix}$$
$$\begin{bmatrix} \varepsilon_1 \\ \varepsilon_2 \\ \gamma_{12} \end{bmatrix} = \begin{bmatrix} m^2 & n^2 & mn \\ n^2 & m^2 & -mn \\ -2mn & 2mn & (m^2 - n^2) \end{bmatrix} \begin{bmatrix} \varepsilon_x \\ \varepsilon_y \\ \gamma_{xy} \end{bmatrix}$$
$$m = \cos\theta$$
$$n = \sin\theta$$

For the off-axis specimen, the loading is only in the axial direction and hence, the stress in the transverse direction and the shear strain are zero. Hence, for this specimen, the compliance matrix is given as follows:

$$\begin{bmatrix} \varepsilon_x \\ \varepsilon_y \\ \gamma_{xy} \end{bmatrix} = \begin{bmatrix} \bar{S}_{11} & \bar{S}_{12} & \bar{S}_{16} \\ \bar{S}_{12} & \bar{S}_{22} & \bar{S}_{26} \\ \bar{S}_{16} & \bar{S}_{26} & \bar{S}_{66} \end{bmatrix} \begin{bmatrix} \sigma_x \\ \sigma_y \\ \tau_{xy} \end{bmatrix}$$

Since the values of σ_y and τ_{xy} are zero for the specimen, the matrix can be reduced as follows:

$$\begin{bmatrix} \varepsilon_x \\ \varepsilon_y \\ \gamma_{xy} \end{bmatrix} = \sigma_x \begin{bmatrix} \bar{S}_{11} \\ \bar{S}_{12} \\ \bar{S}_{16} \end{bmatrix} = \sigma_x \begin{bmatrix} 1/E_x \\ -\nu_{xy}/E_x \\ \eta_{x,xy}/E_x \end{bmatrix}$$

Hence, the engineering constants for the specimen can be obtained as follows:

$$E_x = \frac{\sigma_x}{\varepsilon_x} = \frac{1}{\bar{S}_{11}}$$

$$\nu_{xy} = -\frac{\varepsilon_y}{\varepsilon_x} = -\frac{\bar{S}_{12}}{\bar{S}_{11}}$$

$$\eta_{x,xy} = \frac{\gamma_{xy}}{\varepsilon_x} = \frac{\bar{S}_{16}}{\bar{S}_{11}}$$

The in-plane shear modulus can be calculated as follows where $m = \cos\theta$ and $n = \sin\theta$

$$G_{12} = \frac{\tau_{12}}{\gamma_{12}} = -\frac{mn\sigma_x}{2mn(\varepsilon_y - \varepsilon_x) + (m^2 - n^2)\gamma_{xy}}$$

4.1.2 Effect of end-constraints (tabs) on the test specimen

The off-axis specimen tends to deform at the ends due to the shear when they are free. But, when it is constrained by tabs on the ends, it gets constrained leading to a more complex loading state. This causes the specimen to deform in an S-shape as shown in Figure 21 (in Appendix).

It can be observed that the value of G_{12} can be calculated from the material properties and can be compared against the experimental values. However, these equations assume that the specimen is allowed to freely deform under the load. But, the specimens are gripped using the tabs and hence, they are constrained leading to a complex loading condition as shown in Figure 21. Hence, to correct the effects of the constraint due to tabs on the ends, the following equation is used for the calculation of Young's modulus, where, w is the width of the specimen, E_x is Young's modulus of the unconstrained specimen and L_G is the gauge length:

$$E_x = E_{x,apparent} \left[1 - \frac{1}{\bar{S}_{11}} \left(\frac{3\bar{S}_{16}^2}{3\bar{S}_{66} + 2\bar{S}_{11} \left(\frac{L_G}{w} \right)^2} \right) \right]$$

$$= E_{x,apparent} \left[1 - \left(\frac{3\eta_{x,xy}}{\frac{3E_x}{G_{xy}} + 2 \left(\frac{L_G}{w} \right)^2} \right) \right]$$

It can be observed that as the value of L_G/w approaches infinity, the value of $E_{x,apparent}$ tends towards the value of E_x .

4.1.3 Determination of failure in off-axis specimen

For determining the deformation and failure in the off-axis specimen, there is no single criterion that can be used. The most popular criteria are maximum stress, maximum strain, maximum shear, and Tsai-Wu criterion.

Analysis of the failure characteristics is also very important in order to understand the performance of composite laminates. There are different types of failure criteria that can be used to analyze failure in composite laminates. Figure 22 (in Appendix) shows the plot for the failure envelope for a typical anisotropic material for different failure criteria. The material does not fail as long as the values of stress are within the envelope. The failure index is 1 when the values of the stress lie exactly on the curve.

4.1.3.1 Maximum Stress Failure

Failure happens when the value of any of the stress components in the principal material axes exceeds the value of strength in that direction. The following equations denote the failure in this criterion:

$$\begin{aligned}\sigma_1 &= X_1^T \\ \sigma_1 &= -X_1^C \\ \sigma_2 &= X_2^T \\ \sigma_2 &= -X_2^C \\ \tau_{12} &= S_6 \\ \tau_{12} &= -S_6\end{aligned}$$

Where, X_1^T , X_1^C , X_2^T , X_2^C represent the tensile and compressive strengths in the 1 and 2 directions respectively and S_6 is the strength in 1-2 direction.

4.1.3.2 Maximum Strain Failure

Failure happens when the value of any of the strain components in the principal material axes exceeds the value of ultimate strain (uniaxial tension, compression, and pure shear) in that direction. The following equations denote the failure in this criterion:

$$\begin{aligned}\varepsilon_1 &= e_1^T \\ \varepsilon_1 &= -e_1^C \\ \varepsilon_2 &= e_2^T \\ \varepsilon_2 &= -e_2^C \\ \gamma_{12} &= e_6 \\ \gamma_{12} &= -e_6\end{aligned}$$

Where, e_1^T , e_1^C , e_2^T , e_2^C represent the ultimate tensile and compressive strains in the 1 and 2 directions respectively and e_6 is the ultimate strain in 1-2 direction.

4.1.3.3 Tsai-Wu Failure

The Tsai-Wu failure criteria are used for anisotropic composite materials that have different strengths in the tensile and compressive directions. It is a particular case of the generalized Hill yield criteria. It is used to predict the failure when the failure index in the laminate reaches 1. It is a specialization of the general failure criterion given by Kopnov and Gol'denblat and it is expressed in the following form:

$$F_i \sigma_i + F_{ij} \sigma_i \sigma_j \leq 1$$

Where, i, j range from 1 to 6 and the stresses are represented in Voigt notation, F_{ij} should satisfy the following condition:

$$F_{ii} F_{jj} - F_{ij}^2 \geq 0$$

Hence, F_{ii} must be positive.

For the off-axis specimens, the Tsai-Wu failure criteria can be represented by the following formula:

$$F_1 \sigma_{11} + F_2 \sigma_{22} + F_{11} \sigma_{11}^2 + F_{22} \sigma_{22}^2 + 2F_{12} \sigma_{11} \sigma_{22} + F_{66} \sigma_6^2 = 1$$

The coefficients are calculated as follows:

$$F_1 = \frac{1}{X^T} + \frac{1}{X^C}$$

$$F_2 = \frac{1}{Y^T} + \frac{1}{Y^C}$$

$$F_{11} = -\frac{1}{X^T X^C}$$

$$F_{22} = -\frac{1}{Y^T Y^C}$$

$$F_{66} = \frac{1}{S^2}$$

The value of the interaction coefficient, F_{12} can be predicted from complex experimental methods or can be approximated as follows:

$$F_{12} = -\frac{1}{2}\sqrt{F_{11}F_{22}}$$

The values of F_1 , F_{11} are obtained from the stiffness results of longitudinal tension and compression tests and the values F_2 , F_{22} are obtained from the stiffness results of transverse tension and compression tests. F_{66} is obtained from the shear test.

4.2 Experimental Procedure

Samples were made with 5 different orientations of the lamina, $[15]_8$, $[30]_8$, $[45]_8$, $[60]_8$, $[75]_8$. 6 samples of each orientation were tested. Three measurements were taken of the samples for each of the values of thickness, width and gage length. The coupons were first spray-painted on one side with white color and they were speckled with a dot size of 0.013. to analyze the data with DIC. The relative displacement of these speckles is analyzed to calculate the strain on the specimen.

For the DIC set-up, two cameras and lights were used to focus the specimen. The set-up is calibrated by using a calibration panel and a couple of images were taken of the panel in different orientations so that the relative displacement of the speckle pattern can be observed. Figure 1 shows the DIC set-up for the tensile test.

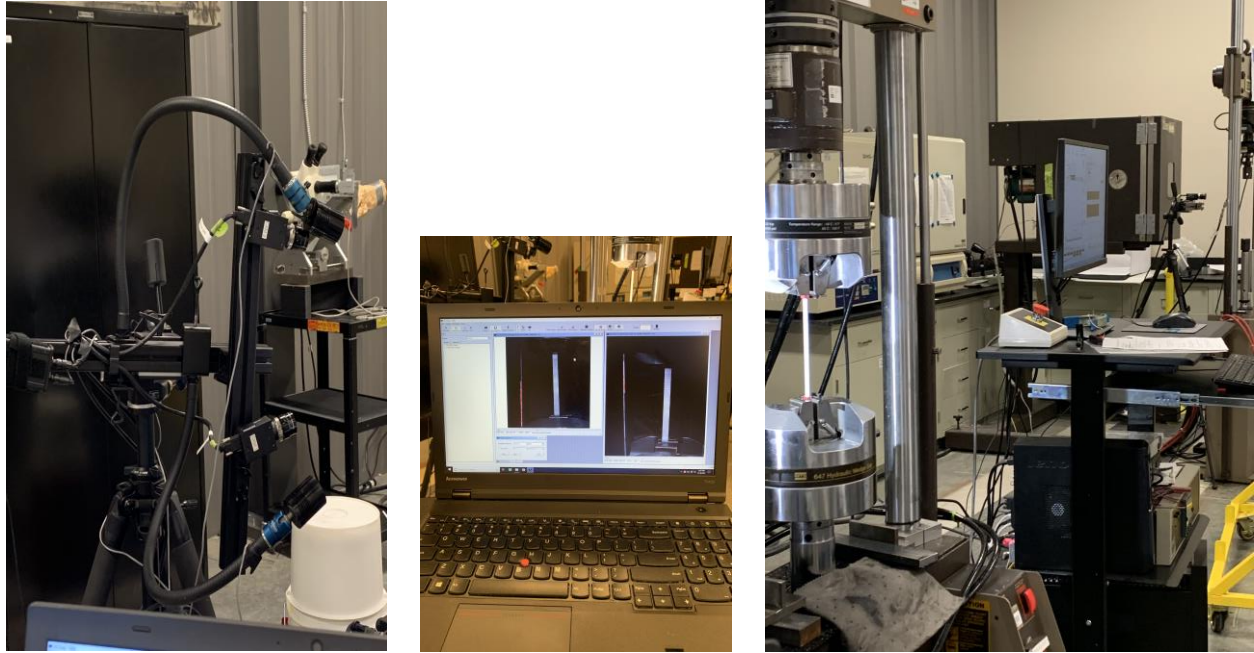


Figure 4.1: DIC Set-up

Tensile tests were conducted on the samples on the 22-kip load frame with a shear rate of 1 mm/min and the samples were tested until failure and the DIC data was analyzed using VIC 3D and the 2D plot was extracted. The images were captured with a frequency of 2 Hz.

4.3 Processing of experimental results

The data from the DIC is exported and is read using a MATLAB script to remove any kind of erroneous data or negative values. The strain data was directly obtained from the DIC and the stresses were calculated as force per unit area. Before conducting the tensile tests, the dimensions of the samples were measured in order to calculate the elastic properties of the specimens. The average values of the dimensions are given as follows in Table 1:

Table 4.1: Off-axis sample dimensions

Sample	Width (mm)	Thickness (mm)	Gauge Length (mm)	X-Sec Area (mm²)
[15] ₈	12.68 ± 0.05	1.34 ± 0.10	152.85 ± 0.14	16.99 ± 1.29
[30] ₈	12.75 ± 0.06	1.73 ± 0.03	152.91 ± 0.06	22.04 ± 0.43
[45] ₈	12.71 ± 0.08	1.35 ± 0.03	152.68 ± 0.07	17.13 ± 0.49
[60] ₈	12.62 ± 0.10	1.31 ± 0.10	152.33 ± 0.14	16.53 ± 1.60
[75] ₈	12.64 ± 0.12	1.30 ± 0.08	152.49 ± 0.11	16.40 ± 1.14

It was observed that the [30]₈ specimens were slightly thicker than the other specimens. This might be due to some human error during the lay-up.

The failure angles of the specimen were analyzed and tabulated as follows in Table 2:

Table 4.2: Failure angles of the off-axis specimens

Sample	Average Failure Angle (°)
[15] ₈	14.84 ± 0.48
[30] ₈	29.78 ± 1.08
[45] ₈	43.14 ± 2.13
[60] ₈	59.32 ± 1.50
[75] ₈	74.44 ± 1.88

It was observed that the failure angles were close to the fiber angles with slight variations. Figure 2 shows the image of the failed samples where the samples are lined up from [15]₈ to [75]₈ from left to right. It can also be observed that none of the fibers break in these samples.

Table 3 shows the parameters obtained from the DIC analysis of the specimens with different fiber orientations. The data for 0 Degree and 90 Degree is obtained from the previous experiments.

Figure 3 shows the stress versus strain curves for the off-axis specimens.



Figure 4.2: Failure angles of specimens

Table 4.3: Off-Axis tensile properties

Fibers	Avg. Shear Modulus	Standard Deviation	Ctd. Avg. Shear Modulus	Avg. Ultimate Strength	Standard Deviation
0°	39.18 GPa*	-	-	1847.4 GPa	-
15°	6.949 GPa	3.299 GPa	7.183 GPa	202.470 GPa	15.077 GPa
30°	2.462 GPa	1.072 GPa	2.545 GPa	105.260 GPa	1.851 GPa
45°	4.814 GPa	1.965 GPa	4.975 GPa	80.568 GPa	3.614 GPa
60°	0.705 GPa	1.761 GPa	0.730 GPa	59.574 GPa	12.020 GPa
75°	0.228 GPa	0.758 GPa	0.236 GPa	59.579 GPa	5.487 GPa
90°	3.439 GPa*	-	-	55.34	-

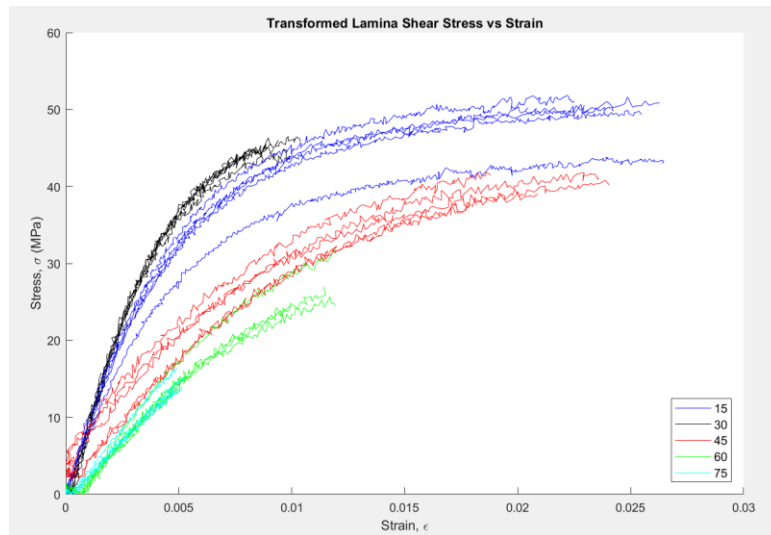


Figure 4.3: Stress Vs Strain curves for off-axis specimens

The shear modulus was calculated from the slope of the shear stress versus shear strain plot for each of the samples. Figure 4 shows the plot of shear modulus versus the angle for all the angles tested. It is observed that the measured values and the corrected values overlap with each other for almost all the angles. The dotted line is from the experimental values of one-inch-wide (25.4 mm) $[45]_8$ laminate.

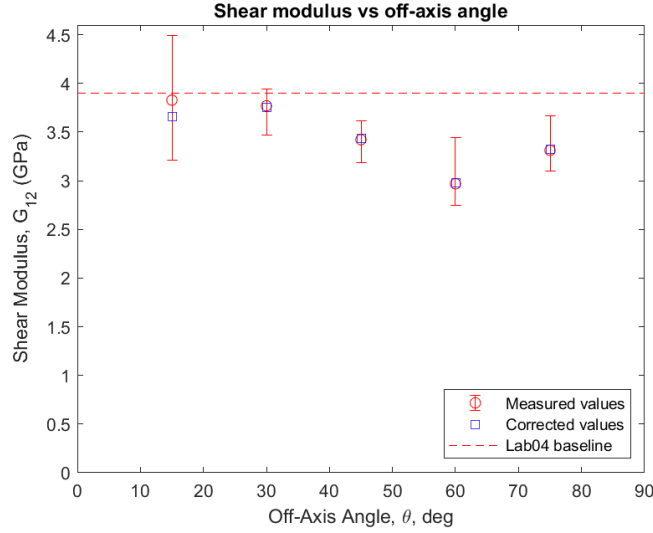


Figure 4.4: Shear modulus Vs Angle

Figure 5 shows the variation of the axial modulus with the angle for the off-axis samples along with 0 and 90 data. It is observed that the axial modulus reduces as the angle increases from 0° to 90° . The slope of the curve is highest between 0° and 15° , hence, the value reduces the most between these values. The line for theoretical data was obtained using the following equation:

$$(E_x)_a = \frac{E_x}{1 - \xi}$$

$$\xi = \frac{1}{\bar{S}_{11}} \left[\frac{3\bar{S}_{16}^2}{3\bar{S}_{66} + 2\bar{S}_{11} \left(L_G/w \right)^2} \right]$$

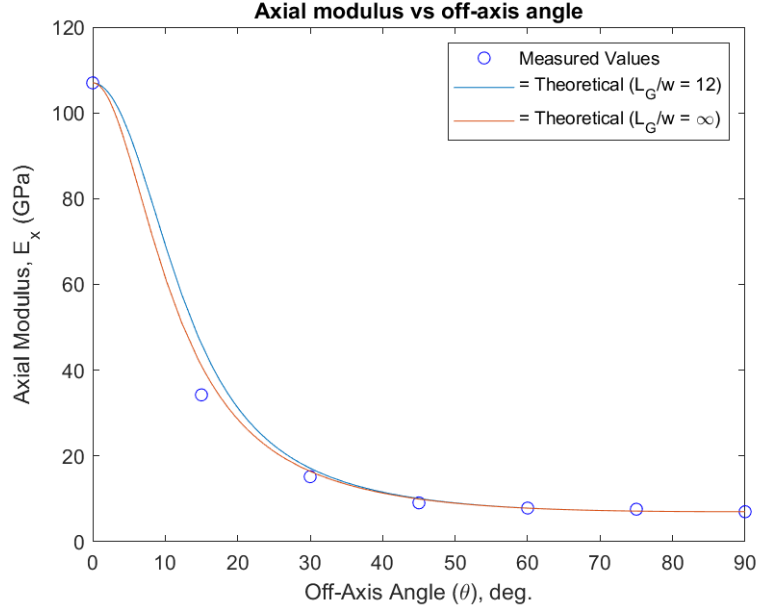


Figure 4.5: Axial Modulus Vs Angle

Figure 6 shows the axial strength versus the off-axis angle. It is observed that the axial strength of the specimens decreases drastically from 0° to 15° and continues to decrease, but at a slower rate until 90°. The specimen loses more than 50% of its strength for a fiber angle of 5° and for a fiber angle of 30°, the strength is only 5% of 0° specimen. Table 3 shows the values of these data along with the standard deviation values for these parameters.

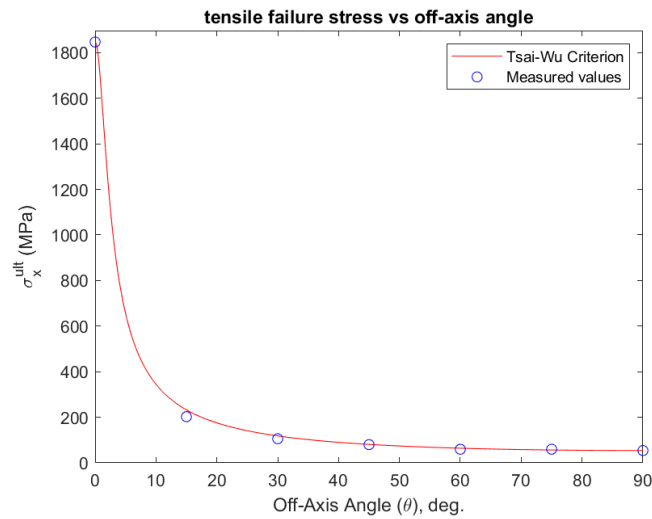


Figure 4.6: Tensile failure strength Vs Angle

Figure 7 shows the variation of Poisson's ratio with the angle. The experimental values were always observed to be higher than the theoretical values, but they follow the same trend. The highest value of experimental Poisson's ratio was observed at 15° and the value reduces after it. The theoretical value was calculated using the following formula:

$$(v_{xy})_a = v_{xy} \left[\frac{1 - \frac{3}{2} \left(\frac{\bar{S}_{26}}{\bar{S}_{11}} \right) \beta}{1 - \frac{3}{2} \left(\frac{\bar{S}_{16}}{\bar{S}_{12}} \right) \beta} \right]$$

$$\beta = \frac{\left(\frac{w}{L_G} \right)^2 \left(\frac{\bar{S}_{16}}{\bar{S}_{11}} \right)}{1 + \frac{3}{2} \left(\frac{w}{L_G} \right)^2 \left(\frac{\bar{S}_{66}}{\bar{S}_{11}} \right)}$$

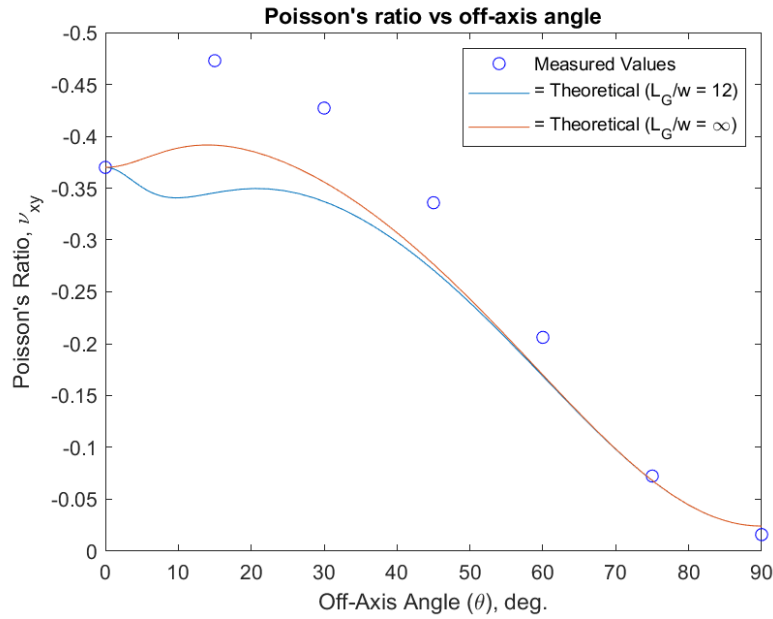


Figure 4.7: Poisson's ratio Vs Angle

Figure 8 shows the variation of shear coupling ratio versus the angle for the specimen. It is determined from the slope of shear strain versus the axial strain. It can be observed that the experimental and theoretical values follow the same trend and are very close to each other. The theoretical values were calculated using the following equation:

$$(\eta_{xy})_a = \left(\frac{\bar{S}_{16}}{\bar{S}_{11}} \right) \left[1 + \frac{3}{2} \left(\frac{w}{L_G} \right)^2 \left(\frac{\bar{S}_{66}}{\bar{S}_{11}} - \left(\frac{\bar{S}_{16}}{\bar{S}_{11}} \right)^2 \right) \right]^{-1}$$

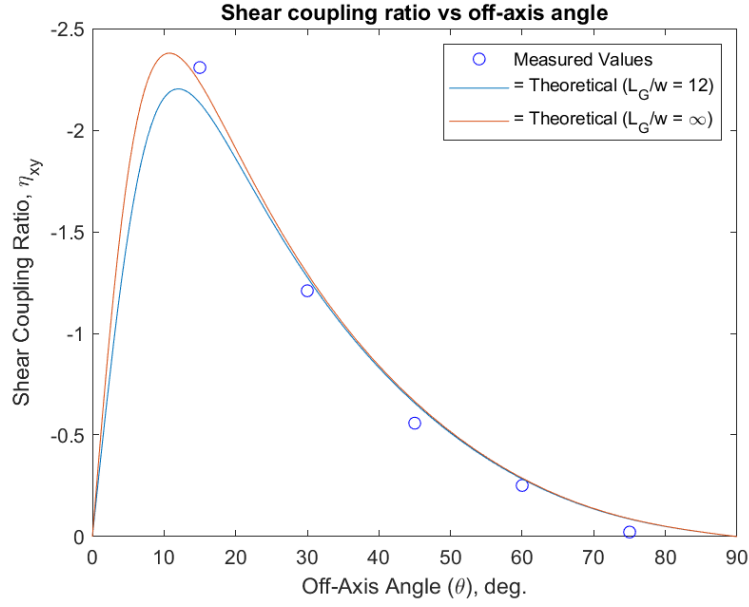


Figure 4.8: Axial modulus vs off-axis angle

Figure 9 shows the variation of the failure stress with the off-axis angles. It considers the Tsai-Wu failure, maximum axial failure, maximum transverse failure, maximum shear criterion and they were compared with the experimental values. It can be observed that the Tsai-Wu failure criterion is in close agreement with the experimental data.

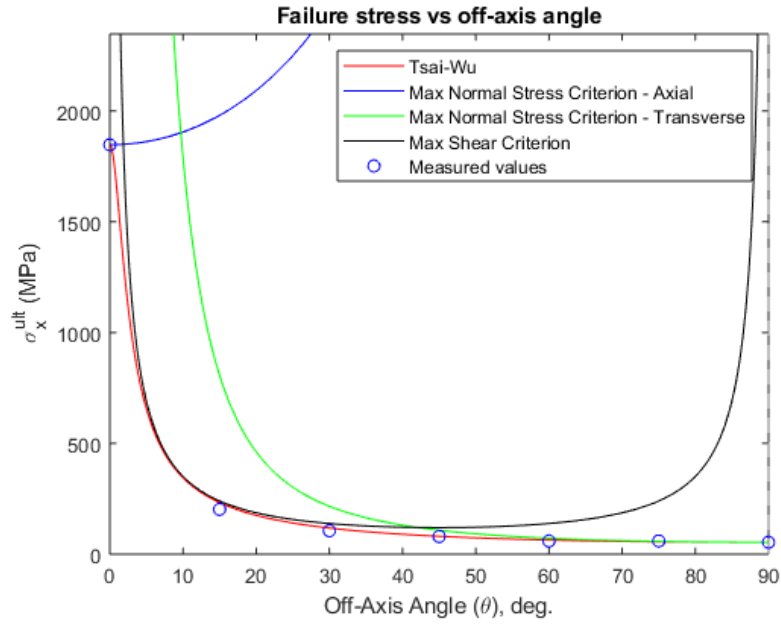


Figure 4.9: Failure stress Vs Angle

It was also observed from the DIC images that the samples undergo transverse displacement before failing. The stress gradient shows that the samples take up an ‘S’ shape. This deformation is very small to be noticed by the human eye but can be noticed from the displacement plots.

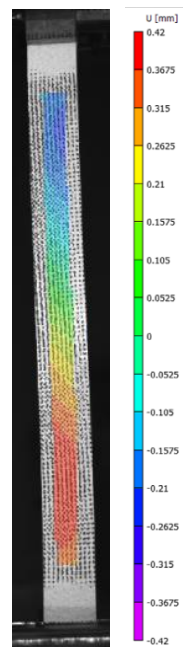


Figure 4.10: DIC image with the transverse displacement of the specimen

4.4 Modeling and analysis of simulation for off-axis test

The magnitudes of the stress and strain were evaluated for these samples by simulating the load and boundary conditions the same as what the test coupon experiences on the MTS. For getting more accurate results, the test coupon was modeled along with the tabs with an assumption that they were bonded perfectly with each other and the interaction of the material and the tabs were analyzed.

The test specimens were modeled as discussed in chapter 2. They were half-inch (12.7 mm) wide and comprised of 8-ply laminates with 5 different orientations as in the experiment. The fiber orientation was assigned individually to each of the plies and hence, for the post-processing of the data, a global coordinate system is created and all the parameters are hence rotated in terms of the global coordinates. The load and boundary conditions for the test are the same as a typical tensile test as discussed in section 2.7. The deformation output has a scale of 12.6987.

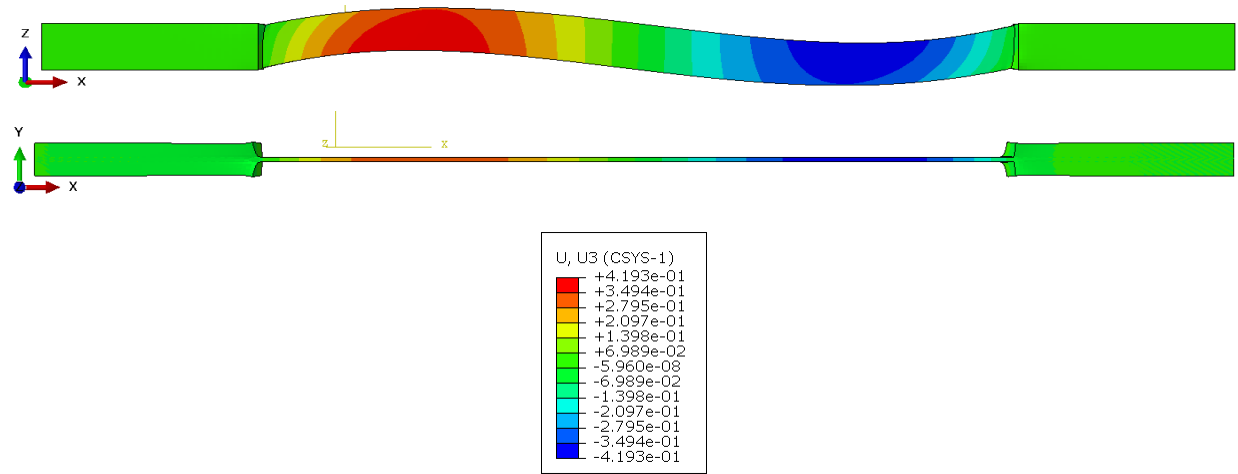
4.4.1 Analysis of simulation results for $[15]_8$, $[30]_8$, $[45]_8$, $[60]_8$, $[75]_8$ laminates

4.4.1.1 Displacement

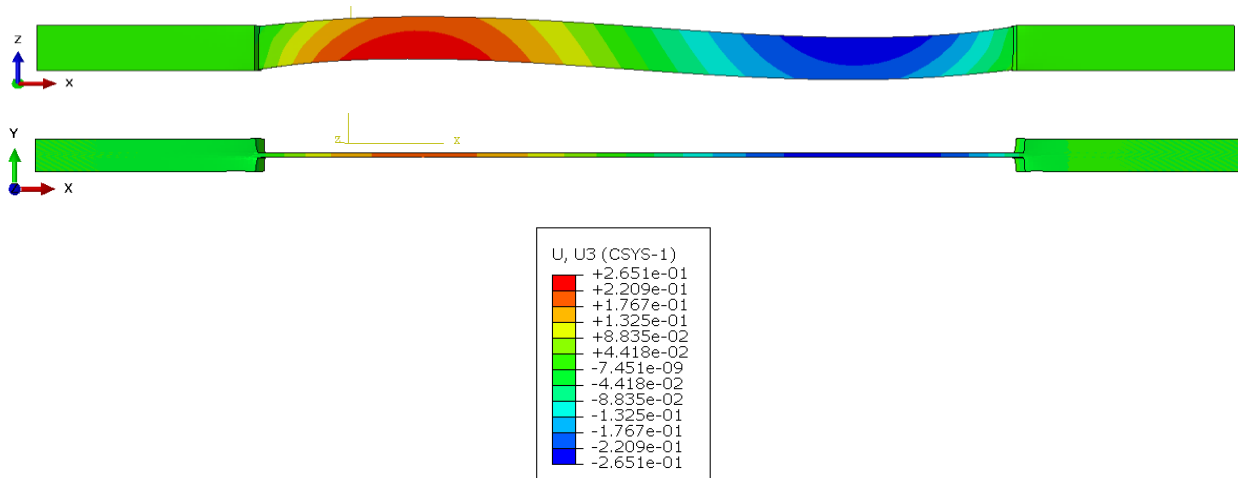
4.4.1.1.1 In-plane deformation

The specimen undergoes in-plane bending that is caused because of coupling between normal and shear deformations. This tends to deform the specimen in shear. But, due to the presence of the grips, the specimen ends do not shear and this leads to in-plane bending in the specimen. It can be observed from Figure 11 that the magnitude of the deformation is very symmetric and uniform with the magnitude decreasing gradually towards the center and there is no deformation at the center of the sample. This hence gives it a characteristic S-shape.

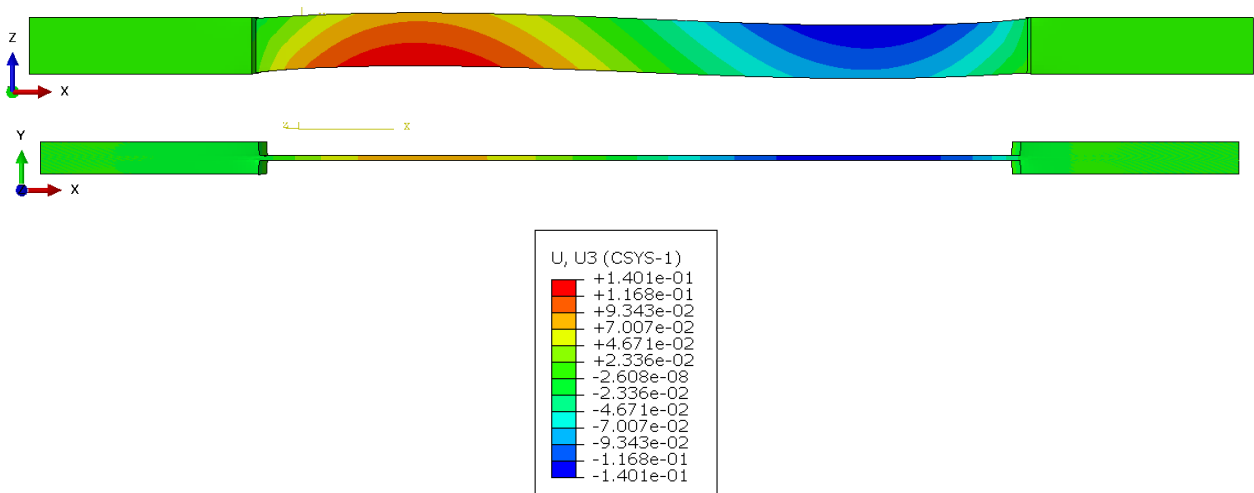
Comparing the states of deformation in the specimen with an increase in the off-axis angle, it can be observed that the magnitude of deformation gradually reduces with an increase in the angle. The maximum in-plane deformation for the $[15]_8$, $[30]_8$, $[45]_8$, $[60]_8$, $[75]_8$ specimen is 0.4193 mm, 0.2651 mm, 0.1401 mm, 0.05657 mm and 0.01105 mm respectively. The side-view of the specimens also shows that there is no out-of-plane deformation in them.



(a) $[15]_8$



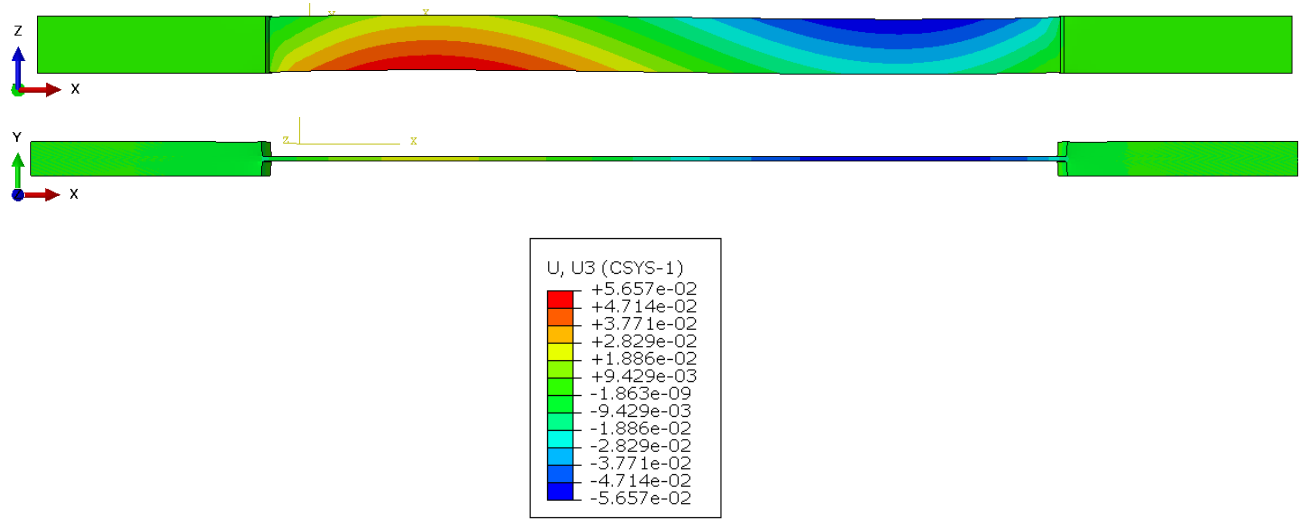
(b) $[30]_8$



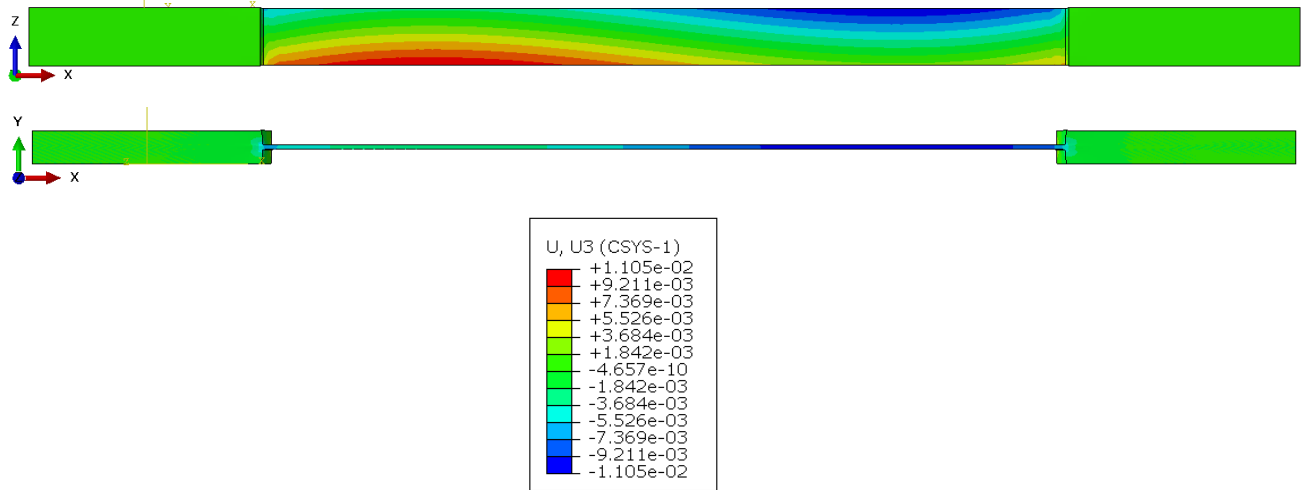
(c) $[45]_8$

Figure 4.11: In-plane deformation (U3) of the off-axis specimen

Figure 4.11 continued



(d) $[60]_8$

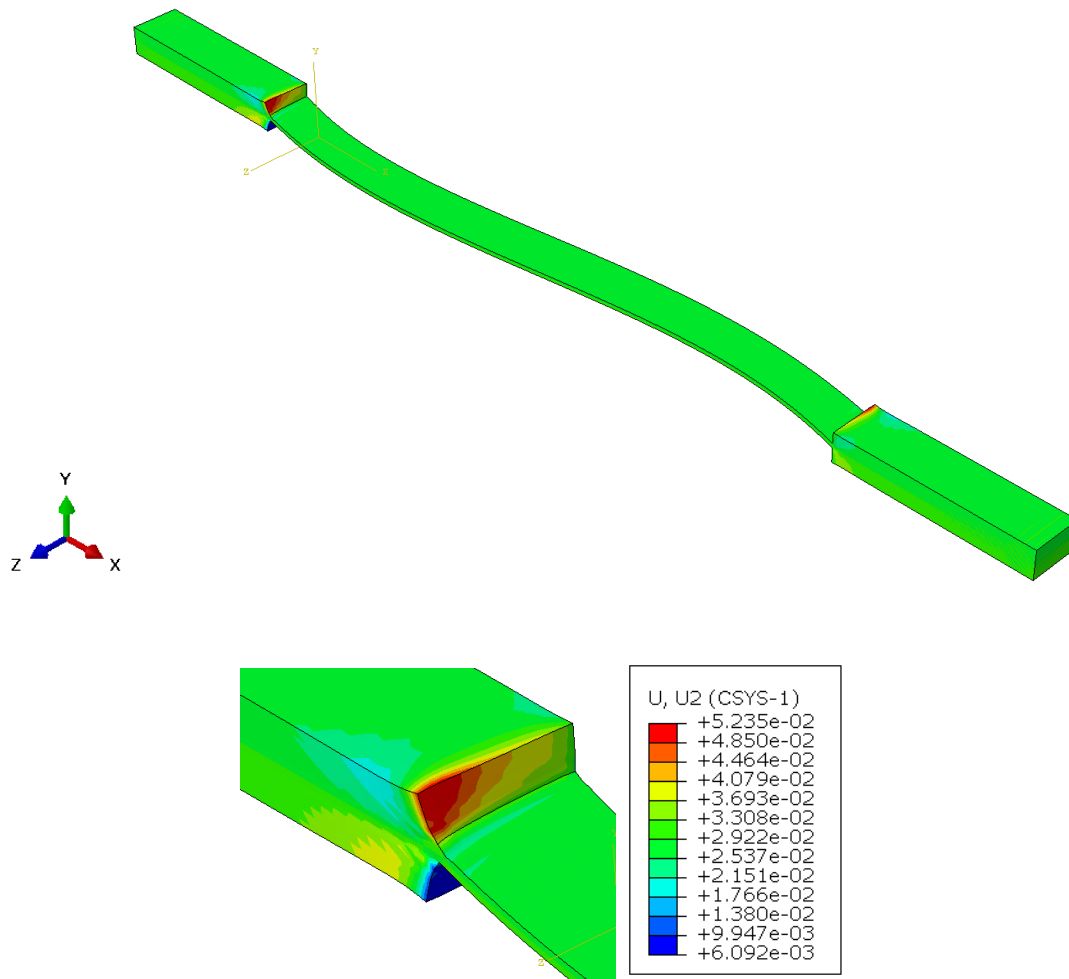


(e) $[75]_8$

4.4.1.1.2 Out-of-plane deformation

The specimen is restricted from moving in the transverse direction by the machine and is gripped in the normal direction by the means of the hydraulic grips. Hence, the tabs are free to move only in the axial direction and there is no displacement in the normal direction, Figure 12 shows that there is no out of plane bending of the sample. There is a slight deformation on the tabs due to the

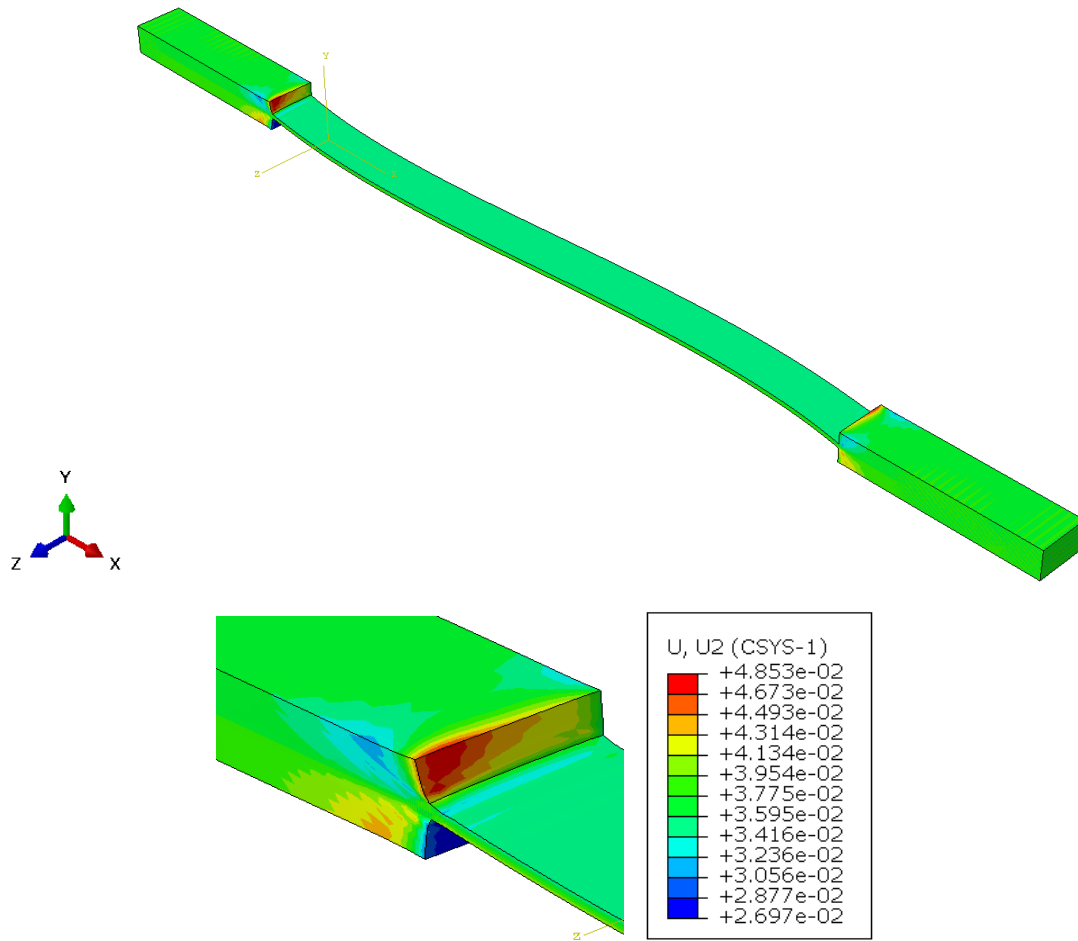
applied pressure on the tab surface. The small magnitude of displacement that is visible is due to the junk values that are projected as an output during the Finite Element simulation in Abaqus.



(a) [15]₈

Figure 4.12: Out-of-plane deformation (U2) of the off-axis specimen

Figure 4.12 continued



(b) $[30]_8$

Figure 4.12 continued

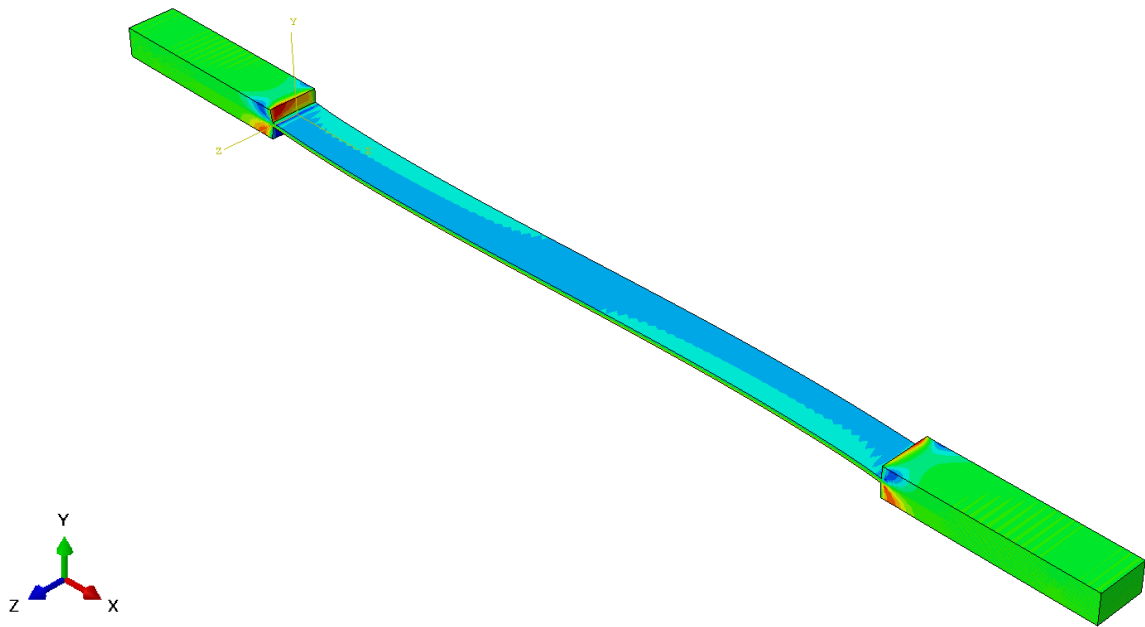
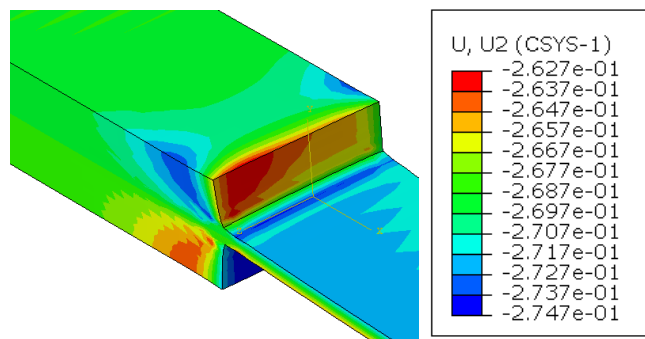
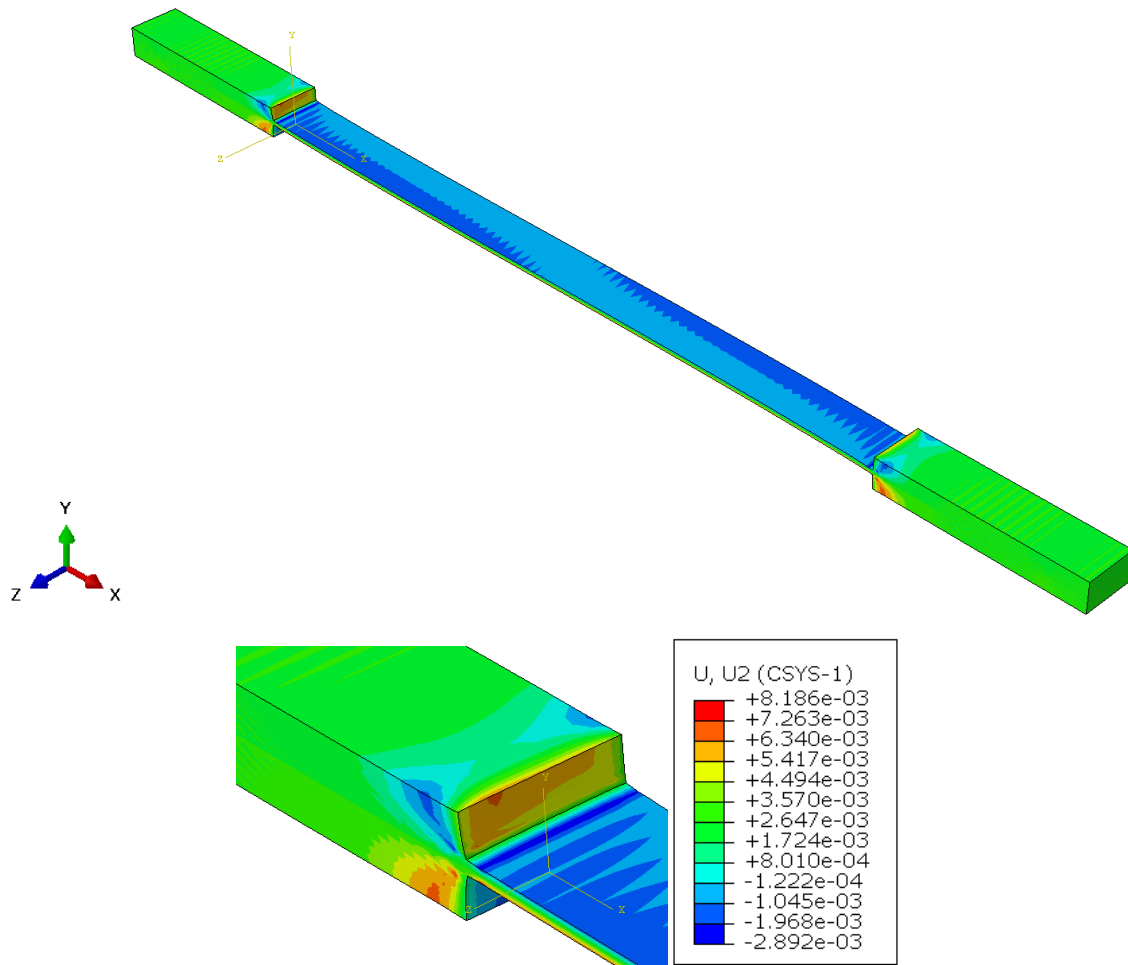


Figure 4.12 continued



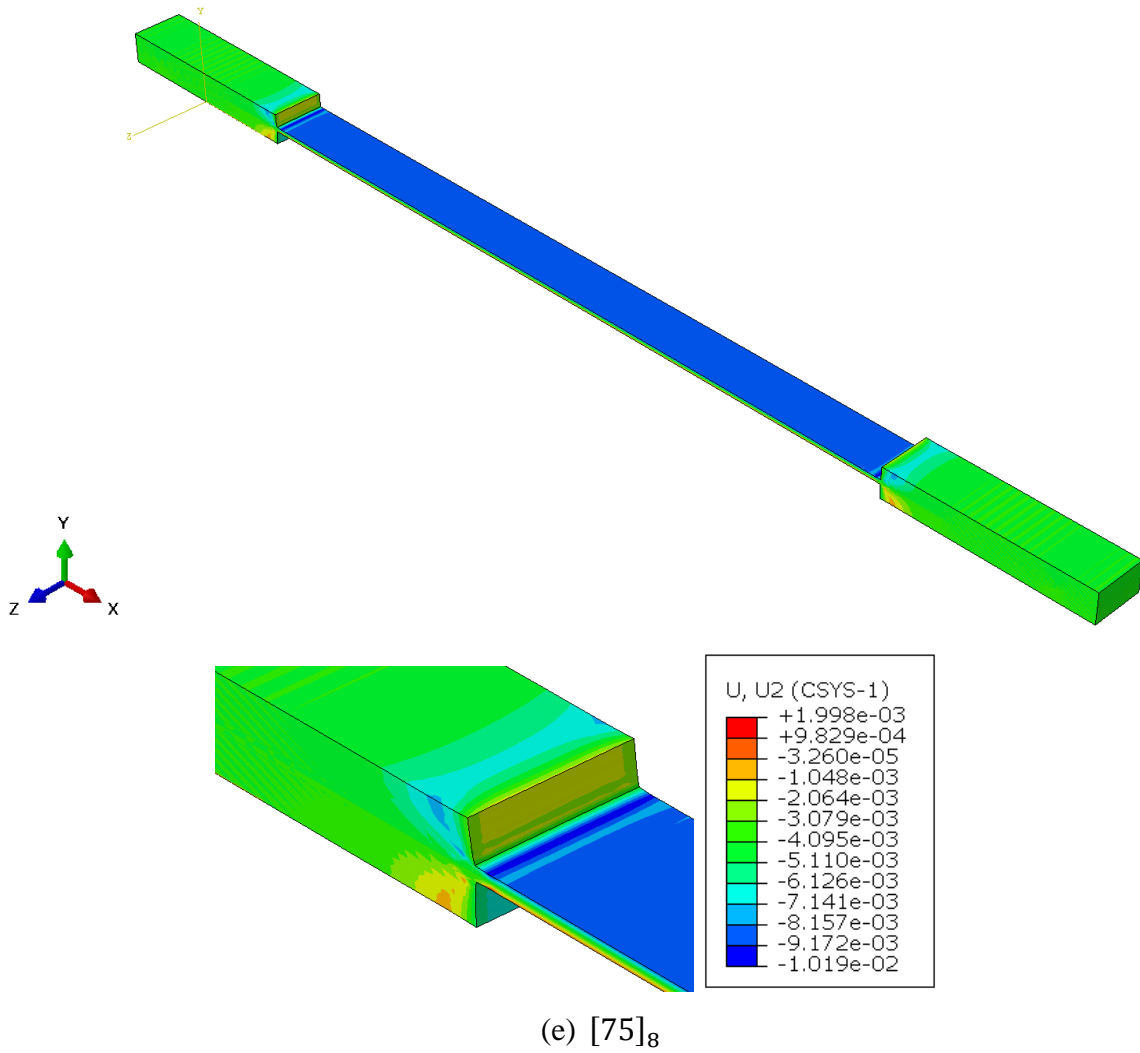
(c) $[45]_8$

Figure 4.12 continued



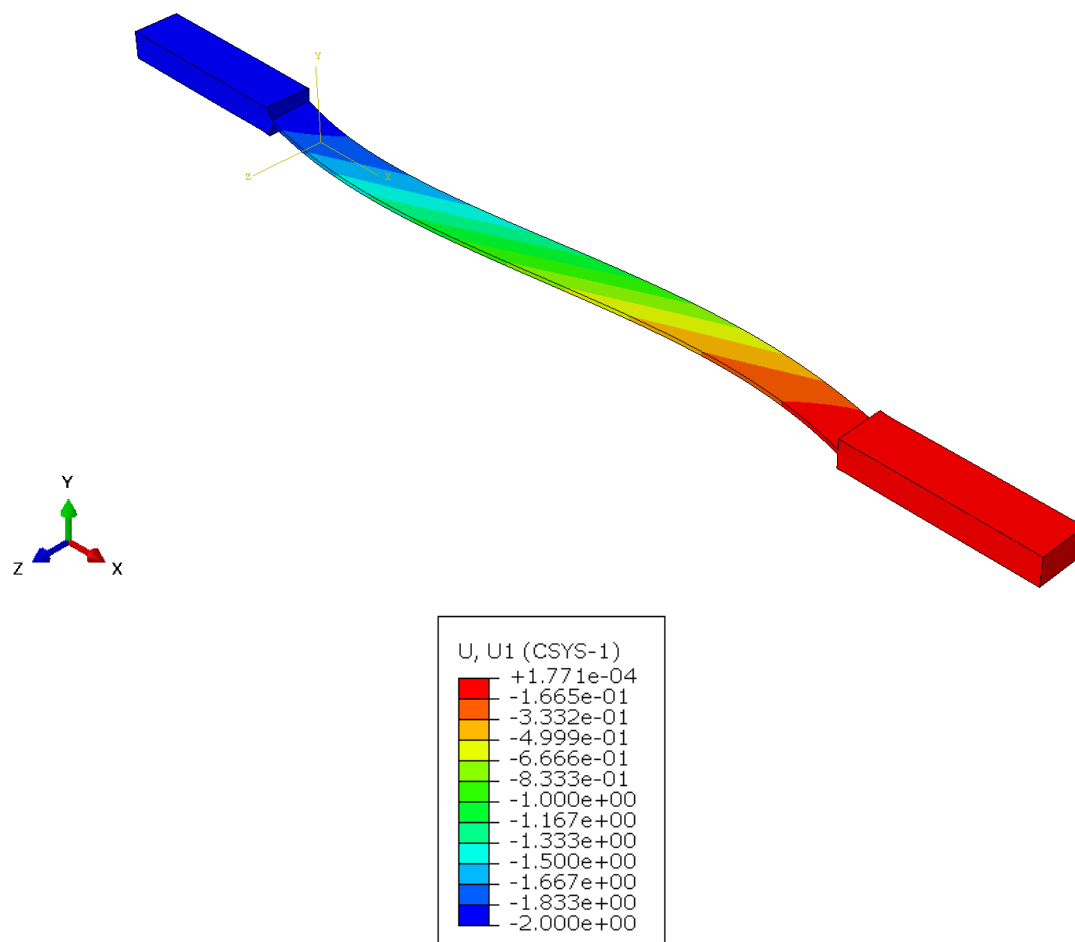
(d) $[60]_8$

Figure 4.12 continued



4.4.1.1.3 Axial deformation

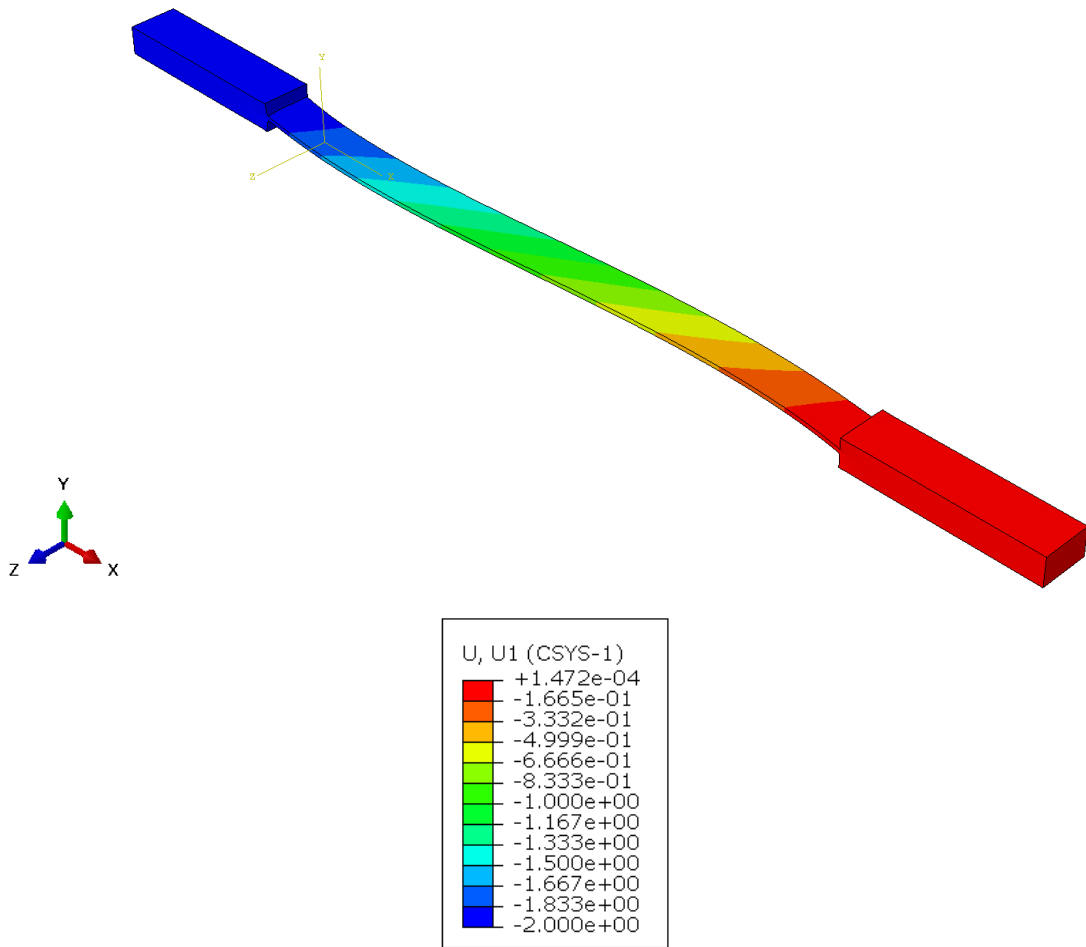
Figure 13 shows the axial deformation. Since one of the sides is completely constrained and the displacement is applied only to the other side of the coupon, it is observed that the axial deformation is zero on the constrained side and the deformation on the other side is equal to the applied displacement which is 2mm. The increase in the magnitude of the displacement is not linear and is uniformly increasing at an angle in the X-Z plane. Similar to the case of out-of-plane deformation, there is a small value of deformation present in the constrained end and these values are attributed to the junk values generated by Abaqus.



(a) $[15]_8$

Figure 4.13: Axial deformation (U1) of the off-axis specimen

Figure 4.13 continued



(b) $[30]_8$

Figure 4.13 continued

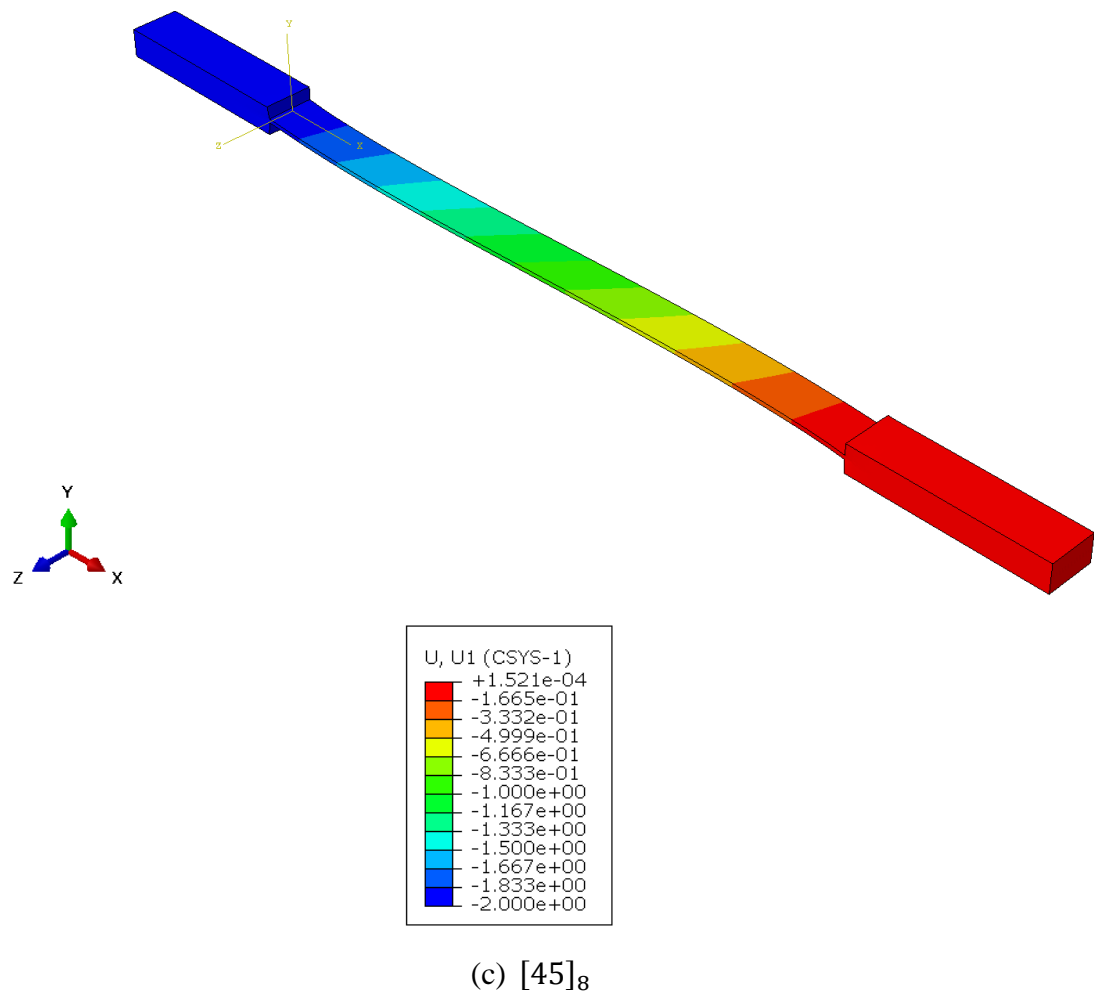
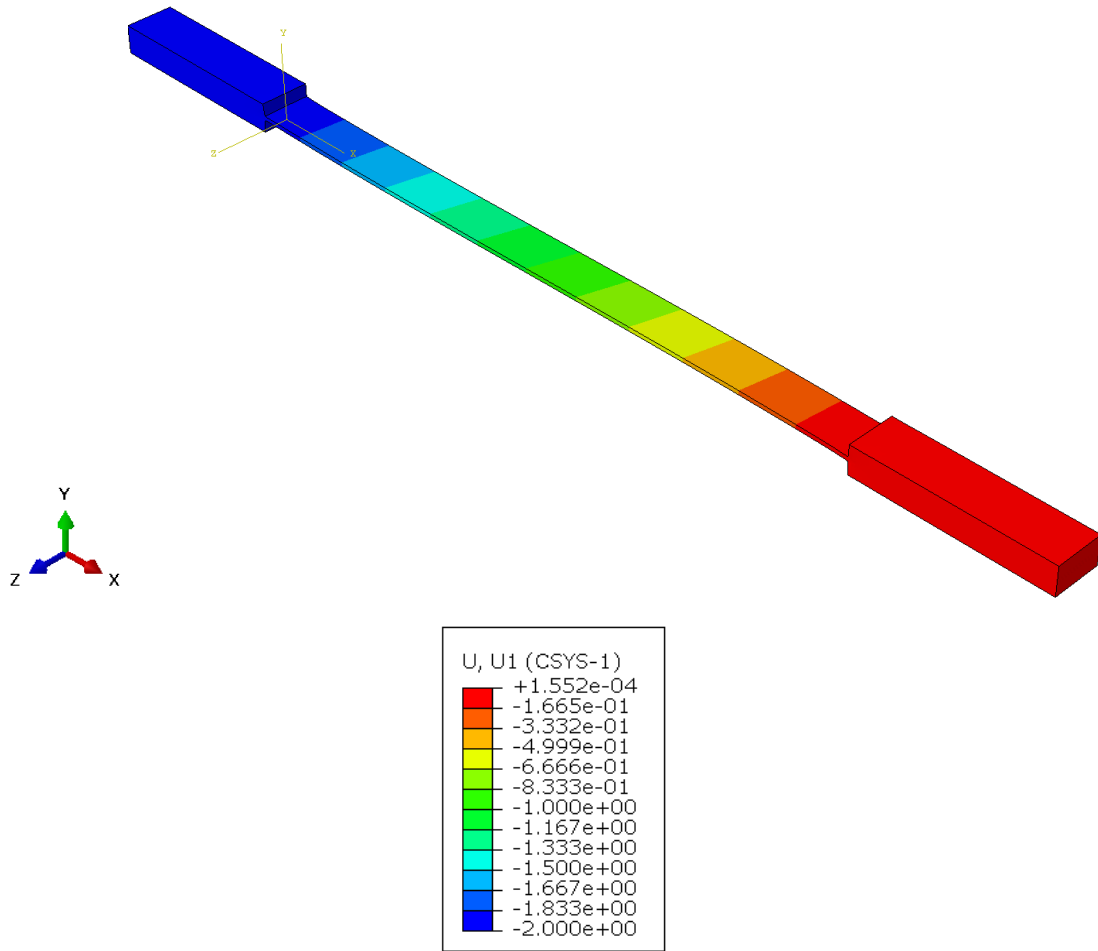
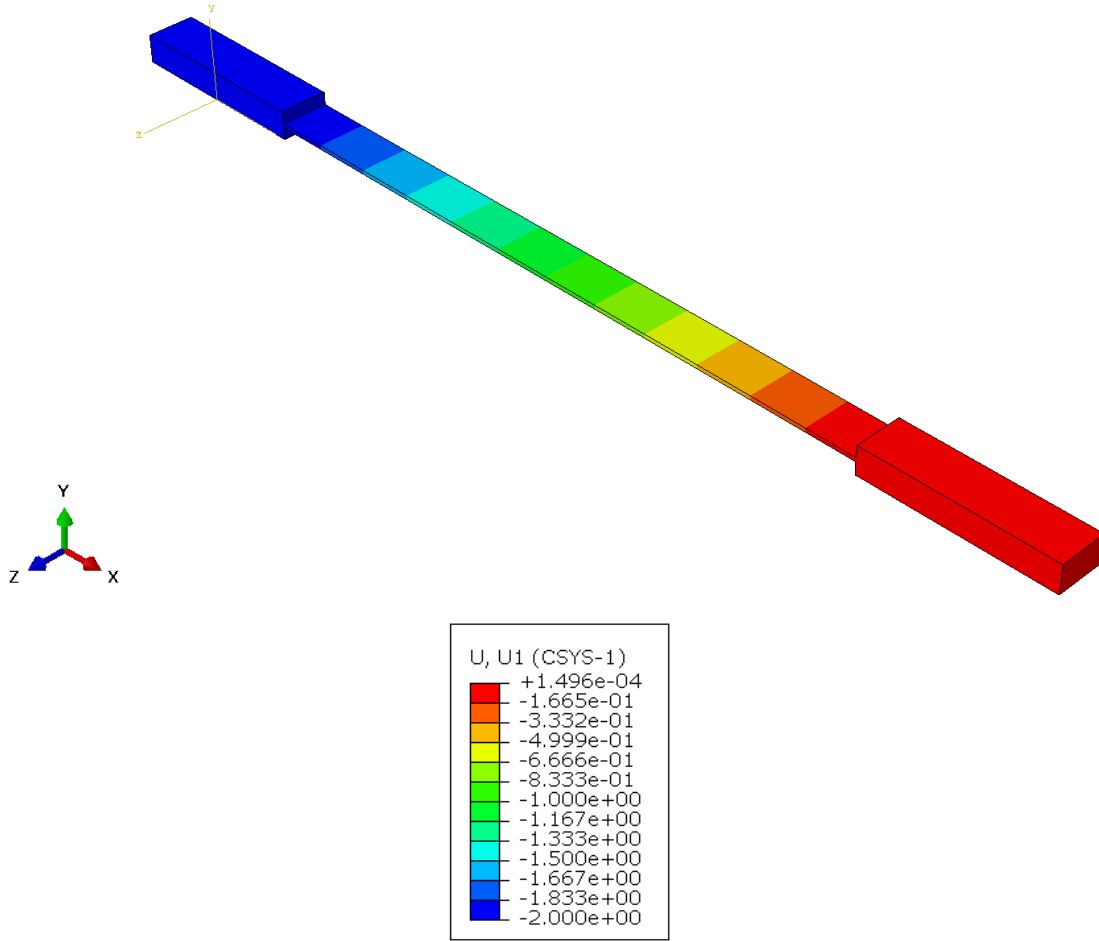


Figure 4.13 continued



(d) $[60]_8$

Figure 4.13 continued



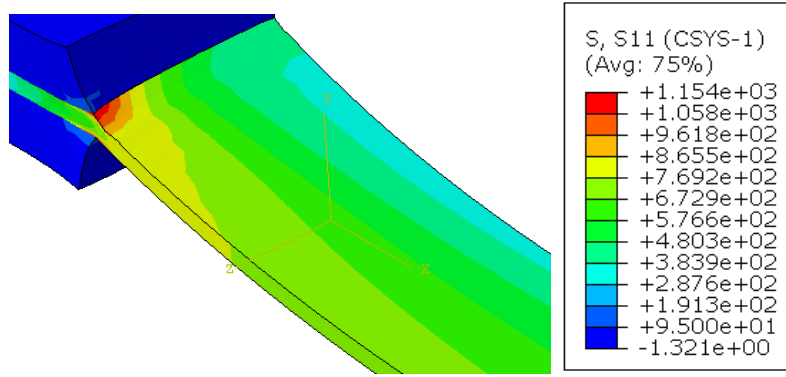
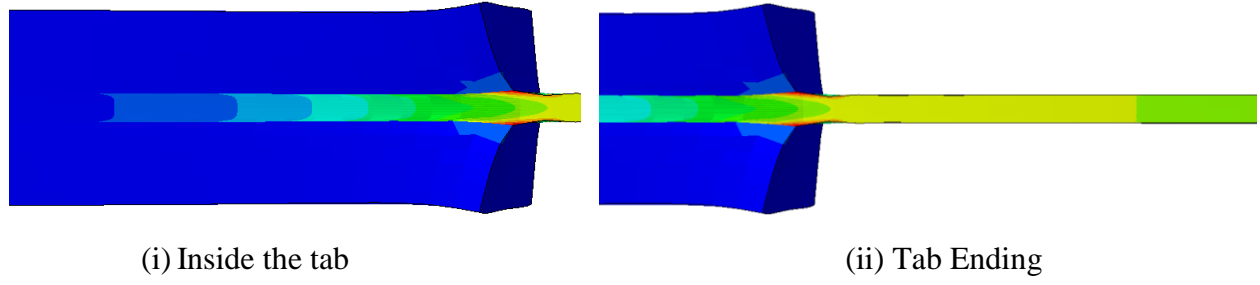
(e) $[75]_8$

4.4.1.2 Stress

4.4.1.2.1 Axial Stress

The in-plane bending causes a variation of axial stress across the width of the sample. The values of σ_{11} vary between 740 MPa to 340 MPa across the width of the $[15]_8$ sample (the variation is shown in Figure 14). The values, however, average to around 540 MPa at the center of the $[15]_8$ specimen. The trend is similar for the specimen with all angles and it can be observed that as the angle increases, the amount of variation of stress across the length and near the tabs reduces. In the $[75]_8$ specimen, the value of stress is almost constant along the length of the sample. The variation of the axial stress across the sample is shown in Figure 14. It can be observed from Figure 16 that the magnitude of axial stress has a parabolic profile and it increases gradually along with

the thickness of the laminate and it reaches a maximum value at the end of the tab. This stress concentration may lead to the debonding of the tabs from the laminate if they are not bonded strongly enough. The magnitude of axial stress is not uniform even after the tab endings. From Figure 14, it can be seen that after the region of high-stress concentration at the tab endings, the magnitude of stress gradually reduces until it becomes uniform at the center of the sample.



(iii) Variation of axial stress across the width

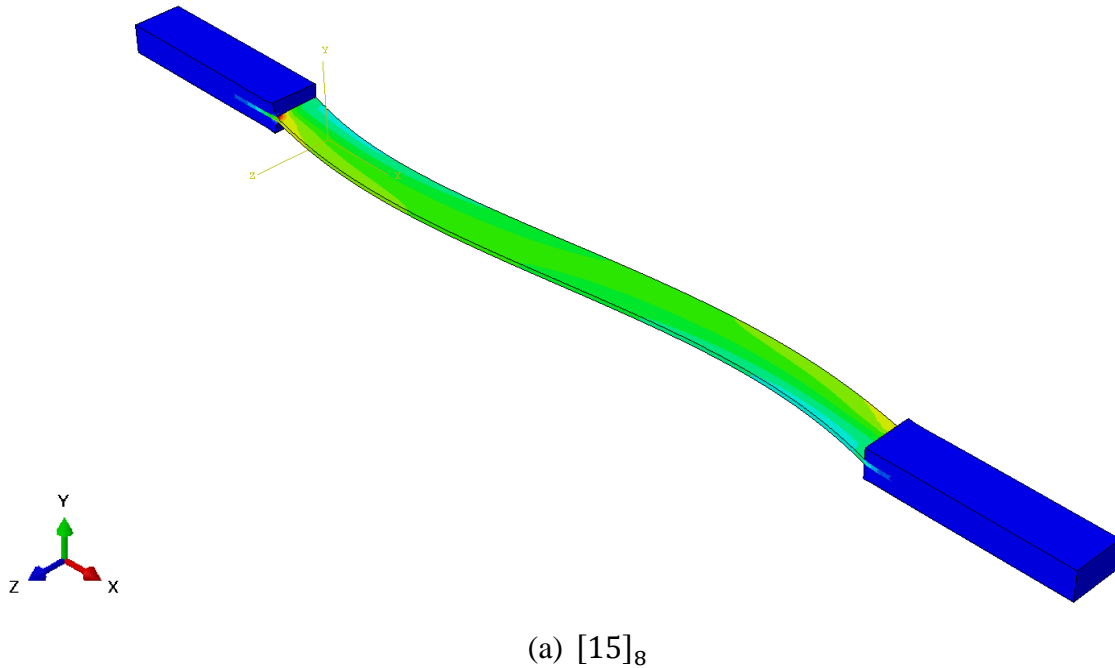
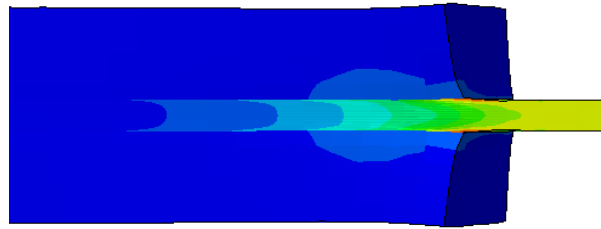
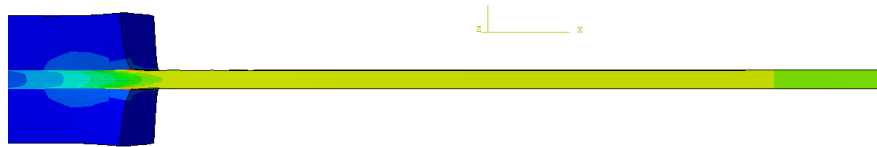


Figure 4.14: Axial stress (σ_{11}) on the off-axis specimen

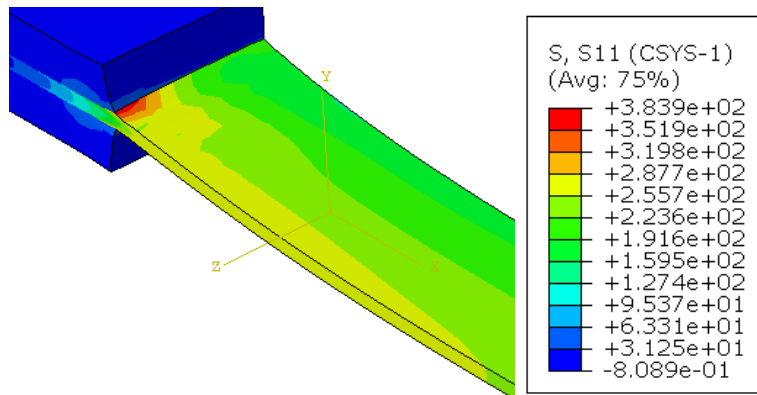
Figure 4.14 continued



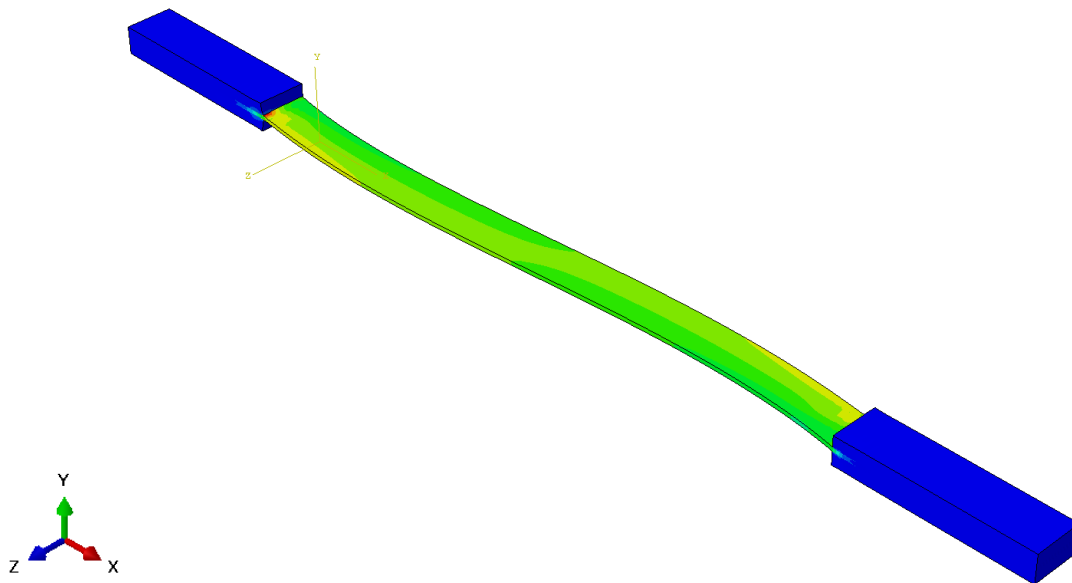
(i) Inside the tab



(ii) Tab Ending

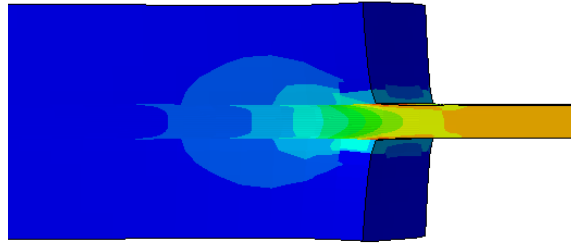


(iii) Variation of axial stress across the width



(b) [30]₈

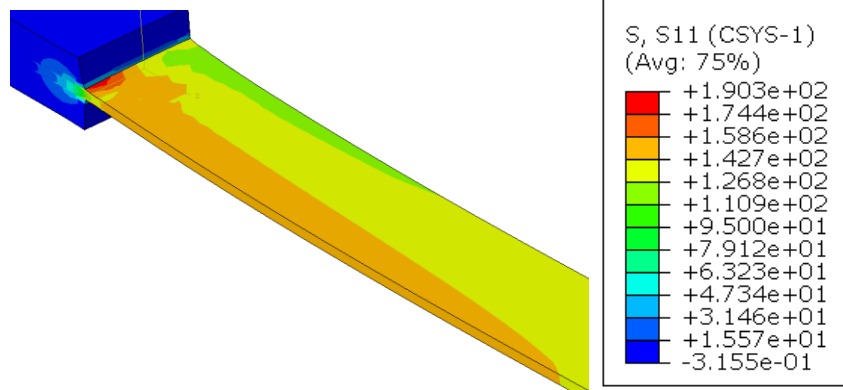
Figure 4.14 continued



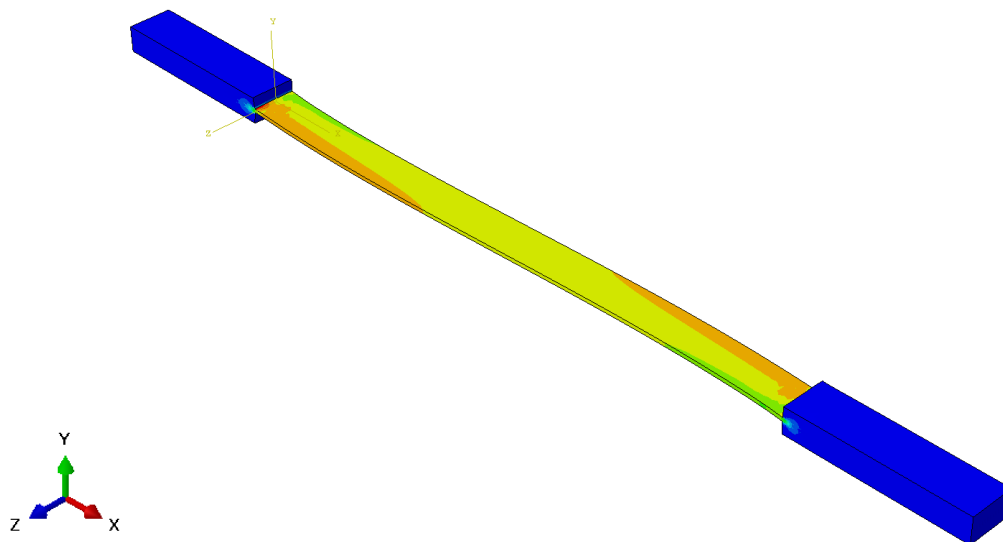
(i) Inside the tab



(ii) Tab Ending

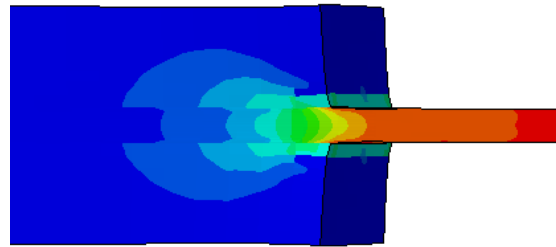


(iii) Variation of axial stress across the width



(c) $[45]_8$

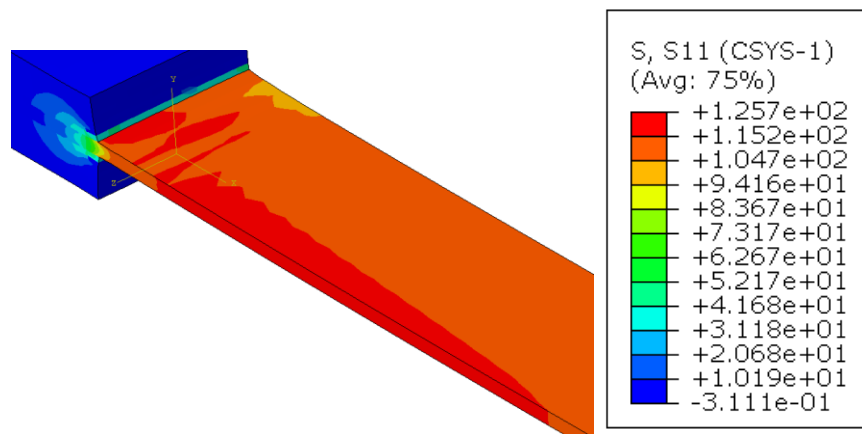
Figure 4.14 continued



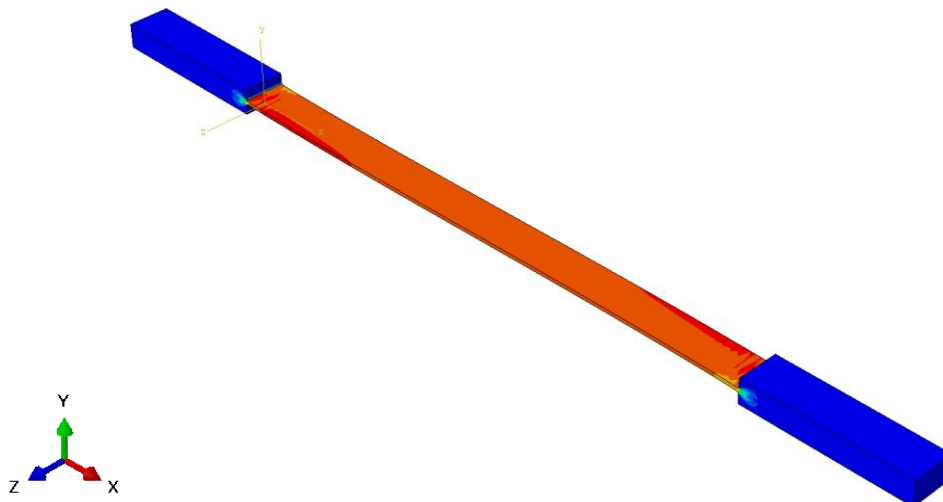
(i) Inside the tab



(ii) Tab Ending

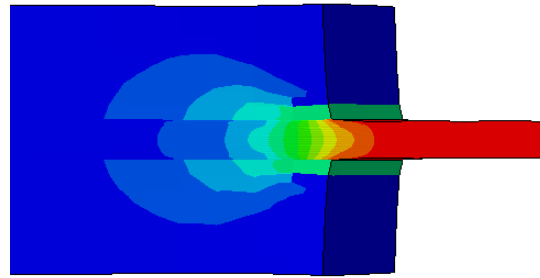


(iii) Variation of axial stress across the width

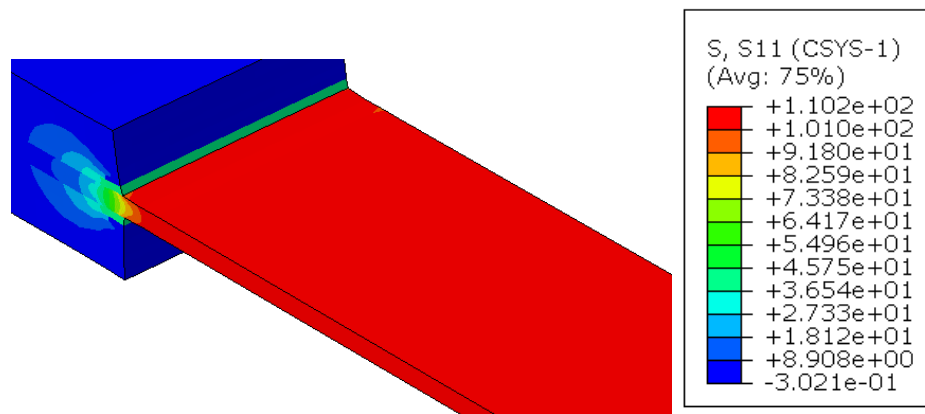


(d) $[60]_8$

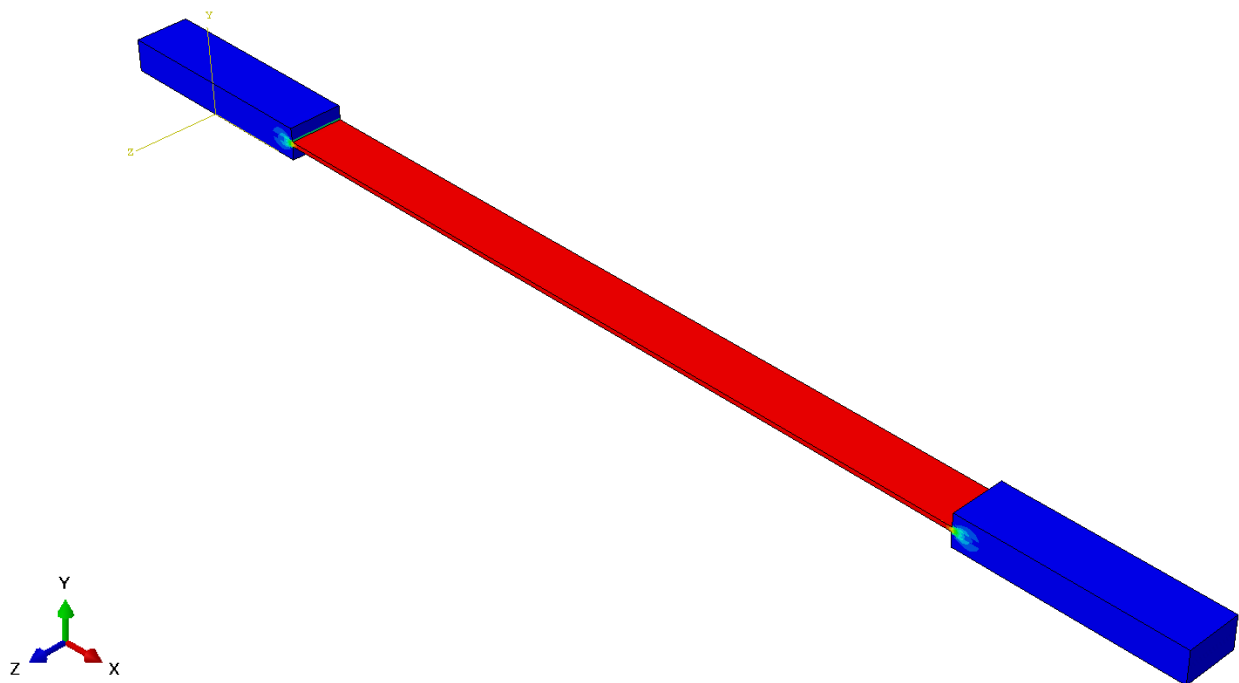
Figure 4.14 continued



(i) Inside the tab



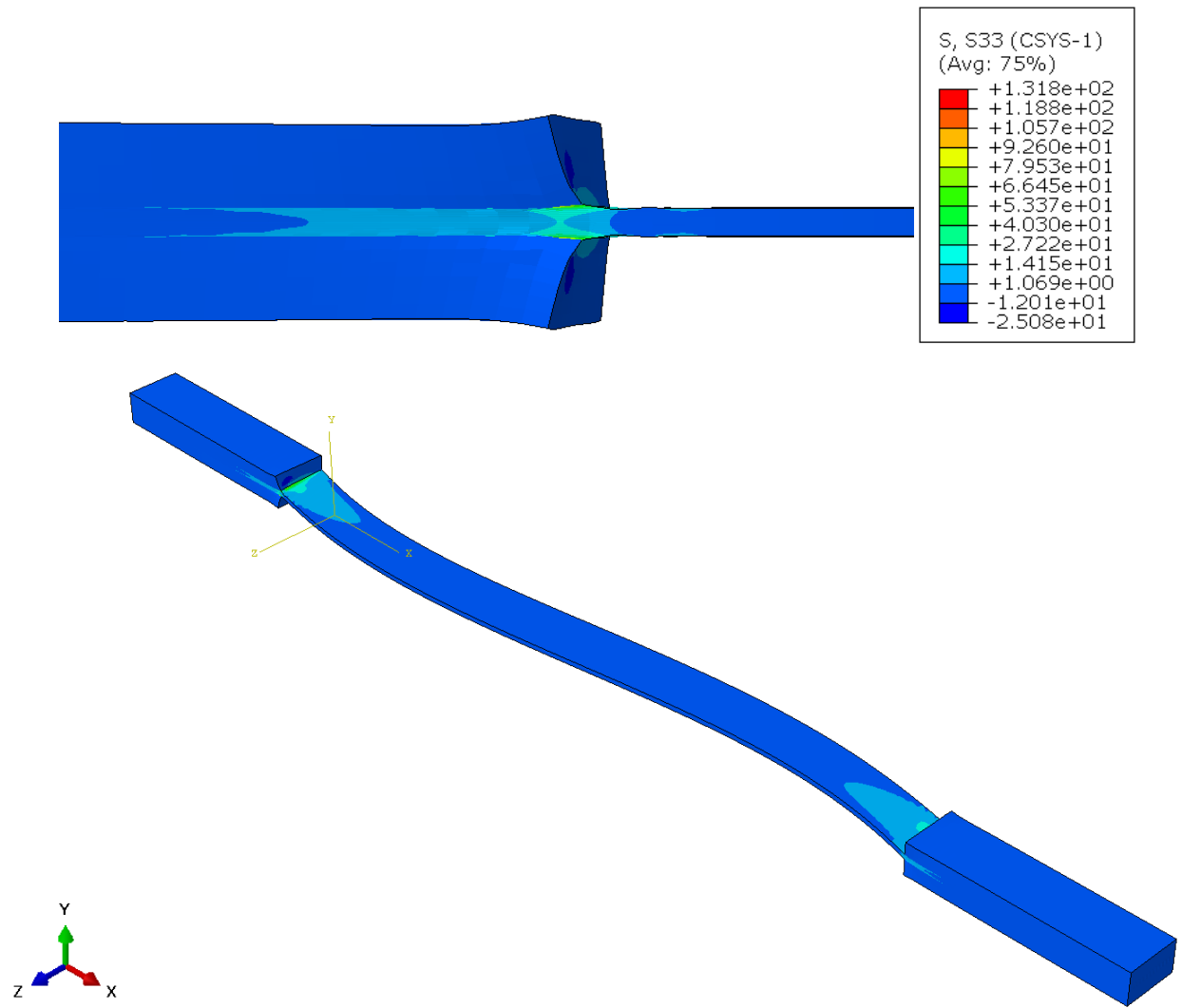
(ii) Variation of axial stress across the width



(e) $[75]_8$

4.4.1.2.2 Transverse Stress

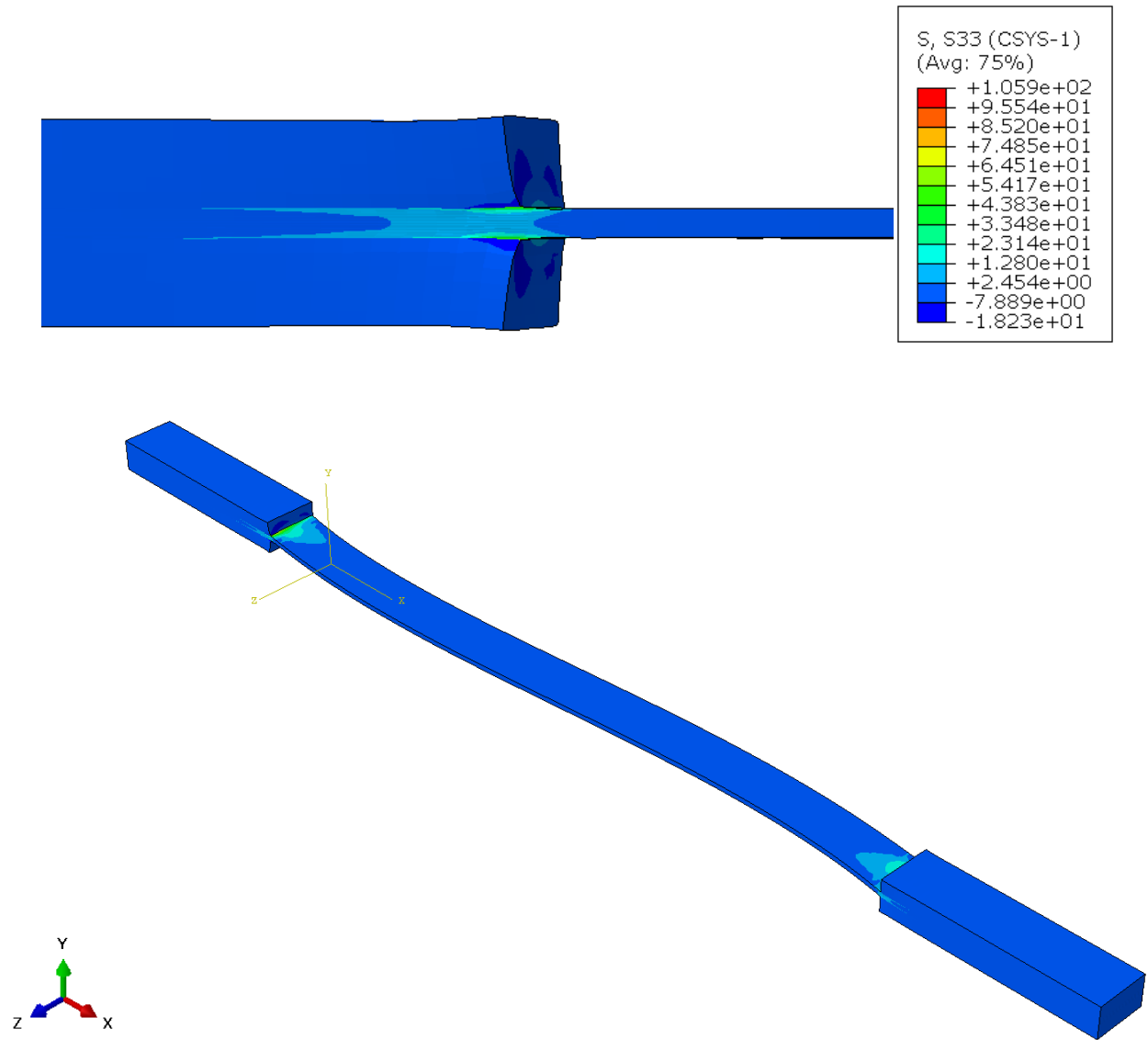
The magnitude of the transverse stress is smaller compared to the axial stress and it is compressive in nature owing to the thinning of the sample as it stretches and the sample has a Poisson's ratio of about 0.4 in the plane of the laminate. But, the magnitude of the stress is slightly high in the tabs (as shown in Figure 15). The laminate is constrained by the tabs and it cannot deform. This induces a stress in the transverse direction in the tabs. The stress is in the state of compression within the tab and gradually it transforms into a state of tension at the tab ending. The magnitude of the stress is uniform in the rest of the laminate. At the region of interaction of the laminate with the tab, the stress has a parabolic profile and the magnitude reduces towards the center of the laminate. The magnitude of stress variation near the tab endings reduces considerably with the increase in the off-axis angle. Similarly, the variation of stress across the thickness of the laminate also reduces with an increase in the angle. For the $[60]_8$ and $[75]_8$ specimen this variation is close to negligible as seen in the side-view of the tabs. The value of stress at the center of the length is very low compared to the tab endings.



(a) $[15]_8$

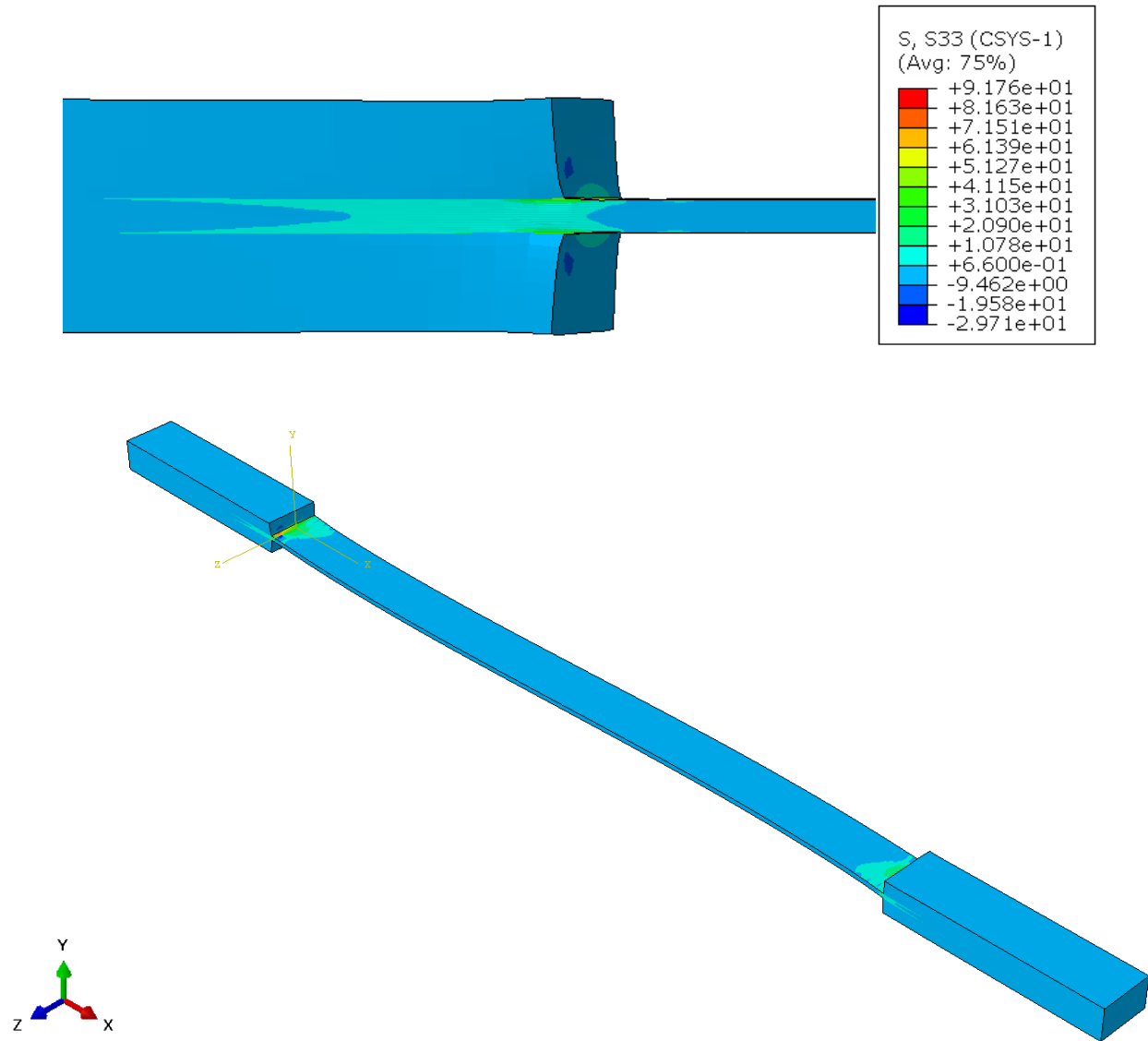
Figure 4.15: Transverse stress (σ_{22}) on the off-axis specimen

Figure 4.16 continued



(b) $[30]_8$

Figure 4.17 continued



(c) $[45]_8$

Figure 4.18 continued

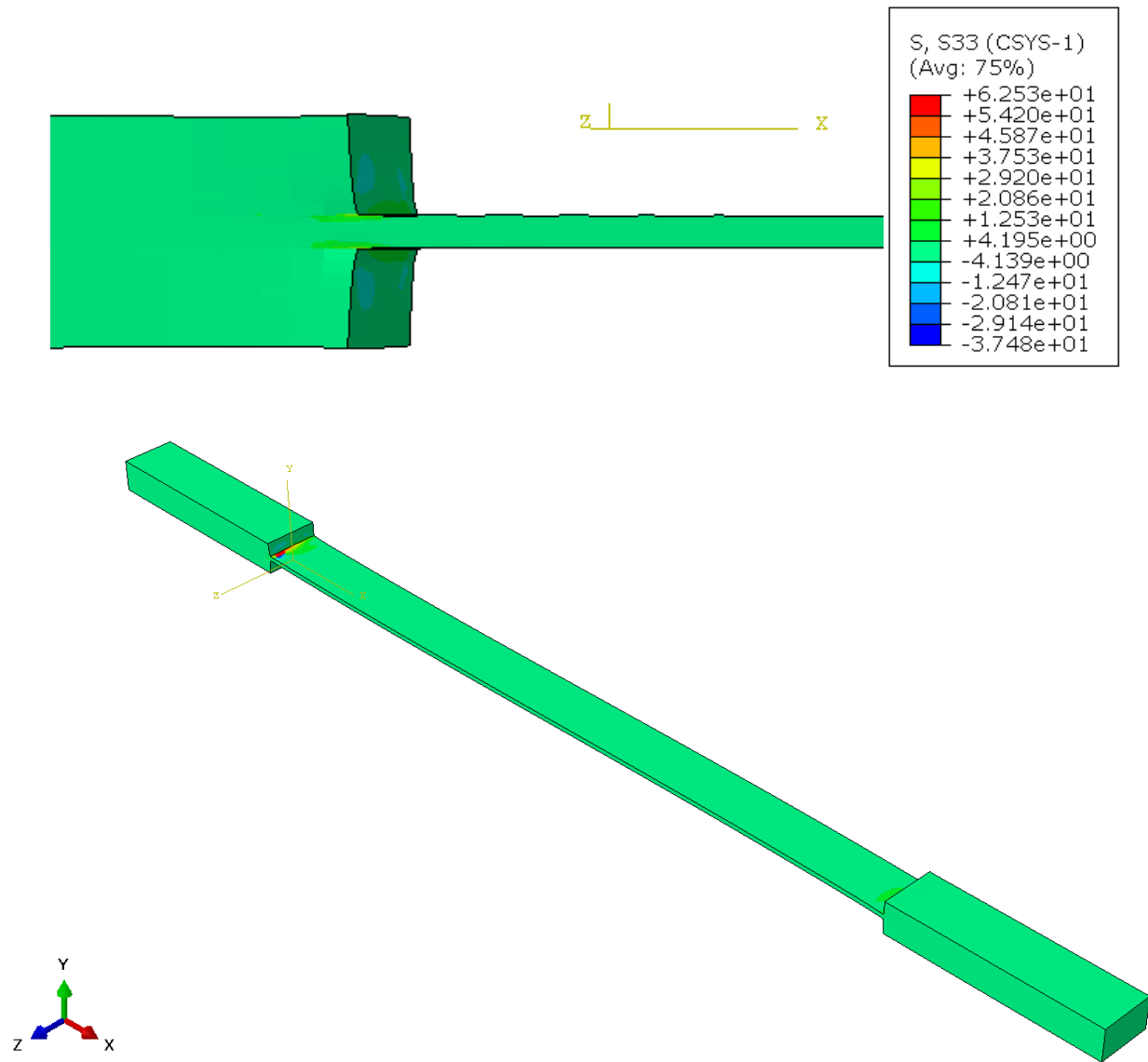
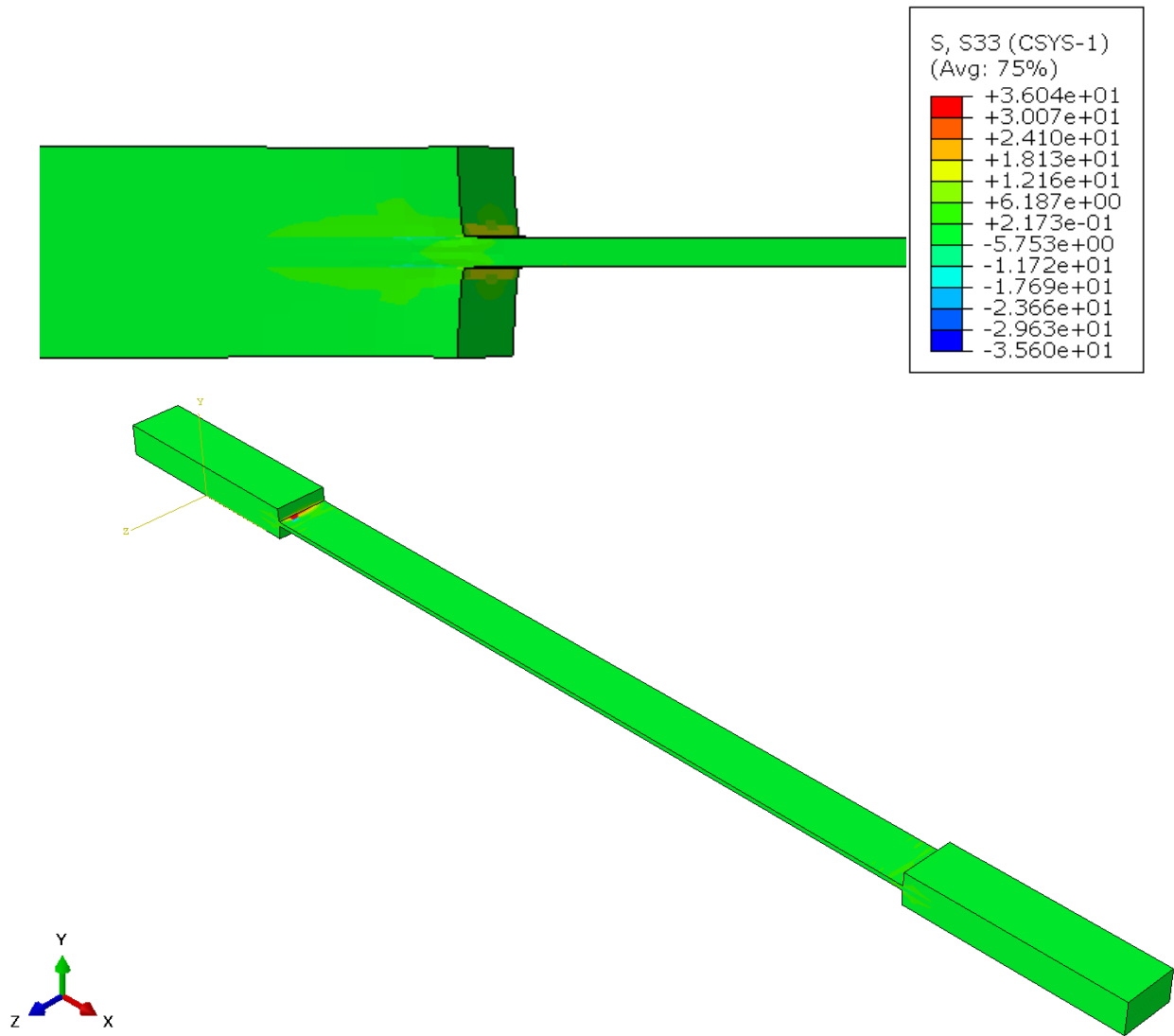


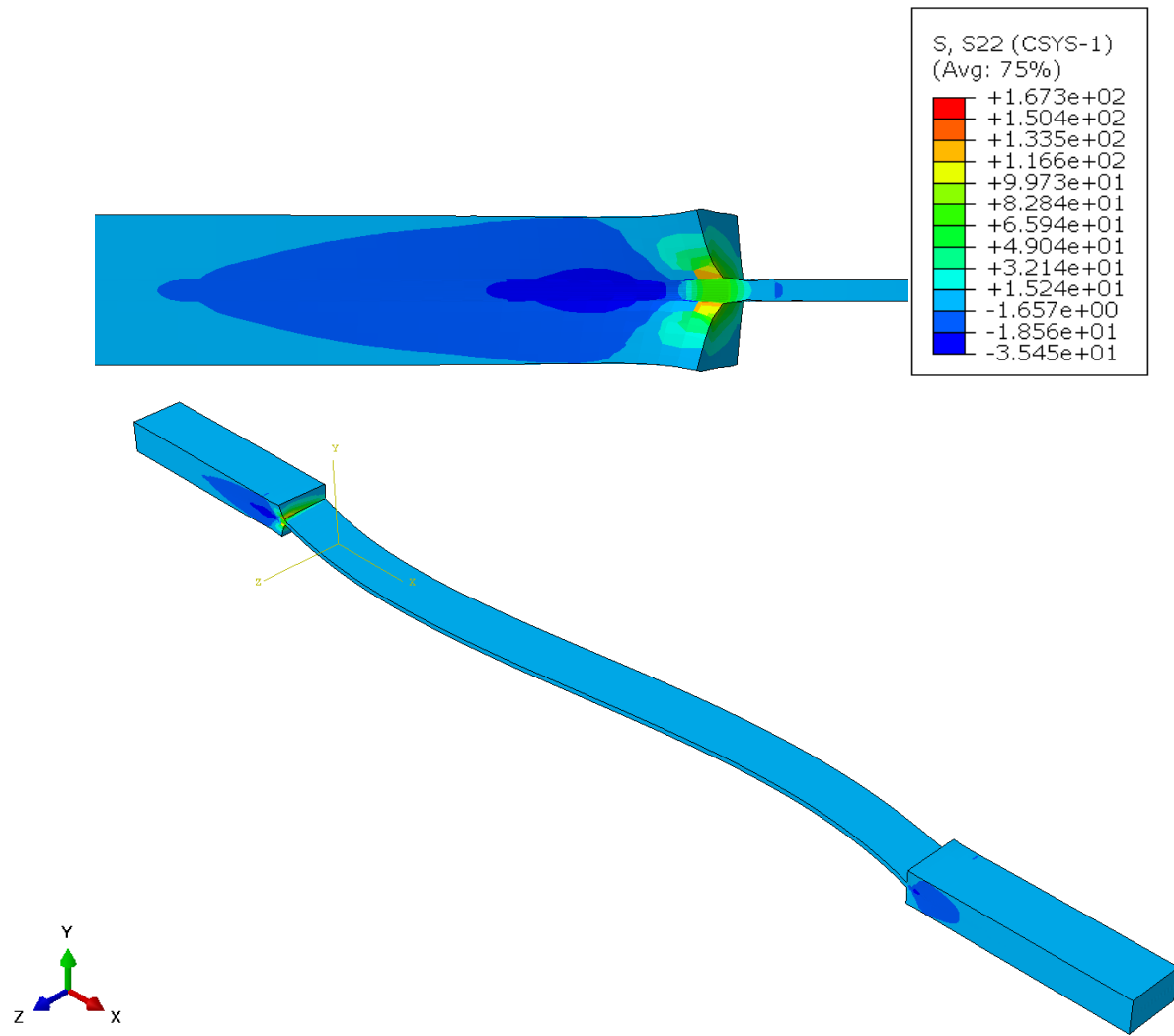
Figure 4.19 continued



(e) [75]₈

4.4.1.2.3 Normal Stress

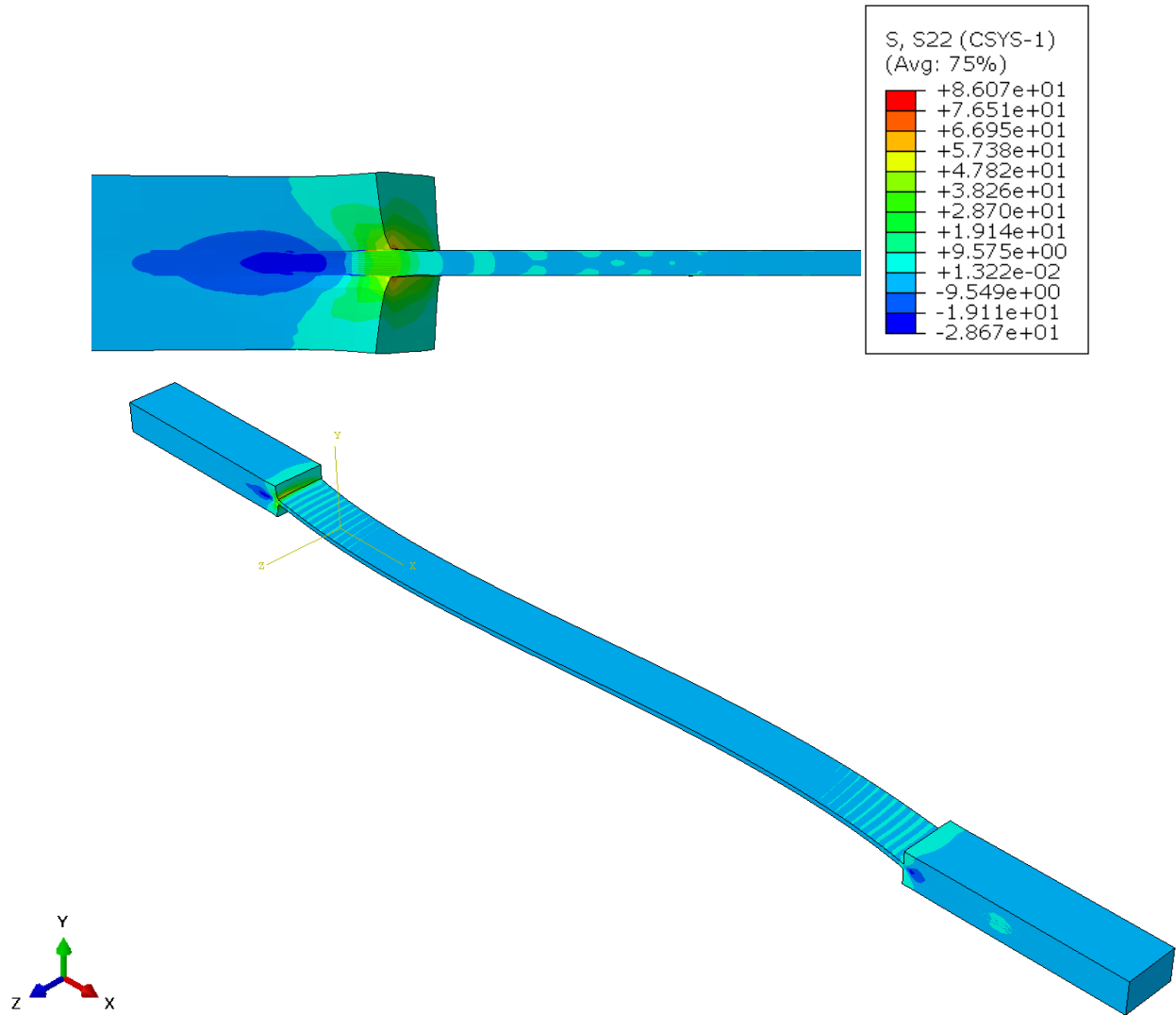
The magnitude of normal stress is also very less compared to axial stress. The stress is dominantly compressive in the tabs (as shown in Figure 16) and this is because of the pressure applied to them by the hydraulic grips in the MTS. At the tab endings, there is a state of tension which indicates that there are more chances for the tabs to de-bond at this region due to the build-up of stress concentration. The magnitude of normal stress is uniform at the rest of the laminate. The variation of this stress in the tabs also reduces with the increase in the off-axis angle.



(a) $[15]_8$

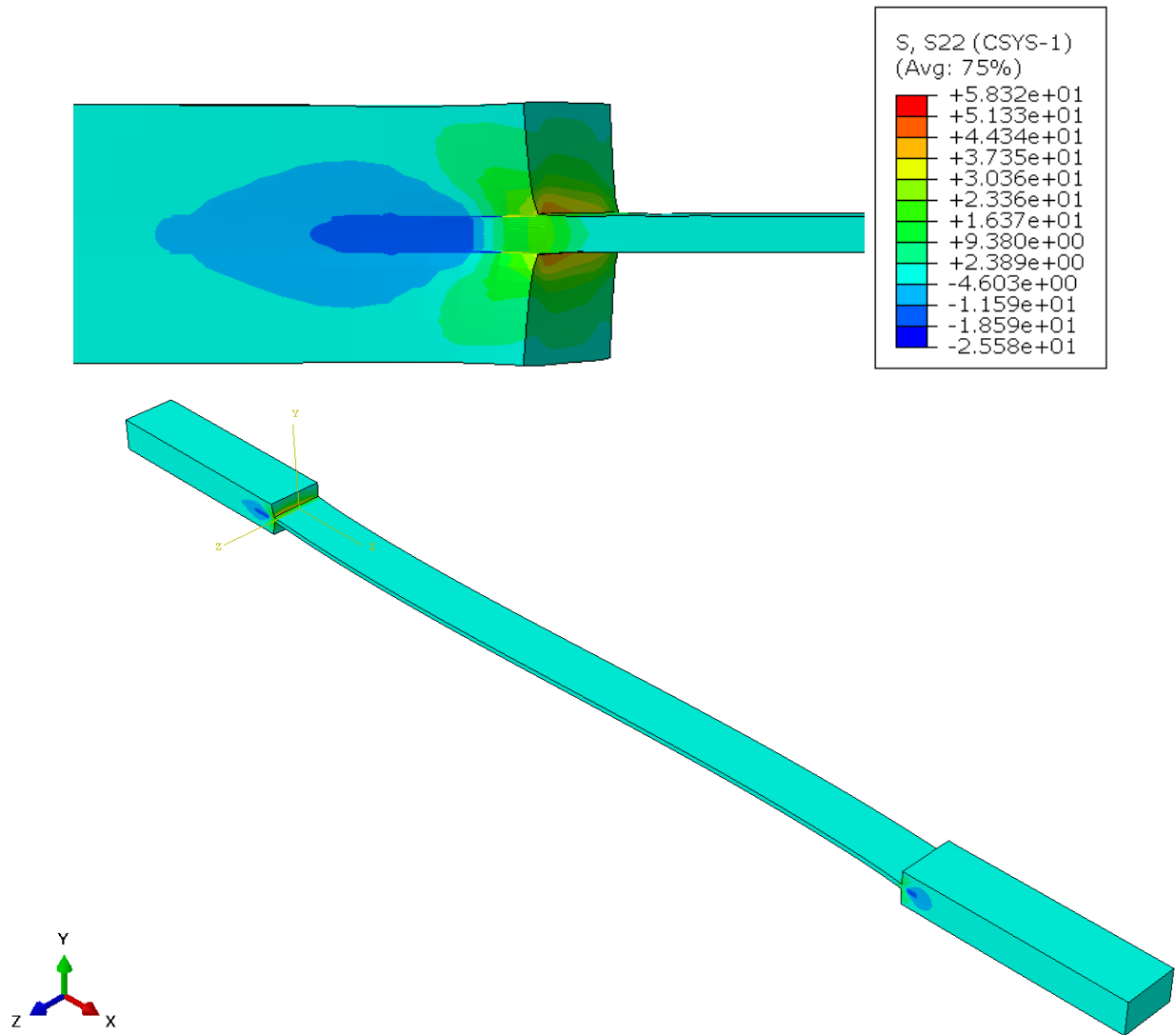
Figure 4.20: Normal stress (σ_{33}) on the off-axis specimen

Figure 4.21 continued



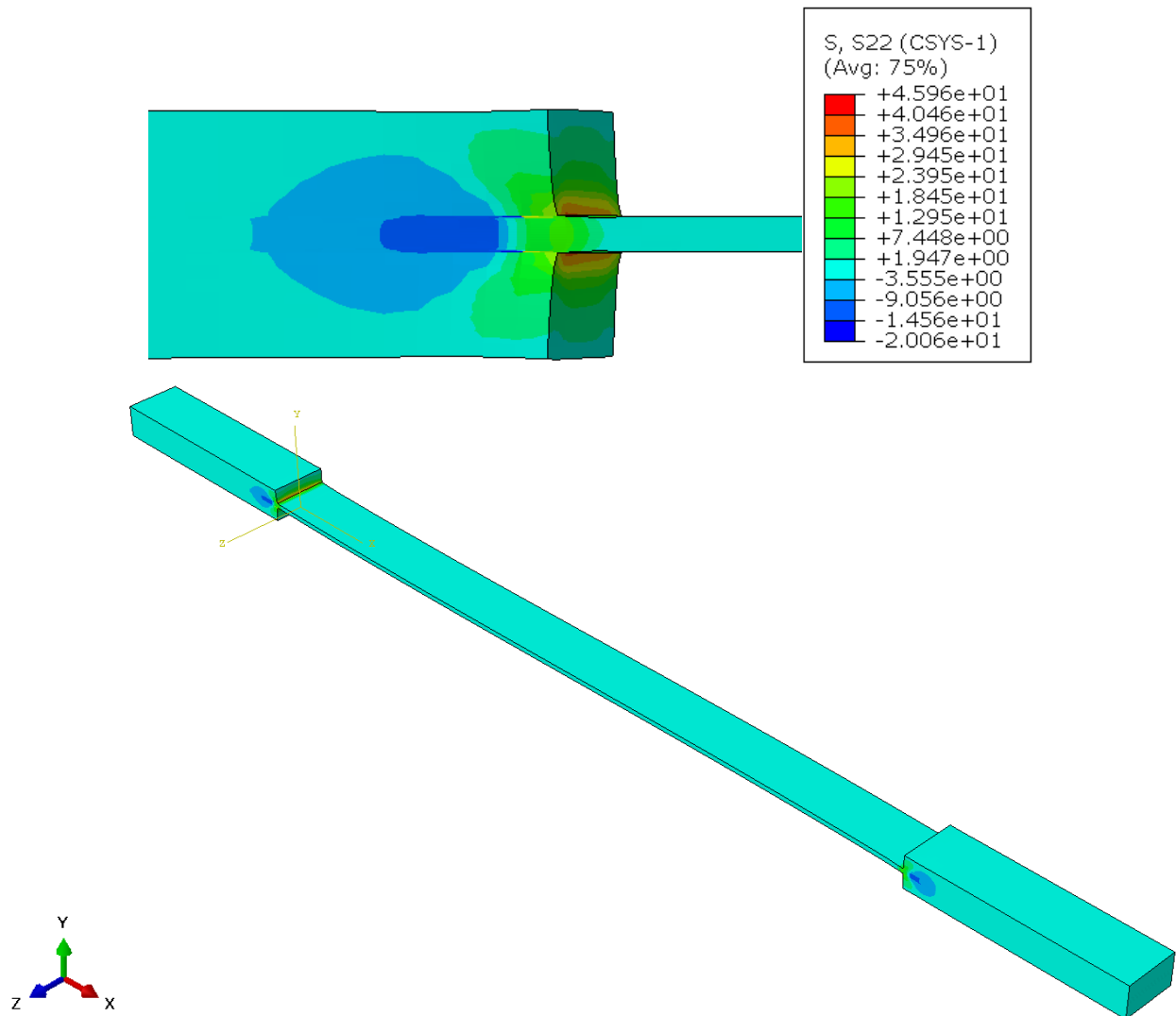
(b) $[30]_8$

Figure 4.22 continued



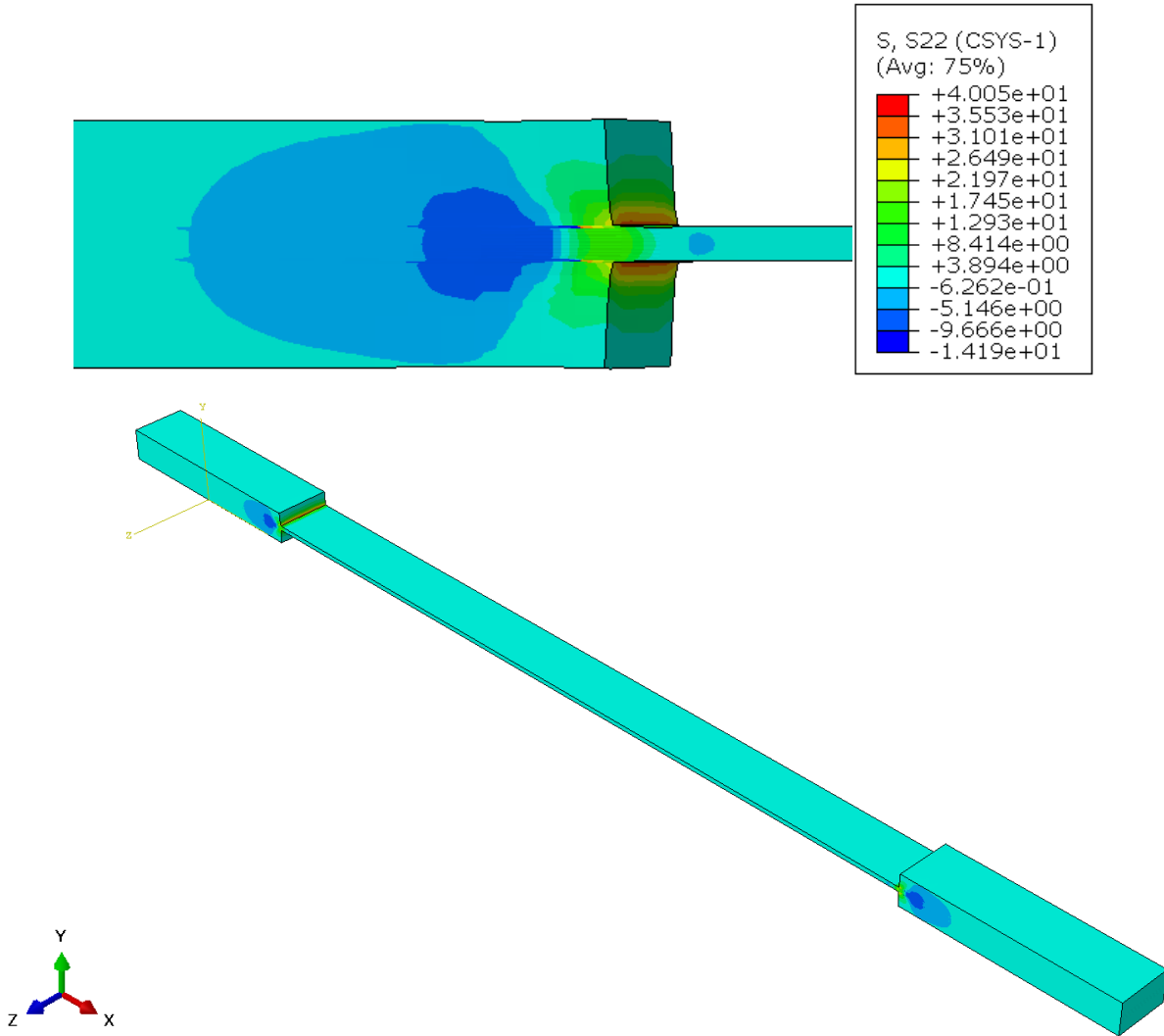
(c) $[45]_8$

Figure 4.23 continued



(d) $[60]_8$

Figure 4.24 continued



(e) [75]₈

4.4.1.2.4 In-plane Shear Stress

The magnitude of the in-plane shear is larger than the transverse and normal components of stress though it is still lower than the axial stress. The magnitude of shear stress is high at the tab endings (as shown in Figure 17) and it can also be observed that at the interaction of the tabs and the laminate towards the tab endings, there is a reversal of the direction of the shear stress and the magnitude gradually increases with a parabolic path. This is a consequence of the in-plane bending of the sample. The magnitude of in-plane shear stress is uniform at the rest of the sample along its length. As the off-axis angle increases, the variation of stress across the thickness of laminate and tabs reduces and for the [75]₈ specimen, this variation is close to negligible across the thickness.

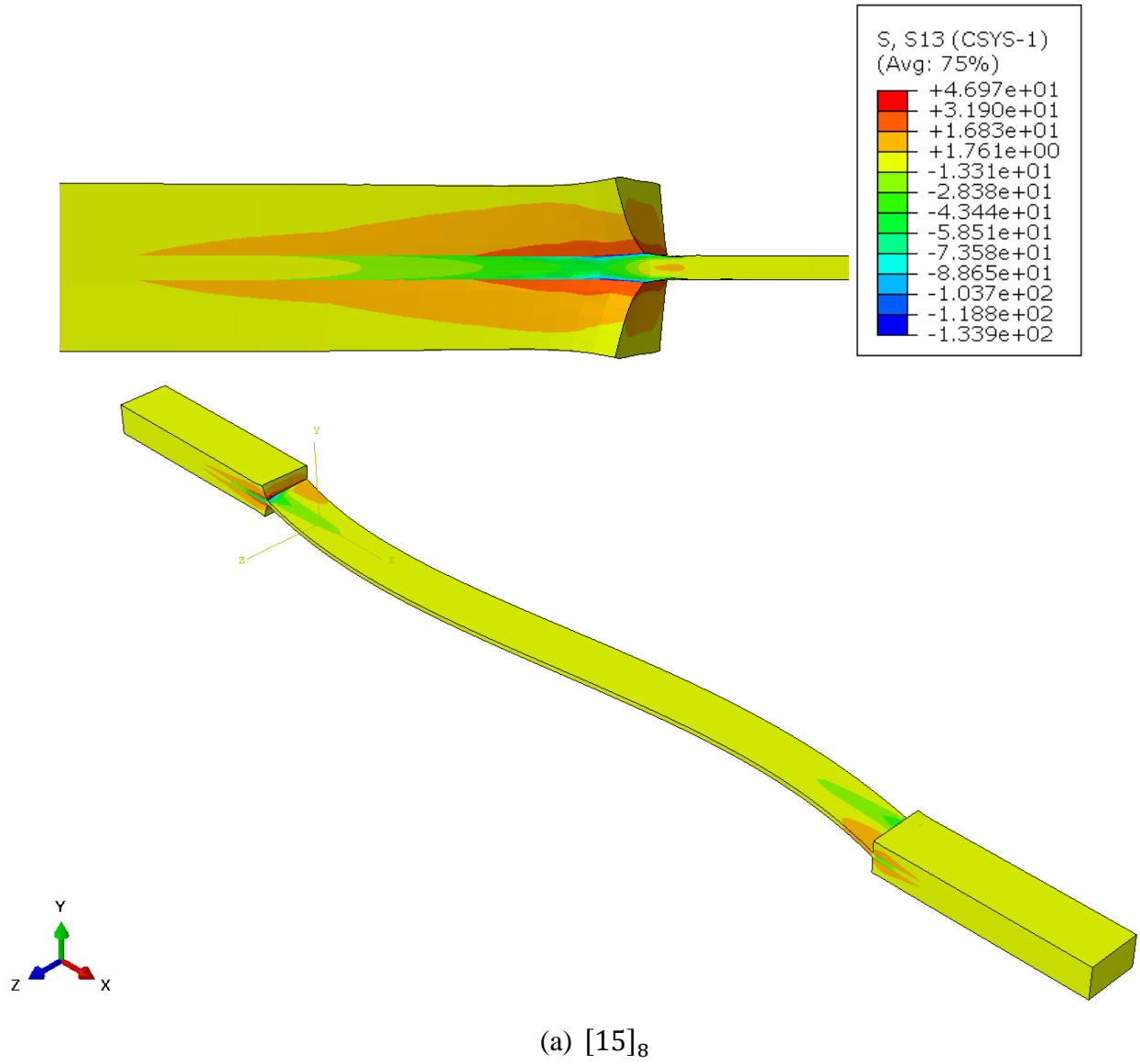
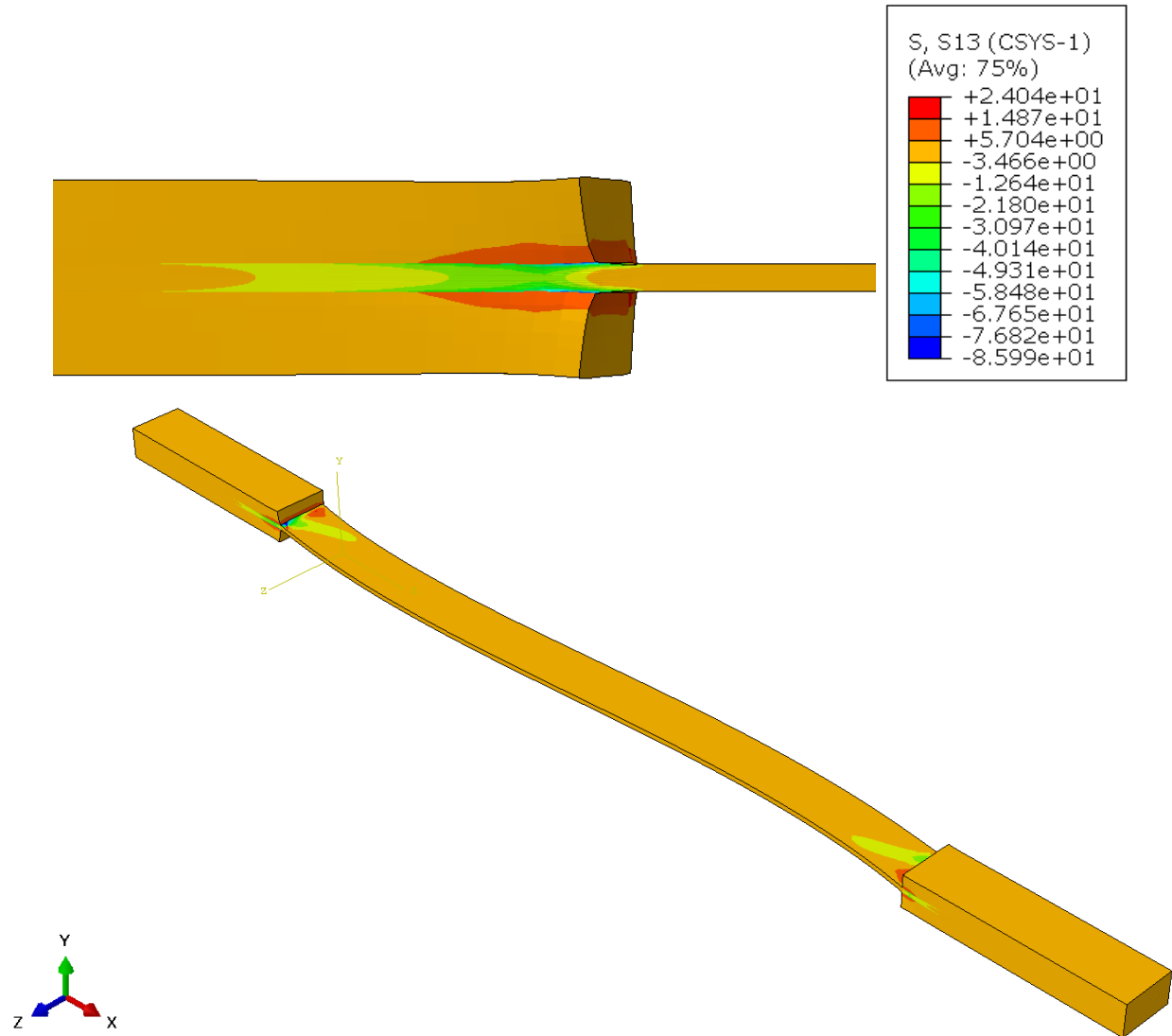


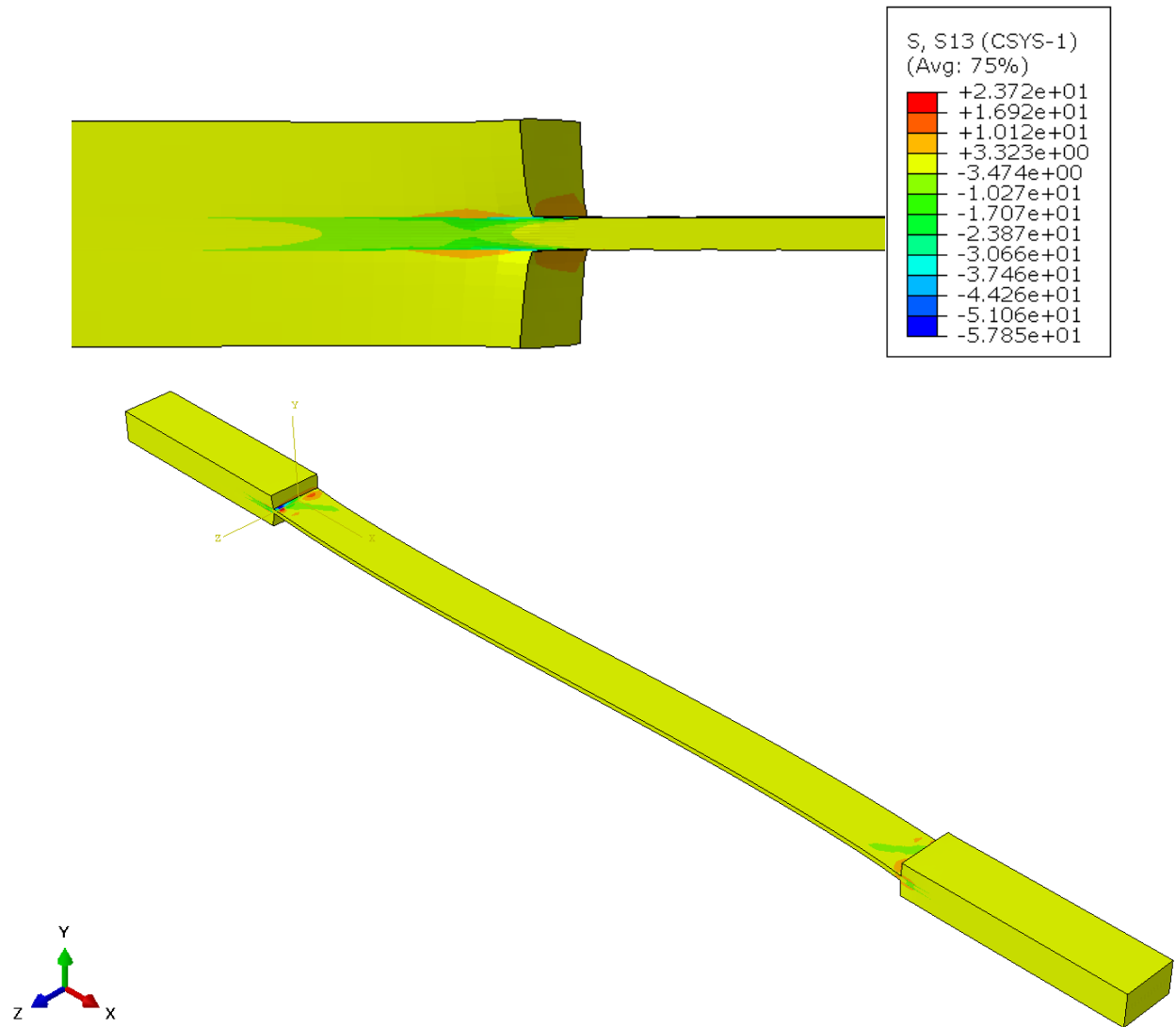
Figure 4.25: In-plane shear stress (σ_{12}) on the off-axis specimen

Figure 4.17 continued



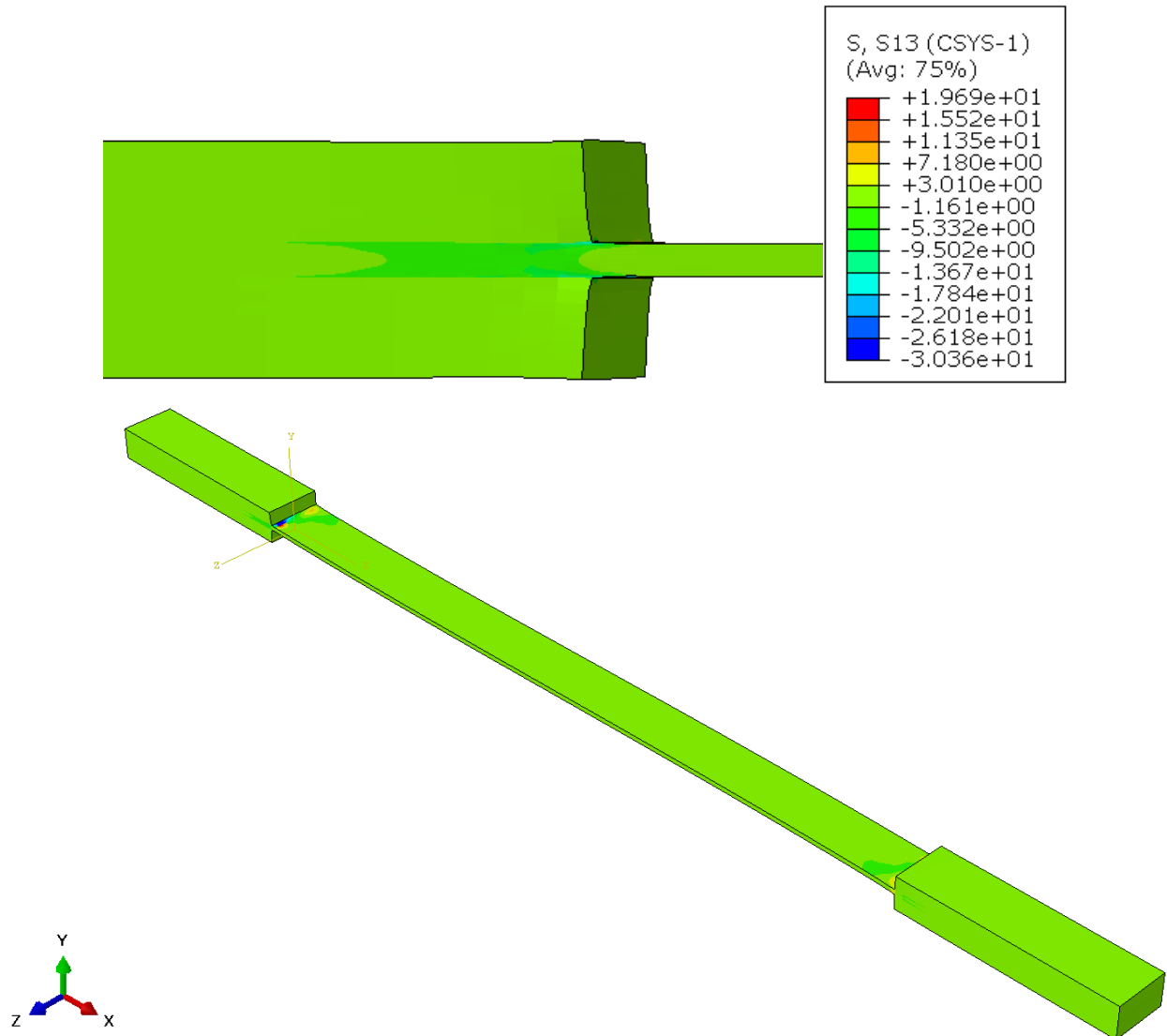
(b) $[30]_8$

Figure 4.17 continued



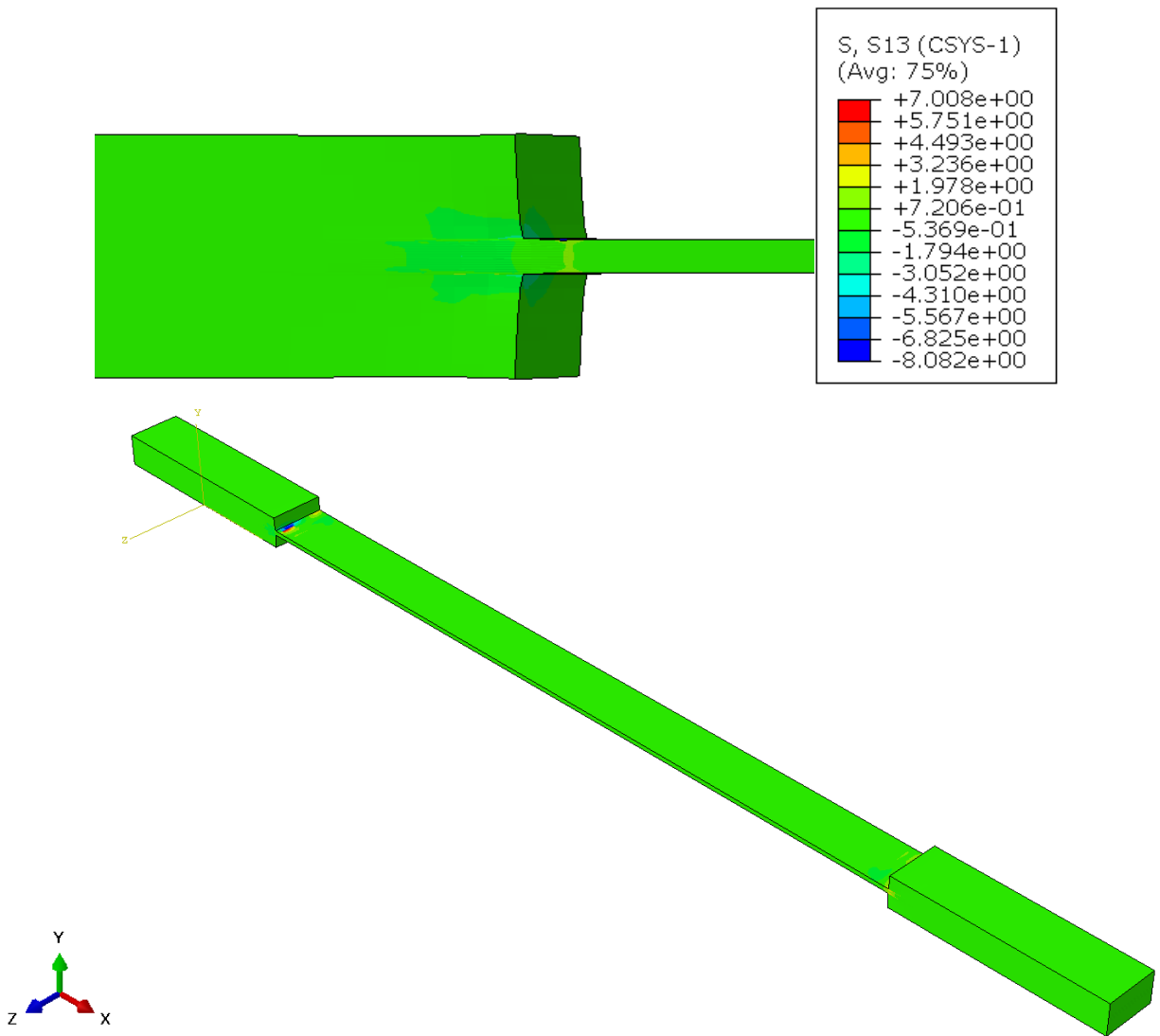
(c) $[45]_8$

Figure 4.17 continued



(d) $[60]_8$

Figure 4.17 continued



(e) $[75]_8$

4.4.1.3 Strain

4.4.1.3.1 Axial Strain

The axial strain in the sample is chiefly due to the in-plane bending in it. It can be seen from Figure 18 that there is a region of high-stress concentration at the edges that have the highest displacement in-plane. The region of strain inside the tabs shows that the laminate is in high amounts of strain at the tab endings at the interface with the laminate. At most of the regions in the tab, there is no strain present and there is strain concentration only at the endings of the tab. The strain is high even after the tab and it propagates to some region onto the laminate. But, the distribution of strain is symmetric and the magnitude reduces uniformly. As the off-axis angle increases, it can be observed that the strain variation in the tabs gradually reduces and also along the gage length of the specimen, the distribution of strain becomes more uniform.

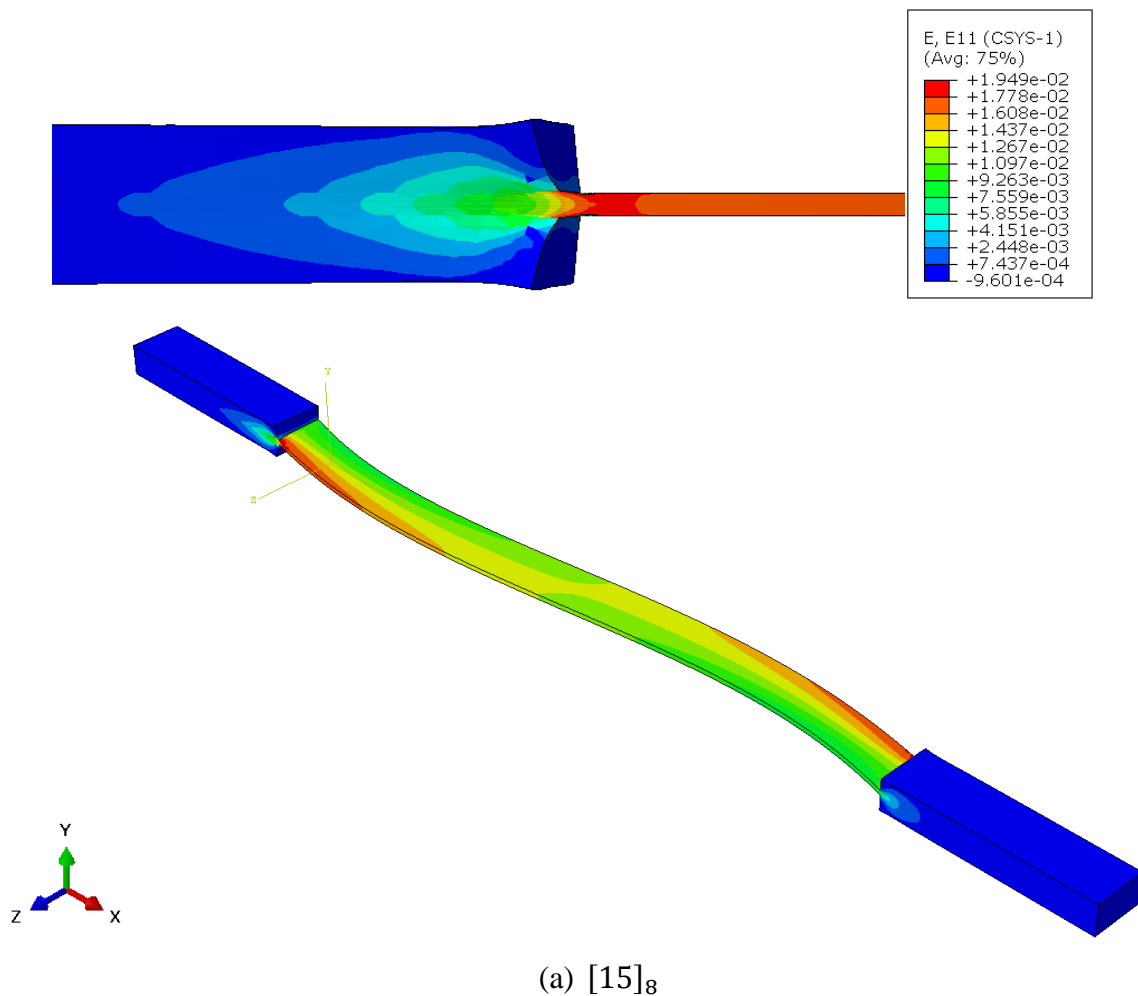
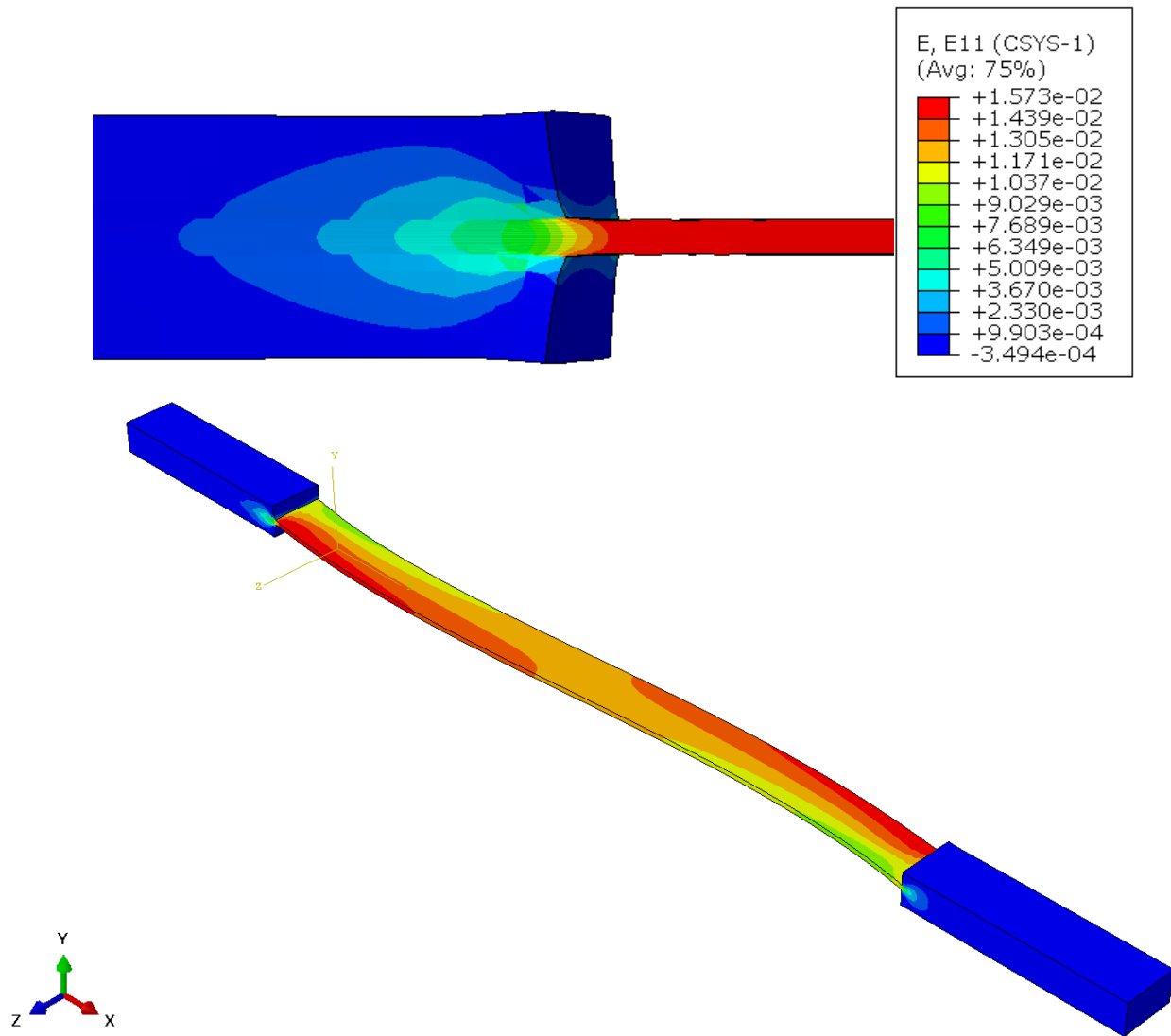


Figure 4.26: Axial strain (ϵ_{11}) on the off-axis specimen

Figure 4.18 continued



(b) $[30]_8$

Figure 4.18 continued

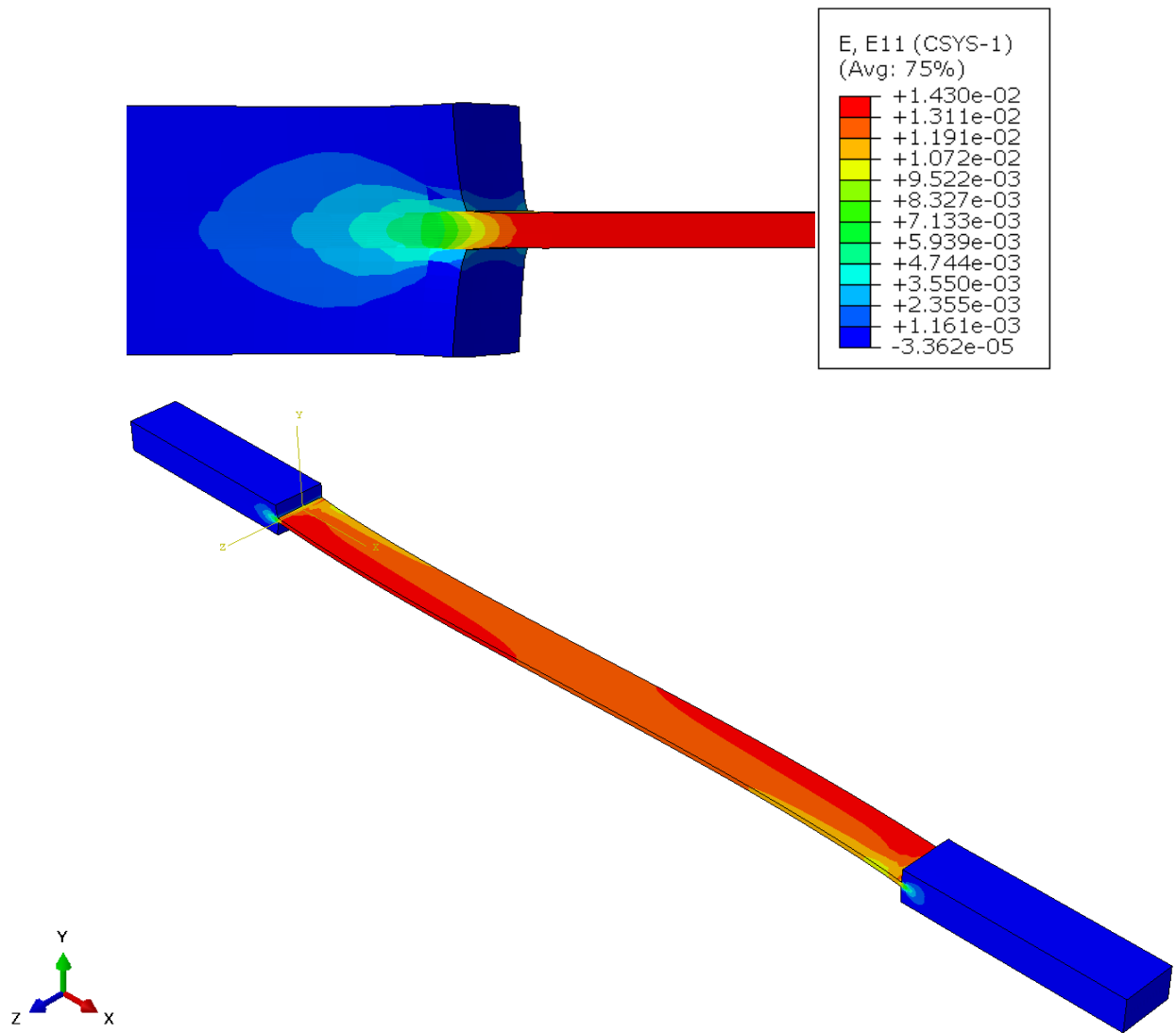
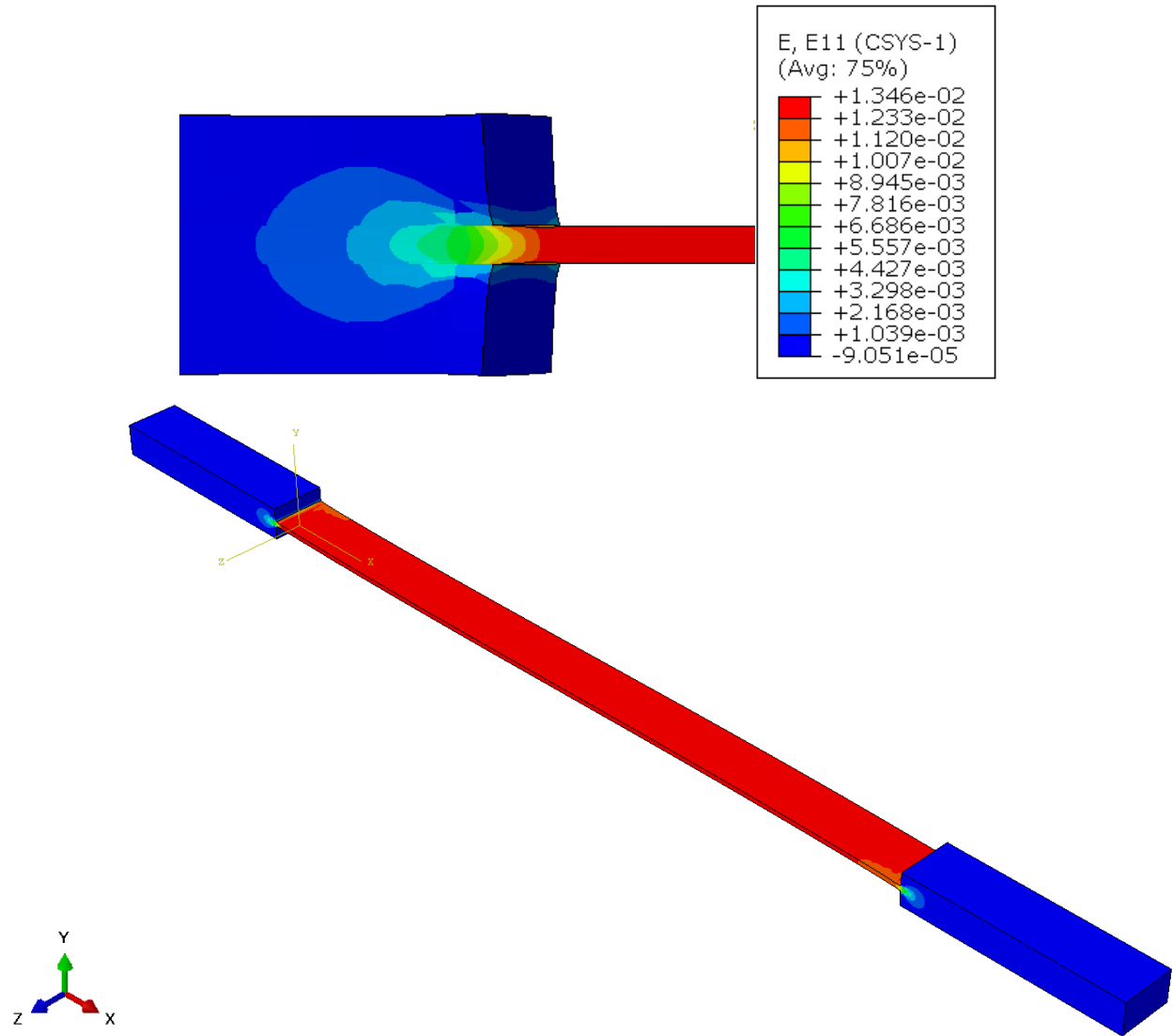
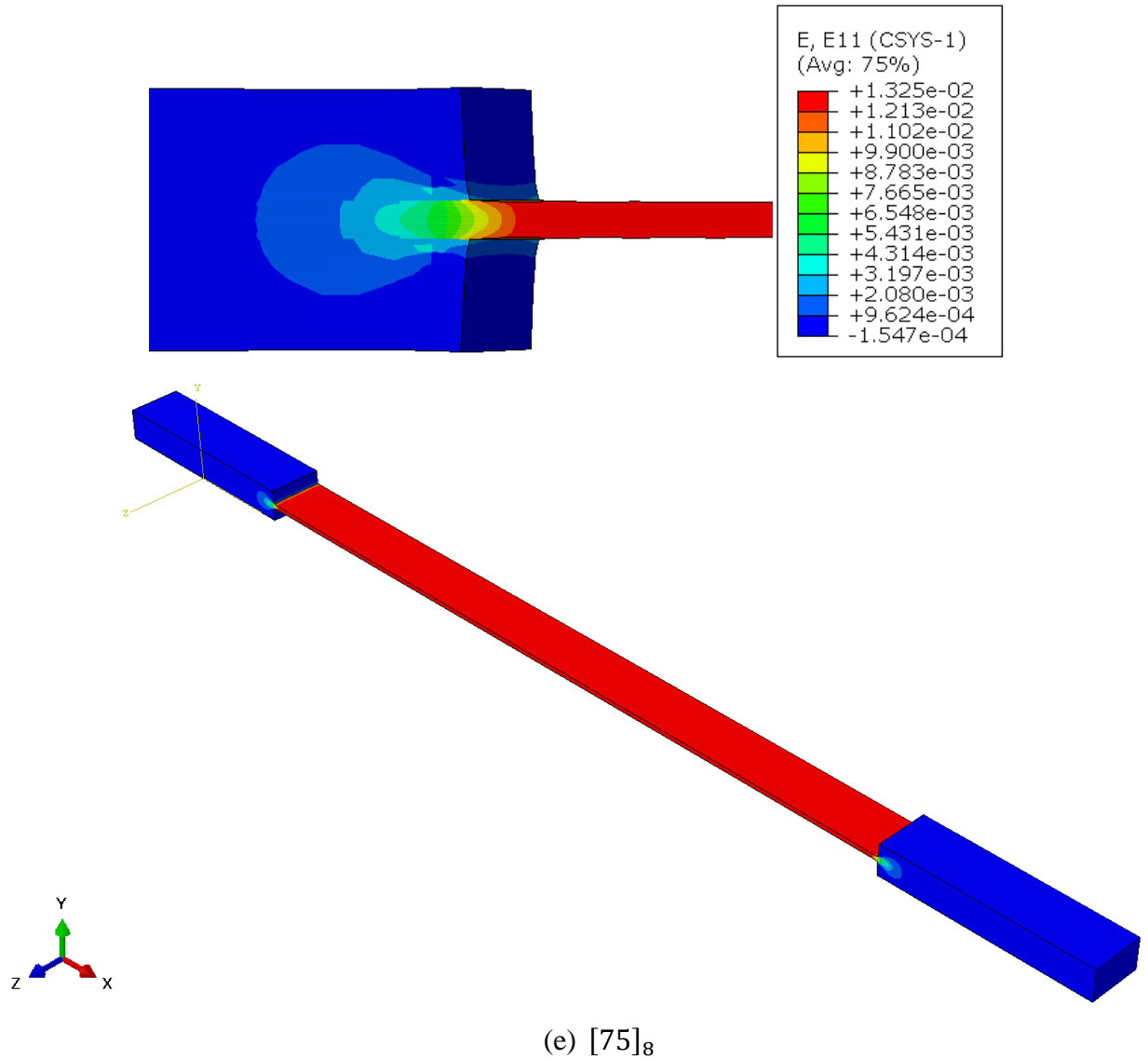


Figure 4.18 continued



(d) $[60]_8$

Figure 4.18 continued



4.4.1.3.2 Transverse Strain

The magnitude of the transverse strain is lower than that of the axial strain and the magnitude is negative as expected. The value of the transverse strain has a high amount of variation across width near the tabs and this variation is because the tabs restrict the shearing of the sample in the transverse direction at the ends. The value of the transverse strain reaches a constant value towards the center of the sample. The strain value is high at the ends across the width of the sample where the transverse displacement is the highest. This variation across the width also reduces as the off-

axis angle increases. The magnitude of strain, however, increases with the increase in the angle. Hence, the $[75]_8$ the specimen has the highest magnitude of strain and the lowest variation across the width of the sample.

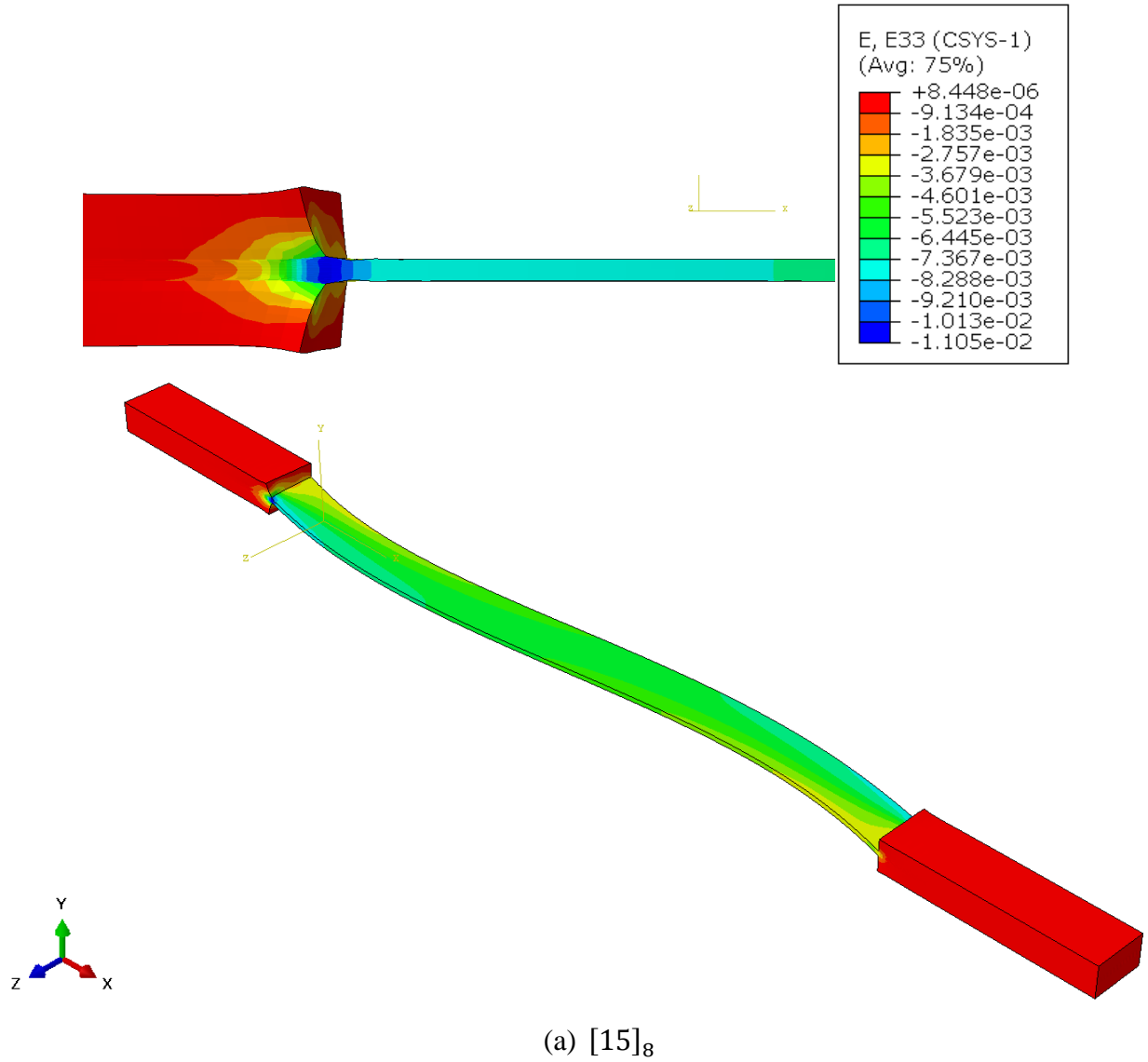
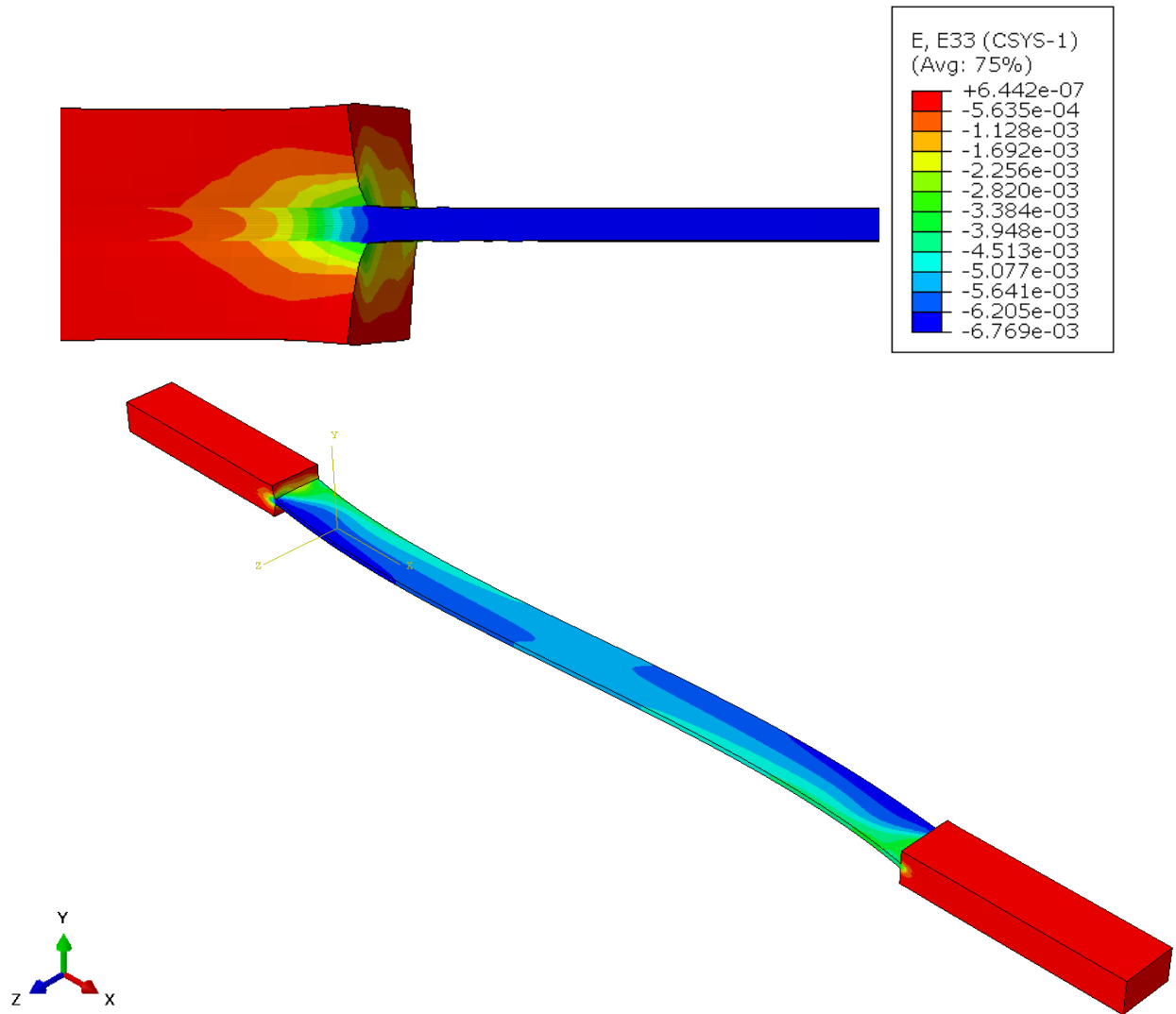


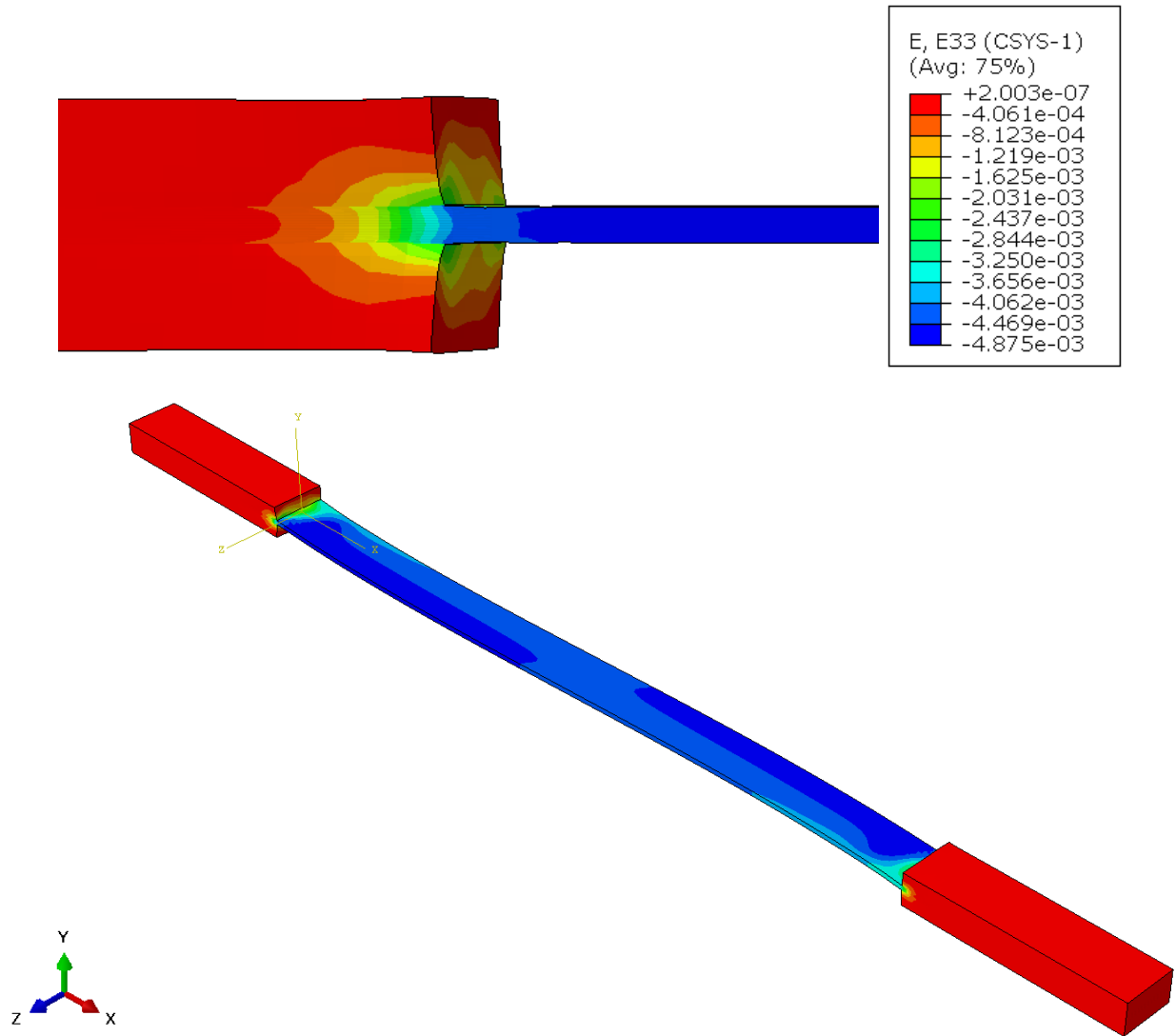
Figure 4.27: Transverse strain (ϵ_{22}) on the off-axis specimen

Figure 4.19 continued



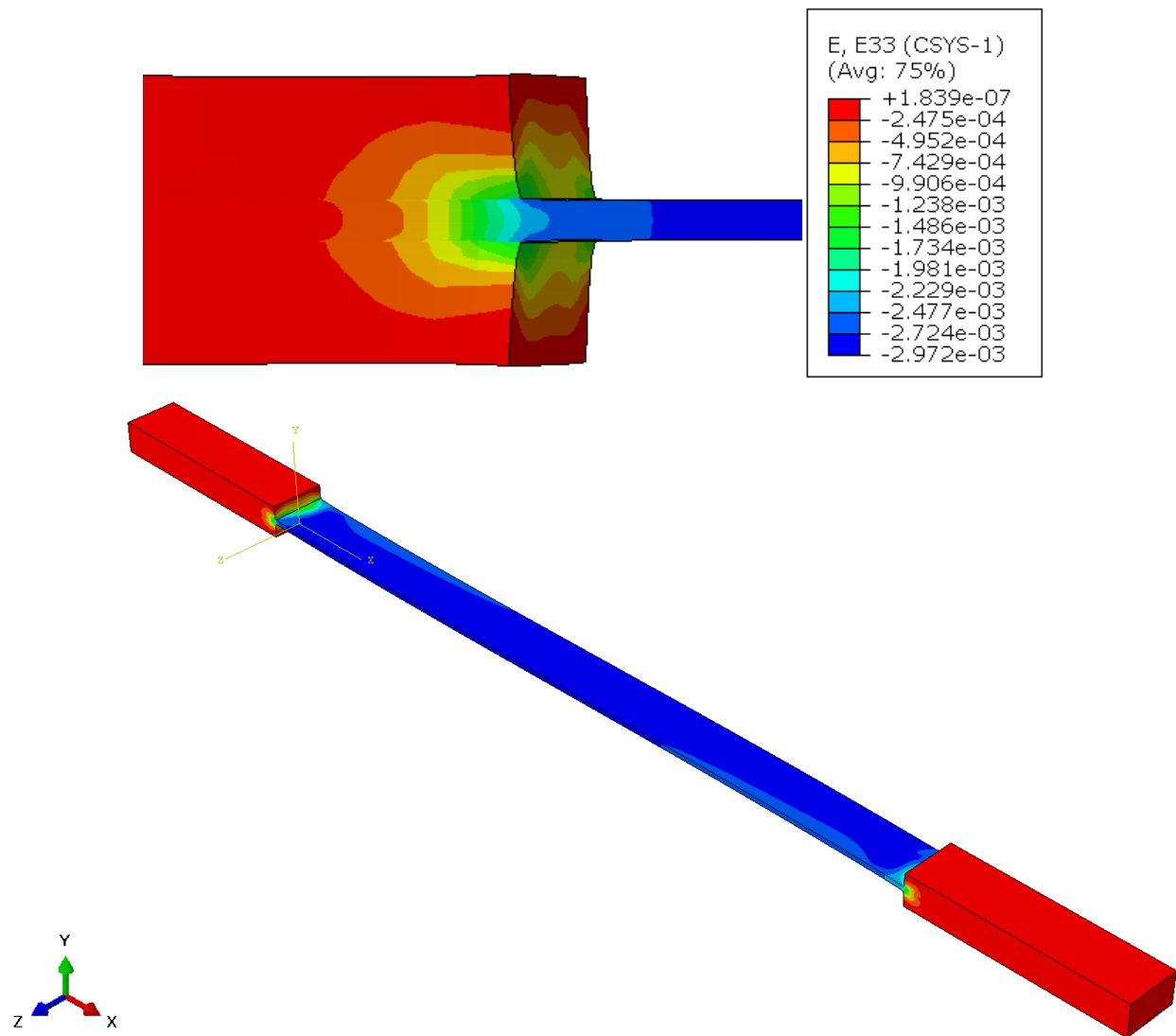
(b) $[30]_8$

Figure 4.28 continued



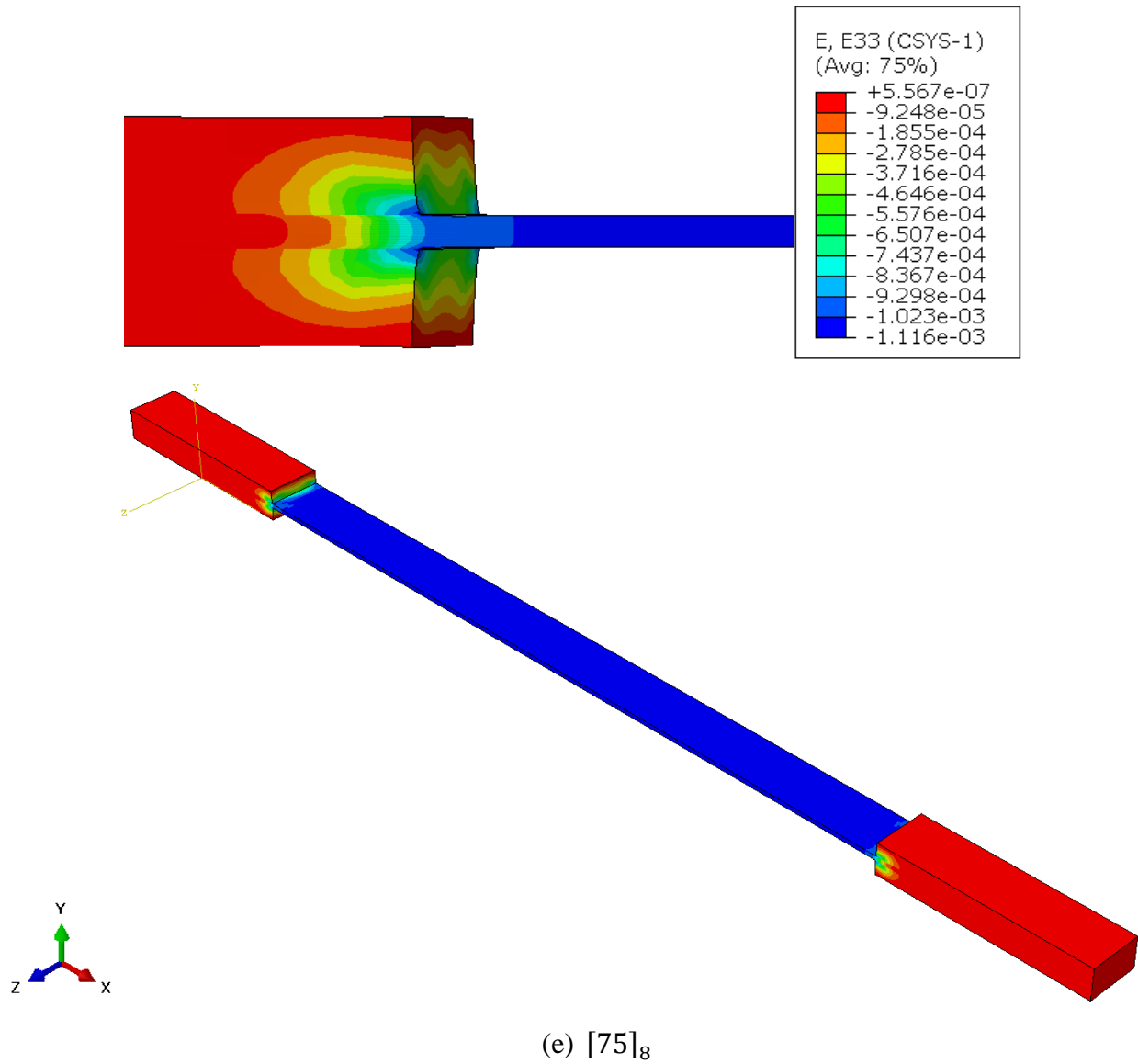
(c) $[45]_8$

Figure 4.29 continued



(d) $[60]_8$

Figure 4.30 continued



4.4.1.3.3 In-plane Shear Strain

The profile of the In-plane shear strain is similar to that of the axial strain but, the magnitude is smaller. The trend is similar to the axial strain where the magnitude keeps increasing in the tab and reaches a maximum at the ends and propagates along the edge of the sample where the displacement is the highest. The distribution of the shear strain also symmetric and the value varies uniformly. The magnitude of in-plane shear strain reduces at the gage length as the off-axis angle

increases. The gradient of the strain also reduces across the laminate within the tabs and the magnitude of the strain becomes almost zero for the $[75]_8$ specimen.

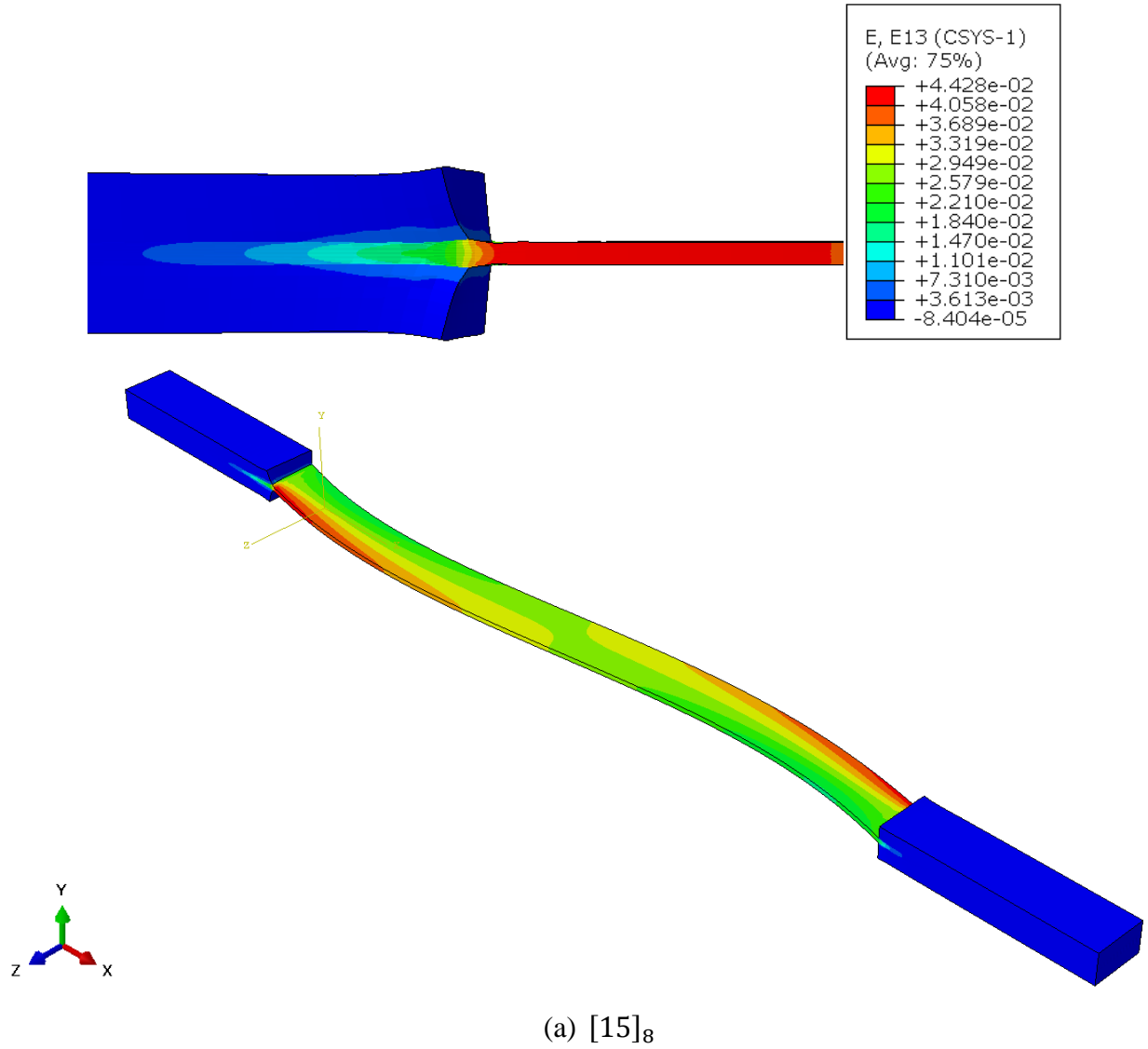
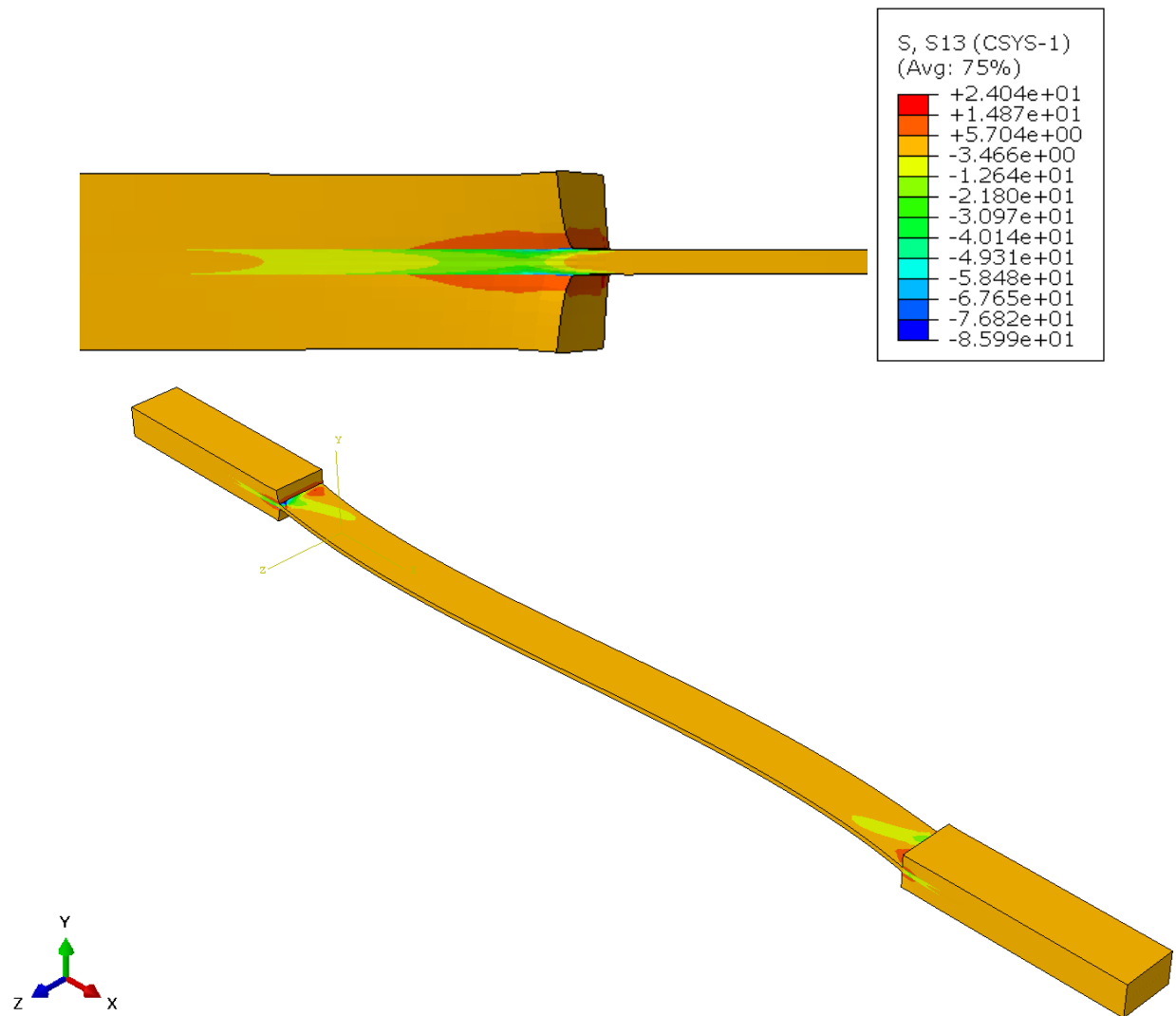


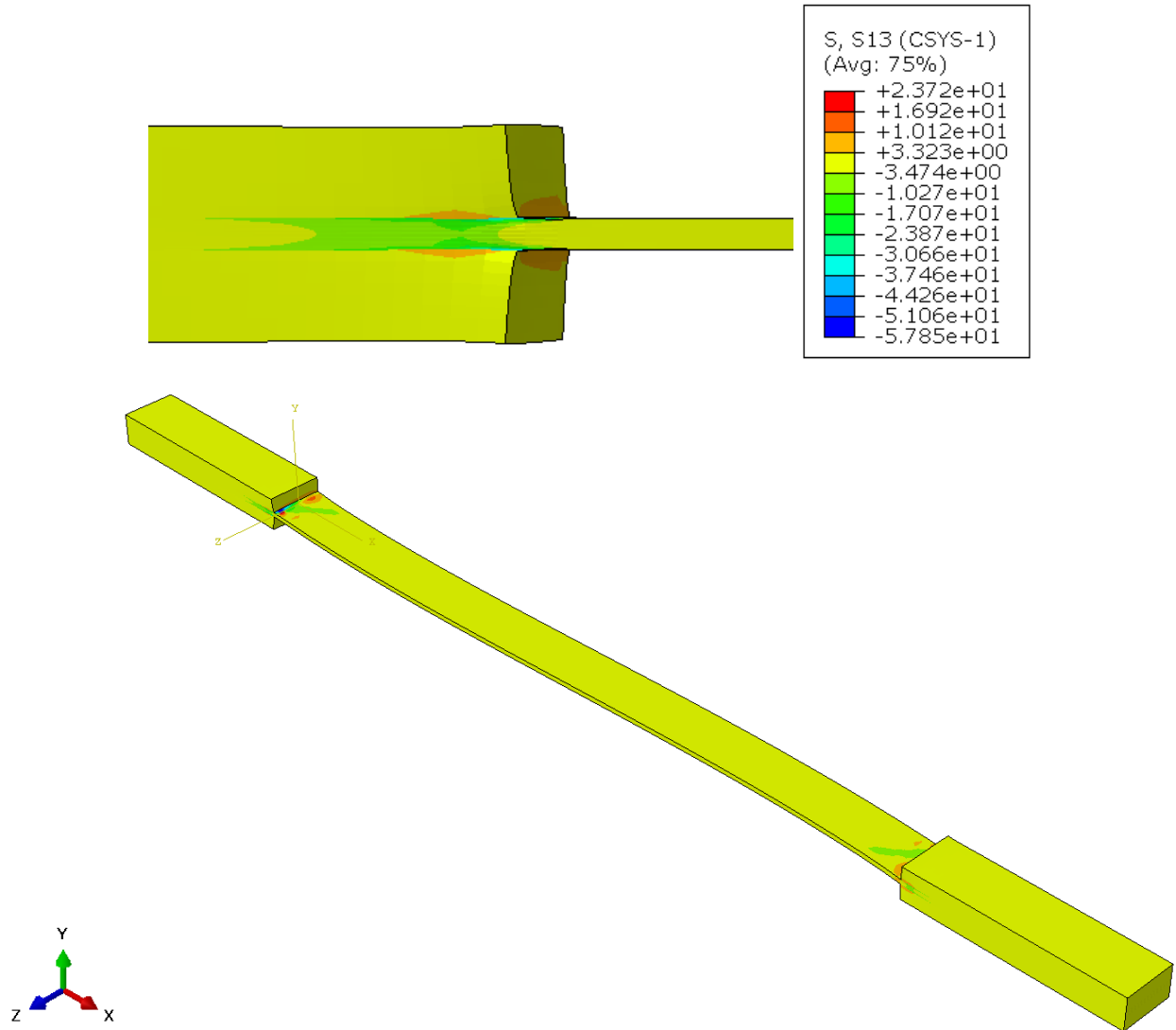
Figure 4.31: In-plane shear strain (ϵ_{12}) on the off-axis specimen

Figure 4.20 continued



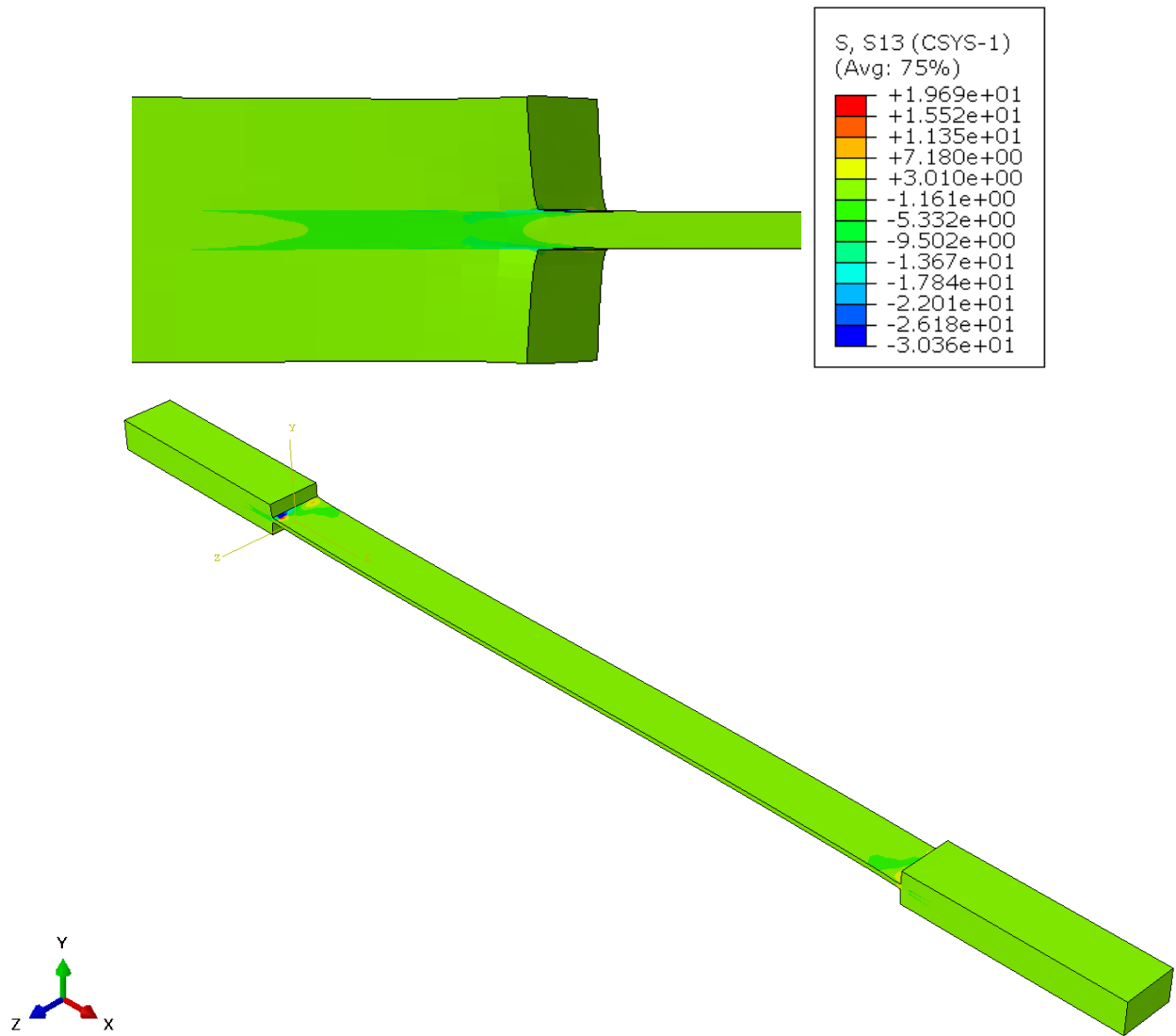
(b) $[30]_8$

Figure 4.20 continued



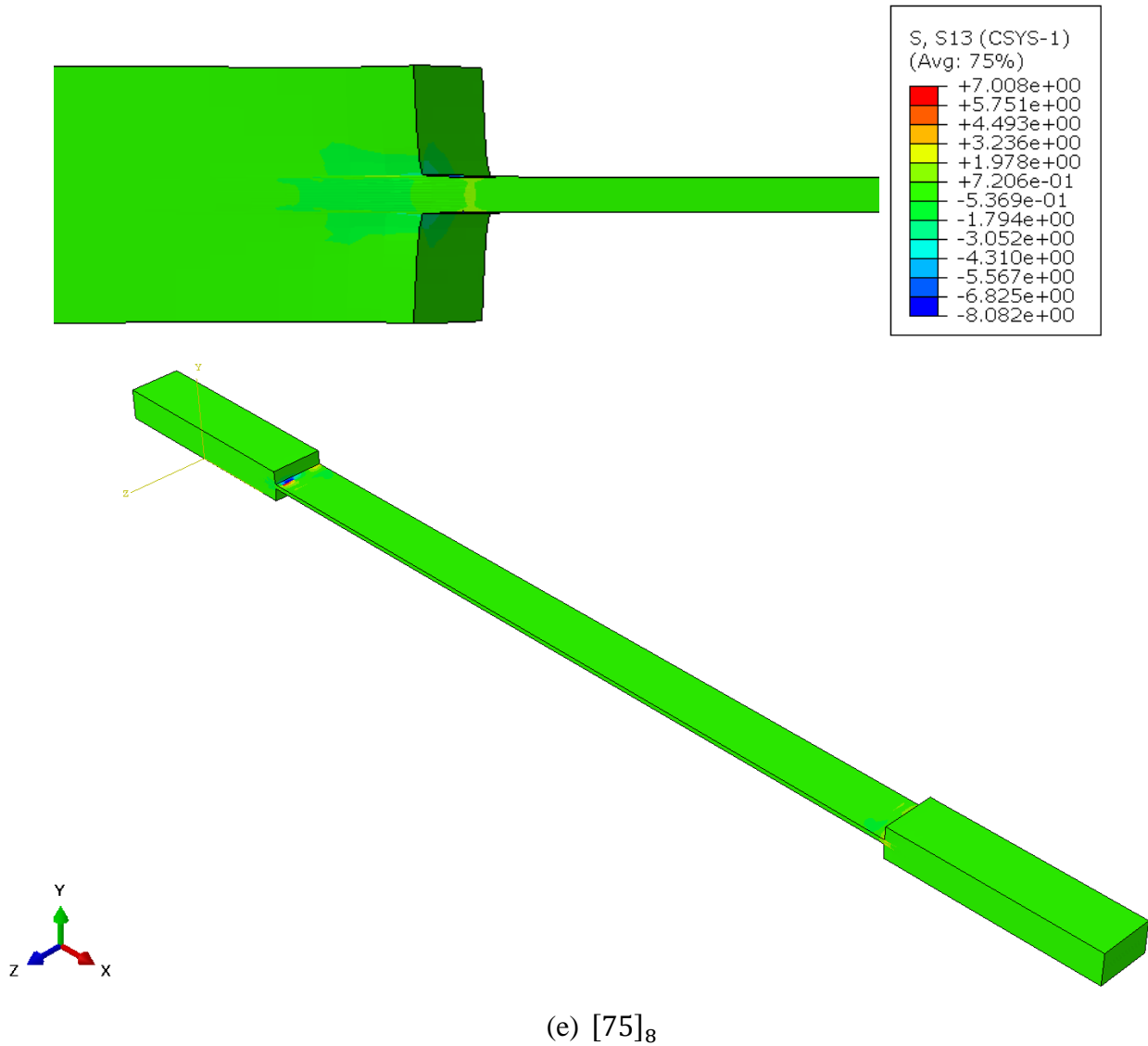
(c) $[45]_8$

Figure 4.20 continued



(d) $[60]_8$

Figure 4.20 continued



4.5 Conclusions

From the experimental data that was obtained from the off-axis tensile specimen, it was observed that by assuming the plane stress condition on them, the effective moduli of the samples can be predicted for a wide range of fiber orientations. The failure angles of the specimens were close to the fiber orientation. None of the fibers were broken during the tensile test. It was observed that the axial modulus and strength decrease with an increase in the off-axis angle and this decrease is very steep in the initial portion of the curve. The Poisson's ratio and shear coupling ratio increase

initially reaching their maximum values at 15° and then reduce gradually. For most of these curves, the data obtained from the experiment was in close agreement with the theoretical data. The highest amount of variation between experimental and theoretical data was observed for the Poisson's ratio. Different failure criteria were applied to these samples to predict their failure under combined stress. It was observed that the experimental data agreed with the Tsai-Wu failure criterion and had variations with the other criteria, especially at the initial angles.

From the simulation results, it can be observed that the off-axis angle plays a very important role in the stress state of the test specimen. The characteristic S-shape that was predicted in the experiment from the DIC analysis is clearly visible as the deformed shape of the specimen. The stress, strain, and displacements of the specimen were analyzed and it was observed that there was a uniform variation in these values and the results were also consistent with the variation of these values in the experiment. The variation of stresses at the tabs was also analyzed to understand the effects of constraining the specimen at the ends. The axial stress, out of plane shear stress τ_{xz} and normal stress is responsible for the failure of the specimen at the tabs in some cases. The magnitude of shear strain is found to be greater than the magnitude of axial strain accounting for the coupling due to constrained ends.

4.6 References

- [1] Carlsson, L. A., Adams, D. F., & Pipes, R. B. (2014). *Experimental characterization of advanced composite materials*. Boca Raton, FL: CRC Press.
- [2] Dr. Wenbin Yu. (2017) Multiscale Structural Mechanics. Wiley-Interscience. John Wiley & Sons, INC., Publication
- [3] Andrea Martin Tovar, Kevin McIver, Philip Steckler 20th September 2019, Friday, Lab 5- Off-Axis Tensile Testing, Presentation
- [4] Dr. Byron Pipes, 16th September 2019, Monday, Failure Theories, Presentation. PPT. (2019)
- [5] Fabrice Pierron & Alain Vautrin, THE 10" OFF-AXIS TENSILE TEST: A CRITICAL APPROACH, (Received 28 September 1995; accepted 14 December 1995), Presentation. PPT. (2019).

4.7 Appendix

4.7.1 Images

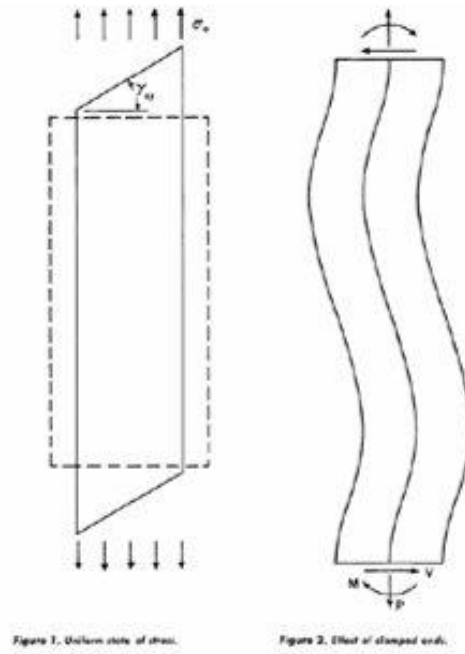


Figure 4.32: Off-axis coupon without and with constraints

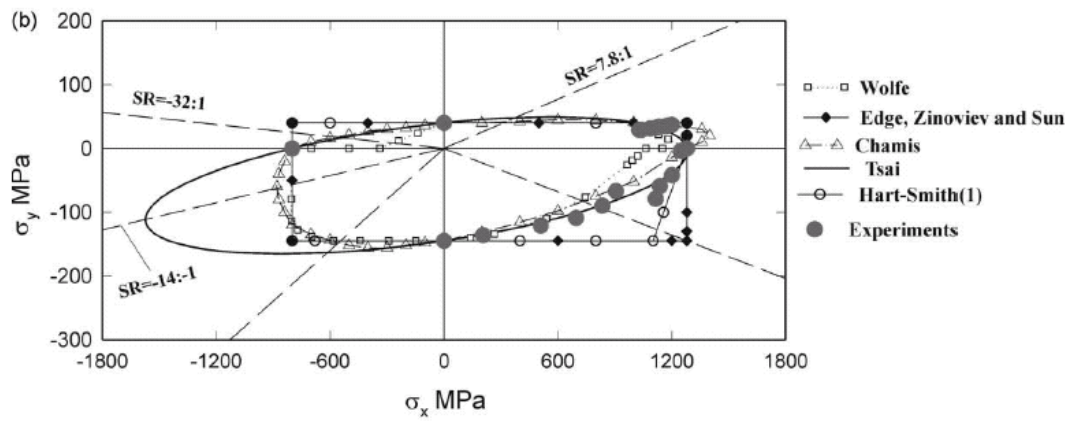


Figure 4.33: Failure envelope for a typical anisotropic material

5. LAMINATE TENSION

5.1 Introduction

5.1.1 Global and Local coordinate systems

A laminate comprises multiple layers of the lamina, which is a thin unidirectional ply of carbon fiber prepreg. As we add more layers in the laminate, we can design it to be symmetric and/or balanced. The laminates are balanced when there is an equal number of positive and negative oriented layers in the laminate and it is symmetric when the lay-up is symmetric about the mid-plane axis. Figure 1 shows the global and local coordinate systems for the analysis of composite laminates.

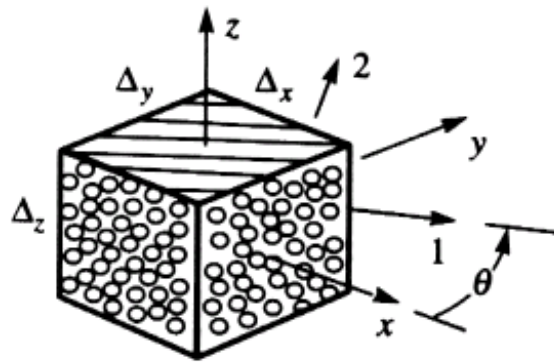


Figure 5.1: Local and global coordinate systems
(Image from Multiscale Structural Mechanics (2017))

X, Y, Z axes are the principal axes and 1, 2, 3 define the local coordinate system, where 1 is along the fiber direction and the angle θ is measured from the laminate principal axis. Figure 2 shows Kirchhoff's observations for the geometric deformations for rotated axes.

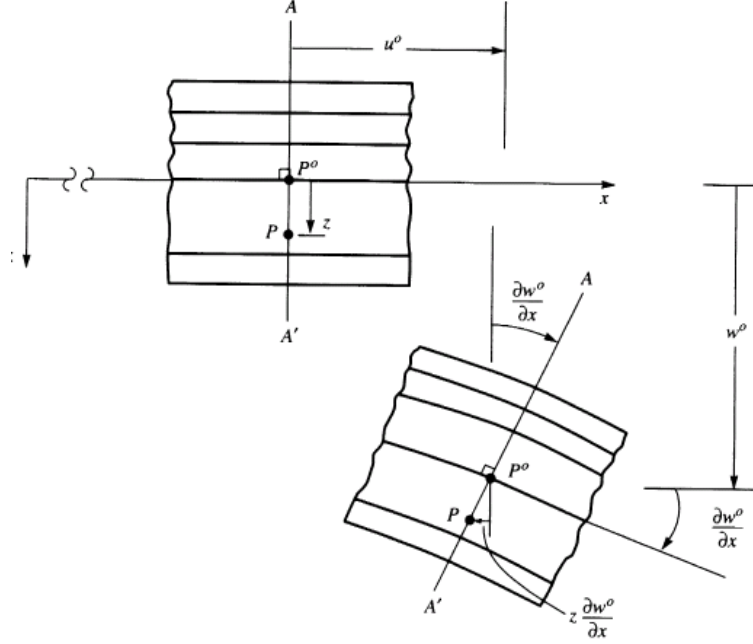


Figure 5.2: In-plane forces and moments
(Image from Multiscale Structural Mechanics (2017))

The strain varies within the plate as a linear function of position with respect to the laminate mid-plane. The strain equations in Kirchhoff's hypothesis are given as follows:

$$\begin{aligned}\varepsilon_x &= \varepsilon_x^0 + z\kappa_x \\ \varepsilon_y &= \varepsilon_y^0 + z\kappa_y \\ \gamma_{xy} &= \gamma_{xy}^0 + z\kappa_{xy}\end{aligned}$$

Where, $\varepsilon_x^0, \varepsilon_y^0, \gamma_{xy}^0$ are the midplane strains and $\kappa_x, \kappa_y, \kappa_{xy}$ are the curvatures. The radii of curvatures are the inverses of respective curvatures. The force resultants can be obtained by the integration of stress through-thickness and the moment resultants are obtained by the integration of the first moment of stress through the thickness. Figure 3 shows the In-plane forces per unit length (N) and moments per unit length (M) in a laminate in the principal coordinate system.

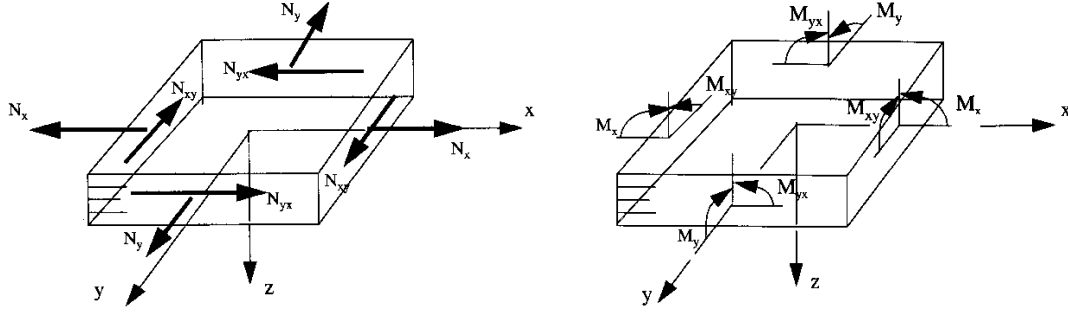


Figure 5.3: In-plane forces and moments per unit length
(Image from Multiscale Structural Mechanics (2017))

The magnitudes of forces and moments are obtained from the following equations:

$$F_x = \int_{-h/2}^{h/2} \sigma_x dz$$

$$F_y = \int_{-h/2}^{h/2} \sigma_y dz$$

$$F_{xy} = \int_{-h/2}^{h/2} \tau_{xy} dz$$

$$M_x = \int_{-h/2}^{h/2} \sigma_x z dz$$

$$M_y = \int_{-h/2}^{h/2} \sigma_y z dz$$

$$M_{xy} = \int_{-h/2}^{h/2} \tau_{xy} z dz$$

5.1.2 Obtaining elastic constants from the stiffness matrix using Classical Laminate Plate Theory (CLPT)

The Classical Laminate Plate Theory assumes that the laminate as a whole acts as a single layer where laminae are perfectly bonded to each other, which enables continuous displacement between the layers so that they do not slip relative to each other. It also assumes that a line that is straight and perpendicular to the middle surface remains straight and normal to the middle surface and the length of the line also remains unchanged during the plate deformation. The constitutive relations of the composite laminate in the laminate coordinate system are given in the form of symmetric matrices as follows:

$$\begin{bmatrix} \sigma_{11} \\ \sigma_{22} \\ \sigma_{33} \\ \sigma_{23} \\ \sigma_{13} \\ \sigma_{12} \end{bmatrix} = \begin{bmatrix} C_{11} & C_{12} & C_{13} & C_{14} & C_{15} & C_{16} \\ C_{12} & C_{22} & C_{23} & C_{24} & C_{25} & C_{26} \\ C_{13} & C_{23} & C_{33} & C_{34} & C_{35} & C_{36} \\ C_{14} & C_{24} & C_{34} & C_{44} & C_{45} & C_{46} \\ C_{15} & C_{25} & C_{35} & C_{45} & C_{55} & C_{56} \\ C_{16} & C_{26} & C_{36} & C_{46} & C_{56} & C_{66} \end{bmatrix} \begin{bmatrix} \varepsilon_{11} \\ \varepsilon_{22} \\ \varepsilon_{33} \\ 2\varepsilon_{23} \\ 2\varepsilon_{13} \\ 2\varepsilon_{12} \end{bmatrix}$$

$$\begin{bmatrix} \varepsilon_{11} \\ \varepsilon_{22} \\ \varepsilon_{33} \\ 2\varepsilon_{23} \\ 2\varepsilon_{13} \\ 2\varepsilon_{12} \end{bmatrix} = \begin{bmatrix} S_{11} & S_{12} & S_{13} & S_{14} & S_{15} & S_{16} \\ S_{12} & S_{22} & S_{23} & S_{24} & S_{25} & S_{26} \\ S_{13} & S_{23} & S_{33} & S_{34} & S_{35} & S_{36} \\ S_{14} & S_{24} & S_{34} & S_{44} & S_{45} & S_{46} \\ S_{15} & S_{25} & S_{35} & S_{45} & S_{55} & S_{56} \\ S_{16} & S_{26} & S_{36} & S_{46} & S_{56} & S_{66} \end{bmatrix} \begin{bmatrix} \sigma_{11} \\ \sigma_{22} \\ \sigma_{33} \\ \sigma_{23} \\ \sigma_{13} \\ \sigma_{12} \end{bmatrix}$$

Applying the plane stress assumption on the laminate, we consider that $\sigma_{i3} = 0$. Hence, constitutive relations reduce to the following:

$$\varepsilon_e = \begin{bmatrix} S_{11} & S_{12} & S_{16} \\ S_{12} & S_{22} & S_{26} \\ S_{16} & S_{26} & S_{66} \end{bmatrix} \sigma_e \equiv S_e \sigma_e$$

$$\varepsilon_t = \begin{bmatrix} S_{13} & S_{23} & S_{36} \\ S_{14} & S_{24} & S_{46} \\ S_{15} & S_{25} & S_{56} \end{bmatrix} \sigma_e \equiv S_{et}^T \sigma_e$$

Where, $\varepsilon_e = \begin{bmatrix} \varepsilon_{11} \\ \varepsilon_{22} \\ 2\varepsilon_{12} \end{bmatrix}$; $\sigma_e = \begin{bmatrix} \sigma_{11} \\ \sigma_{22} \\ \sigma_{12} \end{bmatrix}$; $\varepsilon_t = \begin{bmatrix} \varepsilon_{33} \\ 2\varepsilon_{23} \\ 2\varepsilon_{13} \end{bmatrix}$

S_e is known as the plane stress reduced compliance matrix. The following equation represents the plane stress reduced stiffness matrix (Q):

$$\sigma_e = \begin{bmatrix} Q_{11} & Q_{12} & Q_{16} \\ Q_{12} & Q_{22} & Q_{26} \\ Q_{16} & Q_{26} & Q_{66} \end{bmatrix} \varepsilon_e = Q \varepsilon_e$$

$Q(Q = S_e^{-1})$ matrix can also be obtained from the following equation:

$$Q = C_e - C_{et} C_t^{-1} C_{et}^T$$

Where C_t , C_e and C_{et} are as follows:

$$C_e = \begin{bmatrix} C_{11} & C_{12} & C_{16} \\ C_{12} & C_{22} & C_{26} \\ C_{16} & C_{26} & C_{66} \end{bmatrix}; C_{et} = \begin{bmatrix} C_{13} & C_{14} & C_{15} \\ C_{23} & C_{24} & C_{25} \\ C_{36} & C_{46} & C_{56} \end{bmatrix}; C_t = \begin{bmatrix} C_{33} & C_{34} & C_{35} \\ C_{34} & C_{44} & C_{45} \\ C_{35} & C_{45} & C_{55} \end{bmatrix}$$

These equations are valid for composites that are anisotropic. Laminates are made of plies and they can be approximated as orthotropic in the material coordinate system. It becomes monoclinic

due to rotation of layup angle θ_3 . The constitutive relations for monoclinic system in a laminate coordinate system for plane stress assumption are as follows:

$$\varepsilon_e = \begin{bmatrix} S_{11} & S_{12} & S_{16} \\ S_{12} & S_{22} & S_{26} \\ S_{16} & S_{26} & S_{66} \end{bmatrix} \sigma_e = S_e \sigma_e$$

$$\varepsilon_t = \begin{bmatrix} S_{13} & S_{23} & S_{36} \\ 0 & 0 & 0 \\ 0 & 0 & 0 \end{bmatrix} \sigma_e$$

The transverse shear strains vanish and the transverse normal strain is given by the following relation:

$$\varepsilon_{33} = S_{13}\sigma_{11} + S_{23}\sigma_{22} + S_{36}\sigma_{12}$$

Figure 4 shows the laminate stacking up along the thickness. The plane stress reduced stiffness matrix can be rotated into the lamina coordinate system using the following equation:

$$Q' = R_{\sigma e} Q R_{\sigma e}^T$$

Where the rotation matrix is as follows where $c = \cos\theta$ and $s = \sin\theta$.

$$R_{\sigma e} = \begin{bmatrix} c^2 & s^2 & -2sc \\ s^2 & c^2 & 2sc \\ sc & -sc & c^2 - s^2 \end{bmatrix}$$

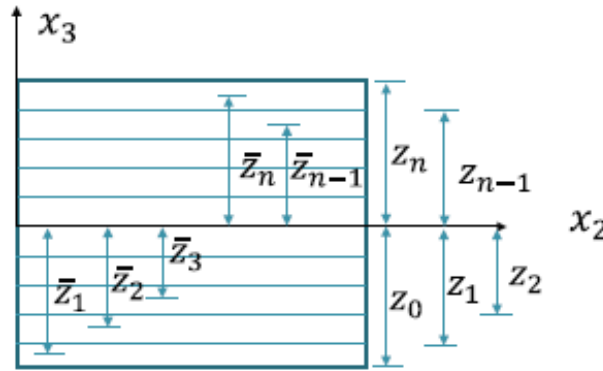


Figure 5.4: Laminate stacking across the thickness
(Image from Multiscale Structural Mechanics (2017))

Q matrix in the lamina coordinate system is used to find the A, B, D matrices as follows:

$$A = \langle\langle Q \rangle\rangle; \quad B = \langle\langle x_3 Q \rangle\rangle; \quad D = \langle\langle x_3^2 Q \rangle\rangle$$

$$A = \sum_{i=1}^n \int_{z_{i-1}}^{z_i} Q_i dx_3 = \sum_{i=1}^n Q_i (z_i - z_{i-1}) = \sum_{i=1}^n Q_i t_i$$

$$B = \sum_{i=1}^n \int_{z_{i-1}}^{z_i} x_3 Q_i dx_3 = \frac{1}{2} \sum_{i=1}^n Q_i (z_i^2 - z_{i-1}^2) = \sum_{i=1}^n Q_i t_i \bar{z}_i$$

$$D = \sum_{i=1}^n \int_{z_{i-1}}^{z_i} x_3^2 Q_i dx_3 = \frac{1}{3} \sum_{i=1}^n Q_i (z_i^3 - z_{i-1}^3) = \frac{1}{3} \sum_{i=1}^n Q_i \left(\left(\bar{z}_i + \frac{t_i}{2} \right)^3 - \left(\bar{z}_i - \frac{t_i}{2} \right)^3 \right)$$

$$D = \sum_{i=1}^n Q_i \left(t_i \bar{z}_i^2 + \frac{t_i^3}{12} \right)$$

The A, B, D matrices collectively form the laminate stiffness matrix as follows:

$$\begin{bmatrix} N_{11} \\ N_{22} \\ N_{12} \\ M_{11} \\ M_{22} \\ M_{12} \end{bmatrix} = \begin{bmatrix} A_{11} & A_{12} & A_{16} & B_{11} & B_{12} & B_{16} \\ A_{12} & A_{22} & A_{26} & B_{12} & B_{22} & B_{26} \\ A_{16} & A_{26} & A_{66} & B_{16} & B_{26} & B_{66} \\ B_{11} & B_{12} & B_{16} & D_{11} & D_{12} & D_{16} \\ B_{12} & B_{22} & B_{26} & D_{12} & D_{22} & D_{26} \\ B_{16} & B_{26} & B_{66} & D_{16} & D_{26} & D_{66} \end{bmatrix} \begin{bmatrix} \epsilon_{11} \\ \epsilon_{22} \\ 2\epsilon_{12} \\ \kappa_{11} \\ \kappa_{22} \\ 2\kappa_{12} \end{bmatrix}$$

$$\begin{bmatrix} N \\ M \end{bmatrix} = \begin{bmatrix} A & B \\ B & D \end{bmatrix} \begin{bmatrix} \epsilon \\ \kappa \end{bmatrix}$$

$$N = \begin{bmatrix} N_{11} \\ N_{22} \\ N_{12} \end{bmatrix}; \quad M = \begin{bmatrix} M_{11} \\ M_{22} \\ M_{12} \end{bmatrix}; \quad \epsilon = \begin{bmatrix} \epsilon_{11} \\ \epsilon_{22} \\ 2\epsilon_{12} \end{bmatrix}; \quad \kappa = \begin{bmatrix} \kappa_{11} \\ \kappa_{22} \\ 2\kappa_{12} \end{bmatrix}$$

Where A = Extension stiffness matrix

B = Extension/Bending Coupling stiffness matrix

D = Bending matrix

N = Laminate resultant forces per unit width

M = Laminate resultant moments per unit width

ϵ = Laminate midplane strain

κ = Laminate midplane curvature

For balanced and symmetric laminates, the elastic constants can be obtained from the Laminate stiffness matrix as follows:

$$E_x = \frac{(A_{11}A_{22} - A_{12}^2)}{A_{22}h}$$

$$E_y = \frac{(A_{11}A_{22} - A_{12}^2)}{A_{11}h}$$

$$\nu_{xy} = \frac{A_{12}}{A_{22}}$$

$$G_{xy} = \frac{A_{66}}{h}$$

5.2 Experimental Procedure

The samples were made in a process similar to the previous tensile test experiments. Four different lay-up sequences were used to analyze the tensile properties of laminates. $[0 / \pm 45 / 90]_s$, $[0_2 / \pm 45]_s$, $[90_2 / \pm 45]_s$, $[\pm 30]_{2s}$. 10 specimens of each lay-up sequence were tested. Figure 5 shows the samples that were used for testing.

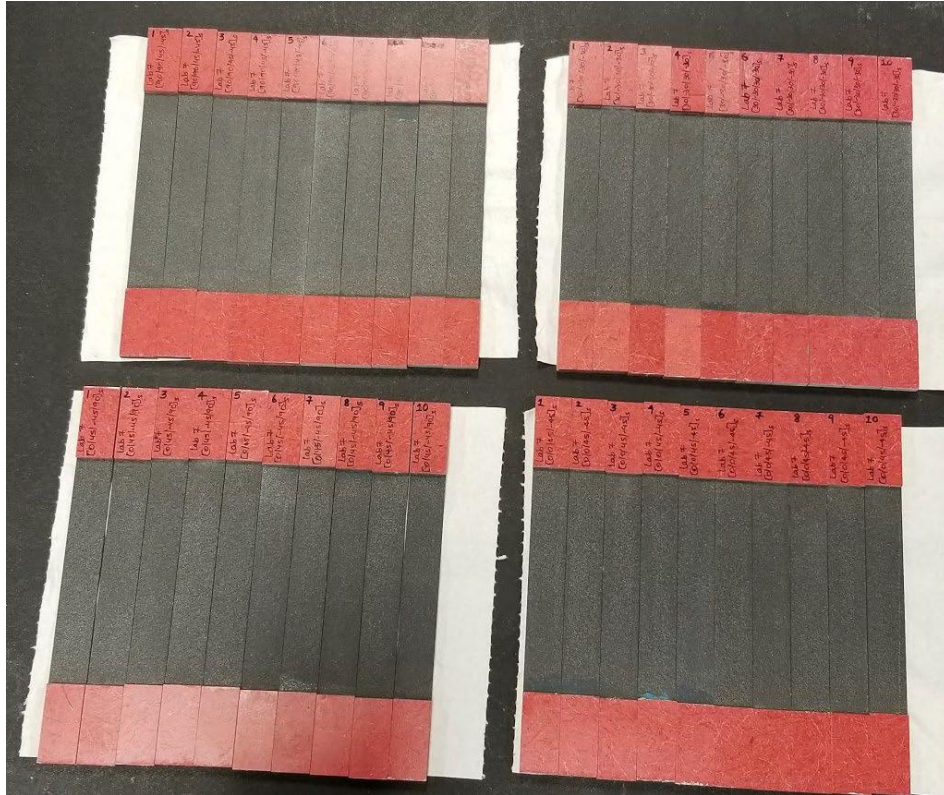


Figure 5.5: Laminate tension samples

The samples were speckled for DIC as shown in Figure 6. They were first spray painted to create a white background for the speckles.

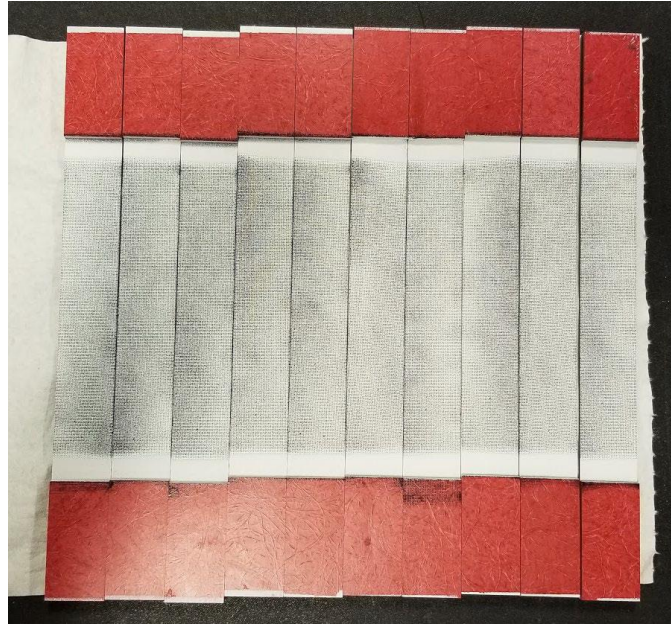


Figure 5.6: Speckled samples for DIC analysis

Table 1 shows the dimensions of the laminates that were tested. It was observed that the $[0_2 / \pm 45]_s$ the laminate was thicker and $[\pm 30]_{2s}$ the laminate was thinner than the expected values and the other 2 laminates.

Table 5.1: Dimensions of the test samples

Layup	Width (mm)	Thickness (mm)	Area (mm ²)	Standard Deviation
$[0 / \pm 45 / 90]_s$	25.41	1.71	43.5	0.297015
$[0_2 / \pm 45]_s$	25.45	1.96	49.93	1.670187
$[90_2 / \pm 45]_s$	25.53	1.7	43.42	0.714842
$[\pm 30]_{2s}$	25.41	1.51	38.26	0.414428

Figure 7 shows the load cell and DIC set-up for the experiment.

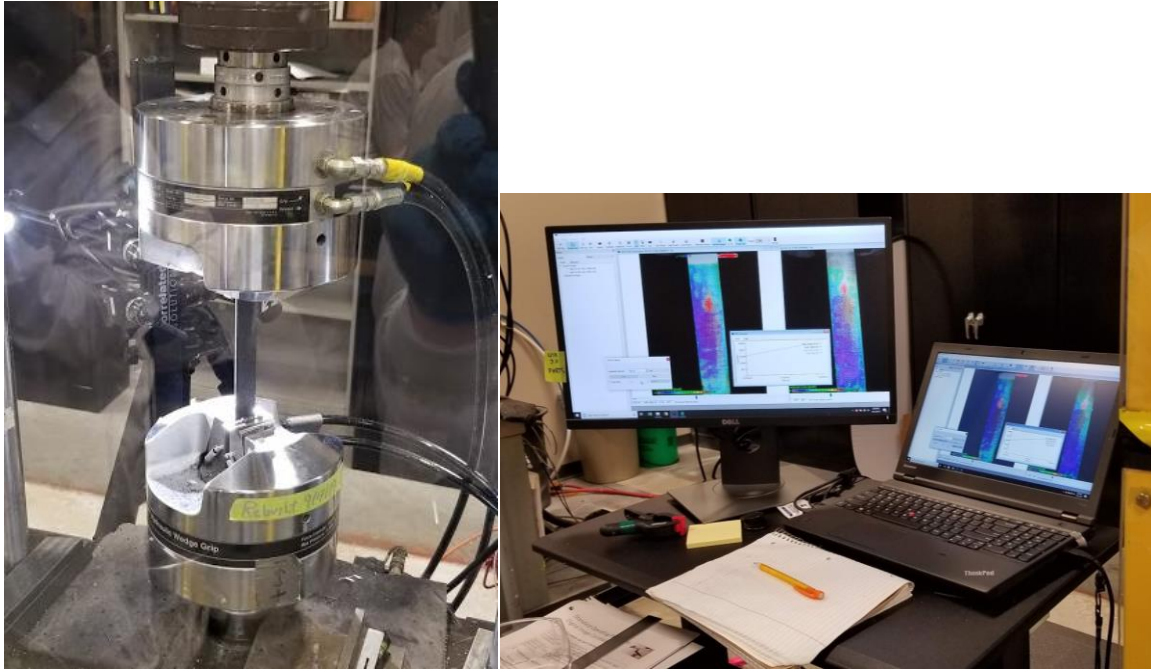
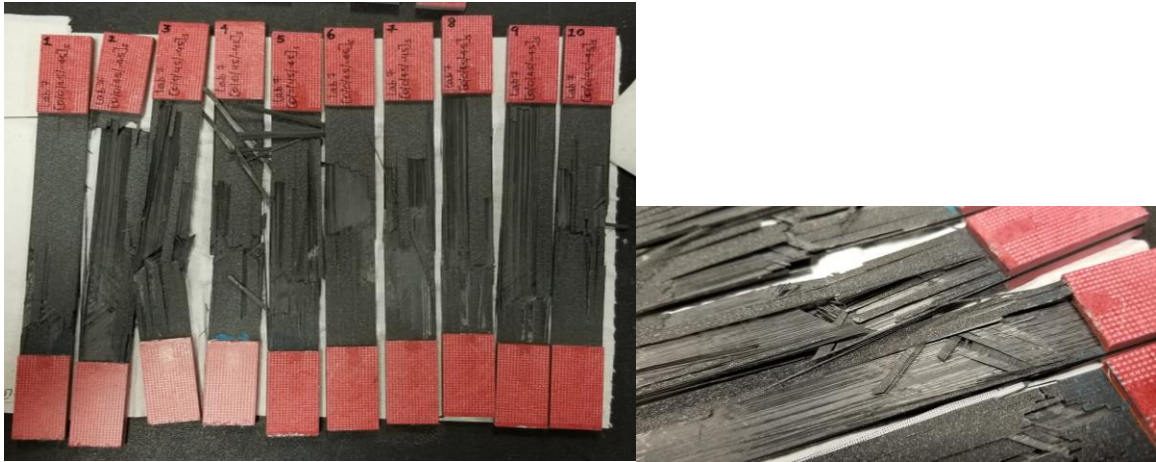


Figure 5.7: Load cell and DIC set-up for the experiment

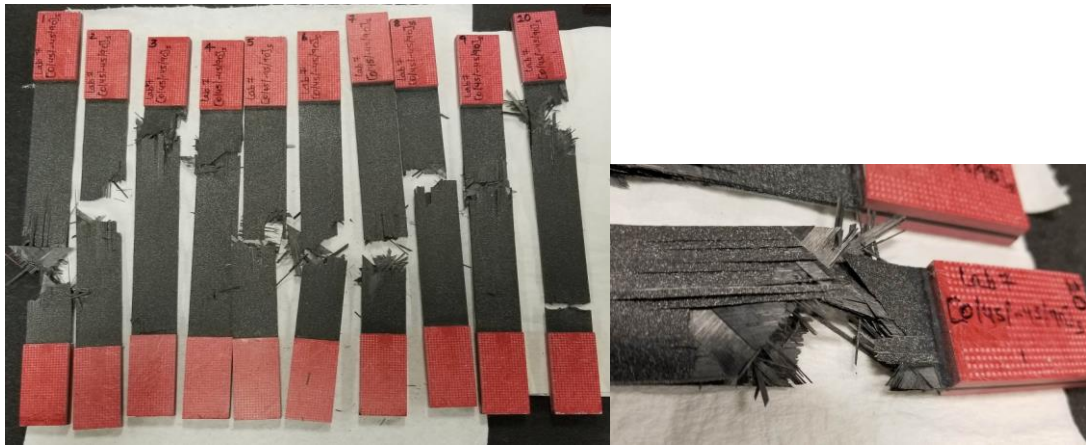
A CLPT analysis was carried out for the laminates using cdmHUB. The axial stress, transverse stress, and shear stress were plotted along the thickness of the laminate.

5.3 Processing of experimental results

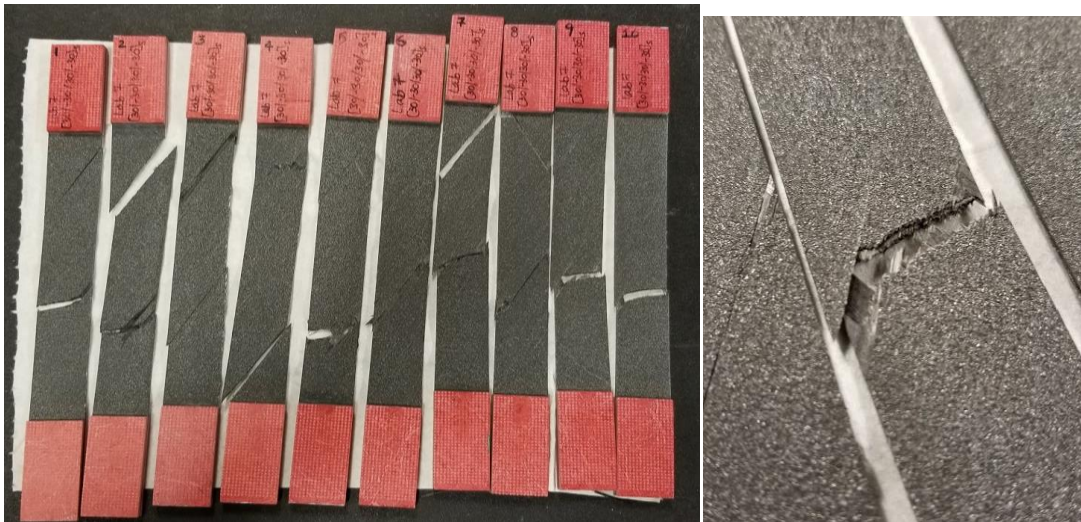
The results obtained from the tensile test were compared to the results of the CLPT analysis. Figure 8 shows the fractured specimens. Every specimen has multiple points of failure. It is a high impact failure where the specimen had exploded into multiple directions. The samples that had 90 plies in them failed in the 90 direction and the samples that did not have 90 plies failed off-axis.



(a) $[0_2 / \pm 45]_s$



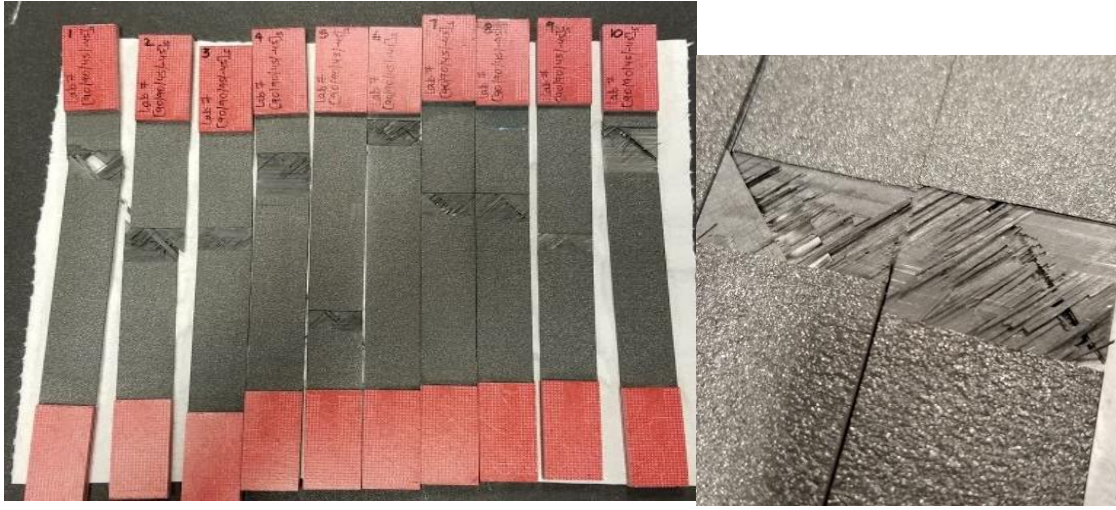
(b) $[0 / \pm 45 / 90]_s$



(c) $[\pm 30]_{2s}$

Figure 5.8: Fractured specimens

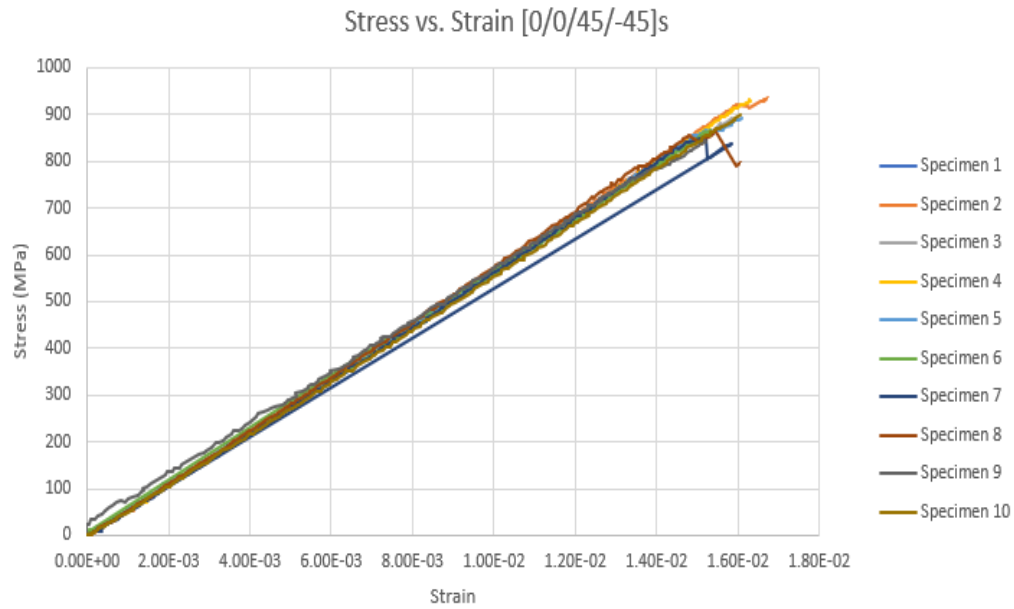
Figure 5.8 continued



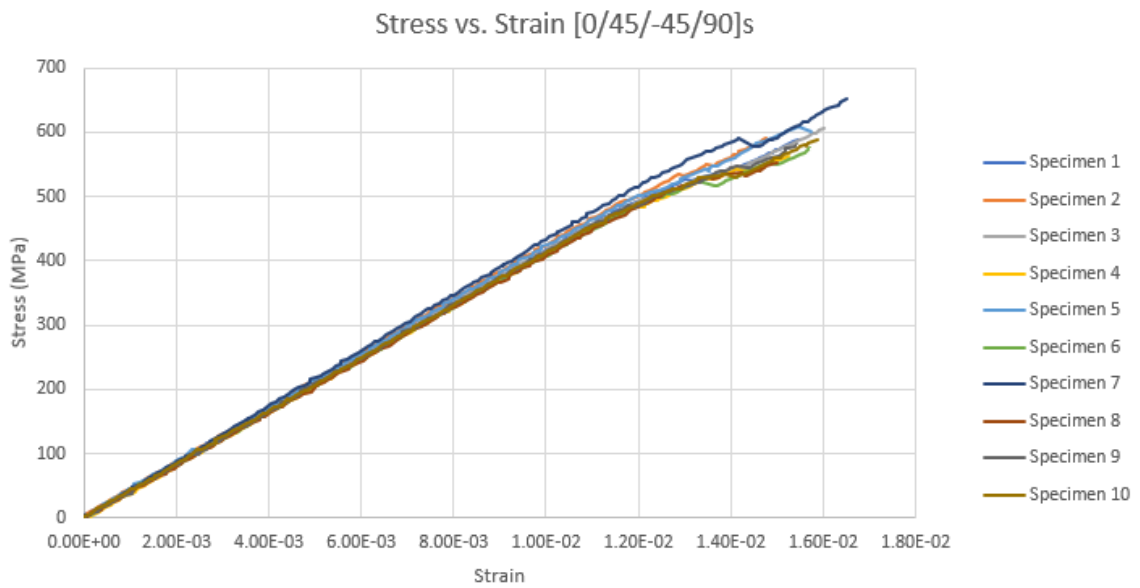
(d) $[90_2 / \pm 45]_s$

5.3.1 Stress-Strain plots of the laminates

Tensile modulus was obtained from the slope of the stress-strain plots for the specimens. Figure 9 shows the stress-strain plots for the laminates. It was observed that the data was coincidental for all the specimens and the plots overlap with each other for a particular lay-up. The values of tensile modulus obtained from the data were compared to the CLPT and SwiftComp results in the later section. The ultimate strength of the $[0_2 / \pm 45]_s$, $[0 / \pm 45 / 90]_s$, $[\pm 30]_{2s}$, $[90_2 / \pm 45]_s$ laminates are 884.3 MPa, 590.0 MPa, 492.2 MPa, and 207.9 MPa respectively. It can be observed that the strength is more for the laminates with a greater number of 0 plies and the strength reduces as the 90 plies increase. A change in slope is observed for the $[90_2 / \pm 45]_s$ laminate and the point where this change happens is called the knee-point which is caused due to failure of the 90 plies, but the laminate has not failed as a whole. Figure 9 shows the stress-strain plots for each of these laminates.



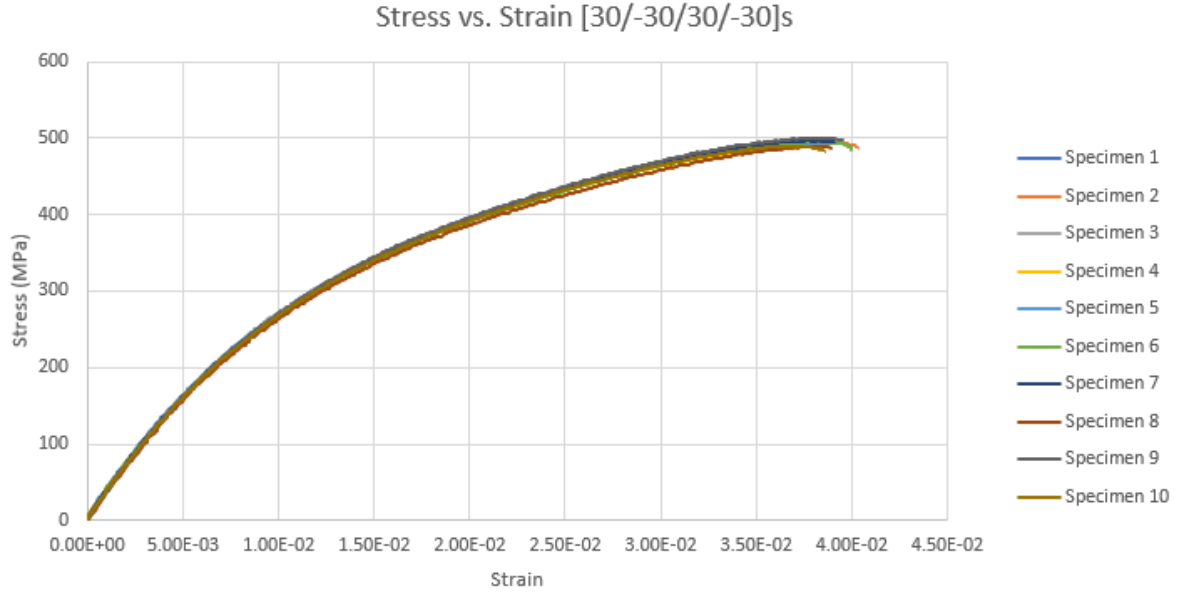
(a) $[0_2 / \pm 45]_s$



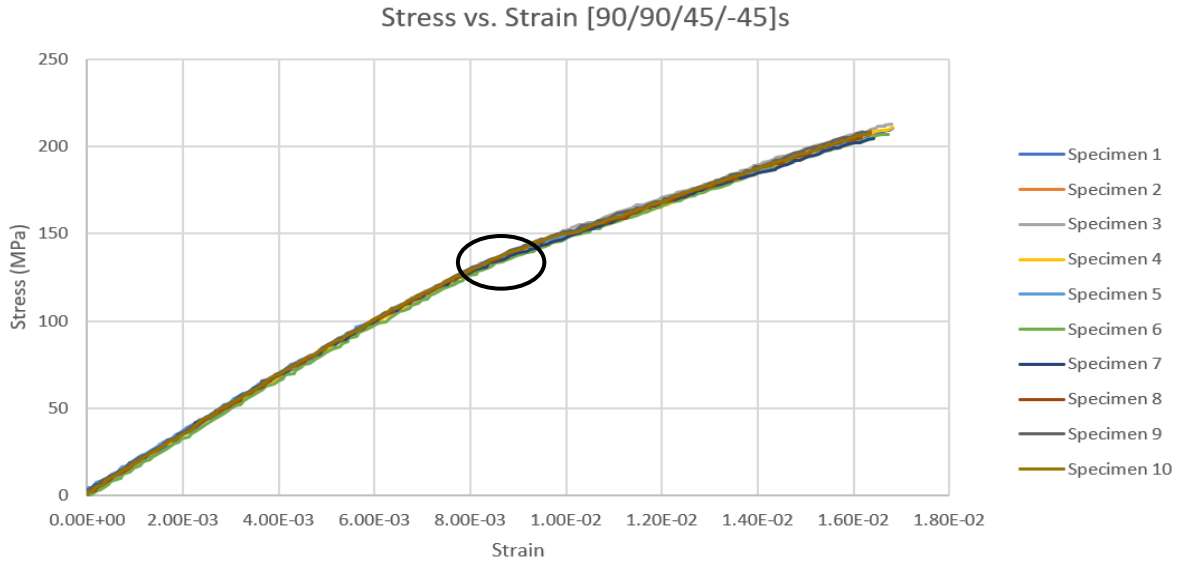
(b) $[0 / \pm 45 / 90]_s$

Figure 5.9: Stress-Strain plots for the laminates

Figure 5.9 continued



(c) $[\pm 30]_{2s}$



(d) $[90_2 / \pm 45]_s$

5.3.2 Transverse Strain-Longitudinal Strain plots for the laminates

Poisson's ratio was obtained from the slope of the transverse strain Vs longitudinal strain plots for the specimens. Figure 10 shows the transverse Vs longitudinal strain plots for the laminates. The values of Poisson's ratio obtained from the data were compared to the CLPT and SwiftComp results in the later section. These plots are not as smooth as the stress-strain plots, but, the data was

coincidental for all the specimens and the plots overlap with each other for a particular lay-up. There is a change in slope for the $[0 / \pm 45 / 90]_s$ laminate. This is because of the failure of 90 plies, but not the laminate as a whole. This increases the transverse strain on the laminate. Poisson's ratio was obtained using the following equation:

$$\nu = \frac{-\varepsilon_{yy}}{\varepsilon_{xx}}$$

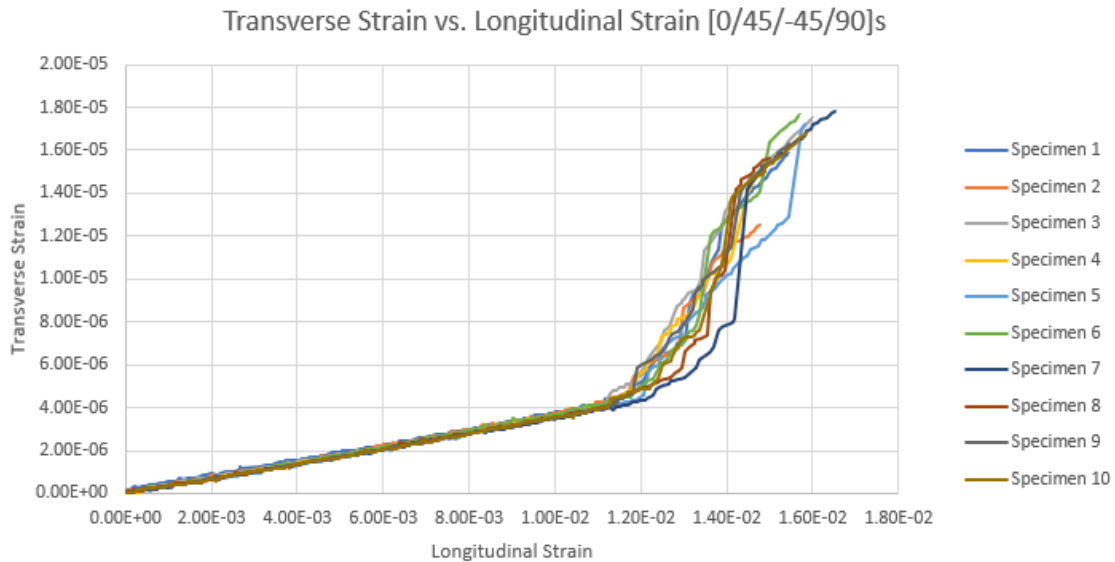
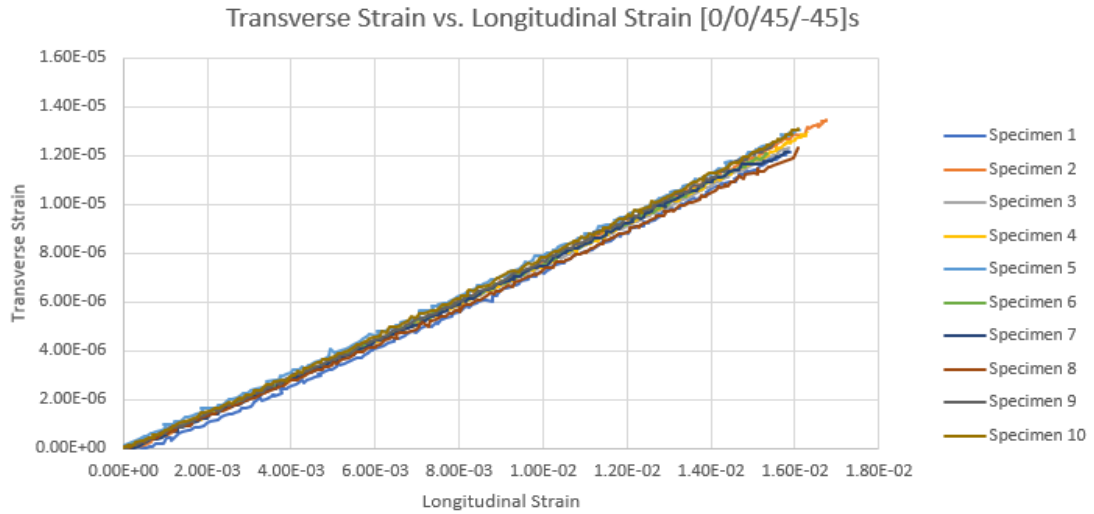
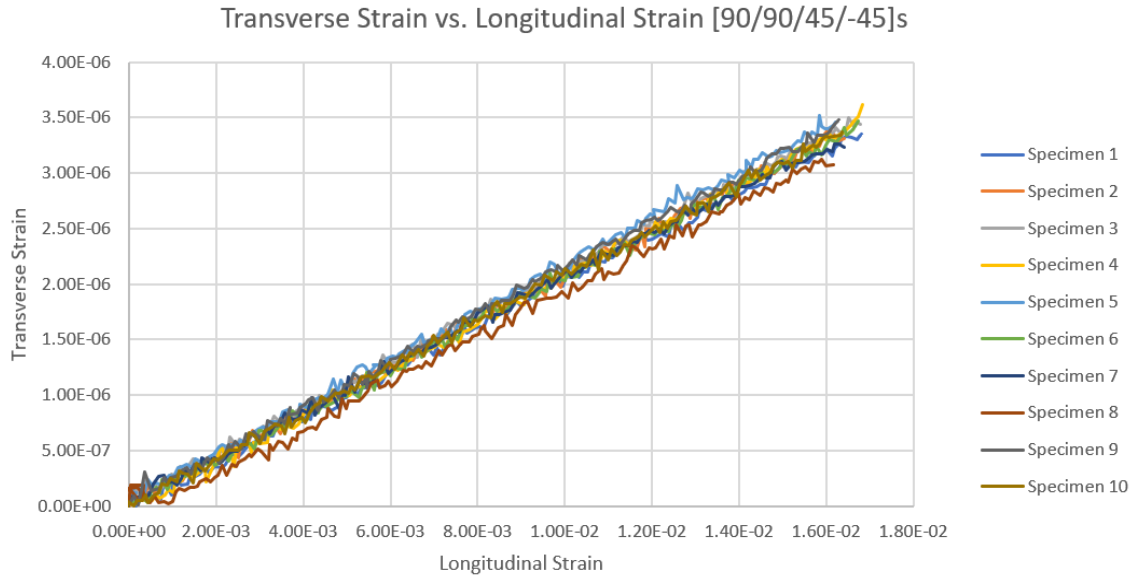
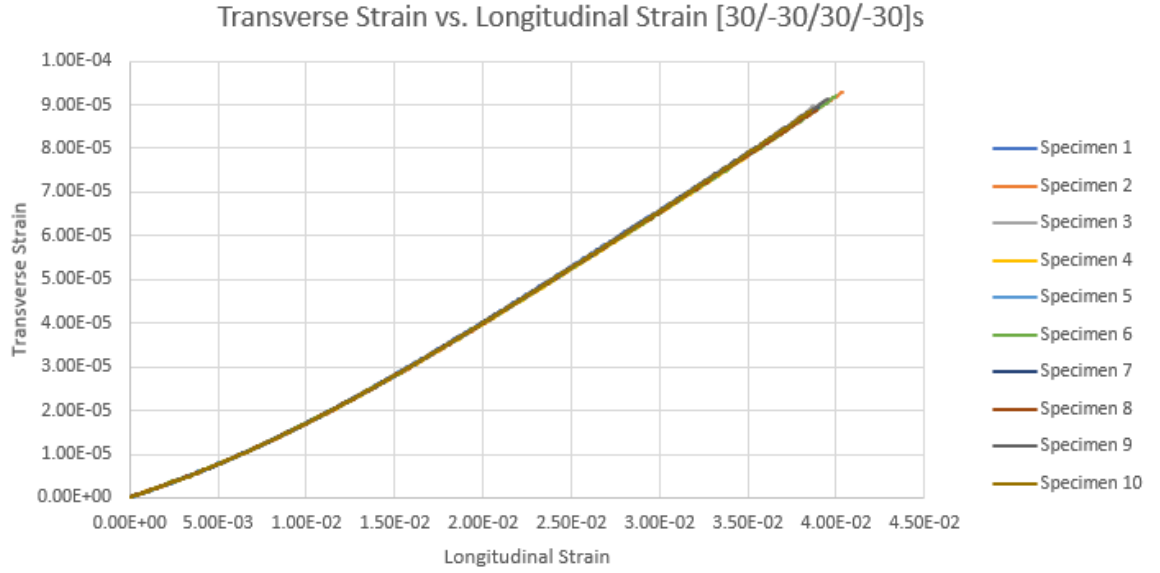


Figure 5.10: Transverse strain Vs Longitudinal strain for the laminates

Figure 5.10 continued



5.3.3 Homogenization of elastic constants for the laminates

Figures 11-14 show the data that was obtained from SwiftComp and CLPT. The results obtained from both these applications are exactly equal to one another. 1-D SG was used for homogenization in SwiftComp. For the $[\pm 30]_{2s}$ laminate, the value of ν_{13} is negative and ν_{12} is 1.48, which is

quite larger than the typical values of Poisson's ratio. The laminates can also be modeled without specifying individual ply orientation, that is, a black-Aluminum approach can be used to determine the behavior of it. In this case, the homogenized material properties can be directly given as input for the laminate. It can also be observed from the results from SwiftComp using the 1D structural genome that each different ply orientation is represented with a different color in it. The values of elastic constants from the results of CLPT and SwiftComp are the same.

The Effective Stiffness Matrix					
9.1523686E+10	2.2651926E+10	7.9577687E+09	0.0000000E+00	0.0000000E+00	-3.3659148E-06
2.2651926E+10	2.9894999E+10	8.6840453E+09	0.0000000E+00	0.0000000E+00	-4.1815540E-06
7.9577687E+09	8.6840453E+09	1.4137972E+10	0.0000000E+00	0.0000000E+00	1.1930486E-07
0.0000000E+00	0.0000000E+00	0.0000000E+00	2.7987644E+09	5.2668459E-09	0.0000000E+00
0.0000000E+00	0.0000000E+00	0.0000000E+00	5.2668459E-09	3.4943262E+09	0.0000000E+00
-3.3659148E-06	-4.1815540E-06	1.1930486E-07	0.0000000E+00	0.0000000E+00	1.9019381E+10
The Effective Compliance Matrix					
1.3477717E-11	-9.7479096E-12	-1.5986217E-12	0.0000000E+00	0.0000000E+00	2.5206717E-28
-9.7479096E-12	4.7765322E-11	-2.3852404E-11	0.0000000E+00	0.0000000E+00	8.9260711E-27
-1.5986217E-12	-2.3852404E-11	8.6282307E-11	0.0000000E+00	0.0000000E+00	-6.0682752E-27
0.0000000E+00	0.0000000E+00	0.0000000E+00	3.5730053E-10	-5.3854354E-28	0.0000000E+00
0.0000000E+00	0.0000000E+00	0.0000000E+00	-5.3854354E-28	2.8617821E-10	0.0000000E+00
2.5206717E-28	8.9260711E-27	-6.0682752E-27	0.0000000E+00	0.0000000E+00	5.2577946E-11
The Engineering Constants (Approximated as Orthotropic)					
E1 =	7.4196540E+10				
E2 =	2.0935690E+10				
E3 =	1.1589862E+10				
G12 =	1.9019381E+10				
G13 =	3.4943262E+09				
G23 =	2.7987644E+09				
nu12=	7.2326116E-01				
nu13=	1.1861220E-01				
nu23=	4.9936655E-01				



(a) SwiftComp

```
Laminate Properties:
Ex (Pa)
7.4197e+10
Ey (Pa)
2.0936e+10
Gxy (Pa)
1.9019e+10
nuxy
0.72
alphax
0
alphay
0
alphaxy
0
```

(b) CLPT

Figure 5.11: Analytical results for $[0_2 / \pm 45]_s$

The Effective Stiffness Matrix						
6.0700016E+10	2.2661253E+10	8.3209070E+09	0.0000000E+00	0.0000000E+00	-3.2682735E-06	
2.2661253E+10	6.0700016E+10	8.3209070E+09	0.0000000E+00	0.0000000E+00	-2.5018118E-06	
8.3209070E+09	8.3209070E+09	1.4137972E+10	0.0000000E+00	0.0000000E+00	1.0374954E-07	
0.0000000E+00	0.0000000E+00	0.0000000E+00	3.1081058E+09	-1.5059350E-07	0.0000000E+00	
0.0000000E+00	0.0000000E+00	0.0000000E+00	-1.5059350E-07	3.1081058E+09	0.0000000E+00	
-3.2682735E-06	-2.5018118E-06	1.0374954E-07	0.0000000E+00	0.0000000E+00	1.9019381E+10	
The Effective Compliance Matrix						
1.9941038E-11	-6.3479355E-12	-8.0002238E-12	0.0000000E+00	0.0000000E+00	2.6352826E-27	
-6.3479355E-12	1.9941038E-11	-8.0002238E-12	0.0000000E+00	0.0000000E+00	1.5758638E-27	
-8.0002238E-12	-8.0002238E-12	8.0148572E-11	0.0000000E+00	0.0000000E+00	-2.8643073E-27	
0.0000000E+00	0.0000000E+00	0.0000000E+00	3.2173937E-10	1.5588870E-26	0.0000000E+00	
0.0000000E+00	0.0000000E+00	0.0000000E+00	1.5588870E-26	3.2173937E-10	0.0000000E+00	
2.6352826E-27	1.5758638E-27	-2.8643073E-27	0.0000000E+00	0.0000000E+00	5.2577946E-11	
The Engineering Constants (Approximated as Orthotropic)						
E1 =	5.0147842E+10					
E2 =	5.0147842E+10					
E3 =	1.2476829E+10					
G12 =	1.9019381E+10					
G13 =	3.1081058E+09					
G23 =	3.1081058E+09					
nu12=	3.1833526E-01					
nu13=	4.0119396E-01					
nu23=	4.0119396E-01					

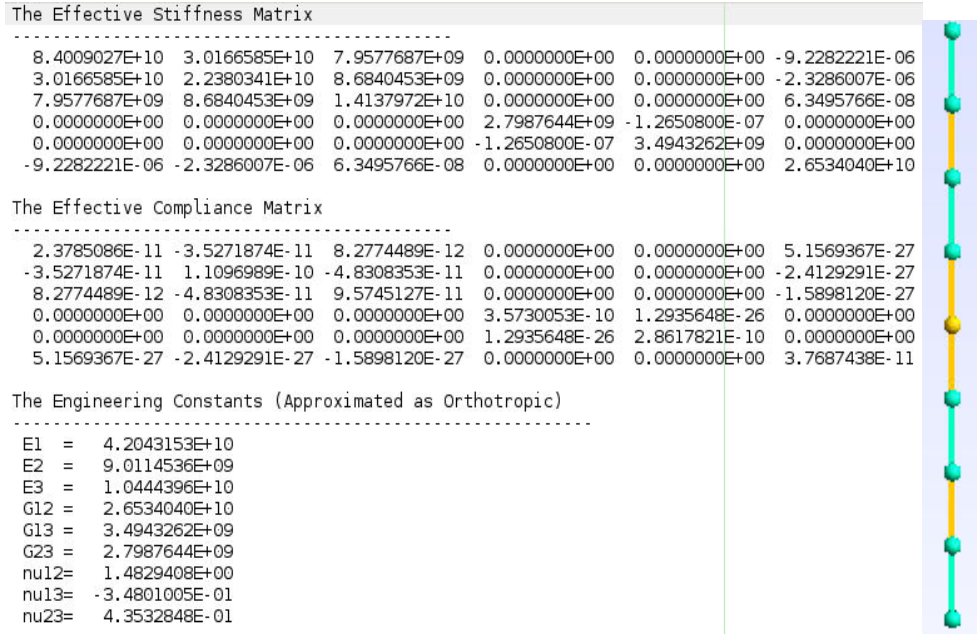


(a) SwiftComp

Laminate Properties:
 Ex (Pa)
 5.0148e+10
 Ey (Pa)
 5.0148e+10
 Gxy (Pa)
 1.9019e+10
 nu_{xy}
 0.32
 alpha_x
 0
 alpha_y
 0
 alpha_{xy}
 0

(b) CLPT

Figure 5.12: Analytical results for $[0 / \pm 45 / 90]_s$

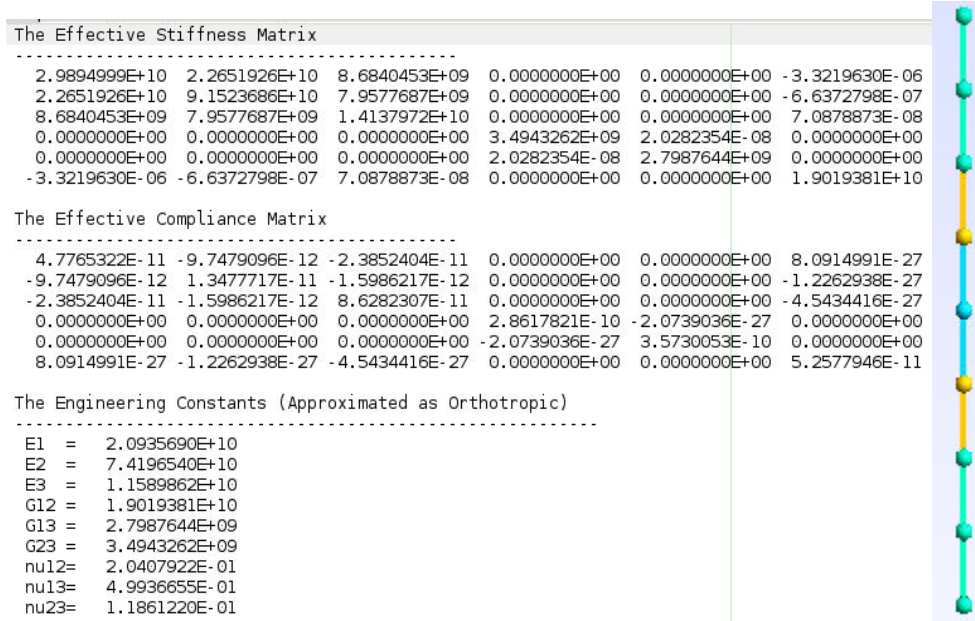


(a) SwiftComp

Laminate Properties:
 Ex (Pa)
 4.2043e+10
 Ey (Pa)
 9.01145e+09
 Gxy (Pa)
 2.6534e+10
 nu_{xy}
 1.48
 alpha_x
 0
 alpha_y
 0
 alpha_{xy}
 0

(b) CLPT

Figure 5.13: Analytical results for $[\pm 30]_{2s}$



(a) SwiftComp

Laminate Properties:
 Ex (Pa)
 2.0936e+10
 Ey (Pa)
 7.4197e+10
 Gxy (Pa)
 1.9019e+10
 nuxy
 0.2
 alphax
 0
 alphay
 0
 alphaxy
 0

(b) CLPT

Figure 5.14: Analytical results for $[90_2 / \pm 45]_s$

5.3.4 Comparison of theoretical and experimental data

Tables 2 and 3 show the comparison of data for axial modulus and Poisson's ratio that was obtained from the experiment with the CLPT and SwiftComp results. The error in the data for most of the parameters is less than or close to 10%. The modulus and Poisson's ratio reduce as the laminate moves more towards the off-axis with the value being the highest for the laminate with more

number of 0 plies. The modulus of $[0_2 / \pm 45]_s$ is half of the modulus obtained for the $[0]_8$ laminate. This is because half of the number of plies in this laminate is 0.

Table 5.2: Comparison of modulus data

Layup	CLPT (GPa)	SwiftComp (GPa)	Experiment (GPa)	Error (%)
$[0 / \pm 45 / 90]_s$	74.197	74.19654	66.47	10.41
$[0_2 / \pm 45]_s$	50.148	50.147842	45.48	9.30
$[\pm 30]_{2s}$	42.043	42.043153	44.62	6.12
$[90_2 / \pm 45]_s$	20.936	20.93569	18.8	10.20

Table 5.3: Comparison of Poisson's ratio data

Layup	CLPT	SwiftComp	Experiment	Error (%)
$[0 / \pm 45 / 90]_s$	0.72	0.72326116	0.785	9.02
$[0_2 / \pm 45]_s$	0.32	0.31833526	0.351	9.68
$[\pm 30]_{2s}$	1.48	1.4829408	1.429	3.44
$[90_2 / \pm 45]_s$	0.2	0.20407922	0.207	3.5

5.4 Modeling and analysis of simulation

The variation of the stress across the thickness both at the edge and the center of the width of the sample was analyzed by simulating the load and boundary conditions the same as what the test coupon experiences on the MTS. This is done to account for and to study the free-edge effects on the edges of the samples as well. Four laminates were modeled for this study from the experimental analysis, $[0_2 / \pm 45]_s$, $[0 / \pm 45 / 90]_s$, $[\pm 30]_{2s}$, $[90_2 / \pm 45]_s$.

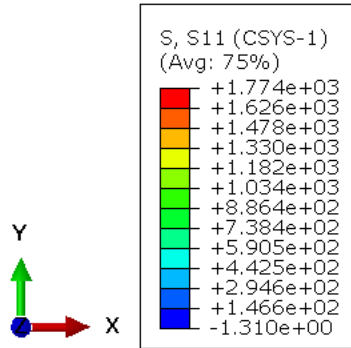
The test specimens were modeled as discussed in chapter 2. They were one-inch (25.4 mm) wide and comprised of 8-ply laminates with 4 different orientations as in the experiment. The fiber orientation was assigned individually to each of the plies and hence, for the post-processing of the data, a global coordinate system is created and all the parameters are hence rotated in terms of the

global coordinates. The load and boundary conditions for the test are the same as a typical tensile test as discussed in section 2.7. The deformation output has a scale of 12.6987.

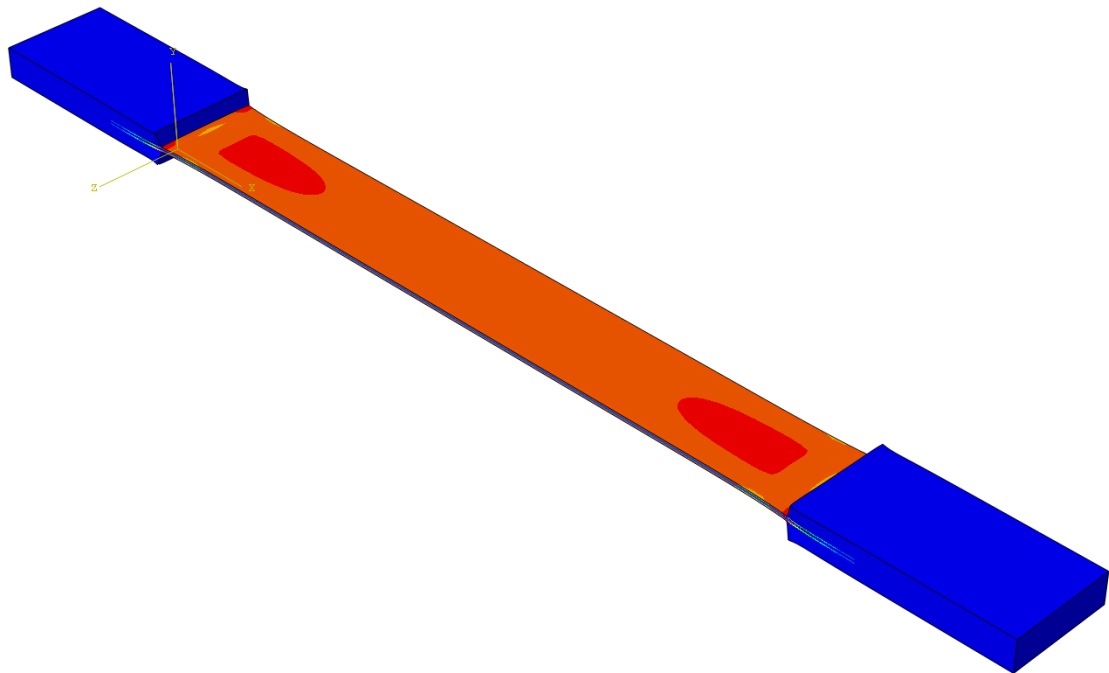
5.4.1 Analysis of simulation results

5.4.1.1 $[0_2 / \pm 45]_s$ Laminate

Figure 15 shows the variation of stresses through the thickness and also the variation through the axial length of the specimen. It can be seen that the 0° plies take the highest axial loads and the 45° plies take all the shear stress. The magnitude of all these stresses does not vary a lot across the length of the specimen. The shear stress changes its direction between the $+45^\circ$ and -45° laminates. The axial and the transverse stresses on the $\pm 45^\circ$ laminates are however the same. The off-axis plies take positive transverse loads whereas, the 0° plies take negative transverse loads denoting the reduction of the width of the specimen with the tensile load applied on it. There is a region of stress concentration near the tabs for the transverse stress case. This is because of the Poisson's effect where the laminate deformation is restricted because of the tabs and hence it cannot reduce its width.



(i) Variation through thickness at the center of the width

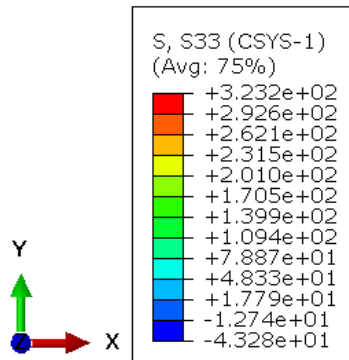


(ii) Axial Variation

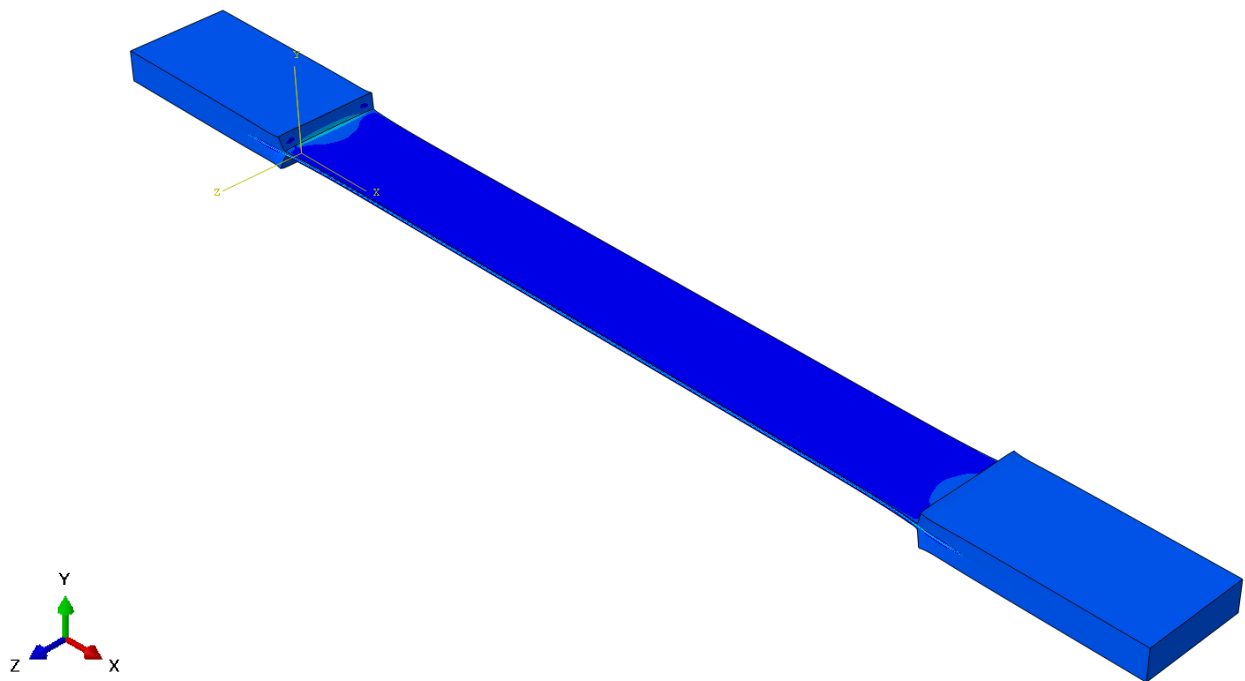
(a) Axial Stress (σ_{11})

Figure 5.15: Variation of stresses for $[0_2 / \pm 45]_s$ laminate

Figure 5.15 continued



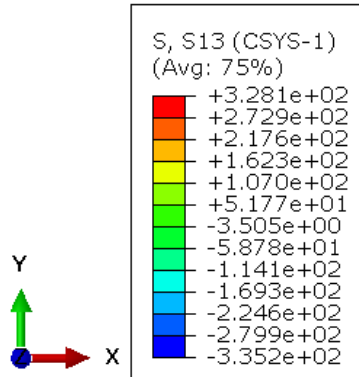
(i) Variation through thickness at the center of the width



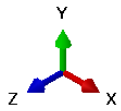
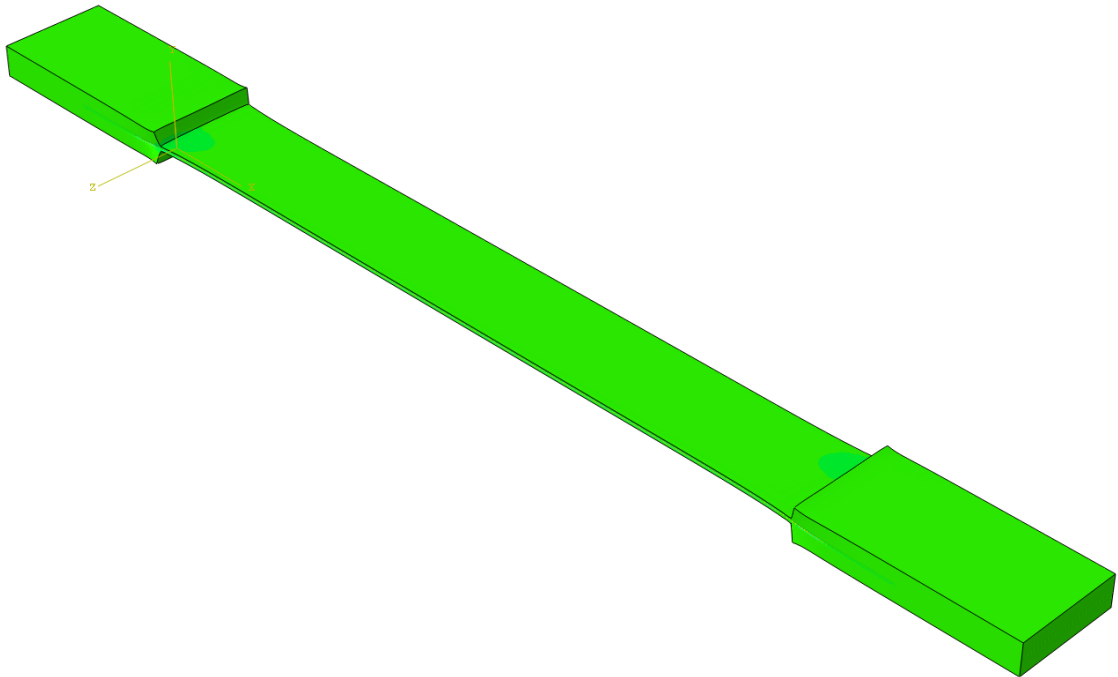
(ii) Axial Variation

(b) Transverse Stress (σ_{22})

Figure 5.15 continued



(i) Variation through thickness the center of the width

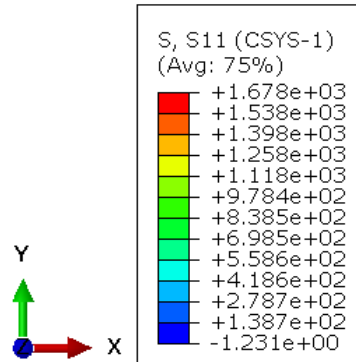


(ii) Axial Variation

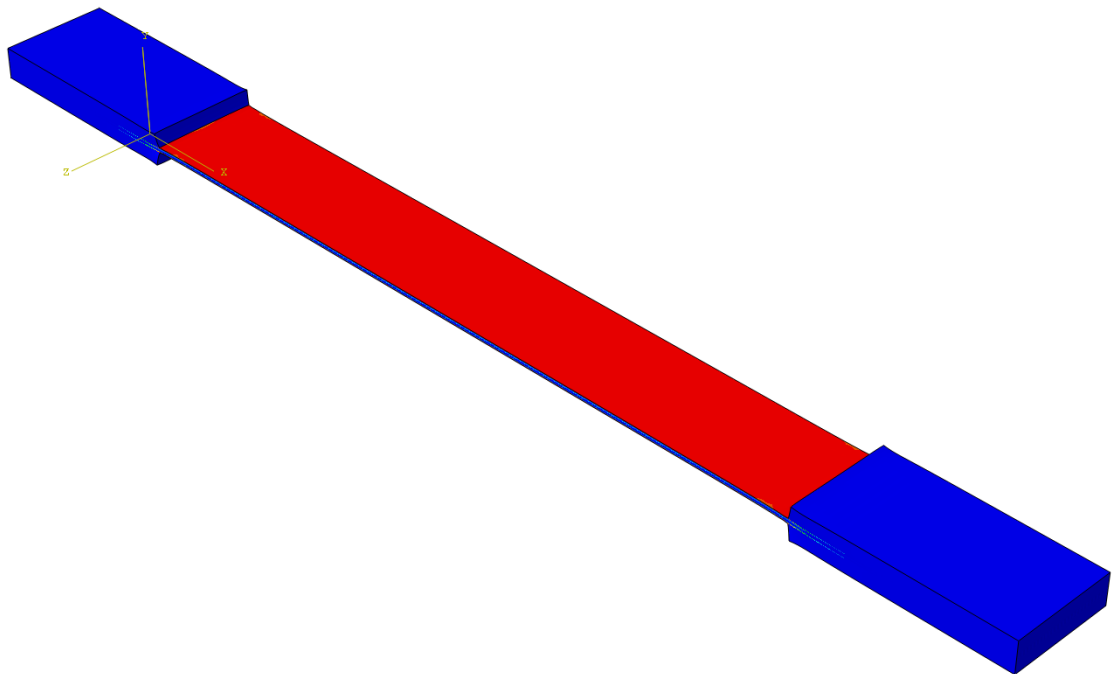
(c) In-plane Shear Stress (σ_{12})

5.4.1.2 $[0 / \pm 45 / 90]_s$ Laminate

Figure 16 shows the variation of stresses through thickness and through the axial length of the laminate. It can be observed that the axial loads are mostly carried by the 0° plies and the 90° plies take the least number of axial loads. All the shear stress is carried by the $\pm 45^\circ$ laminates. They carry the same amount of shear loads. But, the magnitude is opposite in direction. The highest amount of transverse load is carried by the 90° laminates and the magnitude of this stress is negative accounting for its compressive nature and the transverse loads carried by the $\pm 45^\circ$ laminates are positive but of lower magnitude. The free-edge effects are also clearly visible in these images. The variation of these stresses is constant across the length of the specimen and the free-edge effect on the specimen can be clearly visible in the image of transverse stress variation across the length of the sample.



(i) Variation through thickness center of the width

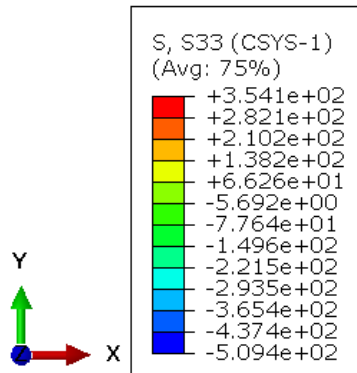


(ii) Axial Variation

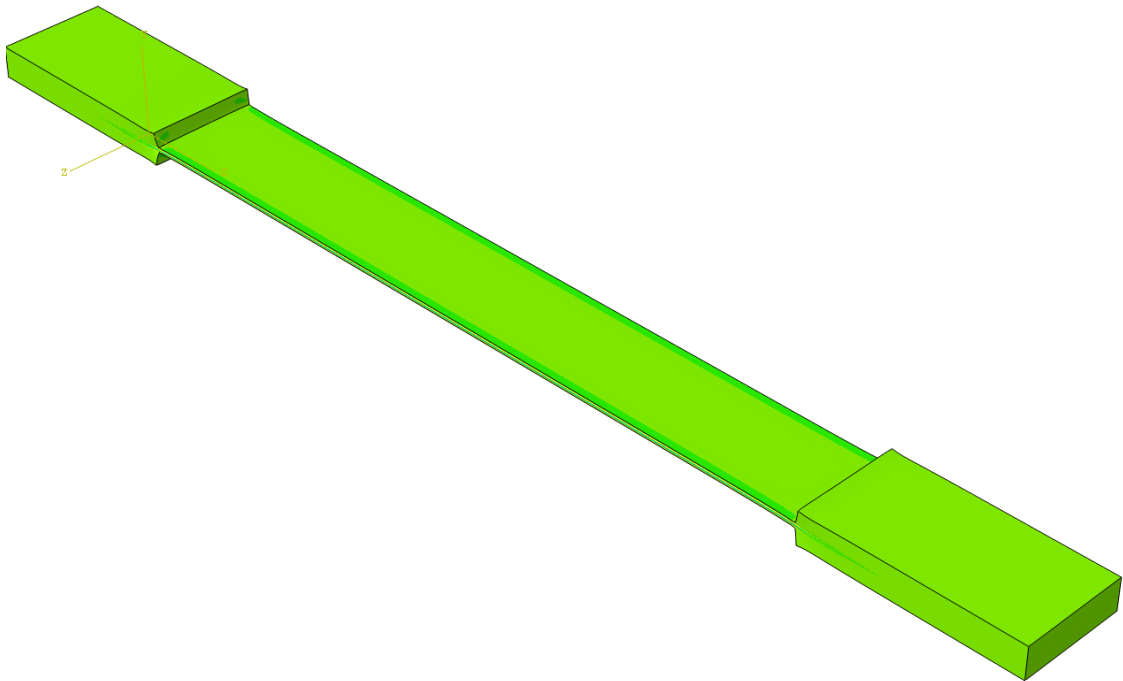
(a) Axial Stress (σ_{11})

Figure 5.16: Variation of stresses for $[0 / \pm 45 / 90]_s$ laminate

Figure 5.16 continued



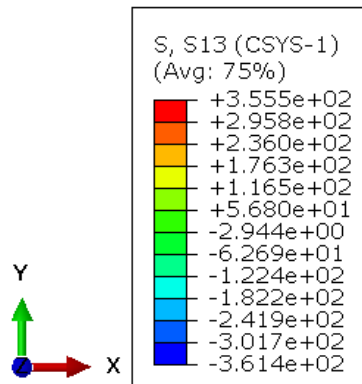
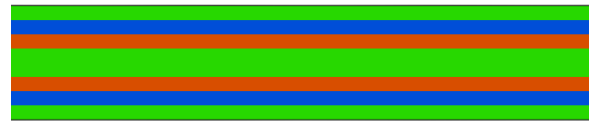
(i) Variation through thickness center of width



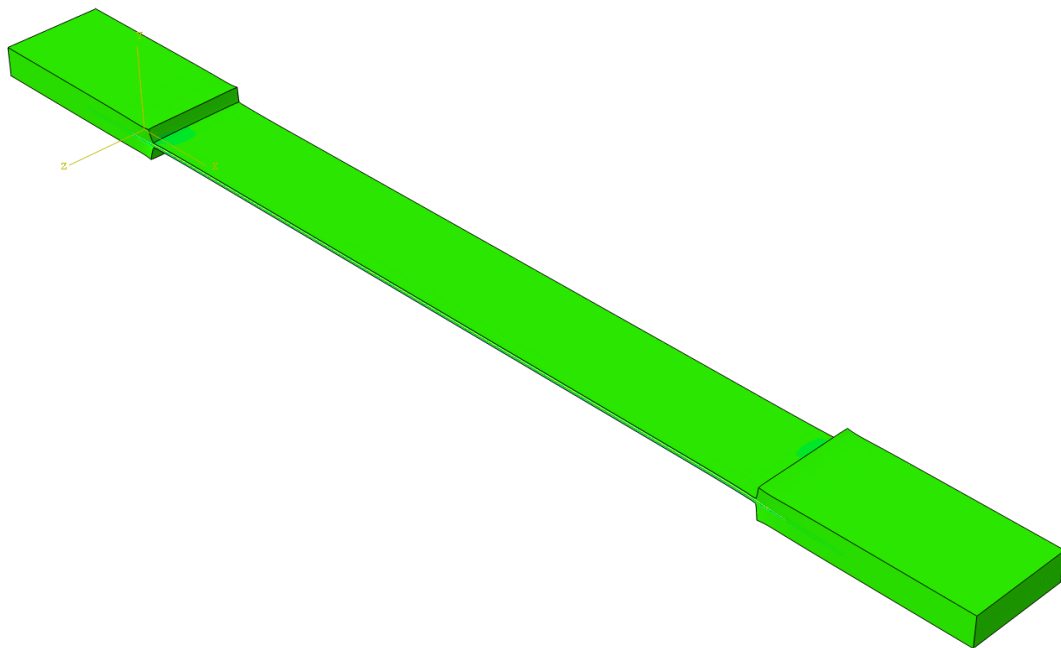
(ii) Axial Variation

(b) Transverse Stress (σ_{22})

Figure 5.16 continued



(i) Variation through thickness center of width

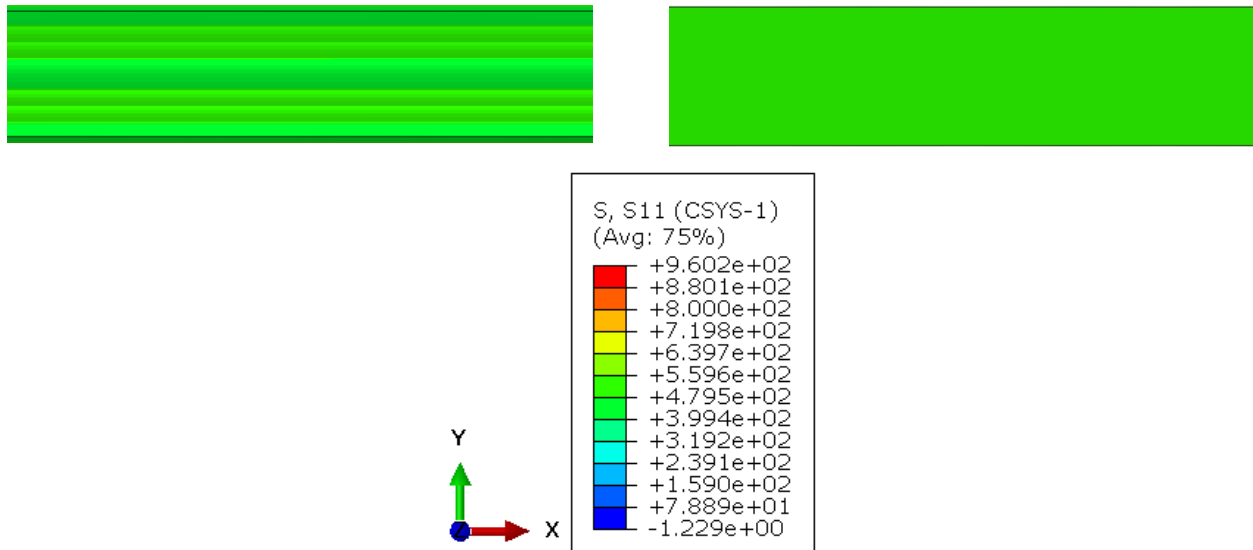


(ii) Axial Variation

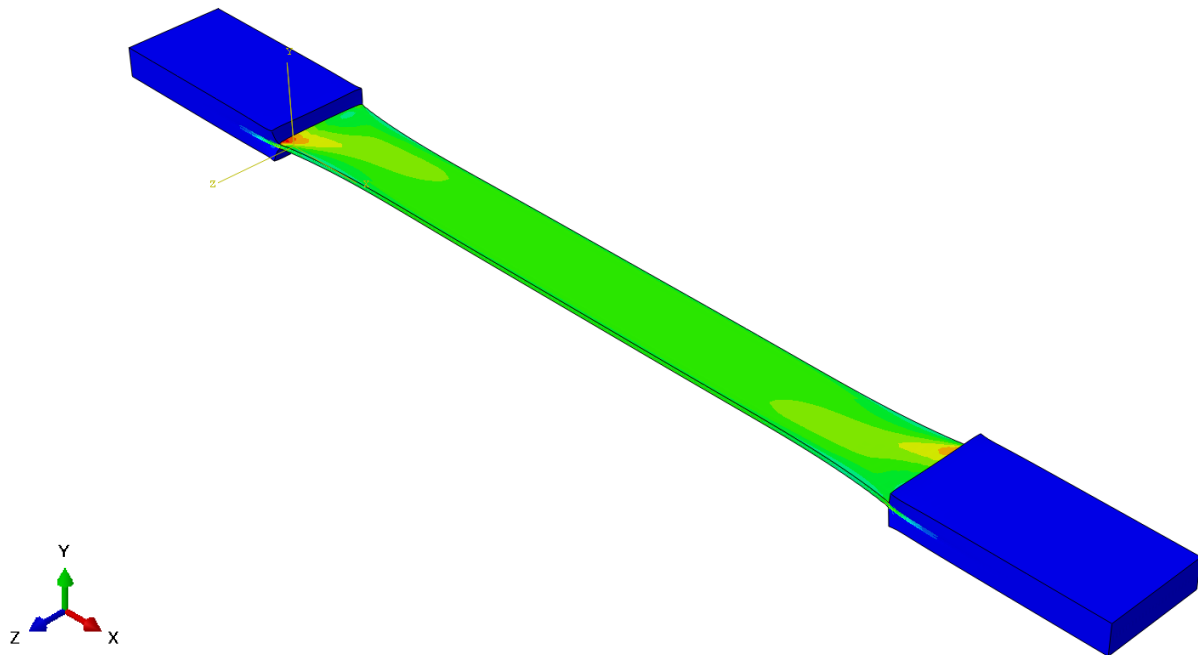
(c) In-plane Shear Stress (σ_{12})

5.4.1.3 $[\pm 30]_{2s}$ Laminate

Figure 17 shows the variation of stresses across the thickness and the axial length of the specimen. It can be observed that the plies undergo a non-uniform displacement at the free-edge, whereas, they deform uniformly at the center of the laminate. The variation of axial stress is constant across the thickness and also across the length of the specimen. The transverse stress on the specimen is zero throughout the thickness of the laminate. At the free-edge, however, there is a slight variation in these values. The direction of shear stress keeps varying between the $\pm 30^\circ$ plies whereas, the magnitude of it remains the same. At the free-edge however, the variation of this stress within a ply varies slightly. The values of these stresses are constant across the gage length of the laminate and the Poisson's effect can be observed to be very distinctly visible as the laminate deforms due to the axial loading. There is a region of stress concentration near the tabs for the transverse stress case. This is because of the Poisson's effect where the laminate deformation is restricted because of the tabs and hence it cannot reduce its width. The axial stress and in-plane shear stress on the specimen are also concentrated at the tabs. This is because of the range of Poisson's ratio the laminate has ($\nu_{12} = 1.4829408, \nu_{13} = -0.34801005$) as discussed in section 5.3.3.



(i) Variation through thickness (Left: Edge, Right: Center of width)

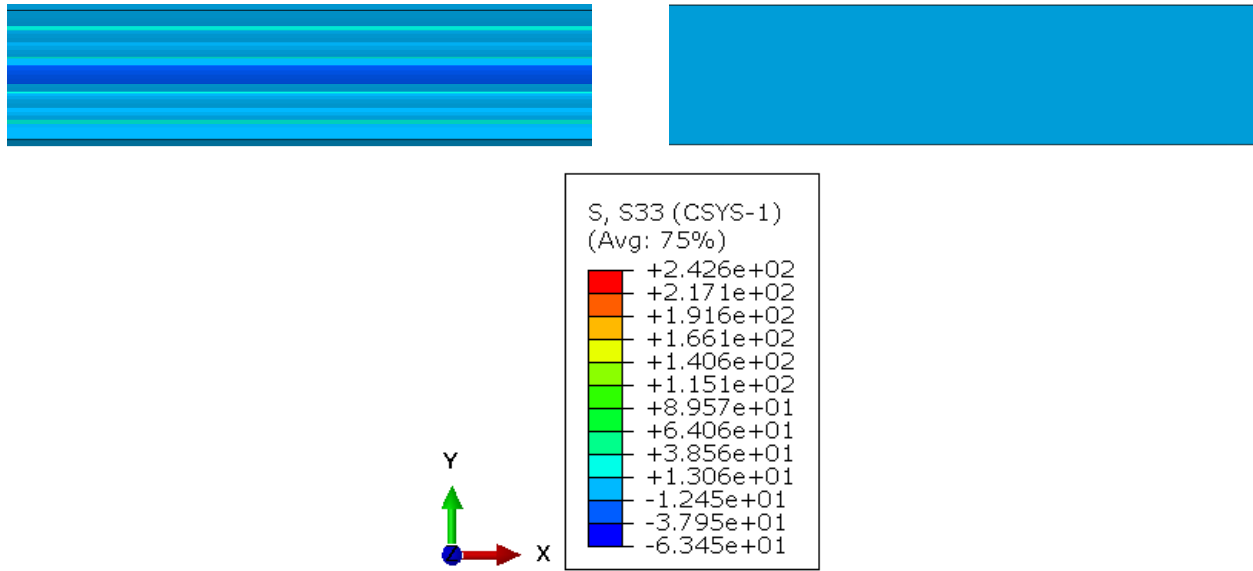


(ii) Axial Variation

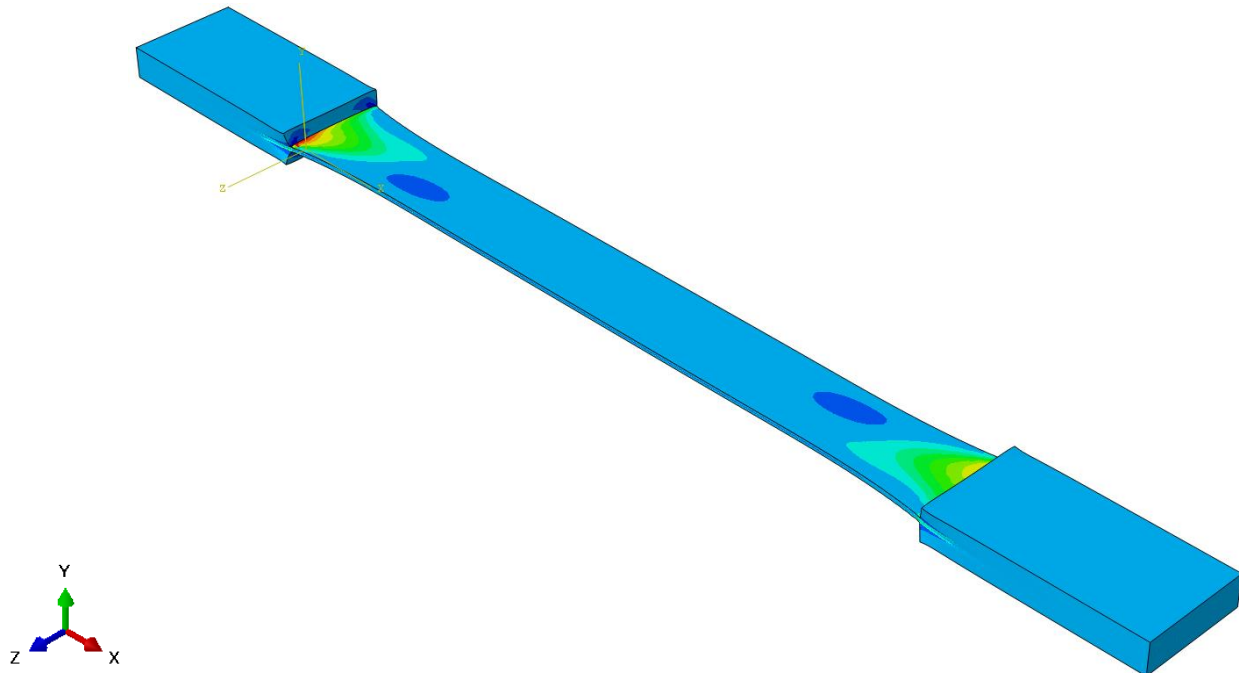
(a) Axial Stress (σ_{11})

Figure 5.17: Variation of stresses for $[\pm 30]_{2s}$ laminate

Figure 5.17 continued



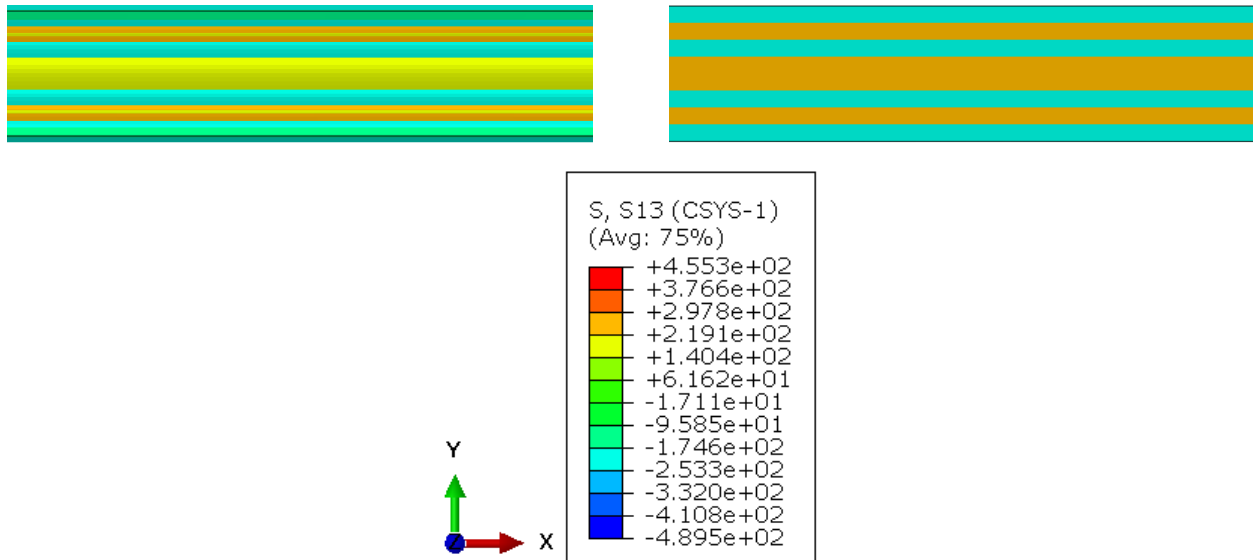
(i) Variation through thickness (Left: Edge, Right: Center of width)



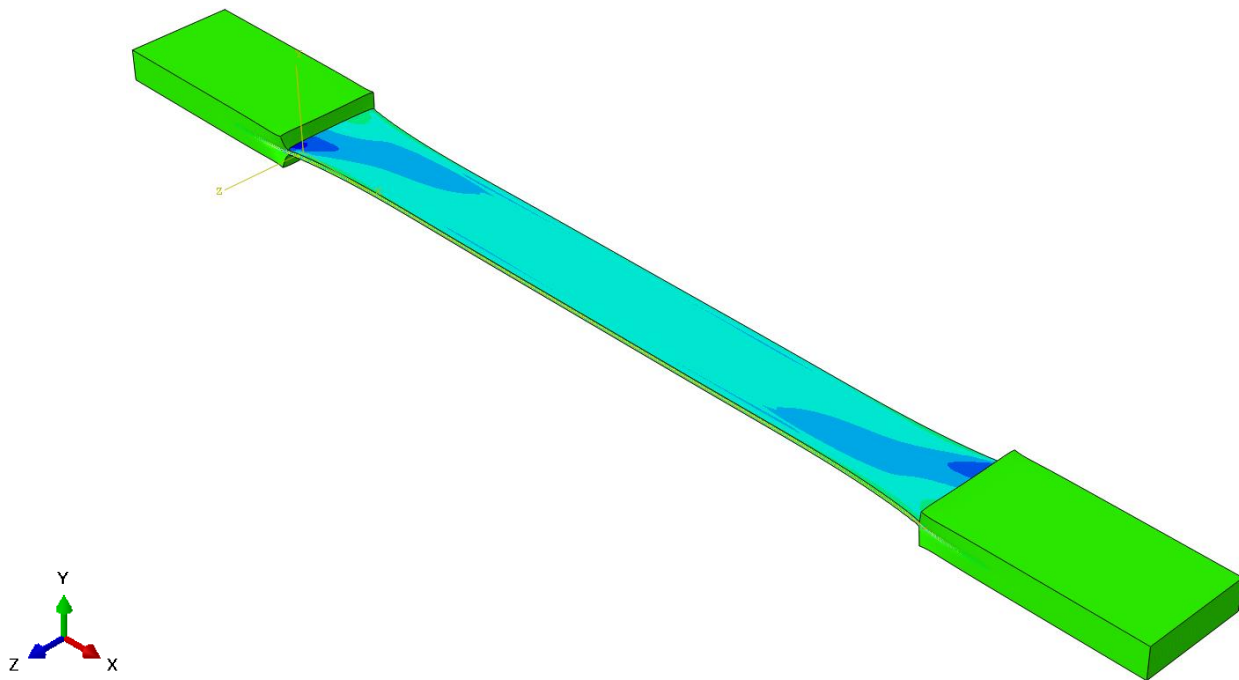
(ii) Axial Variation

(b) Transverse Stress (σ_{22})

Figure 5.17 continued



(i) Variation through thickness (Left: Edge, Right: Center of width)

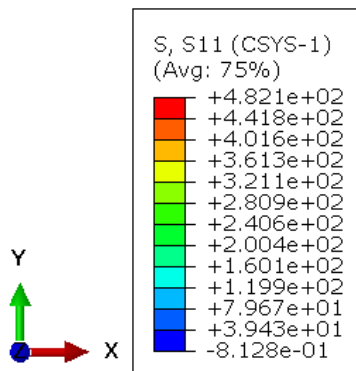
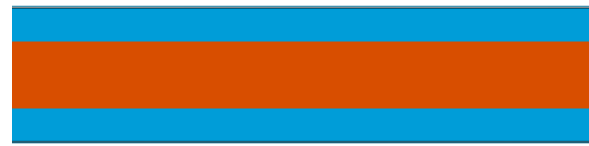


(ii) Axial Variation

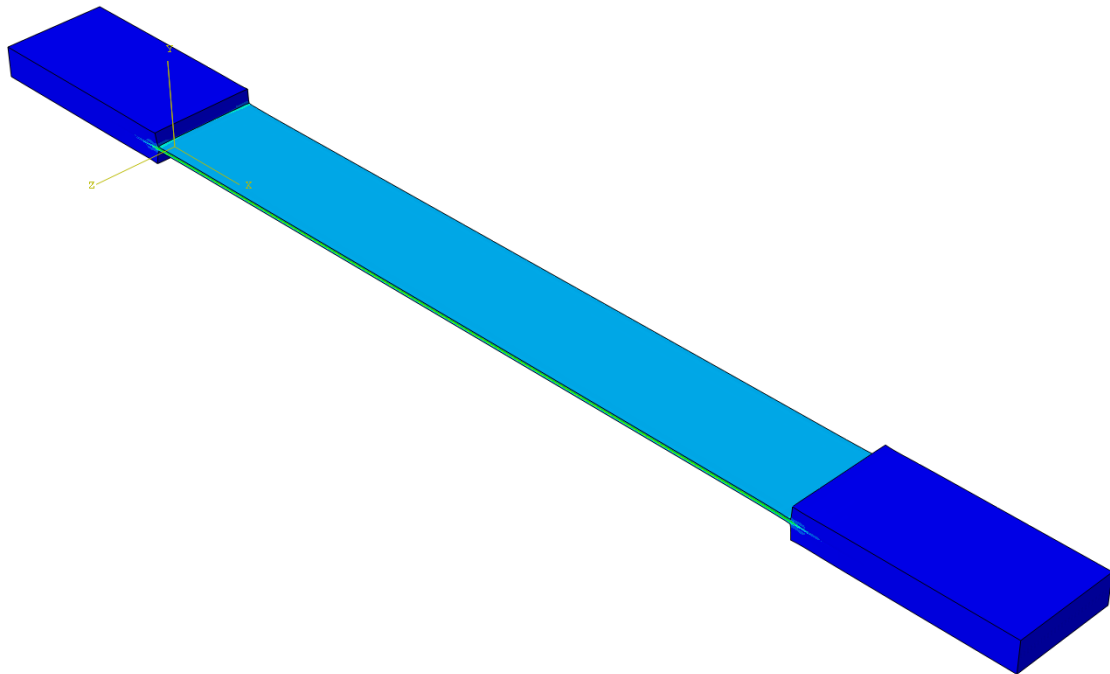
(c) In-plane Shear Stress (σ_{12})

5.4.1.4 $[90_2 / \pm 45]_s$ Laminate

Figure 18 shows the variation of stresses across the thickness and the axial length of the specimen. The $\pm 45^\circ$ carry more axial stress than the 90° laminates. All the shear stress is carried by the $\pm 45^\circ$ laminates, but, the direction of stress is opposite at these plies and the 90° plies do not carry any shear stress. The magnitude of transverse stress is negative at the 90° plies and is positive for the $\pm 45^\circ$ plies. The magnitude is however very close for both the orientations. The transition of these stresses is however not uniform across the thickness of the plies at the free-edge and the deformation of the plies is also not uniform at the edge. In the axial variation of transverse stress, the variation of the stress at the free-edge is clearly visible. In other cases, the variation of stress across the length of the specimen is very less and the value is constant at the gage length.



(i) Variation through thickness center of the width

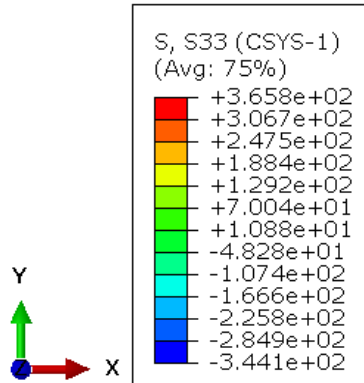
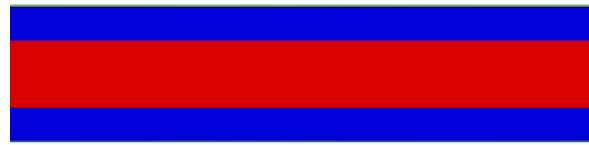


(ii) Axial Variation

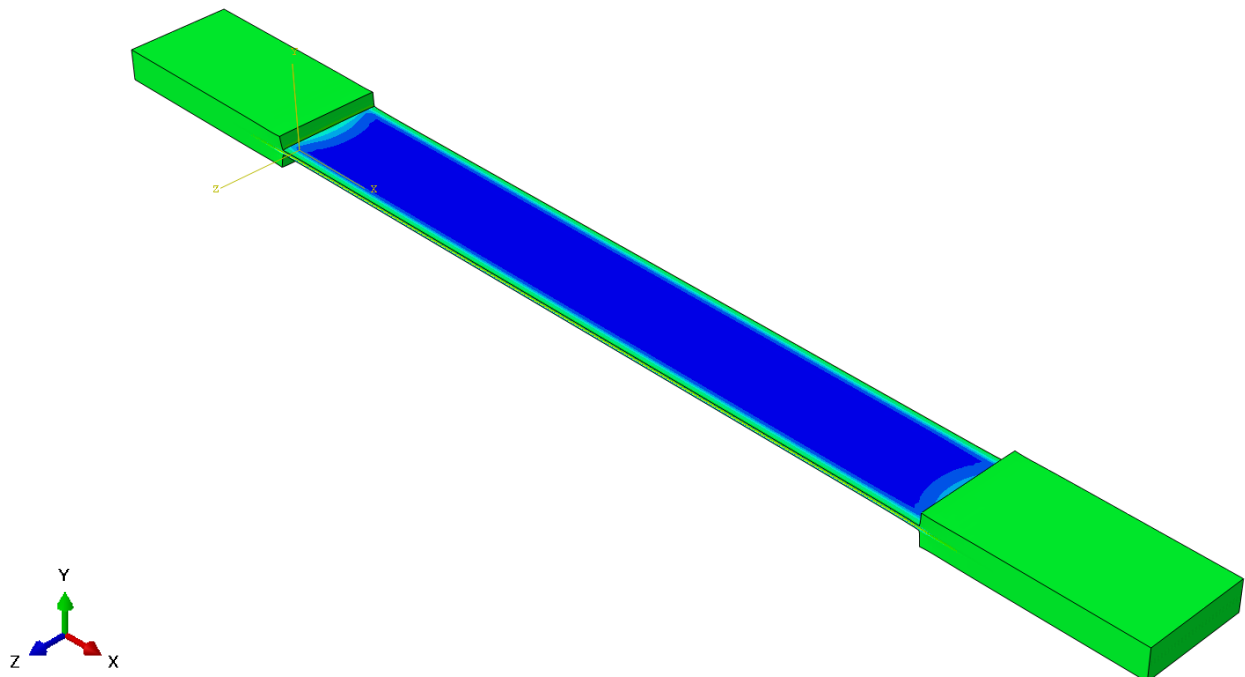
(a) Axial Stress (σ_{11})

Figure 5.18: Variation of stresses for $[90_2 / \pm 45]_s$ laminate

Figure 5.18 continued



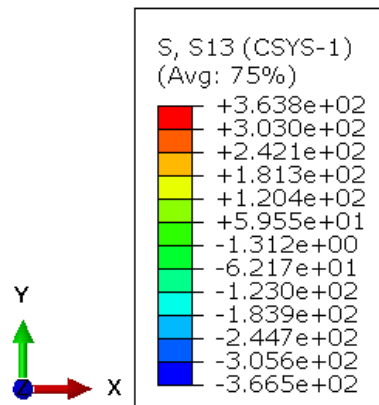
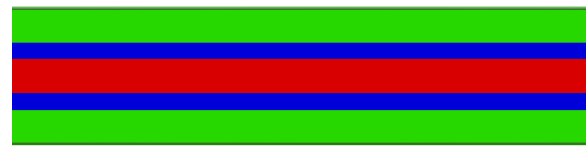
(i) Variation through thickness center of the width



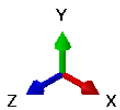
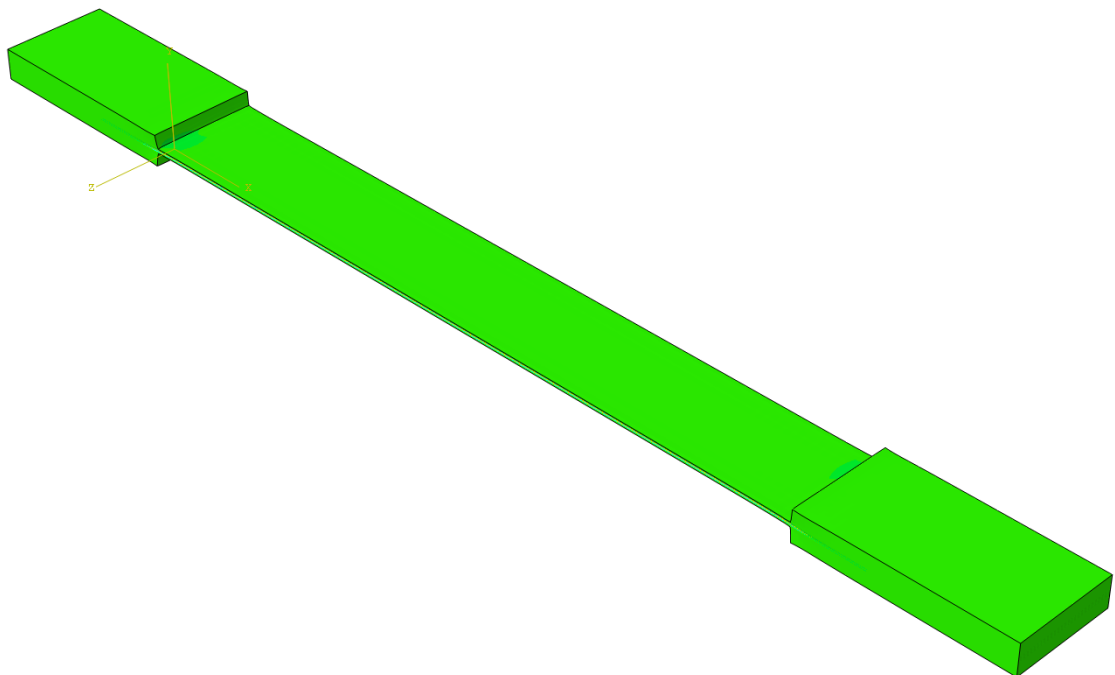
(ii) Axial Variation

(b) Transverse Stress (σ_{22})

Figure 5.18 continued



(i) Variation through thickness center of the width



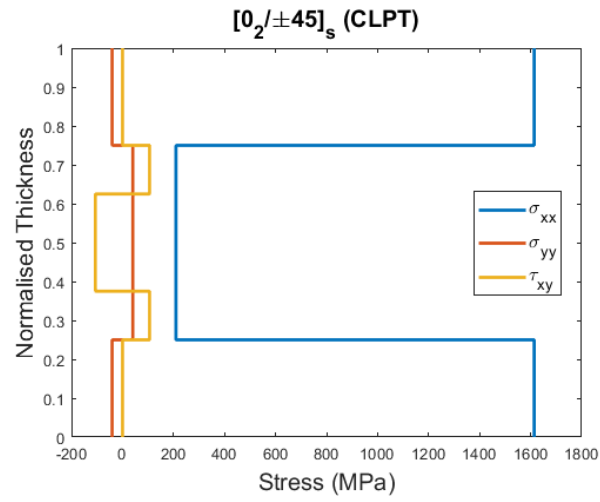
(ii) Axial Variation

(c) In-plane Shear Stress (σ_{12})

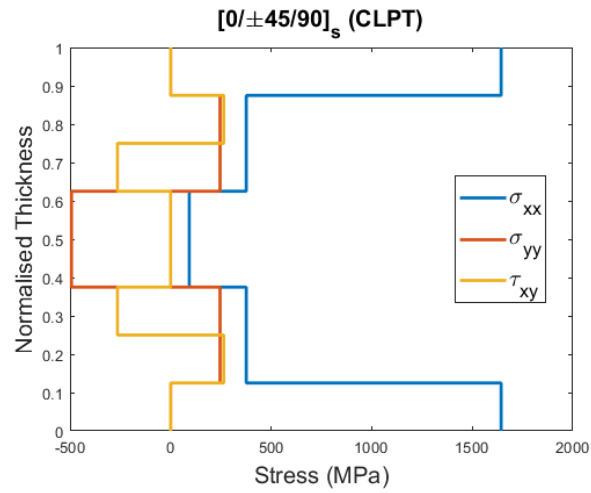
5.5 Comparison between theoretical and simulation results

5.5.1 Theoretical variation of stress through the thickness of the laminate

CLPT application in cdmHub was used to predict the plots of axial stress, transverse stress and shear stress across the thickness of the laminates. The axial load per unit thickness of the laminate was set to be the same as the corresponding value from the experiment. Figure 19 shows the plots for all the laminates. The axial stress is carried mostly by the 0 plies and the least axial stress is carried by the 90 plies. The 0 and 90 plies do not carry the shearing stress and its value is 0 for these plies. The 0 plies also do not carry transverse stress on them. The off-axis plies carry the shear loads on the laminates. It can be observed that the transverse stress is zero throughout the thickness for the $[\pm 30]_{2s}$ laminate. The green, red and blue plots are the shearing stress, transverse stress, and axial stress respectively.



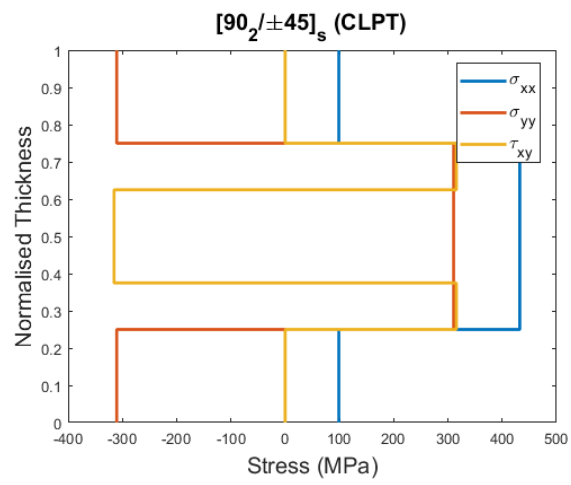
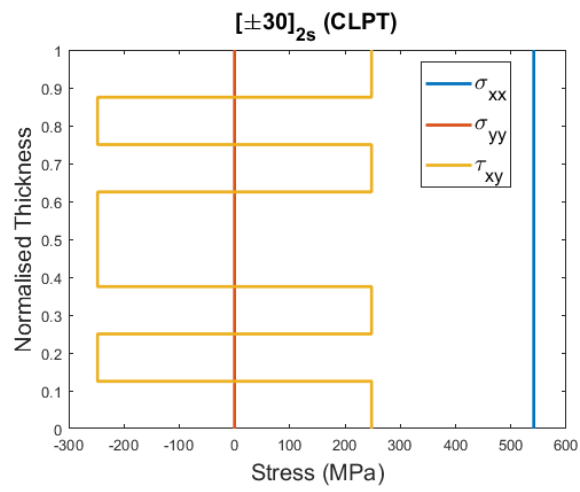
(a) $[0_2 / \pm 45]_s$



(b) $[0 / \pm 45 / 90]_s$

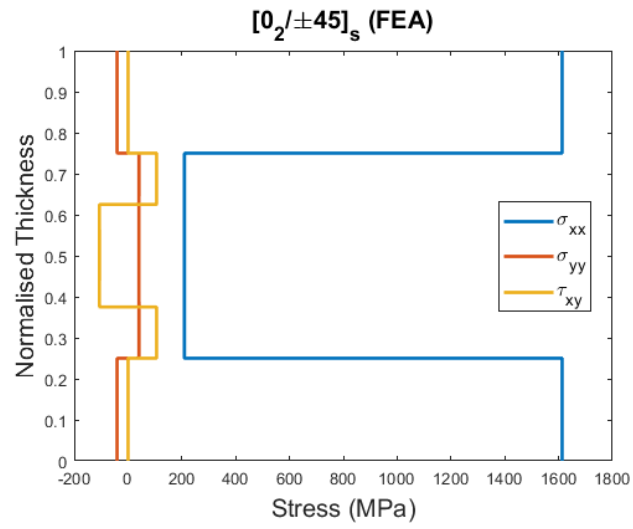
Figure 5.19: Stress Vs thickness plots from CLPT

Figure 5.19 continued

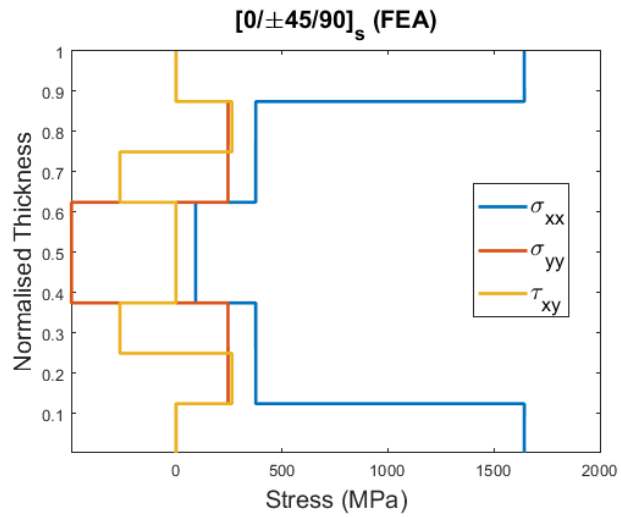


5.5.2 Variation of stress through the thickness of the laminate from the simulation

Figure 20 shows the plots of variation of axial, transverse and in-plane shear stresses with the thickness of the laminate at the center of the width of the laminate. The trend of variation of these stresses is exactly the same as that predicted from CLPT as discussed in section 5.5.1. These plots were made by choosing a set of nodes in the center of the gage length of the laminate. 1, 2 directions correspond to the axial and transverse directions respectively.



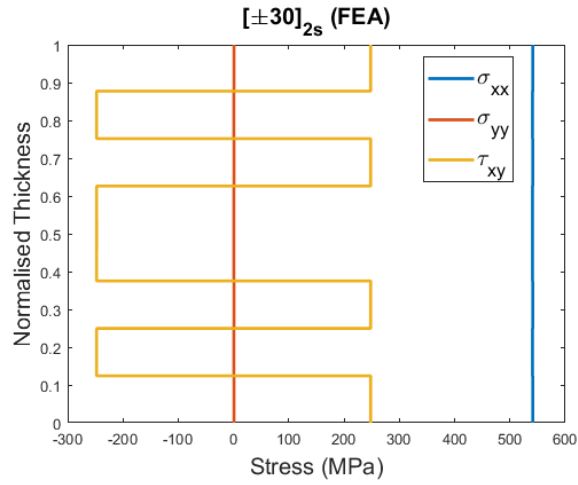
(a) $[0_2 / \pm 45]_s$ center of width



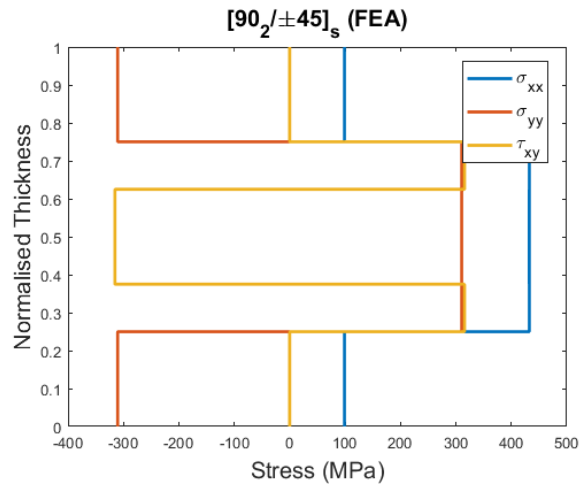
(b) $[0 / \pm 45 / 90]_s$ center of width

Figure 5.20: Stress Vs thickness plots from Simulations

Figure 5.20 continued



(c) $[\pm 30]_{2s}$ center of width



(d) $[90_2 / \pm 45]_s$ center of width

5.6 Conclusions

This experiment was used to determine the tensile modulus, Poisson's ratio and the ultimate tensile strength of the laminates and the experimental data was compared to the results obtained from CLPT and SwiftComp. The error for most of the parameters was obtained to be less than 10%. The axial, shear and transverse stresses were plotted across the thickness of all the specimens using CLPT to check their variation throughout. The samples that have 90 plies in them tend to fail in the 90 direction and other laminates fail in the off-axis direction. Hence, 0 plies have the highest

strength and the number of 0 plies determines the strength of the laminates. The modulus of $[0_2 / \pm 45]_s$ laminate is half of the modulus of the $[0]_8$ laminate. This is because this laminate is half comprised of 0 plies.

Using Abaqus simulations, the variation of these stresses across the thickness and the length of the laminates were analyzed. It was observed this is different at the free-edge and at the center of the laminate. The variation of the stresses across the thickness was found to be the same for the CLPT and the simulation results for all the laminates. The laminates also deformed in a non-uniform manner at the edge. This is to balance the forces at the free surface and this effect is discussed elaborately in chapter 7.

5.7 References

- [1] Carlsson, L. A., Adams, D. F., & Pipes, R. B. (2014). *Experimental characterization of advanced composite materials*. Boca Raton, FL: CRC Press.
- [2] Dr. Wenbin Yu. (2017) Multiscale Structural Mechanics. Wiley-Interscience. John Wiley & Sons, INC., Publication
- [3] Neha Shakelly, Adam Thomason, 4th October 2019, Friday, Lab 7- Laminate Tension, Presentation PPT. (2019).
- [4] Dr. Byron Pipes, 30th September 2019, Monday, Lamination Theory, Presentation PPT. (2019).

6. OPEN HOLE TENSION AND CTE ANALYSIS

6.1 Introduction

6.1.1 Finite and Infinite width specimen

In the practical use of carbon fiber composites, the presence of notch is very common and the strength of the laminate changes to a great extent due to the stress concentrations around the hole in the laminate. The properties of the laminate are also changed by the stacking sequence and size of the hole. These holes are made in the structural composites for fastening purposes. For an infinite plate, this stress concentration factor is independent of the hole size of the laminate. Since the failure modes are complex, the methods discussed are semi-empirical. For an ideally brittle infinite plate, the notched strength can be defined as the failure load over the cross-section area and it can be written as the follows:

$$\sigma_N = \frac{\sigma_0}{K_\infty}$$

Where, σ_0 is the strength of the plate without a hole, σ_N is the strength of the plate with the hole and K_∞ is the stress concentration factor. The stress concentration factor for a plate containing a circular hole of radius R is given by

$$K = \frac{\sigma_x(R, 0)}{\bar{\sigma}_x}$$

For a finite plate, the stress concentration can be defined as the following where there is no dependence on R:

$$K_\infty = 1 + \sqrt{2\left(\sqrt{\frac{E_x}{E_y}} - \nu_{xy} + E_x/(2G_{xy})\right)}$$

Where E_x and E_y are the modulus of elasticity in the loading and the transverse directions respectively, ν_{xy} is the Poisson's ratio and G_{xy} is the shear modulus.

For finite width specimen, as shown in Figure 1, the stress concentration is different from that of an infinite plate. It is given by the following equation:

$$\frac{K}{K_\infty} = \frac{2 + (1 - (D/w))^3}{3(1 - (D/w))}$$

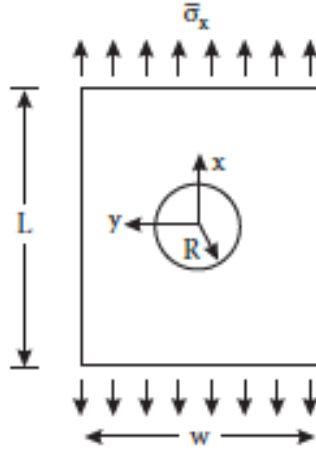


Figure 6.1: Finite plate

(Image from Experimental characterization of advanced composite materials (2014))

Where D is the hole diameter and w is the plate width. The corrected notch strength is as follows:

$$\sigma_N(\infty) = \sigma_N(w)K/K_\infty$$

The approximate stress distribution for an infinite plate containing a circular hole is given as follows:

$$\sigma_x(0, y) = \frac{\sigma_x(\infty)}{2} [2 + \xi^2 + 3\xi^4 - (K_\infty - 3)(5\xi^6 - 7\xi^8)]$$

Where, $\xi = R/y$ and $\sigma_x(\infty)$ is the far-field applied normal stress. Figure 2 shows the distribution of σ_x across the width for quasi-isotropic plates with two different hole sizes ($R/R_0 = 0.1$ and 1.0), where R_0 is the reference radius. The volume of the material that is subjected to high stress is much larger for a plate with a larger hole, increasing the opportunity for damage accumulation and stress distribution and this also explains the reduced notch strength with an increase in hole size.

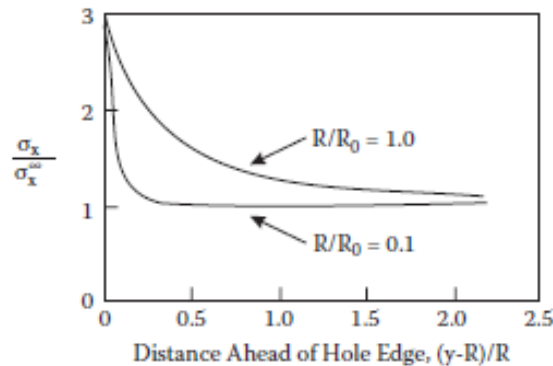


Figure 6.2: Normal stress distribution for quasi-isotropic laminates with 2 hole sizes
(Image from Experimental characterization of advanced composite materials (2014))

The hole size effect was incorporated into two different computationally simple fracture criteria, namely, Point Stress Criterion and Average Stress Criterion.

6.1.2 Point Stress Criteria (PSC)

The laminate is assumed to fail in tension when the stress σ_x , reaches the unnotched laminate strength σ_0 at a distance of d_0 ahead of the hole edge ($x = 0, y = R + d_0$).

$$PSC: \sigma_x(0, R + d_0) = \sigma_0$$

Combining this with the equation of approximate stress,

$$\frac{\sigma_N}{\sigma_0} = \frac{2}{2 + \lambda^2 + 3\lambda^4 - (K_\infty - 3)(5\lambda^6 - 7\lambda^8)}$$

Where, $\lambda = \frac{R}{R+d_0}$

For very large holes, d_0 is small compared to R . Hence, the equation becomes,

$$\frac{\sigma_N}{\sigma_0} = 1/K_\infty$$

The PSC thus contains two parameters (d_0, σ_0) that have to be determined by experiment. Having established d_0 and σ_0 , the PSC allows for strength predictions of laminates containing holes of arbitrary size. Figure 3 shows the experimental data along with the predicted values from PSC for different hole sizes for boron/aluminum composite. Figure 4 shows the graphical representation of PSC.

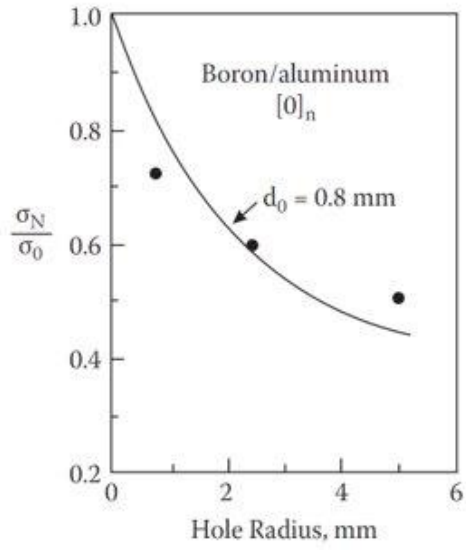


Figure 6.3: Experimental data on predicted values from PSC
(Image from Experimental characterization of advanced composite materials (2014))

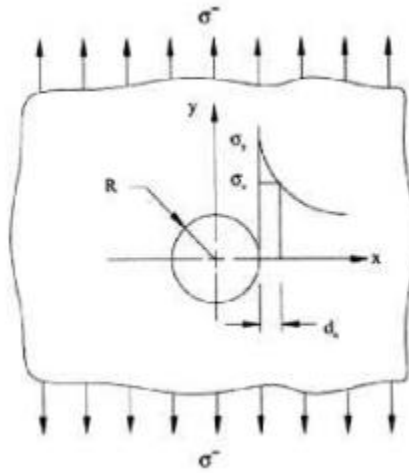


Figure 6.4: Graphical representation of PSC

6.1.3 Average Stress Criteria (ASC)

For the Average Stress Criterion (ASC), the laminate is assumed to fail in tension when the stress, σ_x , averaged over a region spanning from the hole edge ($y = R$) to ($y = R + \sigma_0$), reaches the unnotched laminate strength, σ_0 .

$$ASC: \frac{1}{a_0} \int_R^{R+a_0} \sigma_x(0, y) dy = \sigma_0$$

Substituting the stress equation into the ASC equation, we get the following expression for the notched laminate strength after the integration:

$$\frac{\sigma_N}{\sigma_0} = \frac{2}{(1 + \delta)(2 + \delta^2 + (K_\infty - 3)\delta^6)}$$

Where, $\delta = \frac{R}{R+a_0}$

Figure 5 shows the experimental strength data for a carbon-epoxy laminate with the ASC estimate. It can be observed that the data is in close agreement with each other. Figure 6 shows the graphical representation of ASC.

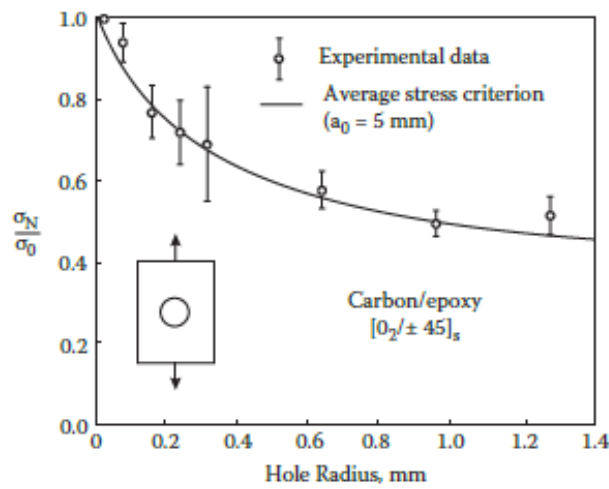


Figure 6.5: Experimental data on predicted values from ASC

(Image from Experimental characterization of advanced composite materials (2014))

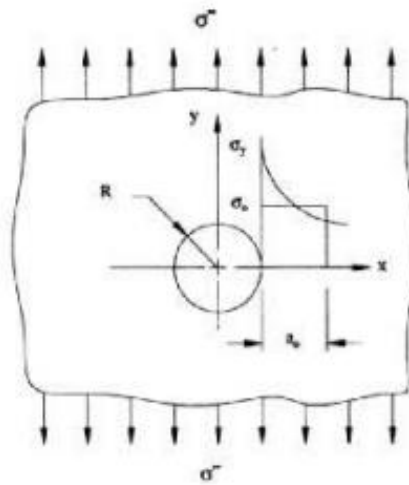


Figure 6.6: Graphical representation of ASC

6.1.4 Modified Point Stress Criteria (MPSC)

PSC was modified to improve the accuracy of the notched strength predictions. The characteristic distance d_0 becomes a power function of the hole radius as follows:

$$d_0 = (R/R_0)^m / C$$

Where, m is the exponential parameter, R_0 is the reference radius, C is the notch sensitivity factor. This model adds the exponential parameter m to the formulation of PSC. The reference radius is arbitrarily chosen to be $R_0 = 1 \text{ mm}$ and the parameter λ becomes as follows:

$$\lambda = 1/(1 + R^{m-1}C^{-1})$$

The parameter m affects the slope of the notch sensitivity curve when the parameter C moves the curve along the $\log R$ axis. The admissible range of m is between 0 and 1 and $C \geq 0$. Figure 7 shows that the experimental and the theoretical data are in close agreement with each other for the carbon-epoxy laminates with $[\pm 45/0/90]_s$ and $[90/0/\pm 45]_s$.

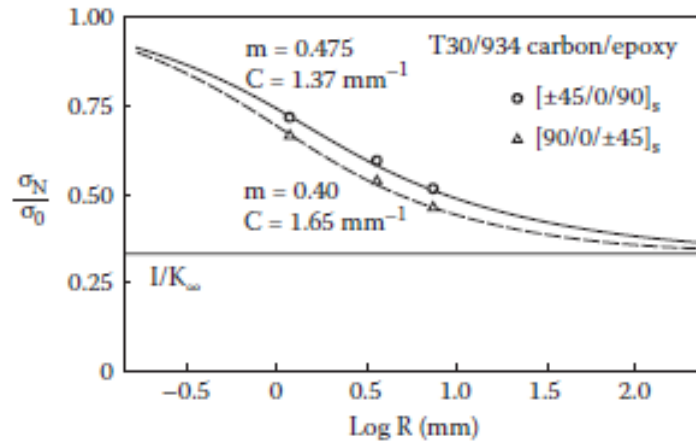


Figure 6.7: Experimental data on predicted values from MPSC

(Image from Experimental characterization of advanced composite materials (2014))

The Notch Sensitivity Factor (C) and exponential parameter (m) are calculated by using the following equation on the curve fit as shown in Figure 8.

$$-\log(1/\lambda - 1) = \log C + (1 - m) \log R$$

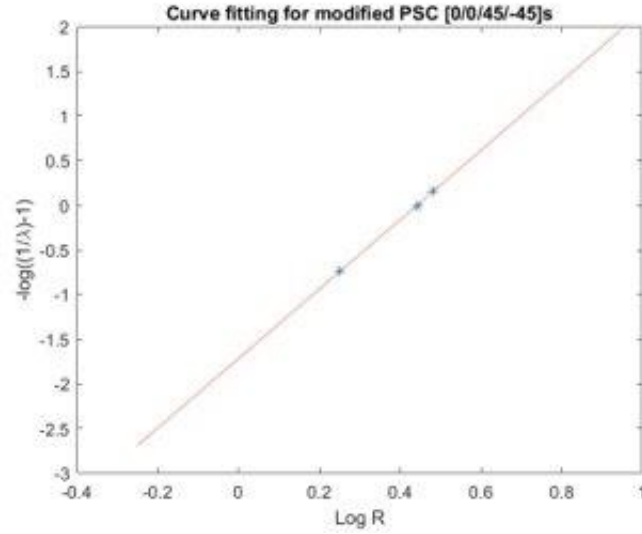


Figure 6.8: Curve fit to calculate parameters in MPSC

6.1.5 CTE for $[\pm 30]_{2s}$ laminate from CLPT

Figure 9 shows the values of CTE predicted from the CLPT application in cdmHub. The parameters that are given as input are the same as the material properties used in the simulations. The value of α_x is negative ($-4.5 \mu\epsilon/\text{°C}$), indicating that the laminate shrinks in the X direction when the temperature is increased. α_y is ($24.1 \mu\epsilon/\text{°C}$), indicating that expansion of the laminate in the Y direction is more than the deformation in the X-direction.

```
Laminate Properties:
Ex (Pa)
4.2043e+10
Ey (Pa)
9.01145e+09
Gxy (Pa)
2.6534e+10
nuxy
1.48
alphax
-4.5e-06
alphay
2.41e-05
alphaxy
0
```

Figure 6.9: Elastic constants and CTE values of $[\pm 30]_{2s}$ laminate

6.2 Experimental Procedure for tensile test

A total of 90 samples were made from three different stacking sequences, $[0_2 / \pm 45]_s$, $[0 / \pm 45 / 90]_s$ and $[\pm 30]_{2s}$. Three different hole sizes were made on the samples, $1/8"$, $3/16"$ and $1/4"$. 10 samples of each of the hole size were made and tested. All the laminates were symmetric and balanced. Out of these samples, 10 of them were speckled for the DIC analysis, which included, 2 large hole specimens for each specimen, 2 medium and small hole specimens for the quasi-isotropic laminate. The specimens were tested with a cross-head rate of 1mm/min. Figure 9 shows the samples that were tested with the DIC to obtain the strain distribution on the samples and Figure 10 shows the setup of DIC and MTS that was used to test the samples.

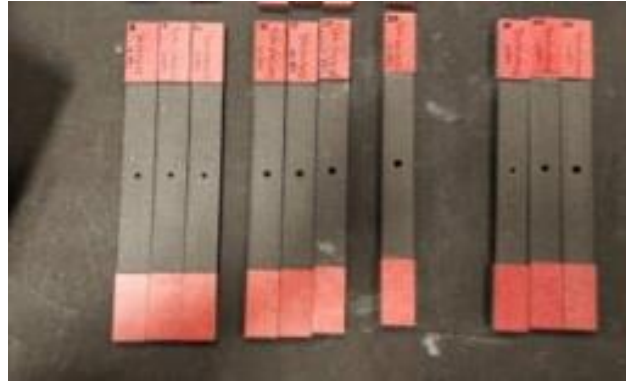
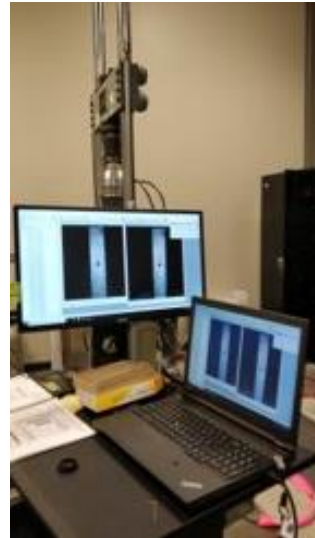


Figure 6.10: Specimen tested with DIC



(a) MTS



(b) DIC

Figure 6.11: Experimental Set-up

The other samples were only tested to get the strength values to compare them with the strengths of the laminates without a hole in them.

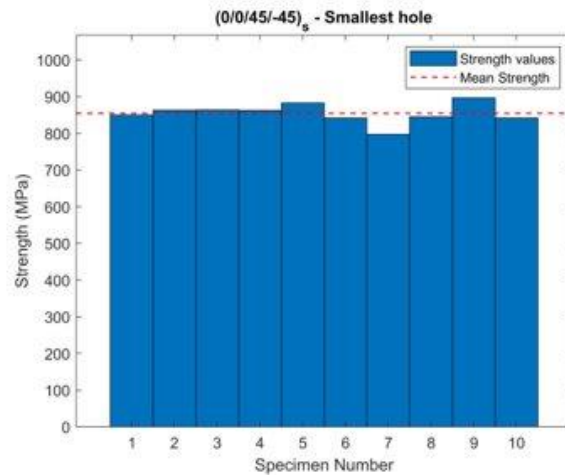
6.3 Experimental procedure for CTE test

The experimental procedure to conduct the CTE test and the experimental set-up for the CTE test are discussed in section 3.2. The values of strain data and displacements around the hole are analyzed using the DIC analysis and section 3.3 discusses the comparison of experimental data with the predicted theoretical values.

6.4 Processing of experimental results for tensile test

6.4.1 $[0_2 / \pm 45]_s$

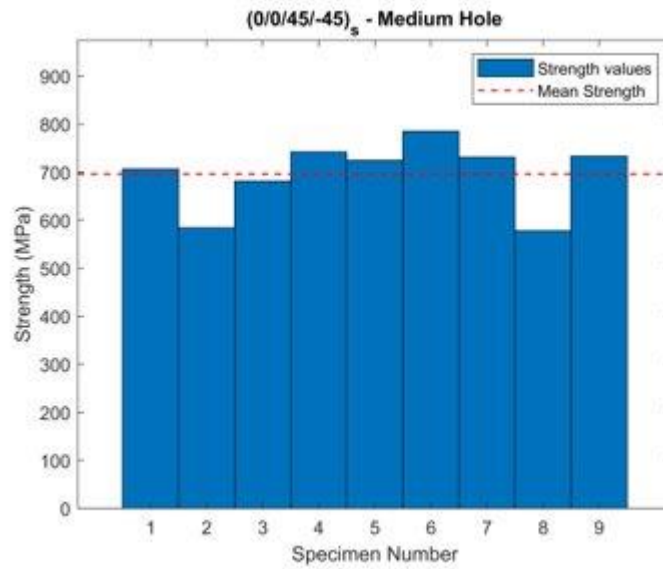
Figure 11 shows the strength distribution of the laminate with three different hole sizes, namely, 3.56 mm, 5.55 mm and 6.39 mm. It can be observed that the strength of the laminate reduces as the size of the hole increases. The strength of the on-notched laminate is 884.3 MPa as obtained from the previous experiments.



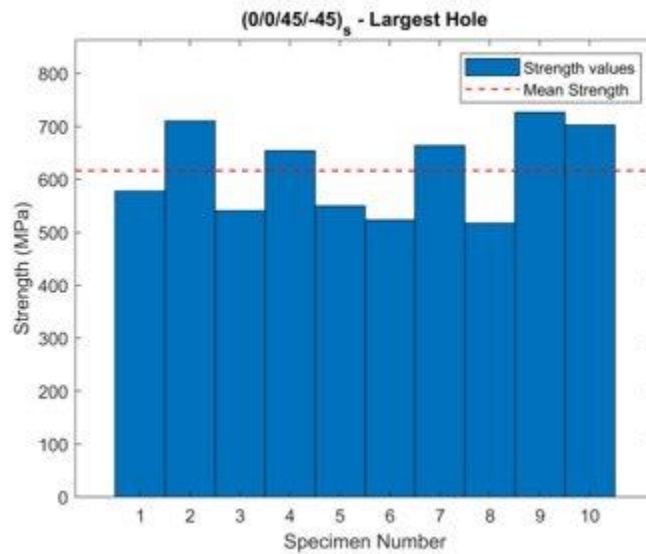
(a) Hole diameter = 3.56 mm

Figure 6.12: Strength distribution for $[0_2 / \pm 45]_s$ laminate

Figure 6.12 continued

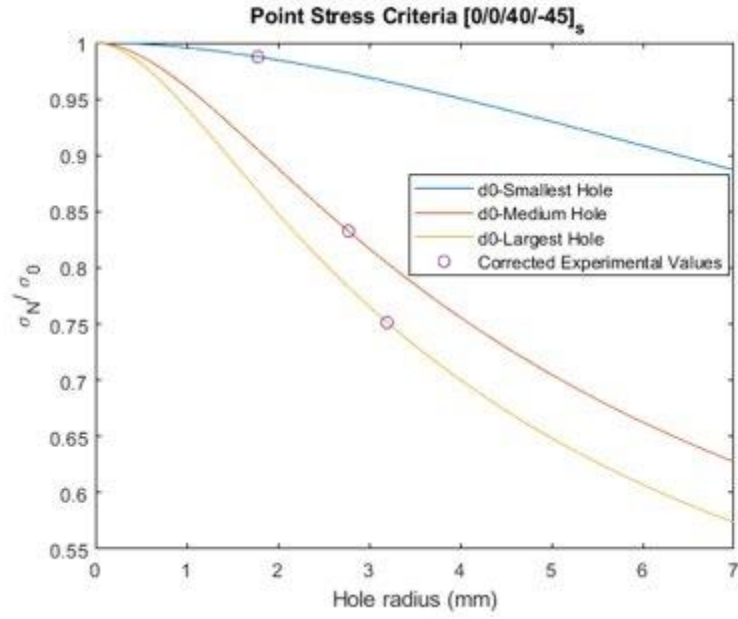


(b) Hole diameter = 5.55 mm

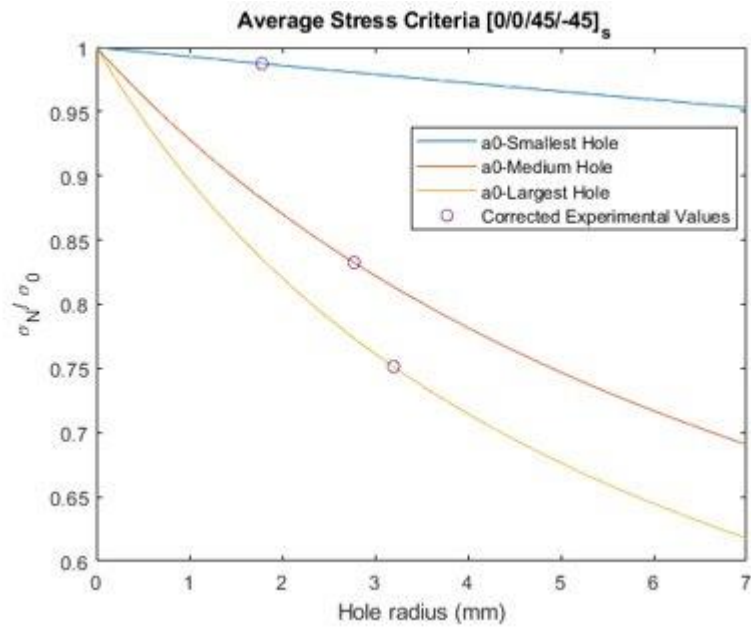


(c) Hole diameter = 6.39 mm

Figure 12 shows the plots of normalized stress calculated from three criteria as discussed in the theory section. The data is then compared to the experimental results that were obtained and they are also plotted along with the theoretical results. Figure 13 shows the failed specimen with different hole sizes for the $[0_2 / \pm 45]_s$ laminate, where small, medium and big holes denote a hole of $d=3.56$ mm, 5.55 mm and 6.39 mm respectively.



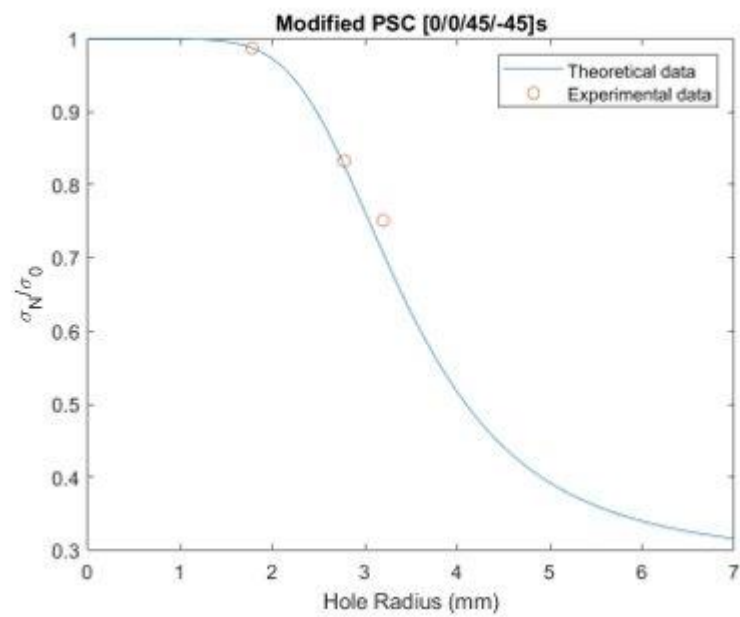
(a) Point Stress criterion



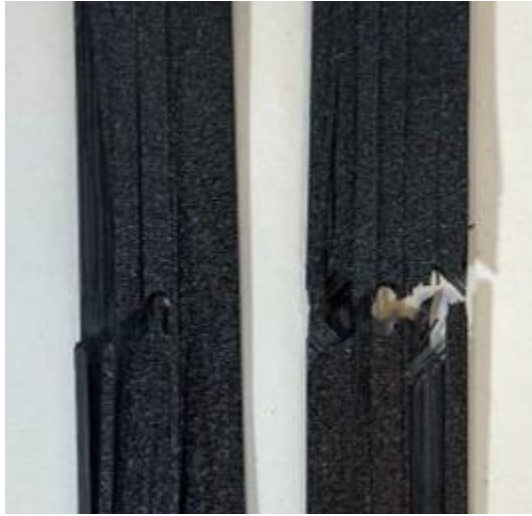
(b) Average Stress Criterion

Figure 6.13: Stress distribution as a function of hole size for $[0_2 / \pm 45]_s$ laminate

Figure 6.13 continued



(c) Modified Stress Criterion



(a) Small hole



(b) Medium hole



(c) Big Hole

Figure 6.14: Failed specimen for $[0_2 / \pm 45]_s$ laminate

It was observed that there was delamination in the first and last plies as shown in Figure 14. This is because the 0-degree plies fail but the 45-degree plies are still intact.



Figure 6.15: Delamination observed in $[0_2 / \pm 45]_s$ laminate

Figure 15 shows the strain distribution around the largest hole on the $[0_2 / \pm 45]_s$ laminate and Figure 16 shows the force versus displacement curves for the specimen with the smallest hole. The curve is linear and there is slight discontinuity and drop in force when there is a failure of a few layers in the laminate but the laminate as a whole is still intact.

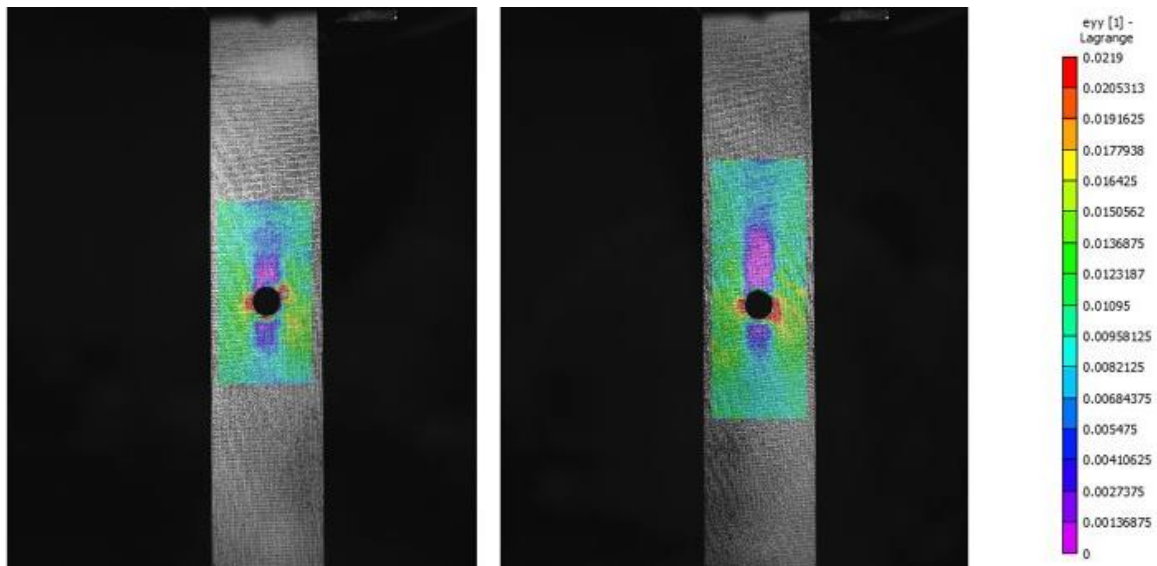


Figure 6.16: Strain distribution around the big hole of $[0_2 / \pm 45]_s$ laminate

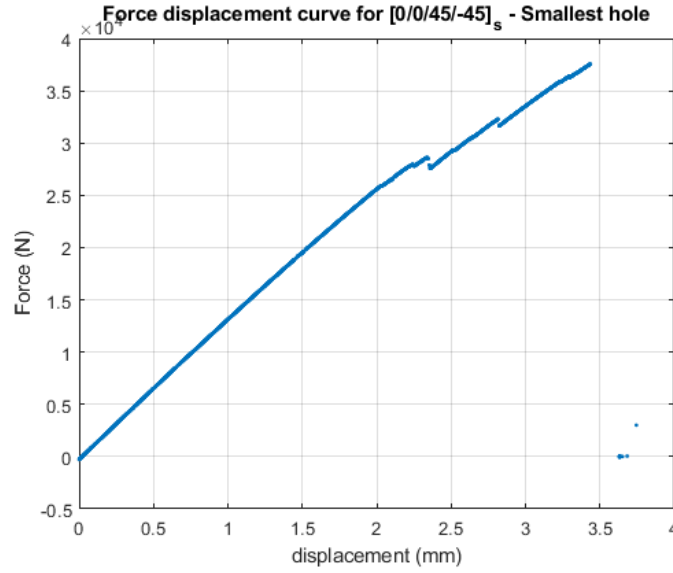
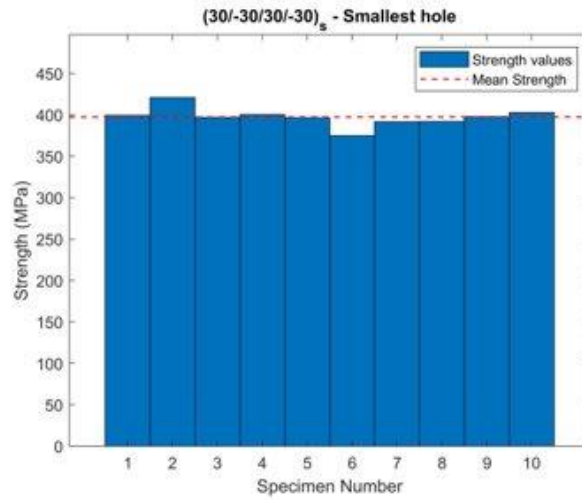


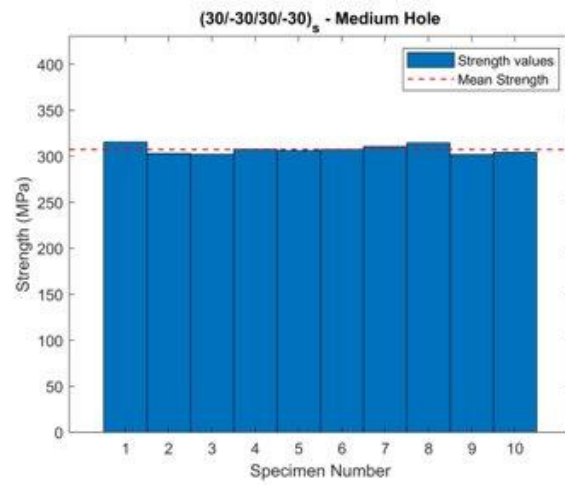
Figure 6.17: Force-displacement curve for $[0_2 / \pm 45]_s$ laminate with smallest hole

6.4.2 $[\pm 30]_{2s}$

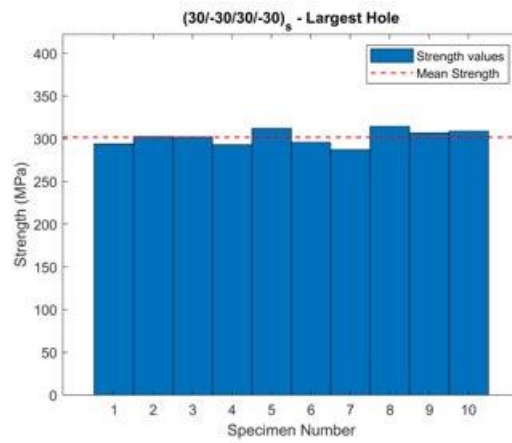
Figure 17 shows the strength distribution of the laminate with three different hole sizes, namely, 3.57 mm, 5.62 mm and 6.48 mm. It can be observed that the strength of the laminate reduces as the size of the hole increases. The strength of the on-notched laminate is 492.2 MPa as obtained from the previous experiments.



(a) Hole diameter = 3.57 mm



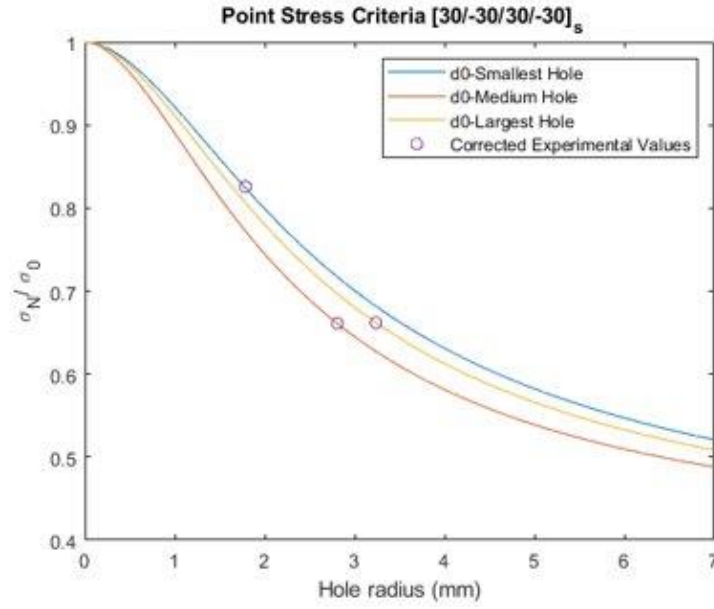
(b) Hole diameter = 5.62 mm



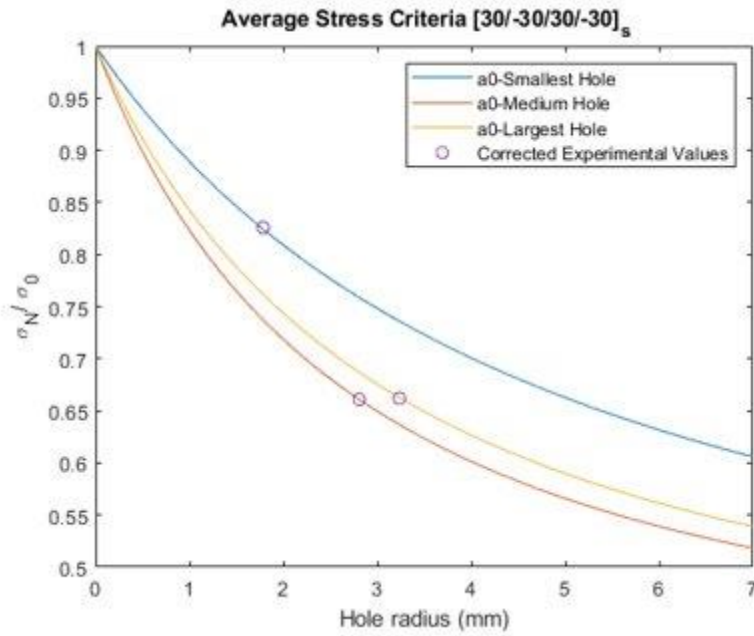
(c) Hole diameter = 6.48 mm

Figure 6.18: Strength distribution for $[\pm 30]_{2s}$ laminate

Figure 18 shows the plots of normalized stress calculated from three criteria as discussed in the theory section. The data is then compared to the experimental results that were obtained and they are also plotted along with the theoretical results. Figure 19 shows the failed specimen with different hole sizes for the $[\pm 30]_{2s}$ laminate, where small, medium and big holes denote a hole of $d=3.57$ mm, 5.62 mm and 6.48 mm respectively.



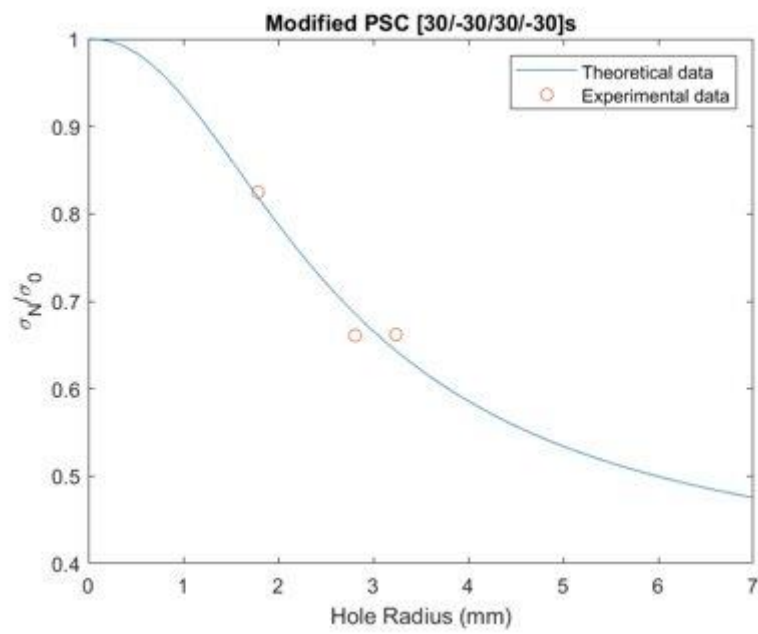
(a) Point Stress criterion



(b) Average Stress Criterion

Figure 6.19: Stress distribution as a function of hole size for $[\pm 30]_{2s}$ laminate

Figure 6.19 continued



(c) Modified Stress Criterion

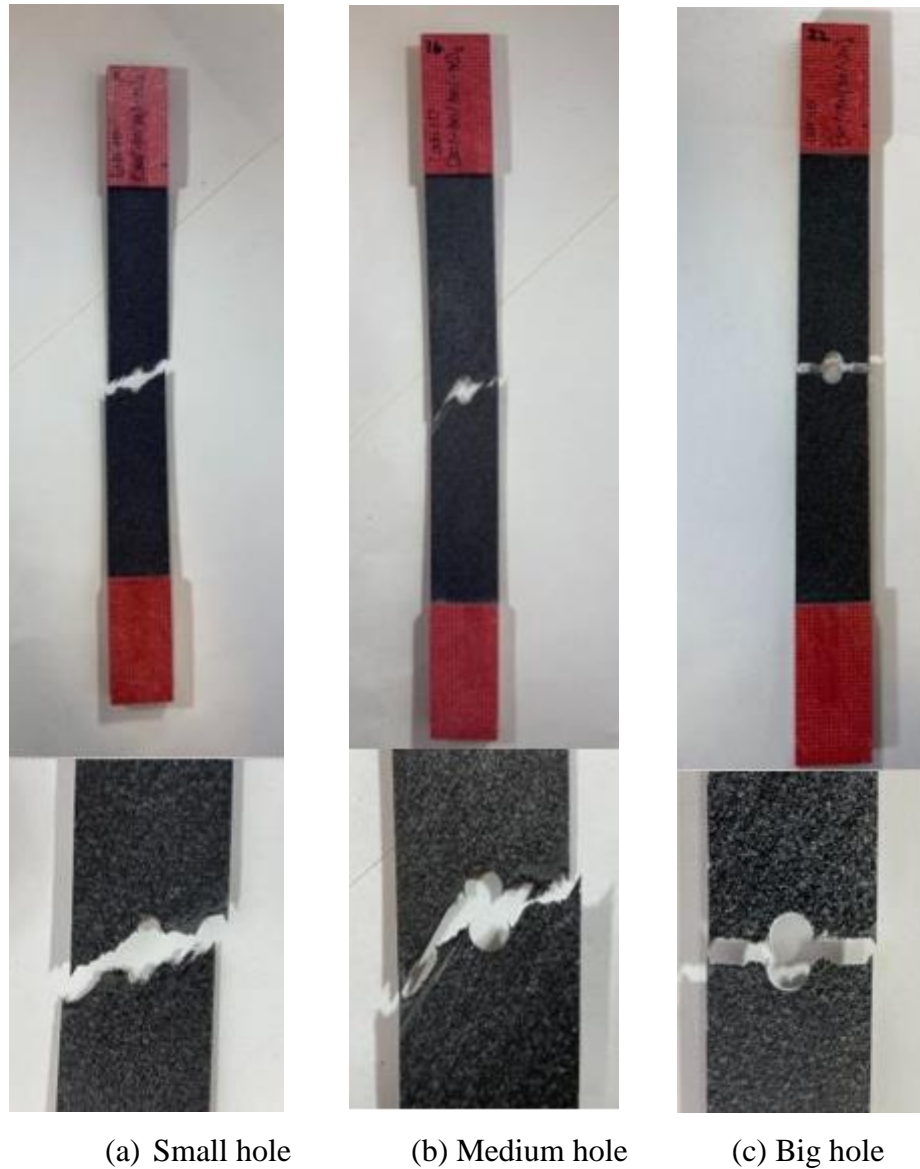


Figure 6.20: Failed specimen for $[\pm 30]_{2s}$ laminate

Figure 20 shows the strain distribution around the largest hole on the $[\pm 30]_{2s}$ laminate and Figure 21 shows the stress versus strain curves for the specimen with the largest hole. It can be observed that the strain distribution is in the shape of a butterfly around the hole and that there is no discontinuity as what was seen in the previous laminate as the laminate fails as a whole and there is no partial failure of the laminate as what was observed in the previous case.

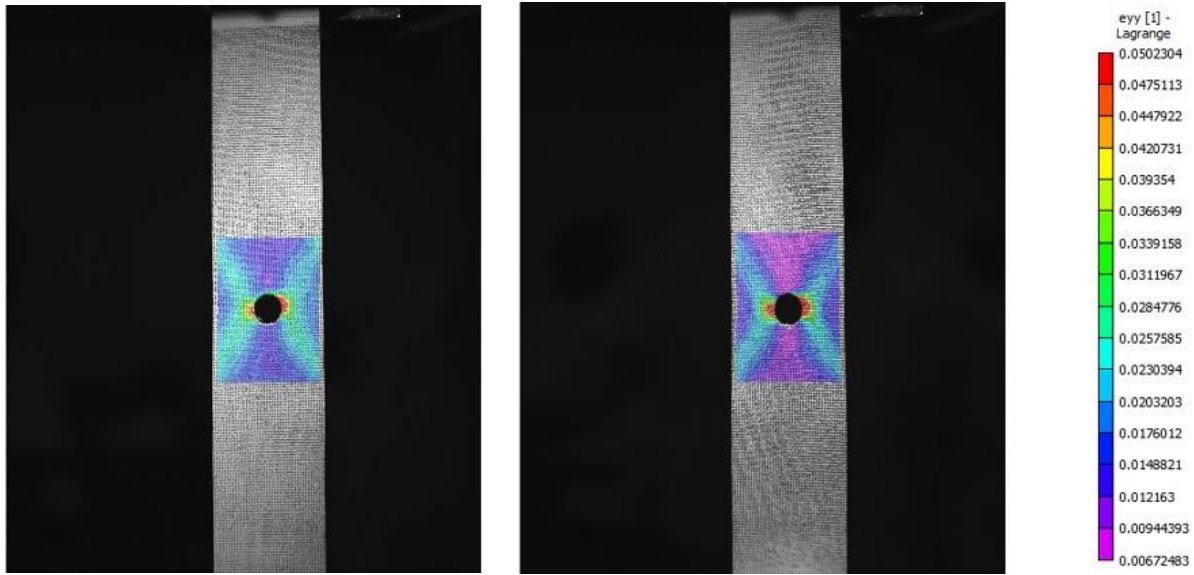


Figure 6.21: Strain distribution around the big hole of $[\pm 30]_{2s}$ laminate

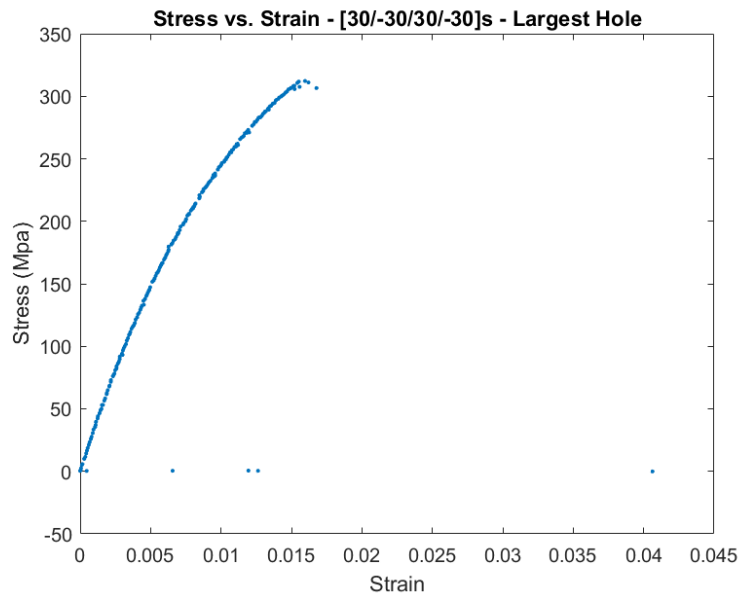
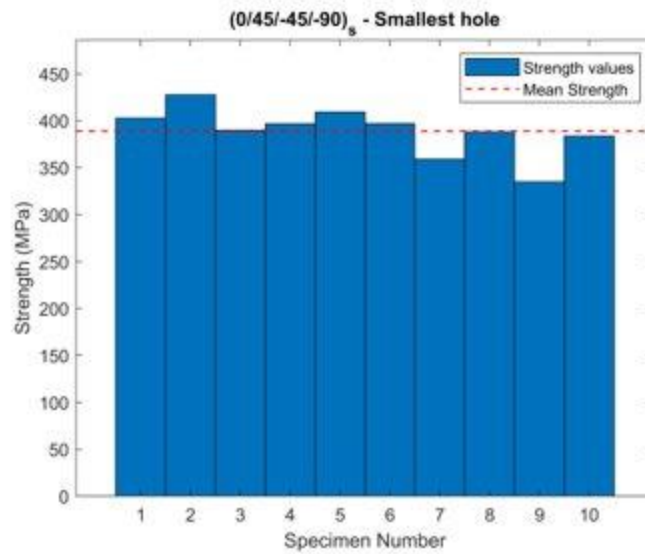


Figure 6.22: Stress-Strain curve for $[\pm 30]_{2s}$ laminate with the largest hole

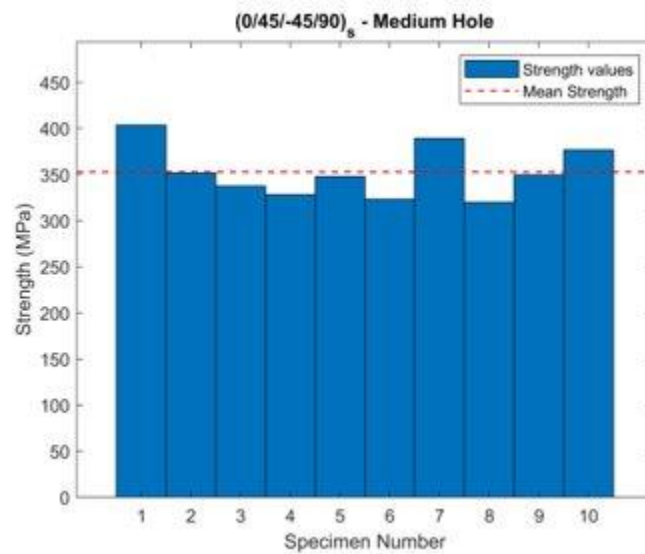
6.4.3 $[0/\pm 45/90]_s$

Figure 22 shows the strength distribution of the laminate with three different hole sizes, namely, 3.66 mm, 5.59 mm and 6.35 mm. It can be observed that the strength of the laminate reduces as

the size of the hole increases. The strength of the on-notched laminate is 590.9 MPa as obtained from the previous experiments.



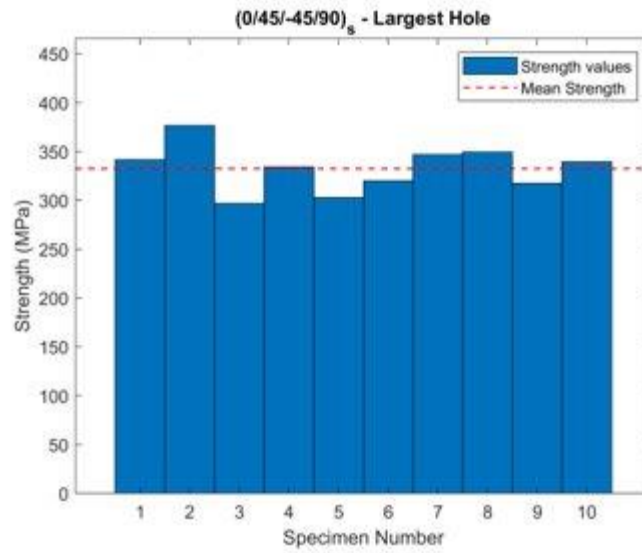
(a) Hole diameter = 3.66 mm



(b) Hole diameter = 5.59 mm

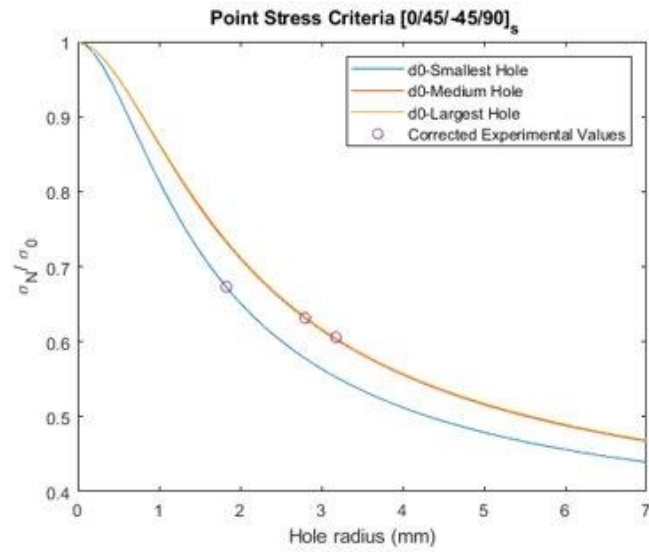
Figure 6.23: Strength distribution for $[0 / \pm 45 / 90]_s$ laminate

Figure 6.23 continued

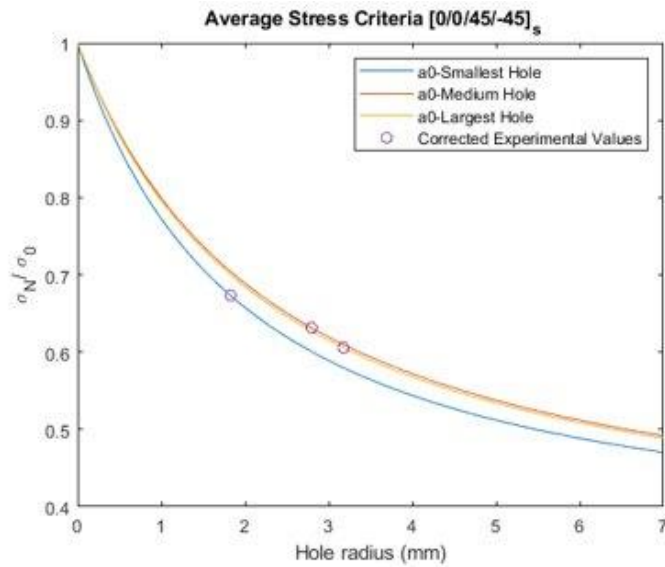


(c) Hole diameter = 6.35 mm

Figure 23 shows the plots of normalized stress calculated from three criteria as discussed in the theory section. The data is then compared to the experimental results that were obtained and they are also plotted along with the theoretical results. Figure 24 shows the failed specimen with different hole sizes for the $[0 / \pm 45 / 90]_s$ laminate, where small, medium and big holes denote a hole of $d=3.66$ mm, 5.59 mm and 6.35 mm respectively.



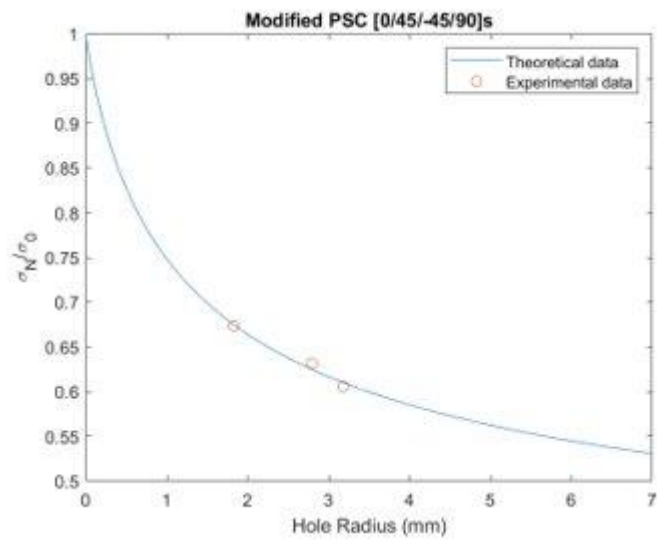
(a) Point Stress criterion



(b) Average Stress Criterion

Figure 6.24: Stress distribution as a function of hole size for [0 / ± 45 / 90]_s laminate

Figure 6.24 continued



(c) Modified Stress Criterion



(a) Small hole



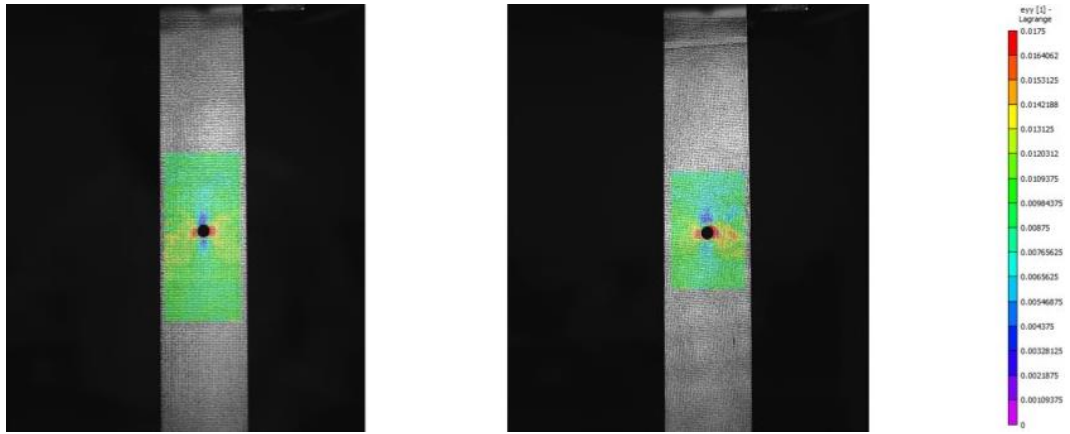
(b) Medium hole



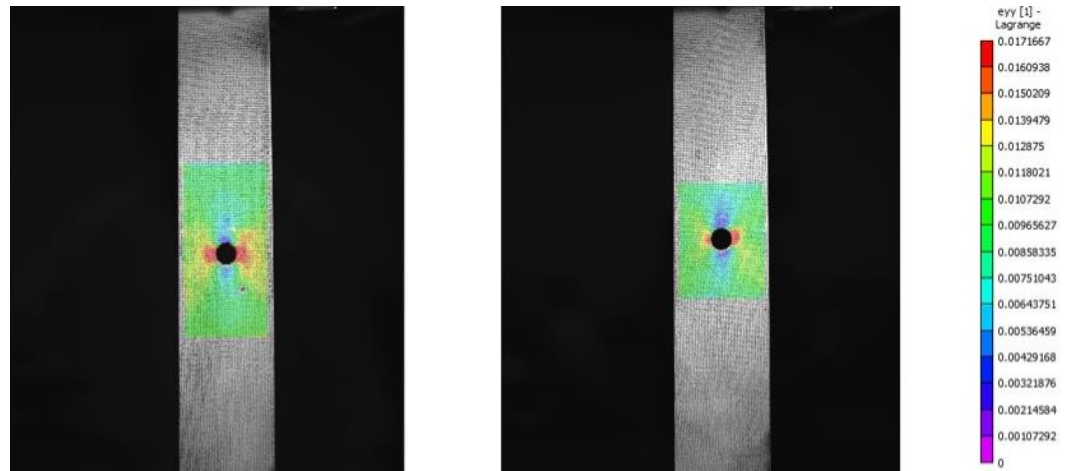
(c) Big hole

Figure 6.25: Failed specimen for $[0 / \pm 45 / 90]_s$ laminate

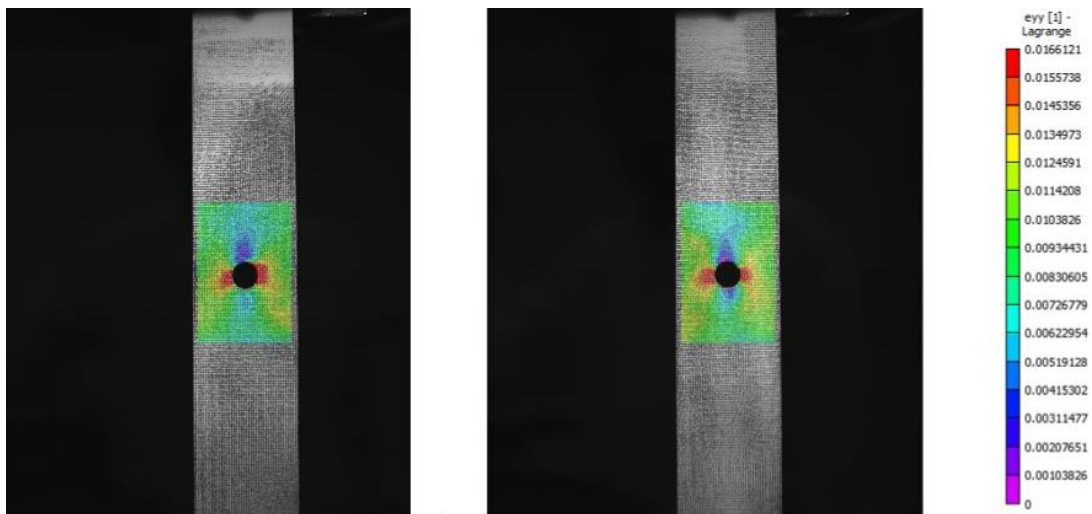
Figure 25 shows the strain distribution around the holes on the $[0 / \pm 45 / 90]_s$ laminate and Figure 26 shows the comparison of the strain around all three hole sizes. It can be observed that the region of high strain increases as the hole size increases. Figure 27 shows the force versus displacement curves for the specimen with holes. It can be observed that there is no discontinuity and the curves appear to be almost linear owing to the quasi-isotropic behavior of the laminate.



(a) Smallest Hole



(b) Medium Hole



(c) Large Hole

Figure 6.26: Strain distribution around the big hole of $[0 / \pm 45 / 90]_s$ laminate

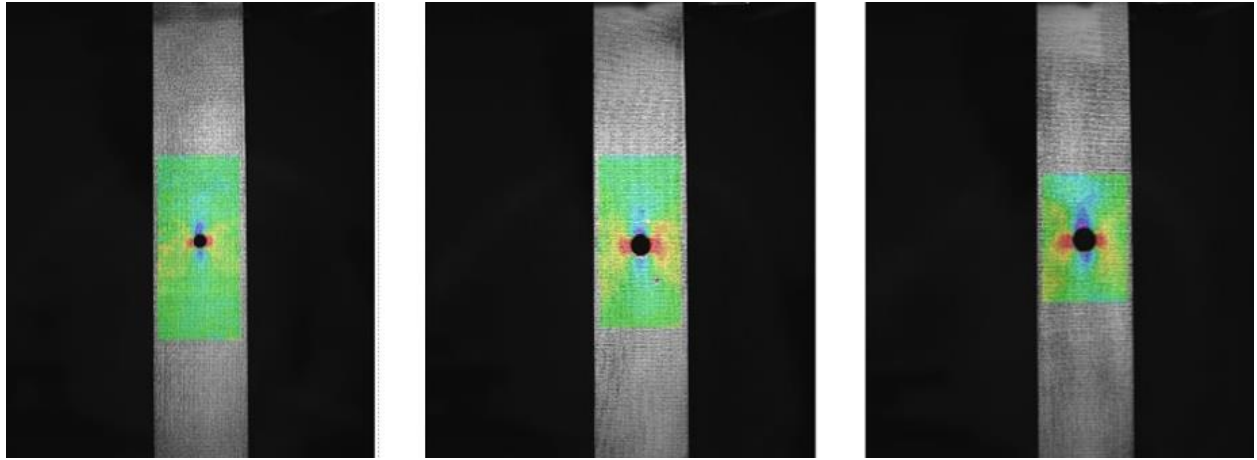
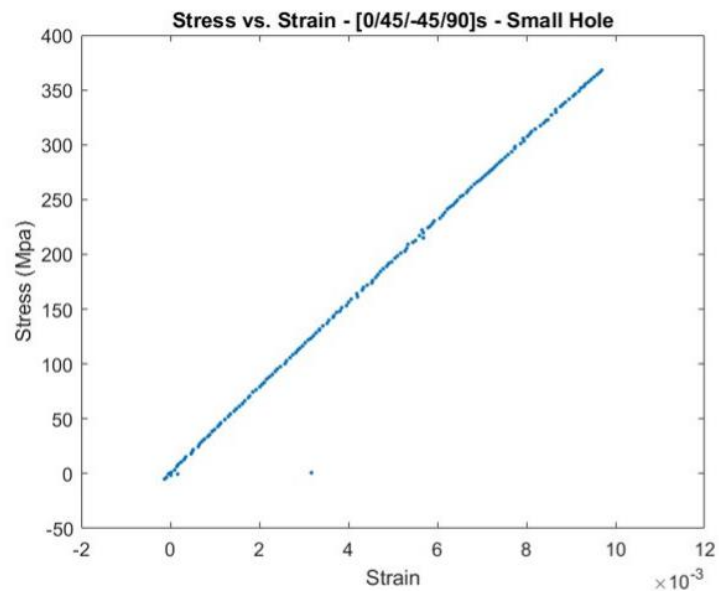


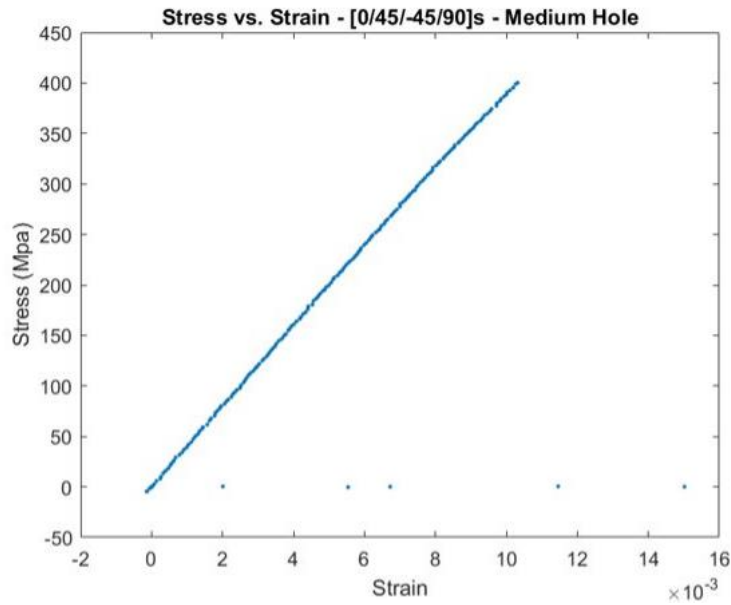
Figure 6.27: Comparison of strain data around the hole in $[0 / \pm 45 / 90]_s$ laminate with hole size increasing from left to right



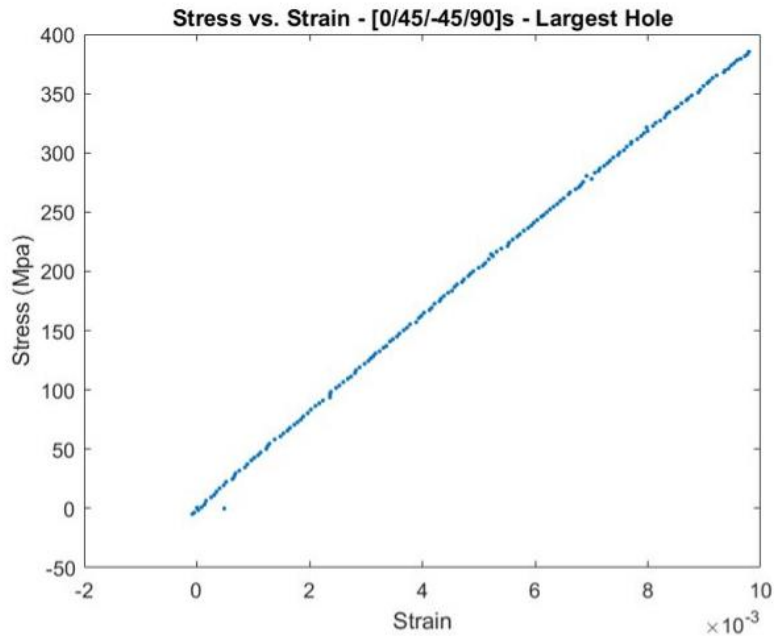
(a) Small Hole

Figure 6.28: Force displacement curve for $[0 / \pm 45 / 90]_s$ laminate

Figure 6.28 continued



(b) Medium Hole



(c) Big Hole

Table 1 shows the comparison of strength data for the three laminates with all the three hole sizes with the un-notched laminate strength. The strength of the laminate reduces as the size of the hole increases and there is a reduction in the strength of the laminate even with the smallest hole size.

$[0 / \pm 45 / 90]_s$ has the highest ultimate strength as it has a larger number of 0° plies and hence, it takes more load.

Table 6.1: Comparison of strength data of notched and un-notched laminates

Ultimate Notched Strength (σ_N) <i>MPa</i>				
Laminate	Small hole	Medium hole	Large hole	Un-notched (<i>MPa</i>)
$[0_2 / \pm 45]_s$	854.47	696.75	616.60	884.30
$[\pm 30]_{2s}$	397.25	307.39	301.69	492.20
$[0 / \pm 45 / 90]_s$	388.84	352.88	332.49	590.90

The parameters a_0 and d_0 obtained for the laminates for all the three hole sizes are tabulated in Table 2.

Table 6.2: Parameters a_0 and d_0 for the laminates with all the hole sizes

a_0			
Laminate	Small hole	Medium hole	Large hole
$[0_2 / \pm 45]_s$	277.07	25.26	16.42
$[\pm 30]_{2s}$	15.09	8.38	9.76
$[0 / \pm 45 / 90]_s$	5.88	7.05	6.87
d_0			
Laminate	Small hole	Medium hole	Large hole
$[0_2 / \pm 45]_s$	19.56	5.71	4.43
$[\pm 30]_{2s}$	3.72	2.96	3.43
$[0 / \pm 45 / 90]_s$	1.95	2.49	2.52

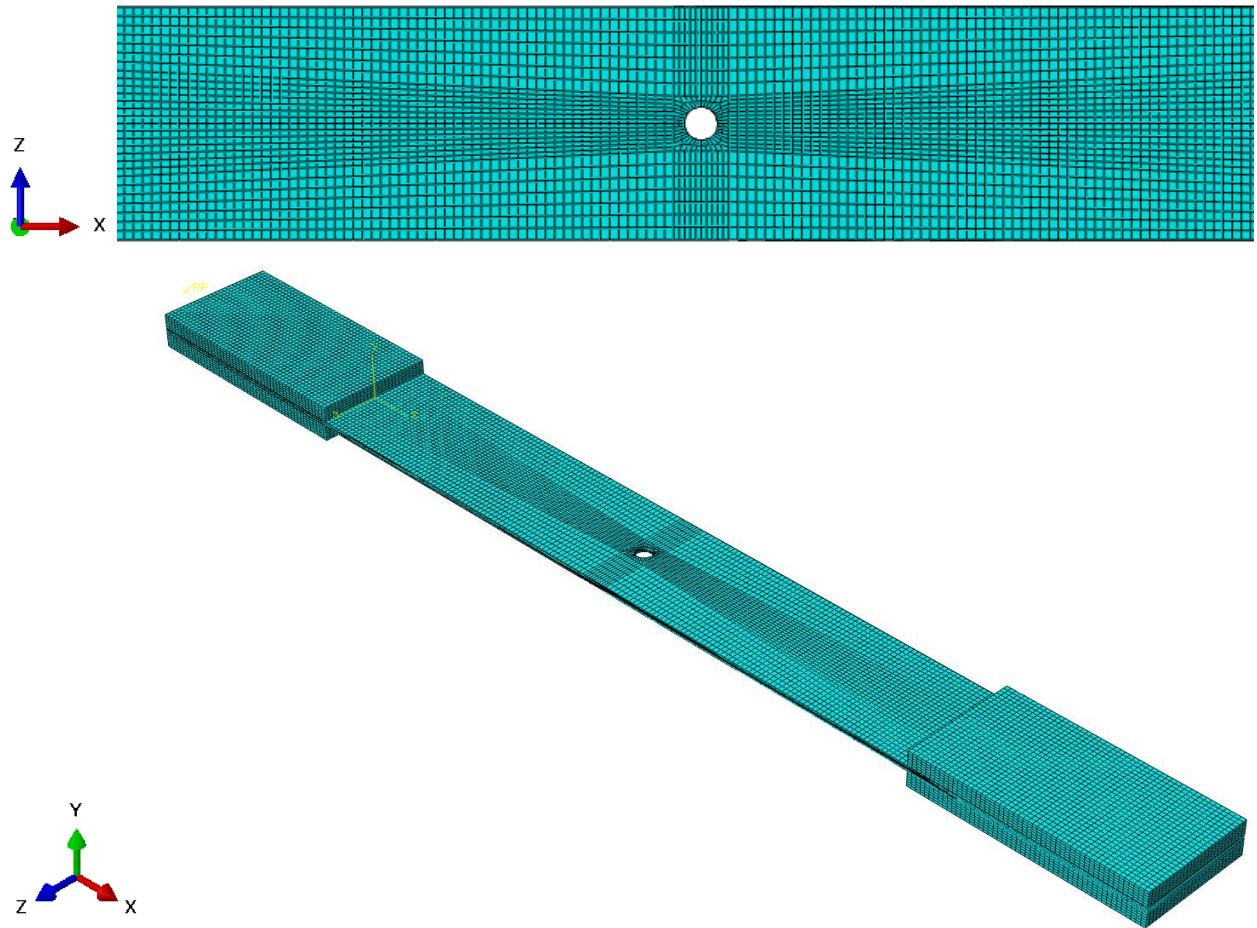
6.5 Modeling the geometry for simulations

6.5.1 Geometry, Load, and Boundary conditions

The specimens were modeled as one-inch (25.4 mm) wide tensile coupons and the holes were made on them at the center of the gage length and width. The average values of the hole diameters from the experimental specimens were chosen to be the diameters of the holes in the models. The hole sizes (diameter) corresponded to be 3.683 mm, 5.715 mm and 6.604 mm. The load and boundary conditions on these models were the same as discussed in section 2.7. Three different laminates with stacking sequences as $[0_2 / \pm 45]_s$, $[0 / \pm 45 / 90]_s$ and $[\pm 30]_{2s}$ were modeled and analyzed with three different hole sizes in each of them.

6.5.2 Mesh

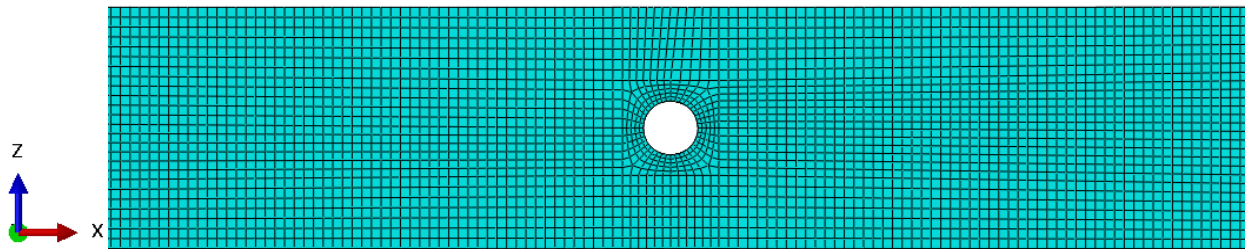
The mesh around the holes was also made structured to get more accurate and better convergence of results. Sections were created around the holes to get the required mesh. The seeding of edges was the same as discussed in section 2.6. The edge along the circumference of the holes was seeded with 40 elements. Figure 29 shows the mesh on the coupons for different hole sizes. The models with hole diameters as 3.683 mm, 5.715 mm and 6.604 mm had 263648, 246736, 246736 elements in them respectively.



(a) Hole diameter = 3.683 *mm*

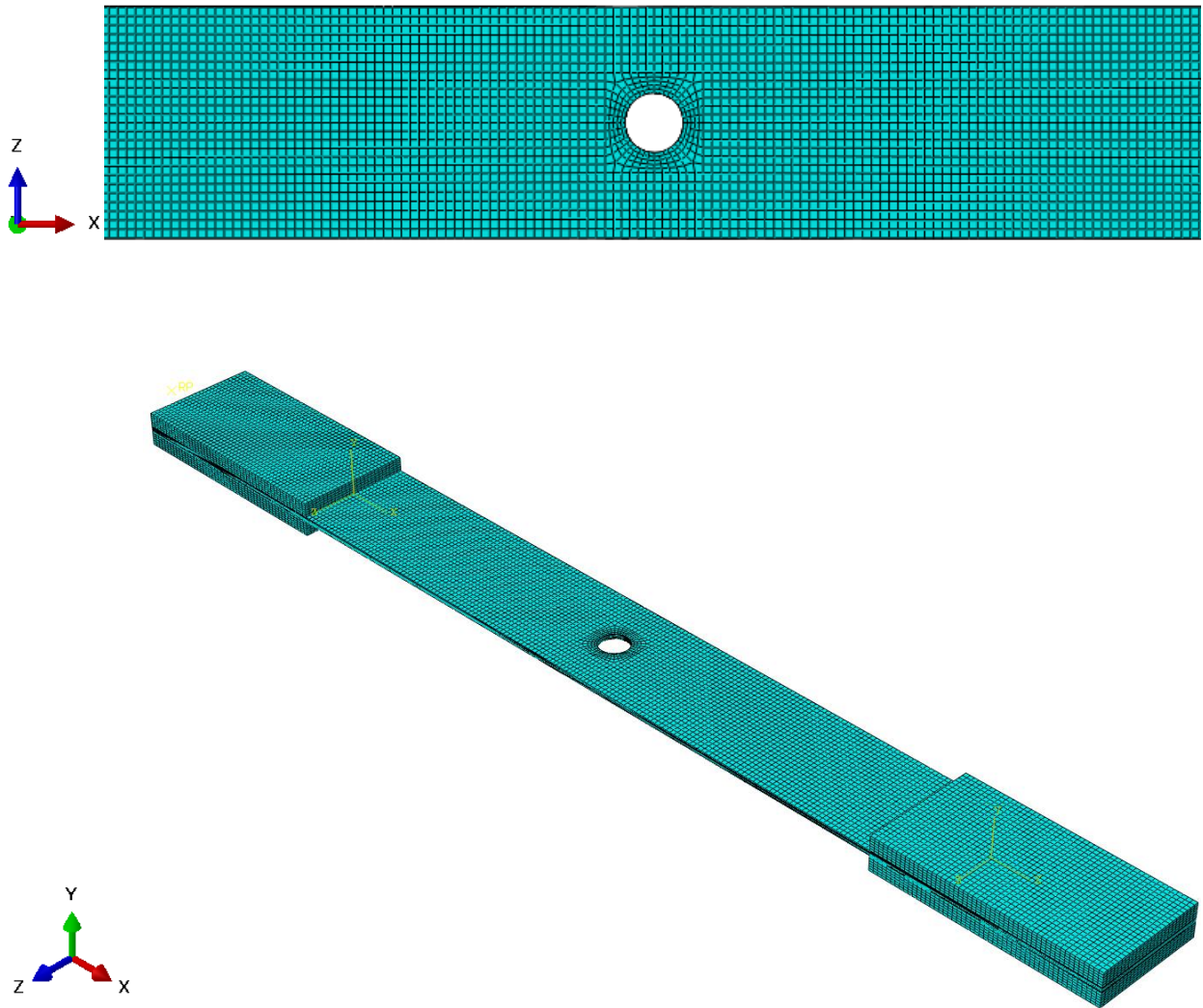
Figure 6.29: Mesh on open-hole tensile test specimen

Figure 6.29 continued



(b) Hole diameter = 5.715 mm

Figure 6.29 continued



(c) Hole diameter = 6.604 *mm*

6.6 Analysis of simulation results for tensile test

As discussed in the previous chapters, the results were first rotated into the global coordinate system as the laminate material orientations were given as an input individually. The default deformation output has a scale of 12.6987 and for the better visualization of results, the scale was reduced to 1.

6.6.1 Distribution of stress on laminates

6.6.1.1 $[0_2 / \pm 45]_s$

Figure 30-32 show the variation of axial stress at the hole and also across the length of the $[0_2 / \pm 45]_s$ laminate. It can be observed that there is compressive and tensile stress around the hole and the magnitude of these stresses increases as the hole size increases. From the (b) part of these images, the free-edge effects at the holes are observed. The 0° plies take more tensile loads than the 45° plies. This agrees with the CLPT results discussed in section 5.5.

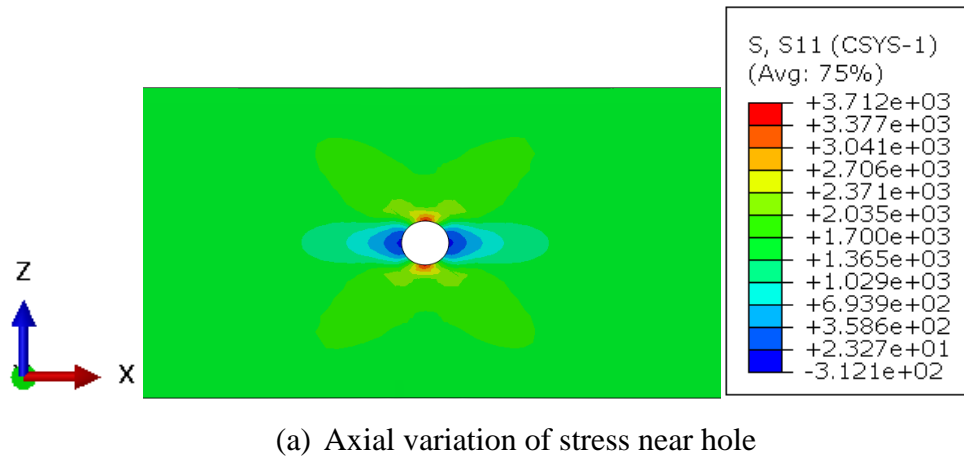
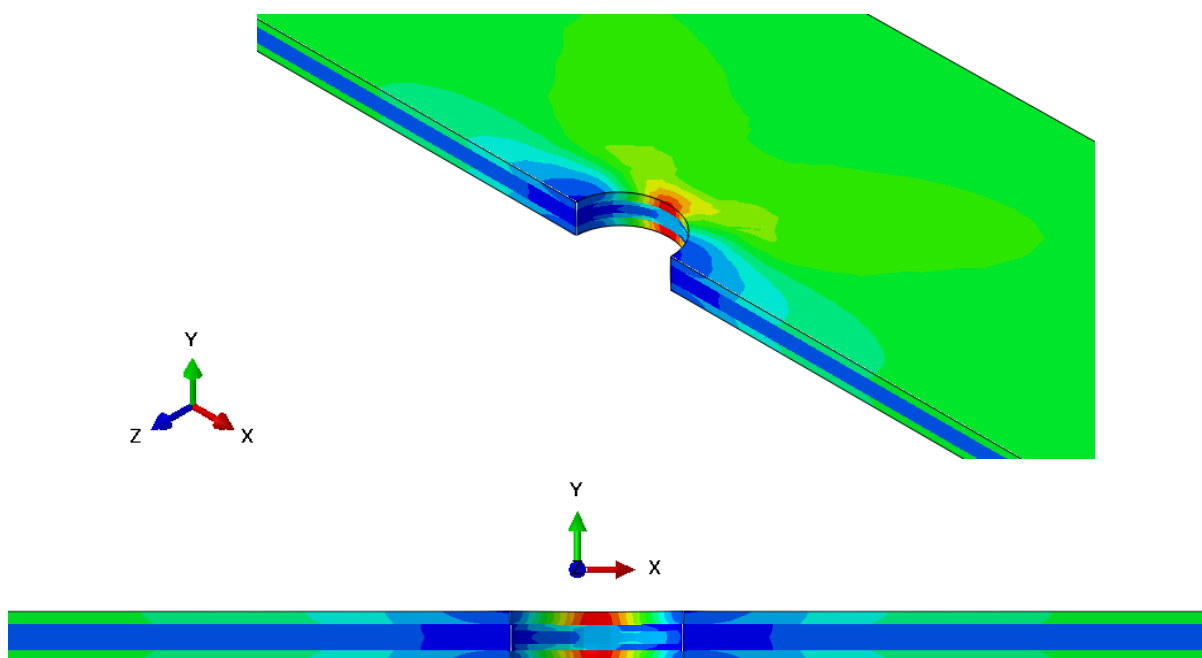
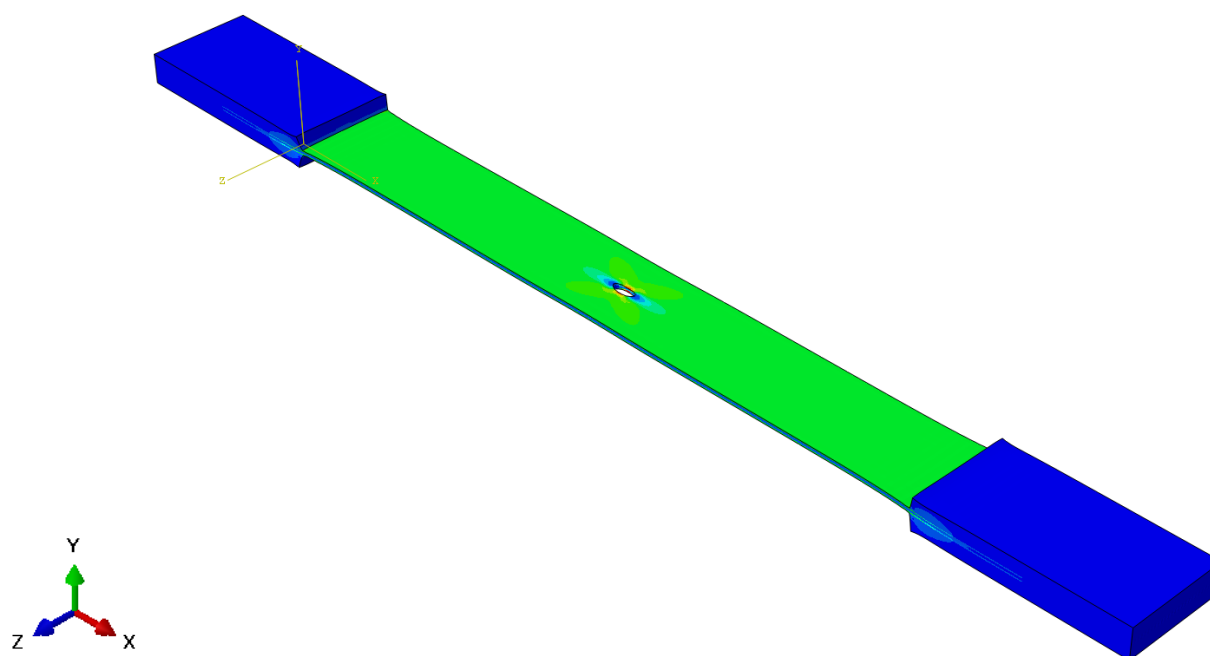


Figure 6.30: Variation of axial stress σ_{11} on the $[0_2 / \pm 45]_s$ laminate with a hole of diameter 3.683 mm

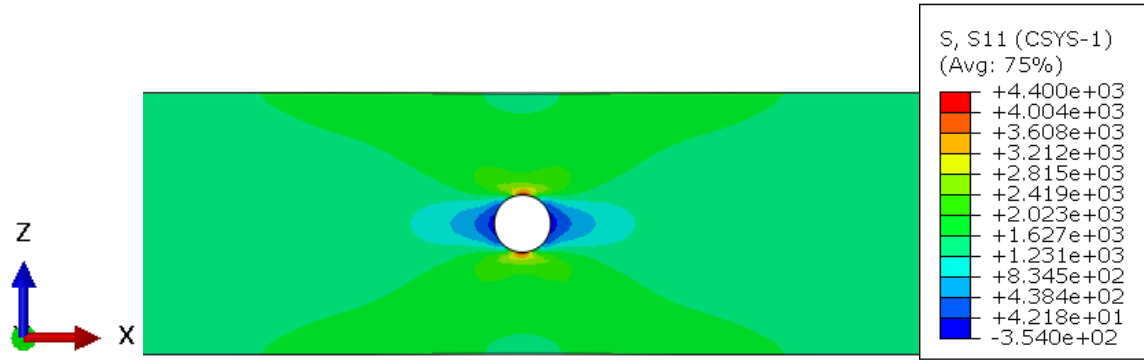
Figure 6.30 continued



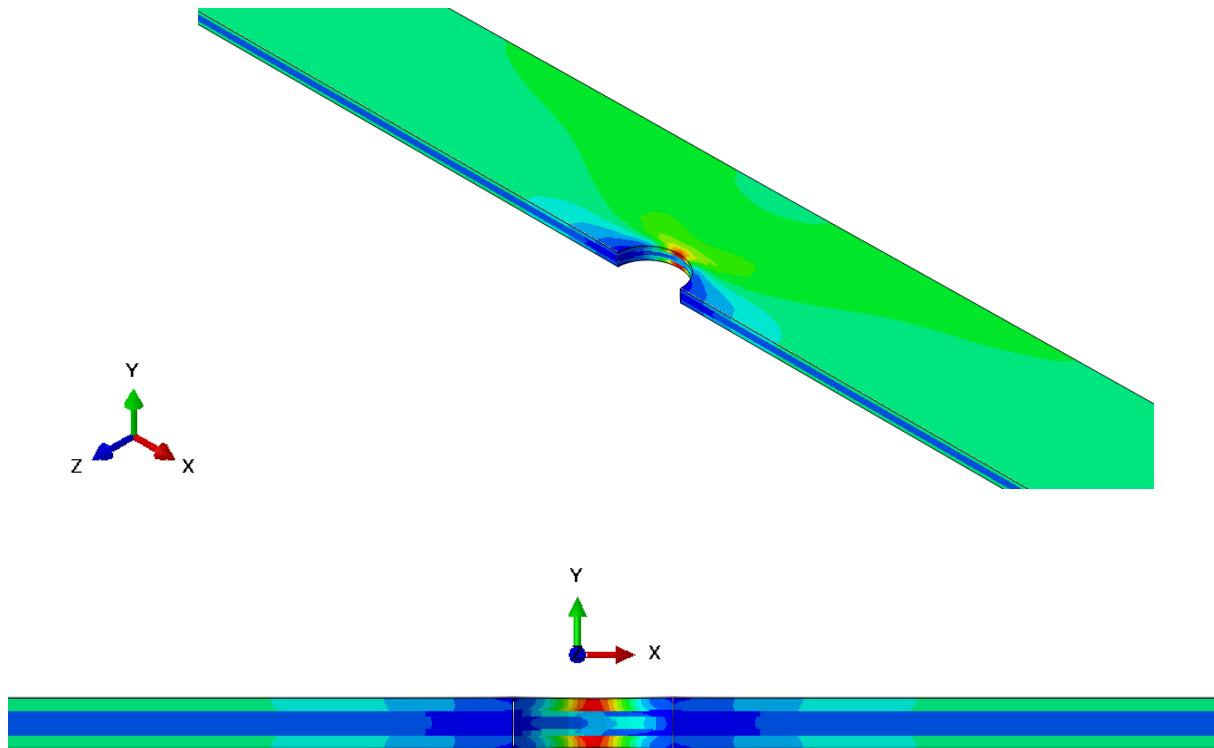
(b) Variation of stress through thickness near the hole



(c) Variation of stress on the entire coupon



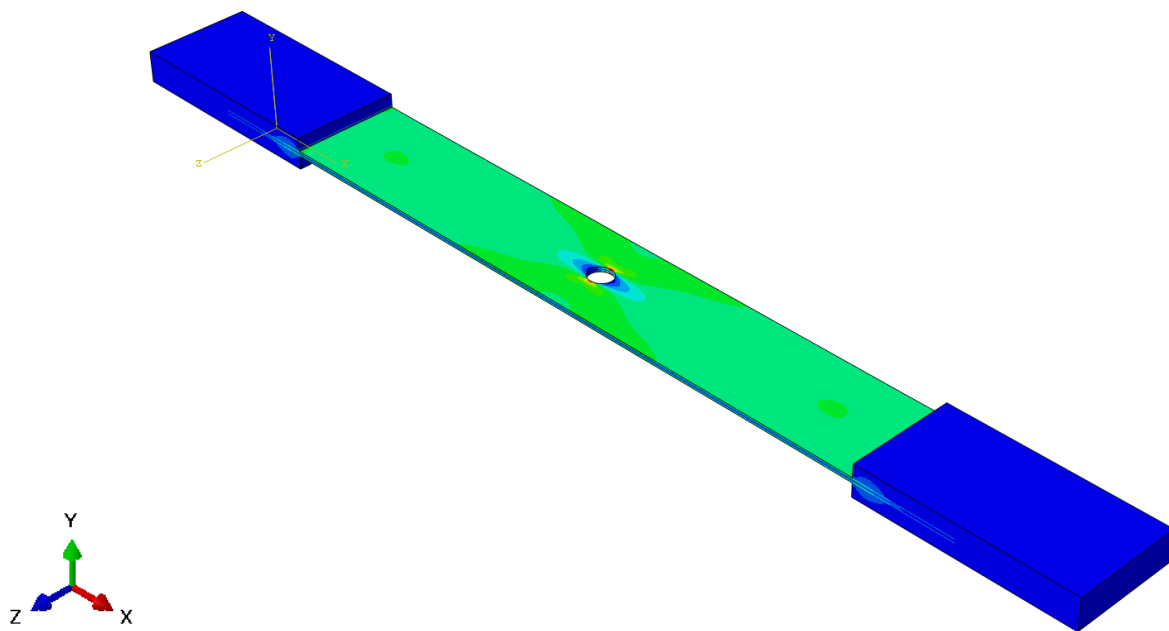
(a) Axial variation of stress near the hole



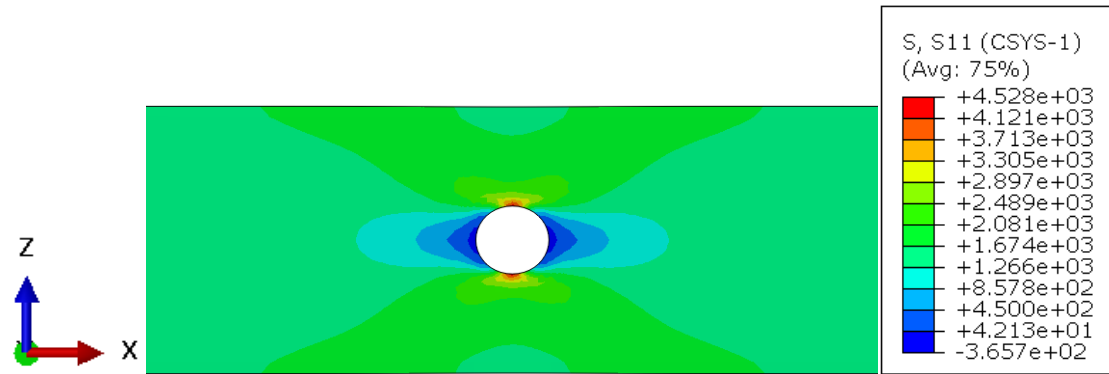
(b) Variation of stress through thickness near the hole

Figure 6.31: Variation of axial stress σ_{11} on the $[0_2 / \pm 45]_s$ laminate with a hole of diameter 5.715 mm

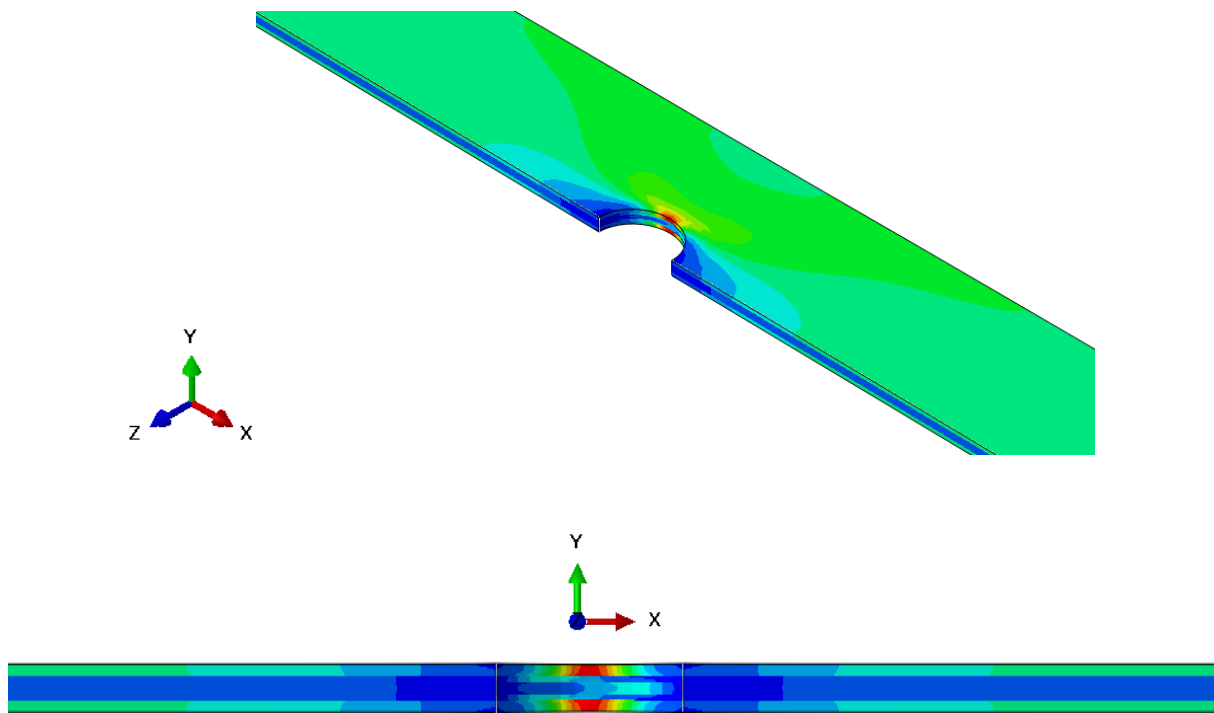
Figure 6.31 continued



(c) Variation of stress on the entire coupon



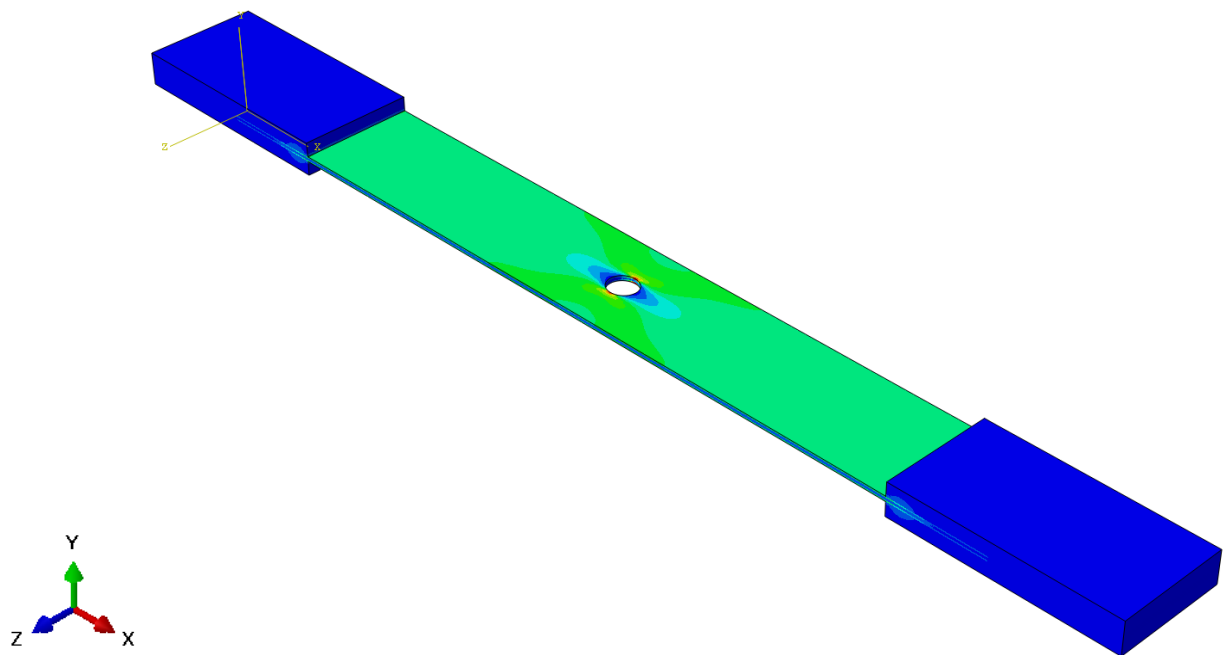
(a) Axial variation of stress near the hole



(b) Variation of stress through thickness near the hole

Figure 6.32: Variation of axial stress σ_{11} on the $[0_2 / \pm 45]_s$ laminate with a hole of diameter 6.604 mm

Figure 6.32 continued



(c) Variation of stress on the entire coupon

6.6.1.2 $[\pm 30]_{2s}$

Figures 33-35 show the variation of axial stresses on the $[\pm 30]_{2s}$ laminate. The gradient of tensile and compressive stresses has an angle with the axial direction and this is along the fiber direction 30° . The magnitude of these stresses also increases with the hole size. The stresses also have a butterfly profile around the hole. The variation of stress across thickness near the holes has an effect of free-edge also on it. This agrees with the results of CLPT.

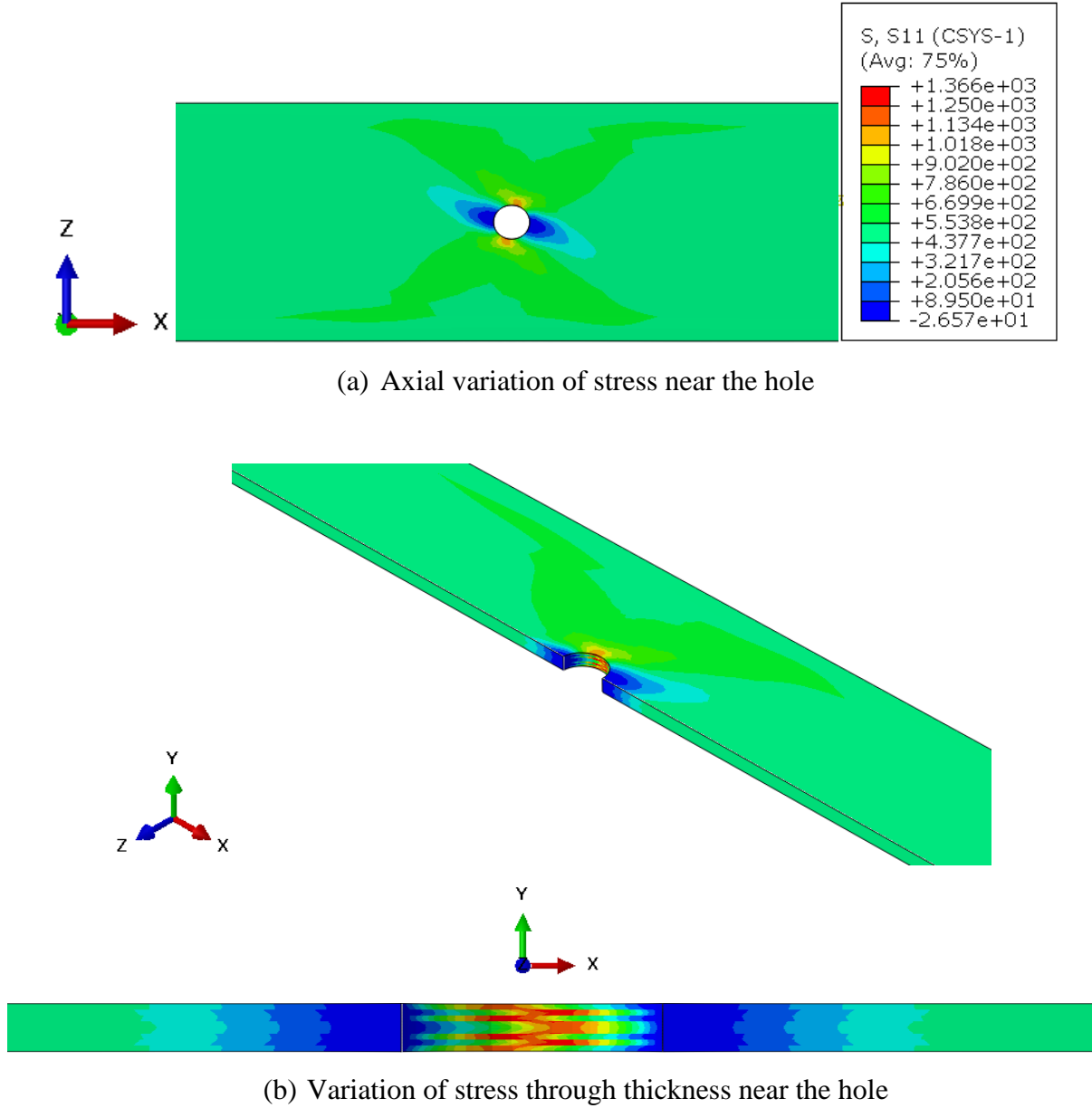
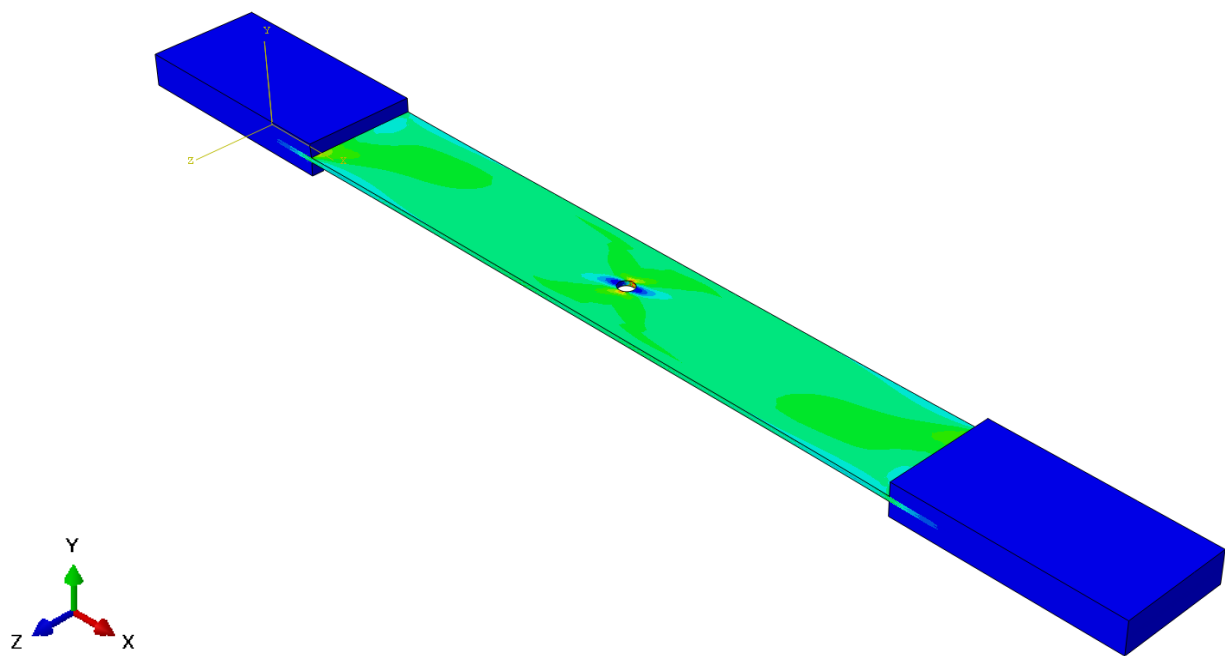
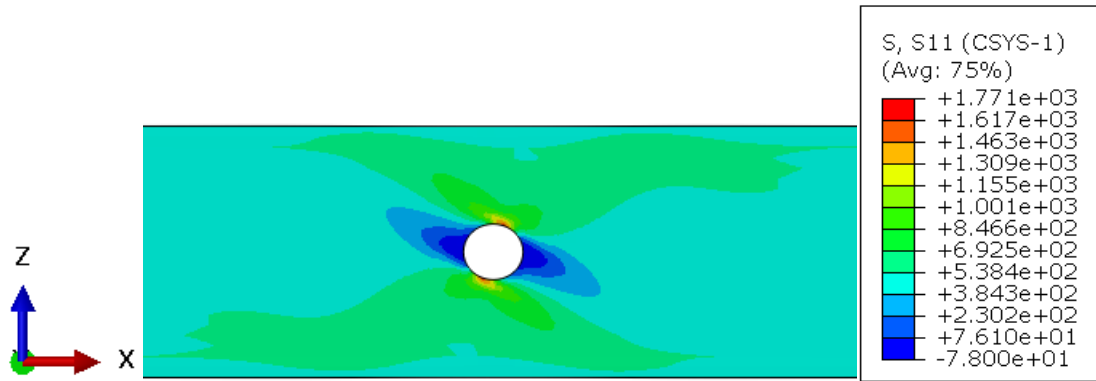


Figure 6.33: Variation of axial stress σ_{11} on the $[\pm 30]_{2s}$ laminate with a hole of diameter 3.683 mm

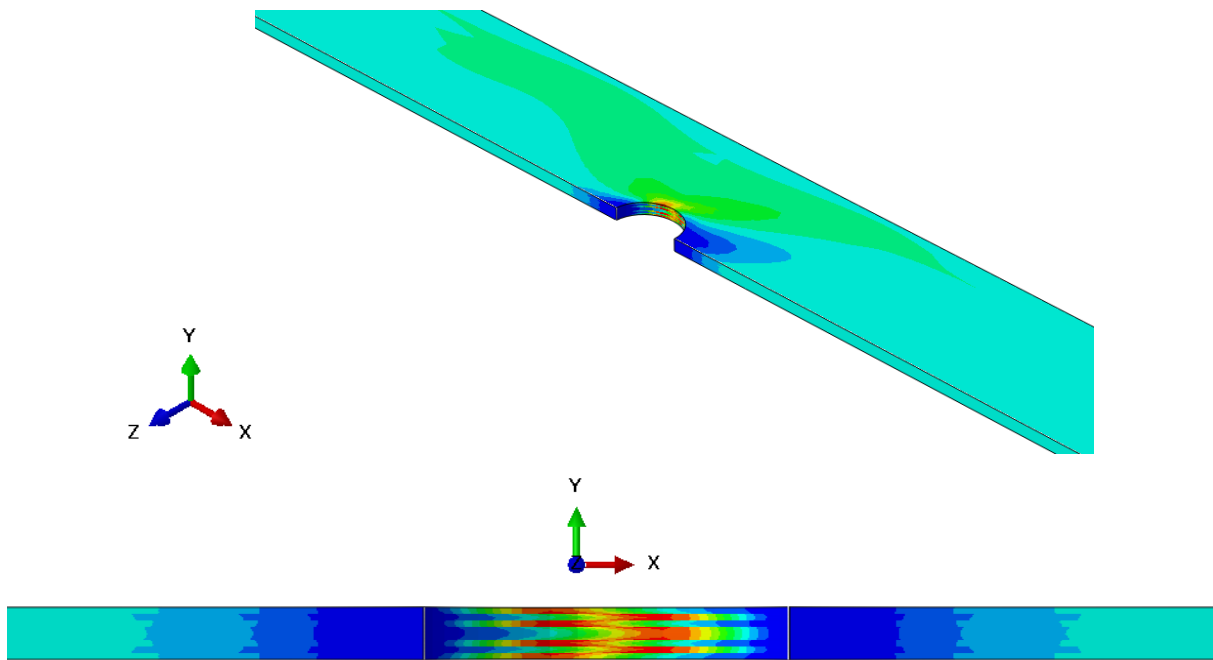
Figure 6.33 continued



(c) Variation of stress on the entire coupon



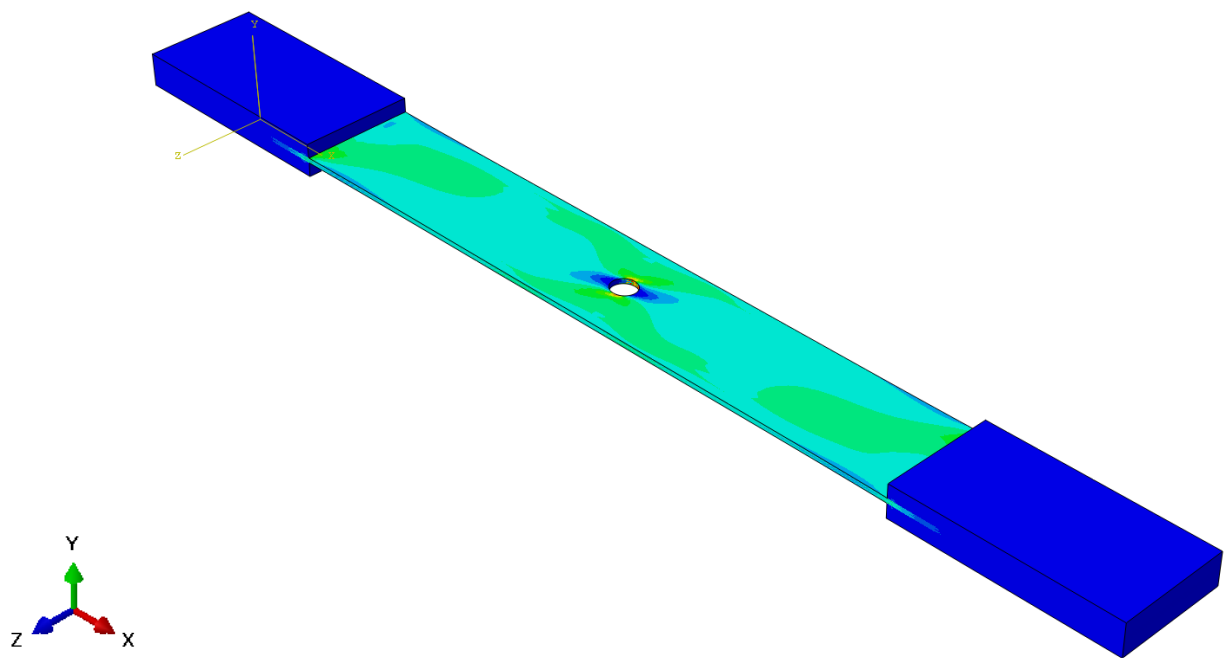
(a) Axial variation of stress near the hole



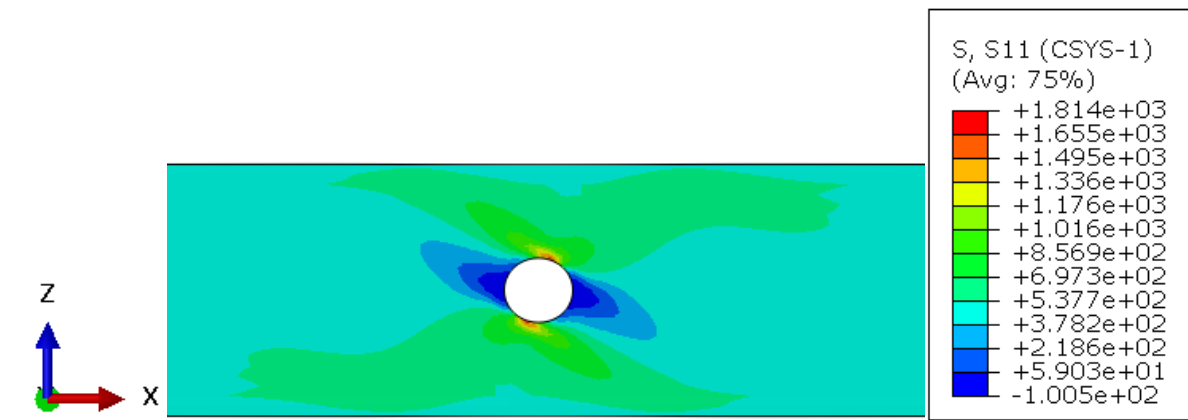
(b) Variation of stress through thickness near the hole

Figure 6.34: Variation of axial stress σ_{11} on the $[\pm 30]_{2s}$ laminate with a hole of diameter 5.715 mm

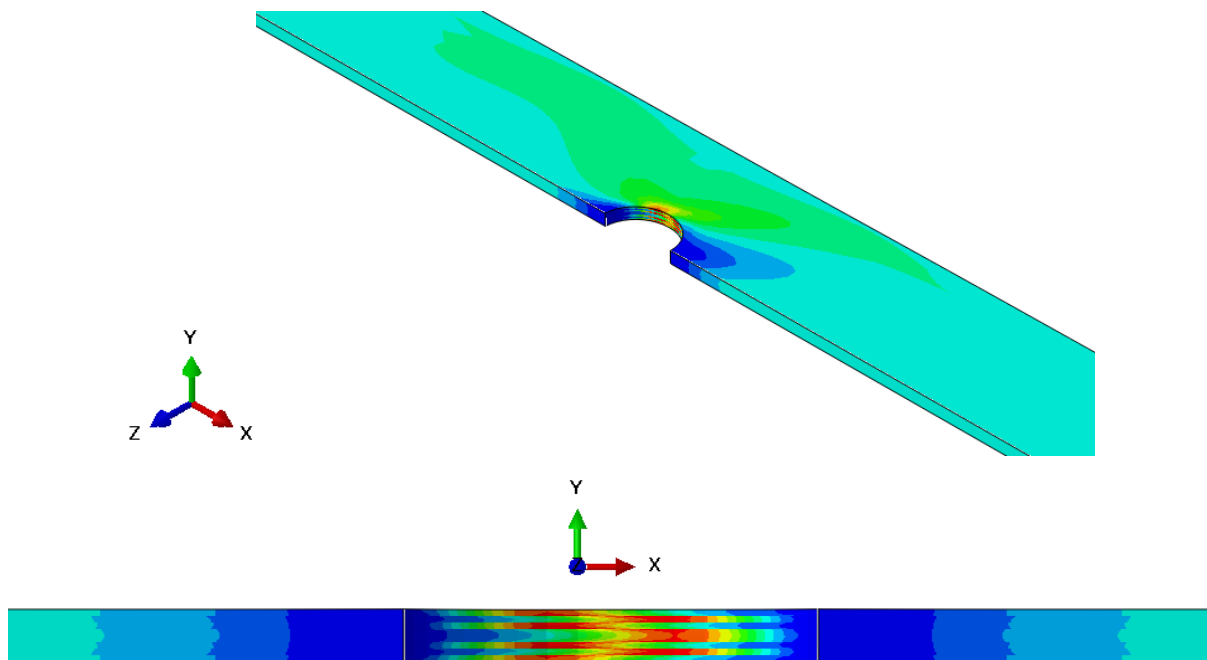
Figure 6.34 continued



(c) Variation of stress on the entire coupon



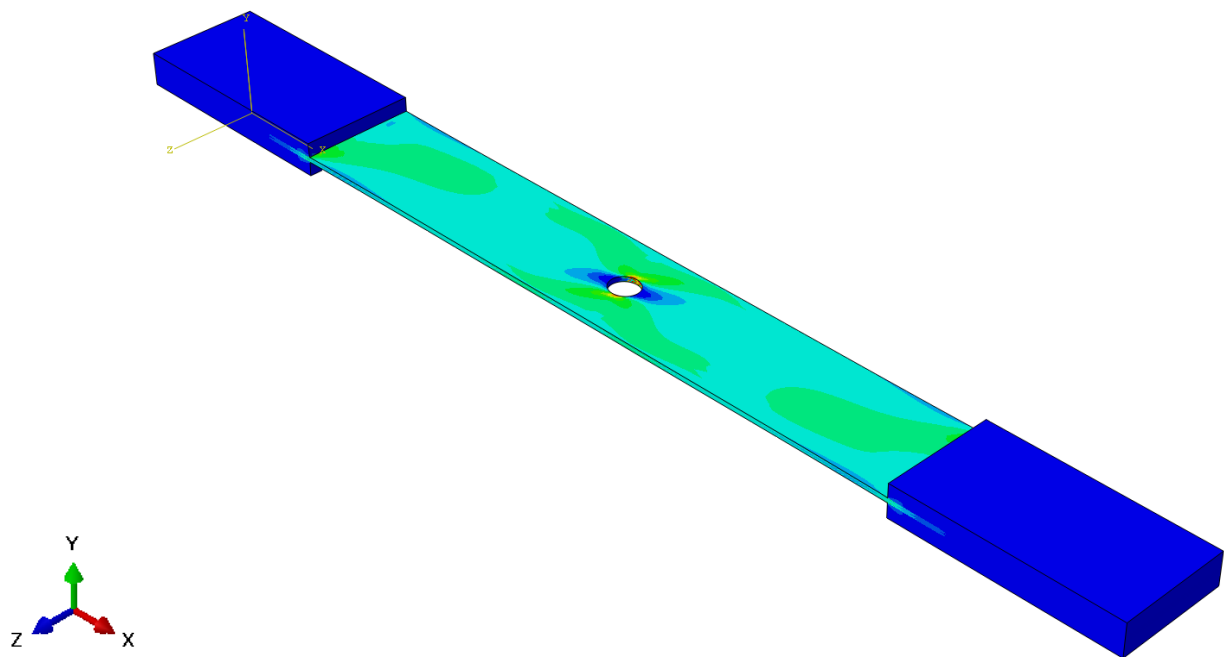
(a) Axial variation of stress near the hole



(b) Variation of stress through thickness near hole

Figure 6.35: Variation of axial stress σ_{11} on the $[\pm 30]_{2s}$ laminate with a hole of diameter 6.604 mm

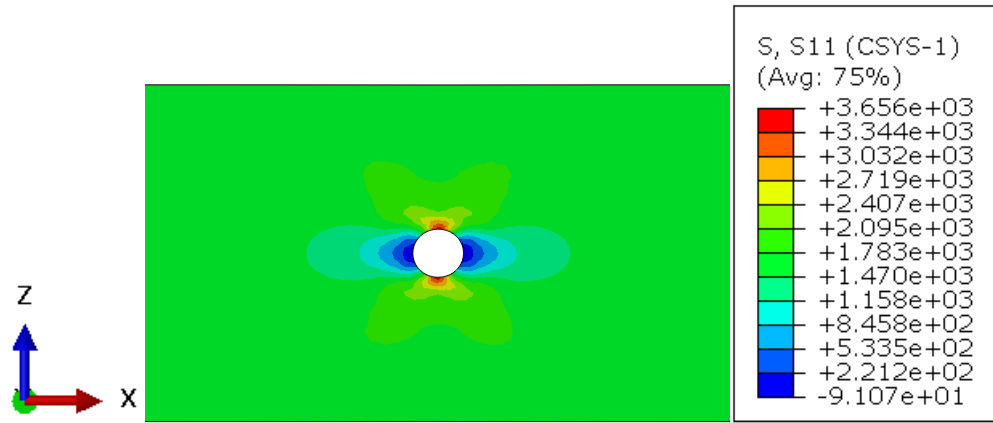
Figure 6.35 continued



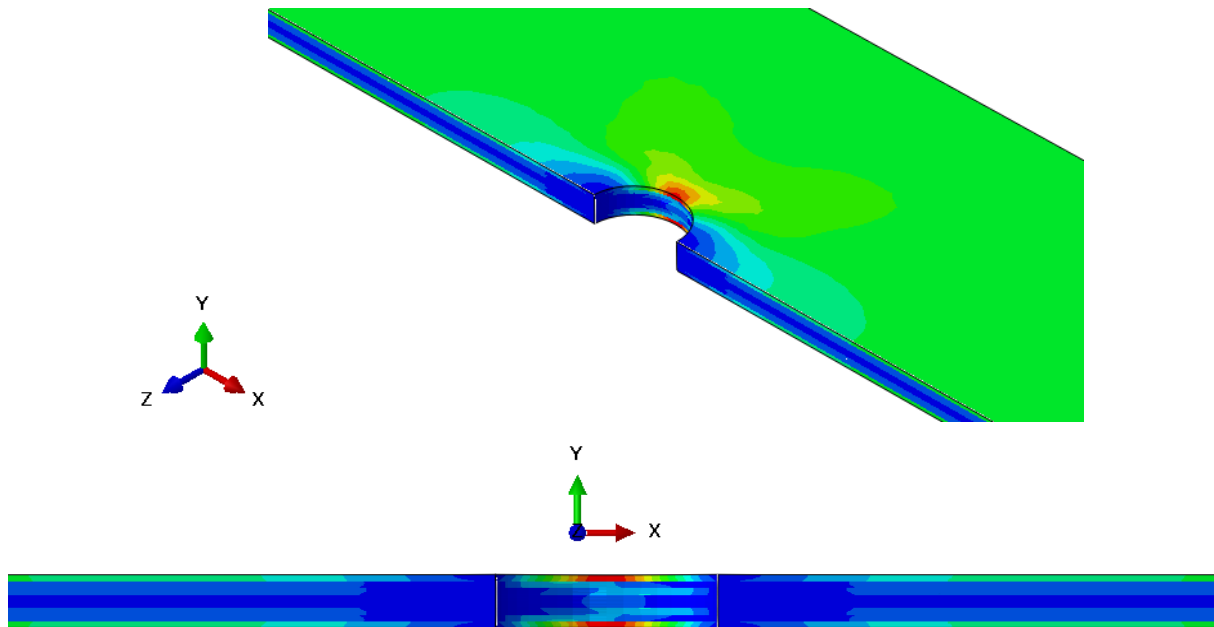
(c) Variation of stress on the entire coupon

6.6.2 $[0/\pm 45/90]_s$

Figure 36-38 shows the variation of stress on the $[0 / \pm 45 / 90]_s$ laminate. As in the previous laminates, there is tension longitudinally and compression transversely around the hole. The magnitude of these stresses increases with the hole size. The region around the hole also has free-edge effects and hence, there is a variation of these stresses across the thickness of the laminate. This variation is also in agreement with the results from CLPT as discussed in the previous chapter.



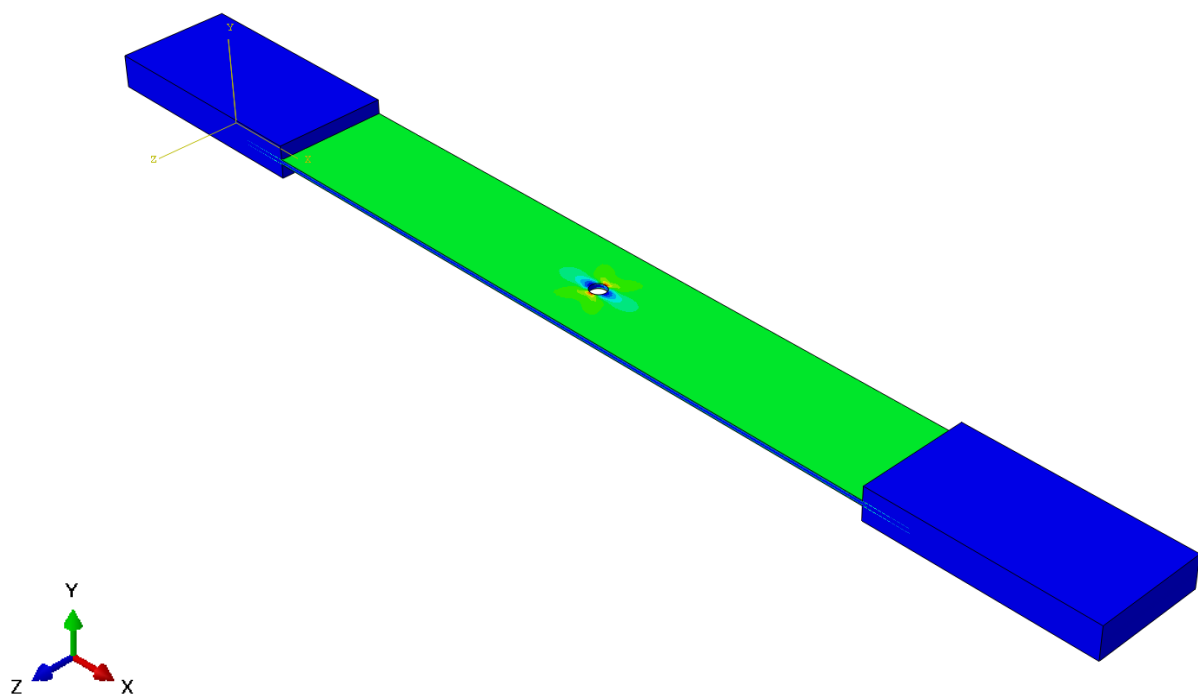
(a) Axial variation of stress near the hole



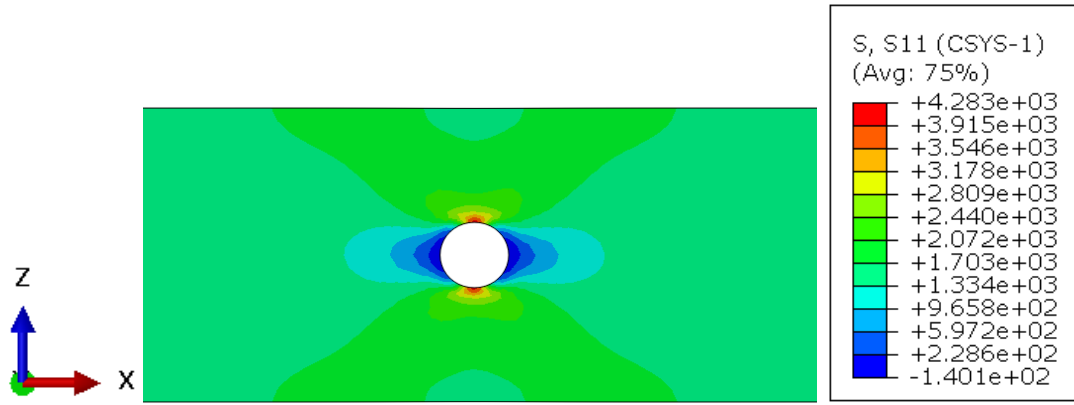
(b) Variation of stress through thickness near the hole

Figure 6.36: Variation of axial stress σ_{11} on the $[0 / \pm 45 / 90]_s$ laminate with a hole of diameter 3.683 mm

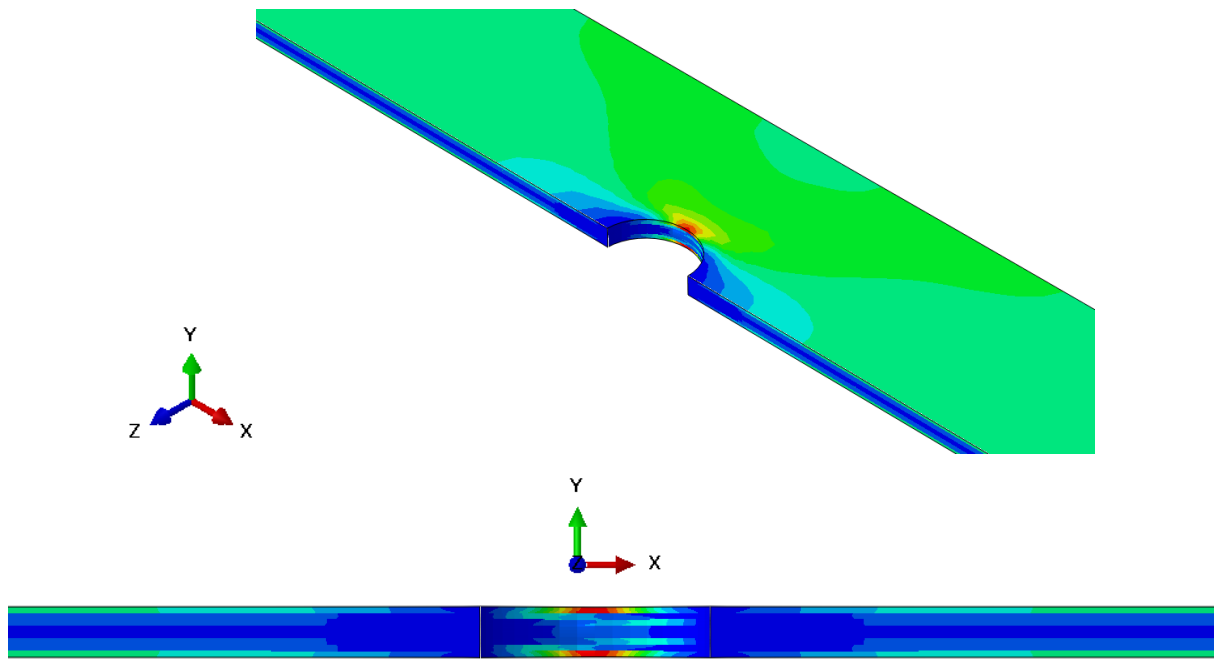
Figure 6.36 continued



(c) Variation of stress on the entire coupon



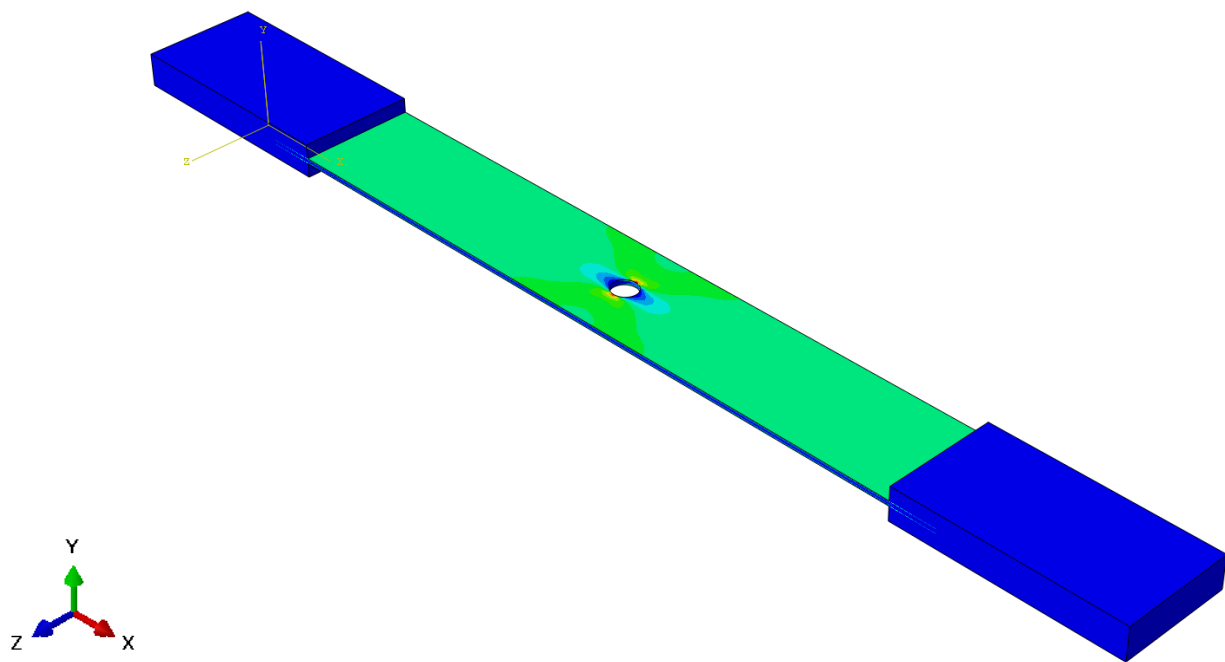
(a) Axial variation of stress near hole



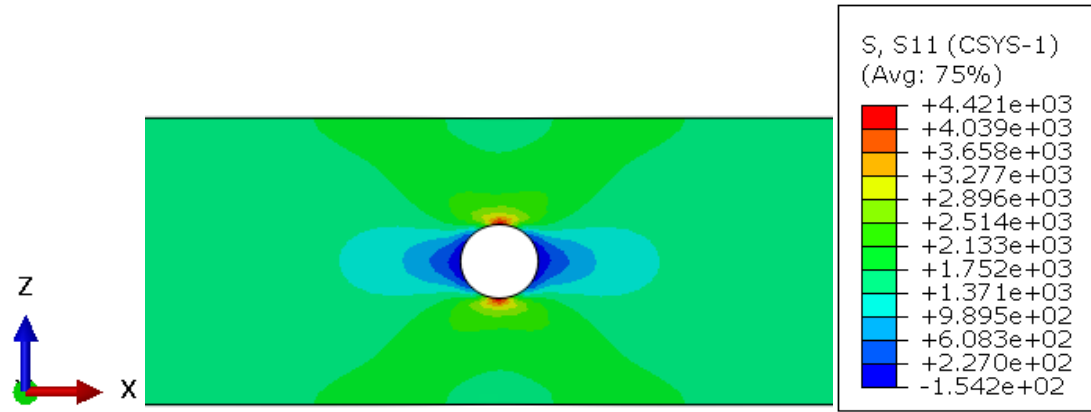
(b) Variation of stress through thickness near hole

Figure 6.37: Variation of axial stress σ_{11} on the $[0 / \pm 45 / 90]_s$ laminate with a hole of diameter 5.715 mm

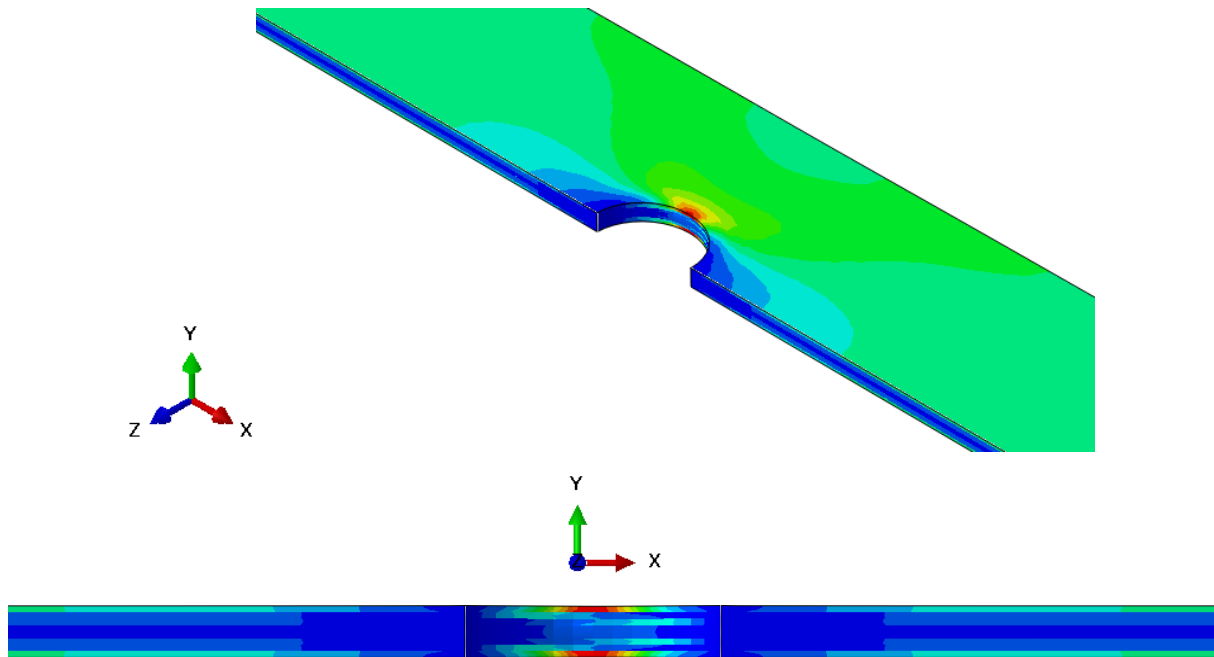
Figure 6.37 continued



(c) Variation of stress on the entire coupon



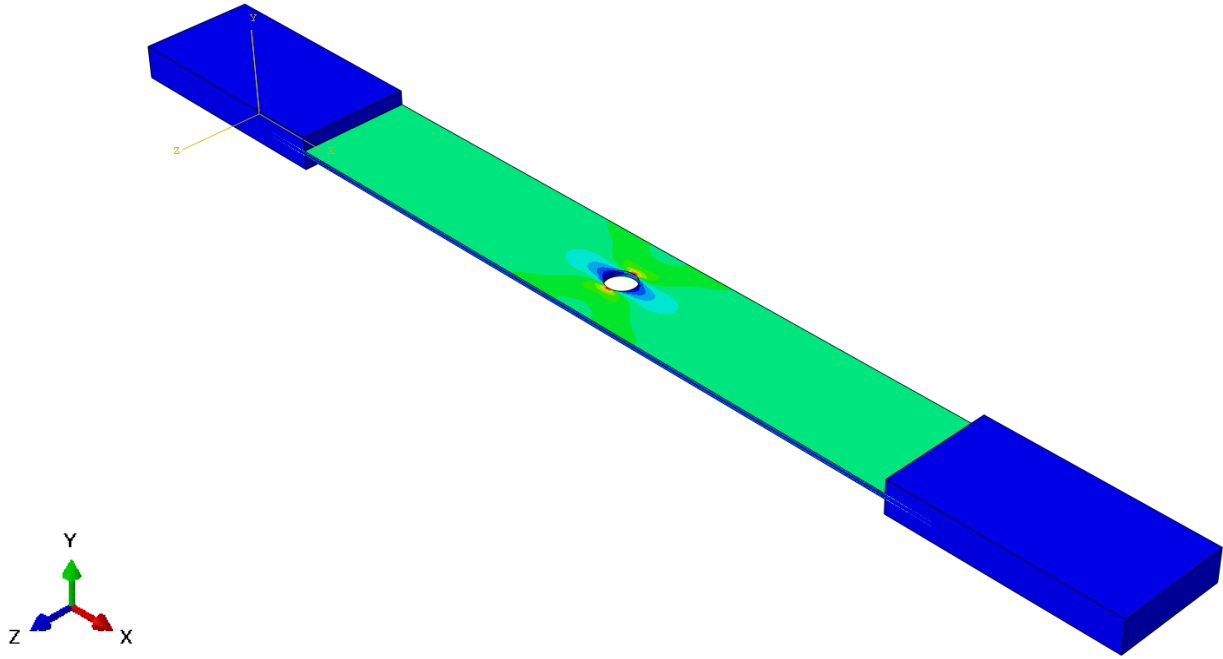
(a) Axial variation of stress near the hole



(b) Variation of stress through thickness near the hole

Figure 6.38: Variation of axial stress σ_{11} on the $[0 / \pm 45 / 90]_s$ laminate with a hole of diameter 6.604 mm

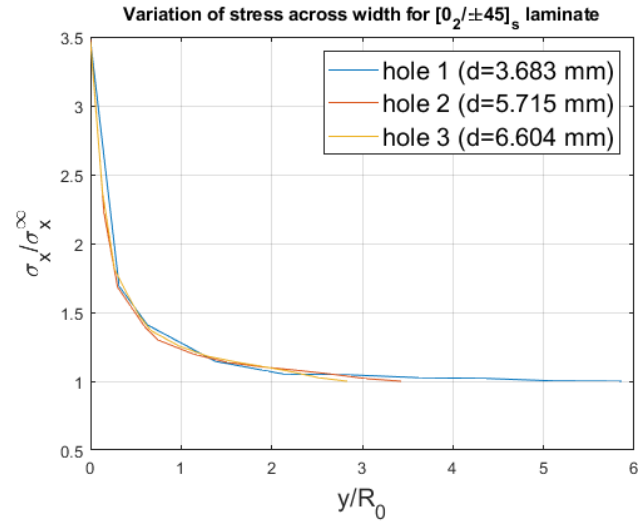
Figure 6.38 continued



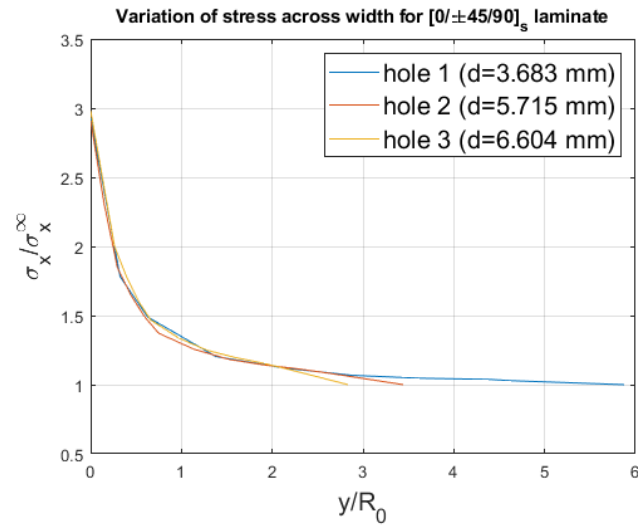
(c) Variation of stress on the entire coupon

6.6.3 Variation of stress across the width of the specimen from the hole

Figure 39 shows the variation of axial stress across the width of the laminates from the hole edge. It can be observed that the stress is maximum at the edge of the hole and the magnitude of the normalized stress increases with the increase in the hole size. The value converges to 1 at the edge of the laminate. The plots for $[0 / \pm 45 / 90]_s$ and $[0_2 / \pm 45]_s$ laminates are similar to each other, whereas, the maximum stress for the $[\pm 30]_{2s}$ laminate is more than these two laminates. The stress concentration factors were observed to be 3.49, 3 and 2.71 for the $[0_2 / \pm 45]_s$, $[0 / \pm 45 / 90]_s$ and $[\pm 30]_{2s}$ laminates and these values are the same as what is predicted from the analytical solution of the stress concentration factor which is independent of the hole size and is only dependent on the laminate material properties.



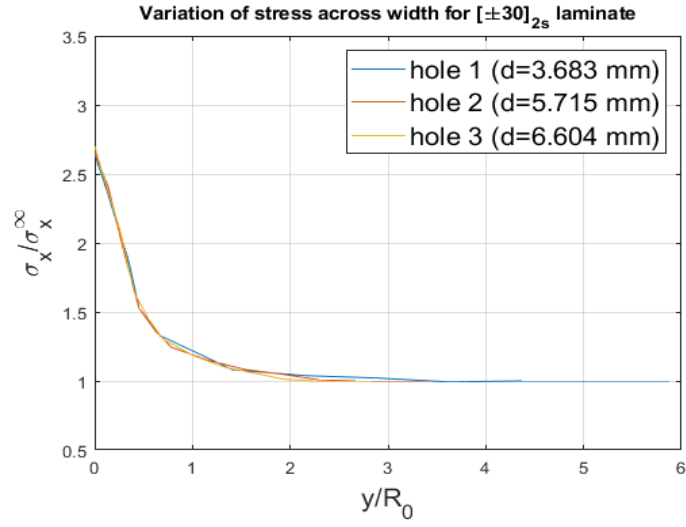
(a) $[0_2 / \pm 45]_s$



(b) $[0 / \pm 45 / 90]_s$

Figure 6.39: Normalized variation of axial stress σ_{11} across the width of the specimen with three different hole sizes

Figure 6.39 continued

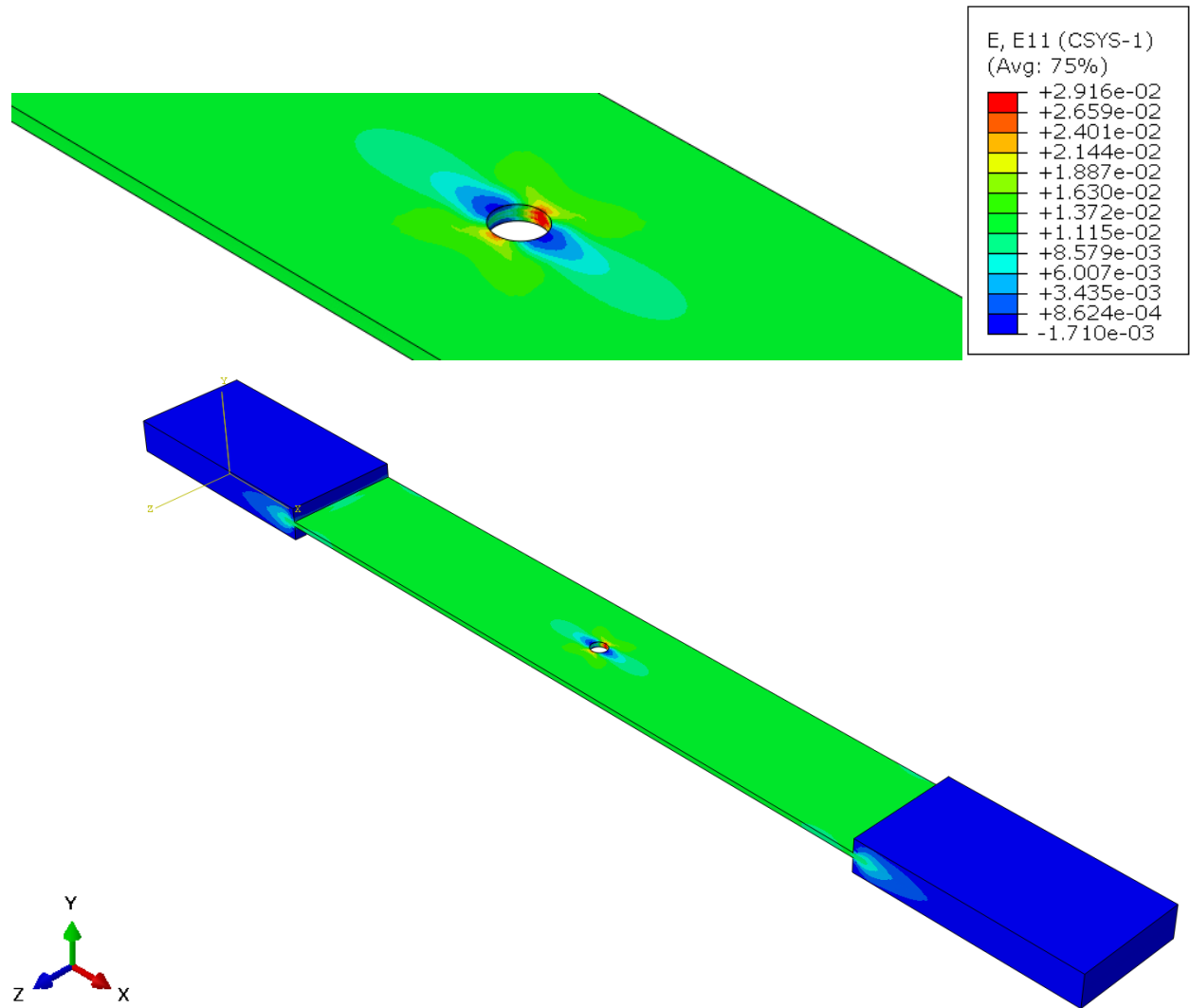


(c) $[\pm 30]_{2s}$

6.6.4 Strain distribution around the hole

6.6.4.1 $[0_2 / \pm 45]_s$

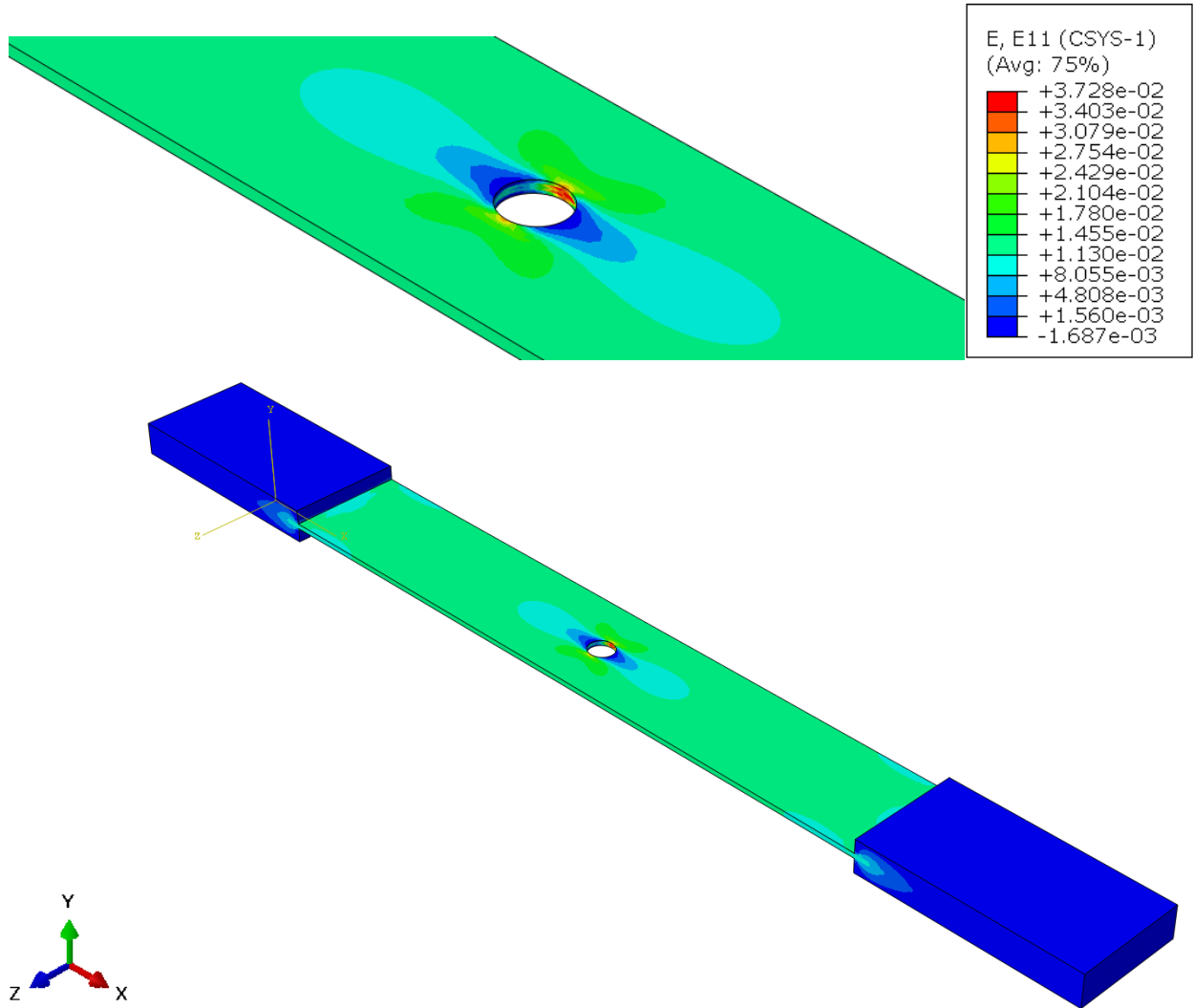
Figure 40 shows the variation of axial strain on the $[0_2 / \pm 45]_s$ laminate. The magnitude of maximum strain increases with the hole size and the variation is identical to the variation of axial stress on the laminate. The images also show the strain variation at the tabs in these specimens.



(a) Hole diameter = 3.683 mm

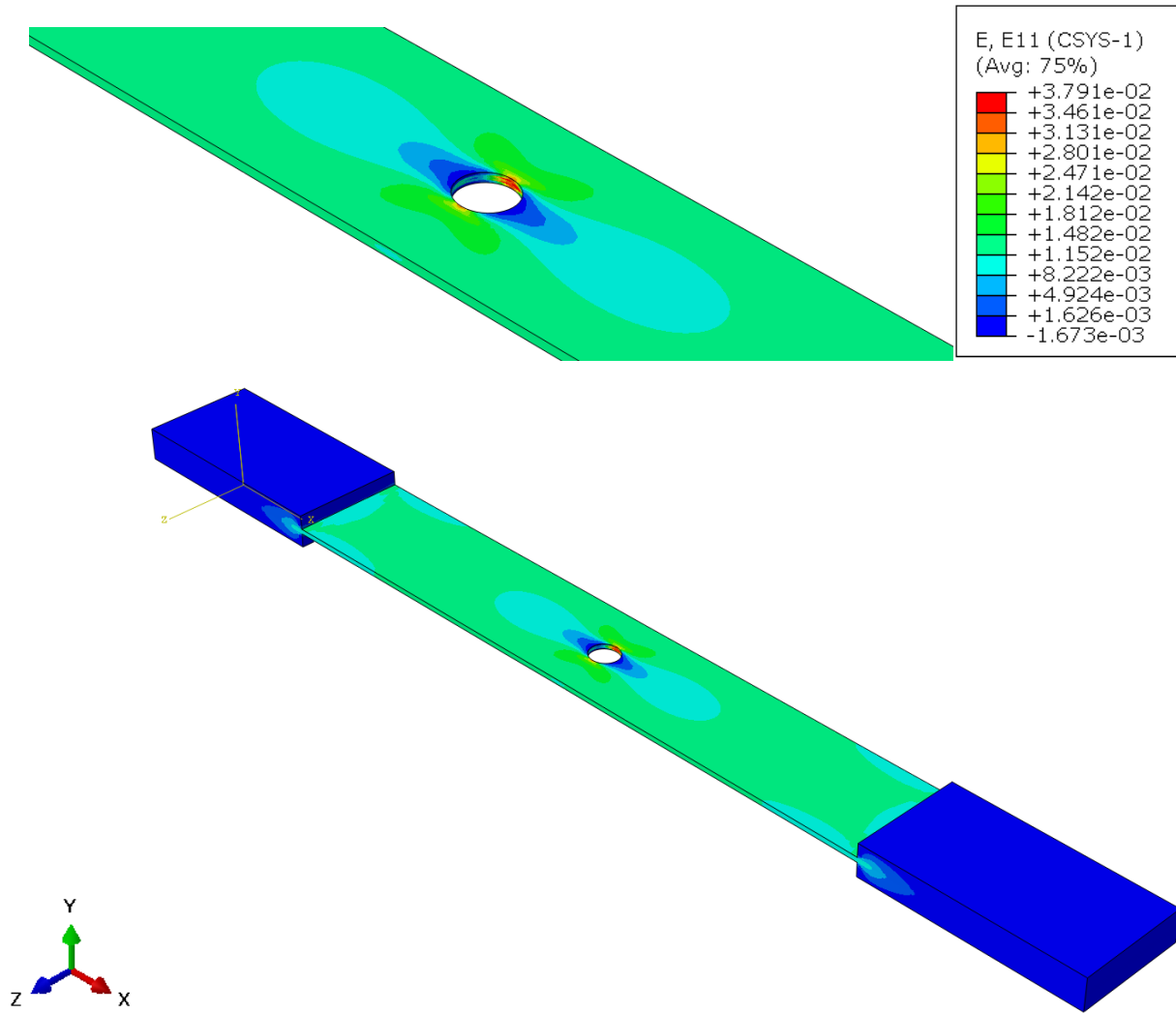
Figure 6.40: Variation of axial strain ε_{11} on the $[0_2 / \pm 45]_s$ laminate for three different hole sizes

Figure 6.40 continued



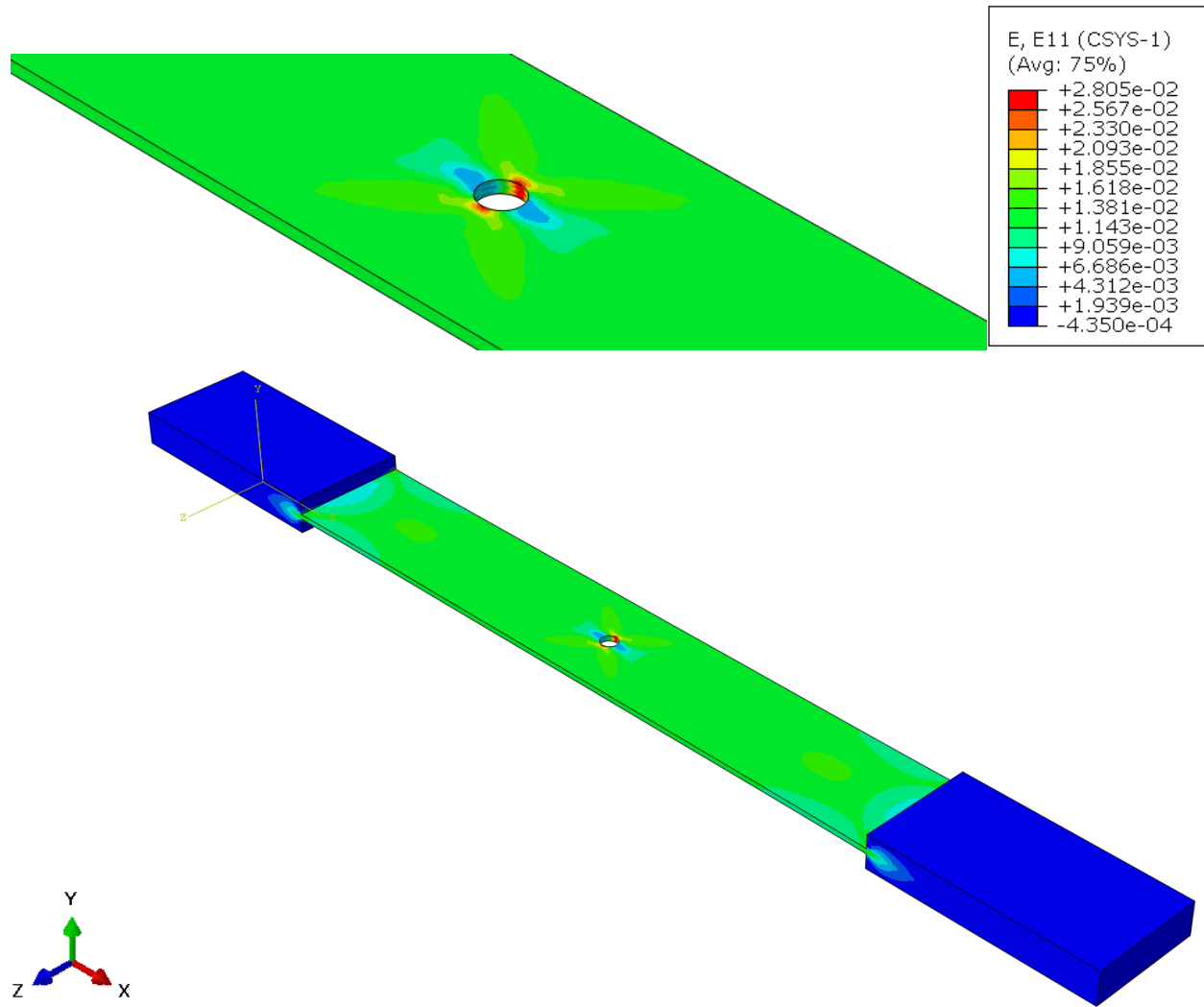
(b) Hole diameter = 5.715 mm

Figure 6.40 continued



6.6.4.2 $[\pm 30]_{2s}$

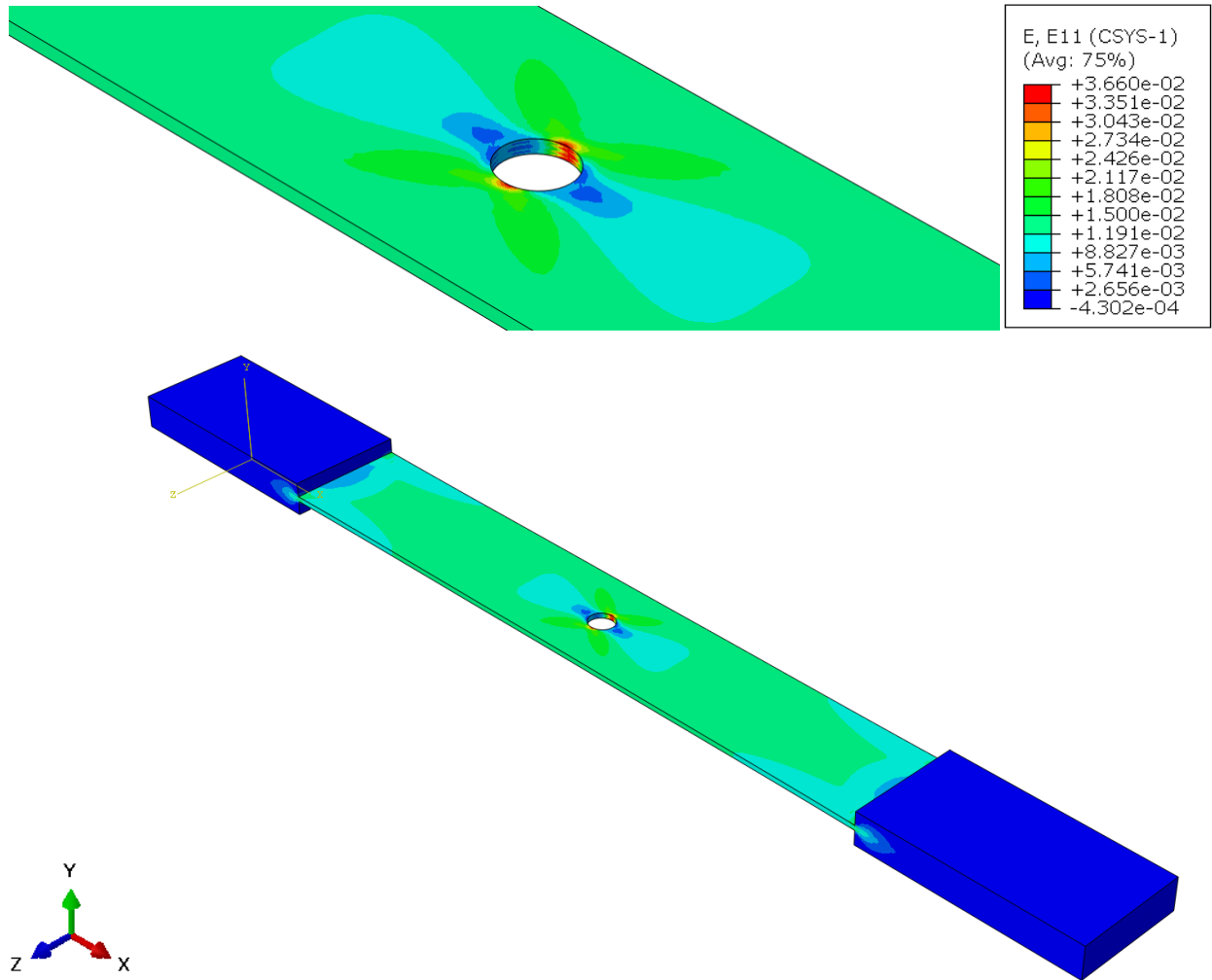
Figure 41 shows the variation of axial strain on the $[\pm 30]_{2s}$ laminate. The magnitude of maximum strain increases with the hole size and the variation is identical to the variation of axial stress on the laminate. The images also show the strain variation at the tabs in these specimens.



(a) Hole diameter = 3.683 mm

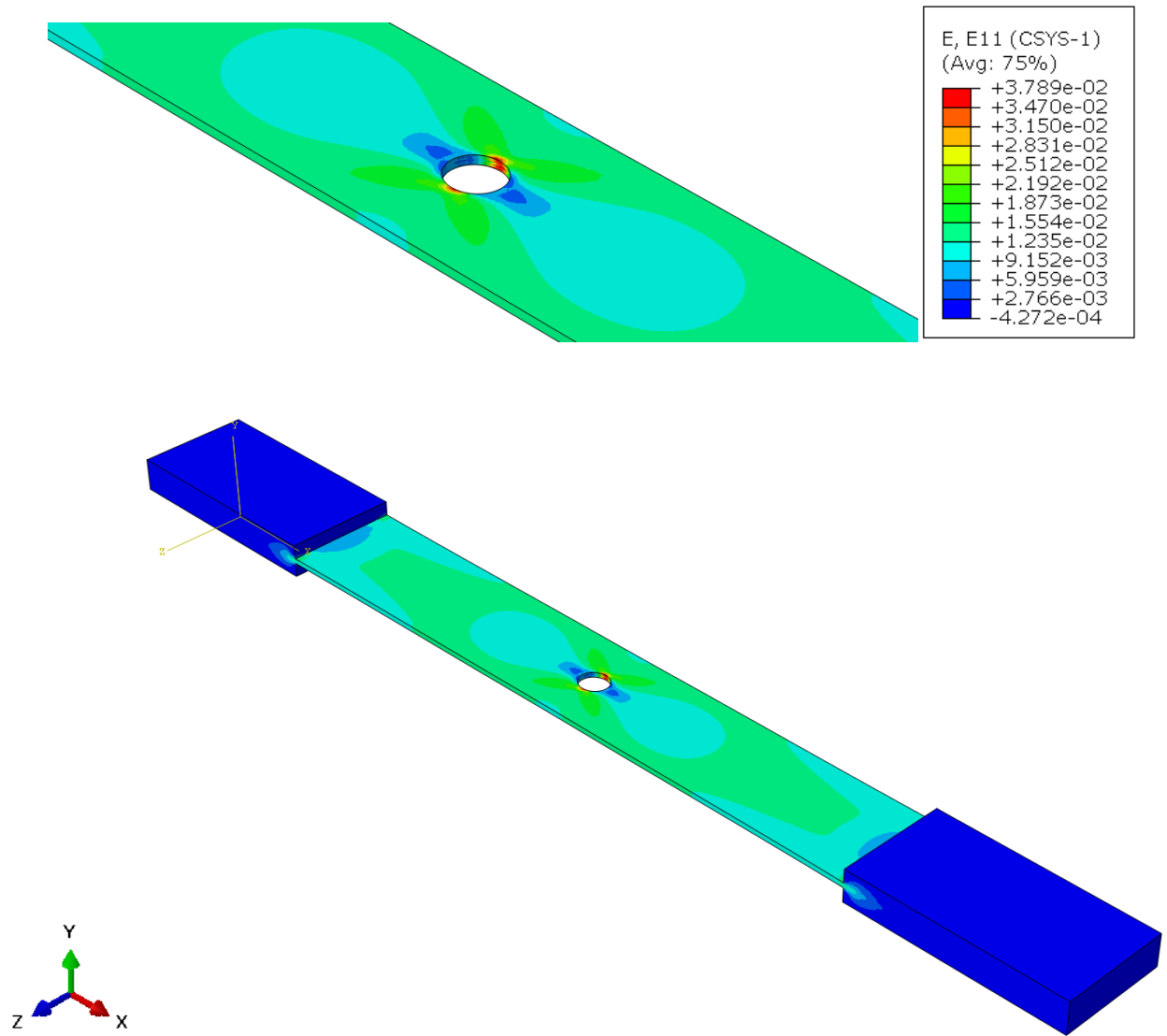
Figure 6.41: Variation of axial strain ϵ_{11} on the $[\pm 30]_{2s}$ laminate for three different hole sizes

Figure 6.41 continued



(b) Hole diameter = 5.715 mm

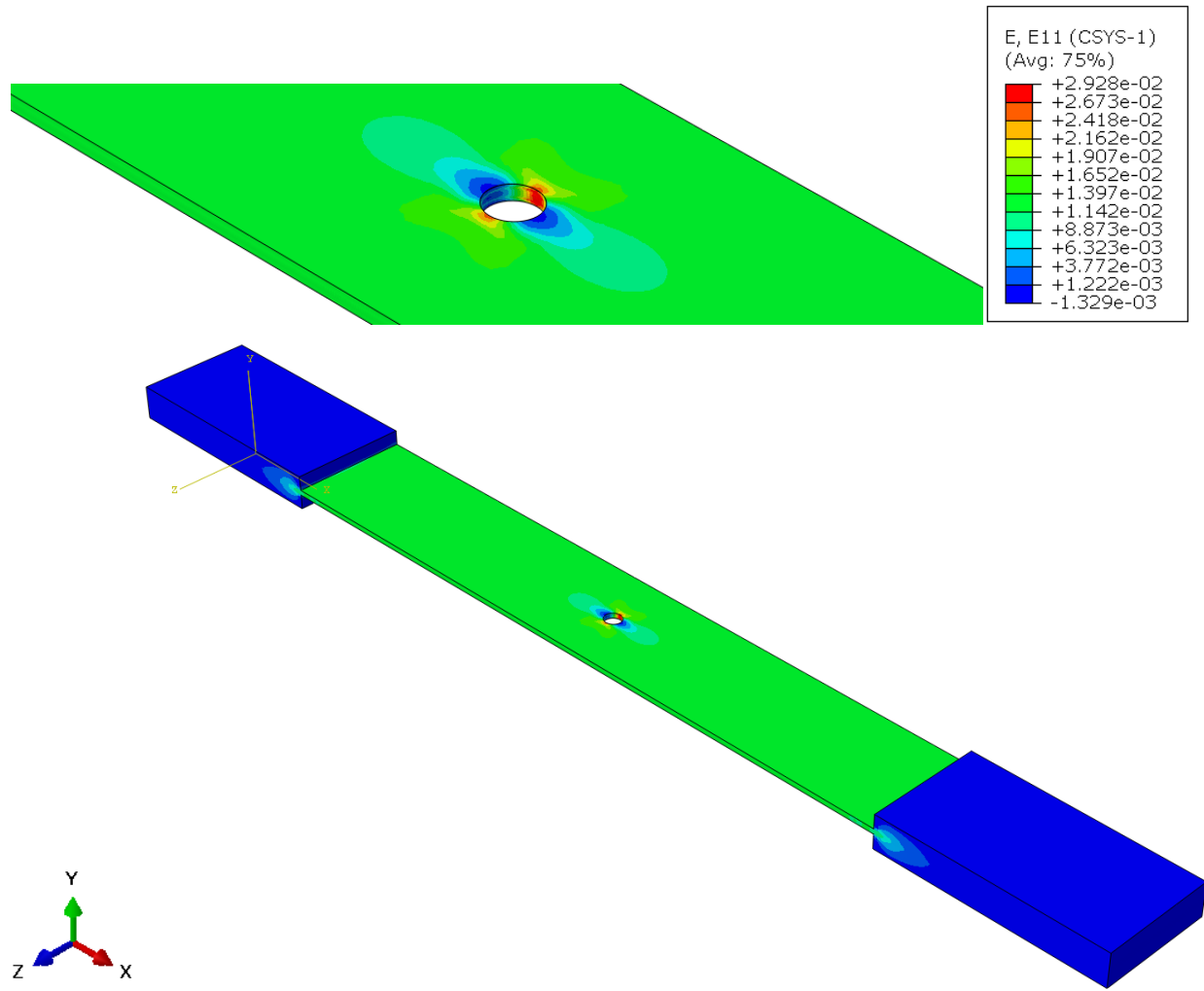
Figure 6.41 continued



(c) Hole diameter = 6.604 mm

6.6.5 $[0/\pm 45/90]_s$

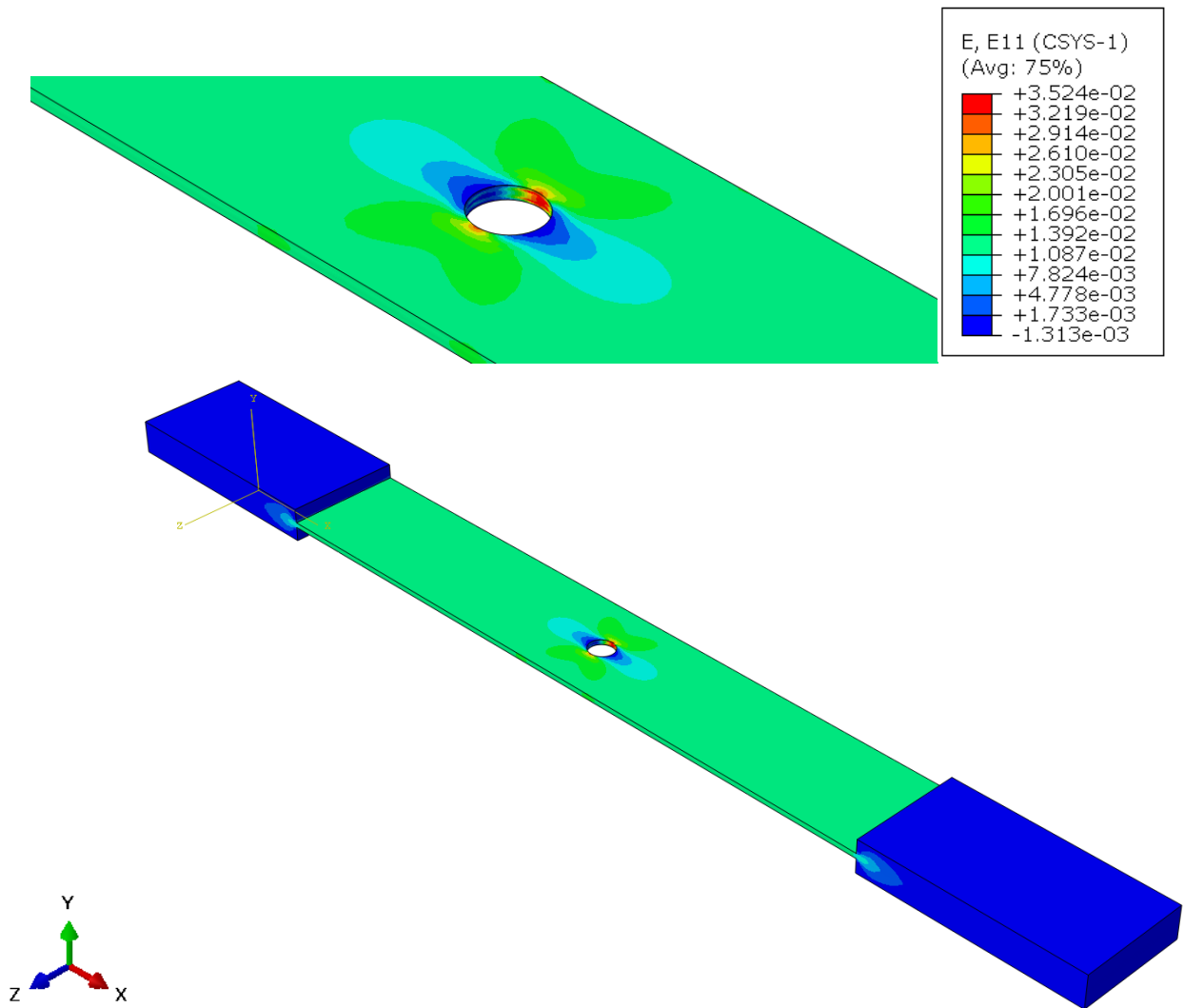
Figure 42 shows the variation of axial strain on the $[0 / \pm 45 / 90]_s$ laminate. The magnitude of maximum strain increases with the hole size and the variation is identical to the variation of axial stress on the laminate. The images also show the strain variation at the tabs in these specimens.



(a) Hole diameter = 3.683 mm

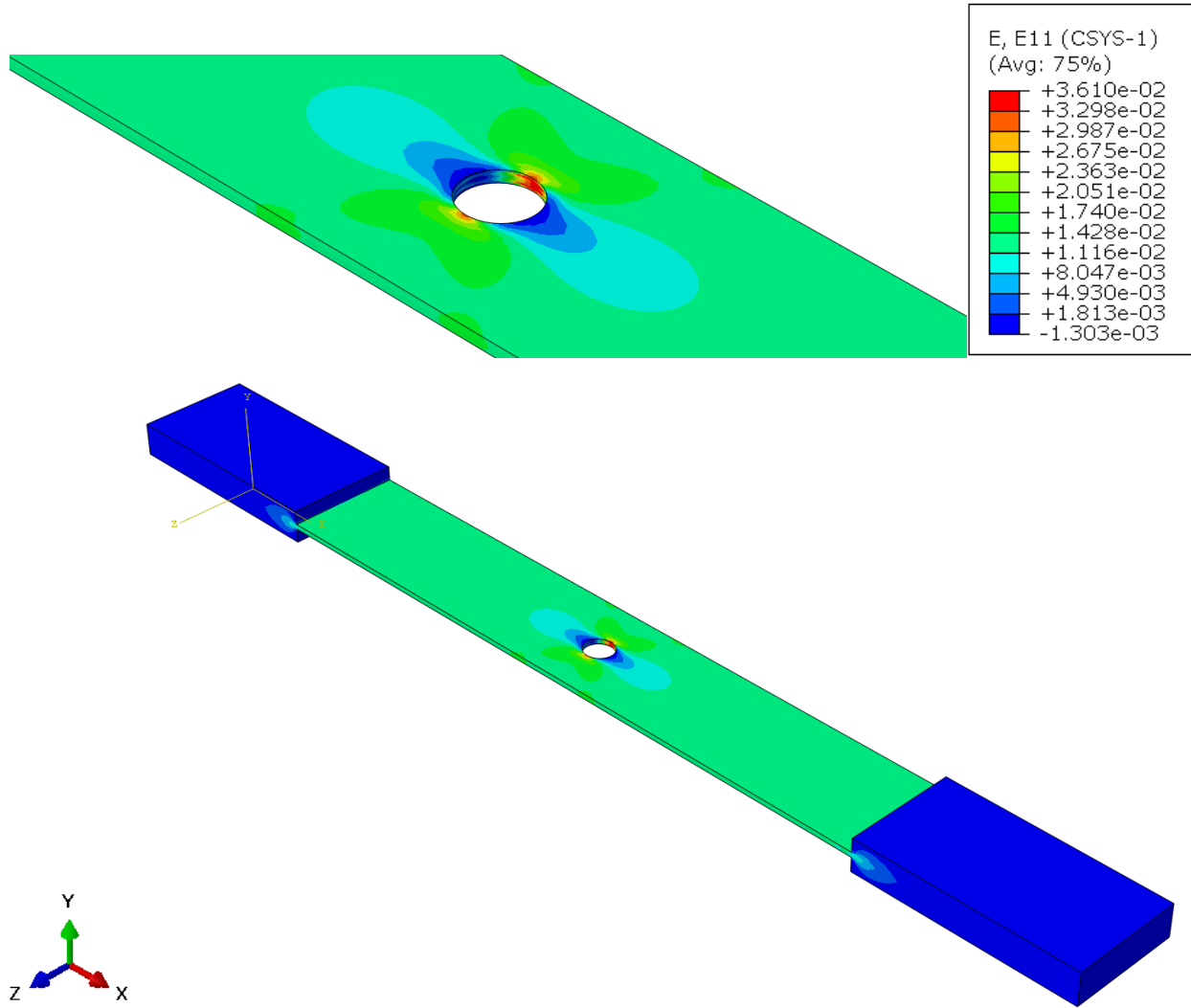
Figure 6.42: Variation of axial strain ϵ_{11} on the $[0 / \pm 45 / 90]_s$ laminate for three different hole sizes

Figure 6.42 continued



(b) Hole diameter = 5.715 mm

Figure 6.42 continued



(c) Hole diameter = 6.604 mm

6.7 Analysis of simulation results for $[\pm 30]_{2s}$ CTE test

The results are obtained for two different cooling cycles which go down up to -100°C & -180°C and the heating cycle runs up to 180°C . There are two different cooling cycles to validate the experimental results and to compare the heating and cooling cycles to the same magnitude of temperatures in the positive and negative scales. For the $[\pm 30]_{2s}$ laminate, α_x is negative ($-4.5 \mu\text{E}/^\circ\text{C}$), α_y is ($24.1 \mu\text{E}/^\circ\text{C}$). Hence, the deformation of it along the Y-axis is much greater than its deformation along X-axis and the laminate shrinks in the X-direction when heated accounting for the negative value of CTE.

6.7.1 Deformation along X-axis

Figure 43 shows the deformation along X-axis on the $[\pm 30]_{2s}$ laminate with two different hole sizes of diameter 3.683 mm & 6.604 mm . The laminate expands more along X-axis in the cooling cycles and shrinks along X-axis in the heating cycle. This accounts for the negative CTE of the laminate in the X-direction. As the temperature is reduced from -100°C to -180°C , the deformation along with the X-axis increases. The range of the variation of deformation is the same for both the hole sizes for a given cycle.

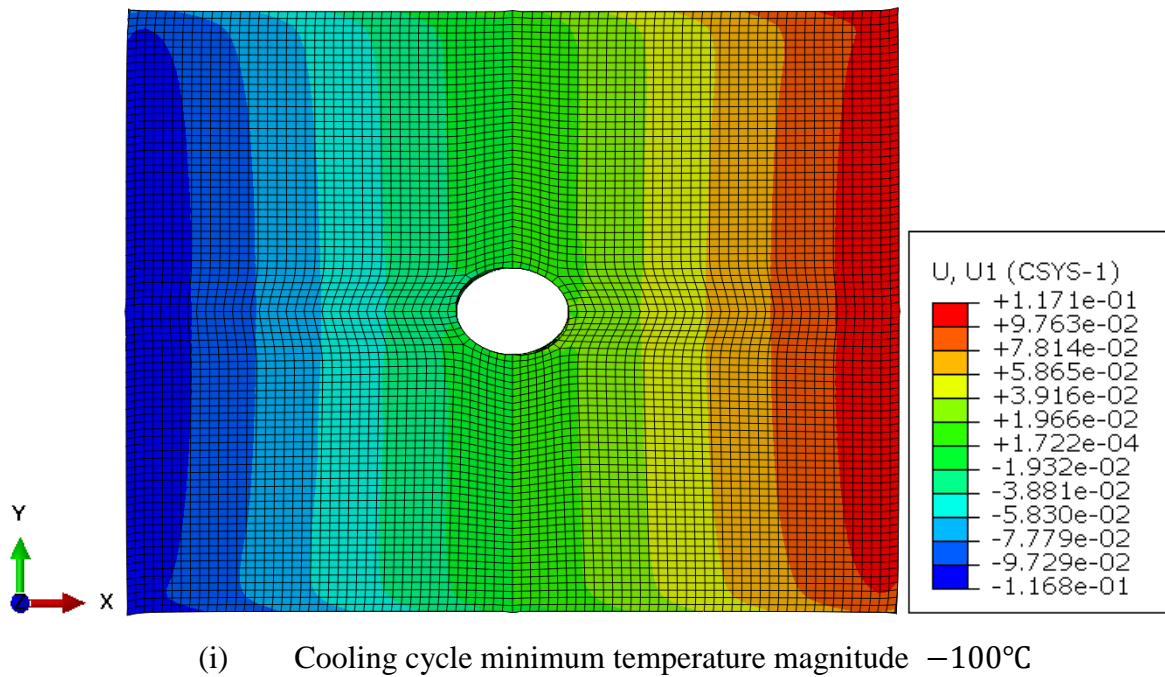
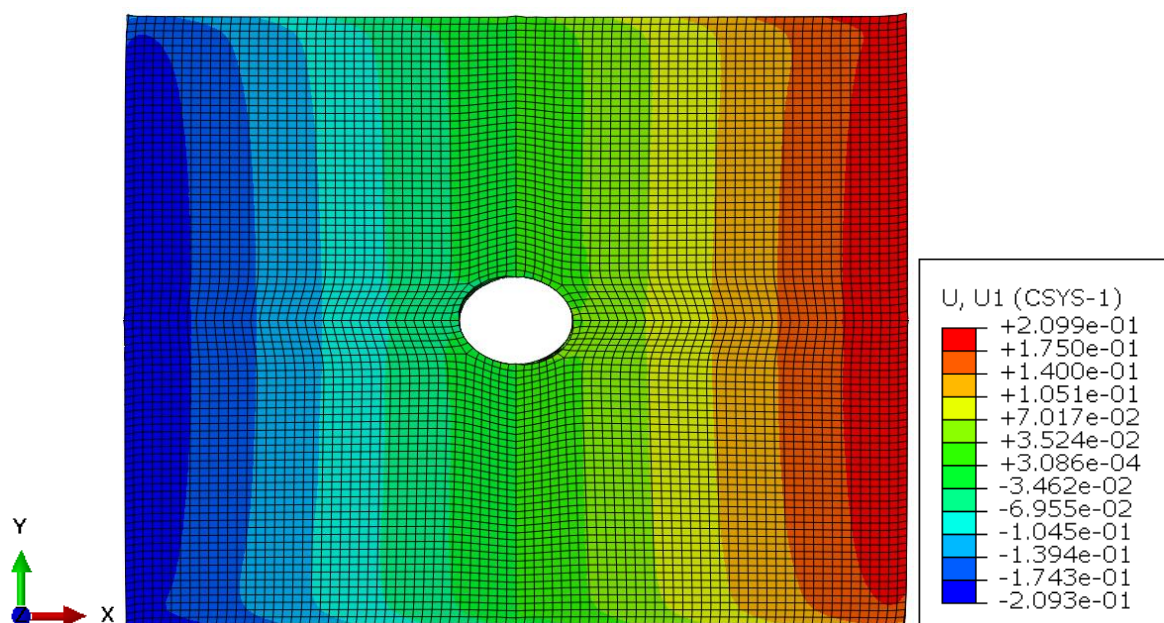
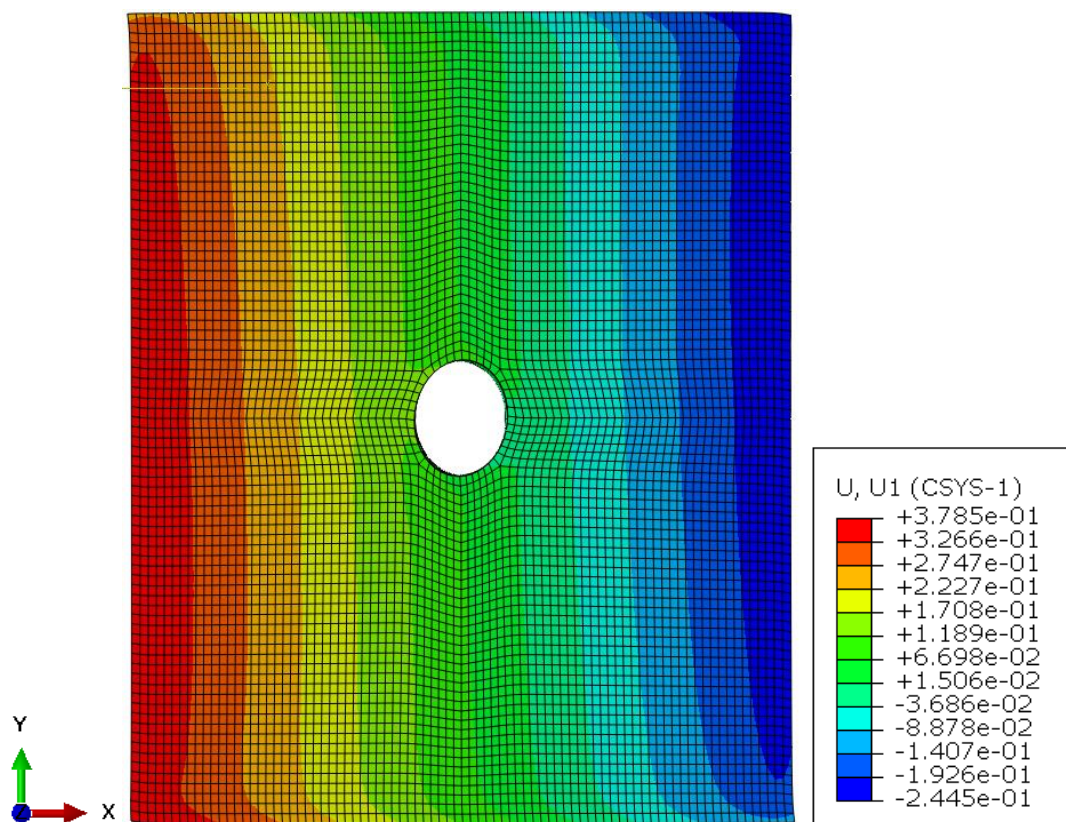


Figure 6.43: Deformation along X-axis U_1 due to temperature change on the $[\pm 30]_{2s}$ laminate for two different hole sizes

Figure 6.43 continued



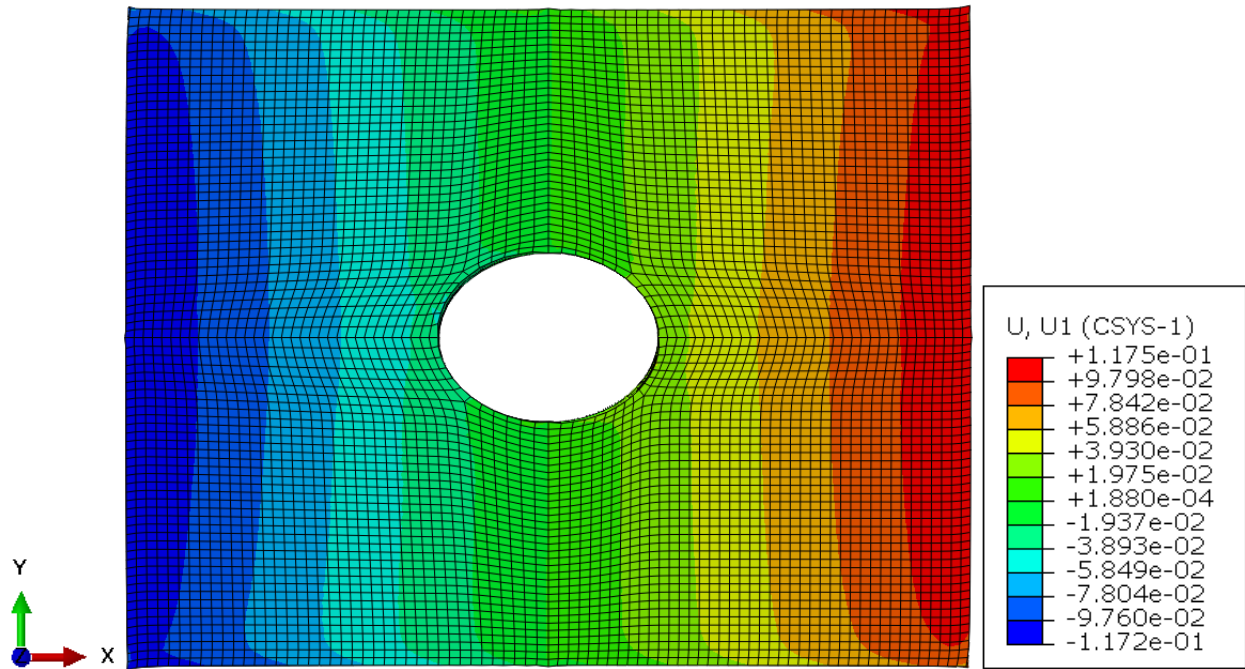
(ii) Cooling cycle minimum temperature magnitude -180°C



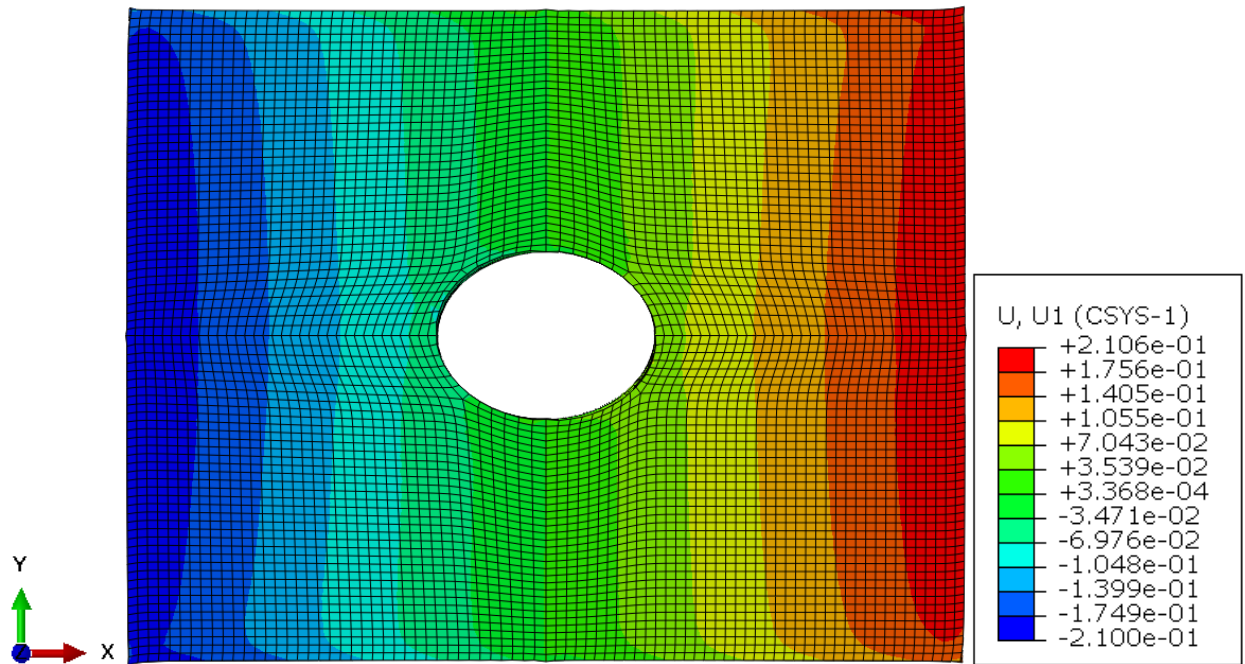
(iii) Heating cycle maximum temperature 180°C

(a) Hole diameter = 3.683 mm

Figure 6.43 continued

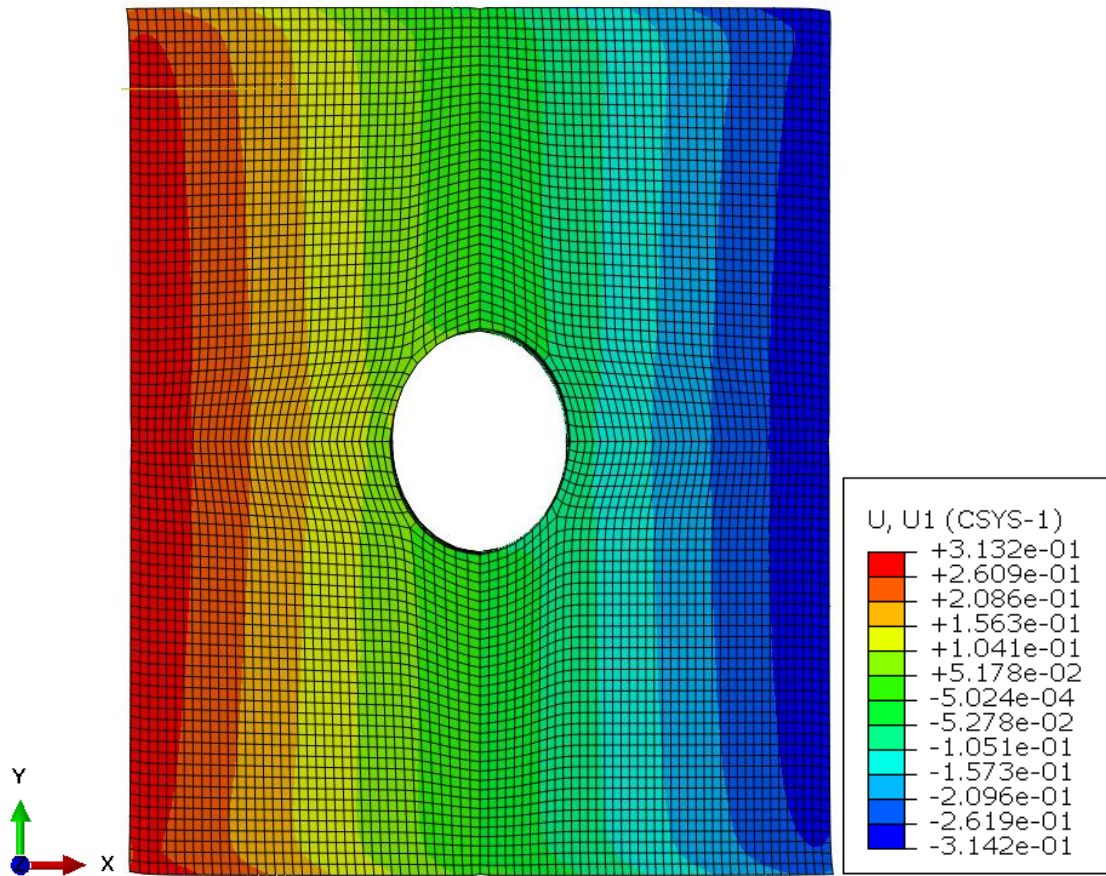


(i) Cooling cycle minimum temperature magnitude -100°C



(ii) Cooling cycle minimum temperature magnitude -180°C

Figure 6.43 continued

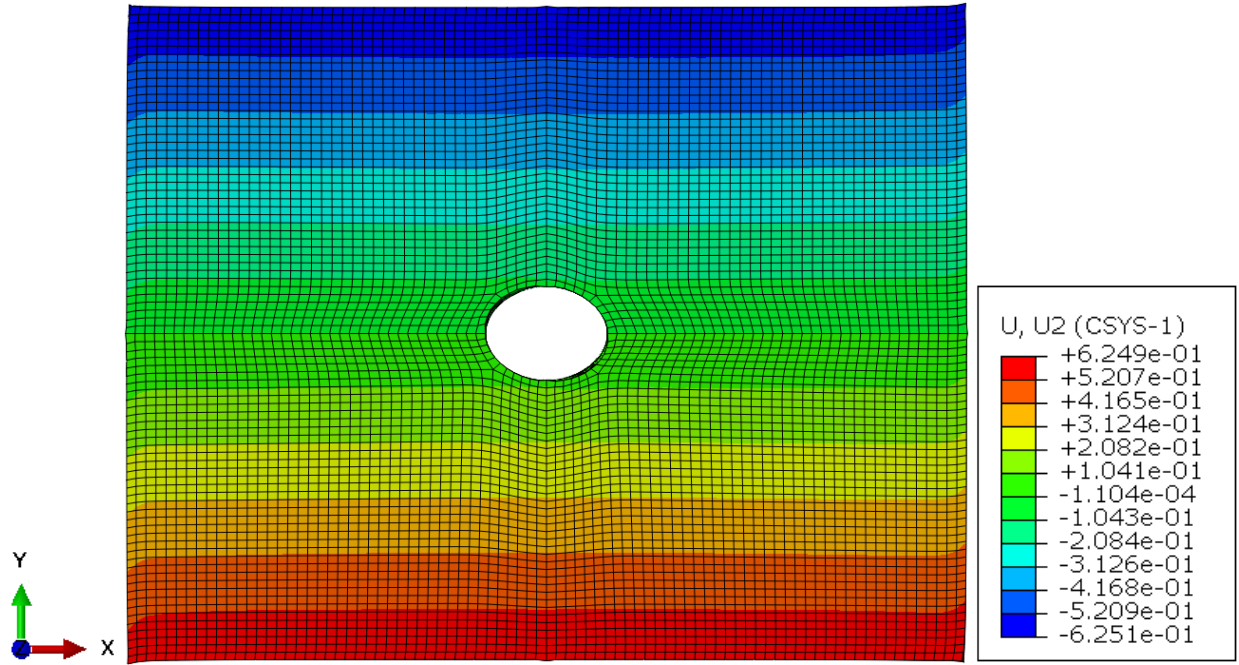


(iii) Heating cycle maximum temperature 180°C

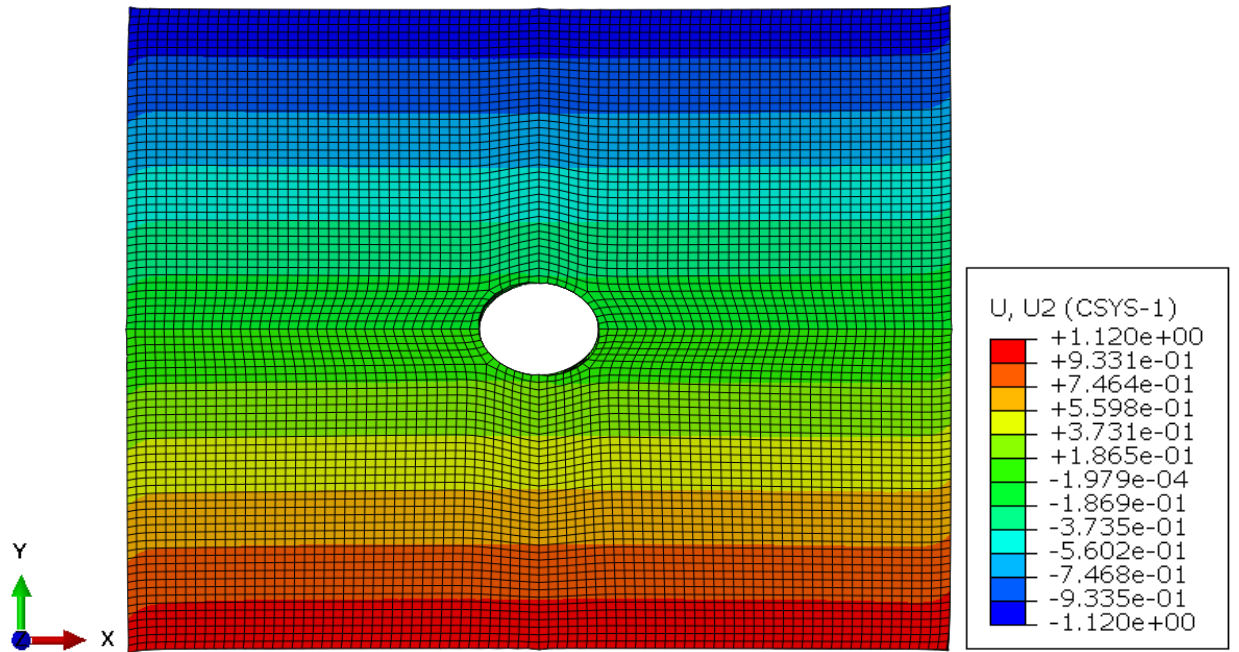
(b) Hole diameter = 6.604 mm

6.7.2 Deformation along Y-axis

Figure 44 shows the deformation along Y-axis on the $[\pm 30]_{2s}$ laminate with two different hole sizes of diameter 3.683 mm & 6.604 mm. The laminate expands more along Y-axis in the heating cycle and shrinks along Y-axis in the cooling cycles. This accounts for the positive CTE of the laminate in the Y-direction. As the temperature is reduced from -100°C to -180°C , the deformation along with the Y-axis increases. The range of the variation of deformation is the same for both the hole sizes for a given cycle. This is much more than the deformation in the X-direction as the CTE in Y-direction is much higher than in X-direction.



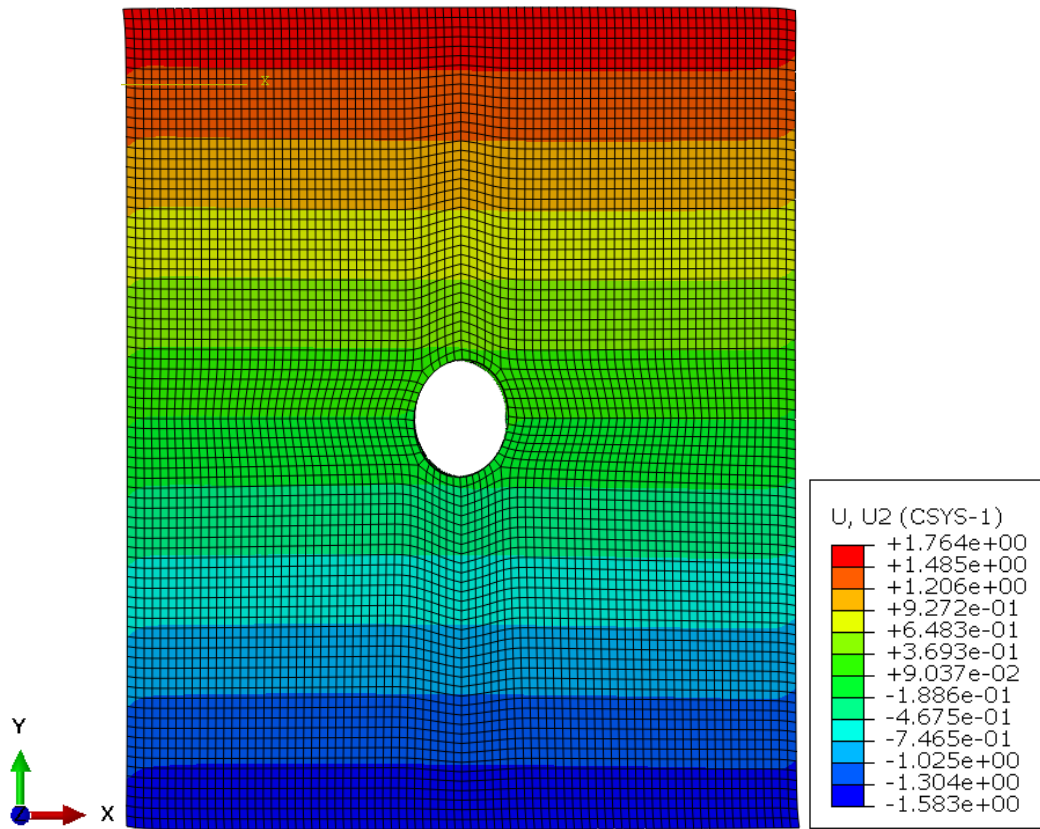
(i) Cooling cycle minimum temperature magnitude -100°C



(ii) Cooling cycle minimum temperature magnitude -180°C

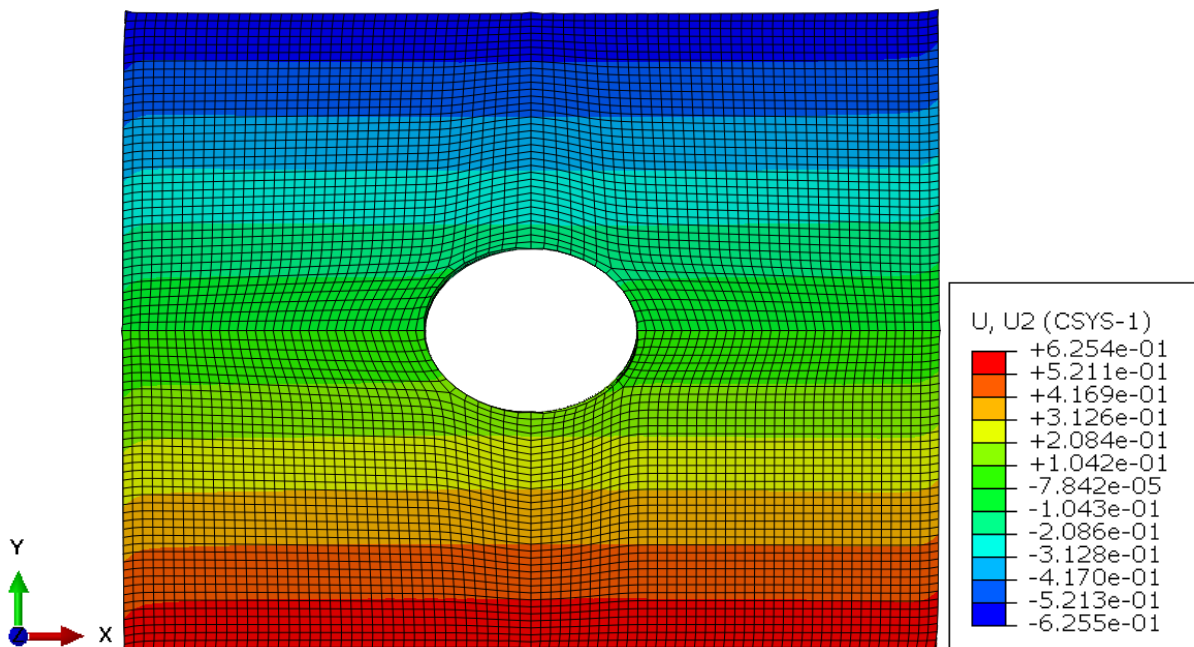
Figure 6.44: Deformation along Y-axis U_2 due to temperature change on the $[\pm 30]_{2s}$ laminate for two different hole sizes

Figure 6.44 continued



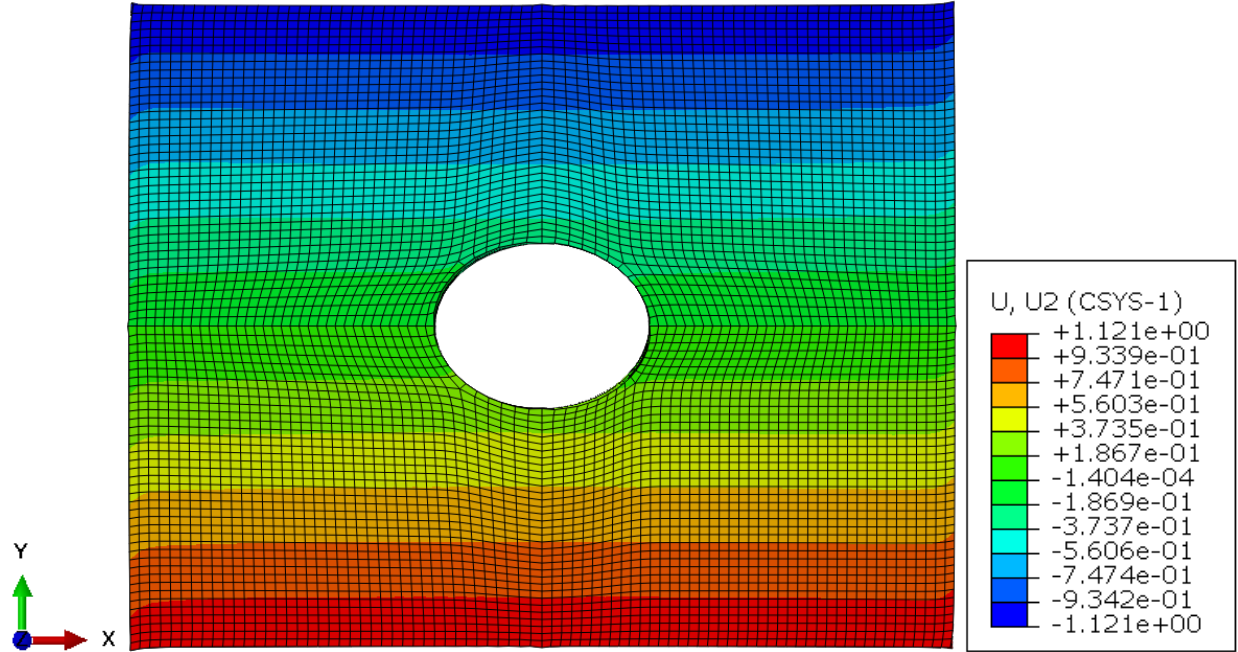
(iii) Heating cycle maximum temperature 180°C

(a) Hole diameter = 3.683 mm

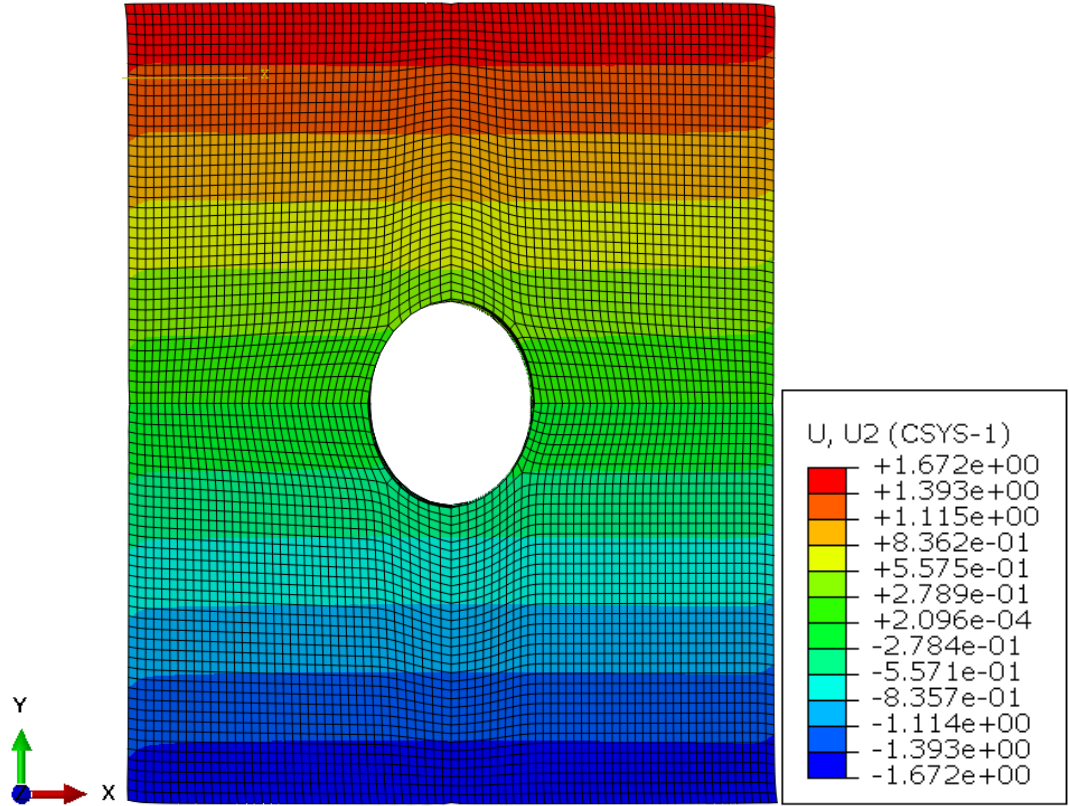


(i) Cooling cycle minimum temperature magnitude -100°C

Figure 6.45continued



(ii) Cooling cycle minimum temperature magnitude -180°C



(iii) Heating cycle maximum temperature 180°C

(b) Hole diameter = 6.604 mm

6.7.3 Stress in X-direction

Figure 45 shows the variation of stress along the X-axis of the specimen. For the heating and cooling cycles, the regions of tensile and compressive stresses are swapped accounting for the swapping of the major and minor axes in these 2 cases. The stresses on the laminate increase as the magnitude of cooling temperature increases. The top edge undergoes tension in the cooling cycles and it undergoes tension in the heating cycles. This is because of the negative CTE the laminate has in X-direction.

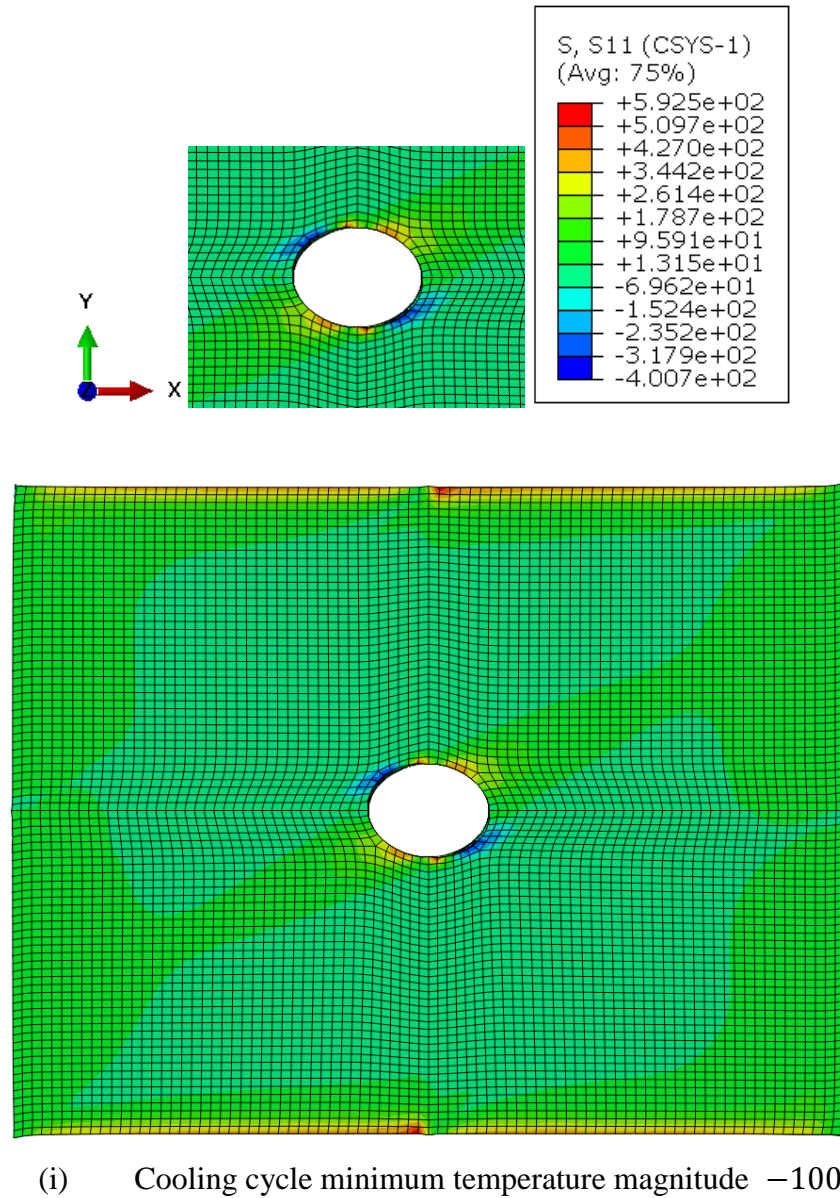
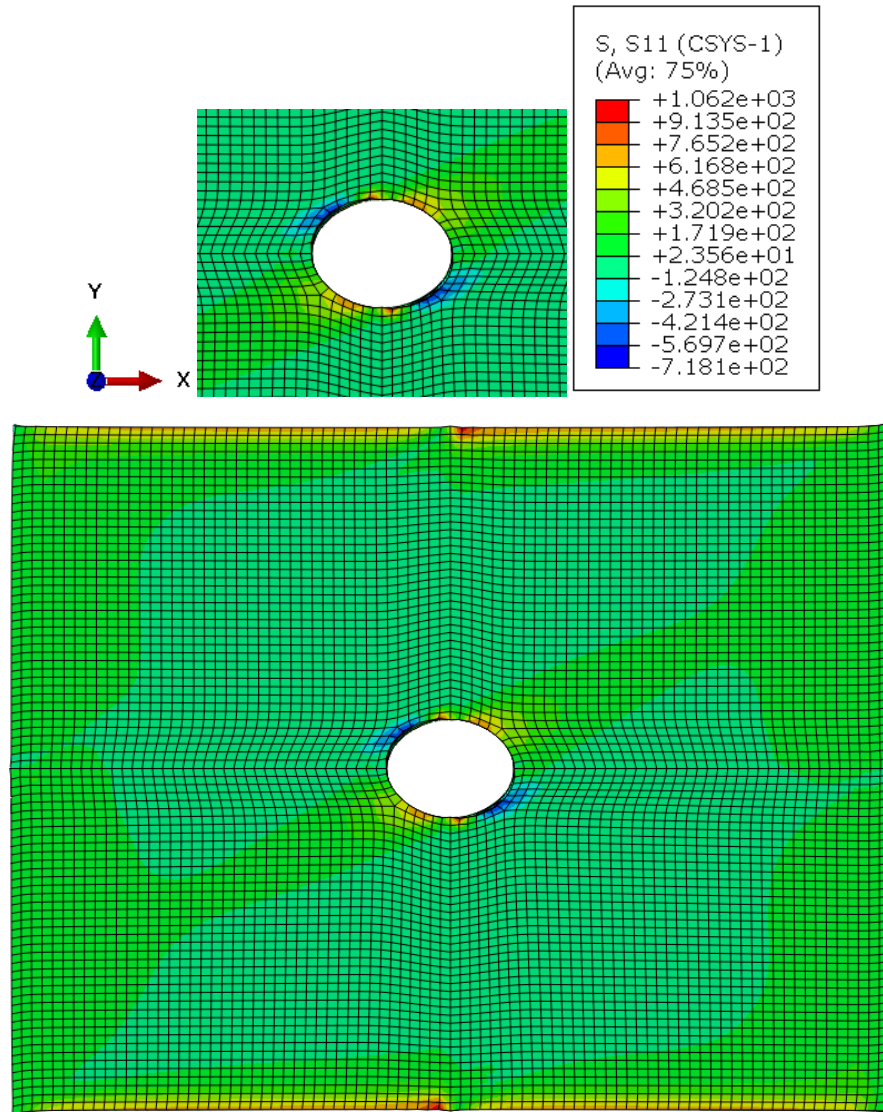


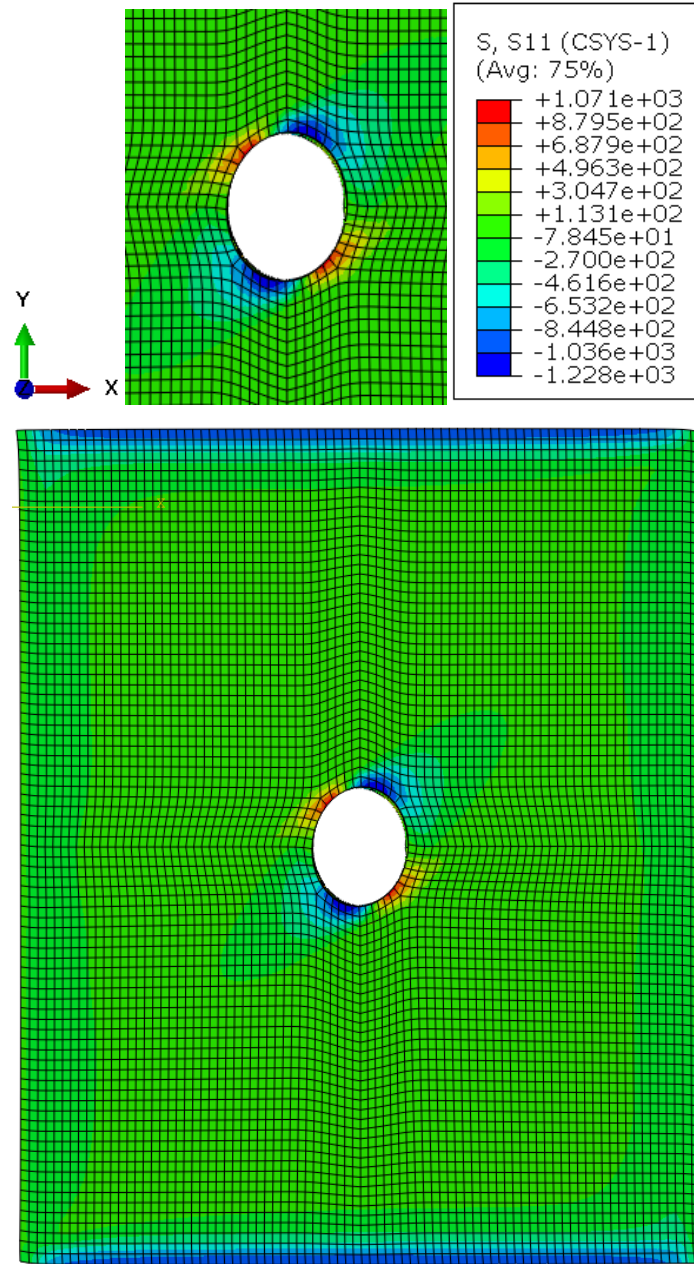
Figure 6.46: Variation of stress in X-direction, σ_{11} due to temperature change on the $[\pm 30]_{2s}$ laminate for two different hole sizes

Figure 6.45 continued



(ii) Cooling cycle minimum temperature magnitude -180°C

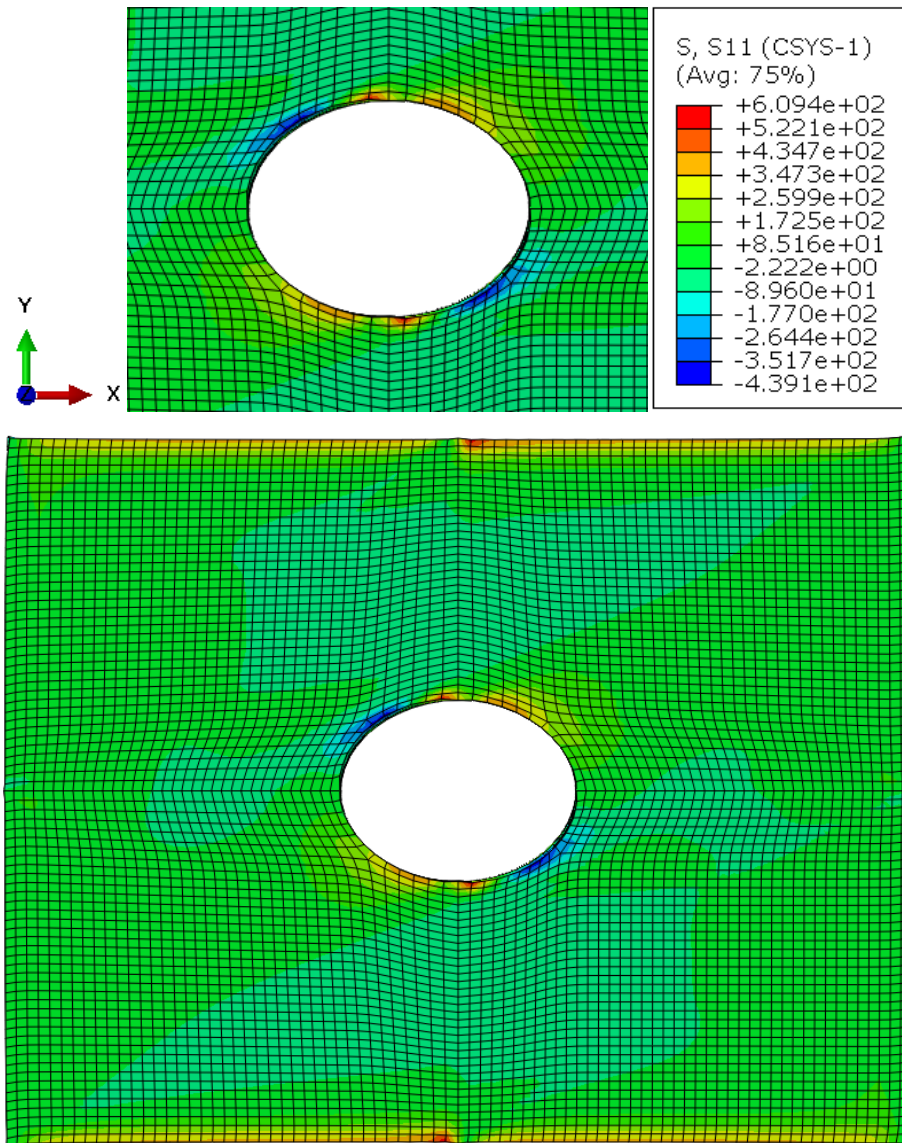
Figure 6.45 continued



(iii) Heating cycle maximum temperature 180°C

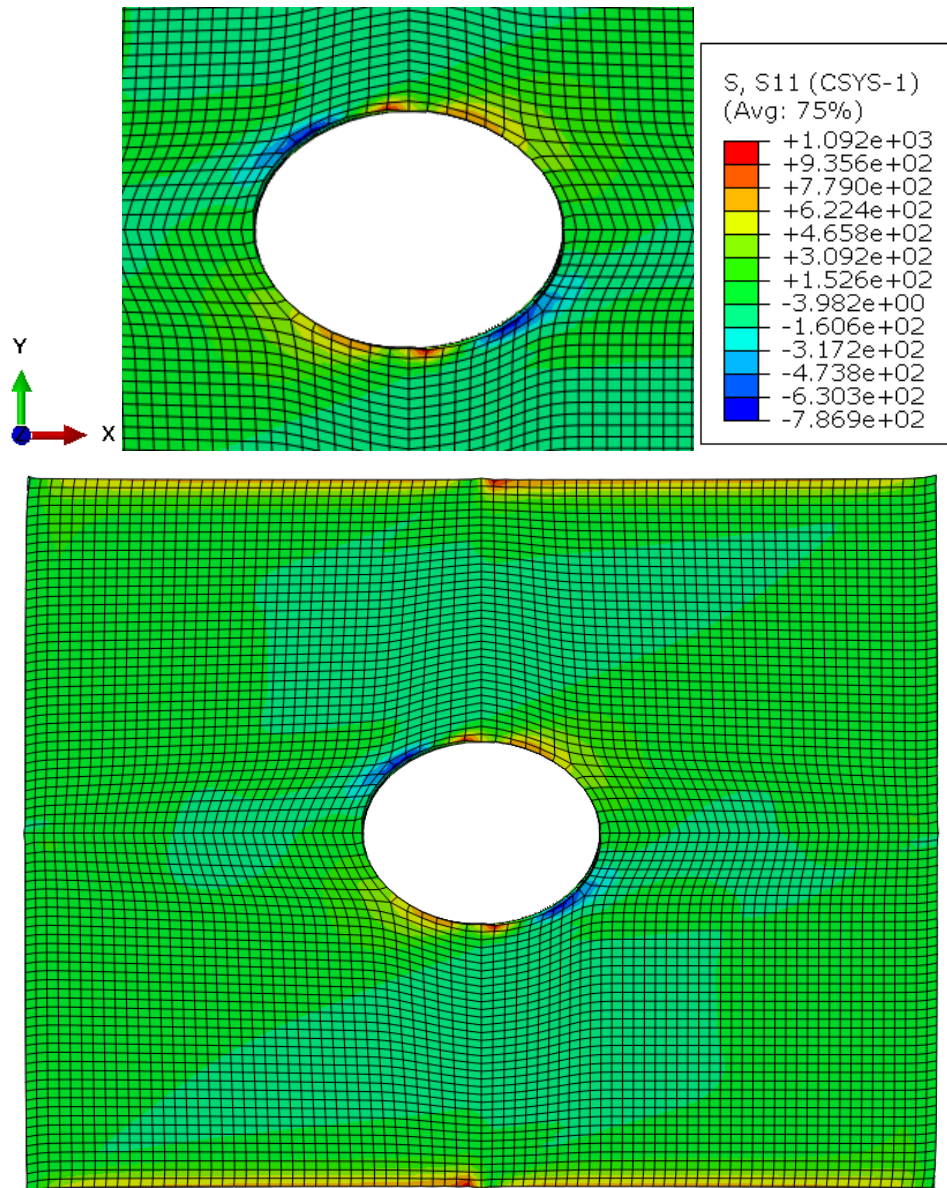
(a) Hole diameter = 3.683 mm

Figure 6.45 continued



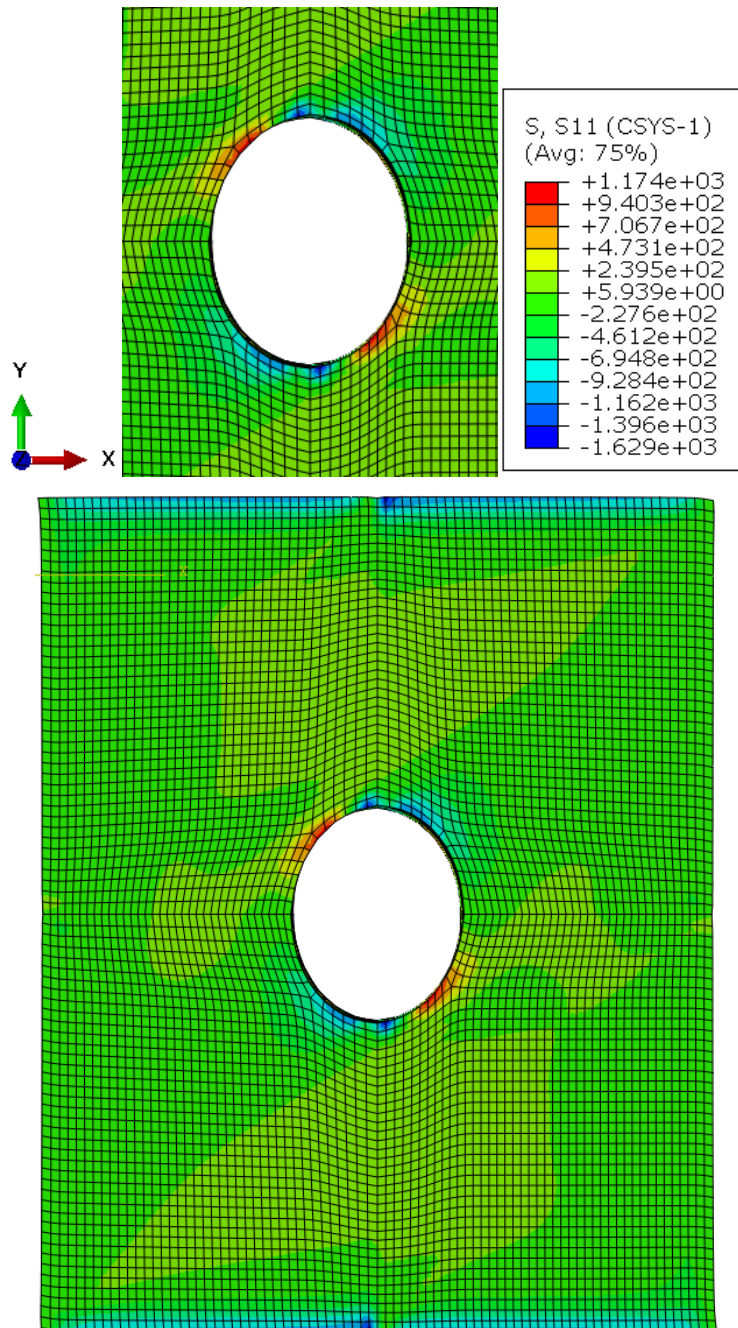
(i) Cooling cycle minimum temperature magnitude -100°C

Figure 6.45 continued



(ii) Cooling cycle minimum temperature magnitude -180°C

Figure 6.45 continued

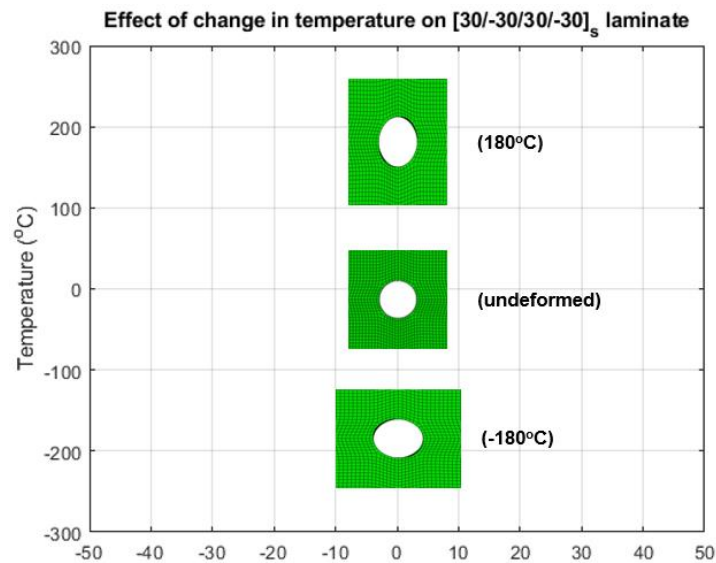


(iii) Heating cycle maximum temperature 180°C

(b) Hole diameter = 6.604 mm

6.7.4 Effect of negative CTE on the deformation of the hole during heating

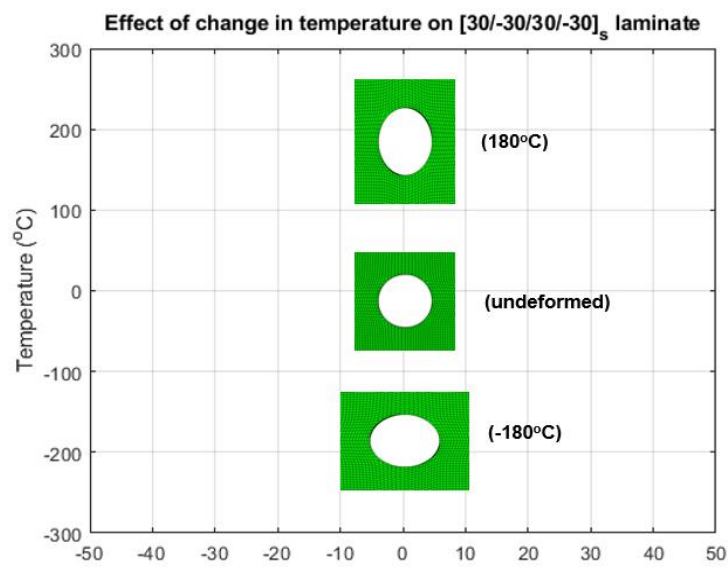
Figure 46 shows the effect of change in temperature on the $[\pm 30]_{2s}$ laminate for two different hole sizes when it is heated and cooled up to 180°C and -180°C respectively. Tables 3 and 4 show the variation of dimensions of both the holes in the heating and cooling cycles. The aspect ratio (major axis/minor axis) for the deformed ellipse at the end of cooling cycles (X deformation/Y deformation) up to -100°C & -180°C is about 1.06 and 1.12 respectively and the aspect ratio at the end of heating cycle (Y deformation/X deformation) up to 180°C for both the holes is about 1.17.



(a) Hole diameter = 3.683 mm

Figure 6.47: Effect of temperature change on the $[\pm 30]_{2s}$ laminate for two different hole sizes

Figure 6.46 continued



(b) Hole diameter = 6.604 mm

Table 6.3: Deformation of holes in the cooling cycle

Cooling (Minimum Temperature) (°C)	Initial diameter (mm)	Deformed (Y) (mm)	Deformed (X) (mm)	Aspect Ratio (X/Y)
-100	3.68	3.49	3.70	1.06
-180	3.68	3.34	3.74	1.12
-100	6.60	6.27	6.65	1.06
-180	6.60	6.00	6.72	1.12

Table 6.4: Deformation of holes in the heating cycle

Heating (Maximum temperature) (°C)	Initial diameter (mm)	Deformed (Y) (mm)	Deformed (X) (mm)	Aspect Ratio (Y/X)
100	3.68	3.87	3.65	1.06
180	3.68	4.02	3.58	1.12
100	6.60	6.93	6.54	1.06
180	6.60	7.28	6.48	1.12

6.8 Conclusions

Holes of three different sizes were made on laminates with three different stacking sequences and the failure modes were determined for them. It was observed that the laminate with stacking sequence $[0_2 / \pm 45]_s$ has the highest strength as it has a greater number of 0° plies in it. The strength was estimated from two different methods, ASC and PSC. A broad range of σ_N/σ_0 were found for different values of a_0 and d_0 for ASC and PSC respectively. It was observed that the modified PSC is a better estimate for the calculations. It gives a single plot for all the hole sizes and it gives a narrower range of estimate compared to the other two cases where there is a wider range of values for σ_N/σ_0 . Once the σ_N/σ_0 was corrected for finite width, they seem to fit the

σ_N/σ_0 estimates better. As the size of the hole increases, the strength of the laminates appears to reduce. Even the laminates with the smallest hole have a significant reduction in the value of strength compared to the un-notched laminate. The stress is the highest at the corner of the hole and it reduces exponentially towards the end of the laminate plate.

The digital twins for the stiffness of the laminates display the detailed variation of stresses on the length of the laminate and across the width of it. The magnitude of normalized stress is the highest for $[0_2/\pm 45]_s$ laminate. The $[\pm 30]_{2s}$ laminate has a negative CTE along X-axis and hence, simulations were run for the deformation of it with an increase and decrease of temperature. It was observed that the hole deforms to an ellipse and the major axis flips for the heating and cooling cycles. As a result, the stress concentrations around these holes also flip directions of tension and compression. A detailed analysis was carried out for the deformation and the stress distribution around the holes of two different sizes.

6.9 References

- [1] Carlsson, L. A., Adams, D. F., & Pipes, R. B. (2014). *Experimental characterization of advanced composite materials*. Boca Raton, FL: CRC Press.
- [2] Dr. Wenbin Yu. (2017) Multiscale Structural Mechanics. Wiley-Interscience. John Wiley & Sons, INC., Publication
- [3] Chen, B.Y., Tay, T.E., Baiz, P.M., Pinho, S.T. (2013). *Numerical analysis of size effects on open hole tensile composite laminates*. Composites: Part A. 47, p. 52-62.
- [4] Hayden Hermes, Swapneel Kulkarni, Akshay Jacob Thomas, 25th October 2019, Friday, Lab 10- Open Hole Strength, Presentation, PPT. (2019).
- [5] Dr. Byron Pipes, 21st October 2019, Monday, Open Hole Tension, Presentation, PPT. (2019).

7. FREE EDGE EFFECTS

7.1 Introduction

7.1.1 Stress distributions at the free edge

With the increasing use of composites in the industry, there is an increasing need to understand and solve different problems that are encountered. Free-edge is one such problem which is very commonly faced. Due to a mismatch in the elastic properties of the neighboring layers in a composite laminate, there are concentrated stresses that arise in the interface of the laminates at the free edges when the laminates are thermally or mechanically loaded. These stress fields are located at the boundary layers of the laminates where there are steep stress gradients and they eventually die out towards the center of the laminate. It is very crucial to obtain the 3D stress field at the edges of the laminate to prevent the premature failure of the laminates as they can result in delamination and transverse cracking of the laminates. Figure 1 shows the variation of stresses on the surface and across the thickness of the laminate. The characterization of the strength of fiber-reinforced composite materials that are laminated shows that the stress state near free-edge is three-dimensional in nature and is not predicted accurately by the laminated plate theory. Some experimental results have shown that the strength of certain angle-ply laminates can be predicted by the laminate strength theories, but the strength of coupons of other fiber orientations cannot be predicted by these theories.

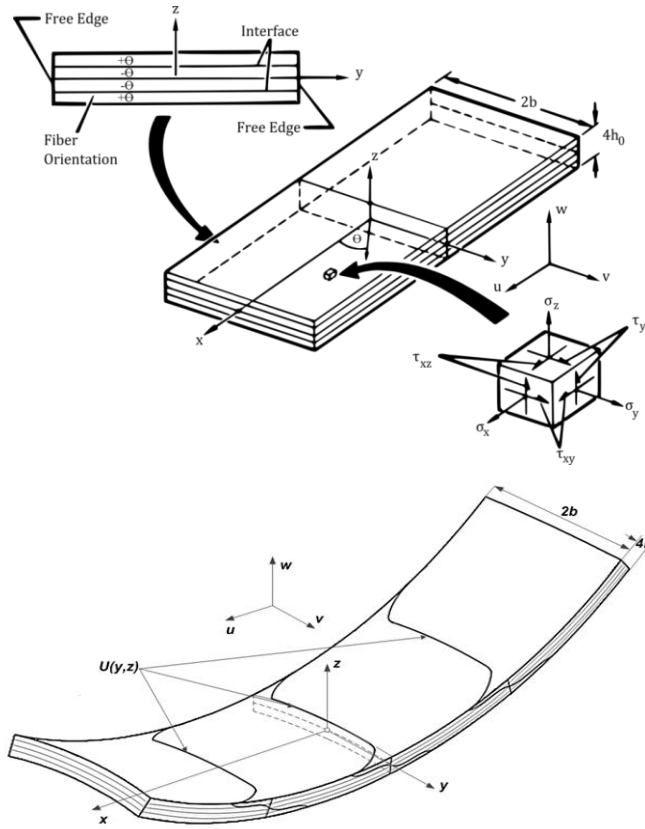


Figure 7.1: Stress state at the free edge of the specimen

(Image from Experimental characterization of advanced composite materials (2014))

7.1.2 Axial displacement and interlaminar shear strain across the thickness

From a few analyses conducted in the past, it was very evident that a cogent amount of interlaminar stress is required to allow shear transfer between layers of an angle-ply laminate that has a fine width. The interlaminar stress is restricted to a narrow region near the free-edge and a uniform stress field as predicted by the lamination theory is recovered from the inner region of the laminate. The location of maximum interlaminar shear stress is found at the interface of the lamina with fiber orientations of $+\theta$ and $-\theta$. The interlaminar normal stress, σ_z , σ_y , τ_{yz} are very small in the angle-ply laminates. When a uniform uniaxial stress is applied to a laminate, it can be proven that the lamina state of stress contains only two components in the laminate coordinate system. These components of stress are σ_x and τ_{xy} .

Figure 2 shows the variation of interlaminar shear strain and Figure 3 shows the variation of axial displacement distribution across the thickness of the laminate. The first Distribution I, corresponds to the elastic analysis and hence to a state of stress-strain at or below the proportional limit. As the load is increased and the material response enters the nonlinear range, the axial displacement distribution changes to a form corresponding to Distribution II. Finally, an interlaminar shear failure results in a separation of the laminae at the interfaces ($z/h_o = \pm 1.0$) and produces the displacement Distribution III. Distribution IV corresponds to the interlaminar shear failure.

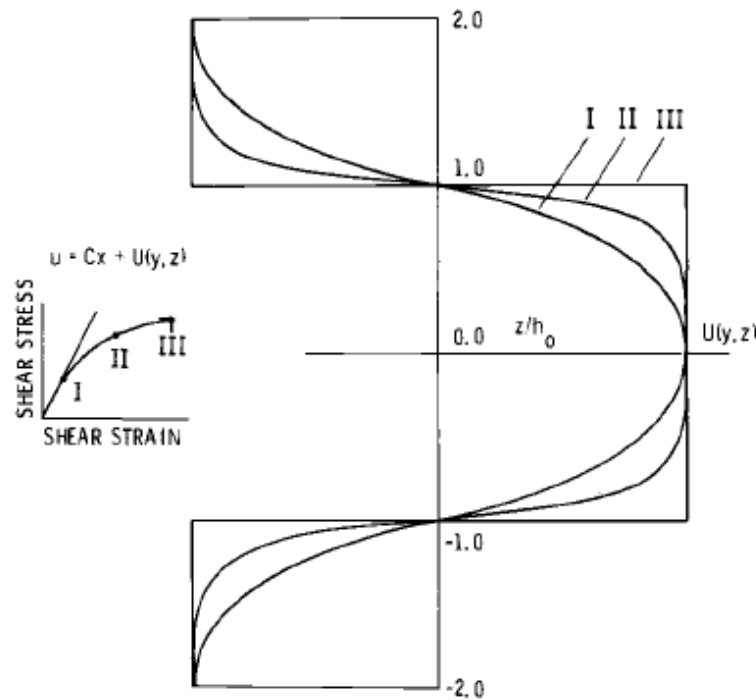


Figure 7.2: Axial displacement across the thickness

(Image from Experimental characterization of advanced composite materials (2014))

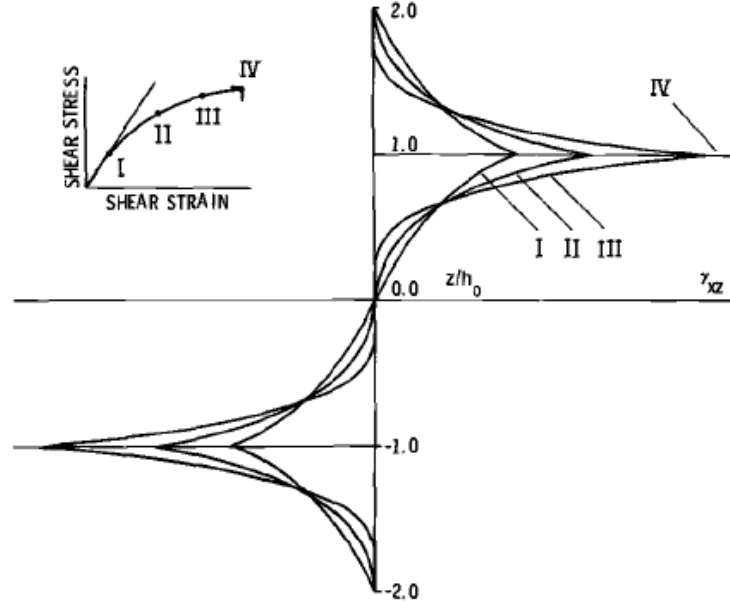


Figure 7.3: Interlaminar shear strain across the thickness

(Image from Experimental characterization of advanced composite materials (2014))

7.1.3 Variation of stresses across the width

When uniform uniaxial stress is applied to a laminate, it can be proven that the lamina state of stress contains only two components in the laminate coordinate system. These components of stress are σ_x and τ_{xy} . Further, it can be shown that σ_y is zero. Also, the direction of the shear stress is the only varying parameter for a lamina of θ and $-\theta$ directions.

Thus, we have

$$\sigma_x(\theta) = \sigma_x(-\theta) = \bar{\sigma}_x$$

$$\tau_{xy}(\theta) = -\tau_{xy}(-\theta)$$

Free edge effects arise to the fact that for finite width specimens to maintain a traction free surface at the edge, there arises interlaminar shear stress.

If the stress state is independent of the x – coordinate (St. Venant's principle) we have

$$\frac{\partial \sigma_x}{\partial x} = 0$$

Thus, the equilibrium equations are given by

$$\frac{\partial \tau_{xy}}{\partial y} + \frac{\partial \tau_{xz}}{\partial z} = 0$$

Since the in-plane shear stress must vanish on the free surface of the specimen, we have

$$\frac{\partial \tau_{xy}}{\partial y} = -\frac{\partial \tau_{xz}}{\partial z}$$

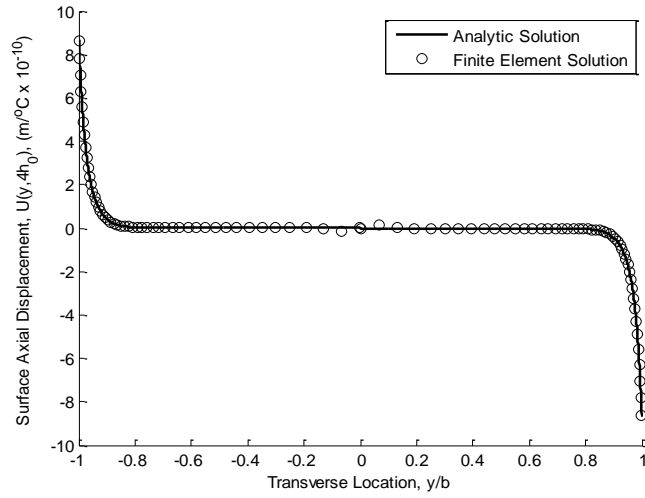
The uniform axial extension form of the strain-displacement relationship is assumed in order to yield stress field independent of the axial coordinate, x

$$\begin{aligned} u &= \varepsilon_0 x + U(y, z) \\ \sigma_y &= \sigma_z = C_{45} = 0 \end{aligned}$$

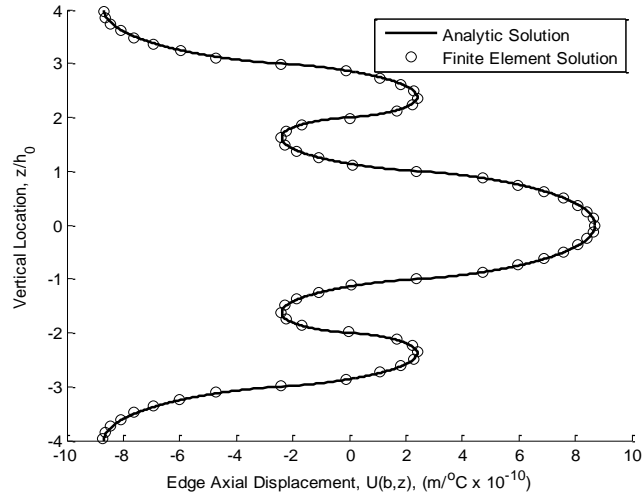
That leads to

$$\begin{aligned} \alpha U_{yy} + U_{zz} &= 0 \\ \alpha &= \frac{S_{11}S_{55}}{[S_{11}S_{66} - S_{16}^2]} \\ \tau_{xz} &\sim S_{16}\varepsilon_0 \sqrt{\frac{1}{S_{11}S_{55}[S_{11}S_{66} - S_{16}^2]}} \end{aligned}$$

It is important to note that the components of the compliance matrix, referred to as S_{ij} are in the laminate coordinate system. The surface deformation in Figure 4 clearly illustrates the nature of the interlaminar phenomenon. Here we see that the axial displacement in the direction of the applied load has an anti-symmetric form that is clearly restricted to as boundary layer. More important, as we saw in analyzing the off-axis tensile coupon, the gradient in displacement in this region reflects the “freedom” of the surface layer to exhibit deformation as if it was not bonded to the rest of the laminate, but free to deform as it would as an off-axis coupon of the same orientation, θ .



(a) Across width



(b) Across thickness

Figure 7.4: Axial displacement across width and thickness of the laminate
(Image from Experimental characterization of advanced composite materials (2014))

The through thickness results show that the interlaminar shear stress is zero on the upper and lower surfaces, as it must be. Note also that the interlaminar shear stress changes sign at the multiple interfaces in much the same way as the in-plane shear stress changes sign for θ and $-\theta$. While a finite maximum value for the interlaminar stress at the free-edge is shown, this is certainly not the case. Rather, the stress at the intersection of the interlaminar planes: $z = +3h$ and $+h$ are unbounded. Namely, a mathematical singularity exists in these positions. This can be seen in Figure 5.

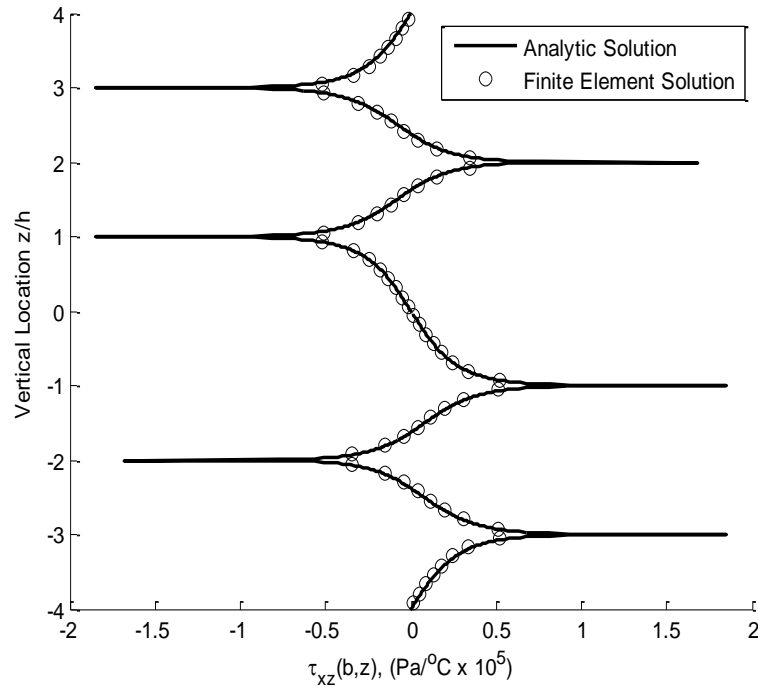
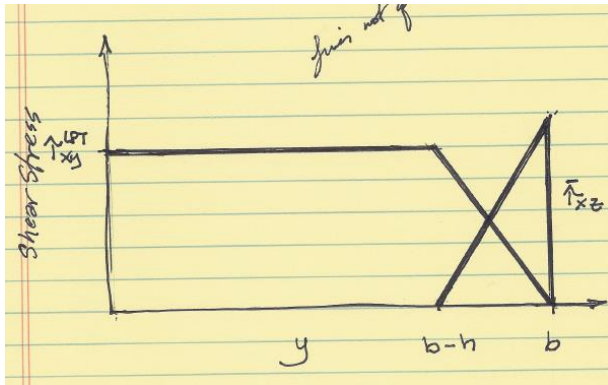


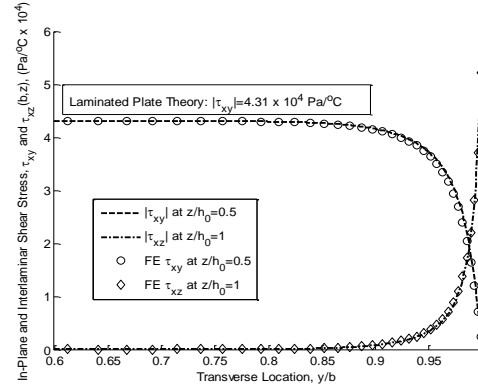
Figure 7.5: Interlaminar shear stresses through the thickness

(Image from Experimental characterization of advanced composite materials (2014))

A simplified shear stress distribution is shown in Figure 6. The mathematical singularity at the free edge can be simplified, wherein τ_{xz} has a finite value at the free-edge and the smooth curves are replaced by linear approximations. This approach will preserve the relationship between the in-plane and interlaminar stresses, but will allow simple relationships to be developed for relating the couples, C_{xz} and C_{xy} to the magnitude of the shear stress at the free edge. Further, Figure 7 shows the variation of complete stress results at the interface of a $[\pm 45]_s$ laminate with the material properties of the laminate specified accordingly.



(a) Simplified



(b) Actual

Figure 7.6: Simplified and Actual shear stress distributions across the width of the sample
(Image from 12a, 12b Free-edge Phenomena, Presentation. PPT. (2019))

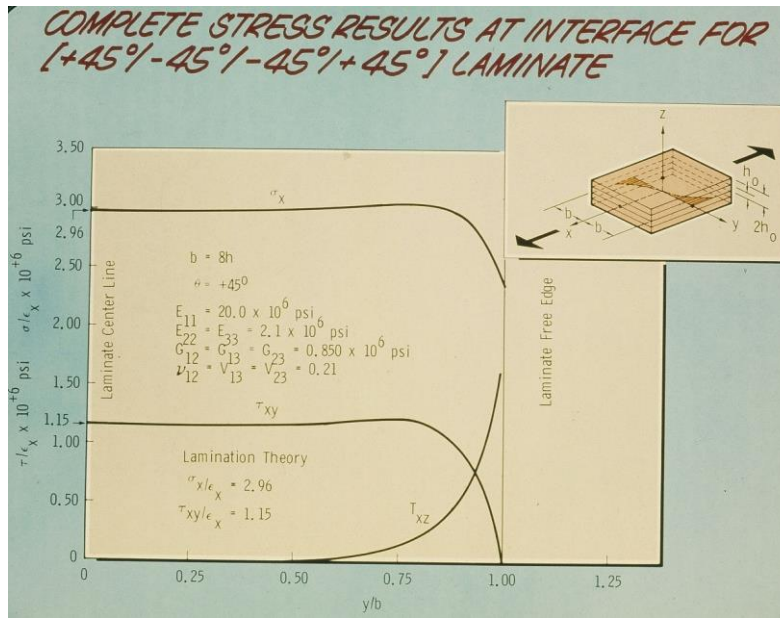


Figure 7.7: Variation of stresses at the interface of $[\pm 45]_s$ laminate
(Image from 12a, 12b Free-edge Phenomena, Presentation. PPT. (2019))

7.2 Experimental Procedure

4 types of laminates were prepared to study the free-edge effects. These were $[\pm 30]_{2s}$, $[\pm 30_2]_{2s}$, $[\pm 30/90_2]_s$, $[\pm 30_2/90_4]_s$. Ten specimens of each laminate were studied. For the calibration of the DIC camera, the position of the samples and the lighting conditions affect

the exposure of the image. The samples were aligned as accurately in the load cell as was possible. The level checked using a spirit level. The load cell was calibrated for a 22kip calibration. The ramp rate for the test was 2 mm/min for the first two samples and was increased to 4 mm/min for the remaining samples. The samples were loaded until failure. There was no speckling on the samples and the data obtained from DIC cameras was used to capture the video of the samples failing. The data reduction was done using the aforementioned formula and the results were compared to those obtained using CDMHub. Figure 8 shows the experimental set-up that was used to test the samples for free-edge effects.



Figure 7.8: Experimental Setup

7.3 Processing of experimental results

The sample dimensions were measured for further calculations to be carried out on the specimen. Table 1 shows the average and standard deviation values of these data for the four laminates that were tested. It can be observed that the sample dimensions are close to each other as the standard deviation values are quite low. The samples with 16 plies have a thickness twice of the samples with 8 plies.

Table 7.1: Average and standard deviation values of sample dimensions

	Specimen Dimensions			
Laminate	$[\pm 30]_{2s}$	$[\pm 30_2]_{2s}$	$[\pm 30/90_2]_s$	$[\pm 30_2/90_4]_s$
Width (mm)	25.39	25.37	25.37	25.32
Width STD	0.04	0.04	0.08	0.06
Thickness (mm)	1.52	3.17	1.62	3.17
T STD	0.04	0.07	0.03	0.08
Length (mm)	152.79	152.70	152.78	152.59
Length STD	0.41	0.28	0.06	0.10
CSA (mm²)	38.48	80.51	41.11	80.21

Load-displacement data was extracted and cleaned using a MATLAB code and plotted per specimen per laminate. The cleaning process only adjusted the offsets on the loads and displacements data by ensuring a start at the origin. The approximate value of the axial strain was taken by dividing the displacement by the mean gauge length of the laminate type. Axial stresses were calculated by dividing the force by the mean cross-sectional area of the laminate type. For the simplified version of calculating the anti-symmetric in-plane shear and interlaminar shear, the following formula was used:

$$h = mh_0$$

$$\tau_{xz} = \frac{2}{m} \left[\frac{b - mh_0/2}{b - mh_0/3} \right]$$

Where h_0 is the thickness of each layer, and b is the half-width of the specimen.

7.3.1 $[\pm 30]_{2s}$ laminate

Figure 9 shows the load versus displacement curves and the axial stress versus strain curves for all the samples made from the $[\pm 30]_{2s}$ laminate. The mean ultimate stress, Young's Modulus, Interlaminar Shear Stress, and Peel Stress values are calculated from the data accordingly.

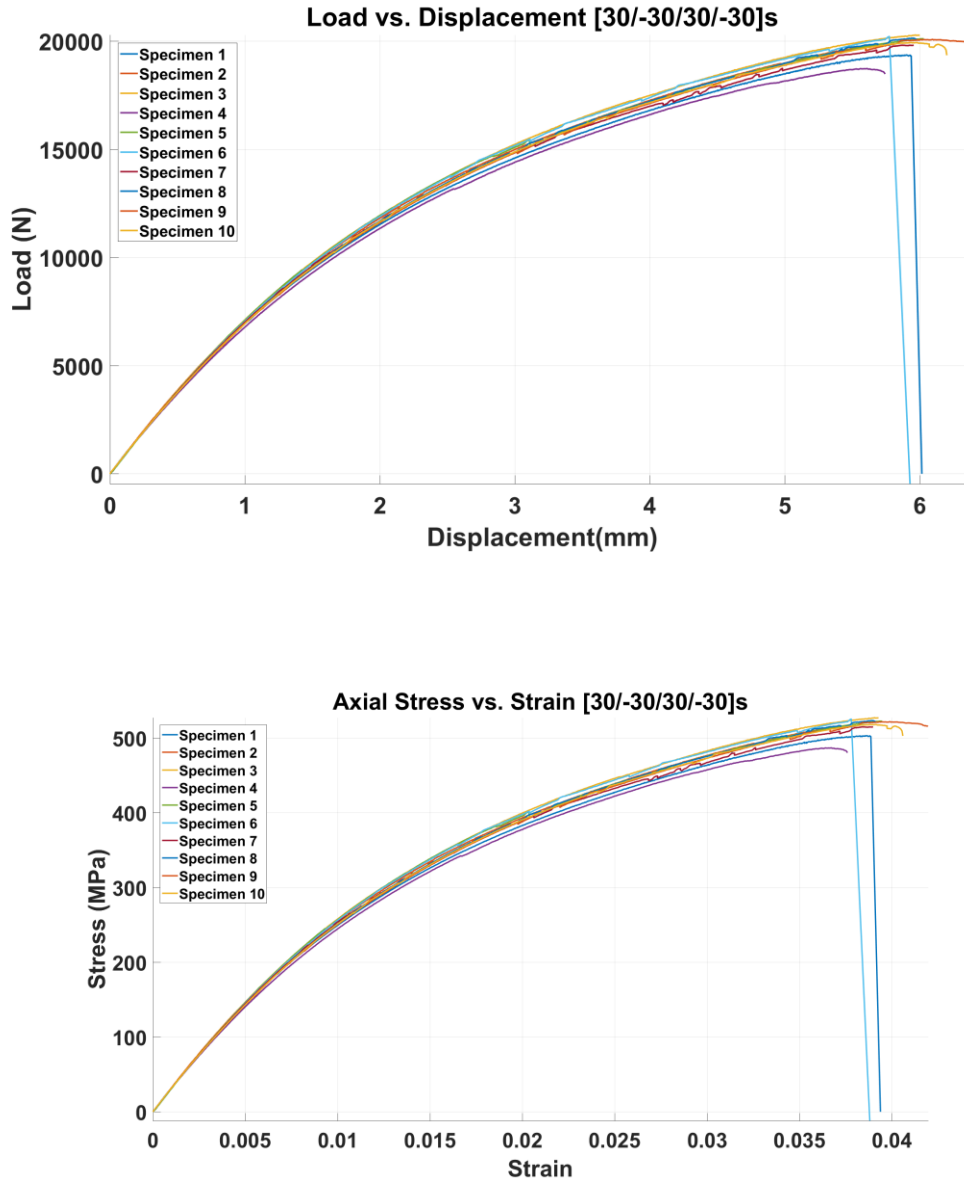


Figure 7.9: Load Displacement and stress-strain plot for $[\pm 30]_{2s}$ laminate

7.3.2 $[\pm 30_2]_{2s}$ laminate

Figure 10 shows the load versus displacement curves and the axial stress versus strain curves for all the samples made from the $[\pm 30_2]_{2s}$ laminate. This laminate has a ply thickness twice of that of the previous laminate. As the thickness of the laminate increases, the strength of it decreases. Hence it can be observed that the ultimate stress of the laminate is lower. The mean ultimate stress, Young's Modulus, Interlaminar Shear Stress, and Peel Stress values are calculated from the data accordingly.

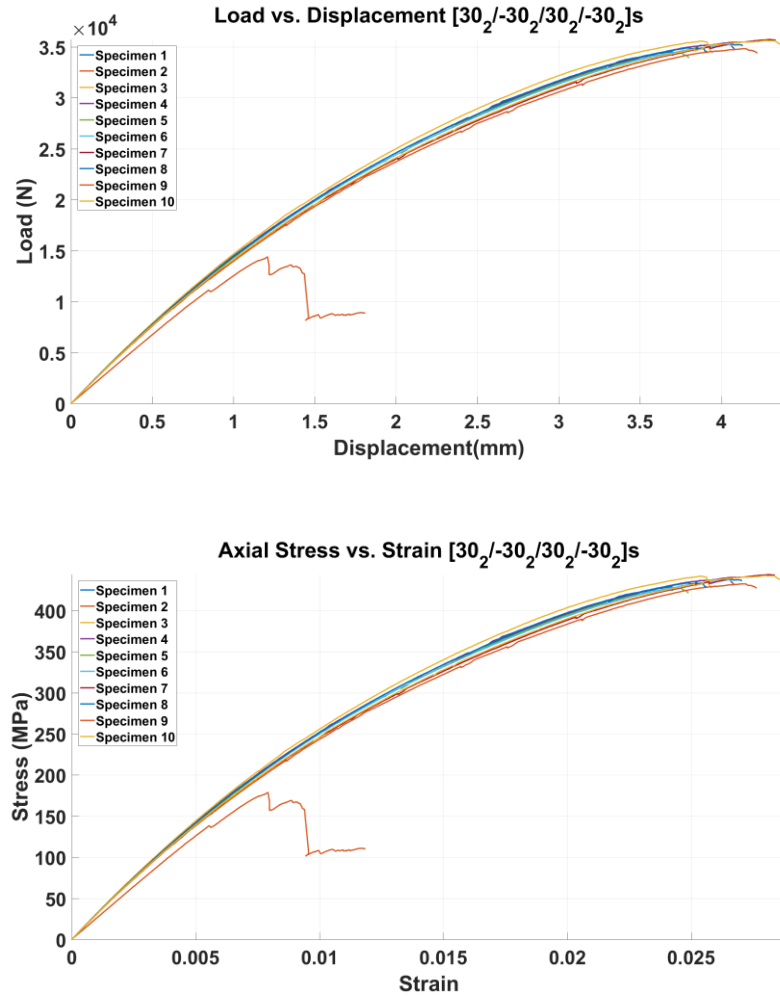


Figure 7.10: Load Displacement and stress-strain plots for $[\pm 30_2]_{2s}$ laminate

From Figure 11 we can see evidence of delamination failure at the edges of the specimen. Since the ply thickness is two times more than the laminate with 8 plies, the delamination is more clearly visible in this case. The simplified version was used for calculating the peel stress. For this laminate, $b = 12.685\text{mm}$, $h = 3.17\text{mm}$, $m=16$ and in-plane shear stress (from CPT) is 558.25 MPa , interlaminar shear stress at failure was 66.61 MPa and peel stress was 7.12 MPa . The mean ultimate stress was calculated to be 411.47 MPa and Young's Modulus was 28.44 GPa .

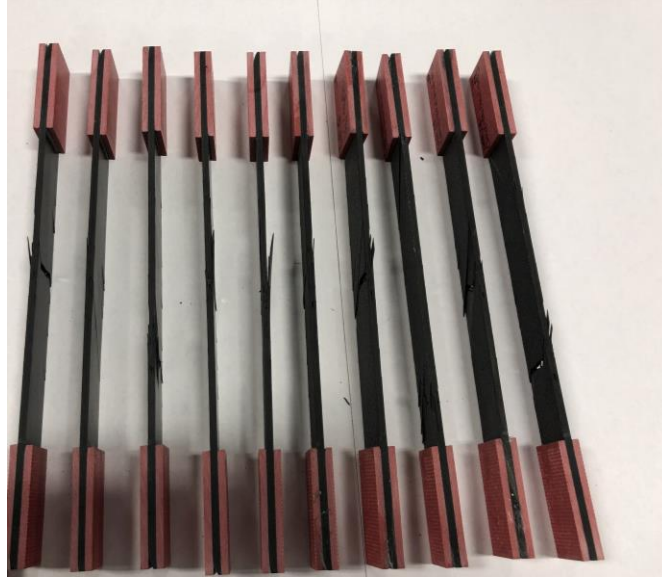


Figure 7.11: Delamination failure at the edge of the specimen for $[\pm 30_2]_{2s}$ laminate

7.3.3 $[\pm 30/90_2]_s$ laminate

Figure 12 shows the load versus displacement curves and the axial stress versus strain curves for all the samples made from the $[\pm 30/90_2]_s$ laminate. The mean ultimate stress and Young's modulus were calculated for this laminate. Since this is not an angled ply laminate, the interlaminar shear stress and peel stress of the laminate is not calculated. The ultimate stress of this laminate is less than the previous laminate with 8 plies because of the presence of 90 oriented plies which reduce the strength of the laminate significantly to about half the previous strength as the number of angled plies are reduced to half in this case. The code in cdmHUB is also not valid for laminates with 90 angled plies. Hence, the plots with the analytical solution are not obtained for this laminate. The average ultimate stress was found to be 299.88 MPa and Young's Modulus was 26.8 GPa.

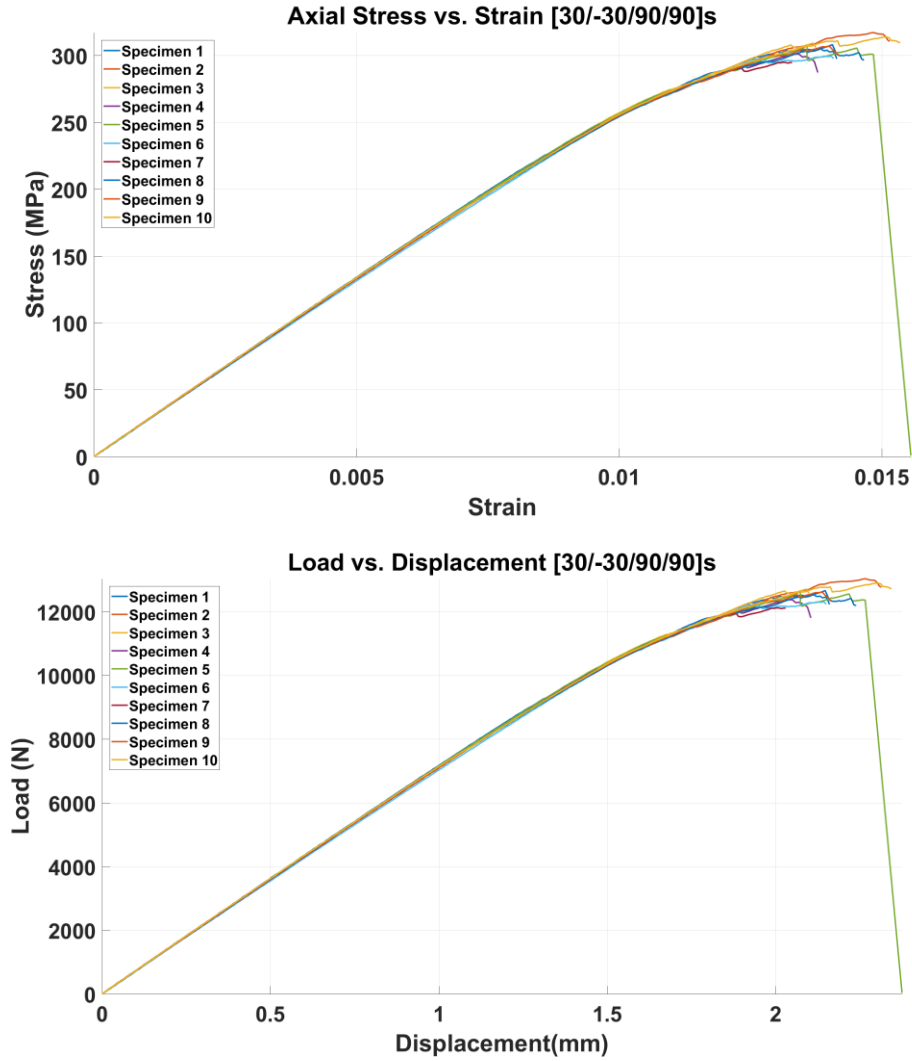


Figure 7.12: Load Displacement and stress-strain plot for $[\pm 30/90_2]_s$ laminate

7.3.4 $[\pm 30_2/90_4]_s$ laminate

Figure 13 shows the load versus displacement curves and the axial stress versus strain curves for all the samples made from the $[\pm 30_2/90_4]_s$ laminate. The mean ultimate stress and Young's modulus were calculated for this laminate. As discussed for the previous laminate, since not plies are angled, the interlaminar shear stresses and the peel stresses of the laminate are not calculated and the analytical results from cdmHUB are also not obtained. The ultimate strength of this laminate is also lower than the laminate with a lower ply thickness. The average ultimate stress was found to be 209.59 MPa and Young's Modulus was 26.21 GPa.

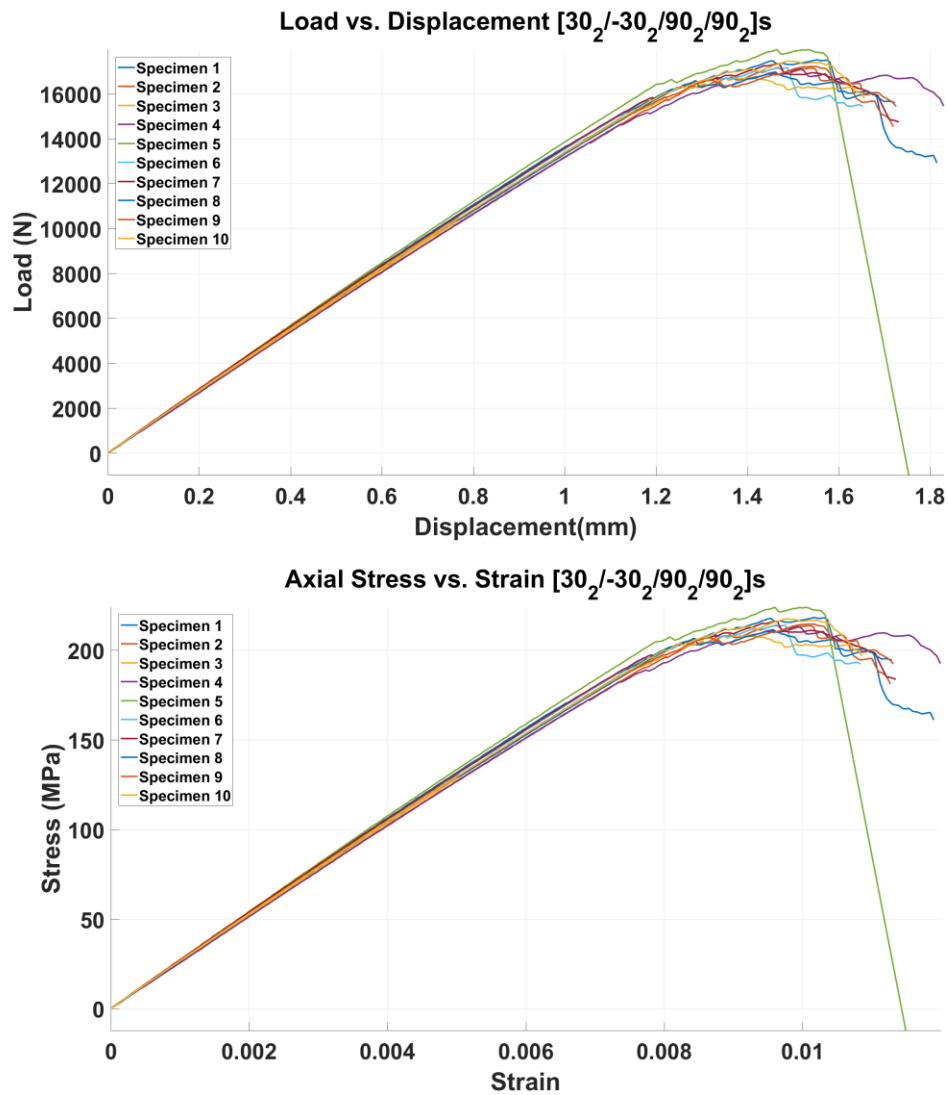


Figure 7.13: Load Displacement and stress-strain plot for $[\pm 30_2/90_4]_s$ laminate

Figure 14 shows the delamination in the $[\pm 30_2/90_4]_s$ laminate. This is not that evident in the laminate with lower ply thickness and it is more visible in this case.

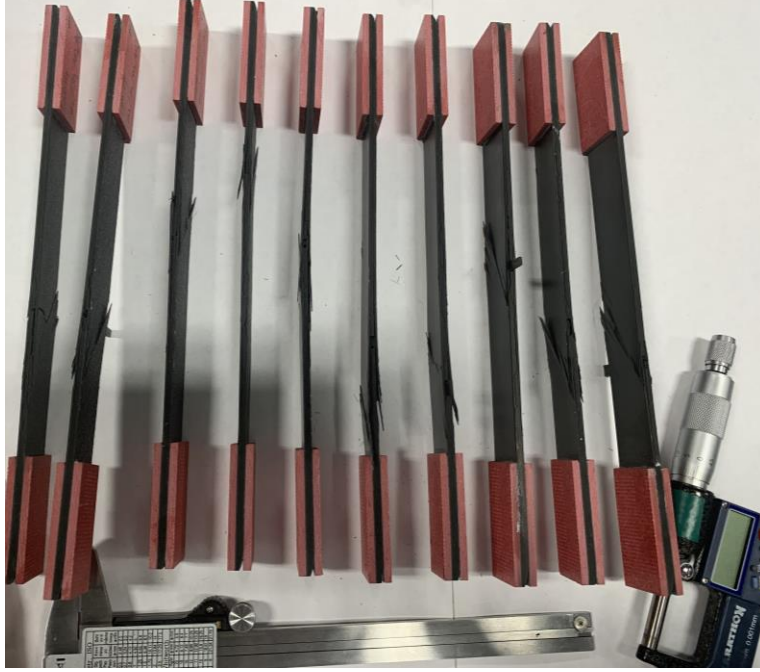


Figure 7.14: Evident delamination at the edges for $[\pm 30_2/90_4]_s$ laminate

7.4 Modeling of geometry for simulations

Laminates with two different stacking sequences, $[\pm 30]_{2s}$ and $[\pm 30/90_2]_s$ were modeled with the same geometry as the experiment with a width of 5.6896 mm, which is 5 times the thickness of the laminate. This was done to have more elements across the width and to capture the free edge effects. The properties of the other two laminates are the same as these but the laminate thickness is twice as them. Hence, to study the deformation and stress properties, it is sufficient to analyze these two. This is done to account for and to study the free-edge effects on the edges of the samples as well. The variation of stresses across the thickness, width is analyzed for both the laminates and the free-edge effects are analyzed.

The fiber orientation was assigned individually to each of the plies and hence, for the post-processing of the data, a global coordinate system is created and all the parameters are hence rotated in terms of the global coordinates. The load and boundary conditions for the test are the same as a typical tensile test as discussed in section 2.7.

7.4.1 Mesh

To capture the free edge effects on the coupon, the mesh was further refined as the width was five times the thickness of the entire laminate. 40 elements are seeded across the width and each

element has a width of one lamina. The geometry was modeled with standard 3D stress elements with a quadratic geometric order (C3D20- 20 node quadratic brick). Reduced integration was used at the tabs to decrease the computation time. There are 1496320 elements on the coupon. Figure 15 shows the images of mesh on the coupon. The tabs were seeded with 4 elements across the thickness.

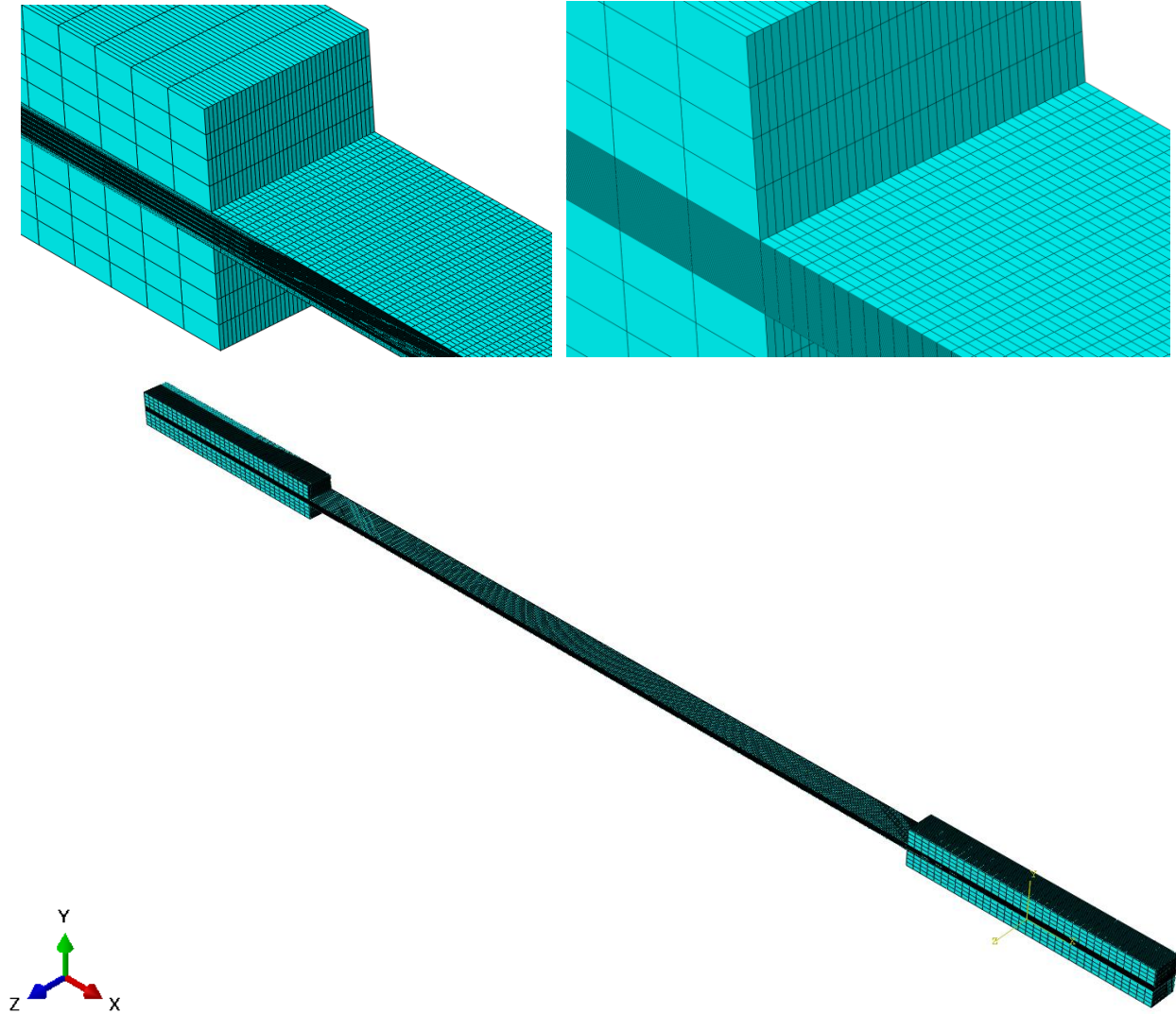


Figure 7.15: Mesh on the edges of free-edge coupon with a width of $5t$

7.5 Analysis of simulation results and comparison with theoretical results

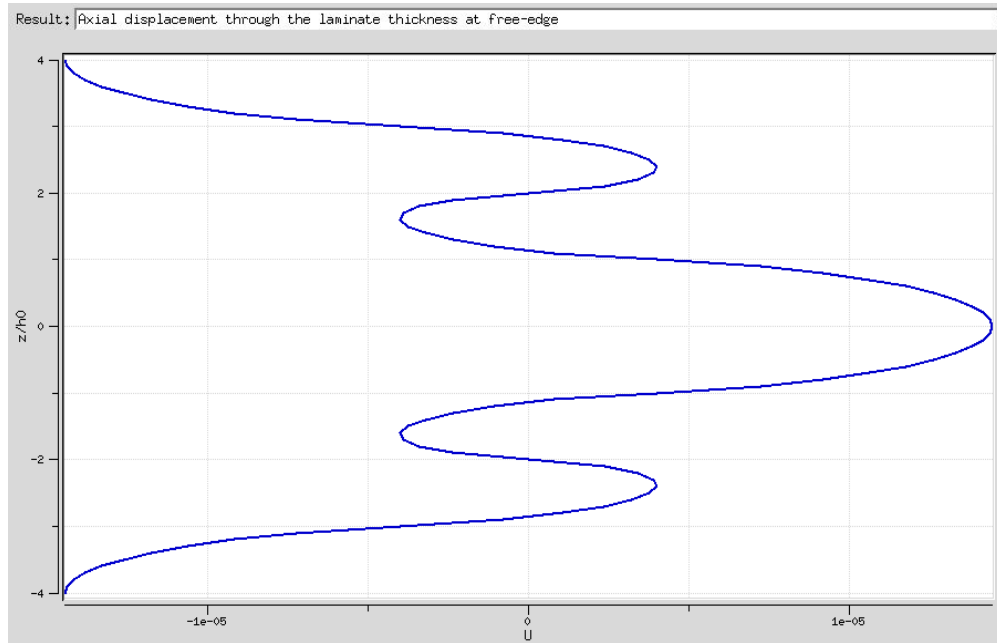
Since the orientation of fibers in the laminate was assigned for individual layers, to get the final properties of the deformed laminate, the parameters were rotated to the global coordinate system. For the analytical results, the free edge elasticity solution application in cdmHub was used with

the material parameters the same as that mentioned in chapter 2. The load was the same as the maximum value of experimental strain that the laminate experiences. The results obtained from the analytical solution and the simulation were compared and validated. For the plots from Abaqus, the location across thickness and width were normalized by dividing the values by 1.13792 and 5.6896 respectively.

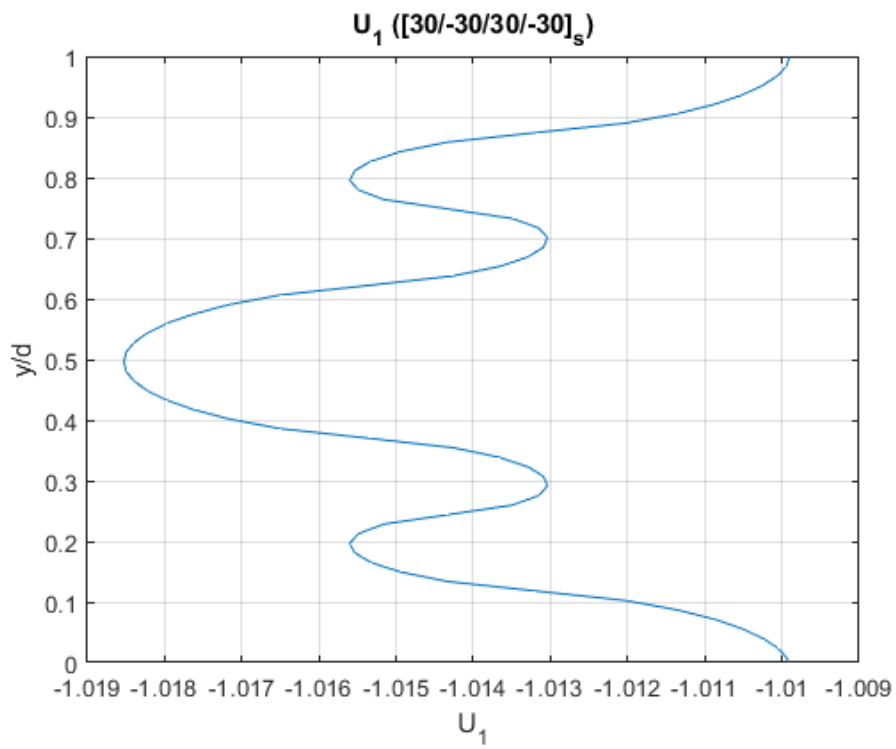
7.5.1 $[\pm 30]_{2s}$ laminate

7.5.1.1 Axial displacement across thickness at the free edge

Figure 16 shows the plots of variation of axial displacement across the thickness from both the analytical solution and from the tensile simulation of the $[\pm 30]_{2s}$ laminate. The laminate has a maximum displacement at the laminate center where there are -30° plies. The -30° plies also have greater displacement than the 30° plies that are present through the thickness of the laminate. This was measured in the middle of the axial length of the laminate. Figure 17 shows the contoured variation of the axial displacement on the entire laminate and the variation across the thickness of the laminate at the gage length.

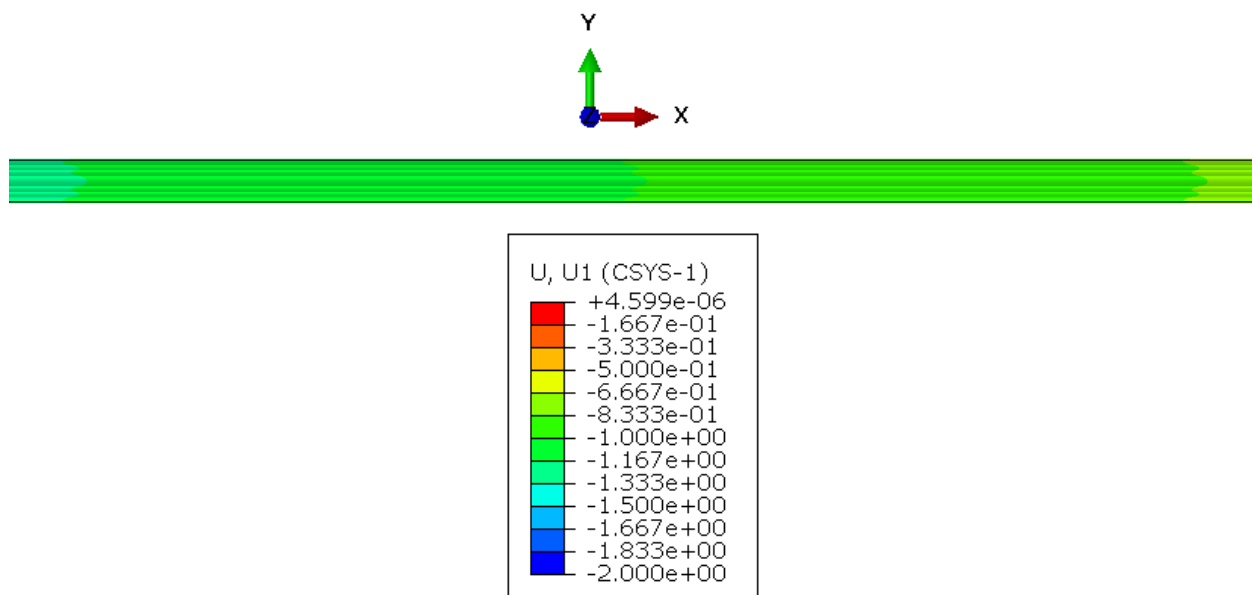


(a) Analytical solution



(b) Abaqus simulation result

Figure 7.16: Variation of axial displacement U_1 across thickness at the free edge of $[\pm 30]_{2s}$ laminate



(a) Axial displacement at gage length

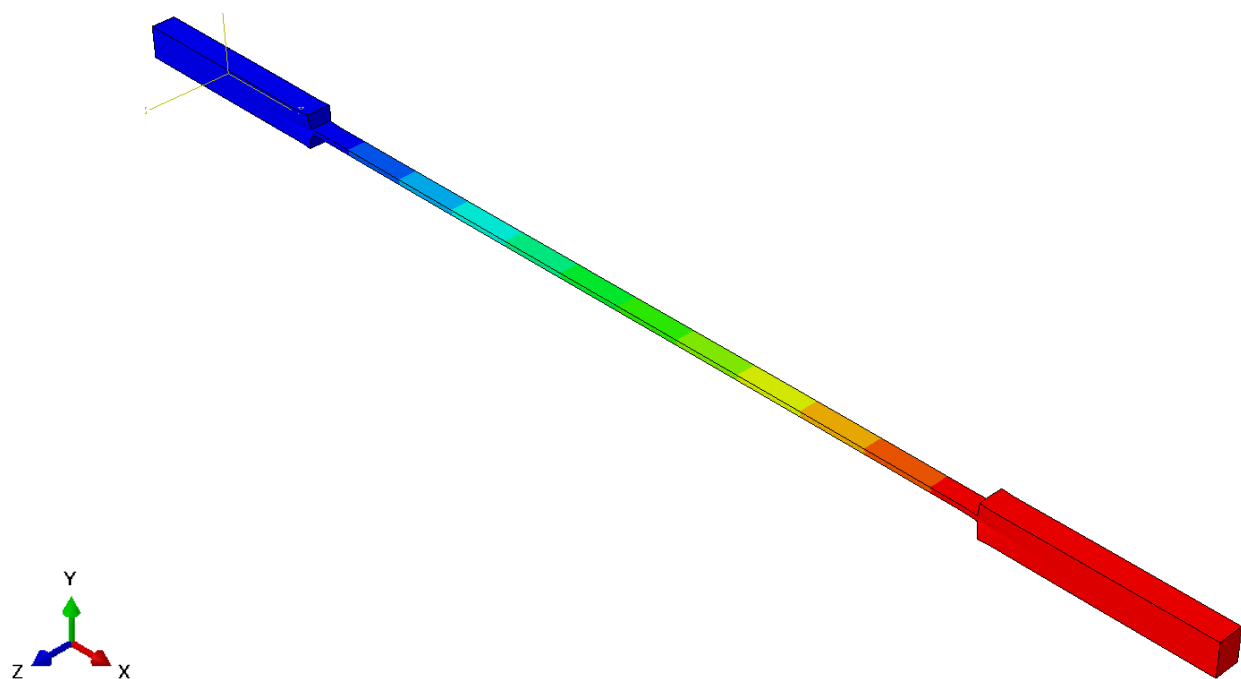
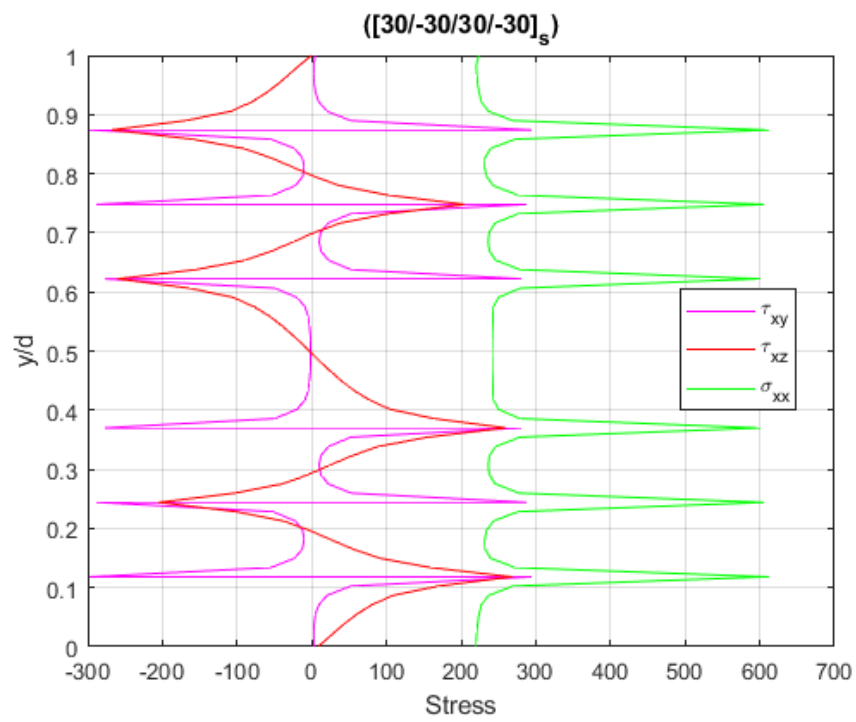
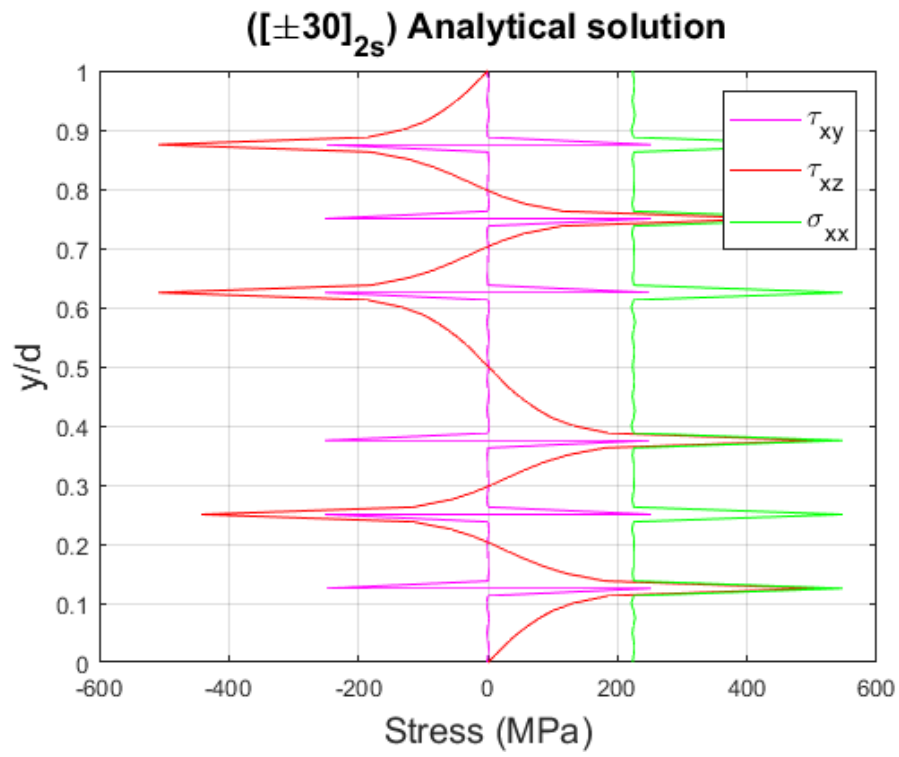
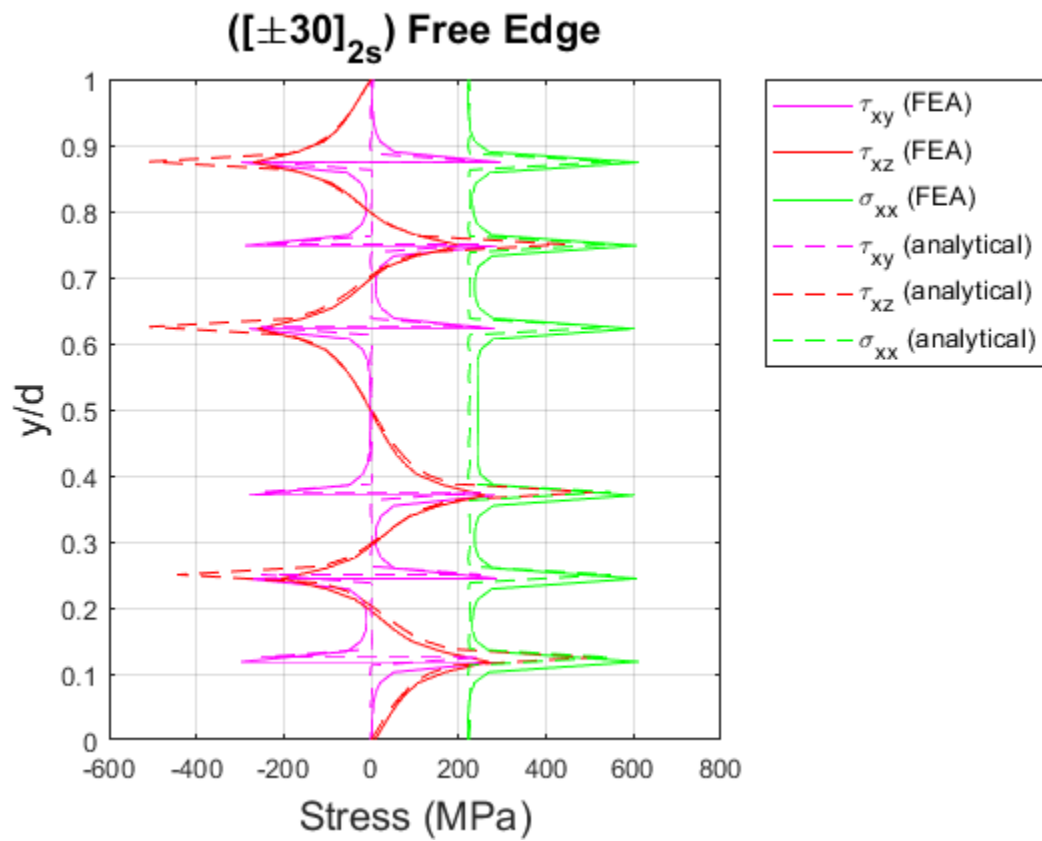


Figure 7.17: Contoured variation of axial displacement U_1 on the $[\pm 30]_{2s}$ laminate

7.5.1.2 Stresses across thickness at the free edge

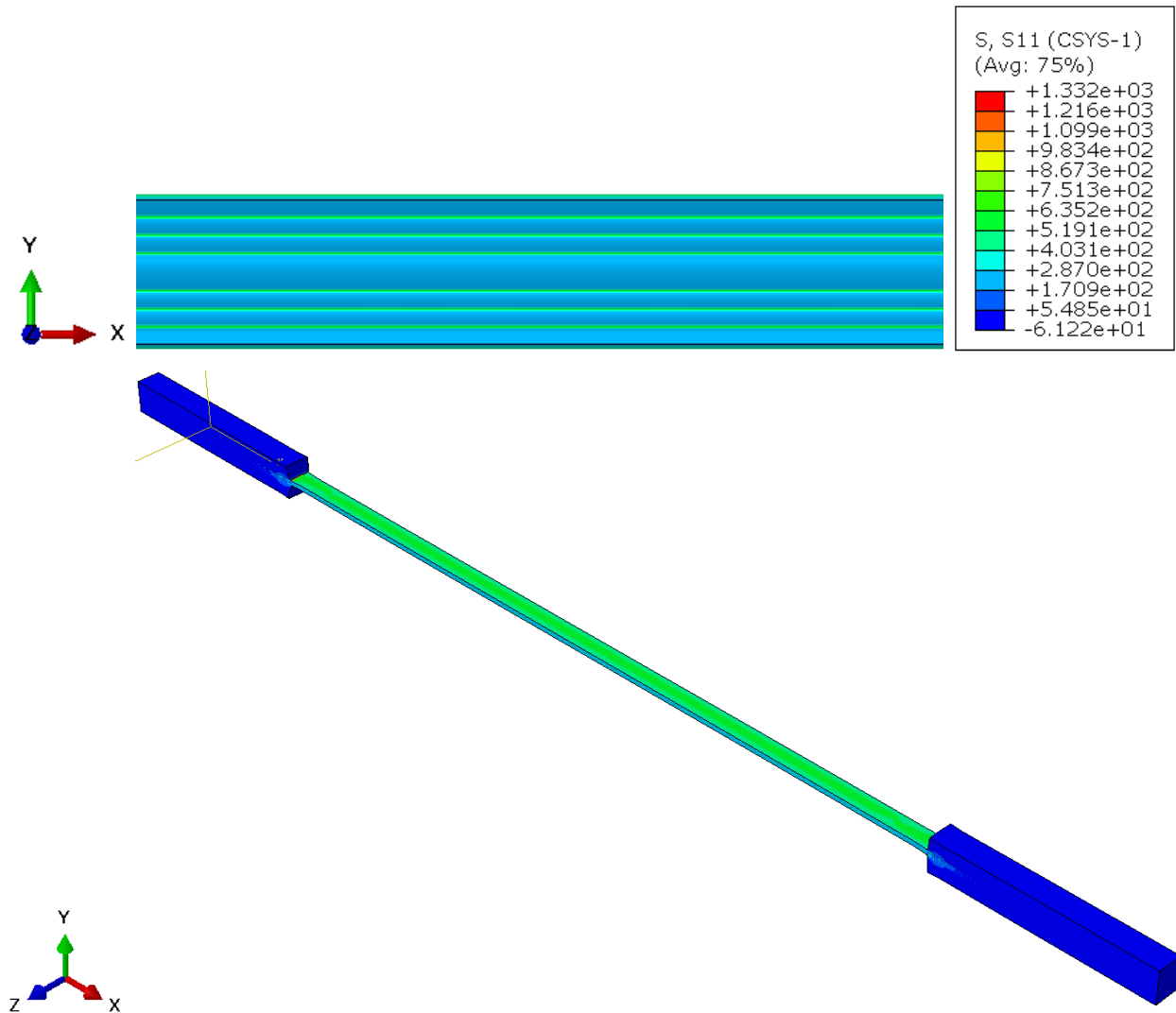
Figure 18 shows the variation of stresses across thickness at the free edge of $[\pm 30]_{2s}$ laminate. The stresses in plots from Abaqus simulation are in MPa. Figure 19 shows the contoured variation of these stresses on the laminate. All of these stresses reach their peak values at the interface between two plies where their orientation changes. The axial and in-plane shearing stresses remain almost constant throughout the thickness of each ply. The interlaminar shearing stress varies through the thickness of the ply and peaks at the interface. The shear stresses also reach 0 at the free surfaces on the top and bottom. The distribution of these stresses is also symmetric with respect to the mid-plane of the laminate. The peak values of the stresses also remain constant as the fiber orientations remain the same with respect to the longitudinal axis. Figure 18c shows the superimposition of the analytical and finite element solution and it can be seen that the peak value of τ_{xz} is more in the analytical solution and this is due to the mathematical singularity in the solution at the interfaces. As the number of Fourier terms is increased the magnitude of this stress increases. The FE solution also approaches this value when the number of terms is increased across the thickness of each ply.





(c) Superimposition of the Analytical and FE solution

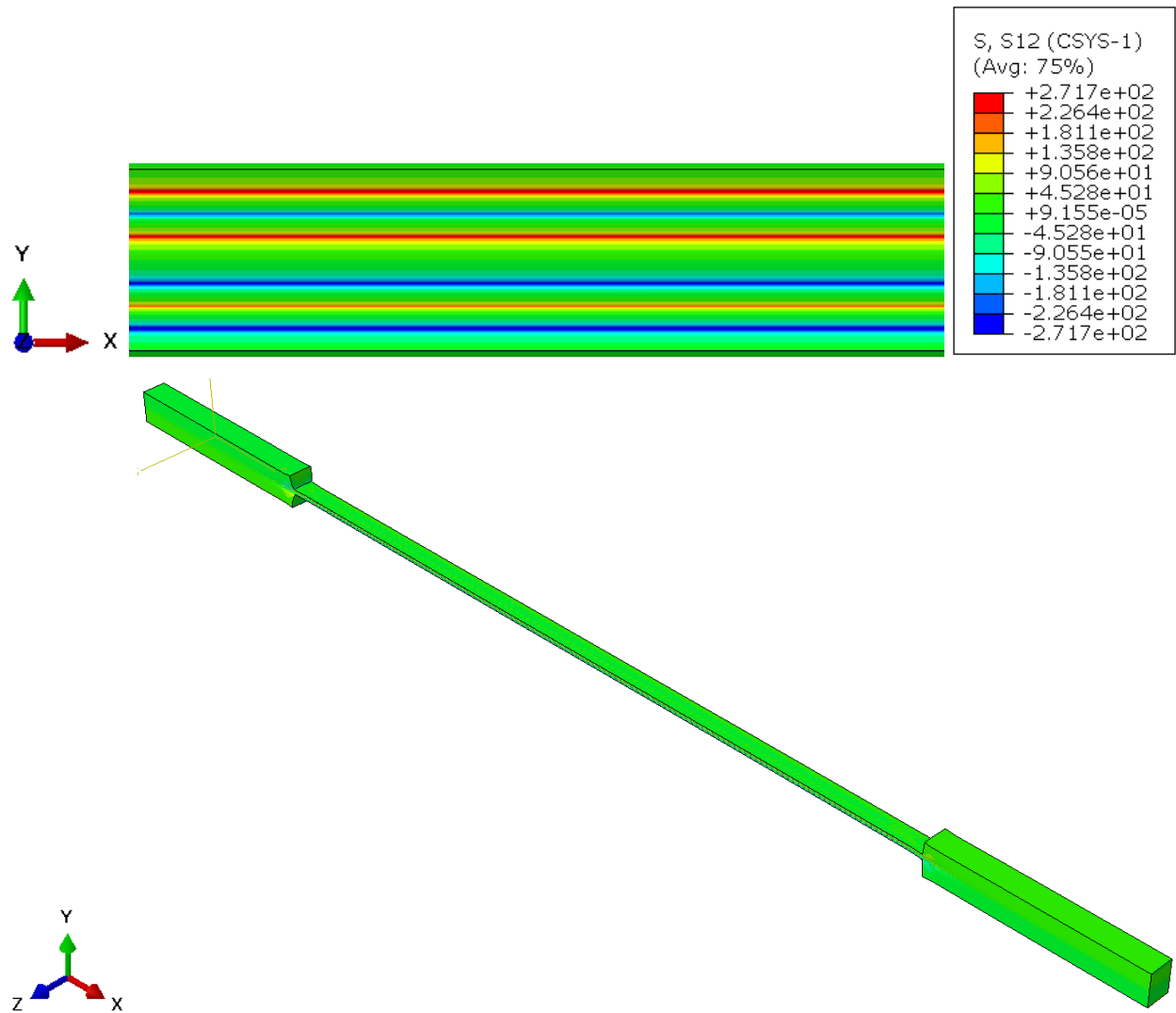
Figure 7.18: Variation of stresses across thickness at the free edge of $[\pm 30]_{2s}$ laminate



(a) Axial stress σ_{xx}

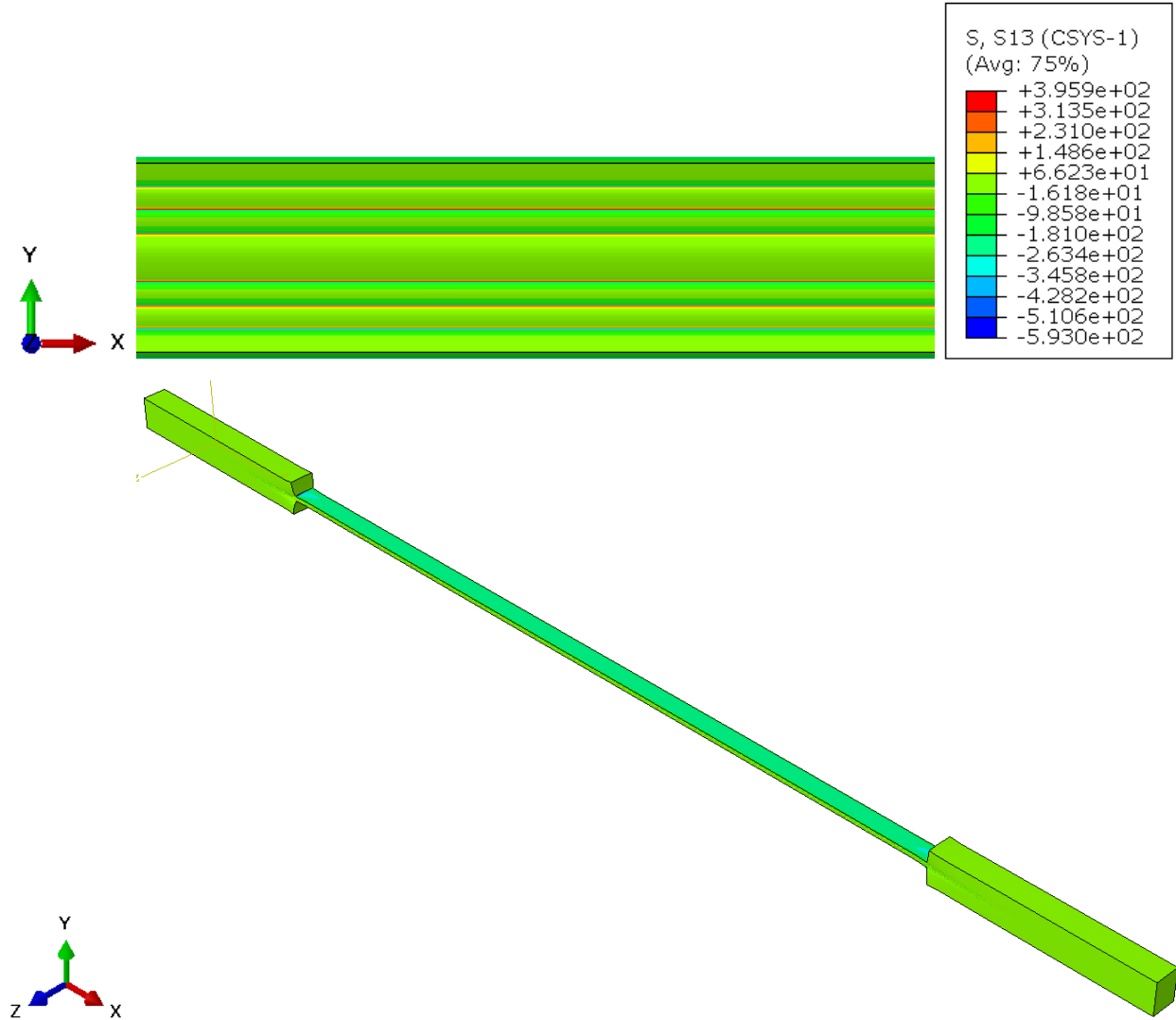
Figure 7.19: Contoured variation of stresses on $[\pm 30]_{2s}$ laminate

Figure 7.19 continued



(b) Interlaminar shearing stress τ_{xz}

Figure 7.19 continued



(c) In-plane shearing stress τ_{xy}

7.5.1.2.1 Variation of normal and transverse stresses through thickness

Figure 20 shows the variation of normal and transverse stresses across the thickness of $[\pm 30]_{2s}$ laminate. The stresses reach zero at the free surfaces on the top and bottom of the laminate. The transverse and out of plane shear stresses are zero across the thickness of the laminate. The value of σ_{zz} peaks at the center of the laminate. Figure 21 shows the contour variation of these stresses at the edge and along the length of the laminate. The analytical solution assumes that the peel stress σ_{zz} is zero across thickness and hence, there is no validation analytical plot for this case.

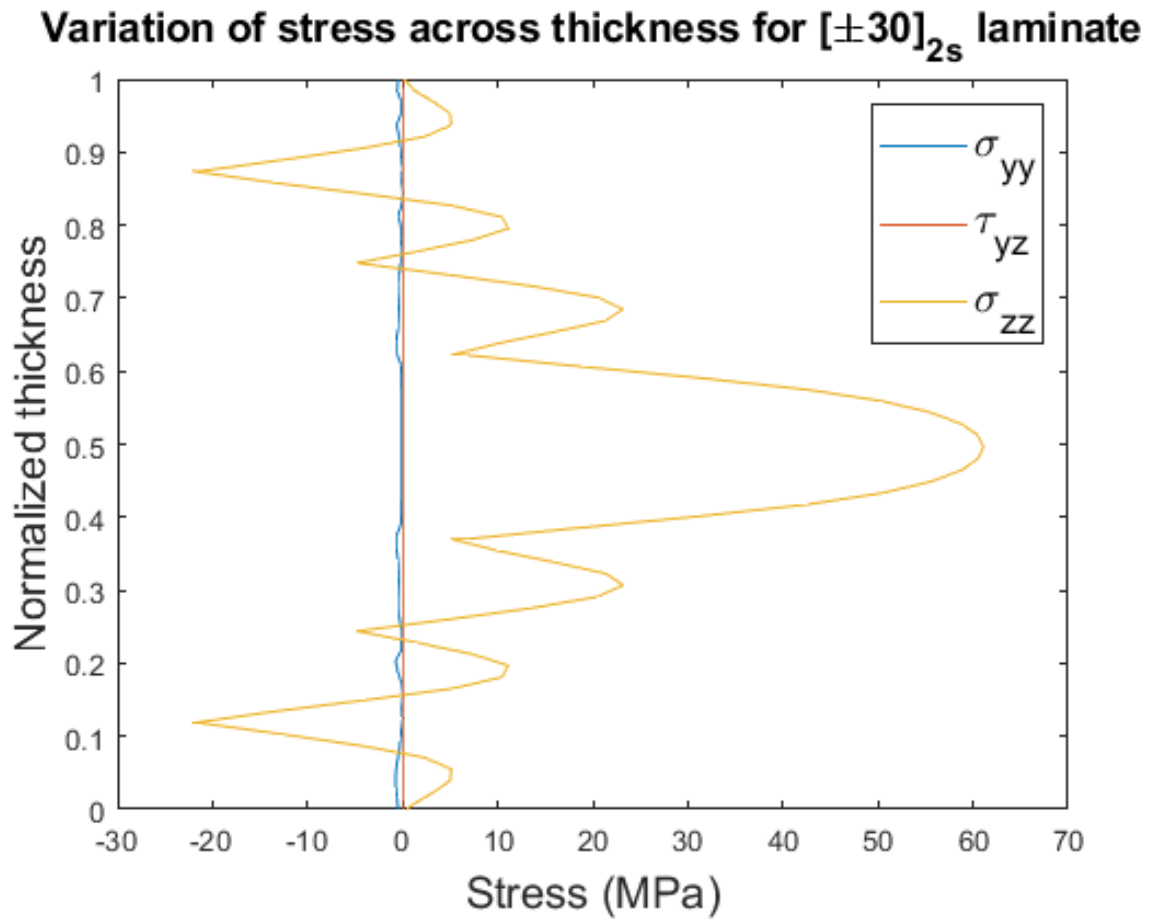
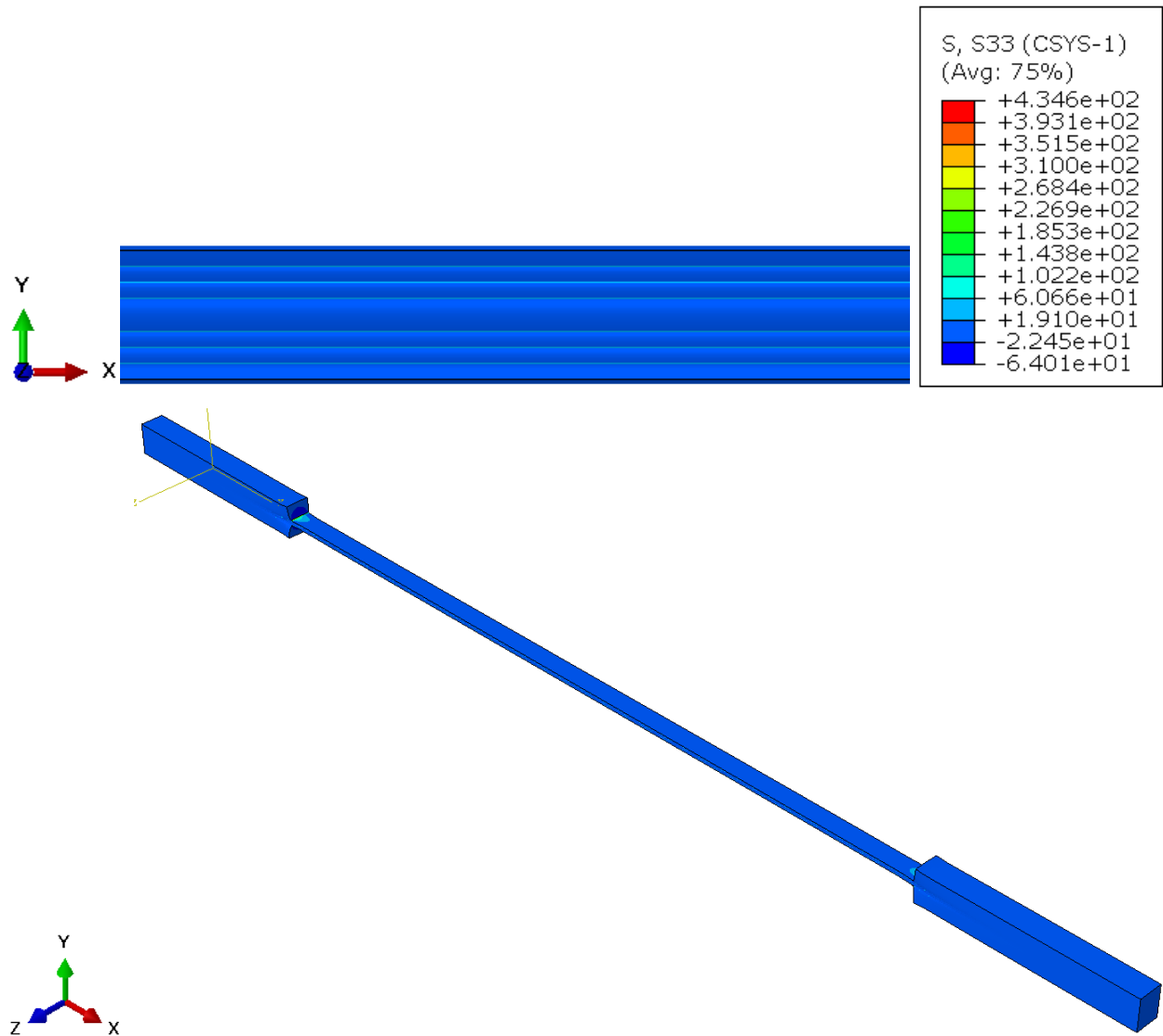


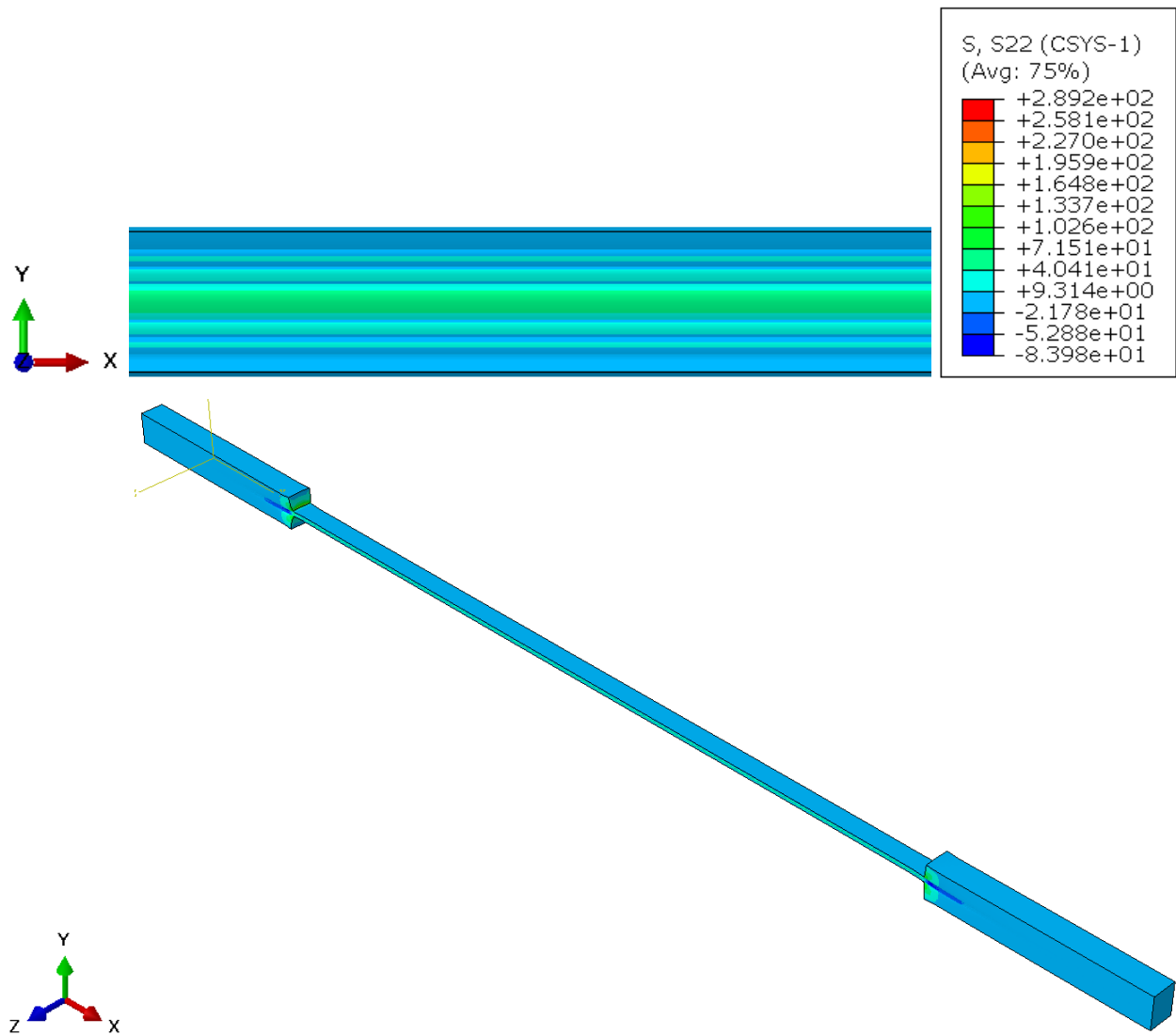
Figure 7.20: Variation of normal and transverse components of stresses across thickness at the free edge of $[\pm 30]_{2s}$ laminate



(a) Transverse stress σ_{yy}

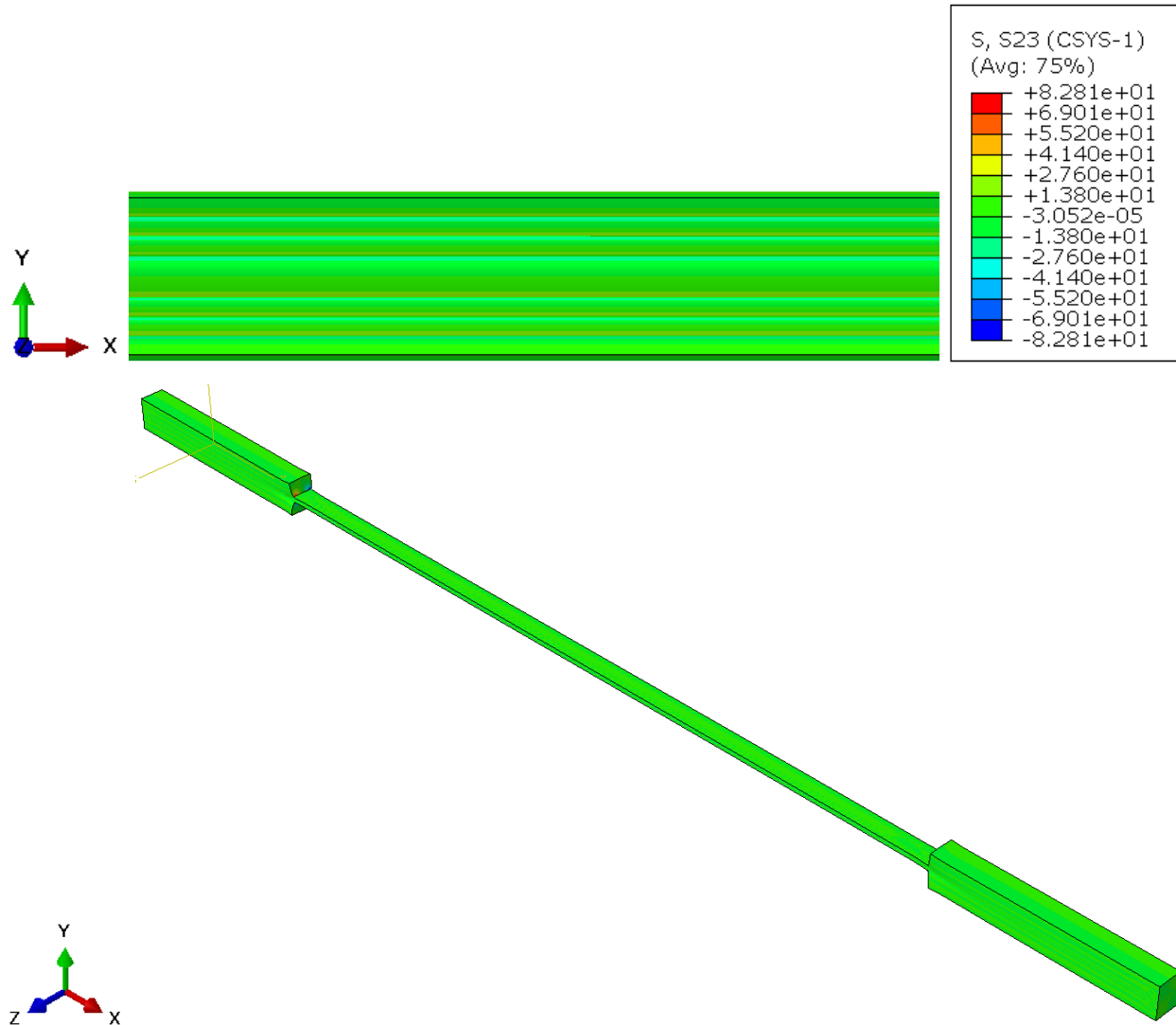
Figure 7.21: Contour variation of normal and transverse components of stresses across thickness at the free edge of $[\pm 30]_{2s}$ laminate

Figure 7.21 continued



(b) Normal stress σ_{zz}

Figure 7.21 continued



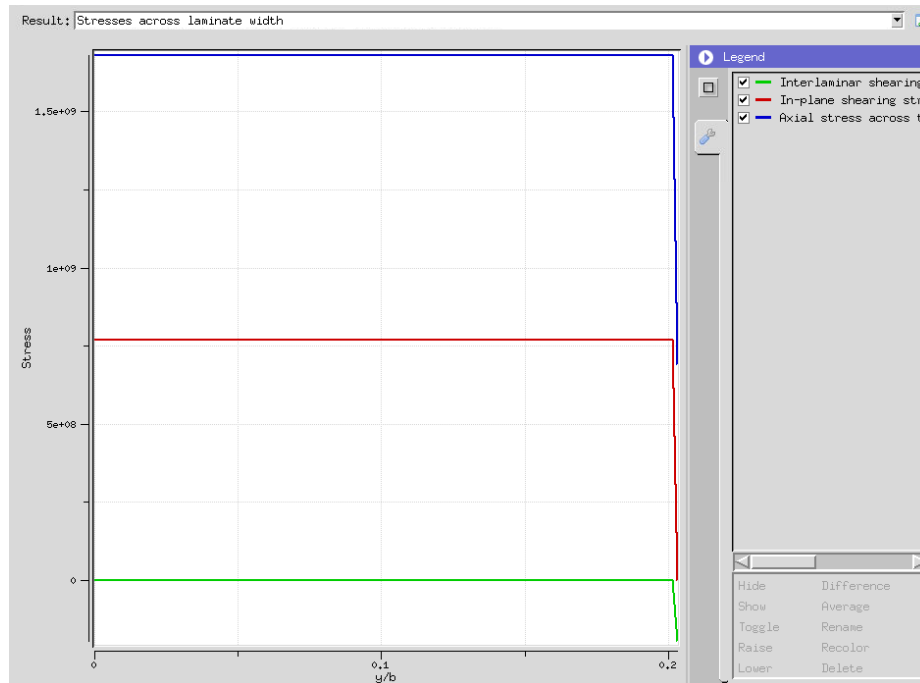
(c) In-plane shearing stress τ_{yz}

7.5.1.3 Stresses across width

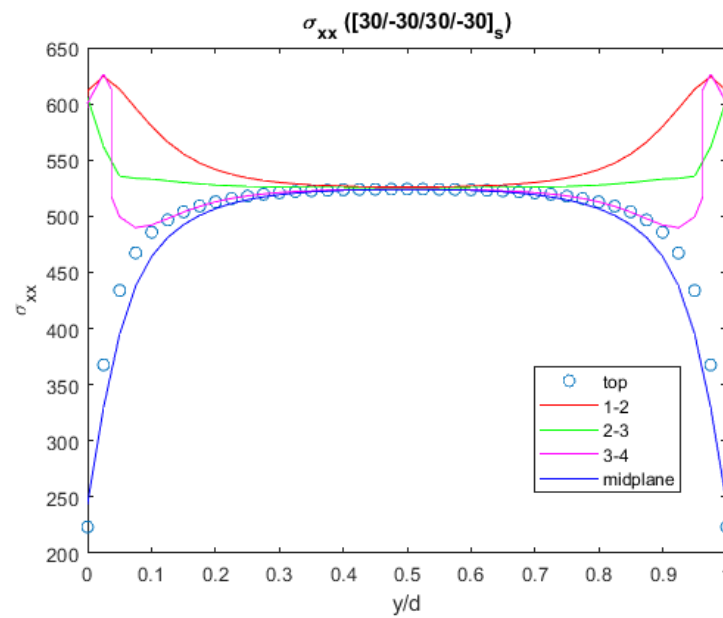
Figure 22 shows the variation of stresses across the width of the specimen from the midplane to the edge of the sample. In the analytical plot, the blue, red and green plots in the analytical solution represent the axial, in-plane shearing and interlaminar shearing stresses respectively. In the Abaqus simulation results, the plots for τ_{xy} are taken from the values of stresses at the middle of each ply and the plots for τ_{xz} and σ_{xx} are plotted by considering the values at the interface between the plies.

In the legends of these plots, the plies are numbered from bottom to top, that is, 1 is the bottom-most ply with an orientation of 30^0 . 2, 3 and 4 represent the subsequent bottom-up plies with orientations -30^0 , 30^0 and -30^0 respectively. The stresses were also plotted at the mid-plane of the laminate and on its top surface. The X-axis of these plots denotes the normalized width of the laminate. It can be clearly seen that there is a boundary layer at the edges before the stresses reach a constant value at the center. This is a consequence of the free-edge effect on the laminate. The sign of the stresses also reverses for the subsequent plies and interfaces.

Figure 23 shows the contour plot of the variation of these stresses across the width of the laminate especially at the free-edge covering the boundary layer.



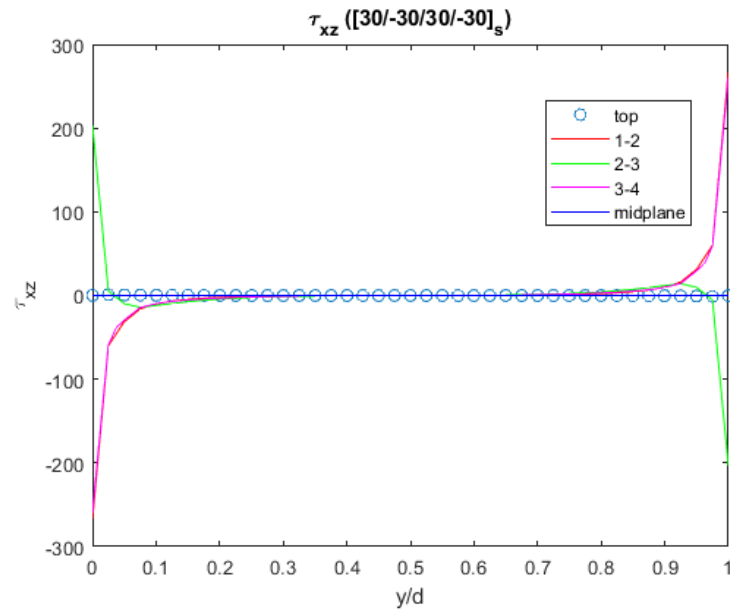
(a) Analytical solution



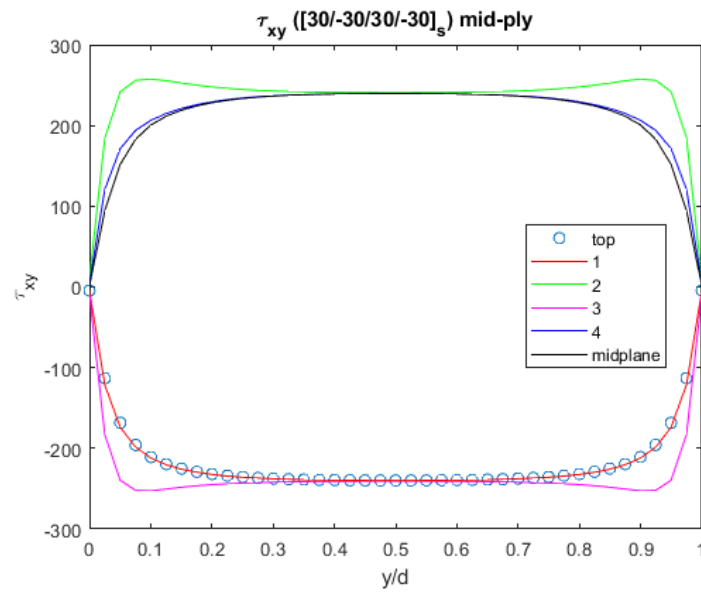
(i) Axial stress σ_{xx}

Figure 7.22: Variation of stresses across the width on $[\pm 30]_{2s}$ laminate

Figure 7.22 continued

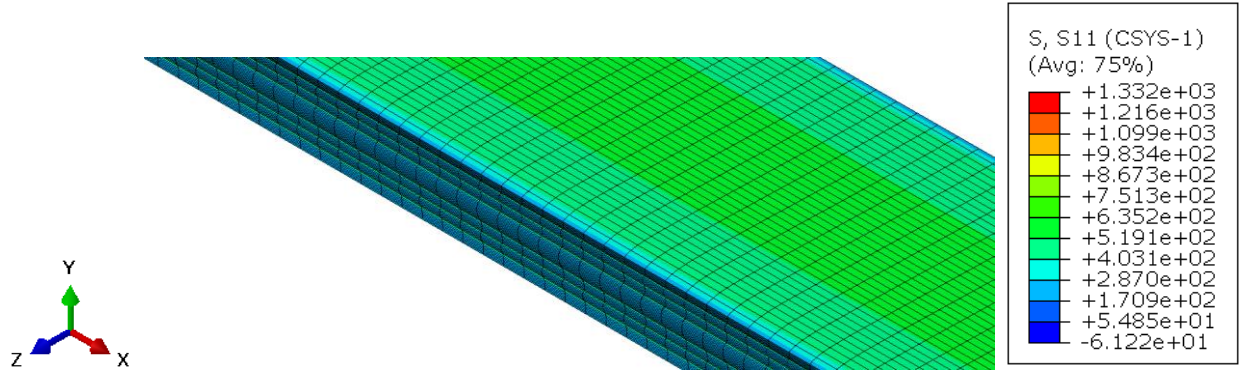


(ii) Interlaminar shearing stress τ_{xz}

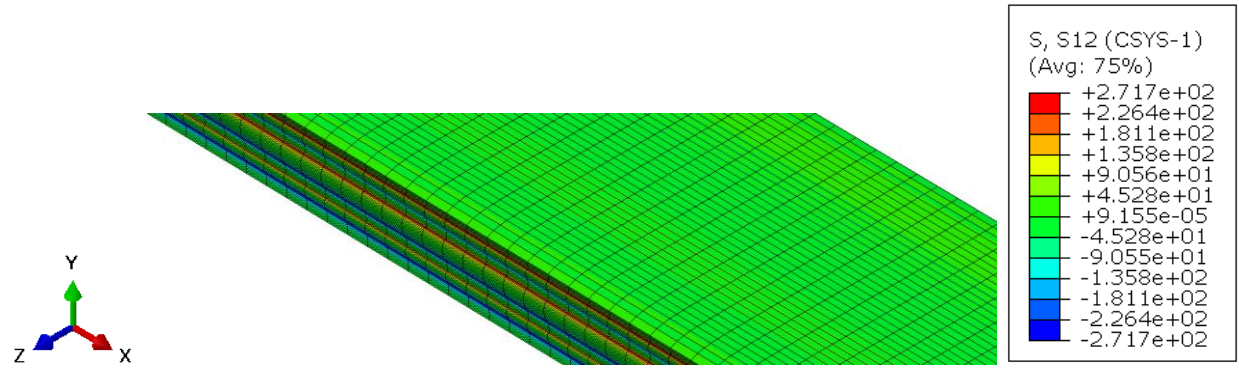


(iii) In-plane shearing stress τ_{xy}

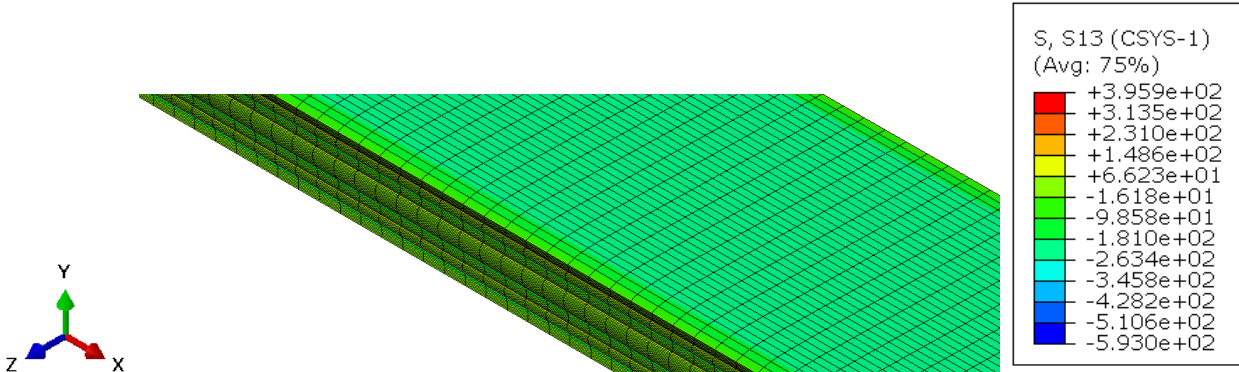
(b) Abaqus simulation result (Stresses in MPa)



(i) Axial stress σ_{xx}



(ii) Interlaminar shearing stress τ_{xz}



(iii) In-plane shearing stress τ_{xy}

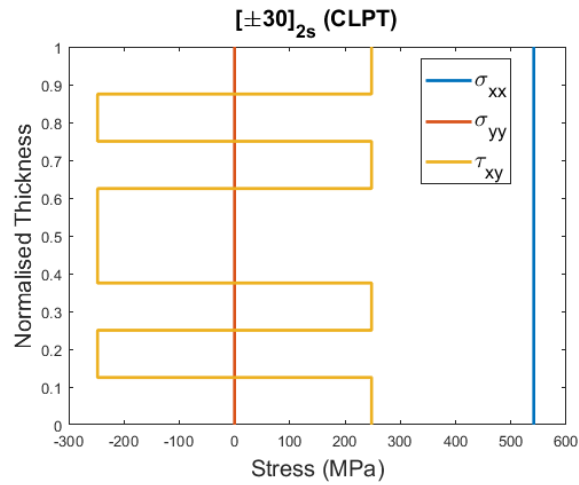
Figure 7.23: Contoured variation of stresses across the width and at the edge of $[\pm 30]_{2s}$ laminate

7.5.1.4 Stresses across thickness at the laminate center

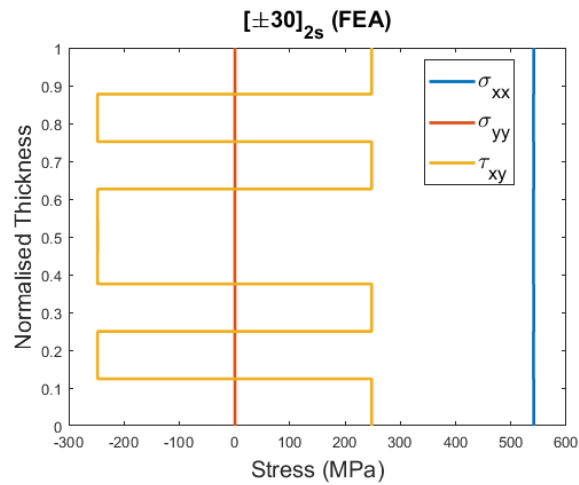
Figure 24 shows the variation of stresses across thickness at the laminate center. In the analytical plots, the blue, red and green plots represent the axial, in-plane shearing and interlaminar shearing stresses respectively. The axial stress is constant across the thickness and the interlaminar shearing

stress is zero throughout the laminate and the in-plane shearing stress has an alternating change in sign across thickness as the sign of the ply reverses.

Figure 25 shows the contour variation of these stresses across the thickness of the laminate at the center.

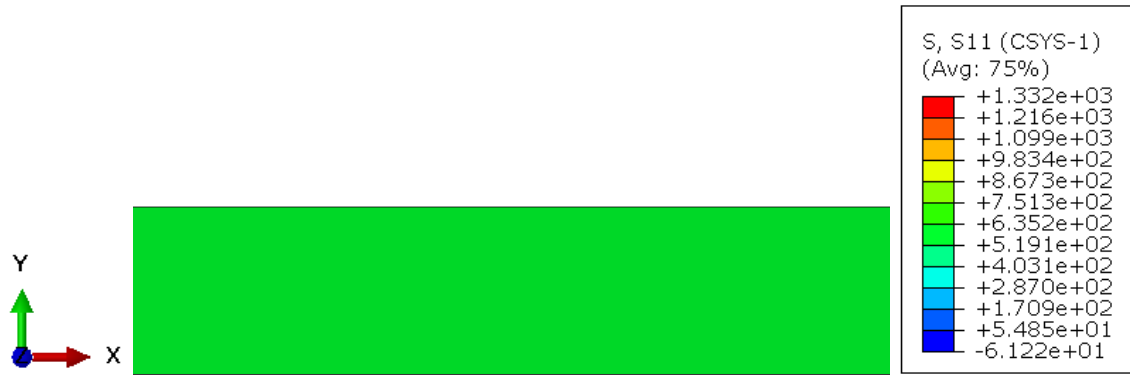


(a) Analytical solution



(b) Abaqus simulation result (Stresses in MPa)

Figure 7.24: Variation of stresses across thickness at the center of $[\pm 30]_{2s}$ laminate



(i) Axial stress σ_{xx}



(ii) Interlaminar shearing stress τ_{xz}

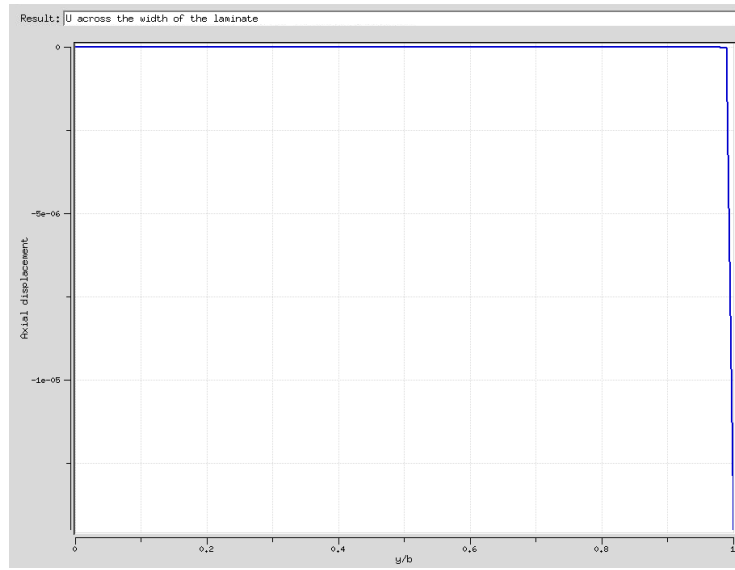


(iii) In-plane shearing stress τ_{xy}

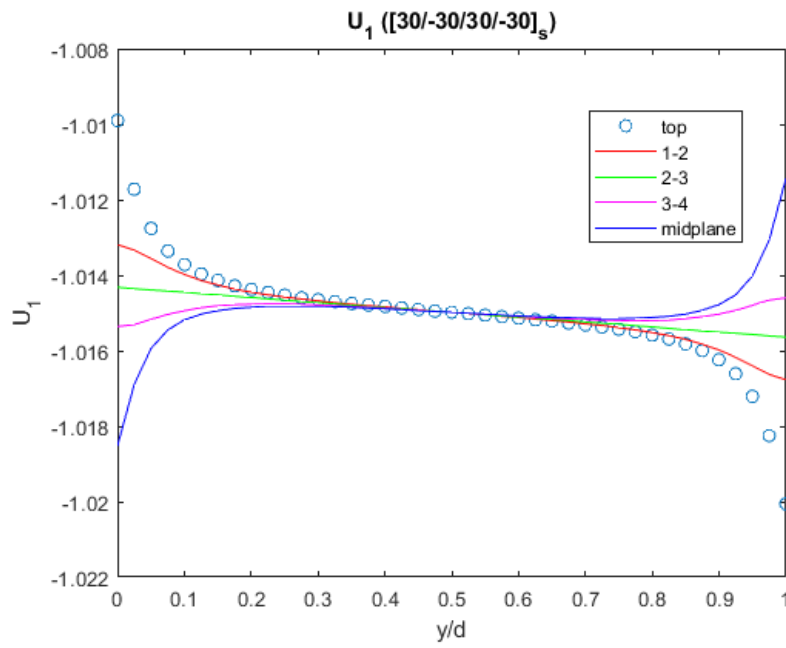
Figure 7.25: Contoured variation of stresses at the center of $[\pm 30]_{2s}$ laminate

7.5.1.5 Axial displacement across the width

Figure 26 shows the variation of axial displacement across the width of $[\pm 30]_{2s}$ laminate. In the plots obtained from the simulation results, the stresses are plotted at the interfaces of the plies and the legends are numbered from bottom to top, that is, 1 is the bottom-most ply with an orientation of 30° . 2, 3 and 4 represent the subsequent bottom-up plies with orientations -30° , 30° and -30° respectively. The stresses were also plotted at the mid-plane of the laminate and on its top surface. There is a boundary layer at the edges of the laminate and hence, the displacement reaches a constant value only at the center of laminate.



(a) Analytical solution



(b) Abaqus simulation result

Figure 7.26: Variation of axial displacement U_1 across width of $[\pm 30]_{2s}$ laminate

7.5.2 $[\pm 30/90_2]_s$ laminate

7.5.2.1 *Axial displacement across thickness at the free edge*

Figure 27 shows the plots of variation of axial displacement across the thickness from the tensile simulation of the $[\pm 30/90_2]_s$ laminate. The laminate has maximum displacement where there are -30° plies. The -30° plies also have greater displacement than the 90° and 30° plies that are present through the thickness of the laminate. This was measured in the middle of the axial length of the laminate. Figure 28 shows the contoured variation of the axial displacement on the entire laminate and the variation across the thickness of the laminate at the gage length. There is no analytical solution available for this laminate as it is available only for the $[\pm\theta]_s$ case.

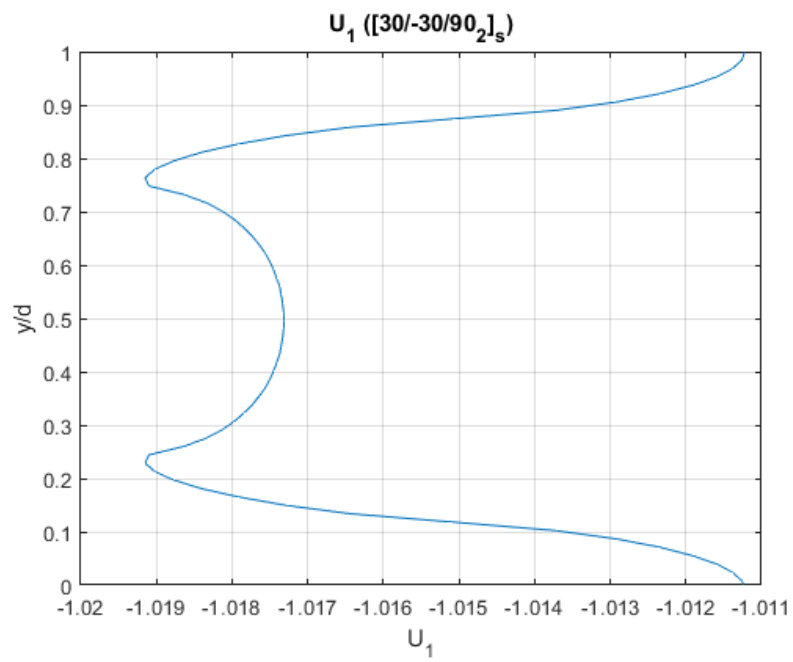
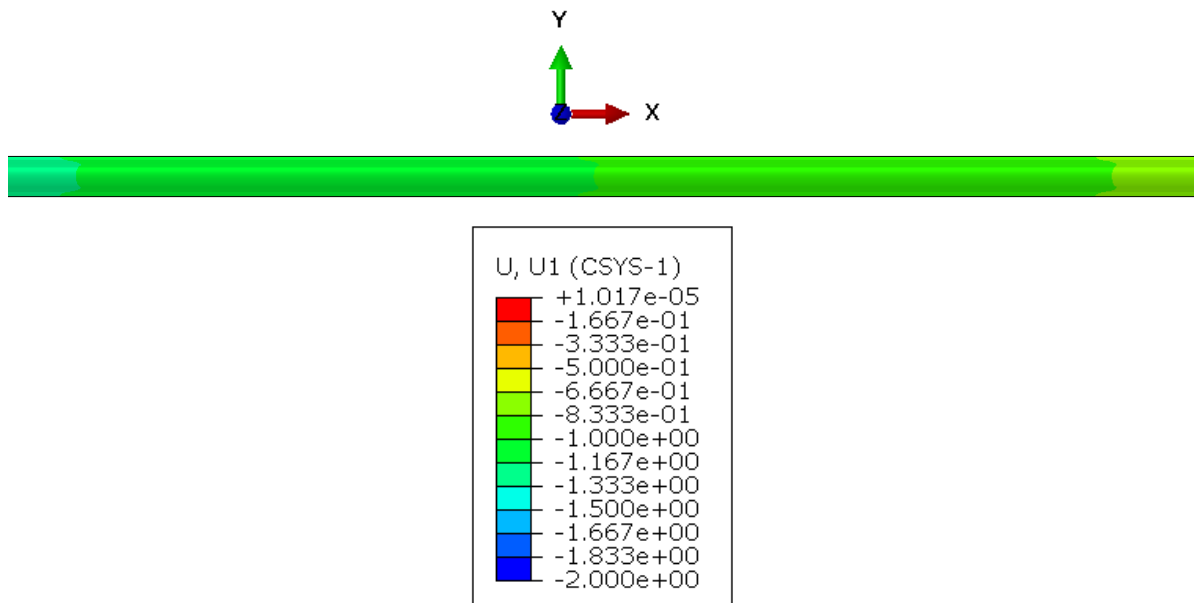


Figure 7.27: Variation of axial displacement U_1 across thickness at free edge of $[\pm 30/90_2]_s$ laminate



(a) Axial displacement at gage length

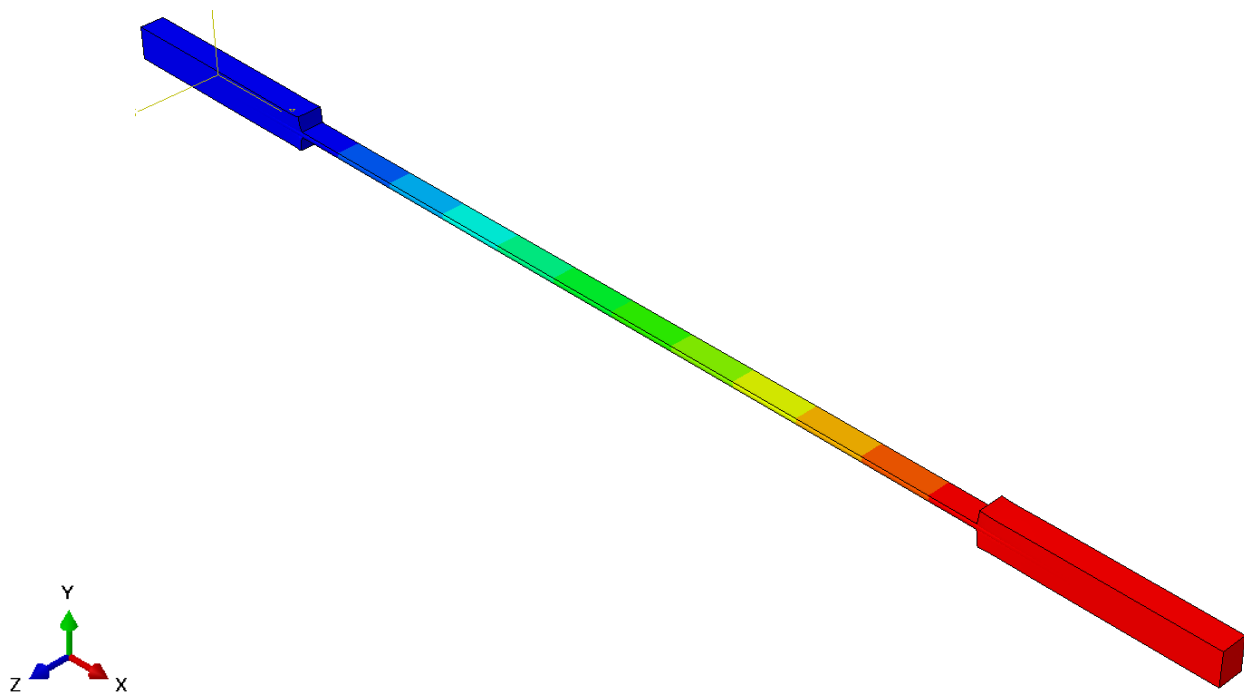


Figure 7.28: Contoured variation of axial displacement U_1 on the $[\pm 30/90_2]_s$ laminate

7.5.2.2 Stresses across thickness at the free edge

Figure 29 shows the variation of stresses across thickness at the free edge of $[\pm 30/90_2]_s$ laminate. The stresses in plots from Abaqus simulation are in MPa. Figure 28 shows the contoured variation of these stresses on the laminate. All of these stresses reach their peak values at the interface between two plies where their orientation changes. The axial and in-plane shearing stresses remain almost constant throughout the thickness of each ply. The interlaminar shearing stress varies through the thickness of the ply and peaks at the interface. The shear stresses also reach 0 at the free surfaces on the top and bottom. The distribution of these stresses is also symmetric with respect to the mid-plane of the laminate. The peak value of stresses at the interface of $\pm 30^\circ$ laminae is more than the peak value of stresses at -30° and 90° laminae. There is no analytical solution available for this laminate as it is available only for the $[\pm\theta]_s$ case.

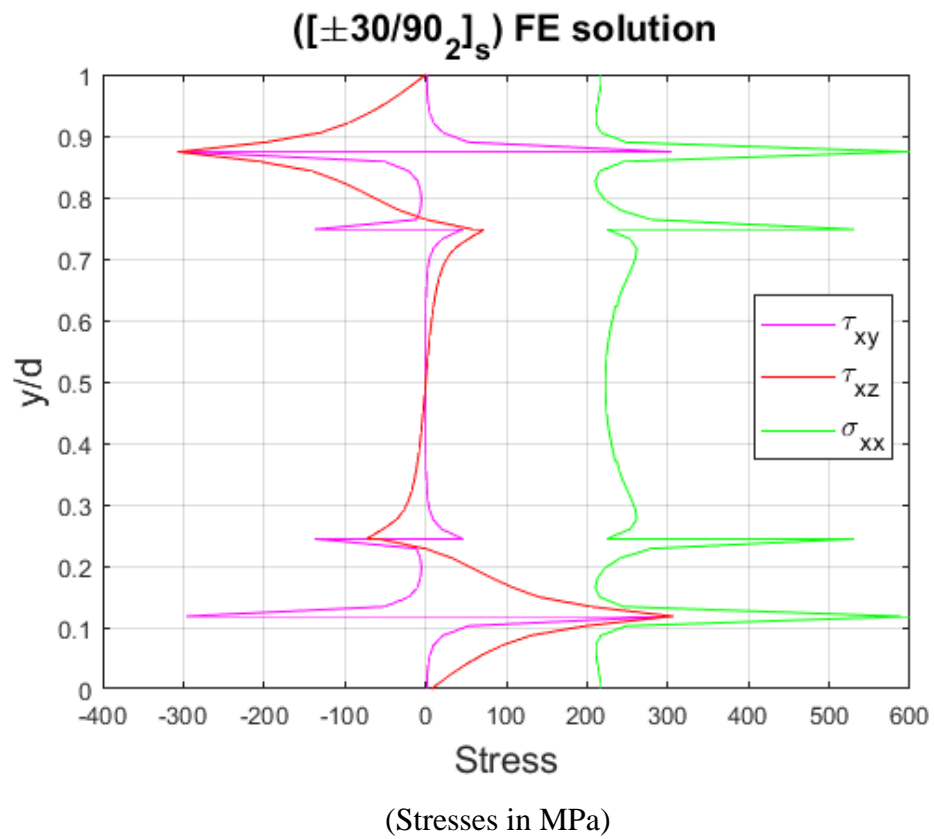
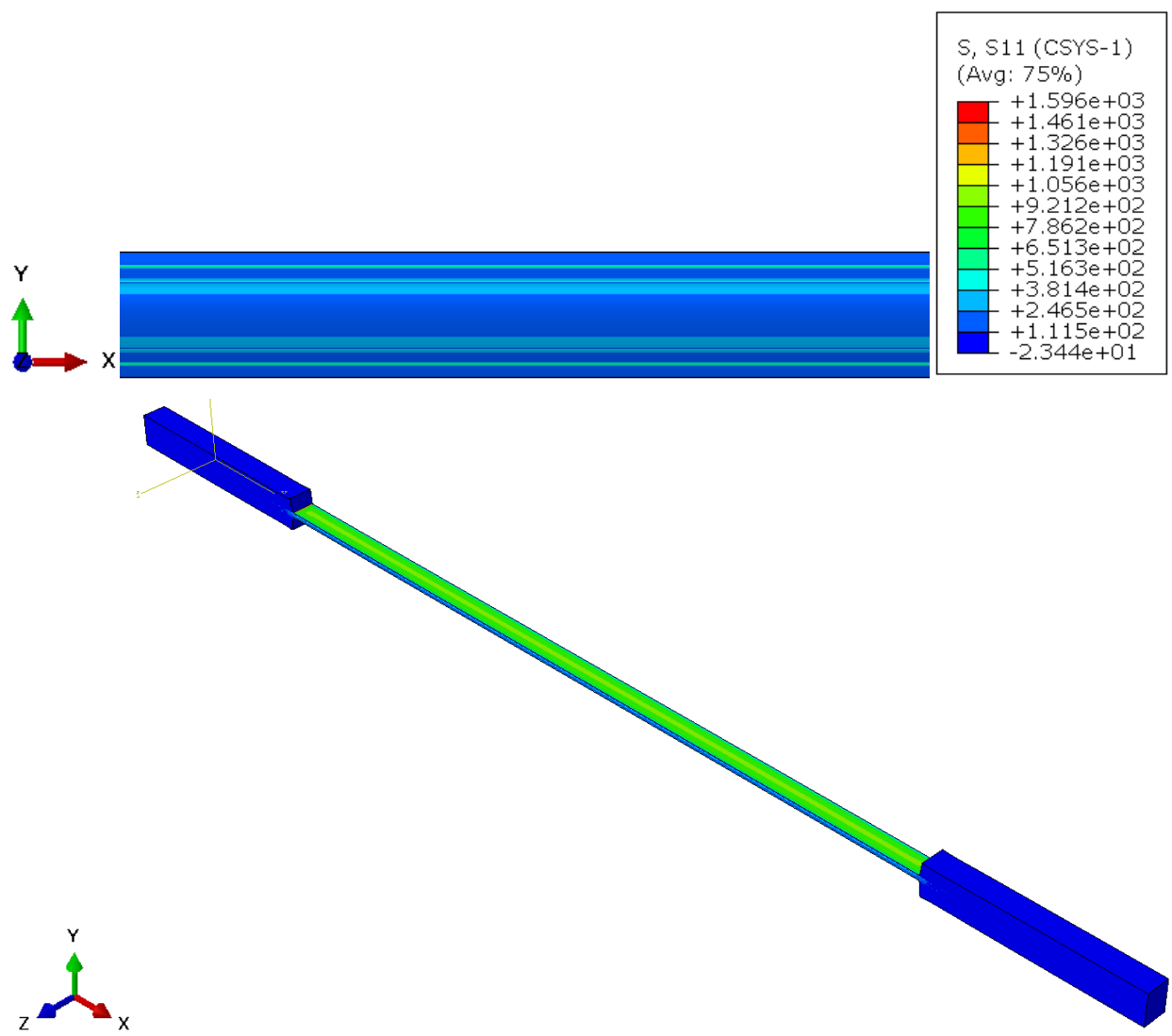


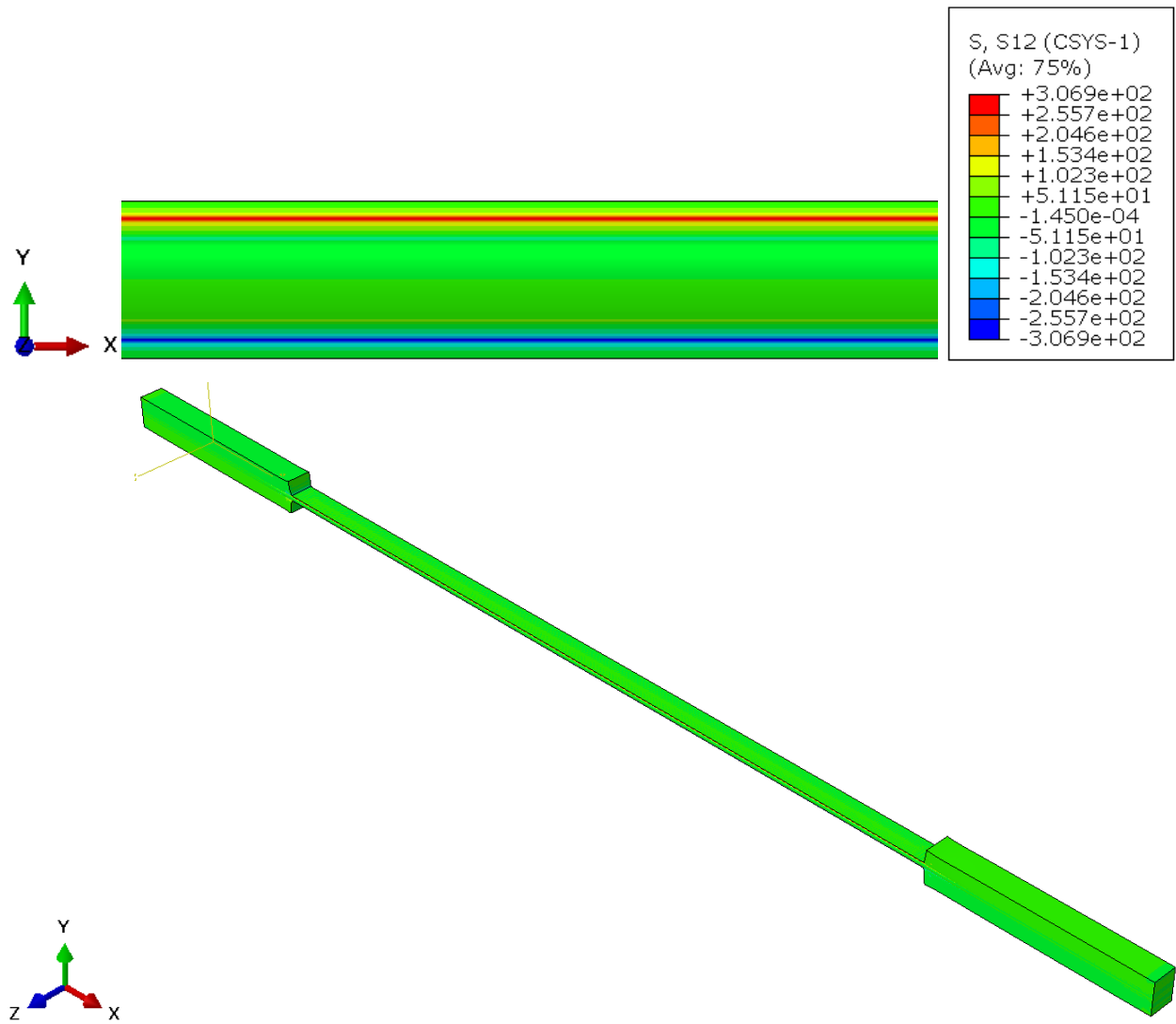
Figure 7.29: Variation of stresses across thickness at the free edge of $[\pm 30/90_2]_s$ laminate



(a) Axial stress σ_{xx}

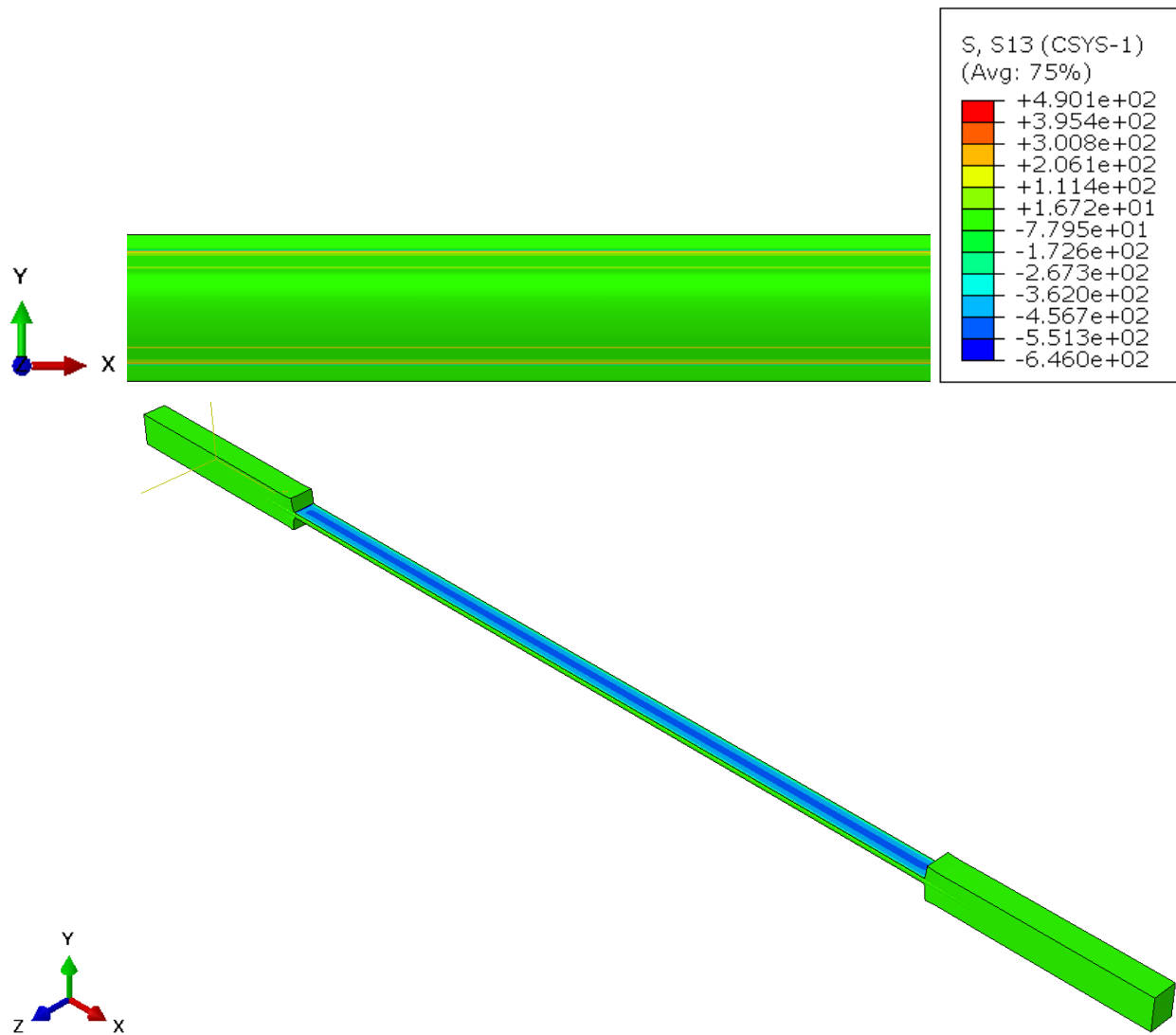
Figure 7.30: Contoured variation of stresses on $[\pm 30/90_2]_s$ laminate

Figure 7.30 continued



(b) Interlaminar shearing stress τ_{xz}

Figure 7.30 continued



(c) In-plane shearing stress τ_{xy}

7.5.2.2.1 Variation of normal and transverse stresses through thickness

Figure 31 shows the variation of normal and transverse stresses across the thickness of $[\pm 30/90_2]_s$ laminate. The stresses reach zero at the free surfaces on the top and bottom of the laminate. The value of σ_{zz} peaks at the interface between -30° and 90° plies. Hence, the peel stress is maximum at these locations. The shear stress τ_{yz} and σ_{yy} are zero across the thickness of the laminate.

Figure 32 shows the contour variation of these stresses at the edge and along the length of the laminate. The peak values of these stresses at the interface of plies are clearly visible in these images.

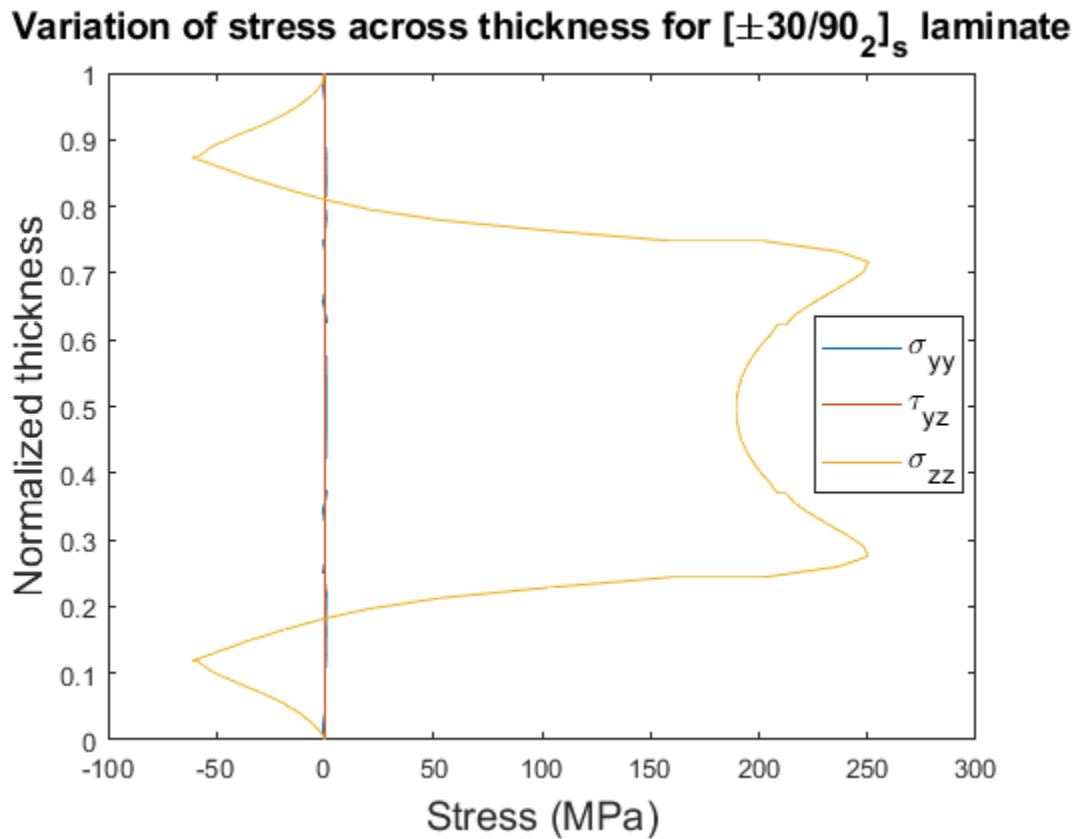


Figure 7.31: Variation of normal and transverse components of stresses across thickness at the free edge of $[\pm 30/90_2]_s$ laminate

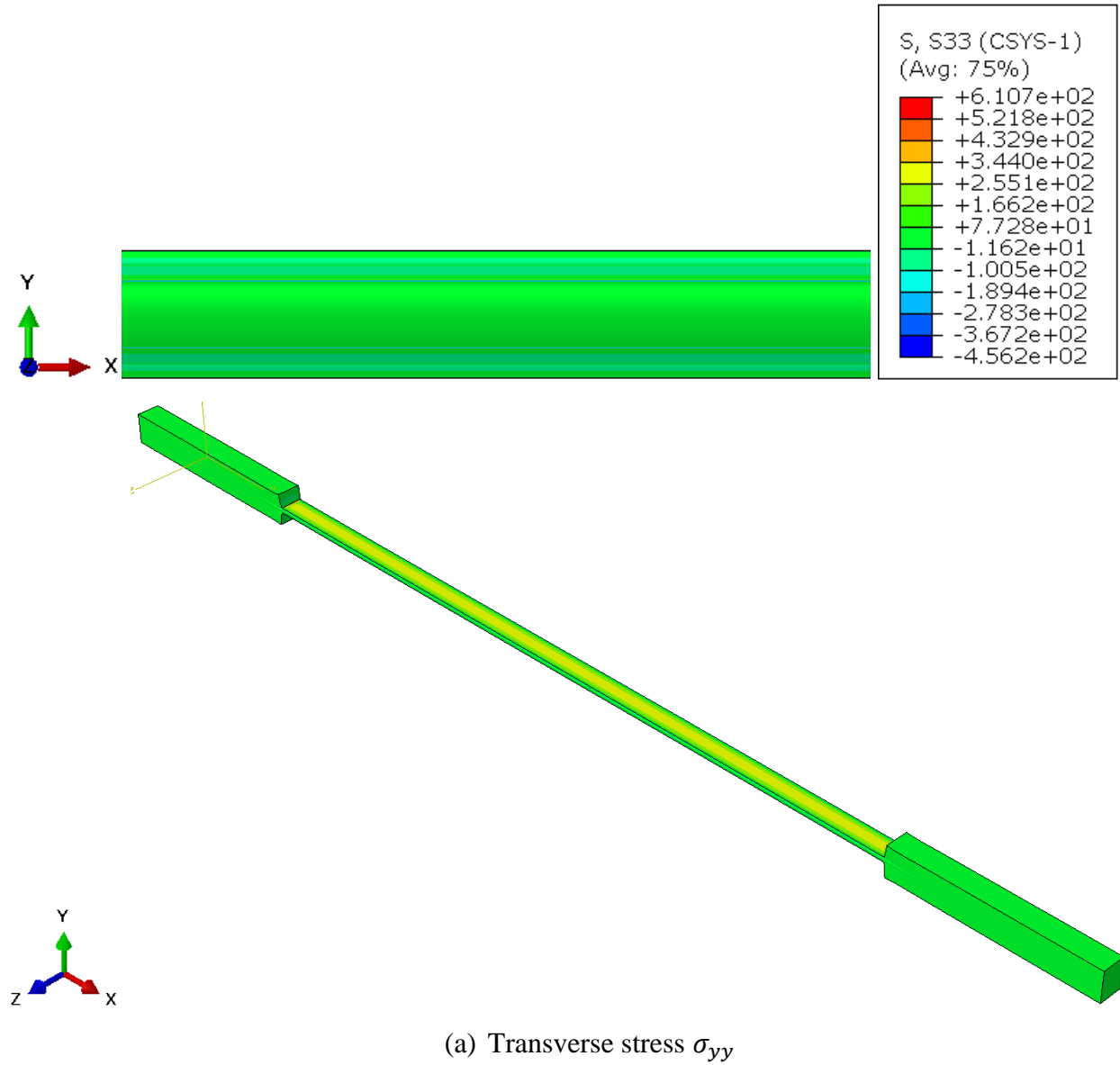
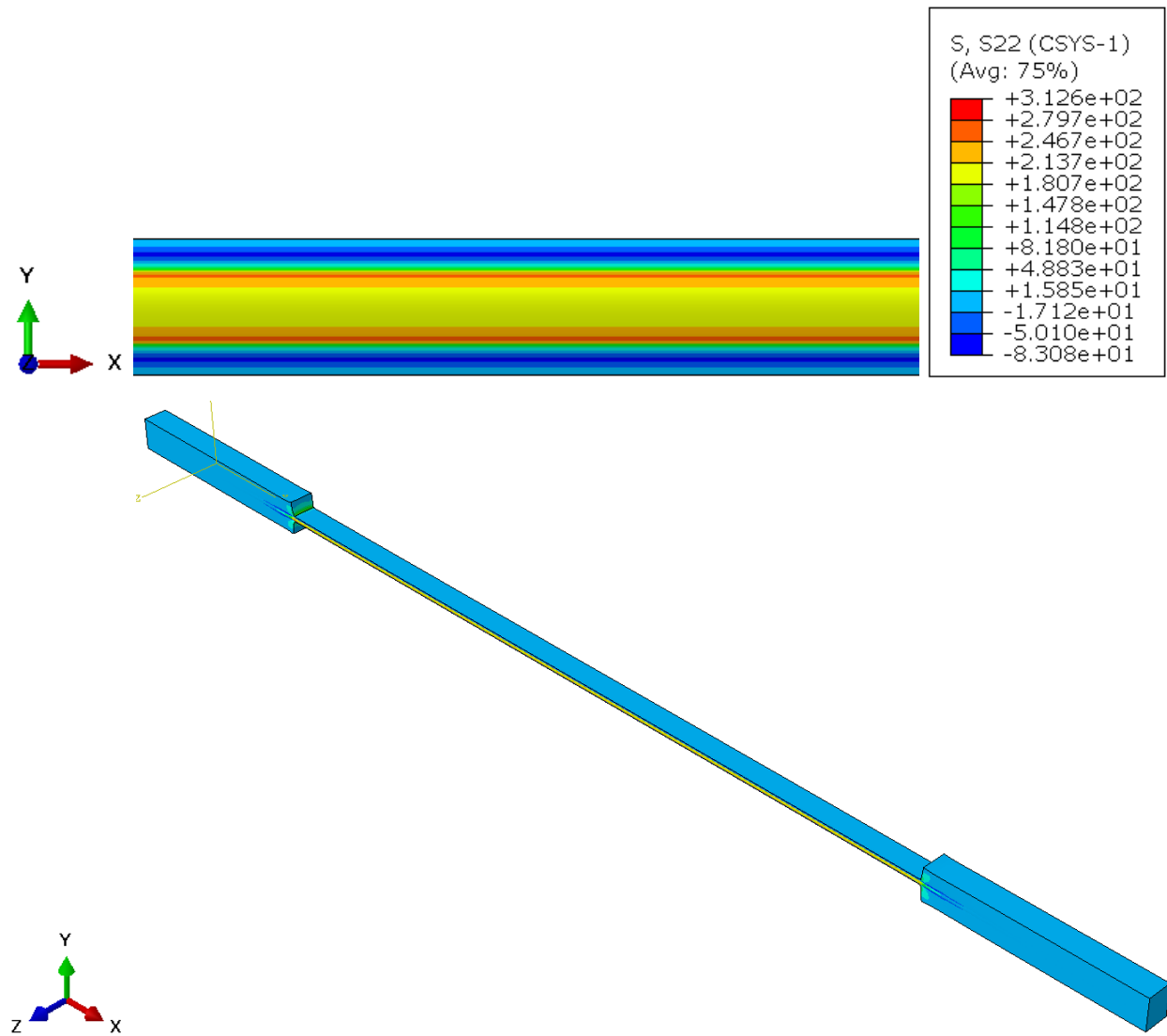


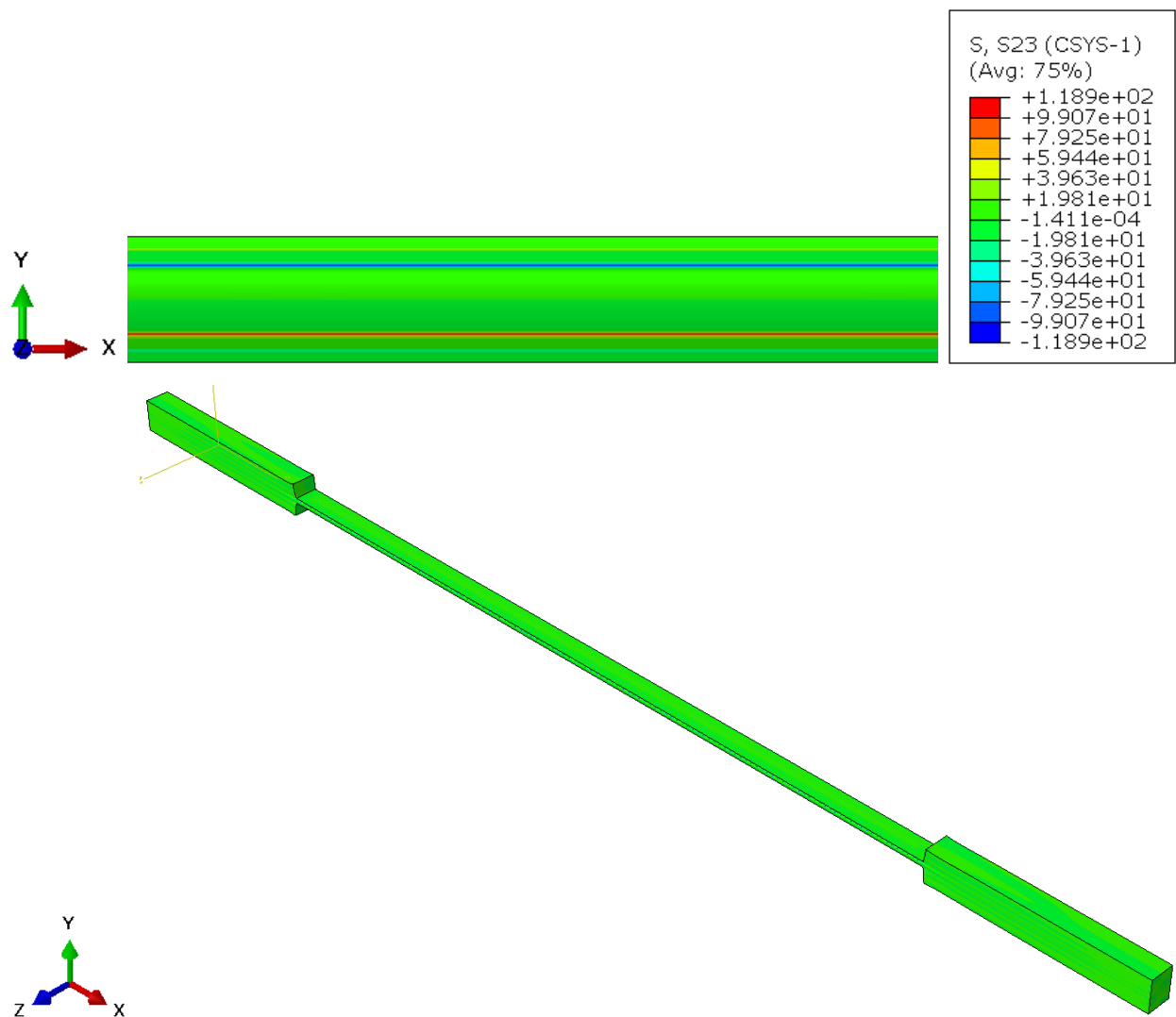
Figure 7.32: Contour variation of normal and transverse components of stresses across thickness at the free edge of $[\pm 30/90_2]_s$ laminate

Figure 7.32 continued



(b) Normal stress σ_{zz}

Figure 7.32 continued



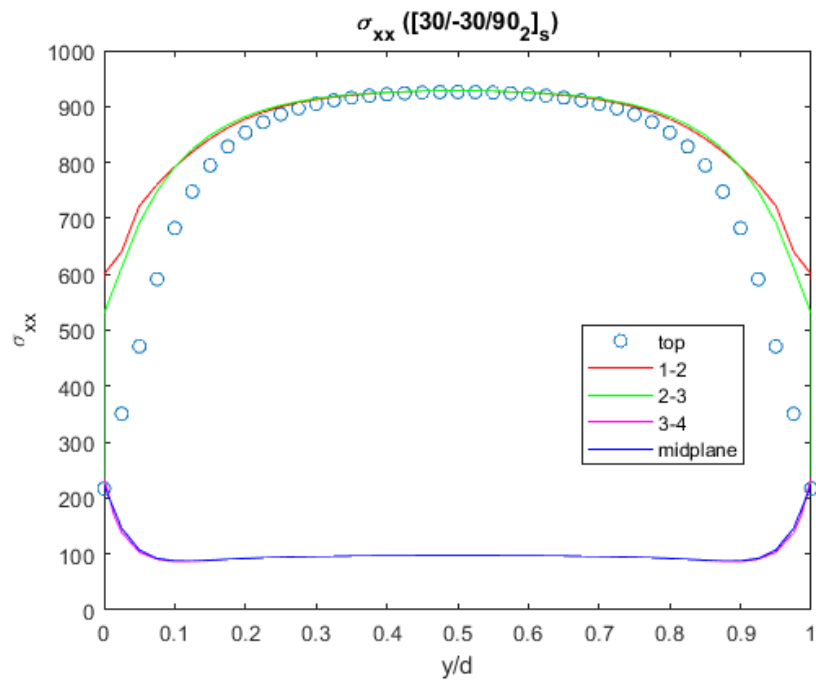
(c) In-plane shearing stress τ_{yz}

7.5.2.3 Stresses across width

Figure 33 shows the variation of stresses across the width of the specimen from the midplane to the edge of the sample. In the analytical plot, the blue, red and green plots in the analytical solution represent the axial, in-plane shearing and interlaminar shearing stresses respectively. In the Abaqus simulation results, the plots for τ_{xy} are taken from the values of stresses at the middle of each ply and the plots for τ_{xz} and σ_{xx} are plotted by considering the values at the interface between the plies.

In the legends of these plots, the plies are numbered from bottom to top, that is, 1 is the bottom-most ply with an orientation of 30° . 2, 3 and 4 represent the subsequent bottom-up plies with orientations -30° , 90° and 90° respectively. The stresses were also plotted at the mid-plane of the laminate and on its top surface. The X-axis of these plots denotes the normalized width of the laminate. It can be clearly seen that there is a boundary layer at the edges before the stresses reach a constant value at the center. This is a consequence of the free-edge effect on the laminate. The sign of the stresses also reverses for the subsequent plies and interfaces.

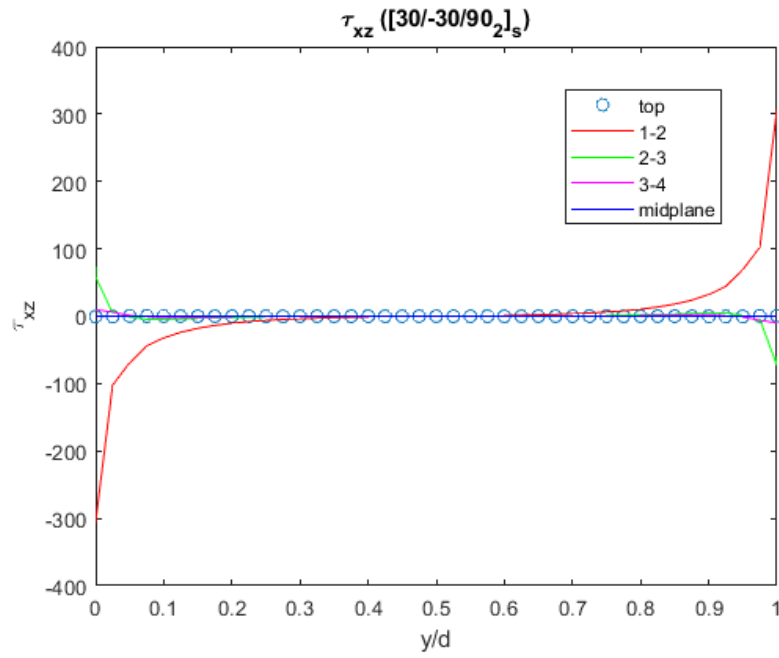
Figure 34 shows the contour plot of the variation of these stresses across the width of the laminate especially at the free-edge covering the boundary layer. There is no analytical solution available for this laminate as it is available only for the $[\pm\theta]_s$ case.



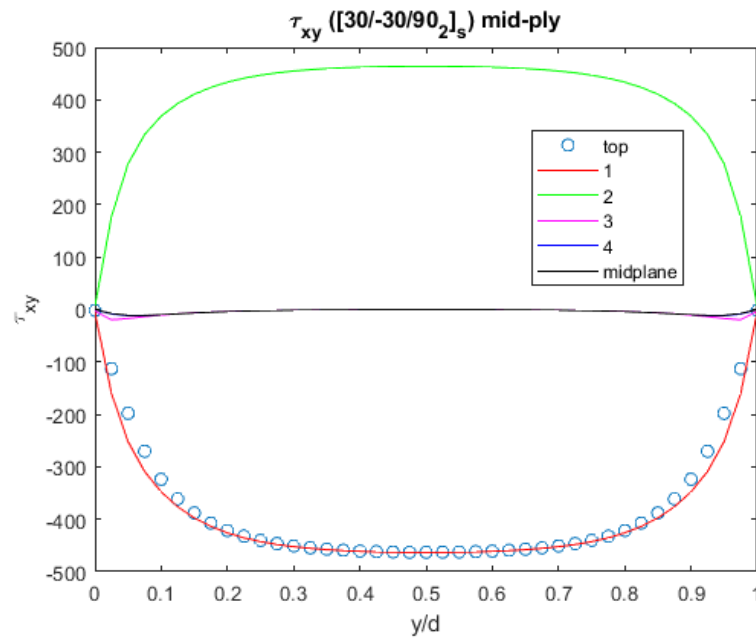
(i) Axial stress σ_{xx}

Figure 7.33: Variation of stresses across width on $[\pm 30/90_2]_s$ laminate

Figure 7.33 continued



(ii) Interlaminar shearing stress τ_{xz}



(iii) In-plane shearing stress τ_{xy}

(Stresses in MPa)

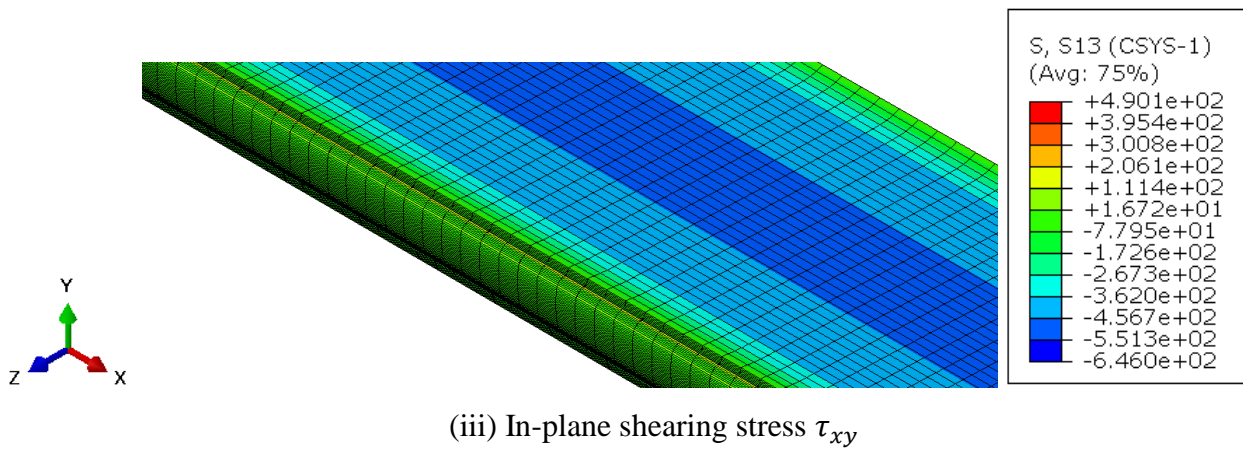
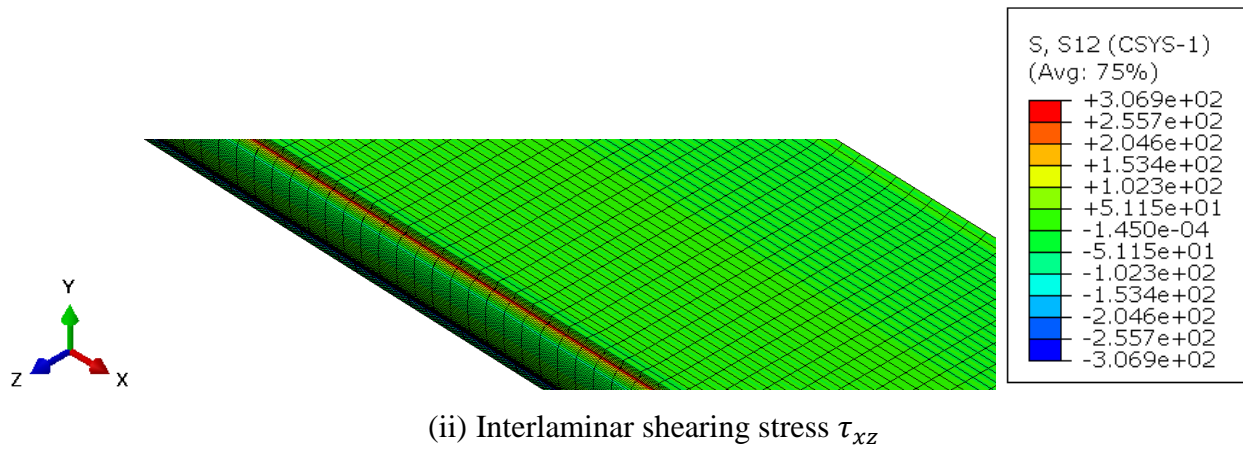
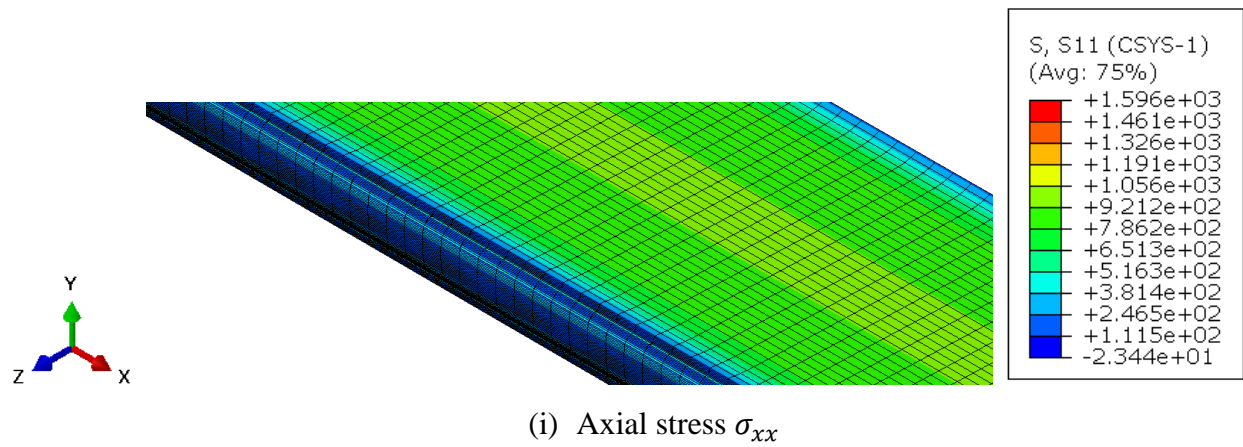
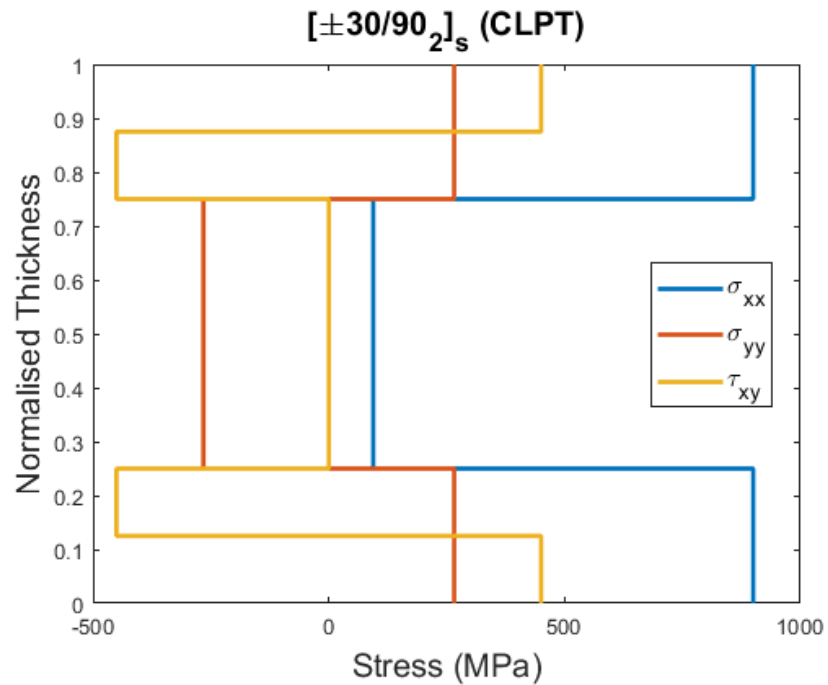


Figure 7.34: Contoured variation of stresses across the width and at the edge of $[\pm 30/90_2]_s$ laminate

7.5.2.4 Stresses across thickness at the laminate center

Figure 35 shows the variation of stresses across thickness at the laminate center. The axial stress is mostly taken by the $\pm 30^\circ$ plies and 90° do not take much axial loads. 90° plies do not take any in-plane shearing stress and all of it is taken by $\pm 30^\circ$ plies with alternating signs of stress between the positive and negative oriented plies.

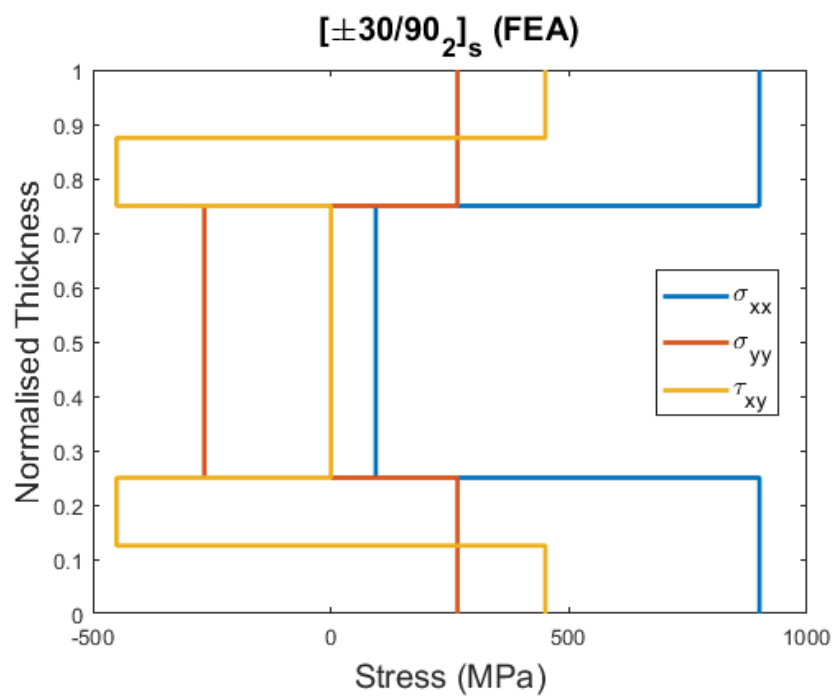
Figure 36 shows the contour variation of these stresses across the thickness of the laminate at the center.



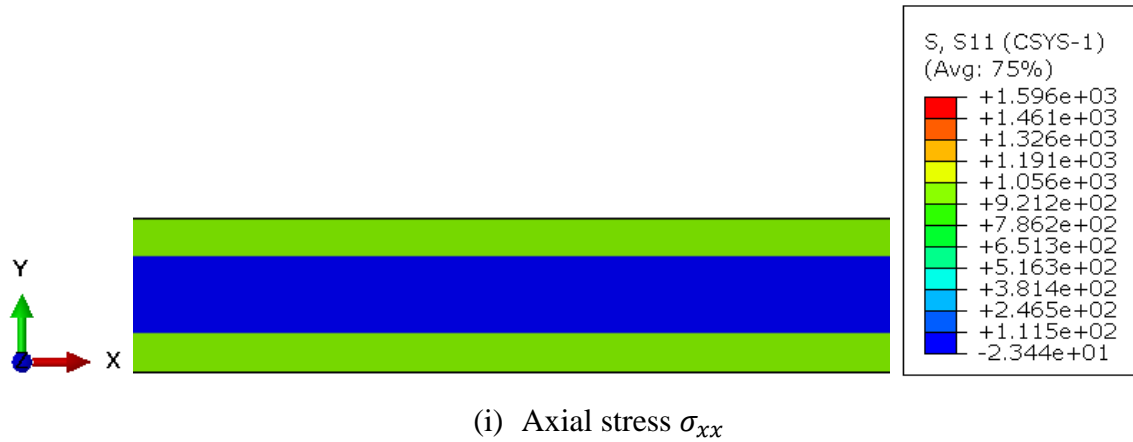
(a) Analytical solution

Figure 7.35: Variation of stresses across thickness at the center of $[\pm 30/90_2]_s$ laminate

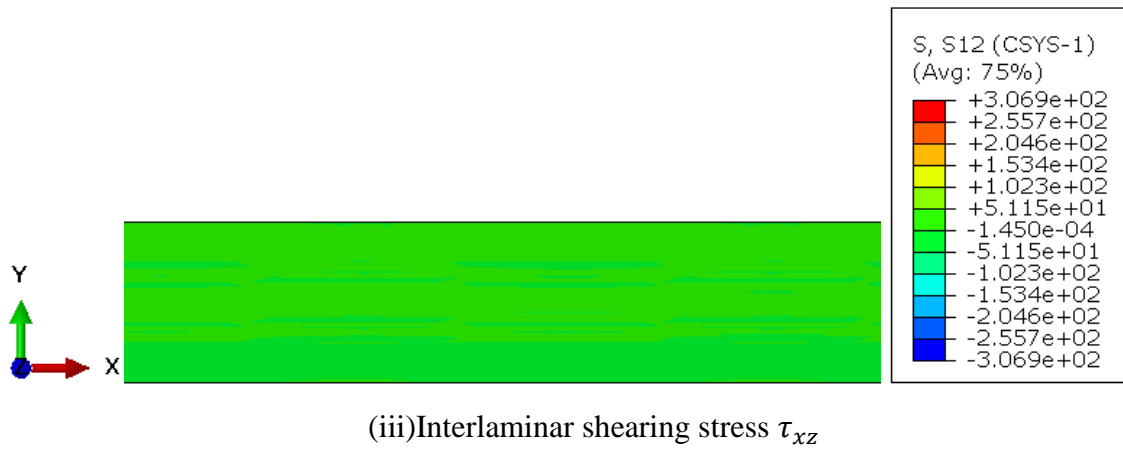
Figure 7.35 continued



(b) Abaqus simulation result (Stresses in MPa)



(ii)



(iv)

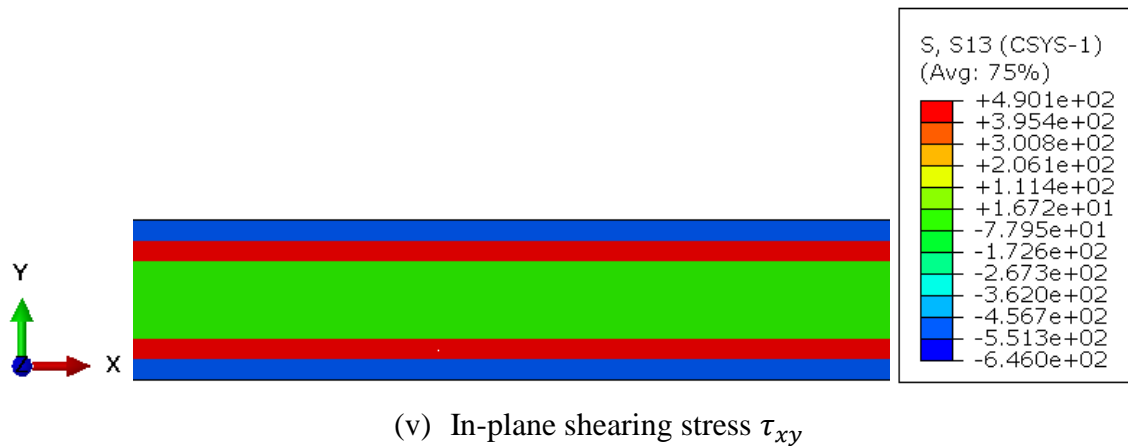
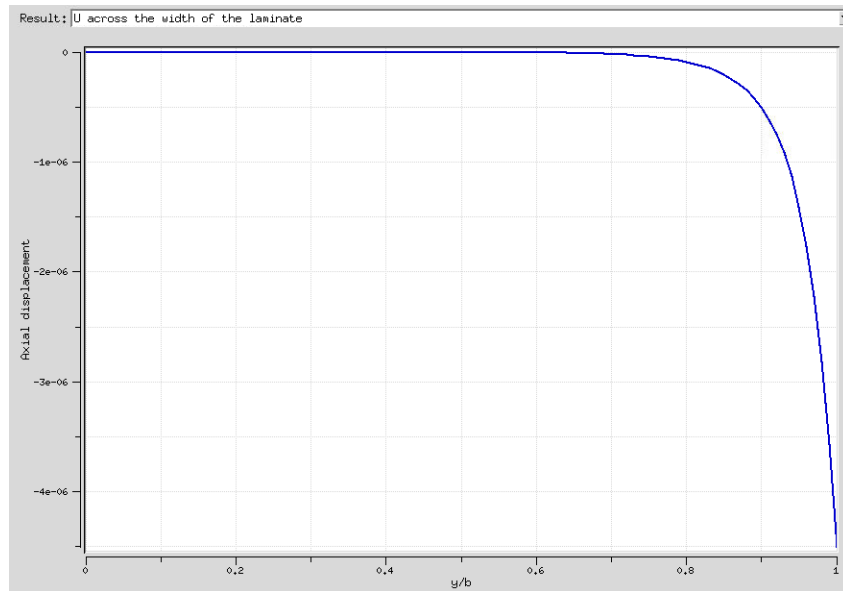


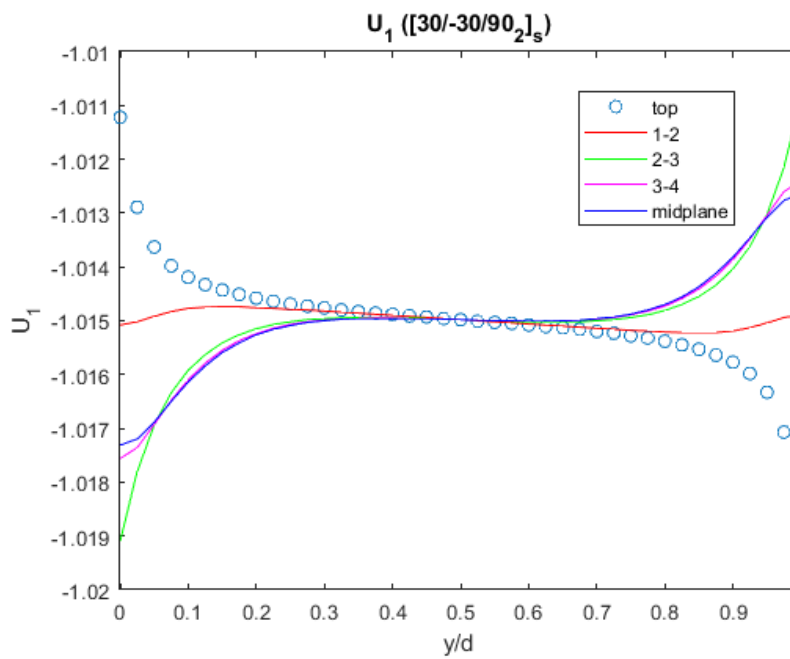
Figure 7.36: Contoured variation of stresses at the center of $[\pm 30/90_2]_s$ laminate

7.5.2.5 Axial displacement across the width

Figure 37 shows the variation of axial displacement across the width of $[\pm 30/90_2]_s$ laminate. In the plots obtained from the simulation results, the stresses are plotted at the interfaces of the plies and the legends are numbered from bottom to top, that is, 1 is the bottom-most ply with an orientation of 30° . 2, 3 and 4 represent the subsequent bottom-up plies with orientations -30° , 90° and 90° respectively. The stresses were also plotted at the mid-plane of the laminate and on its top surface. There is a boundary layer at the edges of the laminate and hence, the displacement reaches a constant value only at the center of laminate.



(a) Analytical solution



(a) Abaqus simulation result

Figure 7.37: Variation of axial displacement U_1 across width of $[\pm 30/90_2]_s$ laminate

7.6 Conclusions

Table 2 shows a summary of all the values calculated for all the laminates. It can be observed that the ultimate stress of the laminates is dependent on the stacking sequence and the thickness of the plies. The strength of the laminate reduces with an increase in thickness and with the number of 90 oriented plies in the laminate. However, the material properties such as Young's modulus do not depend on the ply thickness. The value is hence found to be almost the same for the cases of the same stacking sequence irrespective of the ply thickness.

The interlaminar shear stresses initiate failure for small fiber angles and the strength of the angle-ply laminates could be described in terms of Mode I and Mode II fracture toughness. The lumping plies also result in greater through thickness axial deformation of the laminate.

The failure in these laminates is different from each other. In the $[\pm 30]_{2s}$, $[\pm 30_2]_{2s}$ laminates, there is 'hair-like' delamination that occurs along the flat edges of the sample and in the $[\pm 30/90_2]_s$, $[\pm 30_2/90_4]_s$ laminates, there is delamination between the plies of the laminate and they open up prior to failure and close upon failure.

Table 7.2: Summary of the results

Mean Ultimate Stress (MPa)			
$[\pm 30]_{2s}$	$[\pm 30_2]_{2s}$	$[\pm 30/90_2]_s$	$[\pm 30_2/90_4]_s$
514.97	411.47	299.88	209.59

Young's Modulus (GPa) [Calculated by ASTM D3039 from 1000 $\mu\epsilon$ to 3000 $\mu\epsilon$]			
$[\pm 30]_{2s}$	$[\pm 30_2]_{2s}$	$[\pm 30/90_2]_s$	$[\pm 30_2/90_4]_s$
29.59	28.44	26.80	26.21

Interlaminar Shear Stress (MPa)	
$[\pm 30]_{2s}$	$[\pm 30_2]_{2s}$
136.66	66.61

Peel Stress (MPa)	
$[\pm 30]_{2s}$	$[\pm 30_2]_{2s}$
27.86	7.12

Simulations were carried out to analyze the stress distributions on the $[\pm 30]_{2s}$ and $[\pm 30/90_2]_s$ laminates across the width and across the thickness of the laminate. The free edge effects are visible in these cases and the effect of ply orientation on the stress concentrations are analyzed. The axial displacements and the stresses are validated with the analytical solutions obtained from the free-edge solution on cdmHub. To capture these effects the coupon was modeled with a width of 5 times the thickness of the laminate and the number of elements across the width is increased. There was a presence of a boundary layer at the free edges of the laminates. This is due to the misbalance of stresses at the free surfaces. This phenomenon was also observed in the open-hole tension case where the edge of the hole also experiences free edge effects.

7.7 References

- [1] Carlsson, L. A., Adams, D. F., & Pipes, R. B. (2014). *Experimental characterization of advanced composite materials*. Boca Raton, FL: CRC Press.
- [2] Dr. Wenbin Yu. (2017) Multiscale Structural Mechanics. Wiley-Interscience. John Wiley & Sons, INC., Publication
- [3] ASTM Standard D3039
- [4] Vasudha Kapre, Andrea Martin Tovar, Kevin G. McIver, 15th November 2019, Friday, Lab 13-Free Edge Tension, Presentation. PPT. (2019).
- [5] Dr. Byron Pipes, 11th November 2019, Monday, 12a, 12b Free-edge Phenomena, Presentation. PPT. (2019).

8. MODE I- INTERLAMINAR FRACTURE

8.1 Introduction

8.1.1 Common failure modes in a composite laminate

There are three basic modes in the failure of composite materials. Mode I comprises of the opening mode, mode II comprises of the in-plane shear or the sliding shear mode and Mode III comprises of the out of plane shear mode or twisting shear mode. These failure modes are depicted in Figure 1.

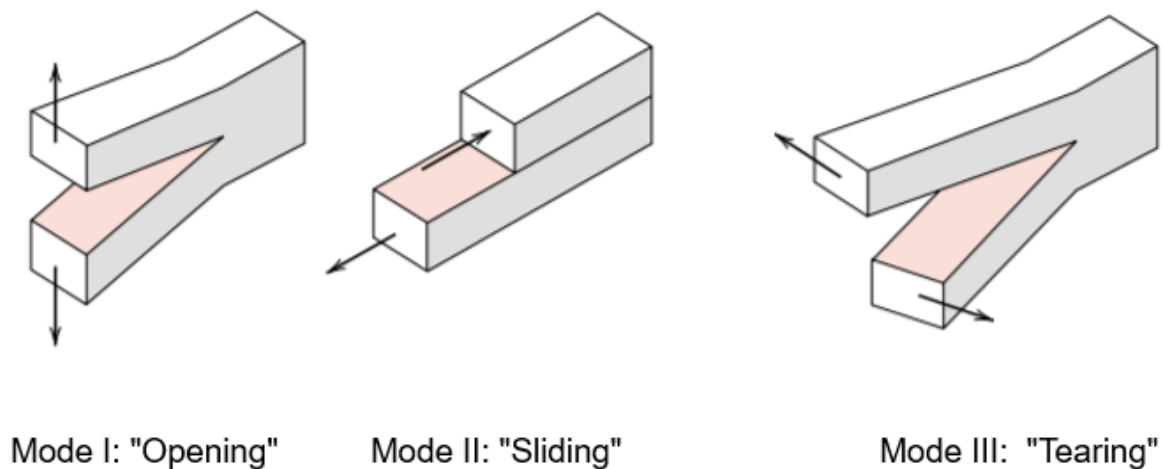


Figure 8.1: Modes of failure in a composite material

(Image from Callister. Materials Science and Engineering: An Introduction. 7th Ed)

Delamination is the phenomenon in which the two adjacent plies in composite laminates get separated. It is one of the most critical failure modes in composite laminates. It represents the crack-like discontinuities in a laminate which can propagate during its laminate and hence, it is a very important factor while determining the damage tolerance and the durability of the laminate. They can be produced during the manufacturing or the handling or even during the service of the laminate. The delamination is produced as a combination or as a single effect of any of the modes described above. It is a “major life-limiting failure process” for a laminate.

As the crack starts to extend, the fibers pull out of the delaminated surfaces ahead of the crack tip and a zone of fibers bridging the gap is formed between the delamination faces. This is formed

directly behind the crack tip. The effect of fiber bridging is more when the crack is small and the effect is very small when the crack propagates to a bigger extent. Figure 2 shows the fiber bridging observed in the specimen. As the delamination progresses, the displacement in the direction of crack opening increases and these bridged fibers continue out pull out and they also break due to the applied tensile stress.

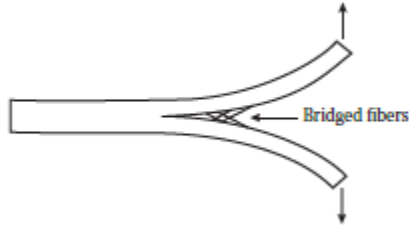


Figure 8.2: Fiber bridging

(Image from Experimental characterization of advanced composite materials (2014))

Linear Elastic Fracture Mechanics (LEFM) is usually used to study the fracture and delamination of the laminates. The main assumption used in this approach is that the material is perfectly elastic. There are two main approaches used in this process. One is energy-based and the other is stress-based. Both of these approaches produce equivalent results for elastic materials. The critical strain energy release rate is generally an accepted measure of the total energy required to initiate delamination in the material and is denoted by G_C . This value is dependent on the mode of delamination of the laminate. Hence, for mode I, mode II and mode III, the G_C values are G_{IC} , G_{IIC} and G_{IIIC} respectively.

8.1.2 Compliance and strain energy release rate for interlaminar fracture

Double Cantilever Beam (DCB) test was used to determine the Mode I failure in the laminates as it is the most commonly used. Mode I delamination is also the most common failure mode among all the 3 failure modes. Figure 3 shows a standard DCB specimen with the hinged loading.

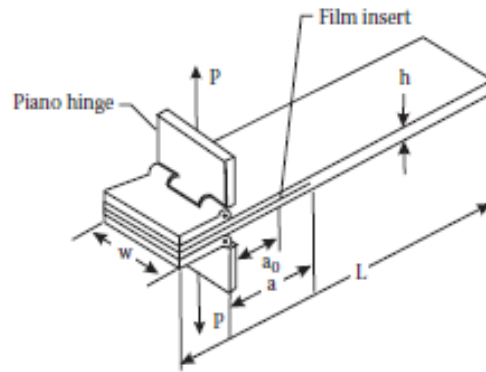


Figure 8.3: DCB specimen with hinge loading

(Image from Experimental characterization of advanced composite materials (2014))

Figure 4 shows the DCB geometry under tensile loading, where $\delta = 2u$.

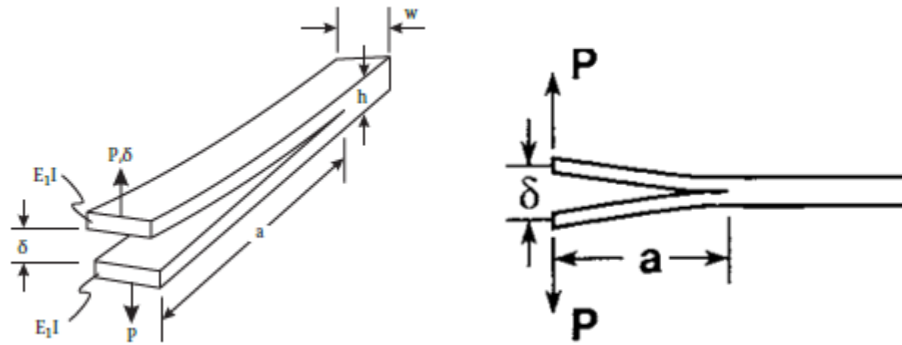


Figure 8.4: DCB specimen under loading

(Image from Experimental characterization of advanced composite materials (2014))

$$\Delta U = \frac{P\Delta u}{2}, \Delta W = P\Delta u$$

$$\Delta H = \Delta W - \Delta U = P\Delta u - \frac{P\Delta u}{2} = \frac{P\Delta u}{2}$$

$$G\Delta A = \frac{P\Delta u}{2} \rightarrow G = \frac{P}{2} \left(\frac{du}{dA} \right)$$

$$u = CP, \quad (C = \text{compliance})$$

$$\frac{du}{dA} = C \left(\frac{dP}{dA} \right) + P \left(\frac{dC}{dA} \right) = P \left(\frac{dC}{dA} \right)$$

$$\frac{dP}{dA} = 0 \quad (\text{fixed load})$$

$$G = \frac{P}{2} \left(\frac{du}{dA} \right) = \frac{P^2}{2} \left(\frac{dC}{dA} \right)$$

From the classical beam theory, the load-point compliance, C (given by δ/P) for the DCB specimen, assuming that it is an ideal slender beam, becomes,

$$C = \frac{2a^3}{3E_1I}$$

Where P is the applied load, δ is the crack opening, E_1 is the modulus of composite in the fiber direction, I is the moment of inertia and a is the crack length. The strain energy release rate, $G = G_I$ is obtained as follows:

$$G = \frac{P^2}{2} \left(\frac{\partial C}{\partial A} \right)$$

$$G = \frac{P^2 a^2}{bE_1I}$$

Figure 5 shows the stress variation near the notch. It can be observed that the plot reaches a peak value near the notch and it reduces exponentially to the value of σ_0 near the end of the plate. For a crack, the radius of curvature approaches zero and hence it is assumed to be a straight line.

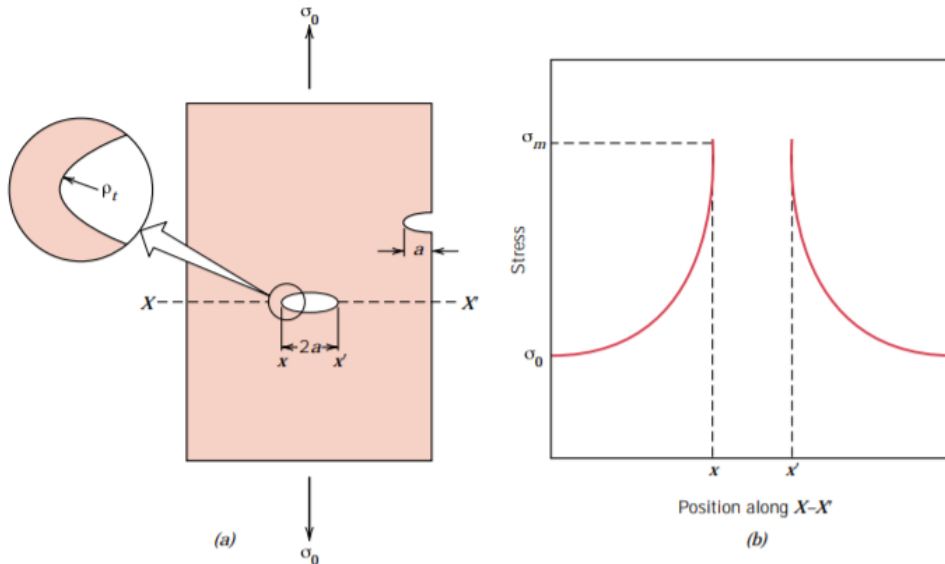


Figure 8.5: Variation of stress from near the notch to the end of the laminate
(Image from Callister. Materials Science and Engineering: An Introduction. 7th Ed)

The stress varies as the following equation:

$$\sigma(x) = \frac{K_I}{\sqrt{2\pi x}}$$

$$\sigma_{yy} = \sigma(1 + \frac{2a}{b})$$

The Mode I stress field equation is given by,

$$\sigma_{yy} = \frac{K_I}{\sqrt{2\pi x}} + O(\sqrt{x})$$

$$\sigma_{xy} = \sigma_{yz} = 0$$

Where K is the stress concentration factor and as x or $b \rightarrow 0$, the stress approaches a value of infinity.

According to Griffith's theory of fracture, $H = W - U$ represents the energy to create new surfaces and $\Delta H \geq G_C \Delta A$, where W is the work done by external forces, U is the elastic strain energy in the body and G_C is the work required to create a new crack of area A. It represents crack propagation and not crack initiation. At the critical condition, $\Delta H = G_C \Delta A$, where,

$$G = \frac{dH}{dA} = \lim_{A \rightarrow 0} \frac{\Delta H}{\Delta A}$$

$$G \geq G_C$$

G, energy release rate is usually in J/mm^2 or N/mm and K, is usually in the units of $MPa \sqrt{mm}$. The energy release rate for plane stress and plane strain cases is as follows:

$$G_I = \begin{cases} \frac{K_I^2}{E} & \text{Plane stress} \\ \frac{(1 - \nu^2)K_I^2}{E} & \text{Plane strain} \end{cases}$$

8.1.3 Load and displacement control for DCB specimen

There are two types of loading for a DCB specimen, load and displacement control. In a load control case, the crack propagates indefinitely for a given applied load and for a displacement control case, the crack stops after it propagates a certain displacement. For stable crack growth,

$$\frac{dG}{da} \leq 0$$

For a load control case:

$$\frac{dG}{da} = \frac{2P^2 a}{bE_1 I}$$

For a displacement control case:

$$\frac{dG}{da} = \frac{-9\delta^2 E_1 I}{ba^3}$$

The initiation value is obtained from the Teflon ‘crack’ that was placed in the laminate while the sample was prepared. This crack is not sharp and it has a pre-defined size. The propagation value is obtained from the cracks that arise from the delamination and the crack is very sharp and difficult to measure.

8.1.4 Calculation of strain energy release rate

There are 4 methods to get the value of G_{IC} for a laminate.

8.1.4.1 Simple Beam Theory

Simple Beam Theory assumes that the beam is perfectly built-in and there is no rotation in it. The value of G_{IC} from the simple beam theory can be obtained from the following equation:

$$G_{IC} = \frac{3}{2} \left(\frac{P\delta}{wa} \right)$$

This expression overestimates G_I because the beam is not perfectly built-in where rotation may occur at the delamination front.

8.1.4.2 Modified Beam Theory

The Modified Beam Theory (MBT) method corrects G_I for this rotation by treating the DCB as if it contained slightly longer delamination, $a + |\Delta|$, where Δ is the correction factor. The value of G_{IC} obtained from this method is given from the following equation:

$$G_{IC} = \frac{3}{2} \left(\frac{P\delta}{w(a + |\Delta|)} \right)$$

The graph of $C^{1/3}$ vs a shifts to the left by $|\Delta|$ as shown in Figure 6.

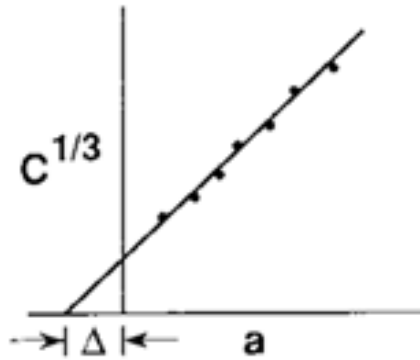


Figure 8.6: MBT with correction factor

The flexural modulus hence becomes,

$$E_{1f} = \frac{64(a + |\Delta|)^3 P}{\delta b h^3}$$

8.1.4.3 Compliance Calibration Method

The Compliance Calibration (CC) Method uses another term called 'n' which is the slope of the least-squares plot of $\log(C)$ vs $\log(a)$. The compliance calibration is shown in Figure 7.

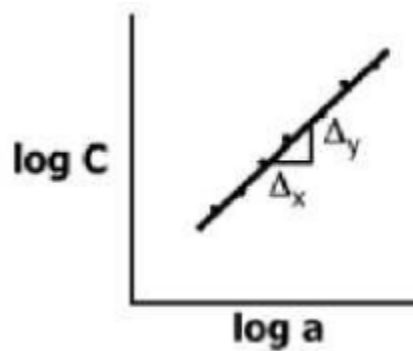


Figure 8.7: Compliance Calibration

Where $n = \Delta_y / \Delta_x$ and the mode I interlaminar fracture toughness is given by the following equation:

$$G_I = \frac{n P \delta}{2 b a}$$

8.1.4.4 Modified Compliance Calibration Method

The Modified Compliance Calibration (MCC) method introduces the term A_1 which is the slope of the least squares plot of the delamination length normalized by specimen thickness, a/h , as a function of the cube root of compliance, $C^{1/3}$ as shown in Figure 8. Mode I interlaminar fracture toughness becomes as shown in the equation below. This method considers Fiber bridging which shows up in the A_1 term.

$$G_I = \frac{3P^2 C^{2/3}}{2A_1 b h}$$

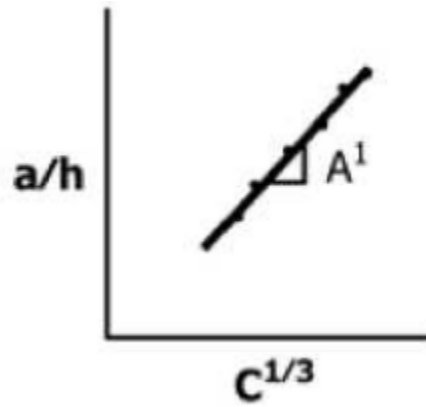


Figure 8.8: Modified Compliance Calibration

8.2 Experimental Procedure

The samples were prepared by the ASTM standards for laminates with stacking sequence as $[0]_{24}$. They were manufactured with a crack in them by inserting a non-adhesive insert such as Teflon on the midplane of the laminate. It serves as the delamination initiator. The length of the insert was set to be 50 mm according to the ASTM standards. The hinges were bonded to one end of the specimen where the crack was formed and hence, the initial crack length in the specimen was 25 mm since the length of the metal hinges was 25 mm and they were attached to the laminate by using an adhesive. Figure 3 shows the schematic diagram of how the specimen looks like after the metal hinges are bonded on them. A total of 10 specimens were made for this test out of which 5 of them were tested. Table 1 shows the dimensions of the specimen that were tested. Figure 9 shows the side view of a DCB specimen with metal hinges on it.

Table 8.1: DCB Specimen Dimensions

Sample	Thickness (mm)	Width
1	3.780	25.643
2	3.793	25.593
3	3.940	25.670
4	3.853	25.653
7	3.767	25.637



Figure 8.9: DCB specimen with hinges

From the ASTM D 5528-01 standard for the DCB test, in Figure 4, the variables to be measured before the DCB test are δ -crack opening, a-crack length, a_0 is the initial crack length and its recommended value is 50 mm, P-applied force, h-thickness, w-width. The specimen was loaded with a cross-head rate of 4 mm/min in the 5-kip load frame as shown in Figure 10.

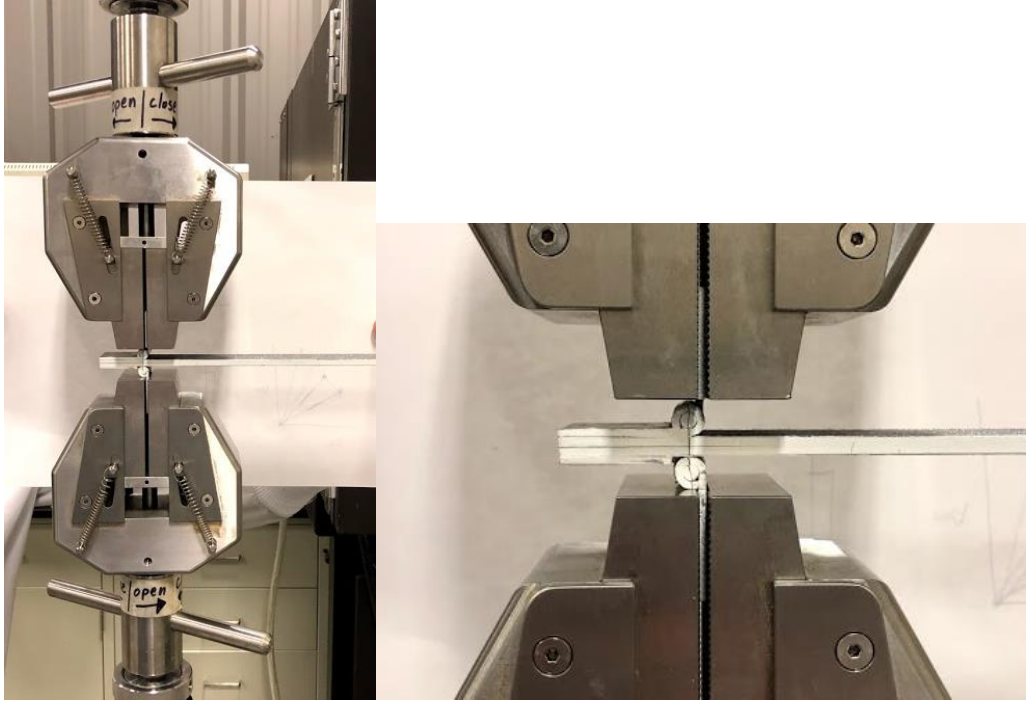


Figure 8.10: Loading of the DCB specimen in the 5-kip load frame

The samples were sprayed on the side faces and the test was performed so that the crack propagation can be accurately measured across the length of the sample. A total of 5 runs were performed on each of the samples where the test was stopped after the crack propagates in each of the cases. The load versus displacement curves were plotted for each of the samples for each of the runs. A linear fit was made on the force versus displacement was done to get the value of $1/C$ for the samples. The plots were made to get the constant values for MBT, CC and MCC methods. The value of G_{IC} was hence calculated for the samples.

8.3 Processing of experimental results

8.3.1 Data reduction from Modified Beam Theory

Figure 11 shows the data reduction from Modified Beam Theory. From Figure 6, we know that the plot needs to be made between $C^{1/3}$ and a and the value of x-intercept is Δ . A linear curve fit was made on the data to obtain this value. The value of Δ was hence obtained to be -8.2983.

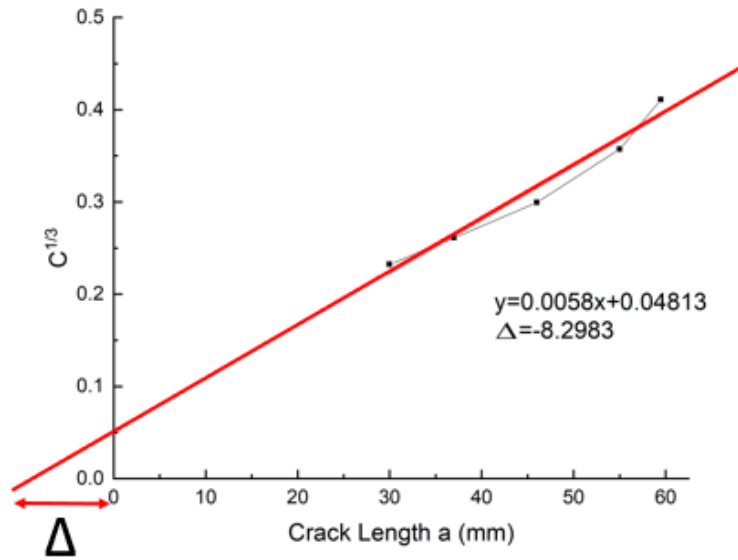


Figure 8.11: Data reduction from Modified Beam Theory

8.3.2 Data reduction from Compliance Calibration

Figure 12 shows the data obtained from the Compliance Calibration where $\log(c)$ versus $\log(a)$ was plotted and the slope of this curve gives the value of n . This plot is expected to look similar to Figure 7. The value of n was hence found to be 2.3995.

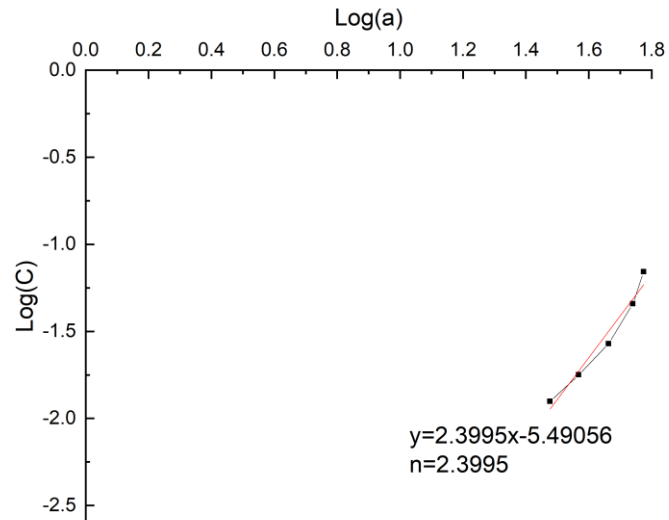


Figure 8.12: Data reduction from Compliance Calibration

8.3.3 Data reduction from Modified Compliance Calibration

Figure 13 shows the data reduction from the modified CC. The normalized crack length a/h is plotted against $C^{1/3}$ and A_1 is obtained from the slope of the curve as shown in Figure 8. The value of A_1 was hence obtained to be 43.91459.

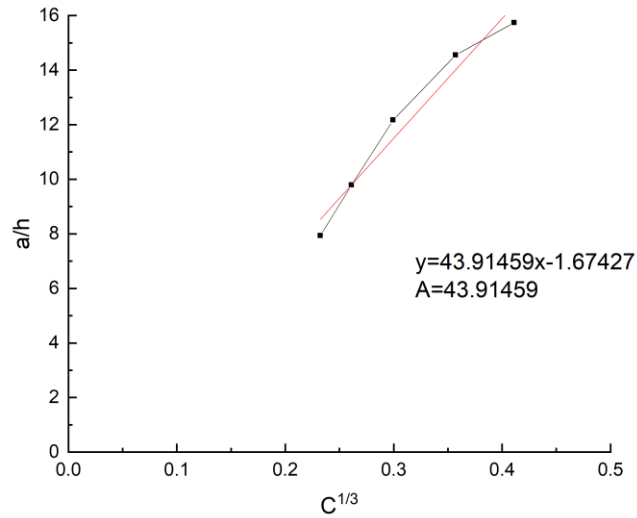
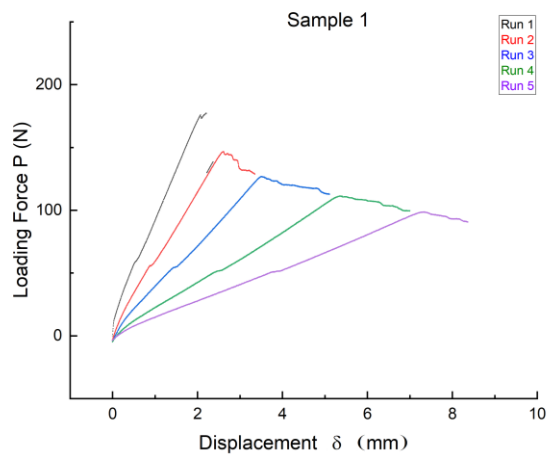


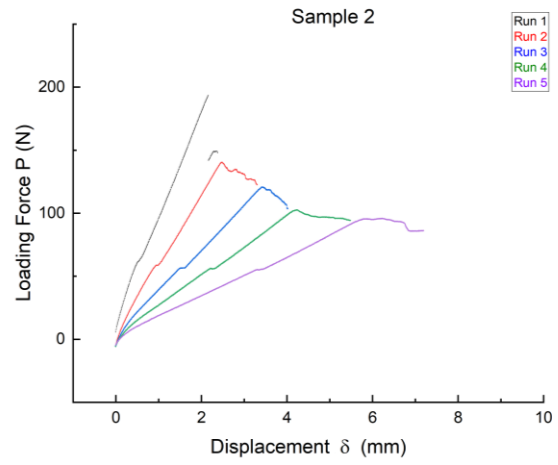
Figure 8.13: Data reduction from Modified Compliance Calibration

8.3.4 Force-displacement plots for the tested samples

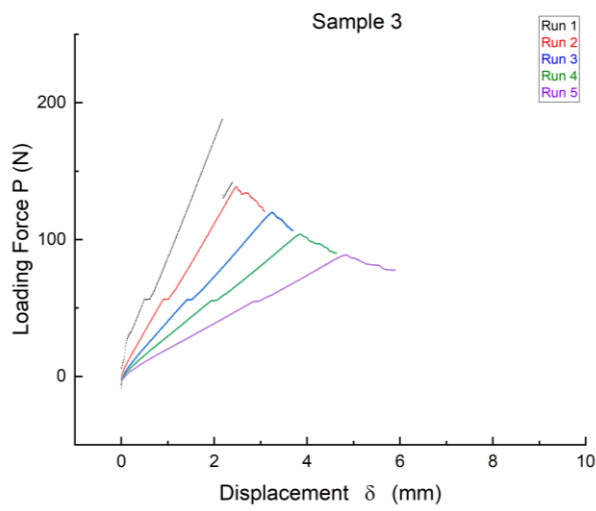
Figure 14 shows the force versus displacement curves for all the 5 samples that were tested.



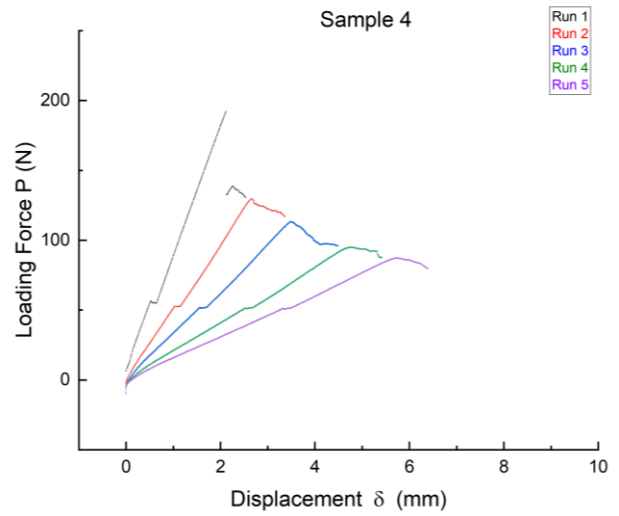
(a) Sample 1



(b) Sample 2



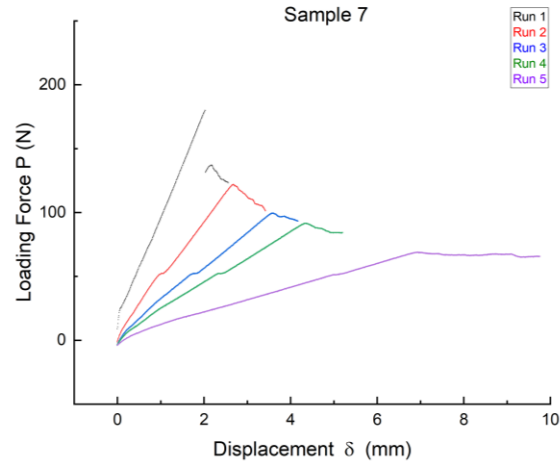
(c) Sample 3



(d) Sample 4

Figure 8.14: Load Vs Displacement curves for the DCB samples

Figure 8.14 continued



(e) Sample 7

8.3.5 G_{IC} calculated from different methods and propagation of the crack

The G_{IC} values were calculated using the three methods as described above and Figure 15 shows the comparison of these plots for sample 7. ASTM standard recommends MBT as it is the most conservative among all the different methods.

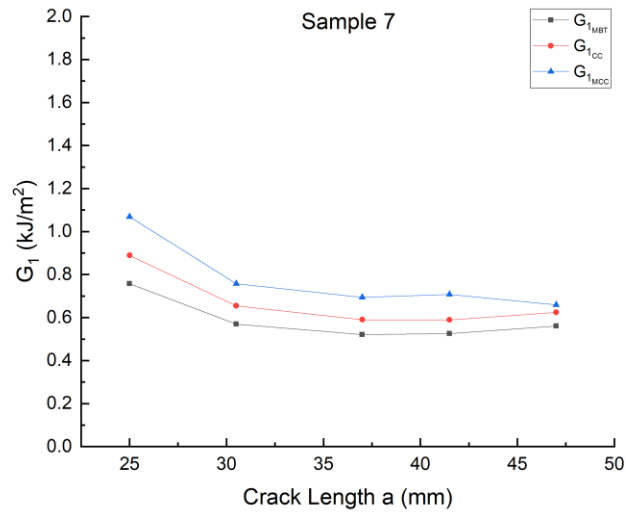


Figure 8.15: Comparison of G_{IC} values obtained from different methods

The propagation of the crack across the length of the sample for each of the runs is shown in Figure 16.

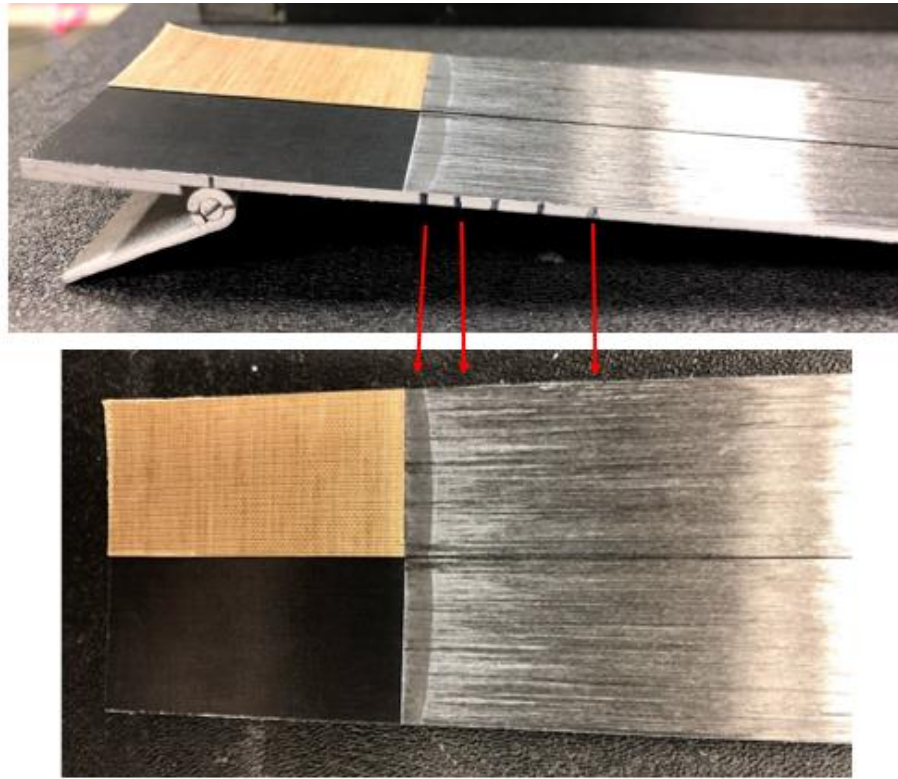


Figure 8.16: Propagation of crack across the length of the sample

The phenomenon of fiber bridging was clearly observed in the samples as the crack propagates and it is shown in Figure 17.



Figure 8.17: Fiber Bridging while testing the DCB samples

For a few samples, the hinges were separated from the sample during the test as shown in Figure 18. This is because of the shearing of the hinges from the samples.

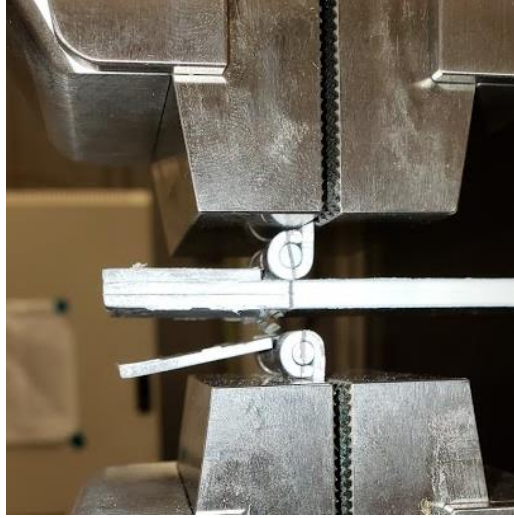


Figure 8.18: Shearing of hinges during the test

Tables 2, 3 and 4 show the data for the values of G_{IC} obtained from the three different methods.

Table 8.2: Results from MBT method

Sample	Run 1 (kJ/m ²)	Run 2 (kJ/m ²)	Run 3 (kJ/m ²)	Run 4 (kJ/m ²)	Run 5 (kJ/m ²)
1	0.596	0.597	0.670	0.876	1.124
2	0.692	0.534	0.539	0.633	0.602
3	0.798	0.611	0.618	0.566	0.533
4	0.840	0.611	0.599	0.589	0.596
7	0.758	0.570	0.521	0.525	0.561

Table 8.3: Results from CC Method

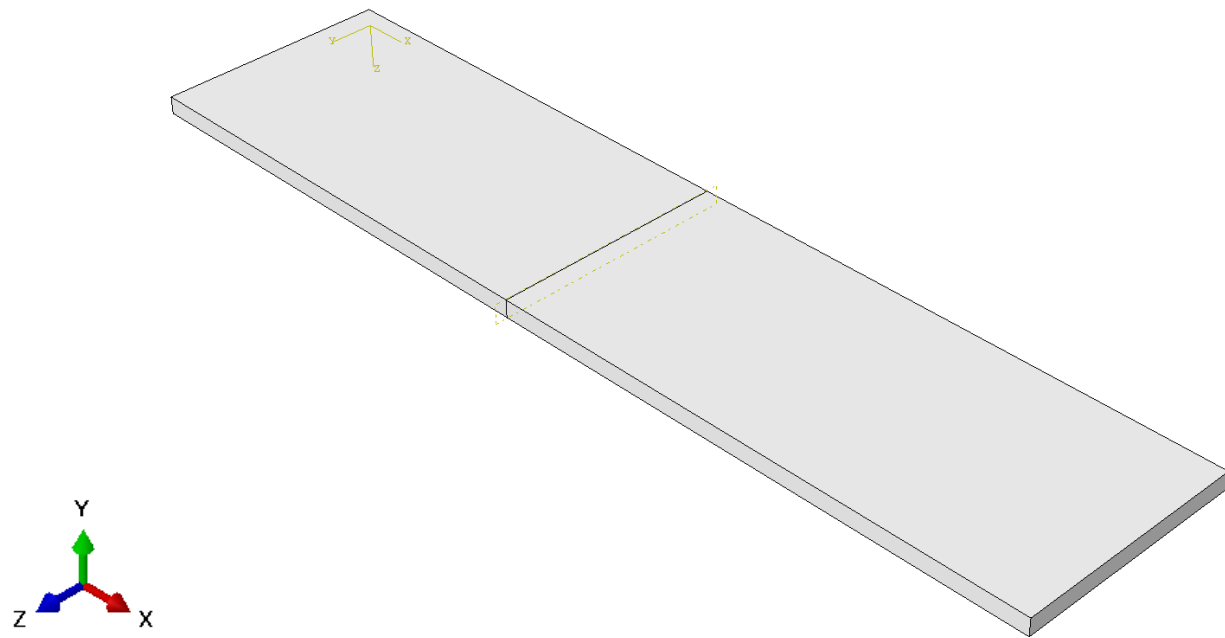
Sample	Run 1 (kJ/m ²)	Run 2 (kJ/m ²)	Run 3 (kJ/m ²)	Run 4 (kJ/m ²)	Run 5 (kJ/m ²)
1	0.609	0.585	0.633	0.807	1.025
2	0.770	0.574	0.544	0.618	0.563
3	0.864	0.647	0.639	0.572	0.528
4	0.887	0.627	0.601	0.581	0.582
7	0.889	0.655	0.590	0.589	0.624

Table 8.4: Results from MCC method

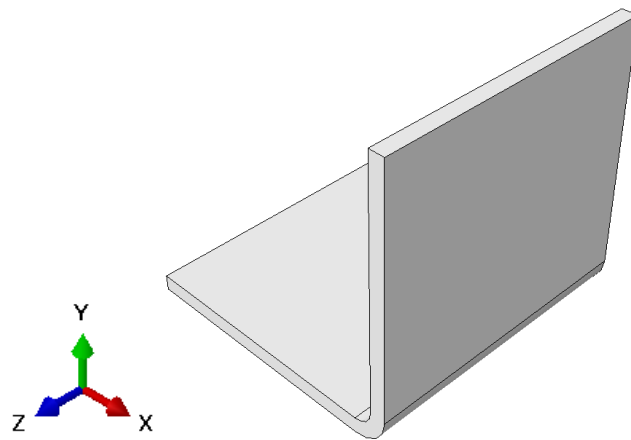
Sample	Run 1 (kJ/m ²)	Run 2 (kJ/m ²)	Run 3 (kJ/m ²)	Run 4 (kJ/m ²)	Run 5 (kJ/m ²)
1	0.598	0.755	0.993	1.413	1.871
2	0.810	0.562	0.569	0.761	0.569
3	0.902	0.726	0.652	0.580	0.552
4	0.824	0.561	0.564	0.527	0.539
7	1.069	0.758	0.694	0.708	0.659

8.4 Modeling of geometry for simulation

The geometry was modeled as two parts. One of them was the dcb-leg and the other one was the hinge. The dimensions of the hinges and the dcb-leg were according to the ASTM D5528 (Standard Test Method for Mode I Interlaminar Fracture Toughness of Unidirectional Fiber-Reinforced Polymer Matrix) standards. A section was created at a distance of 50 mm from the end of the composite laminate in order to account for the pre-incorporated crack in the laminate as in the case of a typical DCB specimen. The laminate was modeled to be 25.4 mm wide and 110 mm long. The hinges were modeled to have a base length of 22.4 mm, inner curvature of 1.6 mm and outer curvature of 3 mm. The laminate was modeled with half thickness and was assembled later to form an entire $[0]_{24}$ laminate by importing two equivalent dcb-leg parts. Hence, each half had a thickness of 1.9 mm and a total thickness is 3.8 mm. This value of thickness was obtained by multiplying the number of plies (12 plies in half of the laminate) with ply thickness as obtained from the material data sheet for a composite material composed of the F155 matrix and AS4C-GP12K fiber. It is a thermosetting composite of the same material that was used for the previous tests. The material properties are given in section 2.5.1. Figure 19 shows the geometry of the two parts, dcb-leg and the hinge that were modeled.



(a) DCB-leg



(b) Hinge

Figure 8.19: Parts modeled for DCB analysis

The parts were then assembled to form the entire geometry as shown in figure 20. The hinges were placed towards the end of the part where there is a crack in the laminate.

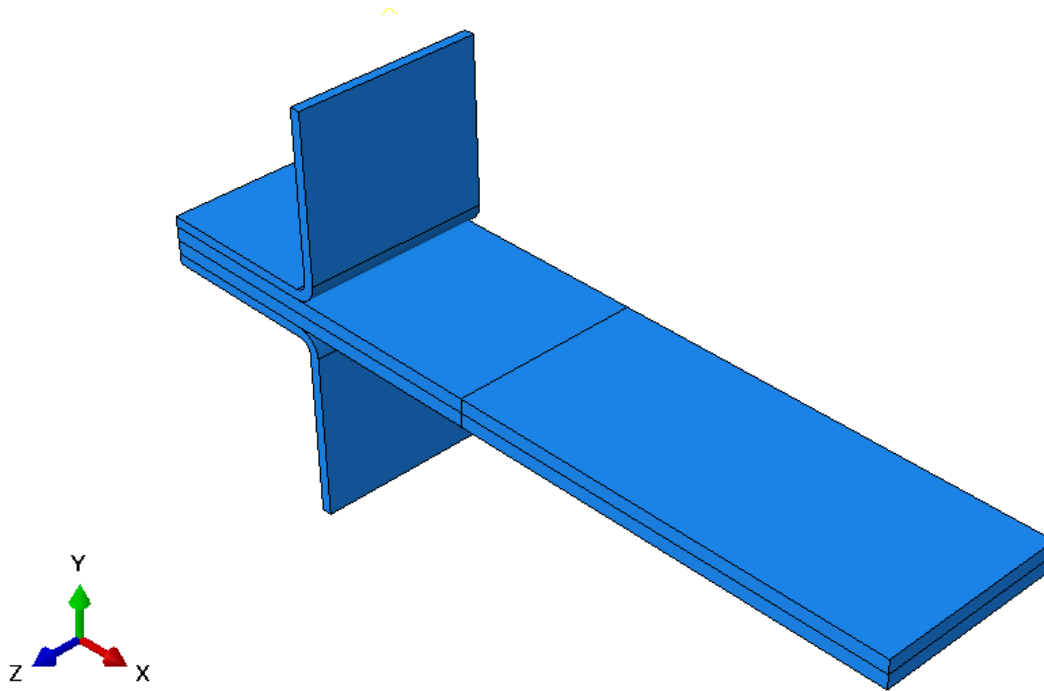


Figure 8.20: DCB part assembly

8.5 Boundary conditions and Interactions

8.5.1 Boundary conditions

The boundary conditions were assigned according to the manner in which the DCB specimen is placed in the test fixture. The bottom hinge is given an encastre boundary condition and a reference point is created above the top hinge where the surface of the hinge is coupled with it for all the degrees of freedom with the surface. It is constrained movement along the X and Z axes and is given a displacement of 7.1902 along the Y-axis. This displacement was given as a ramp. This value is obtained from the experiment that was conducted and the maximum displacement that the hinge has. Figure 21 shows the boundary conditions that were applied to the DCB specimen in accordance with the experiment.

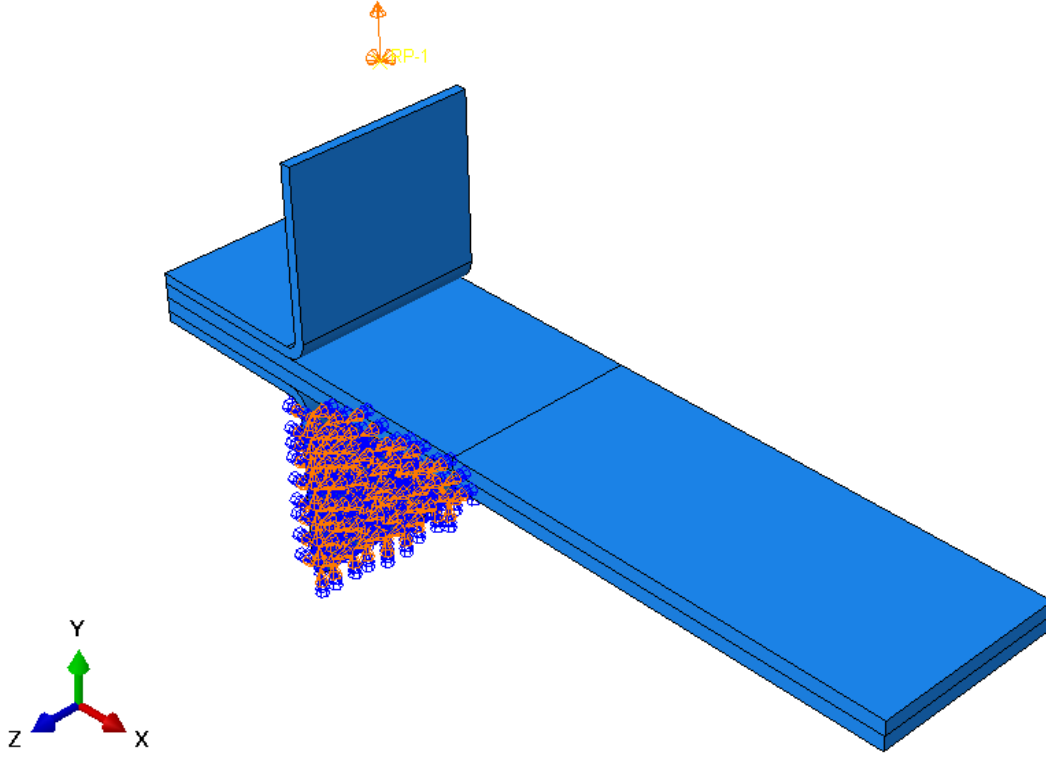


Figure 8.21: Boundary conditions on the DCB specimen

8.5.2 Interaction properties to model cohesion

Two interaction properties were used. One was in between the bottom of the hinges with the laminate. Only a cohesive behavior was defined for these surfaces with stiffness coefficients $k_{nn} = k_{ss} = k_{tt} = 1 * 10^6$. The stiffness coefficients were set to be uncoupled with each other. The eligible slave nodes were set to be default. For the interaction for the DCB laminate where the crack is propagating, four different contact properties were defined, namely, tangential behavior, normal behavior, cohesive behavior, and damage. The friction formulation in tangential behavior was set to be frictionless. In normal behavior, the pressure-overclosure was set to have “Hard” contact and the constraint enforcement method was set to be default with the separation to be allowed after contact. The cohesive behavior in DCB was set to be the same as the cohesive behavior between the hinges and the laminate. With the same values of the stiffness coefficients. For the damage behavior modeling, the damage evolution and stabilization were specified and in the initiation tab, quadratic traction was used where nominal stress for normal only was 70 and was 140 for shear-1 and shear-2 only cases. Under the evolution tab, the type was set to be energy

with a linear softening. A mixed-mode behavior was specified with power law and the mode mix ratio was energy and the power-law/BK exponent was set to be 1. The normal fracture energy was 0.8 and 1st and 2nd fracture energies were set to be 0.9 and 3 respectively. In the stabilization tab, the viscosity coefficient was set to be 0.00002.

Hence, three different interactions were used where these 2 interactions properties were used. For specifying these interactions, sets were created by selecting the respective surfaces. All the three interactions were set to have a standard surface-to-surface contact. The interaction between the hinge bottom and the laminate was modeled with the hinge being the master surface and the dcb-leg being the slave surface. The initial clearance was set to have a uniform value of 1×10^{-10} across the slave surface. For the DCB, the bottom of the top half was set to be the master surface and the top of the second leg was set to be the slave surface.

Figure 22 shows the interactions that were applied to the DCB specimen in accordance with the experiment.

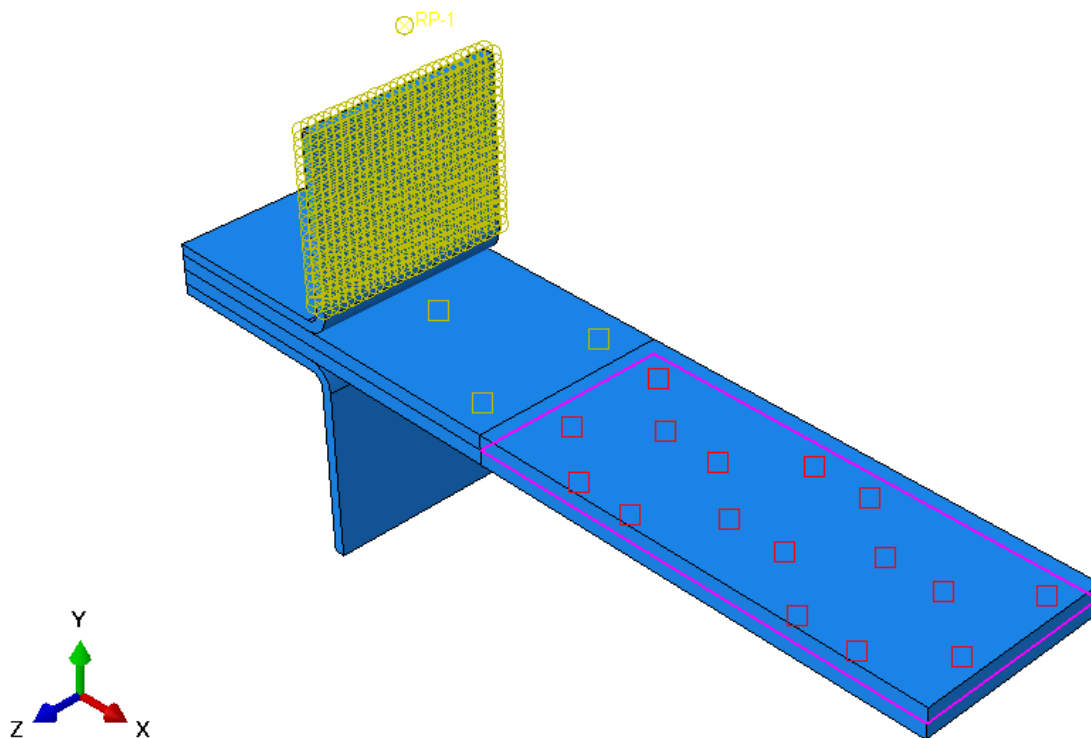


Figure 8.22: Interactions on the DCB specimen

8.6 Mesh parameters and convergence studies

The entire geometry was modeled with a structured mesh with 3D stress solid elements. The hinges were modeled with C3D8 elements (3D stress elements with 8-node linear brick) and the laminate was modeled with C3D8R elements (3D stress elements with 8-node linear brick, reduced integration, hourglass control). The global size on the hinges was 1 and, on the laminate, it was 0.5. The number of elements in each of the hinges was 1225 and the number of nodes was 2600. In each part of the laminate, there are 44880 elements with 57460 nodes. Hence, the total assembly has a total number of 120120 nodes and 92210 elements out of which 89760 elements are linear hexahedral elements of type C3D8R and 2450 elements are linear hexahedral elements of type C3D8. Figure 23 shows the mesh on the part assembly.

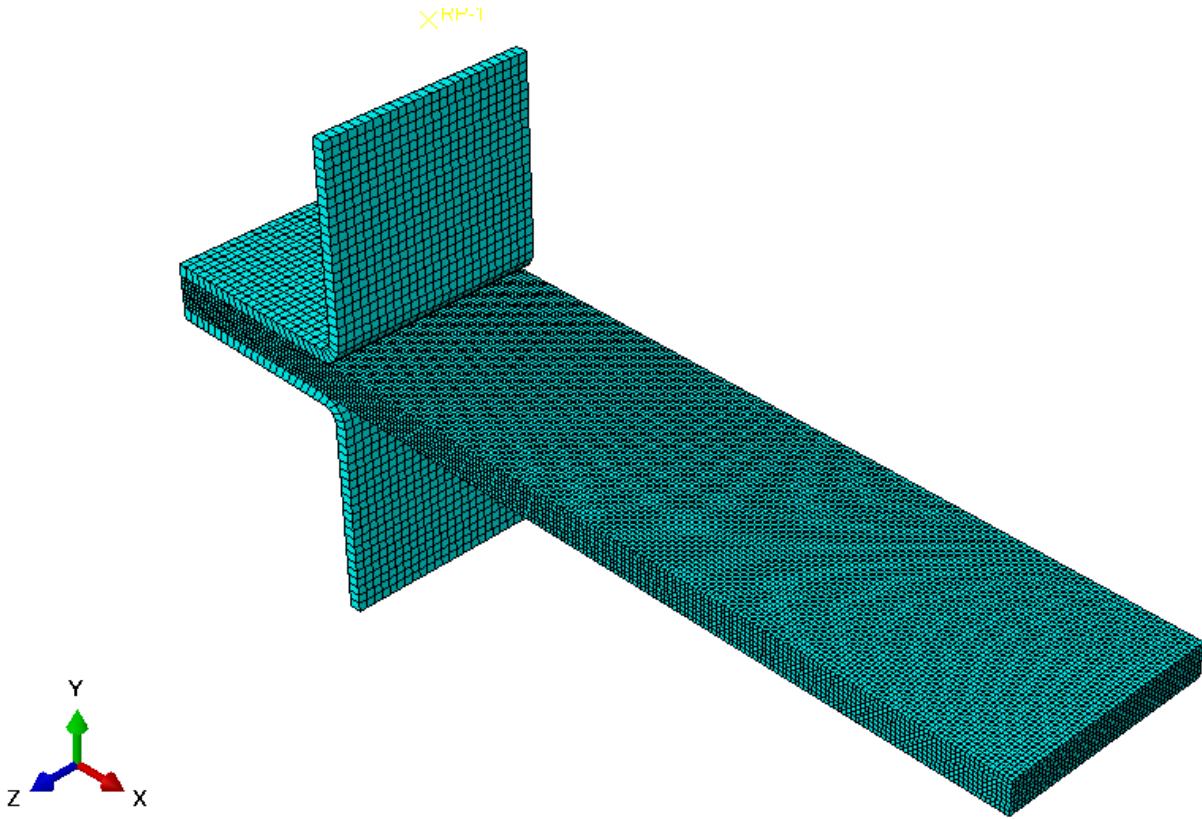


Figure 8.23: Mesh on the DCB part assembly

8.6.1 Convergence studies

A mesh convergence study was carried out for the parameters described in Table 5. Figure 2 also shows the variation of these parameters with the number of elements in the model. The number of elements is varied depending on the global mesh size that was assigned to the geometry. This study was done to check the variation of parameters with the increase in the number of elements in the geometry. Hence, the computational time can be significantly reduced when the number of elements is reduced without significantly reducing the parameters that are studied. Two plots are made as shown in Figure 24 for mesh convergence because of the difference in the scale of the magnitude of the Von Mises stress and hence to make the plots more defined.

Table 8.5: Mesh convergence study data for DCB specimen

Mesh_Size	Number of elements	Number of nodes	Max S. Mises (MPa)	Max S11 (MPa)	Max RF2 (N)	Max RF mag (N)
0.2	1259750	1415760	961.9	428.8	432.8	453.2
0.3	376790	448272	960.8	425.7	431.7	452.4
0.4	175700	217168	958	424	429.5	450.4
0.5	92210	120120	963.6	391.4	428.4	449.7
0.6	48566	68496	926.7	343	412	432
0.75	32438	46640	936.2	338.8	415	435.4
0.8	20114	32722	876.5	280.7	379.3	398.1
0.9	16226	26776	889	284.7	382.9	402.2
1	13450	22516	870.3	278.7	381.7	400.1

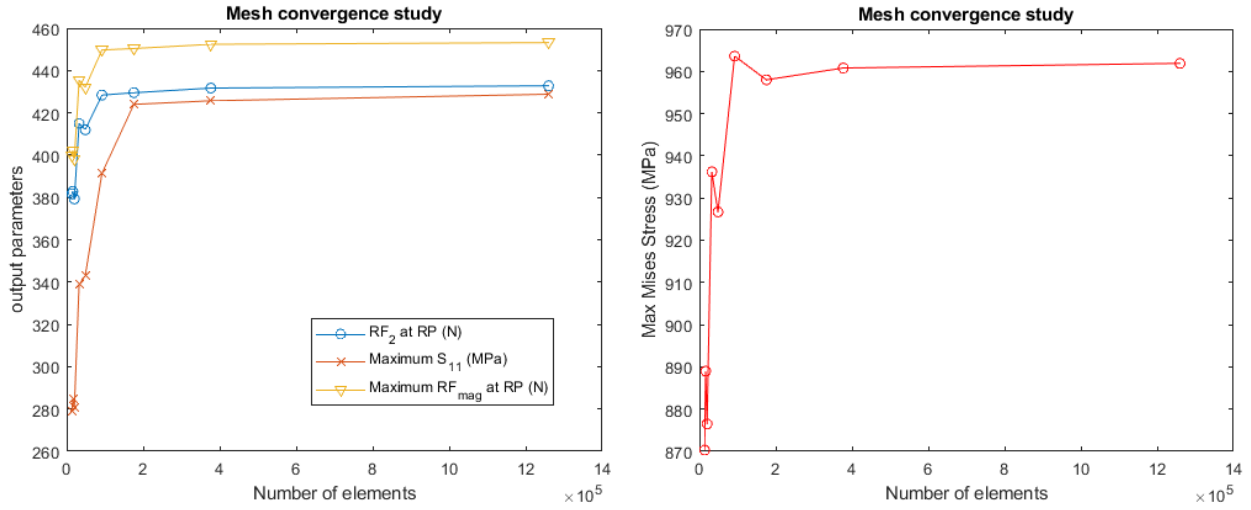


Figure 8.24: Mesh convergence study plots for DCB specimen

8.7 Step Outputs

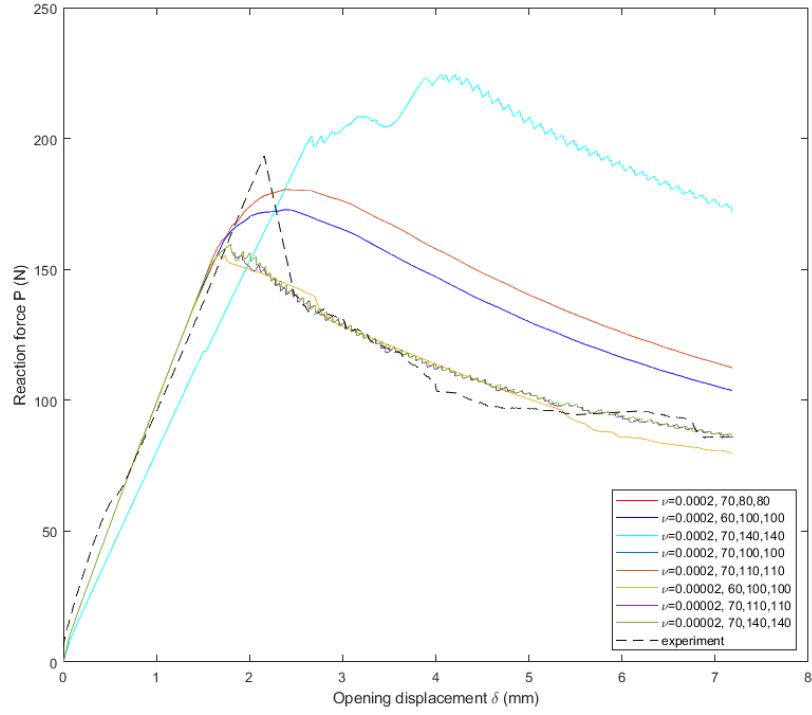
Automatic stabilization was set with a damping factor of 0.0002 and the maximum ratio of stabilization to strain energy was set to be 0.05. The step size was set to be 1 with initial and maximum increment size to be 0.01 and the minimum increment size was $1 * 10^{-15}$. In the field output request, the parameters CSDMG (Scalar stiffness degradation for cohesive surfaces) and CSQUADSCRT (Quadratic traction damage initiation criterion for cohesive surfaces) were requested to see the propagation of the crack and in the history output request, RF2 and U2 were requested at the domain set as the reference point.

8.8 Analysis of simulation results

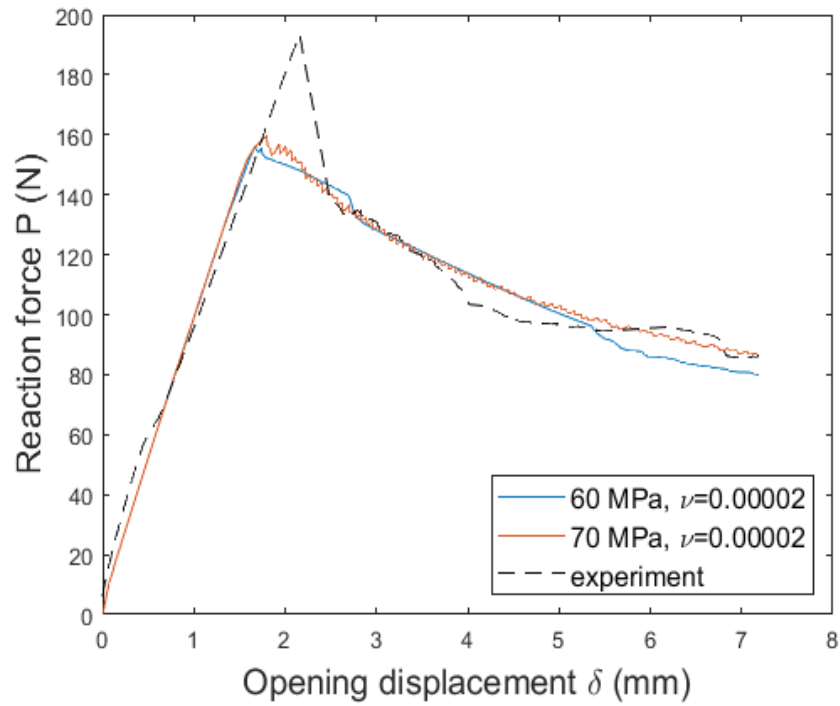
8.8.1 Force-displacement curve

The reaction force and displacement along Y-direction are requested as the history outputs from the simulation to plot the Load versus displacement curves in a DCB specimen (as shown in Figure 25) and to compare it with the experimental results for a DCB. From Figure 25 it can be observed that the load-displacement curve obtained from the history output of the simulation is as expected and this was obtained from the reference point. Various different parameters were tried for the viscosity coefficient and the initiation stress parameters to optimize the force-displacement plots

with respect to the experimental data. The plots were observed to be a close match for the viscosity coefficient of 0.00002 and a normal only coefficient of 70 MPa. The plots are very close to each other when the shear-1 and shear-2 only components are 110 MPa and 140 MPa. The initial peak that is seen in the experimental data is because of the Teflon insert that has a finite thickness to it and hence leading to blunt initial crack propagation. The normal fracture energy was set to be 0.8 KJ/m² and the first shear fracture energy was set to be 0.9 KJ/ m².



(a) Solution convergence Studies



(b) Final values of normal traction

Figure 8.25: Force-displacement plot for crack propagation on DCB specimen for different simulation parameters

8.8.2 Compliance and Strain energy release rate calculations

Tables 6 and 7 show the compliance data from the experimental and simulation data. It can be observed that the compliance data is in the same range since the rates for crack propagation are almost the same for both the cases and this can be seen from the values of crack length a in both the cases.

Figures 26 and 27 show the validation data for force versus crack length and compliance versus crack length for both the experimental and simulation results. The data is observed to be in close agreement and there is a slight variation in the force data for the initial crack propagation because of the Teflon insert in the laminate which acts as the initial crack length for the DCB. The data is in close agreement in the other locations.

Table 8.6: Experimental Compliance data

a(mm)	log(a)	P(N)	δ (mm)	P/δ (N/mm)	Compliance (δ/P)
25	1.40	193.38	2.16	89.60	0.01
28	1.45	140.23	2.48	56.52	0.02
35	1.54	120.71	3.42	35.29	0.03
40	1.60	102.73	4.23	24.26	0.04
49	1.69	95.98	6.23	15.40	0.06

Table 8.7: Simulation Compliance data

a(mm)	log(a)	P(N)	δ (mm)	P/δ (N/mm)	Compliance (δ/P)
25	1.40	150.57	2.16	69.78	0.01
29.5	1.47	139.92	2.48	56.45	0.02
33.5	1.52	122.47	3.42	35.80	0.03
39.5	1.60	109.40	4.24	25.82	0.04
47.5	1.68	91.81	6.24	14.73	0.06

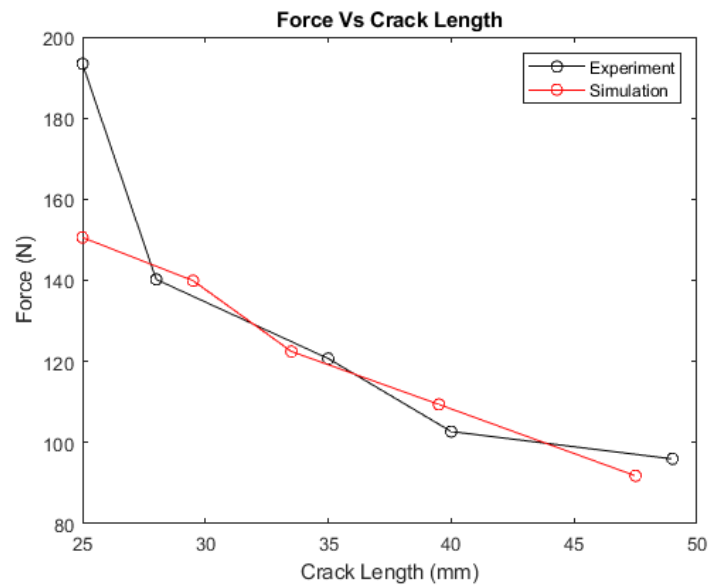


Figure 8.26: Force-crack length validation plot for DCB specimen

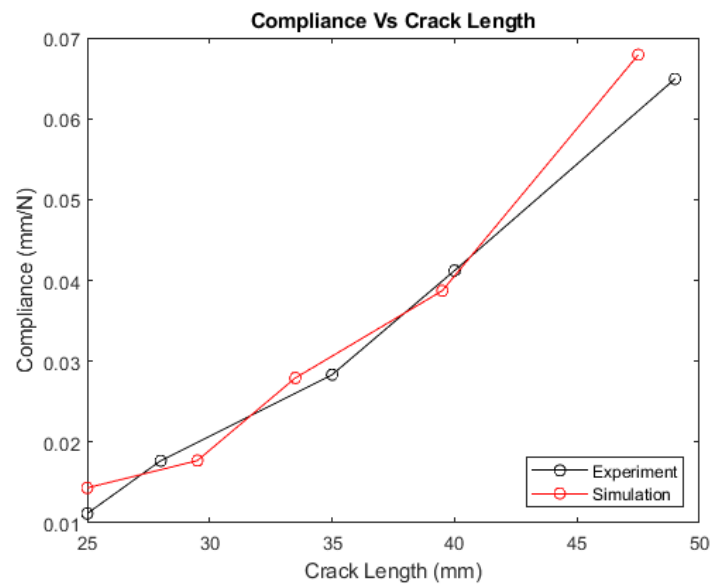


Figure 8.27: Compliance-crack length validation plot for DCB specimen

Tables 8 and 9 show the strain energy release rate G_{IC} calculations from different methods for both the experimental and simulation data. The calculations are done similar to the method explained in section 8.1.4. Table 10 shows the percentage difference between the experimental and simulation results and the values are observed to be very close to each other.

Table 8.8: Experimental Strain energy release rate (KJ/m²) data

a(mm)	G_IC (SBT)	G_IC (MBT)	G_IC (CC)
25	0.98	0.66	0.73
28	0.73	0.51	0.55
35	0.69	0.51	0.52
40	0.64	0.49	0.48
49	0.72	0.57	0.54

Table 8.9: Simulation Strain energy release rate (KJ/m²) data

a(mm)	G_IC (SBT)	G_IC (MBT)	G_IC (CC)
25	0.78	0.64	0.65
29.5	0.69	0.60	0.59
33.5	0.74	0.65	0.63
39.5	0.69	0.62	0.59
47.5	0.71	0.65	0.60

Table 8.10: Percentage error of strain energy release rate using different methods

a (experimental) (mm)	a (simulation) (mm)	SBT (%)	MBT (%)	CC (%)
25	25	21.56	2.39	10.97
28	29.5	4.67	17.34	8.20
35	33.5	6.83	25.61	21.26
40	39.5	8.74	26.12	23.42
49	47.5	0.52	12.46	12.90

8.9 Conclusions

All the DCB samples which were made with $[0]_{24}$ laminates were tested for mode I failure to determine the energy release rate of the laminate. The value of G_{IC} was determined by using 4 different reduction methods. It was observed that it takes less force to displace the crack more. This might be because of some issue in the sample geometry. The ASTM standard recommends a 63 mm insert to ensure that the initial crack length is more than 50 mm. This also ensures the validity of slender beam theory equations. Fiber bridging also occurs in the samples due to which there is an increase in the value of G_{IC} of the laminate. It was observed that the values obtained from Modified Beam Theory were the most conservative and hence the lowest among all the methods. Fiber bridging was observed when the crack propagated across the length of the samples. In 2 of the samples, the hinges broke while the samples were loaded in the MTS. This might be because the hinges were not bonded strongly enough to the laminate and the hinges hence sheared due to the load.

The analysis was carried out for a Double Cantilever Beam specimen by using a cohesive surface interaction between the top and the bottom surface of the laminate. The metal hinges were also modeled on which the load was applied. The value of compliance obtained from the experimental solution was compared to the results obtained from the output data plot of Abaqus to check the validity of the simulation. It was observed that the compliance was in close agreement in both cases. This variation in the results may be because, some parameters while modeling the Cohesive

elements may not be exactly as what is expected from the analytical solution and not all the experimental parameters would have been accounted for while simulating the test.

8.10 References

- [1] Carlsson, L. A., Adams, D. F., & Pipes, R. B. (2014). *Experimental characterization of advanced composite materials*. Boca Raton, FL: CRC Press.
- [2] Dr. Wenbin Yu. (2017) Multiscale Structural Mechanics. Wiley-Interscience. John Wiley & Sons, INC., Publication
- [3] ASTM Standard D5528 – 01
- [4] Peter Hong, Rajan Jain, Zane Smith, 1st November 2019, Friday, Lab 11- Mode-I; Interlaminar Fracture, Presentation, PPT. (2019).
- [5] Dr. Byron Pipes, 28th October 2019, Monday, Fracture Mechanics, Presentation, PPT. (2019).
- [6] Callister, W. D. (2006). *Materials science and engineering: An introduction*. 7th Ed. New York: John Wiley & Sons.

9. FUTURE WORK

The process of making and testing test samples can be a very time-consuming process as it requires a lot of labor for the same. It also requires the utilization of a lot of material to make all the specimens required for conducting the different tests. It might be possible that such amounts of material might not be available for conducting these tests. The way the specimens were modeled in these tests involves taking the input of material properties from the data sheets and hence, it can hence be generalized for any given composite material if the basic properties of the fiber and matrix are available.

1. Each of the properties studied for the characterization of this material is a very deep concept of its own and hence, more detail analysis of the stress and strain conditions at different regions of the specimen can be analyzed to study the distribution of the stresses and strains also near the tabs which have a higher stress concentration.
2. The load was applied as a displacement similar to the way the experiment was conducted for a time period of 1 minute. But, the specimens usually withstand different amounts of deformations up to different time intervals. Hence, it is very crucial to change these parameters while accounting for the failure of the specimen.
3. Different traction separation laws on DCB specimen and tune the cohesive interface properties to get a more precise method of crack propagation. The parameters that were used to model the DCB specimen can be validated by conducting the respective tests so that the results are more optimized.

9.1 Failure Analysis

4. The work done in this thesis covers creating digital twins which account for the similarity in stiffness of the modeled specimen and the experimental specimen. It can be further extended to the failure analysis of the tensile specimen once some basic parameters from the tensile test samples are obtained. This can include the energy-based evolution of the damage variables. A part of this study was started using the Hashin failure criterion. More research can be done on optimizing these parameters for the given material so that perfect

digital twins can be created for all the tests. The damage evolution and damage stabilization variables were approximated as follows:

Table 9.1: Hashin Damage parameters

Longitudinal Tensile Strength (MPa)	Longitudinal Compressive Strength (MPa)	Transverse Tensile Strength (MPa)	Transverse Compressive Strength (MPa)	Longitudinal Shear Strength (MPa)	Transverse Shear Strength (MPa)
1847.405	900	55.34	100	96.52	96.52

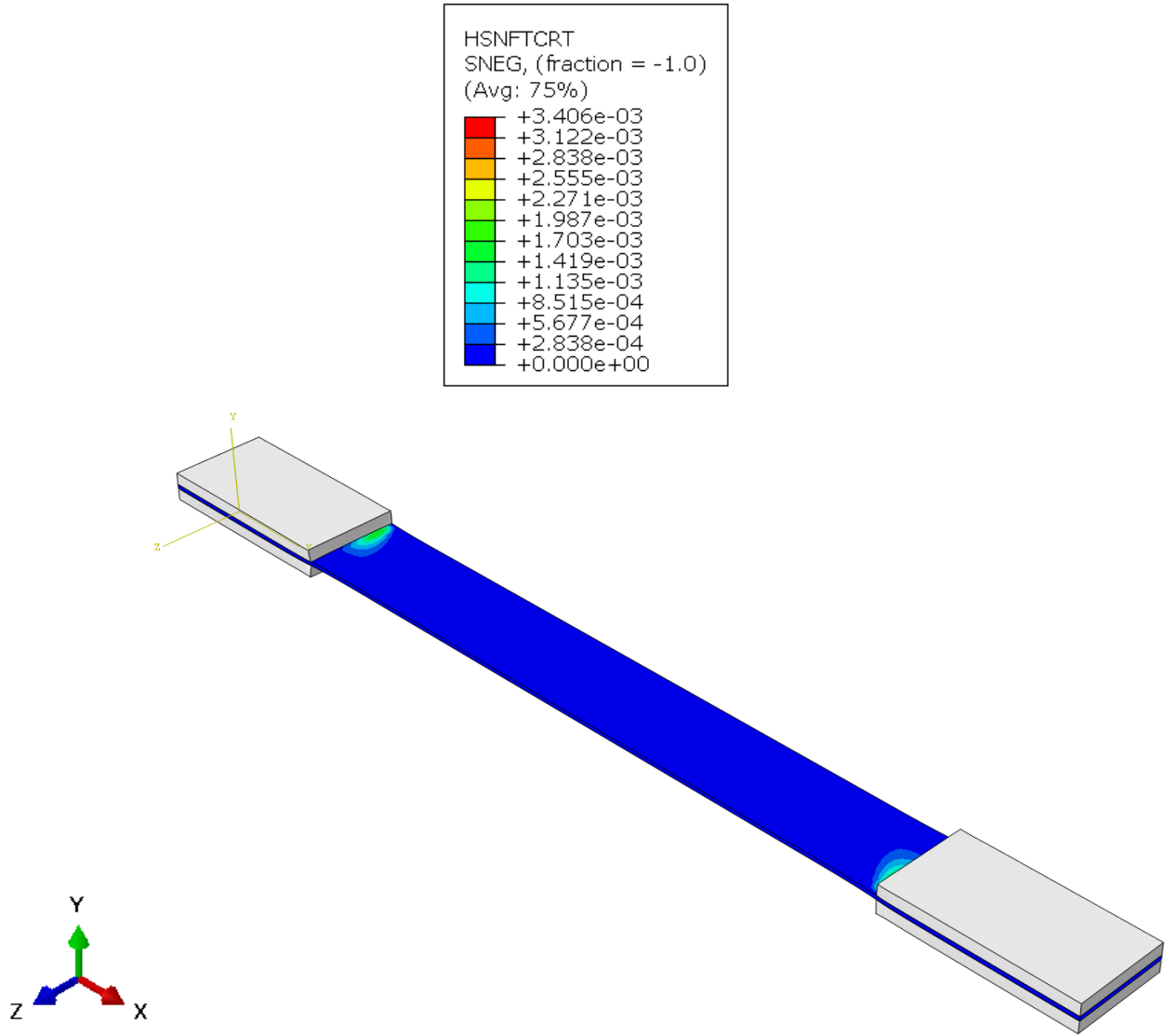
Table 9.2: Damage Evolution parameters

Longitudinal Tensile Fracture Energy	Longitudinal Compressive Fracture Energy	Transverse Tensile Fracture Energy	Transverse Compressive Fracture Energy
12	12	1	1

Table 9.3: Damage Stabilization parameters

Longitudinal Tensile viscosity coefficient	Longitudinal Compressive viscosity coefficient	Transverse Tensile viscosity coefficient	Transverse Compressive viscosity coefficient
0.002	0.002	0.002	0.002

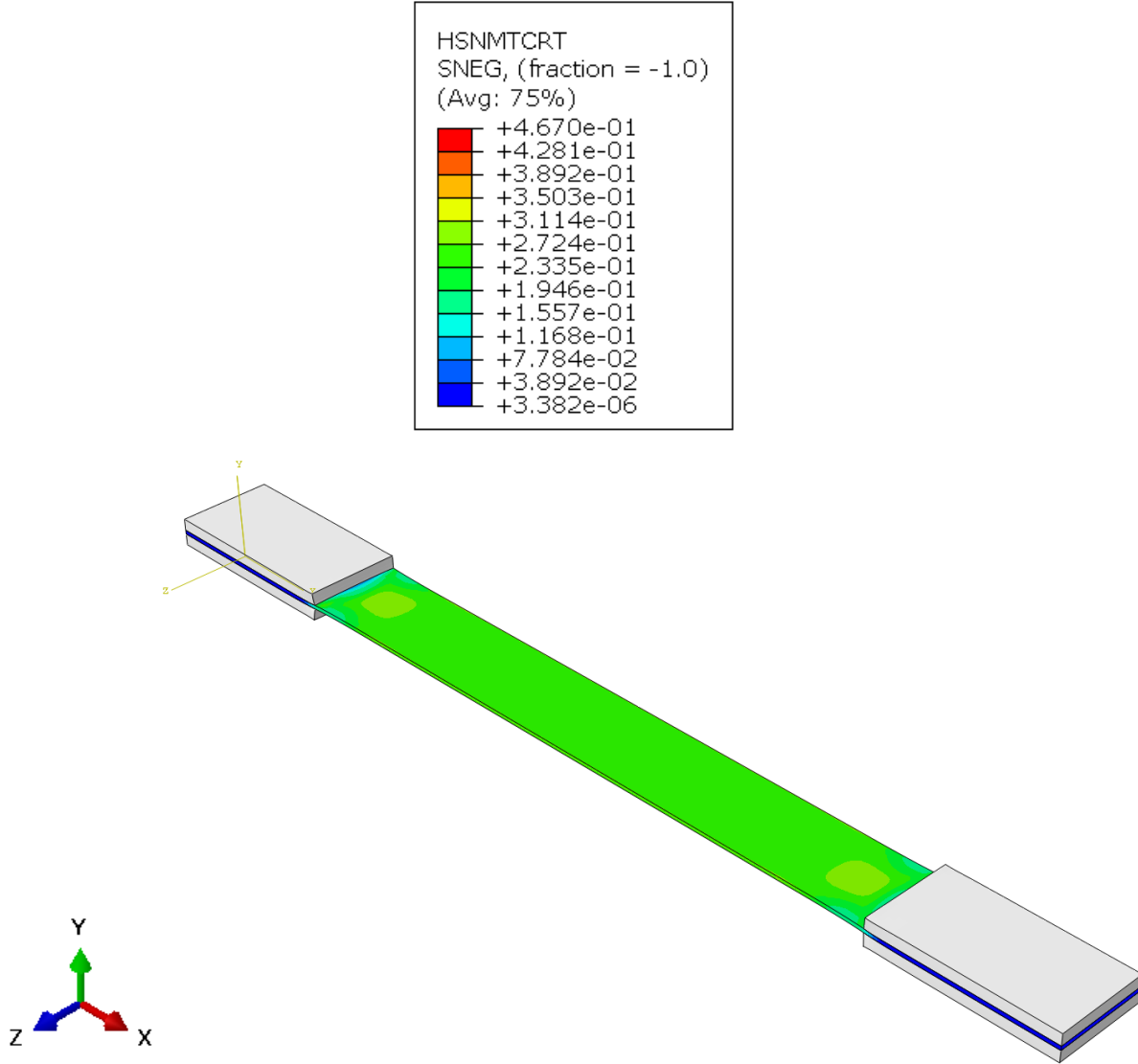
For the same, continuum shell elements were used to model the laminates and the tabs were modeled with 3D stress elements as the failure in them is not analyzed. The Damage and Hashin failure variables were selected to get as a field output. Figure 1 shows the various output variables obtained from the Hashin failure criteria. 0 denotes no failure and 1 denotes complete failure of the $[\pm 30]_{2s}$ laminate. The respective compression parameters show that the damage parameters are 0 on the laminate as it is in a state of tension only. There is no output for the tabs as they are modeled as solid elements.



(a) Hashin Fiber Tension Damage Initiation Criterion (HSNFTCRT)

Figure 9.1: Hashin failure criterion on $[\pm 30]_{2s}$ laminate

Figure 9.1 continued



(b) Hashin Matrix Tension Damage Initiation Criterion (HSNMTCRT)

The stress on this laminate was found to be as shown in Figure 2. The magnitude of stress is lower than that obtained from elastic analysis (section 5.4.1.3). Hence, the potential future work can be to optimize the parameters further to get the values close to the experimental data.

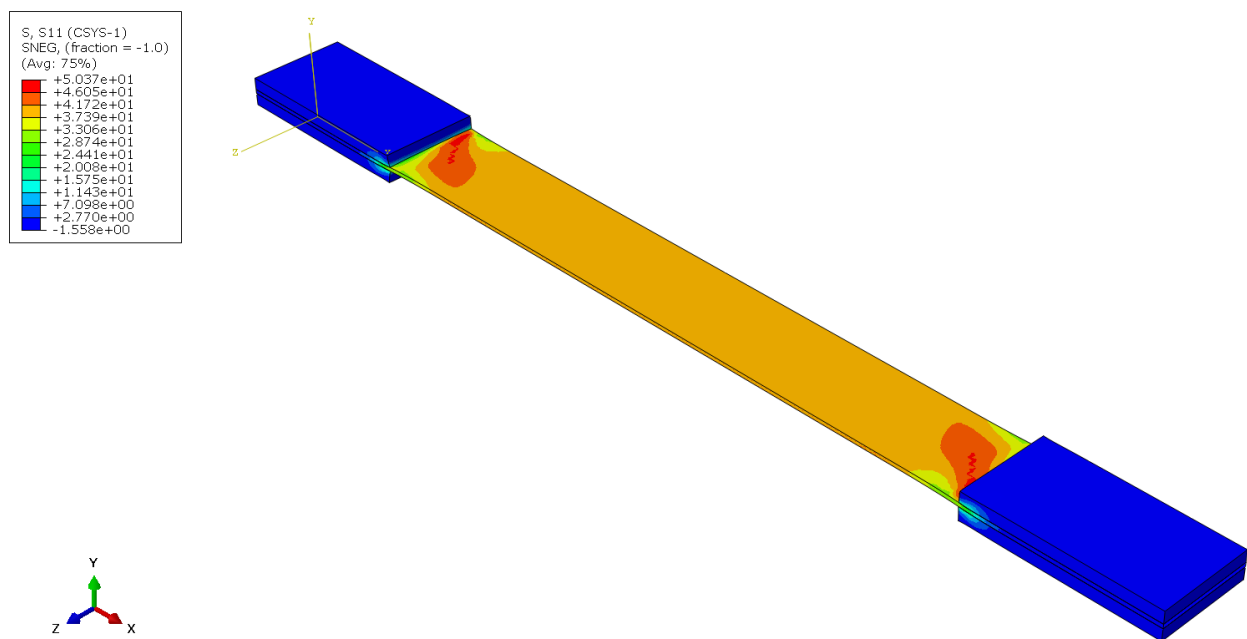


Figure 9.2: Axial stress on $[\pm 30]_{2s}$ laminate